USGS
science for a changing world

Initial Report of the IMAGES VIII/PAGE 127 Gas Hydrate and Paleoclimate Cruise on the RV *Marion Dufresne* in the Gulf of Mexico, 2–18 July 2002

Edited by William J. Winters[1], Thomas D. Lorenson[2], and Charles K. Paull[3]

Open-File Report 2004–1358

U.S. Department of the Interior
U.S. Geological Survey

[1] U.S. Geological Survey, Woods Hole, MA
[2] U.S. Geological Survey, Menlo Park, CA
[3] Monterey Bay Aquarium Research Institute, Moss Landing, CA

Front: Cover posted on board the RV *Marion Dufresne* (shown on a Territory of the French Southern and Antarctic Lands stamp in the upper right corner). The complete ship trackline for the cruise is portrayed on the cachet, including the USGS gas-hydrate leg from Cancun to Florida.

Chapter 1

IMAGES VIII/PAGE 127 Gas Hydrate and Paleoclimate Cruise on the RV *Marion Dufresne* in the Gulf of Mexico, 2–18 July 2002: Introduction

William J. Winters[1], Thomas D. Lorenson[2], and Charles K. Paull[3]

IMAGES VIII/PAGE 127 Gas hydrate and paleoclimate cruise on the RV Marion Dufresne *in the Gulf of Mexico, 2–18 July 2002: Introduction; chapter 1* in *Winters, W.J., Lorenson, T.D., and Paull, C.K., eds., 2007, Initial report of the IMAGES VIII/PAGE 127 gas hydrate and paleoclimate cruise on the RV* Marion Dufresne *in the Gulf of Mexico, 2–18 July 2002: U.S. Geological Survey Open-File Report 2004–1358.*

Abstract

The northern Gulf of Mexico contains many documented gas hydrate deposits near the sea floor. Although gas hydrate often is present in shallow subbottom sediment, the extent of hydrate occurrence deeper than 10 meters below sea floor in basins away from vents and other surface expressions is unknown. We obtained giant piston cores, box cores, and gravity cores and performed heat-flow analyses to study these shallow gas hydrate deposits aboard the RV *Marion Dufresne* in July 2002. This report presents measurements and interpretations from that cruise. Our results confirm the presence of gas hydrate in vent-related sediments near the sea bed. The presence of gas hydrate near the vents is governed by the complex interaction of regional and local factors, including heat flow, fluid flow, faults, pore-water salinity, gas concentrations, and sediment properties. However, conditions appropriate for extensive gas hydrate formation were not found away from the vents.

Introduction

Gas hydrate (fig. 1) is an ice-like crystalline solid containing high concentrations of methane in situ (Sloan, 1998). The amount of gas hydrate in the natural environment is thought to be enormous where conditions of high pressure, low temperature, and sufficient amounts of gas exist (Ginsburg and others, 1995; Booth and others, 1996; Kvenvolden and Lorenson, 2001a, b) (fig. 2). Gas hydrate may represent a potential source of energy (Collett, 2001), exert a control on sea-floor stability (Paull and others, 2000), represent a hazard to hydrocarbon exploration and production (Collett and others, 2000), and influence global climate change (Kennett and others, 2003). At present, however, relatively little is known about its global distribution in shallow marine sediment or even exactly how it forms.

Numerous occurrences of gas hydrate are known near (<7-meter (m) subbottom) the sea bed in the northern Gulf of Mexico (Sassen, 2001; Roberts and others, 2002). The area is characterized by high sedimentation rates, complex stratigraphy, and strata that are disrupted by salt tectonism and

Figure 1. Samples of gas hydrate recovered from Calypso giant piston core MD02-2569.

[1]U.S. Geological Survey, 384 Woods Hole Road, Woods Hole, MA 02543 USA.

[2]U.S. Geological Survey, 345 Middlefield Road, MS-999, Menlo Park, CA 94025 USA.

[3]Monterey Bay Aquarium Research Institute, 7700 Sandholdt Road, Moss Landing, CA 95039 USA.

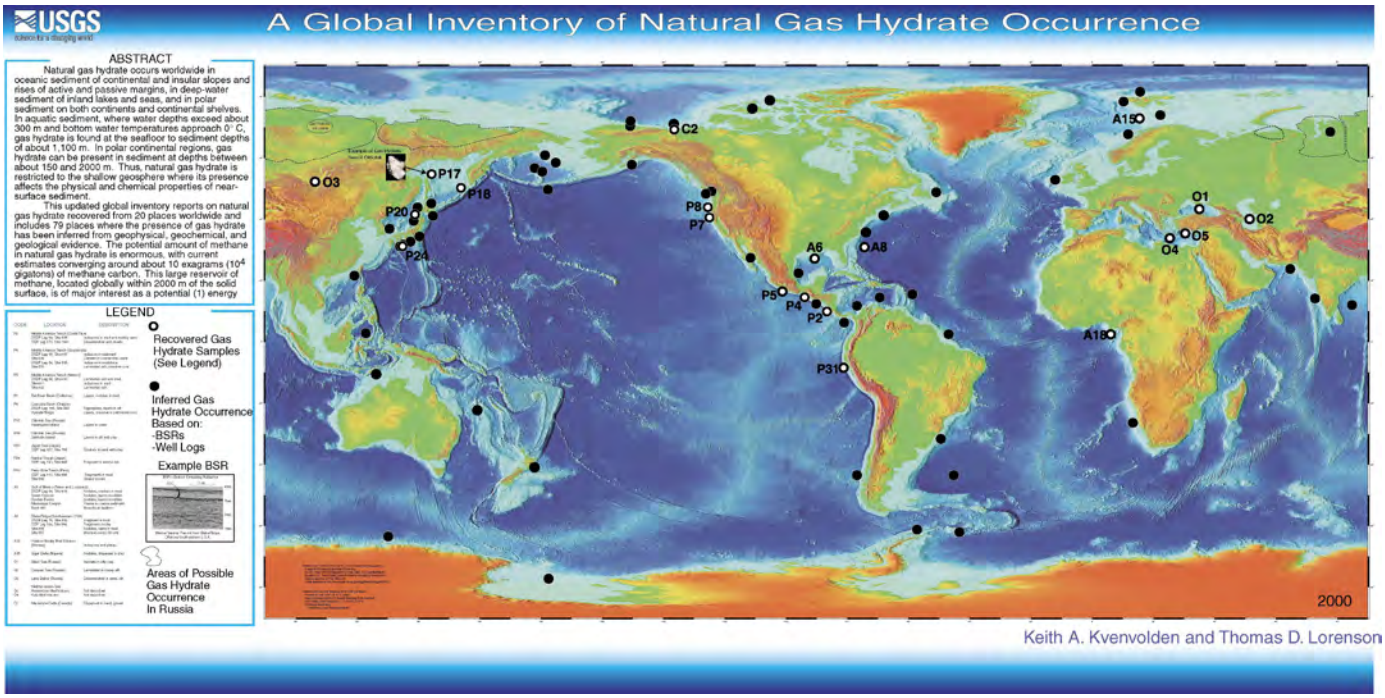

Figure 2. Global inventory map of gas hydrate occurrences (Kvenvolden and Lorenson, 2001b) (*http://walrus.wr.usgs.gov/globalhydrate/index.html*).

common sea-floor failures (Cooper and Hart, 2002). Natural oil and gas seeps also are abundant, usually associated with fault conduits. The resulting numerous hydrocarbon vents are often capped by gas hydrate when the seeps are within the hydrate stability zone. Whereas gas hydrate is relatively common near the sea floor as indicated by extensive sample recovery of hydrate, the lack of diagnostic geophysical indicators on seismic records leaves the existence of deeper gas hydrate unresolved. Thus, we do not know if significant gas hydrate accumulations are present in sediments away from structural conduits inferred to underlie sea-floor mounds. To address this and other questions, we collected samples with the International Marine Past Global Changes Study (IMAGES) and Paleoceanography of the Atlantic and Geochemistry (PAGE) programs aboard the research vessel (RV) *Marion Dufresne* (fig. 3) in July 2002, within four continental-slope regions of the northern Gulf of Mexico (Tunica Mound, Orca and Pigmy Basins, Bush Hill, and the Mississippi Canyon region).

Figure 3. RV *Marion Dufresne* is 120.5 meters in overall length and is 20.6 meters in beam amidships. It has a draft of 6.95 meters and displaces 10,380 tonnes. Coring operations are conducted using the starboard stern A frame.

Scientific Objectives and Conclusions

We recovered 17 giant piston cores, up to 38 m long, two giant box cores up to 10 m long, and four gravity cores up to 9 m long. Gas hydrate-related coring sites were selected along seismic-reflection transects in widely different geologic environments in water depths ranging from about 560 to 1,320 m (table 1). The transects were designed to extend from known sea-floor gas hydrate occurrences across the adjacent basin to thick sediments away from any gas-venting sites. We recovered gas hydrate in four cores from previously known venting areas in subbottom depths of about 3 to 9 m, but none was found in adjacent basins. We made 17 successful passive heat-flow measurements to subbottom depths of 17 m in conjunction with hundreds of pore-water and gas-chemistry measurements to better understand the thermal and geochemical regimes in the sediments and their relations to gas hydrate formation and occurrence.

Results of this work confirm the presence of gas hydrate in vent-related near-sea-bed sediments. However, if results from our limited coring effort can be extrapolated to other Gulf of Mexico sites, it appears that gas hydrate is not pervasive between hydrate outcrops.

Table 1. Core information, including location, water depth, recovered core length, and core type.

[ID, identification; deg, degrees; m, meters; PC, piston core; C2 (box), square box core; GHF, gravity core with heat-flow temperature sensors attached; Grav, gravity core without thermal sensors; **, denotes successful determination of geothermal gradient]

Core ID	Latitude (deg)	Longitude (deg)	Site name	Water depth (m)	Core length (m)	PC	C2 (box)	GHF	Grav	Comments
MD02-2535	27.6198	-92.2410	Tunica Mound	605	37.84	*				
MD02-2536GHF-1	27.6198	-92.2410	Tunica Mound	608	8.88			**		
MD02-2536GHF-2	27.6253	-92.2460	Tunica Mound	564	8.88			**		
MD02-2536GHF-3	27.6270	-92.2375	Tunica Mound	585	8.88			**		
MD02-2537	27.6160	-92.2487	Tunica Mound	600	33.58	*				
MD02-2538G	27.6167	-92.2472	Tunica Mound	599	7.76				*	
MD02-2539	27.6397	-92.1922	Tunica Mound	622	31.1	*				
MD02-2540GHF-1	27.6403	-92.1920	Tunica Mound	617	5.65			**		
MD02-2540GHF-2	27.6402	-92.1952	Tunica Mound	620	-			*		
MD02-2541	27.6325	-92.2123	Tunica Mound	615	35.34	*				
MD02-2542GHF	27.6322	-92.2120	Tunica Mound	617	7.7			**		
MD02-2543G	27.6123	-92.2555	Tunica Mound	579	0.15				*	
MD02-2544G	27.6130	-92.2535	Tunica Mound	584	0.1				*	
MD02-2545G	27.6140	-92.2517	Tunica Mound	588	9.27				*	
MD02-2546	27.6157	-92.2470	Tunica Mound	595	31.21	*				
MD02-2547GHF	27.6165	-92.2483	Tunica Mound	607	5.73			**		
MD02-2548	27.6375	-92.1995	Tunica Mound	610	32.92	*				
MD02-2550C2	26.9462	-91.3457	Orca Basin	2,249	9.09		*			
MD02-2553C2	27.1835	-91.4167	Pigmy Basin	2,259	10.03		*			
MD02-2554	27.7833	-91.4990	Bush Hill Basin	602	31.05	*				
MD02-2555	27.7832	-91.4892	Bush Hill Basin	636	35.68	*				
MD02-2556	27.7830	-91.4775	Bush Hill Basin	654	34.25	*				
MD02-2557GHF-1	27.7830	-91.4987	Bush Hill Basin	613	7.59			**		
MD02-2557GHF-2	27.7830	-91.4890	Bush Hill Basin	639	-			**		
MD02-2557GHF-3	27.7828	-91.4805	Bush Hill Basin	659	-			**		
MD02-2559	28.2225	-89.0882	Kane Spur	1,132	33.39	*				
MD02-2560	28.2433	-89.1550	Kane Spur	1,029	28.24	*				
MD02-2561	28.2052	-89.0202	Kane Spur	1,268	28.8	*				

Table 1. Core information, including location, water depth, recovered core length, and core type. — Continued

[ID, identification; deg, degrees; m, meters; PC, piston core; C2 (box), square box core; GHF, gravity core with heat-flow temperature sensors attached; Grav, gravity core without thermal sensors; **, denotes successful determination of geothermal gradient]

Core ID	Latitude (deg)	Longitude (deg)	Site name	Water depth (m)	Core length (m)	PC	C2 (box)	GHF	Grav	Comments
MD02-2562	28.0798	-89.1402	Kane Spur	1,051	26.09	*				
MD02-2563C2	28.1233	-89.1363	MC853 Diapir	1,070	3.86		*			recovered hydrate (gas bubbles)
MD02-2564GHF-1	28.2433	-89.1545	Kane Spur	1,027	7.63			**		
MD02-2564GHF-2	28.2223	-89.0883	Kane Spur	1,261	-			**		
MD02-2564GHF-3	28.2052	-89.0200	Kane Spur	1,269	-			**		
MD02-2564GHF-4	28.2070	-89.0200	Kane Spur	1,269	-			**		
MD02-2565	28.1235	-89.1395	MC853 Diapir	1,068	22.5	*				recovered hydrate
MD02-2566	28.1192	-89.1032	Kane Spur	1,186	26.05	*				
MD02-2567	28.1002	-89.0198	Kane Spur	1,318	26.65	*				
MD02-2568GHF-1	28.0790	-89.1400	MC853 Diapir	1,049	6.96			**		
MD02-2568GHF-2	28.0810	-89.1370	MC853 Diapir	1,057	-			**		
MD02-2568GHF-3	28.1193	-89.1030	MC853 Diapir	1,190	-			**		
MD02-2568GHF-4	28.1233	-89.1395	MC853 Diapir	1,068	-			*		
MD02-2568GHF-5	28.1235	-89.1362	MC853 Diapir	1,049	-			*		
MD02-2569	28.1522	-89.4797	Mississippi Canyon	1,032	10.35	*				recovered hydrate
MD02-2570	28.0710	-89.6898	West Mississippi	631	28.35	*				
MD02-2571C2	28.0667	-89.7192	West Mississippi	664	10.38		*			
MD02-2572GHF	28.0710	-89.6897	West Mississippi	628	4.9			**		
MD02-2573GHF	28.1520	-89.4798	Mississippi Canyon	1,027	4.2			*		recovered hydrate
MD02-2574	28.6267	-88.2248	East Mississippi	1,963	32.28	*				

Note: Cores obtained during the cruise that are not listed in this table and cores MD02-2548 in Tunica Mound, MD02-2550C2 in Orca Basin, and MD02-2574 in East Mississippi region are IMAGES/PAGE cores, not dedicated USGS cores.

Report Format and Chapter Descriptions

Part 1

This report contains three main sections. The first part (Chapters 2 through 9) describes the interpretation of measurements integrated across all of our sample sites in the northern Gulf of Mexico.

Chapter 2, Geologic Setting: Results of prior USGS seismic-reflection cruises conducted in the northern Gulf of Mexico that provided the stratigraphic framework for the present coring program. Site characteristics of Tunica Mound, Bush Hill, the Mississippi Canyon region, and Pigmy and Orca Basins are discussed.

Chapter 3, Coring and Gas Hydrate Operations: An illustrated record of the procedures used to acquire, subsample, and process sediment samples from the various sampling devices used during the cruise. Special emphasis is placed on safety-related aspects dealing with dissociating gas hydrates.

Chapter 4, Physical Properties: Results of shear strength, electrical resistivity, texture, carbon content, and index property tests performed at sea and in a shore-based laboratory.

Chapter 5, Sedimentology: Sedimentologic descriptions and discussion of longitudinally split cores obtained during the cruise. In addition, techniques used to obtain Multi-Sensor Core Logs (MSCL), core photographs, and spectrophotometric logs are presented.

Chapter 6, Heat Flow: Results of instrumented gravity core penetrations of the sea floor. Geothermal gradients and heat-flow parameters at 17 locations distributed throughout the three main study areas.

Chapter 7, Thermal Conductivity: Methods and results of thermal conductivity (TC) tests performed on whole-round sections from 23 cores.

Chapter 8, Pore-Water Geochemistry: Interpretations of chloride, sulfate, and methane concentration in relation to sub-bottom depth of 483 water samples squeezed from sediment of Tunica Mound, Bush Hill, and the Mississippi Canyon region.

Chapter 9, Sediment Gas Geochemistry: Results of hydrocarbon and carbon dioxide gas analyses of sediment samples taken from four distinct regions in order to constrain concentrations and sources of gas that may form gas hydrate. Gas from dissociated hydrate, gas dissolved in sediment pore water, and gas from voids in the core were analyzed.

Part 2

The second part of this report (Chapters 10 through 14) is related to analyses that were performed on just one or a limited number of cores.

Chapter 10, Microbiology: An analysis of the archaeal small-subunit ribosomal RNA gene diversity from core MD02-2571C2, located near a gas chimney at a site west of the Mississippi Canyon.

Chapter 11, Biostratigraphy: A preliminary age-depth model for core MD02-2570 (west flank of the Mississippi Canyon), based on datums defined by the regional biostratigraphic zonation of planktonic foraminifers.

Chapter 12, Scanning Electron Microscopy (SEM): SEM analyses of natural gas hydrate nodules from core MD02-2569, from a site west of the Mississippi Canyon. Similarities in grain and pore structure were compared with images of laboratory-synthesized gas hydrates.

Chapter 13, Pollution Transport: Results of textural analyses of samples from Pigmy Basin and from low-oxygen, hyper-saline Orca Basin. Trace metal compositions of basin sediments were determined using a variable-pressure scanning electron microscope (SEM) equipped with energy-dispersive spectroscopy (EDS).

Chapter 14, Carbonate Mineralogy and Isotopes: Analyses of carbonates sampled from various subbottom depths at Tunica Mound and the Mississippi Canyon.

Part 3

The third part of this report consists of appendixes that typically, but not exclusively, present information and data produced at sea. Most of the at-sea data sets required the use of proprietary software that was not available for post-cruise editing and, thus, are in their original, unedited formats.

Appendix A, Cruise Logistics: A table of core information, core and sediment recovery statistics, photographs, and contact information for cruise participants.

Appendix B, Maps: Regional and local bathymetric maps showing core locations.

Appendix C, Combined Station Results: Compiled, measured properties, and information for individual core sites.

Appendix D, Seismic profiles/Track lines: Regional and local core-specific seismic profiles and track lines.

Appendix E, Core Summaries: Information about individual core recovery and sediment observations.

Appendix F, Lithologic Descriptions: Unedited lithologic descriptions produced at sea of longitudinally split cores.

Appendix G, Core Photographs: At-sea photographs of freshly exposed longitudinally split cores (combined from individual digital files representing 0.5-m long core sections).

Appendix H, Multi-Sensor Core Logger (MSCL) Results: Individual core at-sea records of unedited acoustic velocity and amplitude, density, magnetic susceptibility, and related properties.

Appendix I, Spectrophotometry Results: Unedited, at-sea spectrophotometry records of individual cores.

Appendix J, Photographs: Digital photographs of shipboard activities.

Appendix K, U.S. Geological Survey (USGS) Video Press Release: Produced for the USGS in Tampa Bay.

Appendix L, Gas Hydrate Stability Models: Gas hydrate stability models related to gas type and geothermal conditions.

Appendix M, Metadata: Cruise logistics and information.

Appendix N, Abbreviations and Symbols: Selected abbreviations and symbols used in this report.

There is some redundancy in information between chapters so that readers can concentrate on those chapters that are of pri-

mary interest. Thus, readers may not need to read the chapters in numerical order.

USGS Cruise Participants

Participants of the USGS-supported part of the cruise: USGS, Menlo Park; USGS, Woods Hole; USGS, St. Petersburg; Monterey Bay Aquarium Research Institute (MBARI); University of Victoria, British Columbia, Canada; College of William and Mary; Moscow State University; University of Tokyo; and Texas A&M University.

Acknowledgments and Notes

We thank Captain Jean-Michel Nicolas, Yvon Balut (coring supervisor), and the crew of the RV *Marion Dufresne* for their assistance in performing shipboard activities. Cruise logistical support was provided by the French Polar Institute [Institut Polaire Francais – Paul-Emile Victor (IPEV)].

Considerable at-sea help was provided by an international group of about 40 scientists working under the IMAGES (International Marine Past Global Changes Study) and PAGE (Paleoceanography of the Atlantic and Geochemistry) programs. The IMAGES program is an international effort to understand the mechanisms and consequences of climatic changes using the oceanic sedimentary record.

Financial support of USGS-related activities was provided by the USGS Coastal and Marine Geology Program, the USGS Energy Program, and the U.S. Department of Energy's Gas Hydrate Program.

The U.S. Minerals Management Service provided information used to determine core locations and avoid existing sea-floor infrastructure (pipelines, etc.).

The Integrated Ocean Drilling Program (IODP) provided facilities to store and archive recovered cores.

Metadata from the cruise, including navigation, personnel, core locations, are available on the Internet at the USGS Web site: *http://walrus.wr.usgs.gov/infobank/d/d102gm/html/d-1-02-gm.meta.html* .

References Cited

Booth, J.S., Rowe, M.M., and Fischer, K.M., 1996, Offshore gas hydrate sample database with an overview and preliminary analysis: U.S. Geological Survey Open-File Report 96–272, 23 p.

Collett, T.S., 2001, Natural-gas hydrates; resource of the twenty-first century? American Association of Petroleum Geologists Memoir, v. 74, p. 85–108.

Collett, T.S., and Dallimore, S.R., 2000, Identification and remediation of gas hydrate induced drilling and production hazards: Annual Meeting Expanded Abstracts—American Association of Petroleum Geologists, v. 2000, p. 30.

Cooper, A.K., and Hart, P.E., 2002, High-resolution seismic-reflection investigation of the northern Gulf of Mexico gas-hydrate-stability zone: Marine and Petroleum Geology, v. 19, no. 10, p. 1275–1293.

Ginsburg, G.D., and Soloviev, V.A., 1995, Submarine gas hydrate estimation; theoretical and empirical approaches: Proceedings—Offshore Technology Conference, v. 27, p. 513–518.

Kennett, J.P., Cannariato, K.G., Hendy, I.L., and Behl, R.J., 2003, Methane hydrates in Quaternary climate change—The Clathrate Gun Hypothesis: Washington, DC, American Geophysical Union, 216 p.

Kvenvolden, K.A., and Lorenson, T.D., 2001a, The global occurrence of natural gas hydrate, *in* Paull, C.K., and Dillon, W.P., eds., Natural gas hydrates occurrence, distribution, and detection, Geophysical Monograph 124: Washington, DC, American Geophysical Union, p. 3–18.

Kvenvolden, K.A., and Lorenson, T.D., 2001b, Global occurrences of gas hydrate: The Proceedings of the International Offshore and Polar Engineering Conference, v. 11, p. 462–467.

Paull, C.K., Ussler, W., III, and Dillon, W.P., 2000, Potential role of gas hydrate decomposition in generating submarine slope failures, coastal systems and continental margins—Natural gas hydrate in oceanic and permafrost environments: Dordrecht, Kluwer Academic Publishers, p. 149–156.

Roberts, H.H., Coleman, J.M., Hunt, J.L., Shedd, W.W., Sassen, R., and Milkov, A., 2002, Gas hydrate deposits in a complex geologic setting, northern Gulf of Mexico slope: Transactions—Gulf Coast Association of Geological Societies, v. 52, p. 860.

Sassen, R., 2001, Gas hydrates in the Gulf of Mexico, A geochemical perspective, *in* McKay, M., Nides, J., and Vigil, D., eds., 2001, Proceedings—Twentieth Annual Gulf of Mexico Information Transfer Meeting, December 2000, New Orleans: U.S. Department of the Interior, Minerals Management Service, Outer Continental Shelf Region, MMS 2001-082, p. 92–105.

Sloan, E.D., Jr., 1998, Clathrate hydrates of natural gases: New York, Marcel Dekker, Inc., 705 p.

Chapter 2

Geologic Setting and Context of Cores Taken During the IMAGES VIII/PAGE 127 Cruise of the RV *Marion Dufresne* in the Northern Gulf of Mexico

Thomas D. Lorenson[1], Alan K. Cooper[1], Patrick E. Hart[1], and William J. Winters[2]

Geologic setting and context of cores taken during the IMAGES VIII/PAGE 127 cruise of the RV Marion Dufresne *in the northern Gulf of Mexico; chapter 2* in *Winters, W.J., Lorenson, T.D., and Paull, C.K., eds., 2007, Initial report of the IMAGES VIII/PAGE 127 gas hydrate and paleoclimate cruise on the RV* Marion Dufresne *in the Gulf of Mexico, 2–18 July 2002: U.S. Geological Survey Open-File Report 2004–1358.*

Introduction

The northern Gulf of Mexico contains some of the best documented occurrences of gas hydrates in the world; gas hydrate samples have been recovered in near-sea-floor sediments at more than 50 locations associated with active sea-floor hydrocarbon seeps (Sassen, Sweet, Milkov, and others, 2001b). However, years of geophysical prospecting for hydrocarbons in the northern Gulf of Mexico have failed to reveal the vertical distribution of gas hydrate. Prior sampling studies in the region have focused principally on basin-edge structures with little emphasis on the extensive areas of the basin floors.

Background

In July 2002, the International Marine Past Global Changes Study (IMAGES) VIII/Paleoceanography of the Atlantic and Geochemistry (PAGE) 127 program cruise collected cores for the purpose of characterizing the hydrate stability zone in collaboration with the U.S. Geological Survey (USGS). Seventeen giant Calypso piston cores of up to 38 meters (m) in length and two box cores were collected. About 500 m of piston core were recovered, and 14 m of box core sediment were obtained for USGS-related studies. Gravity cores with thermal sensors welded to the core barrel also were obtained mainly to acquire heat-flow information from 17 cores at 9 stations.

The core locations for the cruise primarily were selected using seismic records obtained from two previous Department of Energy (DOE)-funded USGS cruises over the upper- and middle-continental slope (Cooper and Hart, 2003) described in more detail below. Targeted sites were chosen to help answer three main questions: First, what is the lateral extent of gas hydrate between near-surface hydrate deposits and in adjacent basins? Second, are there significant gas hydrate deposits in reservoir sediments at depth in these basins? Third, does gas hydrate have any effect on known submarine slides near the Mississippi Canyon where deep offshore platforms might be at risk?

Coring sites were chosen from (1) transects on the upper slope going from structural highs into minibasin environments, (2) a transect down the middle of a submarine slide feature, (3) the summits of diapirs and sea-floor mounds, (4) above seismically imaged gas chimneys, and (5) locations where gas hydrate had been previously recovered, which typically corresponded to areas noted in number 3 above. In addition, 11 cores were taken by other research interests of the IMAGES group within and around this study area. In particular, four cores were taken in Pigmy and Orca Basins, part of the middle slope region, for environment and climate studies.

Geologic Framework of the Gulf of Mexico

The complex geologic setting of the northern Gulf of Mexico results largely from interactions of active salt tectonics, rapid sedimentation, and gravity slope-failures (Diegel and others, 1995; Prather and others, 1998; Winker and Booth, 2000). The resulting suite of minibasin and ridge features are being actively modified by both deep-seated (kilometers) and shallow (meters) faults that are being buried by mass-transport debris flows and hemipelagic-draped deposits. Sediment types and deposition rates are highly variable in the minibasins,

[1]U.S. Geological Survey, 345 Middlefield Road, MS-999, Menlo Park, CA 94025 USA.

[2]U.S. Geological Survey, 384 Woods Hole Road, Woods Hole, MA 02543 USA.

depending on fluvial input to the adjacent shelf and slope, and on input from slope failures. A large Gulf of Mexico salt basin extends from the coastal salt dome province to the lower continental slope. A series of smaller interior salt basins extends onshore from south Texas to Alabama. The basins formed during Late Triassic rifting and during Middle Jurassic marine incursions were filled by sediment of the Louann and Werner Formations (Salvador, 1987). Structural style is profoundly influenced by the effects of salt movement caused by rapid deposition of overlying siliciclastic sediment.

The Gulf of Mexico continental shelf is characterized by numerous salt domes. In deeper waters, the continental slope is affected by large sheet-like salt thrusts that extend from the shelf edge across the continental slope to the Sigsbee Escarpment, near the shallow limit of the abyssal plain (Worrall and Snelson, 1989). In general, the basins are areas of salt withdrawal, and the intervening ridges are areas of salt piercement or structural folds (Rowan, 1995). Structural pathways for upward-migrating fluids and gases are most common along ridge flanks, around isolated diapiric highs, near edges of basins, and close to slope failures. Where faults extend to the sea floor, the sea-floor morphology is characterized by vents, sea-floor mounds, pockmarks, authigenic carbonate deposits, gas hydrate mounds, debris flows, chaotic reflection zones, and other features related to water and hydrocarbon seeps (Roberts and Carney, 1997; Roberts, 2001). By contrast, basin floors usually do not show evidence of active seepage. Instead, alternating sections of chaotic sediments commonly overlie laminated sediments. The chaotic sediments are the result of mass transport deposits shed from the basin sides (Berryhill and others, 1987).

The geology of the Gulf of Mexico slope is conducive to seepage and venting from deeply buried petroleum systems to the sea floor because hydrocarbon generation took place geologically recently within the deep sediment section beneath the salt thrust and on the upper abyssal plain (Sassen, Losh, and others, 2001; Sassen, Sweet, DeFreitas, and others, 2001; Sassen, Sweet, Milkov, and others, 2001a, b). Hydrocarbons migrated vertically through the salt withdrawal basins that pierce the salt sheets. Rapid sedimentation in Pleistocene depocenters (Galloway and others, 2000) activates migration conduits from depth to the sea floor. Fractures and faults associated with moving salt provide efficient migration conduits for fluid flow of gas, oil, and brines to the sea floor. Hydrocarbon seepage manifests itself on the sea floor as gas hydrate, oil-stained sediments, authigenic carbonate rock with carbon depleted in carbon-13 (^{13}C), and hydrocarbon-driven chemosynthetic communities (for example, MacDonald and others, 1989; Roberts and Aharon, 1994; Aharon and others, 1997; Roberts and Carney, 1997; Sassen, Joye, and others, 1999).

Gas Hydrate in the Gulf of Mexico

Gas hydrate deposits commonly are associated with salt domes or other salt-related tectonics. Geophysical evidence for gas hydrate in the region is equivocal. Where sea-floor exposure of gas hydrate deposits are known from submersible observations and coring near sea-floor vents and diapirs, high-resolution seismic data indicate localized strong sea-floor reflections and shallow subbottom acoustic wipeout zones (for example, Roberts and others, 1999; Sager and others, 1999). Over the same regions, deep-tow side-scan sonar images show zones of high backscatter that are associated with diagenetic-carbonate, chemosynthetic-community, and gas hydrate deposits (Cooper and others, 1999; Sager and others, 1999), and sea-floor reflectance values derived from 3–D seismic surveys commonly show varied amplitudes and reversed polarity indicative of near-sea-floor gas (Roberts and others, 1992; Roberts, 1996). While sea-floor exposures of gas hydrate have clear seismic signatures, buried gas hydrate deposits are not as easily imaged with seismics. Bottom simulating reflections (BSRs), the most commonly cited evidence for gas hydrate, are rare in the northern Gulf of Mexico and typically are documented on the continental rise of the western and central Gulf of Mexico (Shipley and others, 1979; Hedberg, 1980).

Milkov and Sassen (2001) provided a conceptual model to explain the distribution of gas hydrate in the Gulf of Mexico. They proposed that thermogenic and biogenic gases are focused along basin-edge structures and that only disseminated bacterial gas is present in the centers of minibasins. Most prior gas hydrate studies in the northern Gulf of Mexico have focused on basin-edge structures containing active hydrocarbon venting. There have been few studies of the extensive areas of basin flanks and centers. The basin edges and structural highs are where the sea-floor gas hydrate mounds occur, and where gas hydrate has been sampled at subsurface depths of a few meters (Sassen, Sweet, Milkov, and others, 2001b), although disseminated bacterial gas hydrate was found in the Orca basin from 20 to 40 meters below sea floor (mbsf) (Pflaum and others, 1986). Toward the basin centers, there are few common geophysical markers (for example, BSRs) that indicate the presence of gas hydrate, although numerous discontinuous zones of enhanced reflectivity occur, possibly suggesting that gas might be trapped within or beneath the gas hydrate stability zone (Cooper and Hart, 2003). Geochemical studies in conjunction with this cruise and by others have demonstrated that salt inhibition is an important constraint on gas hydrate formation in the northern Gulf of Mexico (Paull and others, 2005; Ruppel and others, 2005). Models of gas hydrate stability using measured pore-water salt content and geothermal gradients (Appendix L) clearly show the shoaling of the gas hydrate stability zone caused in large part by the high salt concentration in pore water.

Pre-Cruise USGS Seismic Surveys

Extensive seismic surveys have been conducted by the oil and gas industry in the northern Gulf of Mexico, but most modern high-resolution seismic data are proprietary. Published seismic-reflection surveys across these regions by the USGS

and others (for example, Berryhill and others, 1987; EEZ-SCAN, 1987; Weimer and others, 1998) are either not in digital format or are of lower resolution than required for this study. High-resolution seismic-reflection surveys of areas around gas hydrate deposits (for example, Roberts and others, 1999; Sager and others, 1999) do not extend across basin flanks and centers.

In 1998 and 1999, the USGS conducted high-resolution seismic investigations of the Mississippi Canyon and Garden Banks-Green Canyon regions of the upper- and middle-continental slope to evaluate the distribution of gas hydrate, associated free gas, and their effects on slope stability (fig. 1). Track lines crossed several continental slope basins, including areas of known occurrences of gas hydrate, shallow water flows, chemosynthetic communities, and sea-floor slides. The region location names used above and throughout this report correspond to names of lease block areas defined by the Minerals Management Service (Minerals Management Service, 2002).

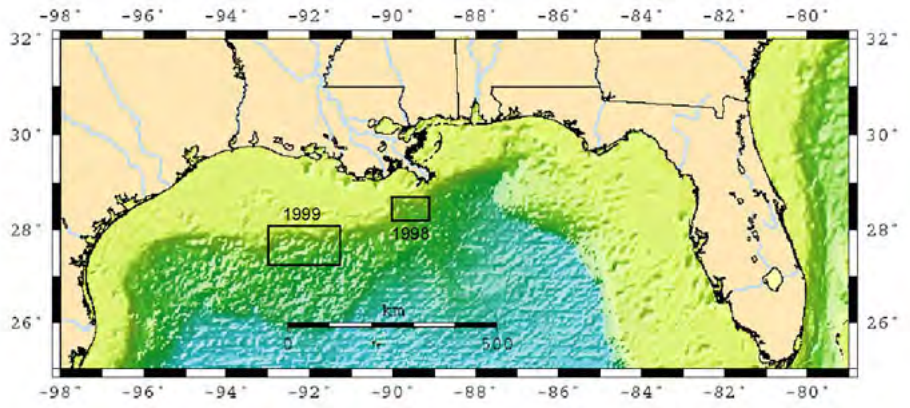

Figure 1. Previous (1998 and 1999) cruise areas studied by the USGS. Both areas were occupied during the 2002 cruise conducted aboard the RV *Marion Dufresne*.

In 1998, multichannel high-resolution seismic-reflection data were acquired in the Mississippi Canyon region by using either a 35-cubic-inch dual-chamber airgun (that is, GI gun) or a 15-cubic-inch water gun and a 250-m long 24-channel solid-core streamer. The data imaged to depths greater than 1,300-m subbottom with nearly 5-m resolution. Single-channel data were recorded by a Huntec deep-tow boomer towed at 100- to 200-m subsea-surface, and achieved penetration greater than 200-m subbottom resolution and 0.25-m vertical resolution. A detailed ocean bottom seismometer (OBS) survey also was conducted on the west side of the Mississippi Canyon in an area where sea-floor gas hydrate deposits are known (Neurauter and Bryant, 1990).

The 1999 USGS cruise in the Garden Banks and Green Canyon region acquired multichannel high-resolution seismic-reflection data with the same water gun and streamer as used in 1998, and Huntec deep-tow boomer data and deep-tow side-scan and chirp seismic data also were recorded. The chirp seismic data penetrated to about 40-m subbottom with a resolution of about 0.1 m. Images and digital data for multichannel seismic-reflection data from both cruises are accessible on the Internet (Hart and others, 2002).

Both the 1998 and 1999 studies found widespread occurrence within the upper 500 to 700 m of the sedimentary sections of chaotic units with disrupted reflections that have high reflectivity zones that can be diffuse in places. Cooper and Hart (2003) refer to these as high reflectivity zones (HRZs). The report gives examples of the high-resolution seismic data across HRZs and discusses possible causes of these zones with regard to likely concentrations of free gas that may be a source for gas hydrate deposits in the gas hydrate stability zone (GHSZ). The report also describes evidence for fault and stratigraphic conduits, and evidence for the coincidence of HRZs with deep-seated faults, diapiric structures, shallow water flows, and décollements beneath sea-floor slides in the study areas. These may be important features in explaining fluid and gas flow through the GHSZ and, hence, the distribution of possible gas hydrates.

RV *Marion Dufresne* Piston Coring

The research vessel (RV) *Marion Dufresne* (fig. 2) has an unobstructed starboard main deck that allows the deployment and recovery of Institut Polaire Français' (IPEV) "Calypso" corer. The piston-coring system, driven by a 6-tonne weight stand, has obtained cores as long as 64.5 m. In the Gulf of Mexico, 17 giant Calypso piston cores as long as 38 m were collected at Tunica Mound, at Bush Hill, and near or within the Mississippi Canyon (fig. 3). Four gravity cores, up to 9 m long, were taken in areas suspected of being composed of carbonate or gas hydrate-hardened sediment. Box cores,

Figure 2. The RV *Marion Dufresne*.

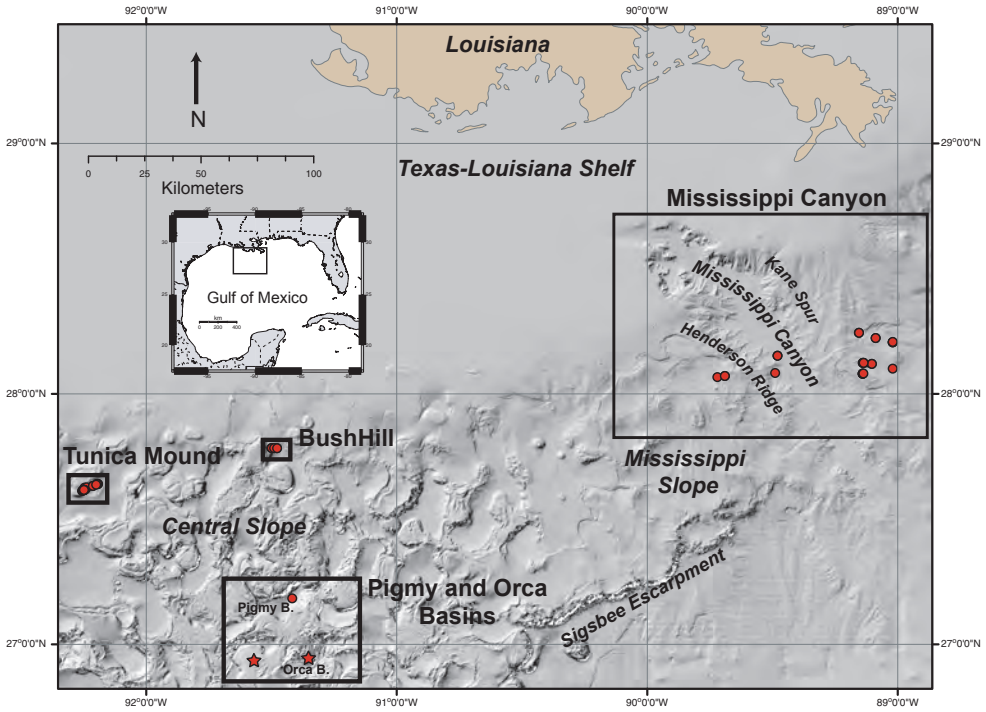

Figure 3. Coring sites. Boxes denote areas of interest and more detailed maps. Circular symbols represent dedicated USGS cores. Star symbols represent cores taken primarily for other studies.

up to 10 m long, were also recovered. These box cores were useful in obtaining the best surface record possible for climate and pollution history studies that were conducted by other researchers on board. Two box cores were recovered for gas hydrate studies; each targeted potential surficial gas hydrate. An additional 17 gravity cores at 9 stations were made to provide heat-flow and thermal gradient measurements at or near selected piston core sites. Metadata from the cruise, including navigation, personnel, and core locations, are available in Appendix M and on the Internet at the USGS Web site: *http://walrus.wr.usgs.gov/infobank/d/d102gm/html/d-1-02-gm.meta.html* .

Site Characterization: Mississippi Canyon Region

The east and west sides of the Mississippi Canyon (fig. 4) are characterized by extreme sedimentation rates up to 15 to 20 meters per thousand years (m/k.y.), pelagic drape, and mass wasting over the last 20 thousand years (ka), when the principal filling of the ancestral Mississippi Canyon and its side canyons occurred (Goodwin and Prior, 1989). The age of the sedimentary sections in the upper 600 to 700 m (that is, the estimated GHSZ) in our operating areas is likely younger than late Pleistocene age (Goodwin and Prior, 1989).

East Side of Mississippi Canyon, Kane Spur, MC853 Diapir

A large slide, about 15 kilometers (km) wide and at least 15 km long, covering at least 225 square kilometers (km^2) is a prominent feature on Kane Spur on the east side of the canyon. Extensional faults occur at the head of the slide. In addition, there is a 1- to 2-km wide shear zone along the southwest edge of the slide. The subbottom is cut by two categories of faults: a suite of high-angle faults that converge with depth and extend beyond the depth of seismic-reflection data, and a set of faults that appear to be related to stratigraphic sliding within the upper sedimentary section. Cooper and Hart (2003) infer that the high-angle faults are rooted in deep-seated salt that is the principal driving mechanism for the sea-floor slide. The shallow faults sole out within a chaotic unit at about 2.2 seconds (sec) subbottom, where they partly accommodate the slide motion that includes extension near the slide's head and compression near the toe.

The slide lies within a broader zone of extensional subsidence of salt withdrawal. The western edge of the subsidence zone is marked by a number of boundary faults, one of which is the probable conduit for a large elliptical diapir-like structure present in lease blocks MC853 and MC852. Gas hydrate was cored at the sea floor from the diapiric structure and is suspected to exist within other smaller sea-floor mounds

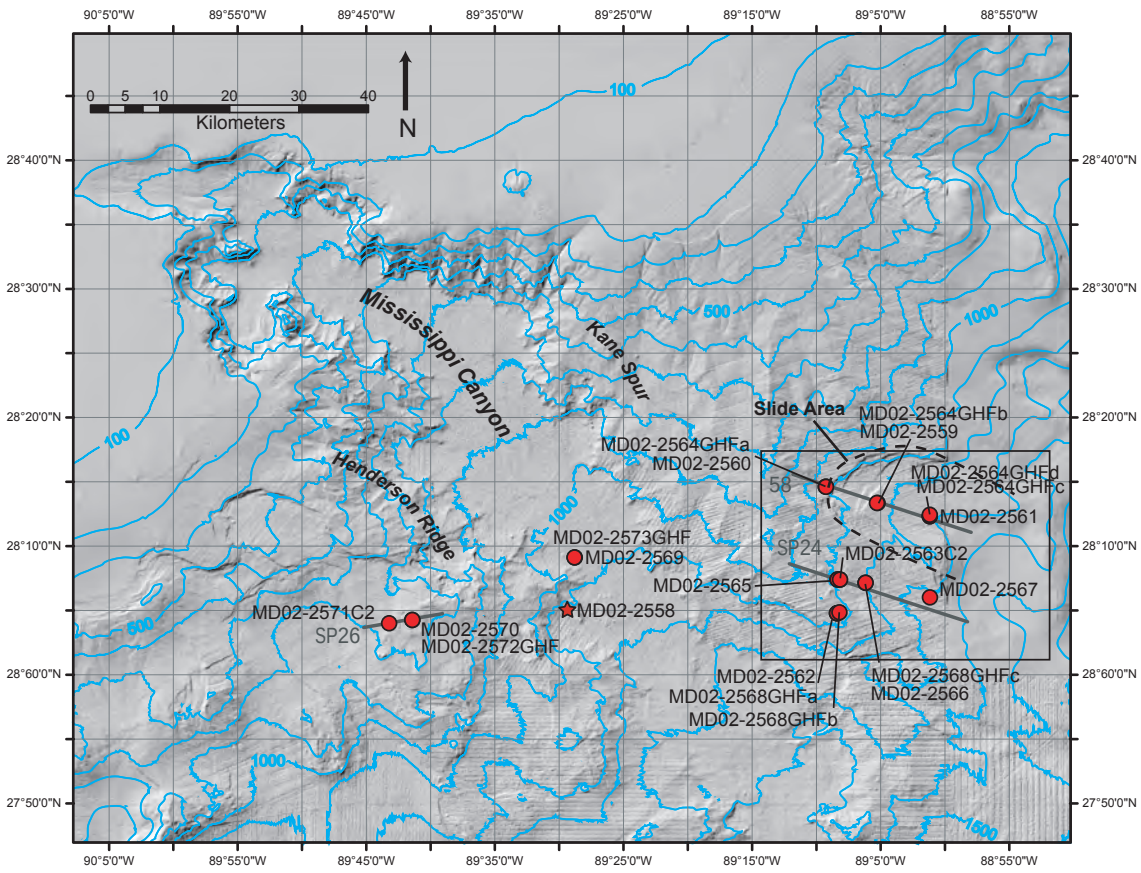

Figure 4. Coring locations in and around Mississippi Canyon. Boxed area indicates area of detail shown in figure 5. Gray lines denote seismic lines shown in figures 6 and 7. Core MD02-2558, part of the IMAGES program, is shown for reference.

over nearby faults within the slide's shear and extension zones (Sager and Kennicutt, 2000; Sassen, Sweet, Milkov, and others, 2001a).

Within the boundaries of the extensional subsidence zone, a chaotic stratigraphic unit occurs with disrupted reflections and high reflectivity zones (HRZ). The top of the HRZ under the slide lies at a subbottom depth of about 500 to 550 milliseconds (ms; 440 to 480 m), is about 100 to 150 ms (90 to 130 m) thick, and generally mimics the sea floor. The high reflectivity zones occur mostly where reflections are discontinuous and chaotic. The unit can be traced regionally, but reflectivity is greatest under the slide and near large fault zones. Drilling at multiple sites along the southwest side of the slide during development of the Ursa Field encountered wet sands from about 300 mbsf to 550 mbsf, with overpressure shallow-water flows and some gas (Eaton, 1999). Such shallow-water flows are common in the northern Gulf of Mexico (Minerals Management Service, 2001).

Our coring effort on the eastern Mississippi Canyon focused on two primary objectives: (1) A transect of the Kane Spur slide beginning above the headwall, into the main body, and ending in the toe (MD02-2560, -2559, and -2561, respectively, fig. 5). The watergun-sourced USGS 2–D seismic section, including these core locations, is shown in figure 6. (2) A transect from the summit of the MC853 diapiric structure known to be roofed by gas hydrate and oil-laden sediments, proceeding southeast into deeper waters along a previous USGS seismic line (MD02-2565, -2563C2, and -2566, respectively, fig. 5, with a chirp seismic section seen in fig. 7).

The seismic sections summarize important findings of the cruise. Each section shows the location of cores with the relative penetration into sediments at scale, the measured geothermal gradient, and the calculated base of the gas hydrate stability zone (BGHSZ) (fig. 7). The calculations of gas hydrate stability are given in more detail in Appendix L. Important features included measured geothermal gradient, pore water salinity (chlorinity as proxy) measured and projected to depth, the observed bottom water temperature, and gas compositions reflecting pure methane and wet gas compositions from Bush Hill and Mississippi Canyon given in Cooper and Hart (2003).

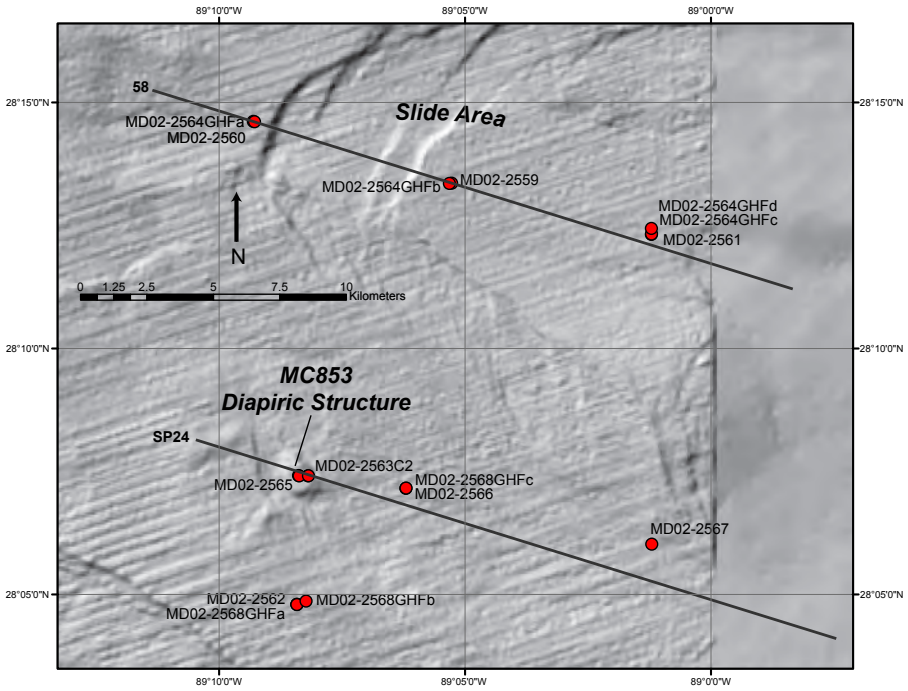

Figure 5. Detailed map of the east side of Mississippi Canyon coring area showing the core sites relative to the sea-floor slide, Kane Spur, and the MC853 diapiric structure.

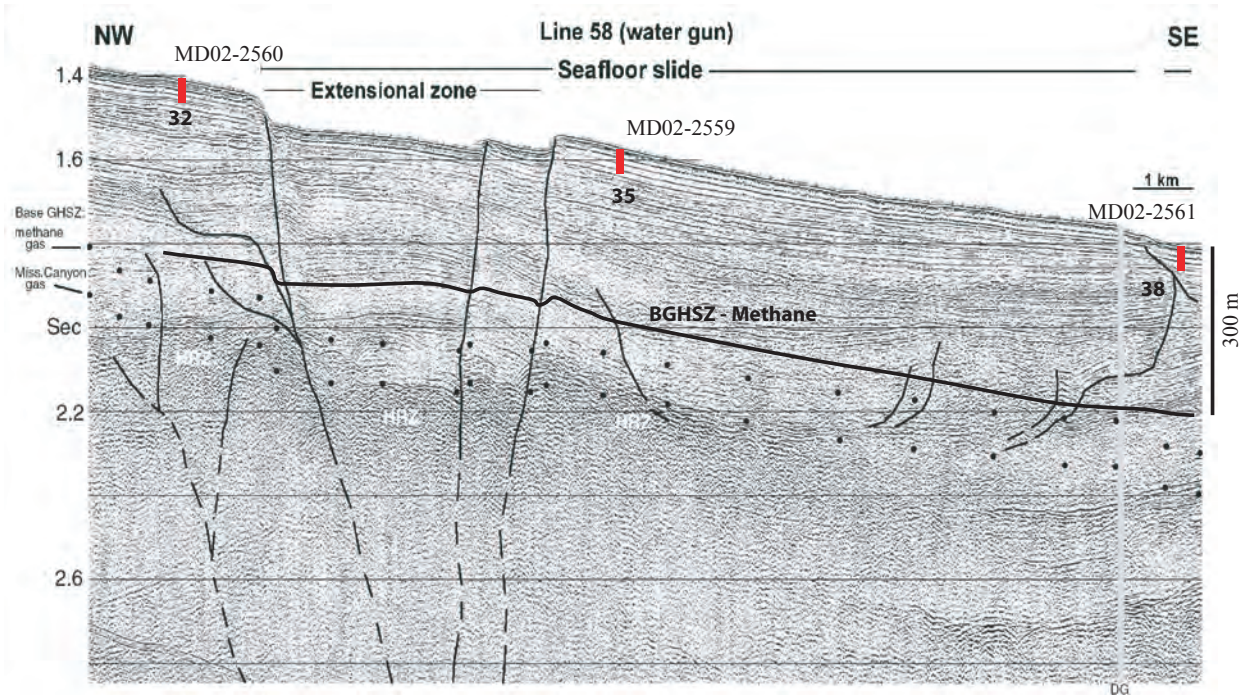

Figure 6. Watergun 2–D seismic line 58 from east of the Mississippi Canyon modified from Cooper and Hart (2003). Red lines denote the location and penetration of recovered cores. Interpreted faults are indicated as solid and dashed lines; dotted lines indicate theoretical base of gas hydrate as given by Cooper and Hart (2003). Measured geothermal gradients (degrees Celsius per kilometer) are given next to core sites. The line labeled BGHSZ is the calculated theoretical base of gas hydrate for structure I methane hydrate based on the measured geothermal gradient. The lack of any significant methane concentrations measured in pore water or sediment by Ussler and others, this volume, chapter 8; and Lorenson and others, this volume, chapter 9, make it unlikely gas hydrate exists near these locations.

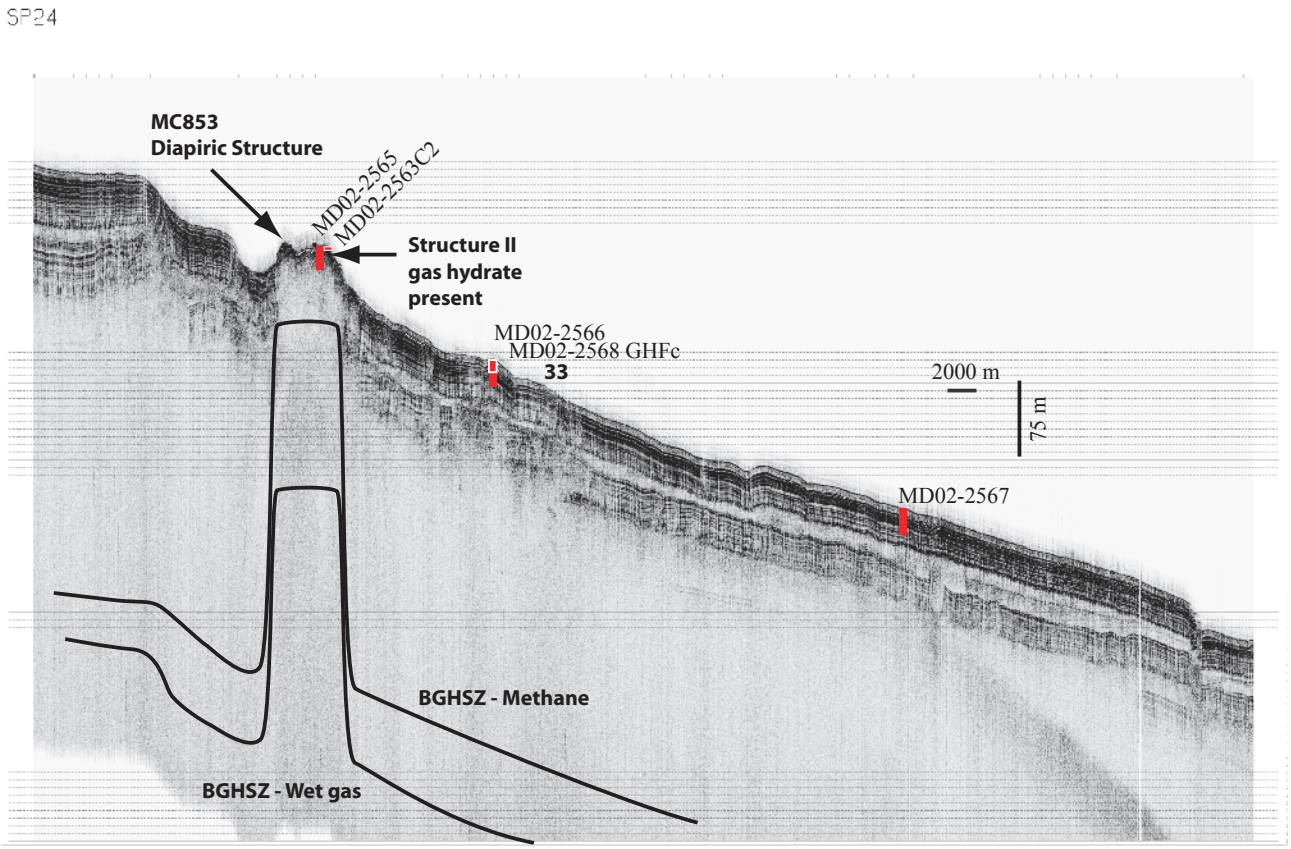

Figure 7. Chirp seismic line SP24 recorded during the cruise showing core locations east of the Mississippi Canyon, the position and penetration of selected cores, and the calculated base of the gas hydrate stability zone for methane and Mississippi Canyon wet gas compositions. Calculations are based on measured geothermal gradients (degrees Celsius per kilometer) shown, the bottom water temperature recorded at the time of coring, and the salinity of pore water both measured and extrapolated to depth.

Two additional sites were cored to the south primarily for researchers at Pennsylvania State University for studies of over-pressured shallow-water flows and sediment physical properties. These sites were subsequently drilled as part of the Integrated Ocean Drilling Program Leg 309 expedition in June 2005.

West Side of Mississippi Canyon

High-resolution seismic-reflection data were recorded in 1998 (Hart and others, 2002; Cooper and Hart, 2003) over a strongly deformed area on the west side of the canyon where shallow structures and sea floor deformation are common and gas hydrate is known from sea-floor cores. Here, irregular and diffuse HRZs lie within the upper 0.6-second (s) subbottom above diapiric structures, along fault zones, laterally within layered and chaotic stratal units bounded by faults, and adjacent to acoustic "wipeout" zones. Gas hydrate was cored from the westernmost diapir (Sassen and others, 1994). In other areas of the Gulf of Mexico's upper continental slope where acoustic wipeout zones and diffuse HRZs are seen, massive deformation, flow units, gas hydrate, and diagenetic carbonates are found within the near-sea-floor sediments (Roberts, 2001).

A detailed seismic survey, including ocean bottom seismometers, was conducted during the 1999 USGS cruise across a small semi-circular basin where Neurauter and Bryant (1990) cored gas hydrate from a sea-floor mound that directly overlies a shallow HRZ (Cooper and others, 1998). Their high-resolution profiles across this area illustrated that many near-vertical faults extend to the sea floor and delineate different reflection packages of both enhanced reflectivity and diminished reflectivity zones. In the higher-resolution Huntec boomer data, the upper 90-ms subbottom is characterized by acoustic "chimney" features with diffractions and abrupt reflectivity changes that cut through the layered stratigraphy, which may denote local accumulations of gas (and gas hydrate) (for example, Anderson and Bryant, 1990). Directly below (that is, between 90- to 200- ms subbottom), the boomer data indicate few reflections in an apparent wipeout zone directly above the HRZ. Strata here may be deformed or contain gas (and gas hydrate), as suggested for wipeout zones

in other parts of the Gulf of Mexico (for example, Roberts and others, 1999).

On the western Mississippi Canyon, we cored two gas-rich sites previously identified by gas chimneys (MD02-2570 and 2571C2) (fig. 8). Important objectives were to determine if gas hydrate was present within and above gas chimneys and to determine the microbial communities around the sulfate methane interface. One additional site (MD02-2569) known to be a gas hydrate mound was cored in the thalweg of Mississippi Canyon (MC802) resulting in the best hydrate recovery of the cruise.

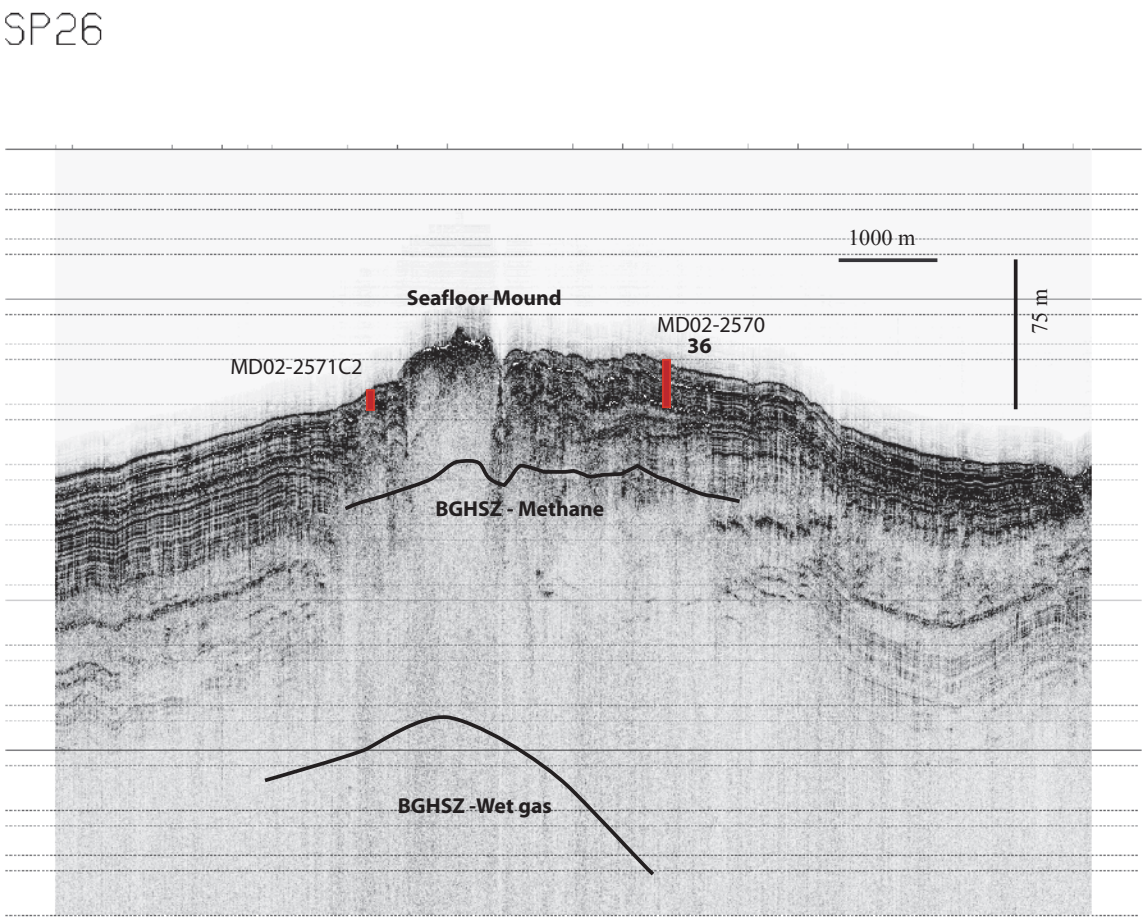

Figure 8. Chirp seismic line recorded during the cruise showing core locations MD02-2570 and MD02-2571C2 located west of the Mississippi Canyon. The line bisects a semicircular ridge of about 3 kilometer diameter that is dotted with mounds such as this one. Approximate depth of core penetration is indicated. Core MD02-2571C2 penetrated about 10 meters of gas-charged sediments on the flank of a sea-floor mound. Core MD02-2570 penetrated laminated sediments, also gas-charged, starting at depths below about 5 meters. Also indicated are the calculated base of the gas hydrate stability zone for methane and Mississippi Canyon wet gas compositions. Calculations are based on measured geothermal gradients (degrees Celsius per kilometer) shown, the bottom water temperature recorded at the time of coring, and the salinity of pore water both measured and extrapolated to depth.

Site Characterization: Green Canyon Region

The Green Canyon region, like the Mississippi Canyon region, is also known for locally high sedimentation rates of 7 to 11 m/k.y. for the upper sedimentary section, extensive late Neogene salt deformation, and slope failures with mass-wasting along oversteepened parts of the continental slope (Rowan and Weimer, 1998). Sediment ages in the upper 600 to 700 mbsf are likely no older than 0.5 million years (m.y.) in the study area (Berryhill and others, 1987; Weimer and others, 1998). This region includes the Tunica Mound and Bush Hill coring sites.

The upper sedimentary section of the continental slope in the Green Canyon region is characterized by layered and chaotic units that are faulted near basin edges, and by slope failures on basin flanks. Deformation is greater near salt structures and on oversteepened slopes. The HRZs are common and may be broad and diffuse with associated wipeout regions, especially where salt deformation is greatest beneath the uppermost slope (Cooper and Hart, 2003). Elsewhere in the northern Gulf of Mexico, on a local scale (for example, near fault scarps and sea-floor mounds) such wipeout zones are documented as sites of gas expulsion, gas hydrate, authigenic carbonates, and(or) chemosynthetic communities (Sager and others, 1999; Roberts, 2001).

Tunica Mound

Downslope from the diffuse HRZ under the shelf edge, well-layered reflections at 150- to 300-ms subbottom have many vertical acoustic "chimney" features (that is, small faults) and are encased by chaotic units directly below and above. The underlying chaotic unit has HRZs that are dispersed within chaotic stratal units and similar to those in other slope basins at about the same depth. "Chimney" features extend up from this chaotic unit to the overlying chaotic unit, which has low seismic amplitudes and evidence of faulting and sliding.

A transect of nine gravity and piston cores was taken along the southern flank of Tunica Mound verging toward but not entering the basin to the east (fig. 9). Tunica Mound is about 14 km square with a fault running through the southwest to northeast corners. The northwest side of the mound is uplifted in contrast to the southeast corner. The transect runs for about 7 km at a subparallel angle to the fault in the southeast quadrant. Water depths along the transect range from about 600 m to 630 m. Figure 10 shows the chirp seismic section, SP2, annotated with core locations, geothermal gradients, and the base of the gas hydrate stability zone for methane and Bush Hill gas compositions. All sites on the transect remain within the confines of the dome; however, the site to the northeast appears to enter the basin between Tunica Mound and Caddo Mound to the east. Most of the gravity cores were taken on or near a subsidiary mound with features that indicate active fluid flow, for example, authigenic carbonate, sea-floor relief, and seismic indications of gas. Piston cores were obtained from the sub-mound. As seen in figure 10, the BGHSZ does not necessarily follow the contours of the sea floor; instead, it can be quite variable. This is the consequence mainly of large changes of the geothermal gradient over short distances and the shoaling effects of increased salinity in pore water that drastically decreases the depth of the gas hydrate stability zone.

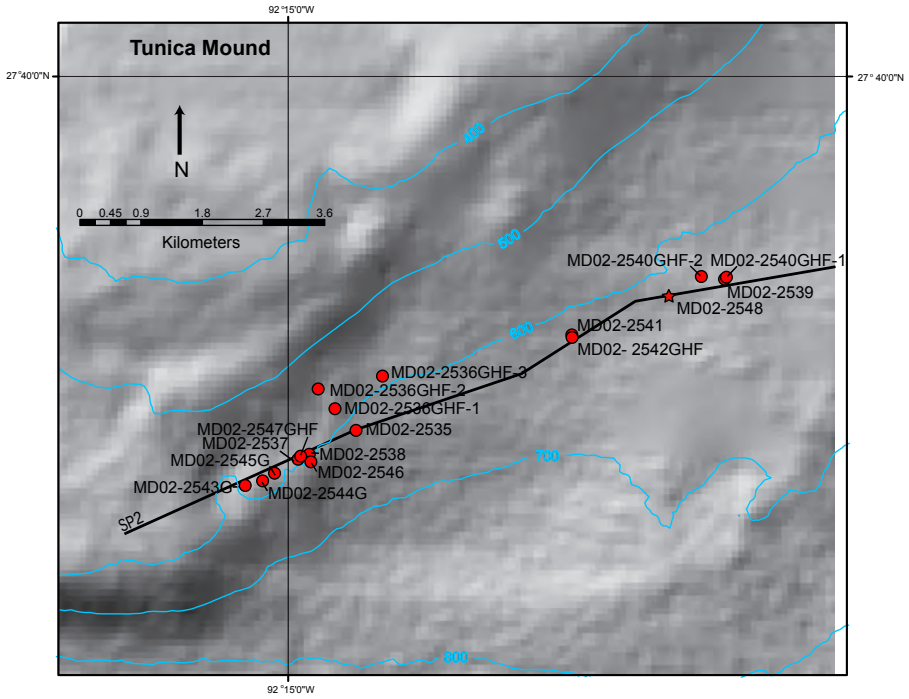

Figure 9. Coring locations in and around Tunica Mound. Gray line denotes the seismic lines shown in figure 10. IMAGES core MD02-2548 is shown for reference.

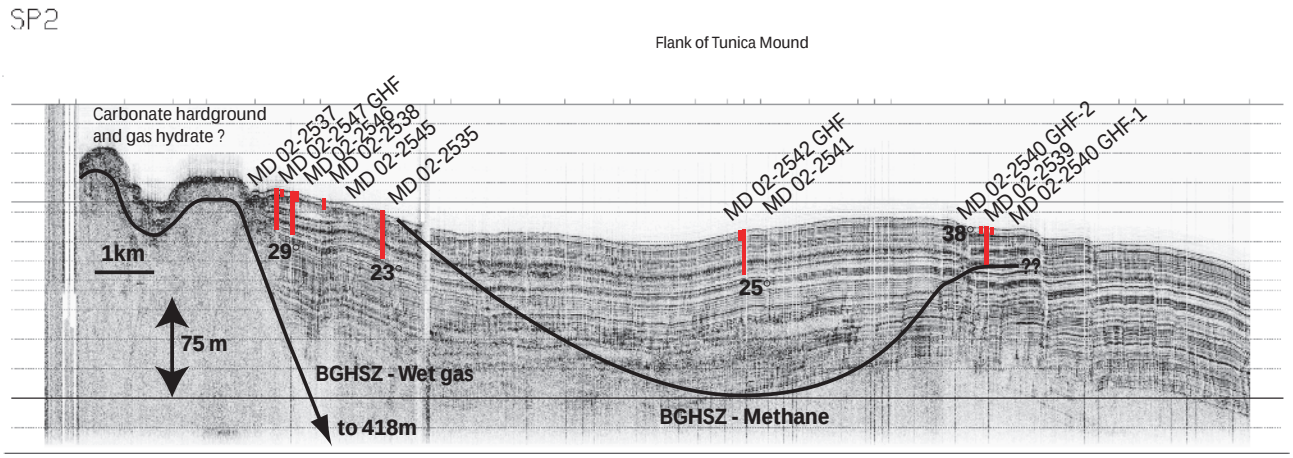

Figure 10. Chirp seismic line SP2 recorded during the cruise showing core locations, the penetration of selected cores, and the calculated base of the gas hydrate stability zone for methane and Bush Hill wet gas compositions. Calculations are based on measured geothermal gradients (degrees Celsius per kilometer) shown, the bottom water temperature recorded at the time of coring, and the salinity of pore water both measured and extrapolated to depth.

Bush Hill Mound and Adjacent Basin

The Bush Hill Mound, interpreted as a sea-floor-piercing mud diapir (Neurauter and Bryant, 1990), is located along the boundary between GC blocks 184 and 185, and is a fault-related seep mound at a water depth of ~540 m. Subbottom profiles of 3.5 kilohertz across the Bush Hill Mound indicate that the structure is acoustically amorphous with abrupt lateral contacts and is surrounded by upturned stratified reflectors (Neurauter and Bryant, 1990; Lee, 1995). Well-defined vertically oriented acoustic wipeout zones are recorded both at shallow acoustic profiles (Lee, 1995) and deep 3–D seismic profiles (Roberts, 2001). Acoustic profiles suggest the occurrence of hard substrate below the sea floor commonly associated with carbonates (Roberts and Carney, 1997) and gas hydrate (Sager and others, 1999). Deep seismic profiles (Roberts, 2001) suggest that reflections are disturbed below Bush Hill, which suggests the presence of a mud diapir or gas-charged sediments to a depth of at least 700 m.

An antithetic fault related to a major growth fault (Neurauter and Bryant, 1990; Cook and D'Onfro, 1991) at Bush Hill is structurally related to nearby growth faults that constitute the structural trap at Jolliet Field just a few kilometers to the south (Cook and D'Onfro, 1991). These faults are active conduits for vertically migrating hydrocarbons. There appears to be a larger area of numerous, shallow faults serving as migration conduits for fluids that surround the Bush Hill mound area (Neurauter and Bryant, 1990). The oil and gas at the Bush Hill site correlate with reservoirs of Pliocene to Pleistocene age at ~2 to 3 km depth in the Jolliet Field (for example, Kennicutt and others, 1988; Cook and D'Onfro, 1991; Sassen, Losh, and others, 2001).

The Bush Hill area is a complex location where thermogenic gas hydrate was first recovered by piston cores in the Gulf of Mexico (Brooks and others, 1984; Brooks and others, 1986). Previous research focused on vent gas, gas hydrate, and chemosynthetic communities (MacDonald and others, 1989, 1994, 1996; Roberts and Carney, 1997; Roberts, 2001; Sassen and others, 1993, 1998; Sassen, Joye, and others, 1999; Sassen, Sweet, and others, 1999; Sassen, Losh, and others, 2001; Sassen, Sweet, Milkov, and others, 2001a, b).

Chemosynthetic organisms and authigenic carbonate rocks are widely distributed across the area at water depths of 250 to 880 m (Kennicutt and others, 1985; Roberts, and others, 1990). Only thermogenic structure II and H gas hydrates containing methane through pentane hydrocarbon gases have been found in the area (Sassen and MacDonald, 1994). Mounds of structure II gas hydrate outcrop on the sea floor and have been persistently observed since 1991 (Sassen and others, 2004). Gas hydrate occurs as sea-floor mounds (1–2 m across) and at shallow depth in sediments (MacDonald and others, 1994), mainly around Bush Hill. Gas hydrate gas and vent gas collected at the Bush Hill site have molecular and isotopic properties that correlate with hydrocarbon gases from reservoirs of Jolliet Field (Sassen, Sweet, Milkov, and others, 2001a).

Sparse data of gas hydrate concentration in the sediment at Bush Hill indicate that 5 to 20 percent by volume of gas hydrate may be present in the upper 6 m of sediments. Gas hydrate mounds (90-percent gas hydrate by volume) crop out at the sea floor. Gas hydrate concentration in sediments below 6 m is largely unknown. Models based on molecular composition of Jolliet reservoir gas, vent gas, and hydrate-bound gas suggest that gas hydrate concentration remains constant throughout the upper part of the GHSZ and decreases at the base of the GHSZ (Chen and Cathles, 2003).

Previously recovered piston cores taken on the Bush Hill mound contain oil-saturated silty mud with small (1 to

2 millimeters (mm)) deposits of yellowish hydrate up to large 40- to 50-mm diameter nodules of hydrate (Brooks and others, 1986; Neurauter and Bryant, 1990). Gas is abundant in cores recovered from Bush Hill (Lee, 1995), as well as in the water column just above the mound (Sassen, Losh, and others, 2001). Shallow sediment is under-consolidated hemipelagic mud with near-normal salinity (~38 parts per thousand (ppt)), high concentration of hydrogen sulfide (as much as 20.3 millimoles [mM]), and high pH (8.3–9.0) (Aharon and Fu, 2000). Sassen, Losh, and others (2001) report that piston cores collected in the area of reflections contain expansion cracks and a strong hydrogen sulfide smell, both evidence of abundant gas in the sediments.

Coring commenced in the small basin just east of Bush Hill (fig. 11) along an east-west transect with three cores spaced about 2 km apart. The primary objectives of the transect were to investigate the occurrence, if any, of thermogenic gases and surficial gas hydrate along a track into the adjacent basin, and to determine if gas hydrate is likely to exist at depth in the basin. Figure 12 shows the chirp seismic profile (SP17) annotated with core locations, geothermal gradients, and the calculated BGHSZ. The BGHSZ methane remains deep within the basin and shoals abruptly near Bush Hill, reflecting the increased geothermal gradient near the mound. The lack of any recovered gas hydrate in cores suggests that the structure II and H gas hydrates reported on Bush Hill are not widespread in the adjacent basin. However, the presence of methane in the shallow sediments of the adjacent basin suggest that gas hydrate could be present in small concentrations at depths greater than 10 to 20 mbsf.

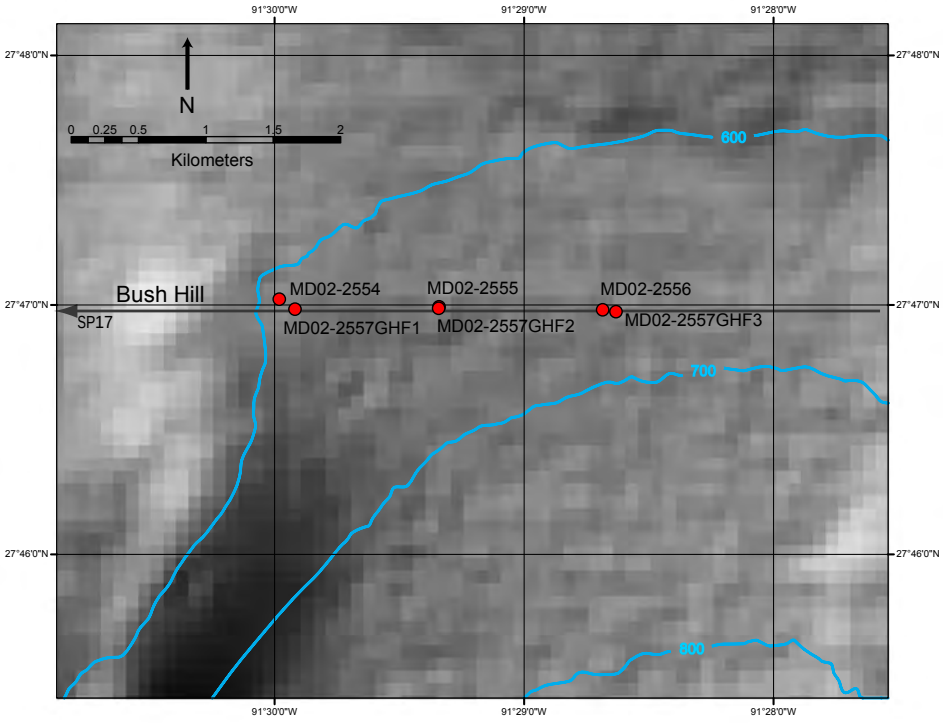

Figure 11. Coring locations east of Bush Hill (GC185). Dark gray line denotes the seismic line shown in figure 12.

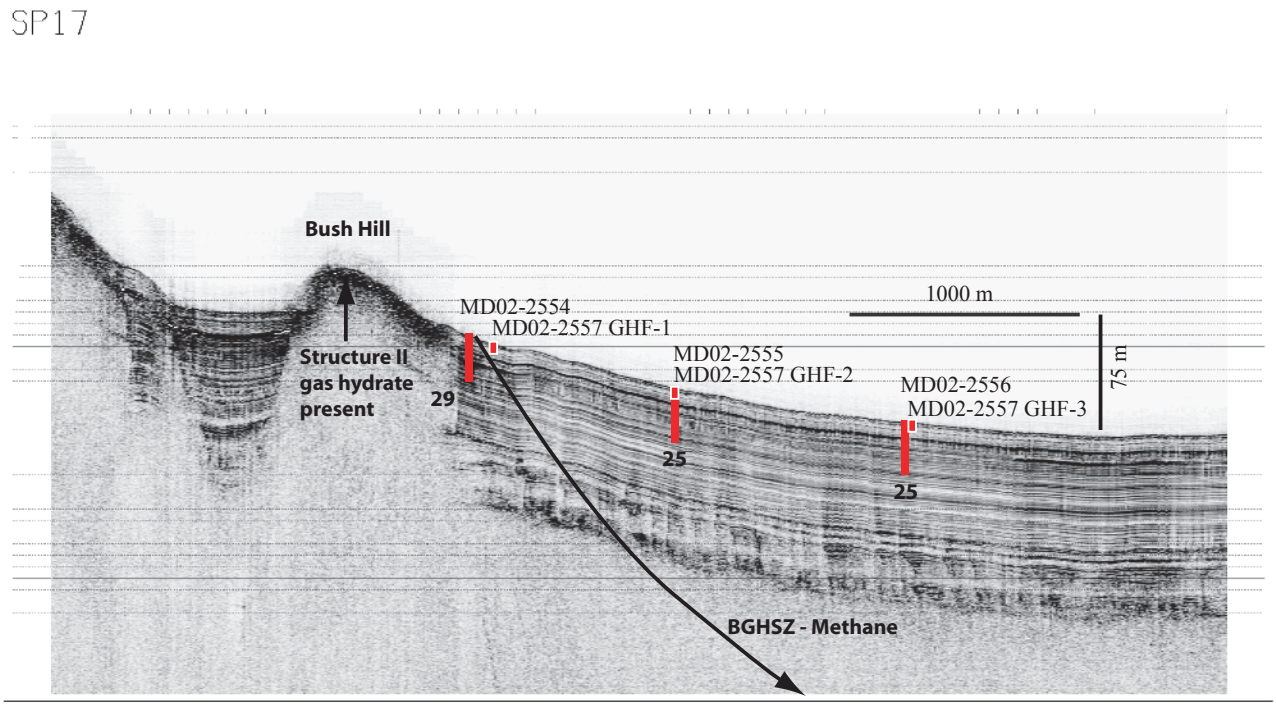

Figure 12. Chirp seismic line SP17 recorded during the cruise showing core locations, the penetration of selected cores, and the calculated base of the gas hydrate stability zone for methane and Bush Hill wet gas compositions. Calculations are based on measured geothermal gradients (degrees Celsius per kilometer) shown, the bottom water temperature recorded at the time of coring, and the salinity of pore water both measured and extrapolated to depth.

Site Characterization—Pigmy and Orca Basins

Coring in Pigmy and Orca basins was conducted for paleoceanographic research studies (fig. 13). The basins presumably have similar depositional histories. However, Orca basin has been submerged by a seawater brine for an unknown time, which has resulted in an anoxic environment and organic preservation. In contrast, Pigmy basin has been subject to oxic conditions. USGS researchers at St. Petersburg, Florida, obtained samples to study the pollution history of the Mississippi River as revealed by sediments in the two basins having contrasting redox potentials.

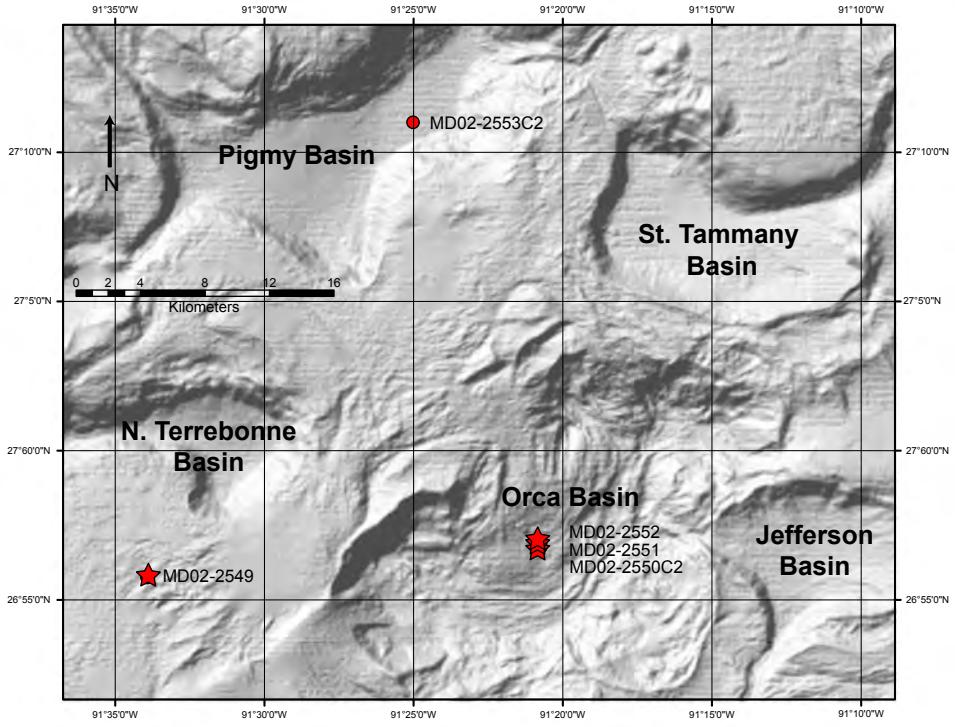

Figure 13. Coring locations in Pygmy and Orca basins. IMAGES core MD02-2549 is shown for reference.

Summary

Piston coring during the RV *Marion Dufresne* cruise was designed primarily to look at a series of three transects extending from known gas hydrate mounds in regions where high reflectivity zones have been identified. We found that the lateral extent of gas hydrate between near-surface hydrate deposits and in adjacent basins was limited. Surficial gas hydrates found on sea-floor mound tops did not extend into the adjoining basins. We were not able to confirm or deny that any significant gas hydrate deposits occur in reservoir sediments at depth in these basins. A lack of methane (and gas hydrate) in sediments in and around the Kane spur slide suggest that gas hydrate dissociation had little or no effect on known submarine slides near the Mississippi Canyon where deep offshore platforms might be at risk.

Acknowledgments

We thank Captain Jean-Michel Nicolas, Yvon Balut (coring supervisor), and the crew of the RV *Marion Dufresne* for their assistance in performing shipboard activities. Cruise logistical support was provided by the French Polar Institute [Institut Polaire Francais – Paul-Emile Victor (IPEV)].

Considerable at-sea help was provided by an international group of about 40 scientists working under the IMAGES and PAGE programs. The IMAGES program is an international effort to understand the mechanisms and consequences of climatic changes using the oceanic sedimentary record.

Financial support of USGS-related activities was provided by the USGS Coastal and Marine Geology Program and the USGS Energy Program. Significant funding for the cruise was provided by the U.S. Department of Energy without whose support the cruise would not have been possible.

Special thanks to Bill Dillon for initiating the cruise.

The U.S. Minerals Management Service graciously provided access to 3–D seismic information prior to the coring.

References

Aharon, P., and Fu, B., 2000, Microbial sulfate reduction rates and sulfur and oxygen isotope fractionations at oil and gas seeps in deepwater Gulf of Mexico: Geochimica et Cosmochima Acta, v. 64, p. 233–246.

Aharon, P., Schwarcz, H.P., and Roberts, H.H., 1997, Radiometric dating of hydrocarbon seeps in the Gulf of Mexico: Geolical Society of America Bulletin, v. 109, p. 568–579.

Anderson, A.L., and Bryant, W.R., 1990, Gassy sediment occurrence and properties—northern Gulf of Mexico: Geo-Marine Letters, v. 10, p. 209–220.

Berryhill, H.L., Suter, J.R., and Hardin, N.S., 1987, Late Quaternary facies and structure, northern Gulf of Mexico: AAPG Studies in Geology, no. 23, 289 p.

Brooks, J.M., Cox, H.B., Bryant, W.R., Kennicutt, M.C., II, Mann, R.G., and McDonald, T.J., 1986, Association of gas hydrates and oil seepage in the Gulf of Mexico: Organic Geochemistry, v. 10, p. 221–234.

Brooks, J.M., Kennicutt, M.C., II, Fay, R.R., McDonald, T.J., and Sassen, R., 1984, Thermogenic gas hydrates in the Gulf of Mexico: Science, v. 225, p. 409–411.

Chen, D.F., and Cathles, L.M., III, 2003, A kinetic model for the pattern and amounts of hydrates precipitated from a gas steam; application to the Bush Hill vent site, Green Canyon block 185, Gulf of Mexico: Journal of Geophysical Research, B, Solid Earth and Planets, v. 108, no. 1, 14 p.

Cook, D., and D'Onfro, P., 1991, Jolliet Field thrust structure and stratigraphy, Green Canyon block 184, offshore Louisiana: Gulf Coast Association of Geological Societies, Transactions, v. 41, p. 100–121.

Cooper, A.K., and Hart, P.E., 2003, High-resolution seismic-reflection investigation of the northern Gulf of Mexico gas-hydrate-stability zone: Marine and Petroleum Geology, v. 19, p. 1275–1293.

Cooper, A.K., McGee, T., Hart, P., and Pecher, I., 1998, Seismic investigation of gas hydrate in the Mississippi Canyon region, northern Gulf of Mexico—cruise M1-98-GM: U.S. Geological Survey Open-File Report 98–506, 33 p.

Cooper, A.K., Twichell, D., and Hart, P., 1999, A seismic-reflection investigation of gas hydrate and seafloor features of the upper continental slope of the Garden Banks and Green Canyon regions, northern Gulf of Mexico—report for cruise G1-99-GM (99002): U.S. Geological Survey Open-File Report 99–570, 20 p.

Diegel, F.A., Karlo, J.F., Schuster, D.C., Shoup, R.C., and Tauvers, P.R., 1995, Cenozoic structural evolution and tectono-stratigraphic framework of the northern Gulf Coast continental margin, *in* Jackson, M.P.A., Roberts, D.G., and Snelson, S., eds., Salt tectonics—a global perspective: American Association of Petroleum Geologists Memoir 65, p. 109–155.

Eaton, L.F., 1999, Drilling through shallow water flow zones at Ursa: Conference Proceedings Shallow Water-Flows, Oct. 6–8, 1999, PennWell, Tulsa, OK, 600 p.

EEZ-SCAN 85 Scientific Staff, 1987, Atlas of the U.S. Exclusive Economic Zone, Gulf of Mexico and eastern Caribbean areas: U.S. Geological Survey Miscellaneous Investigation I-1864A, 103 p., scale 1:500,000.

Galloway, W.E., Ganey-Curry, P.E., Li, X., and Buffler, R.T., 2000, Cenozoic depositional history of the Gulf of Mexico Basin: American Association of Petroleum Geologists Bulletin, v. 84, p. 1743–1774.

Goodwin, R.H., and Prior, D.B., 1989, Geometry and depositional sequences of the Mississippi Canyon, Gulf of Mexico: Journal of Sedimentary Petrologists, v. 59, no. 2, p. 318–329.

Hart, P.E., Cooper, A.K., Lee, M.W., and Agena, W.F., 2002, High-resolution multichannel seismic-reflection data acquired in the northern Gulf of Mexico, 1998–99: U.S. Geological Survey Open-File Report 02–0368. *http://pubs.water.usgs.gov/ofr02-368*

Hedberg, H.H., 1980, Methane generation and petroleum migration, *in* Roberts, W.H., and Cordell, R.J., eds., Problems of petroleum migration: American Association of Petroleum Geologists Studies in Geology, no. 10, p. 179–206.

Kennicutt, M.C., II, Brooks, J.M., Bidigare, R.R., Fay, R.R., Wade, T.L., and MacDonald, T.J., 1985, Vent type taxa in a hydrocarbon seep region on the Louisiana slope: Nature, v. 317, p. 351–353.

Kennicutt, M.C., II, Brooks, J.M., and Denoux, G.J., 1988, Leakage of deep, reservoired petroleum to the near surface of the Gulf of Mexico continental slope: Marine Chemistry, v. 24, p. 39–59.

Lee, C.S., 1995, Geology of hydrocarbon seeps on the northern Gulf of Mexico continental slope: College Station, TX, Texas A&M University, Ph.D. dissertation, 115 p.

MacDonald, I.R., Boland, G.S., Baker, J.S., Brooks, J.M., Kennicutt M.C., II, and Bidigare, R.R., 1989, Gulf of Mexico hydrocarbon seep communities, II. Spatial distribution of seep organisms and hydrocarbons at Bush Hill: Marine Biology, v. 101, p. 235– 247.

MacDonald, I.R., Guinasso, N.L., Jr., Sassen, R., Brooks, J.M., Lee, L., and Scott, K.T., 1994, Gas hydrate that breaches the sea floor on the continental slope of the Gulf of Mexico: Geology, v. 22, p. 699–702.

MacDonald, I.R., Reilly J.F., Jr., Best, S.E., Venkataramaiah, R., Sassen, R., Amos, J., and Guinasso, N.L., Jr., 1996, A remote-sensing inventory of active oil seeps and chemosynthetic communities in the northern Gulf of Mexico, *in* Schumacher, D., and Abrams, M.A., eds., Hydrocarbon migration and its near-surface expression: American Association of Petroleum Geologists Memoir 66, p. 27– 37.

Milkov, A.V., and Sassen, R., 2001, Economic geology of the Gulf of Mexico and the Blake Ridge gas hydrate provinces: Gulf Coast Association of Geological Societies Transactions, LI, p. 219–228.

Minerals Management Service, 2001, Shallow water flows in the northern Gulf of Mexico, available online at *http://www.gomr.mms.gov/homepg/offshore/safety/wtrflow.html*

Minerals Management Service, 2002, Gulf of Mexico lease block areas, available online at *http://www.gomr.mms.gov/homepg/gomatlas/atlas.html*

Neurauter, T.W., and Bryant, W.R., 1990, Seismic expression of sedimentary volcanism on the continental slope, northern Gulf of Mexico: Geo-Marine Letters, v. 10, p. 225–231.

Paull, C.K., Ussler, W., III, Lorenson, T., Winters, W., and Dougherty, J., 2005, Geochemical constraints on the distribution of gas hydrates in the Gulf of Mexico: Geo-Marine Letters, v. 25, DOI: 10.1007/s00367-005-0001-3.

Pflaum, R.C., Brooks, J.M., Cox, H.B., Kennicutt, M.C., II, Sheu, D., and Bouma, A.H., 1986, Molecular and isotopic analysis of core gases and gas hydrates, deep sea drilling project Leg 96; initial reports of the deep sea drilling project covering Leg 96 of the cruises of the drilling vessel Glomar Challenger, Ft. Lauderdale, Florida, to Galveston, Texas, September–November 1983: Initial Reports of the Deep Sea Drilling Project, v. 96, p. 781–784.

Prather, B.E., Booth, J.R., Steffens, G.S., and Craig, P.A., 1998, Classification, lithologic calibration and stratigraphic succession of seismic facies of intraslope basins, deep-water Gulf of Mexico: American Association of Petroleum Geologists Bulletin, v. 85, p. 701–728.

Roberts, H.H., 1996, 3D-seismic for interpretation of seafloor geology (Louisiana slope): Gulf Coast Association of Geological Societies Transactions, v. 46, p. 353–366.

Roberts, H.H., 2001, Fluid and gas expulsion on the northern Gulf of Mexico continental slope—mud-prone to mineral-prone responses, *in* Paull, C.K., and Dillon, W.P., eds., Natural gas hydrate—occurrence, distribution, and dynamics: American Geophysical Union Monograph Series, v. 24, p. 145–161.

Roberts, H.H., and Aharon, P., 1994, Hydrocarbon-derived buildups of the northern Gulf of Mexico—a review of submersible investigations: Geo-Marine Letters, v. 14, p. 135–148.

Roberts, H.H., Aharon, P., Carney, R., Larkin, J., and Sassen, R., 1990, Sea floor response to hydrocarbon seeps, Louisiana continental slope: Geo-Marine Letters, v. 10, p. 232–243.

Roberts, H.H., and Carney, R., 1997, Evidence of episodic fluid, gas and sediment venting on the northern Gulf of Mexico continental slope: Economic Geology, v. 92, p. 863–879.

Roberts, H.H., Cook, D.J., and Sheedlo, M.K., 1992, Hydrocarbon seeps of the Louisiana continental slope—seismic amplitude signature and seafloor response: Gulf Coast Association of Geological Societies, v. 42, p. 349–361.

Roberts, H.H., Kohl, B., Menzies, D., and Humphrey, G.D., 1999, Acoustic wipe-out zones—a paradox for interpreting seafloor geologic/geotechnical characteristics (An example for Garden Banks 161): Proceedings Offshore Technology Conference, Houston, Texas, Offshore Technology Conference Paper 10921, p. 1–12.

Rowan, M.G., 1995, Structural styles and evolution of allochthonous salt, central Louisiana outer shelf and upper slope, *in* Jackson, M.P.A., Roberts, D.G., and Snelson, S., eds., Salt tectonics—a global perspective: American Association of Petroleum Geologists Memoir 65, p. 199–228.

Rowan, M.G., and Weimer, P., 1998, Salt-sediment interaction, northern Green Canyon and Ewing Bank (Offshore Louisiana), northern Gulf of Mexico: American Association of Petroleum Geologists Bulletin, 82/5B, p. 1055–1082.

Ruppel, C., Dickens, G.R., Castellini, D.G., Gilhooly, W., and Lizarralde, D., 2005, Heat and salt inhibition of gas hydrate formation in the northern Gulf of Mexico: Geophysical Research Letters, v. 32, no. 4, L04605 DOI:10.1029/2004GL021909, 4 p.

Sager, W.W., and Kennicutt, M.C., II, 2000, Proposal for ocean drilling program research on gas hydrate in the Gulf of Mexico: Proceedings Offshore Technology Conference, Houston, TX, Offshore Technology Conference Paper 12111, p. 587–603.

Sager, W.W., Lee, C.S., MacDonald, I.R., and Schroeder, W.W., 1999, High-frequency near-bottom acoustic reflection signatures of hydrocarbon seeps on the northern Gulf of Mexico continental slope: Geo-Marine Letters, v. 18, p. 267–276.

Salvador, A., 1987, Late Triassic-Jurassic paleogeography and origin of Gulf of Mexico basin: American Association of Petroleum Geologists Bulletin, v. 71, p. 419–451.

Sassen, R., Brooks, J.M., MacDonald, I.R., Kennicutt, M.C., II, Guinasso, N.L., Jr., and Requejo, A.G., 1994, Association of oil seeps and chemosynthetic communities with oil discoveries, upper continental slope, Gulf of Mexico: Gulf Coast Association of Geological Societies Transactions, v. 44, p. 349–355.

Sassen, R., Joye, S., Sweet, S.T., DeFreitas, D.A., Milkov, A.V., and MacDonald, I.R., 1999, Thermogenic gas hydrates and hydrocarbon gases in complex chemosynthetic communities, Gulf of Mexico continental slope: Organic Geochemistry, v. 30, p. 485–497.

Sassen, R., Losh, S.L., Cathles, L.M., III, Roberts, H.H., Whelan, J.K., Milkov, A.V., Sweet, S.T., and DeFreitas, D.A., 2001, Massive vein-filling gas hydrate—relation to ongoing gas migration from the deep subsurface of the Gulf of Mexico: Marine and Petroleum Geology, v. 18, p. 551–560.

Sassen, R., and MacDonald, I.R., 1994, Evidence of structure H hydrate, Gulf of Mexico continental slope: Organic Geochemistry, v. 22, p. 1029–1032.

Sassen, R., MacDonald, I.R., Guinasso, N.L., Joye, S., Requejo, A.G., Sweet, S.T., Alcala-Herrera, J., DeFreitas, D.A., and Schink, D.R., 1998, Bacterial methane oxidation in sea-floor gas hydrate—significance to life in extreme environments: Geology, v. 26, p. 289–293.

Sassen, R., MacDonald, I.R., Requejo, A.G., Guinasso, N.L., Kennicutt M.C., II, Sweet, S.T., and Brooks, J.M., 1994, Organic geochemistry of sediments from chemosynthetic communities, Gulf of Mexico slope: Geo-Marine Letters, v. 14, p. 110–119.

Sassen, R., Roberts, H.H., Aharon, A., Larkin, J., Chinn, E.W., and Carney, R., 1993, Chemosynthetic bacterial mats at cold hydrocarbon seeps—Gulf of Mexico continental slope: Organic Geochemistry, v. 20, p. 77–89.

Sassen, R., Roberts, H.H., Carney, R., Milkov, A.V., DeFreitas, D.A., Lanoil, B., and Zhang, C., 2004, Free hydrocarbon gas, gas hydrate, and authigenic minerals in chemosynthetic communities of the northern Gulf of Mexico continental slope—relation to microbial processes: Chemical Geology, v. 205, p. 195–217.

Sassen, R., Sweet, S.T., DeFreitas, D.A., Morelos, J.A., and Milkov, A.V., 2001, Gas hydrate and crude oil from the Mississippi Fan Foldbelt, downdip Gulf of Mexico salt basin—significance to petroleum system: Organic Geochemistry, v. 32, p. 999–1008.

Sassen, R., Sweet, S.T., Milkov, A.V., DeFreitas, D.A., and Kennicutt, M.C., II, 2001a, Thermogenic vent gas and gas hydrate in the Gulf of Mexico slope—Is gas hydrate decomposition significant? Geology, v. 29, p. 107–110.

Sassen, R., Sweet, S.T., Milkov, A.V., DeFreitas, D.A., and Kennicutt, M.C., II, 2001b, Stability of thermogenic gas hydrate in the Gulf of Mexico—constraints on models of climate change, *in* Paull, C.K., and Dillon, W.P., eds., Natural gas hydrates—occurrence, distribution, and detection: American Geophysical Union, Washington, DC, p. 131–143.

Sassen, R., Sweet, S.T., Milkov, A.V., DeFreitas, D.A., Salata, G.G., and McDade, E.C., 1999, Geology and geochemistry of gas hydrates, central Gulf of Mexico continental slope: Gulf Coast Association of Geological Societies Transactions, v. 49, p. 462–468.

Shipley, T.H., Houston, M.H., Buffler, R.T., Shaub, F.J., McMillen, K.J., Ladd, J.W., and Worzel, J.L., 1979, Seismic reflection evidence for the widespread occurrence of possible gas-hydrate horizons on continental slopes and rises: American Association of Petroleum Geologists Bulletin, v. 63, p. 2204–2213.

Weimer, P., Crews, J.R., Crow, R.S., and Varnai, P., 1998, Atlas of petroleum fields and discoveries, northern Green Canyon, Ewing Bank, and Southern Ship Shoal northern Gulf of Mexico, 1998: American Association of Petroleum Geologists Bulletin, v. 82, p. 878–917.

Winker, C.D., and Booth, J.R., 2000, Sedimentary dynamics of the salt-dominated continental slope, Gulf of Mexico; integration of observations from the seafloor, near-surface, and deep subsurface: AAPG 2000 annual meeting, Annual Meeting Expanded Abstracts, American Association of Petroleum Geologists, v. 2000, p. 158.

Worrall, D.M., and Snelson, S., 1989, Evolution of the northern Gulf of Mexico with emphasis on Cenozoic growth faulting and the role of salt, *in* Bally, A.W., and Palmer, E.R., eds., The geology of North America—an overview: Boulder, CO, Geological Society of America, v. A, p. 97–138.

Chapter 3

Coring and Gas Hydrate-Related Operations During the IMAGES VIII/PAGE 127 Gas Hydrate and Paleoclimate Cruise on the RV *Marion Dufresne* in the Gulf of Mexico, 2–18 July 2002

William J. Winters[1], Thomas D. Lorenson[2], Charles K. Paull[3], and Yvon Balut[4]

Coring and gas hydrate-related operations during the IMAGES VIII/PAGE 127 gas hydrate and paleoclimate cruise on the RV Marion Dufresne *in the Gulf of Mexico, 2–18 July 2002; chapter 3* in *Winters, W.J., Lorenson, T.D., and Paull, C.K., eds., 2007, Initial report of the IMAGES VIII/PAGE 127 gas hydrate and paleoclimate cruise on the RV* Marion Dufresne *in the Gulf of Mexico, 2–18 July 2002, U.S. Geological Survey Open-File Report 2004–1358.*

Abstract

This chapter is an illustrated overview of activities related to coring, subsequent sediment analyses, sample preservation, and safety-related issues dealing with the handling and storage of gas hydrate samples at sea. During this cruise, 17 giant piston cores up to 38 meters long, 4 giant box cores up to 10 meters long, and 4 gravity cores up to 9 meters long were recovered along high-resolution seismic reflection transects in widely different geologic environments and in water depths ranging from about 560 to 2,260 meters. Gas hydrate was recovered in three cores at subbottom depths of about 3 to 9 meters, and gas bubbles indicative of gas hydrate dissociation were noticed in a fourth core. Seventeen successful passive heat-flow measurements to subbottom depths of 17 meters were also made at locations near piston-core sites.

Introduction

Gas hydrate, an ice-like crystalline solid containing high concentrations of methane, is a potential energy resource. It is also a potential hazard to hydrocarbon exploration and production, and may influence global climate change. Although the amount of gas hydrate in the natural environment is inferred to be enormous, little is known about its distribution in shallow sediment or even exactly how it forms. Exploring these and other questions were among the goals of a July 2002 cruise conducted within three continental slope regions of the northern Gulf of Mexico (Tunica Mound, Bush Hill, and the east and west flanks of Mississippi Canyon). The work was supported by the French Polar Institute [Institut Polaire Francais – Paul-Emile Victor (IPEV)] and the U.S. Geological Survey (USGS), and employed a giant piston coring system using the 120.5-meter (m)-long French research vessel (RV) *Marion Dufresne* (fig. 1).

Figure 1. RV *Marion Dufresne* is 120.5 meters in overall length and is 20.6 meters in beam amidships. It has a draft of 6.95 meters and displaces 10,380 tonnes. Coring operations are conducted using the starboard stern A frame.

[1]U.S. Geological Survey, 384 Woods Hole Road, Woods Hole, MA 02543 USA.

[2]U.S. Geological Survey, 345 Middlefield Road, MS–999, Menlo Park, CA 94025 USA.

[3]Monterey Bay Aquarium Research Institute, 7700 Sandholdt Road, Moss Landing, CA 95039 USA.

[4]Institut Polaire Francais – Paul-Emile Victor, Technopole Brest Iroise – BP75, Plouzane, 29280 France.

Seventeen giant Calypso piston cores of up to 38 m in length (500 m total recovery) and 2 box cores (14 m total recovery) were collected for gas hydrate-related studies (tables 1, 2). The cores were used for study of the potential distribution of natural gas hydrate using geochemical analyses of pore water (Ussler and Paull, this volume, chapter 8) and gas samples (Lorenson and others, this volume, chapter 9). In addition, physical property (Winters and others, this volume,

Table 1. Core information including location, water depth, recovered core length, and core type.

[ID, identification; deg, degrees; m, meters; PC, piston core; C2 (box), square box core; GHF, gravity core with heat-flow temperature sensors attached; Grav, gravity core without thermal sensors; **, denotes successful determination of geothermal gradient]

Core ID	Latitude (deg)	Longitude (deg)	Site name	Water depth (m)	Core length (m)	PC	C2 (box)	GHF	Grav	Comments
MD02-2535	27.6198	-92.2410	Tunica Mound	605	37.84	*				
MD02-2536GHF-1	27.6198	-92.2410	Tunica Mound	608	8.88			**		
MD02-2536GHF-2	27.6253	-92.2460	Tunica Mound	564	8.88			**		
MD02-2536GHF-3	27.6270	-92.2375	Tunica Mound	585	8.88			**		
MD02-2537	27.6160	-92.2487	Tunica Mound	600	33.58	*				
MD02-2538G	27.6167	-92.2472	Tunica Mound	599	7.76				*	
MD02-2539	27.6397	-92.1922	Tunica Mound	622	31.1	*				
MD02-2540GHF-1	27.6403	-92.1920	Tunica Mound	617	5.65			**		
MD02-2540GHF-2	27.6402	-92.1952	Tunica Mound	620	-			*		
MD02-2541	27.6325	-92.2123	Tunica Mound	615	35.34	*				
MD02-2542GHF	27.6322	-92.2120	Tunica Mound	617	7.7			**		
MD02-2543G	27.6123	-92.2555	Tunica Mound	579	0.15				*	
MD02-2544G	27.6130	-92.2535	Tunica Mound	584	0.1				*	
MD02-2545G	27.6140	-92.2517	Tunica Mound	588	9.27				*	
MD02-2546	27.6157	-92.2470	Tunica Mound	595	31.21	*				
MD02-2547GHF	27.6165	-92.2483	Tunica Mound	607	5.73			**		
MD02-2548	27.6375	-92.1995	Tunica Mound	610	32.92	*				
MD02-2550C2	26.9462	-91.3457	Orca Basin	2,249	9.09		*			
MD02-2553C2	27.1835	-91.4167	Pigmy Basin	2,259	10.03		*			
MD02-2554	27.7833	-91.4990	Bush Hill Basin	602	31.05	*				
MD02-2555	27.7832	-91.4892	Bush Hill Basin	636	35.68	*				
MD02-2556	27.7830	-91.4775	Bush Hill Basin	654	34.25	*				
MD02-2557GHF-1	27.7830	-91.4987	Bush Hill Basin	613	7.59			**		
MD02-2557GHF-2	27.7830	-91.4890	Bush Hill Basin	639	-			**		
MD02-2557GHF-3	27.7828	-91.4805	Bush Hill Basin	659	-			**		
MD02-2559	28.2225	-89.0882	Kane Spur	1,132	33.39	*				
MD02-2560	28.2433	-89.1550	Kane Spur	1,029	28.24	*				
MD02-2561	28.2052	-89.0202	Kane Spur	1,268	28.8	*				
MD02-2562	28.0798	-89.1402	Kane Spur	1,051	26.09	*				
MD02-2563C2	28.1233	-89.1363	MC853 Diapir	1,070	3.86		*			recovered hydrate (gas bubbles)
MD02-2564GHF-1	28.2433	-89.1545	Kane Spur	1,027	7.63			**		
MD02-2564GHF-2	28.2223	-89.0883	Kane Spur	1,261	-			**		
MD02-2564GHF-3	28.2052	-89.0200	Kane Spur	1,269	-			**		

Table 1. Core information including location, water depth, recovered core length, and core type. — Continued

[ID, identification; deg, degrees; m, meters; PC, piston core; C2 (box), square box core; GHF, gravity core with heat-flow temperature sensors attached; Grav, gravity core without thermal sensors; **, denotes successful determination of geothermal gradient]

Core ID	Latitude (deg)	Longitude (deg)	Site name	Water depth (m)	Core length (m)	PC	C2 (box)	GHF	Grav	Comments
MD02-2564GHF-4	28.2070	-89.0200	Kane Spur	1,269	-			**		
MD02-2565	28.1235	-89.1395	MC853 Diapir	1,068	22.5	*				recovered hydrate
MD02-2566	28.1192	-89.1032	Kane Spur	1,186	26.05	*				
MD02-2567	28.1002	-89.0198	Kane Spur	1,318	26.65	*				
MD02-2568GHF-1	28.0790	-89.1400	MC853 Diapir	1,049	6.96			**		
MD02-2568GHF-2	28.0810	-89.1370	MC853 Diapir	1,057	-			**		
MD02-2568GHF-3	28.1193	-89.1030	MC853 Diapir	1,190	-			**		
MD02-2568GHF-4	28.1233	-89.1395	MC853 Diapir	1,068	-			*		
MD02-2568GHF-5	28.1235	-89.1362	MC853 Diapir	1,049	-			*		
MD02-2569	28.1522	-89.4797	Mississippi Canyon	1,032	10.35	*				recovered hydrate
MD02-2570	28.0710	-89.6898	West Mississippi	631	28.35	*				
MD02-2571C2	28.0667	-89.7192	West Mississippi	664	10.38		*			
MD02-2572GHF	28.0710	-89.6897	West Mississippi	628	4.9			**		
MD02-2573GHF	28.1520	-89.4798	Mississippi Canyon	1,027	4.2			*		recovered hydrate
MD02-2574	28.6267	-88.2248	East Mississippi	1,963	32.28	*				

Note: Cores obtained during the cruise that are not listed in this table and cores MD02-2548 in Tunica Mound, MD02-2550C2 in Orca Basin, and MD02-2574 in East Mississippi region are IMAGES/PAGE cores, not dedicated USGS cores.

Table 2. Core and sample list.

[cm, centimeters; m, meters]

Core dimensions:
Box core cross section: 25 cm x 25 cm
Calypso piston core, gravity core, gravity heat-flow core size: 10.1-cm diameter
White opaque PVC liner: 10.1-cm-inside diameter, 11.4-cm-outside diameter
Number of cores recovered:
Calypso piston: 17
Box: 4
Gravity: 4
Gravity heat flow: 21 penetrations at 9 stations produced 17 successful determinations of geothermal gradient
Length of core sediment recovered:
Calypso piston: 500 m
Box: 33 m (approx)
Gravity: 17 m
Gravity heat flow: 57 m
Number of samples acquired:
Pore water: 483
Water content/geotechnical: 1,100 (approx.)

chapter 4) and other measurements have been made on core subsamples. Gravity cores were obtained mainly to acquire heat-flow information (Labails and others, this volume, chapter 6) from sensors attached to the perimeter of the core barrel. Detailed station location maps for each area are located in Appendix B of this report. Chirp seismic-reflection data were acquired at all core sites (this volume, Appendix D).

Nine- and 10-m-long box cores were also collected from Orca and Pigmy Basins, respectively, for studies related to the International Marine Past Global Changes Study (IMAGES) program, and Paleoceanography of the Atlantic and Geochemistry (PAGE) program, and for measuring anthropogenic contaminant input of Holocene age to the northern Gulf of Mexico from the Mississippi River (Flocks and Swarzenski, this volume, chapter 13). In addition, the RV *Marion Dufresne* obtained two cores in Tampa Bay for the USGS Tampa Bay project for climate-history studies. Cores collected for paleoclimate studies as part of the IMAGES and PAGE programs were interspersed with the USGS sites.

Figure 3. Calypso piston corer ready to be lowered. Notice the yellow-colored trigger arm attached to the main cable above the weight stand. The main corer is held in position until a weight suspended from the trigger arm contacts the sea floor. As tension on the trigger arm is reduced, the main corer is released and is driven into the sea floor by the massive weight stand.

Piston and Box Coring Systems

The RV *Marion Dufresne* has an unobstructed starboard main deck that allows the deployment (figs. 2, 3) and recovery (figs. 4–6) of IPEV's "Calypso" giant piston corer (fig. 7). This piston-coring system, driven by a 6-tonne weight stand (fig. 8), has recently obtained cores as long as 64.5 m. Much longer cores are obtained with piston-coring systems compared to gravity corers because they use a piston (fig. 9) inside the core liner, which theoretically remains near the level of the sea floor during the coring process (fig. 10). The piston creates a vacuum at the sediment surface that helps overcome the frictional forces between the cored sediment and the internal wall of the barrel liner.

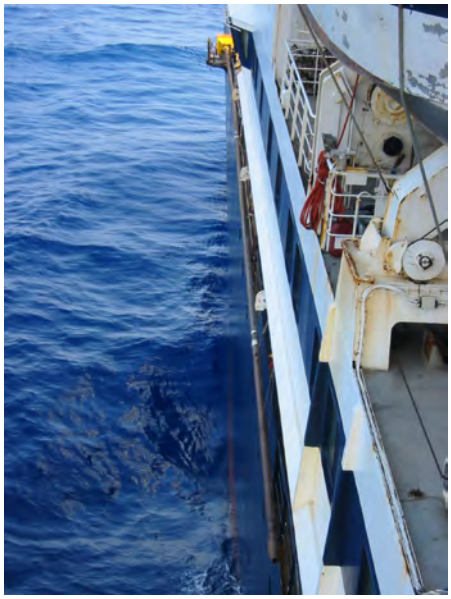

Figure 2. Calypso piston corer about to be pivoted into a vertical position for coring.

A newly designed 11-m-long box core was also used to recover large (25 centimeter (cm) by 25 cm in cross section) sediment samples from shallow subbottom depths (fig. 11). The box cores were driven into the sea floor by using the same weight stand as the piston corer.

Figure 4. Recovery of a Calypso piston corer.

Figure 5. Recovered Calypso piston corer being lowered to the deck.

Figure 6. Recovered Calypso corer ready to be dismantled.

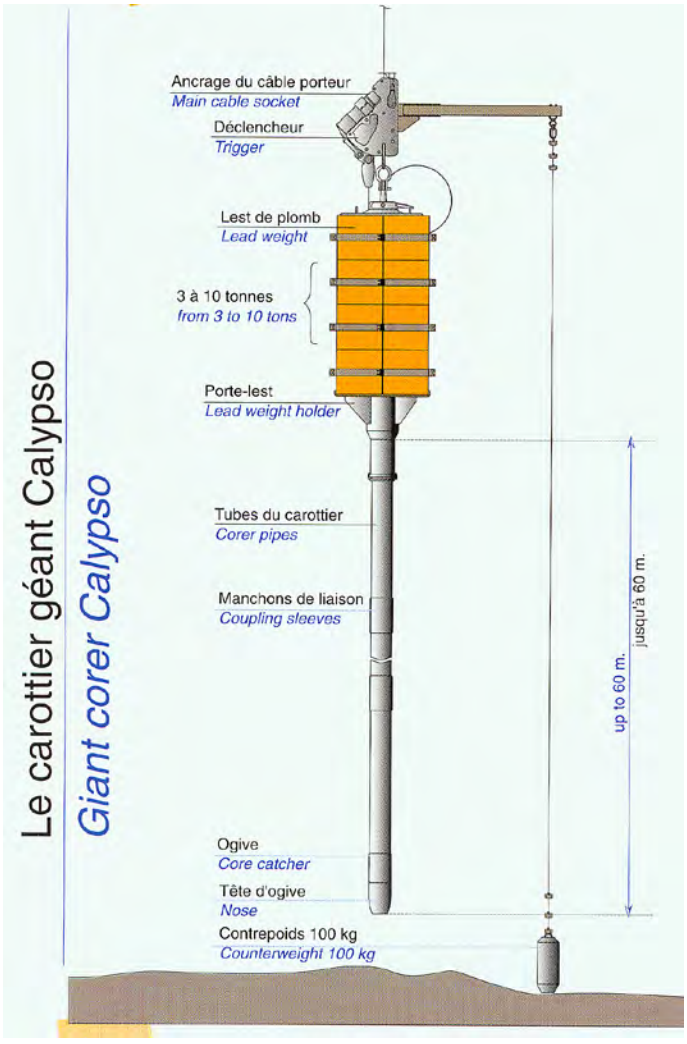

Figure 7. Components of a Calypso giant piston corer (illustration courtesy of Institut Polaire Francais – Paul-Emile Victor).

Figure 8. Weight stand used to drive the core barrel into the sea floor.

Figure 9. A critical component of a piston-coring system is the piston that theoretically remains near the level of the sea floor during sediment penetration by the core barrel. The vacuum that develops between the bottom of the piston and the sediment surface helps overcome the frictional forces between the cored sediment and the internal wall of the barrel liner.

Figure 10. Operation of a Calypso giant piston corer (illustration courtesy of Institut Polaire Francais – Paul-Emile Victor).

Heat-Flow Measurements Using Gravity Corers

Gravity cores (fig. 12) with staggered temperature sensors and recorders (figs. 13–14) were used to determine geothermal gradients to about 17-m-subbottom depth at 17 locations near piston-core sites (table 1). Thermal gradients are important in determining the subbottom extent of gas hydrate stability. Gravity cores obtained during heat-flow measurements supplemented the shallow sediment sections collected at nearby piston-coring sites. Occasionally, multiple heat-flow penetrations were made without changing barrels. A used barrel, containing a sediment core, was slowly towed to another site and dropped, sometimes multiple times. Sediment-related results from these multiple-dropped cores were treated with caution because of the potential for additional sediment penetration at the base of an existing core. For more information about the heat-flow measurement program and results see Labails and others (this volume, chapter 6).

Figure 12. Gravity core with staggered outrigger heat-flow sensors.

Figure 11. Deployment of a box corer.

Figure 13. Installation of a heat-flow sensor onto an outrigger welded to a gravity corer.

Figure 14. Side view of a heat-flow temperature sensor.

Core Handling and Gas Hydrate Recovery

Piston Cores

After Calypso piston cores were brought on deck, a number of procedures were performed sequentially to ensure safe and efficient core processing (fig. 15). To reduce hazards associated with gas overpressures and the presence of toxic gas before general core-related activities began, a small number of scientists used a safety protocol on most of the 17 piston cores recovered for the USGS. As the piston core liner was being removed from the metal core barrel, the liner surface temperature was monitored using an infrared temperature sensor (fig. 16). Holes were drilled at about 1-m

CORE FLOW DIAGRAM

Created 04July2002

INTACT CORE

Core on deck (MD staff)
Core catcher removed and bagged (MD staff)
Liner pulled from barrel (MD staff)
Assess gas hazard (for explosion and H_2S)
(Core cutters must wear safety glasses)
Wipe down liner
Scan core with IR thermal sensor
Determine voids with stud finder
Mark cold sections on liner in colored pen*
Drill holes in liner for temperature probes and to relieve gas *
Insert temperature probes*
Option to cut out cold sections*
Mark missing sections on liner*
Split removed liner containing potential GH* and(or)
Flash freeze in LN_2, or
Conduct dissociation experiments, or
Preserve GH in pressure vessel*
Drill pilot hole and take gas sample
Insert boat hook in top end
Cut at top surface with rotary cutter
Tape cap on top of core
Rotate core so line is on top
Tape measure taped along core
Mark 1.5-m increments from top (account for missing sections)
Mark sections to cut out (10 cm at bottom of each core section and as directed)
Cut out whole round sections
Mark section with core#, interval, and "UP" arrow
Label sections with Top, Base, A, W (archive half is toward the center of the ship, working is toward the water
Label depth intervals, "MD02-core no", sect no (Roman numeral from top)
Cut 1.5-m sections with rotary core cutter and cap ends (cut on
even 150-cm depth marks: 150, 300, 450, 600,…)

Figure 15. Calypso piston core flow diagram.

Move sections to bench by MST van
Place depth labels along longitudinal line for length of core
Mark depth intervals
Bring to thermal conductivity lab
Let temperature equilibrate >4–6 hours
Perform thermal conductivity measurements (on whole round sections)
Move core to bench by MST van
Split section along depth-interval tape

WORKING HALF	ARCHIVE HALF
Bring to phys props lab	Carry to F deck or use lift
Vp, Vs, ER, VS, TV, PP	Scrape core
WC, GD, BD	Sedimentologic description (paper form)
Subsampling	Photograph core (50 cm per shot)
Cover with Saran wrap	Cover with Saran wrap
Place in heavy plastic sleeve and tape ends	Spectrophotometry (every ~1–2 cm)
Place in labeled D tube	MST lab (Main deck)
Place in reefer on Heliport (Deck F)	Temp equilibration (for >1 hour)
	Vp, Mag susc, GRAPE, ER
	Paleomag U-channel
	Place in heavy plastic sleeve and tape ends
	Place in labeled D tube
	Place in reefer on Heliport (Deck F)

* - As needed
Subsamples - in **bold**

BD - Bulk density
ER - Electrical resistivity
GD – Grain density
Mag susc – Magnetic susceptibility
PP – Pocket penetrometer

PV – Pressure vessel
TV – Torvane
Vp – P-wave velocity
Vs – Shear wave velocity
VS – Vane shear strength

Figure 15 (Continued). Calypso piston core flow diagram.

Figure 16. The surface temperature of the core liner was measured with an infrared sensor after it was removed from the metal core barrel.

spacing to relieve potential hazardous gas pressures (figs. 17, 18) and to collect gas samples (figs. 19, 20) for later isotopic analyses (see Lorenson and others, this volume, chapter 9). Digital temperature probes were inserted into the holes after the gas pressure dissipated (figs. 21, 22) and were monitored to find small thermal anomalies suggestive of gas hydrate dissociation. Much of the recovered sediment was highly gas charged, as evidenced by the abrupt expulsion of sediment (figs. 23, 24) (view video*) and gas (fig. 25) (view video*) from holes drilled in the core liner. On occasion, expanding gas also caused sediment to extrude beyond the core liner after it was cut (figs. 26, 27). Because of the highly toxic nature of hydrogen sulfide gas (table 3), we checked cores and subsamples for its presence (fig. 28) to ensure that safe levels were not exceeded on deck or in the inboard laboratories. A few core subsamples had to be removed from laboratories because hydrogen sulfide (H_2S) may have exceeded the safety threshold. A general note on description of "Hazards Associated with Core Overpressures and Hydrogen Sulfide Gas" is presented at the end of this chapter.

*Video is also accessible at AppendixJ/Winters/Mudworms_gas. Software to view video can be downloaded from *http://www.microsoft.com/downloads* (Windows Media Player) or *http://www.apple.com/downloads* (QuickTime).

Figure 17. Immediately after the PVC core liner is pulled from the metal core barrel the surface temperature was determined with a hand-held infrared thermal sensor.

Figure 18. Holes were drilled in the liner at 1-meter intervals to relieve potential gas overpressures, and a digital thermometer was inserted to record internal sediment temperature.

Figure 19. Gas sample being collected from a hole drilled in a Calypso PVC core liner.

Figure 20. Syringe filled with gas to be later analyzed for isotopic composition.

Figure 21. Thermometers were monitored to determine low thermal anomalies suggestive of gas hydrate dissociation.

Figure 22. Digital thermometers were inserted at 1-meter intervals down core.

Figure 23. Highly gas-charged sediment resulted in “mud worms” being extruded from holes drilled in the core liner.

Figure 24. Click here to view video* of gas-charged sediment "mud worms" being extruded from holes drilled in the core liner.

Figure 25. Click here to view video* of gas being extruded from holes drilled in the core liner.

Figure 26. Sediment that "self-extruded" because of gas expansion sometimes needed to be collected on a half-round PVC liner.

Table 3. Hydrogen sulfide characteristics.

Concentration in air		Effects
Percent	Parts per million	
0.001	10	Obvious and unpleasant odor; safe for 8 hours exposure.
0.002	20	Safe for 4 hours exposure.
0.01	100	May not be smelled in 3–15 minutes; may sting eyes and throat.
0.02	200	May not be smelled in a very short period of time; stings eyes and throat.
0.05	500	Dizziness; breathing ceases in minutes; need prompt artificial respiration.
0.07	700	Unconsciousness occurs quickly; death will result if not rescued promptly.
0.1	1,000	Unconsciousness occurs nearly immediately; death occurs within minutes.

Note: For more information on hydrogen sulfide safety, see Foss and Julson, 1993, ODP Technical Note 19, Revised H_2S Drilling Contingency Plan, Ocean Drilling Program, College Station, TX.

Figure 27. Occasionally gas expansion caused sediment to self extrude.

Figure 28. Cores and sediment samples were checked for dangerous levels of hydrogen sulfide gas.

*Video is also accessible at AppendixJ/Winters/Mudworms_gas. Software to view video can be downloaded from *http://www.microsoft.com/downloads* (Windows Media Player) or *http://www.apple.com/downloads* (QuickTime).

Following the safety-related procedures, the white PVC core liner was removed from the metal core barrel, labeled, and cut into 1.5-m lengths using a rotary pipe cutter (fig. 29). Whole-round samples, 10-cm to 25-cm long, were cut from the ends of core sections every 1.5 m (fig. 30). Most of the sediment from the whole rounds was placed in two types of squeezers (fig. 31) to obtain pore water for chloride ion, sulfate ion, and methane concentration analyses, performed within a mobile geochemistry van operated by the Monterey Bay Aquarium Research Institute (MBARI) (fig. 32). A total of 483 pore-water samples were obtained during the cruise. Other sediment was frozen for microbiological studies (Hallam and others, this volume, chapter 10). The remaining intact whole-round (and split) sections were stored at 4 degrees Celsius (°C) (fig. 33) for subsequent shore-based testing, including stress history and other geotechnical studies. Intact whole-round samples were also retained for isotopic gas geochemistry analyses to determine the source of the gas (Lorenson and others, this volume, chapter 9).

Figure 29. After the PVC core liner was removed from the metal core barrel, it was labeled and cut into 1.5-meter lengths.

Figure 32. Pore water samples extracted from sediment were analyzed for the concentration of chloride and sulfate ions in a portable geochemistry van.

Figure 30. Whole-round samples, 10-centimeter to 25-centimeter long, were cut from the ends of core sections every 1.5 meters.

Figure 33. Core sections were refrigerated at approximately 4 degrees Celsius during storage.

Figure 31. Laboratory containing multiple Reeburg-style squeezers to extract pore water from sediment samples.

After whole-round samples were removed on deck, the remaining sections were measured for thermal conductivity (fig. 34) after temperature equalization. Then the cores were split longitudinally (fig. 35). The archive half was brought into the sedimentology lab (fig. 36) where its lithology was described (Bout-Roumazeilles and Trentesaux, this volume, chapter 5), color recorded with a spectrophotometer (fig. 37), digitally photographed, and run through a Multi-Sensor Core Logger (MSCL) (fig. 38) for measurement of density, P-wave velocity, magnetic susceptibility, and electrical properties (Bout-Roumazeilles and Trentesaux, this volume, chapter 5; Winters and others, this volume, chapter 4).

Figure 34. Thermal conductivity measurements were performed on whole-round core sections using a needle probe after the sediment temperature equilibrated.

Figure 35. The core was longitudinally split after whole-round sections were removed.

Figure 36. The archive half of longitudinally-split cores were lithologically described, recorded for color with a spectrophotometer, and digitally photographed in the sedimentology laboratory.

Figure 37. Sediment color on the archive-half split core was recorded with a spectrophotometer.

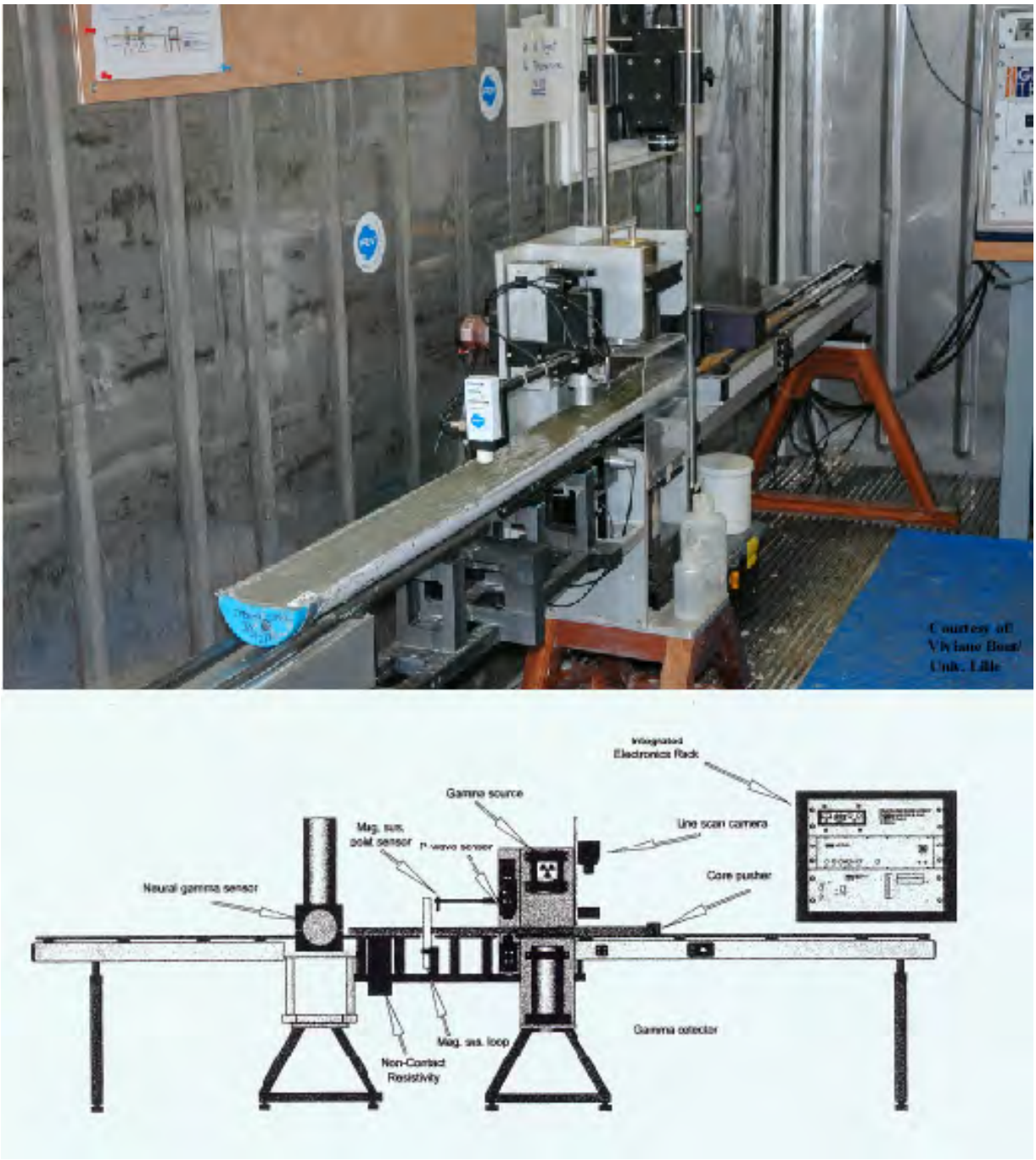

Figure 38. Multi-Sensor Track (MST) used for determining physical properties on a longitudinally-split core section.

The working half of the core was brought into the physical properties laboratory for the determination of electrical resistivity, P-wave velocity, water content, and shear strength by mini-lab vane (fig. 39), torvane (fig. 40), and pocket penetrometer. Approximately 1,100 water-content samples were acquired during the cruise. Post-cruise grain-density and grain-size analyses were conducted in USGS laboratories in Woods Hole, MA (Winters and others, this volume, chapter 4).

The core-barrel length used at each site was determined after viewing seismic records, which are indirectly related to sea-floor hardness and potential core penetration. Occasionally, core barrels did not achieve optimal penetration. If the length of core barrel remaining above the sea floor after penetration was too long, the barrel would buckle, bend (fig. 41), or even break (figs. 42, 43) due to the force exerted by the mass of the essentially unsupported weight stand. These bent cores were difficult to recover and resulted in extra time being spent to cut the barrels into manageable lengths (fig. 44).

Figure 39. A suite of physical property measurements were made on the working half of the cores. A mini-vane shear machine is located in the foreground.

Figure 40. The working half of the split cores was subsampled for water content and other properties. A Torvane test is being performed in the foreground.

Figure 43. Although most of the core barrel broke during the coring operation, enough strength existed in the remaining barrel and liner to enable retrival of the core.

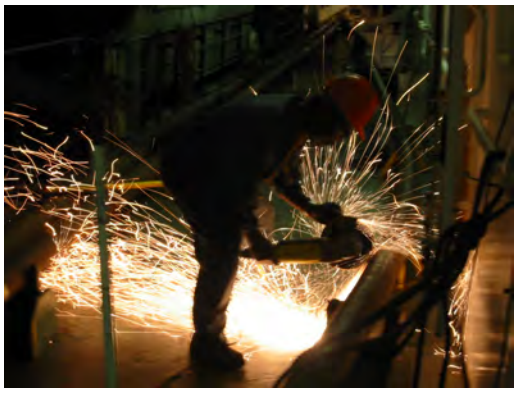

Figure 44. Bent barrels were cut into more manageable lengths after recovery.

Figure 41. Bent core barrels required special handling procedures.

Figure 42. The core barrel would actually break if enough stress was placed on it during the coring and recovery process.

Box Cores

Removable panels that covered one side of the box core frame were not pressure tight (fig. 45); thus, the box cores are not likely to become overpressured after recovery. However, the cores were checked for the presence of hydrogen sulfide gas.

After the metal side panels were removed from the IMAGES cores (fig. 46), the sediment surface was scraped (fig. 47), U-channels were pushed into the sediment (fig. 48), and the core was tipped on its side (figs. 49, 50). Archive U-channel

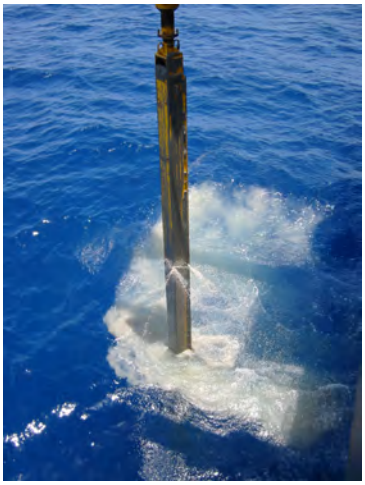

Figure 45. Recovery of a box core. Notice the spray of water exiting between joints in the frame. Unlike Calypso piston cores, box cores could not be overpressured from gas expansion or gas hydrate dissociation.

Figure 46. Top panels being removed from a box corer. Notice the pyramid shape to the recovered sediment at the bottom of the core.

Figure 47. Sediment surface being scraped to enhance interpretation of stratigraphic features.

cores were removed (fig. 51) and processed in the sedimentology lab. Working U-channel cores were sampled for paleoclimate and other analyses. Sediment remaining in the corer was subsampled for various studies (fig. 52), including physical properties and pore-water geochemistry (fig. 53). Strength was also determined using a pocket penetrometer. Dedicated gas hydrate box cores were not tipped on their side during subsampling. As with piston cores, sediment temperature was measured using digital-reading probes (fig. 54). Hydrocarbon presence was noticed in some box cores (figs. 55–58).

Figure 51. Removal of a U-channel from a box core.

Figure 48. U-channels being pushed into a box core.

Figure 49. A box core about to be tipped onto its side.

Figure 52. Subsampling a box core. After removal of U-channel samples.

Figure 50. A box core on its side. Notice the styofoam plug at the top of the core used to stabilize the soft sediment surface.

Figure 53. Sediment from a box core being placed into a sample holder that will be used to squeeze pore water from the sediment pore spaces.

Figure 54. A dedicated USGS box core being subsampled. Sediment in the foreground is being placed into a pore water sample holder. This core, MD02-2563C2, located on a large diapir in the MC853 lease area, was saturated with liquid hydrocarbons.

Figure 57. The hydrocarbons had a sticky consistency that did not allow easy removal from surfaces.

Figure 55. Hydrocarbons recovered in box core MD02-2563C2.

Figure 58. Hydrocarbons recovered in box core MD02-2563C2. Notice the pen tip in the lower right corner of the photograph.

Figure 56. Hydrocarbons recovered in box core MD02-2563C2. Notice the filament-like, viscous nature of the hydrocarbons.

Gas Hydrate Recovery

A hand-held infrared camera was used to measure surface core-liner temperatures during extrusion from the metal core barrel. A decrease in temperature, resulting from the endothermic cooling caused by gas hydrate dissociation, typically is the first indication of the presence of hydrate. In order to retrieve samples of gas hydrate, short sections were cut out of the cores at locations of temperature anomalies (fig. 59). For example, in core MD02-2565, typical liner temperatures of 23 to 24 °C were measured. However, temperatures between 10 and 19 °C were observed proximal to gas hydrate occurrences. A thermometer inserted into the hydrate-containing sediment layer displayed an internal temperature of 4 °C. Temperatures recorded on the liner surface for core MD02-2569 typically ranged from 23 to 24 °C, except near gas hydrate-bearing zones, which had liner-surface temperatures of 19 to 21 °C.

Gas hydrate was recovered in three different cores at a maximum subbottom depth of about 8.2 m. The gas

Figure 59. Removal of core sections containing gas hydrate was based on low sediment liner surface or internal sediment temperature anomalies. Samples were immediately placed in the liquid nitrogen Dewar shown next to the core.

hydrate in core MD02-2565 was disseminated within fine-grained sediment and was associated with the presence of nearby hydrocarbons, whereas the gas hydrate recovered in core MD02-2569 consisted of massive veins that filled the entire cross section of the core liner (figs. 60, 61). Those pieces typically were at least 2 cm thick. This implies that we cored continuous layers of gas hydrate of some unknown lateral extent. Hydrate samples recovered from cores were preserved in liquid nitrogen (fig. 62) or in a freezer kept at a temperature of –80 °C for post-cruise, shore-based laboratory testing.

Figure 60. Gas hydrate chunks recovered from Calypso giant piston core MD02-2569. The sediment clinging to the gas hydrate was washed away with water from the bottle.

Figure 61. Gas hydrate chunks recovered from Calypso giant piston core MD02-2569.

Figure 62. Recovered hydrate samples were preserved in liquid nitrogen.

The generation of gas caused by hydrate dissociation was spectacularly demonstrated when the upper several meters of core MD02-2565 blew vertically out the end of the core barrel as the weight stand was removed, flew at least 10 m into the air, and landed in the waters next to the ship. The gas hydrate remained on the surface of the water because of its low density and floated away as it dissociated.

The recovered cores are currently available for further scientific study upon application to the Integrated Ocean Drilling Program at Texas A&M University in College Station, TX.

Summary

During this cruise, 17 giant piston cores (as much as 38-m long), 4 giant box cores (4 to 10-m long), and 4 gravity cores were recovered in widely different geologic environments in water depths ranging from about 560 to 2,260 m. The cores were used to predict the regional distribution of natural gas hydrate using geochemical analyses of pore water and gas samples. Physical properties and a host of other measurements were also obtained from at-sea and shore-based analyses. Gravity cores, instrumented with temperature-sensing outriggers, were attempted at 21 different sites adjacent to piston-core locations. From those penetrations, 17 successful determinations of geothermal gradient were obtained.

Gas hydrate was recovered in three cores at subbottom depths of about 3 to 9 m, and gas bubbles indicative of gas hydrate dissociation were noticed in a fourth core. Safety protocols to relieve potential sediment overpressures and to monitor hazardous gas concentrations were implemented on cores that could potentially contain gas hydrate.

Box cores from Orca and Pigmy Basins were collected for measuring anthropogenic contaminant input of Holocene age to the northern Gulf of Mexico from the Mississippi River. Cores collected for paleoclimate studies were interspersed with the USGS sites as part of the IMAGES and PAGE programs.

Acknowledgments

Captain Jean-Michel Nicolas and the crew of the RV *Marion Dufresne* are thanked for their assistance in performing shipboard activities. Cruise logistical support was provided by the French Polar Institute [Institut Polaire Francais – Paul-Emile Victor (IPEV)].

Considerable at-sea help was provided by an international group of about 40 scientists under the IMAGES and PAGE programs. The IMAGES program is an international effort to understand the mechanisms and consequences of climatic changes using the oceanic sedimentary record.

Financial support of USGS-related activities was provided by the USGS Coastal and Marine Geology Program, the USGS Energy Program, and the U.S. Department of Energy's Gas Hydrate Program.

The U.S. Minerals Management Service provided information used to determine core locations and avoid existing sea-floor infrastructure.

The Integrated Ocean Drilling Program provided facilities to store and archive recovered cores.

Metadata from the cruise, including navigation, personnel, and core locations, are available on the Internet at the USGS Web site *http://walrus.wr.usgs.gov/infobank/d/d102gm/html/d-1-02-gm.meta.html* .

A Note on the Hazards Associated with Core Overpressures and Hydrogen Sulfide Gas: Safety Procedure Applied During RV *Marion Dufresne* Giant Piston Coring Operations

Some unusual hazards can be associated with cores collected from gas and gas hydrate-rich environments. These include problems associated with generating very elevated gas pressures and with the release of hydrogen sulfide, a highly poisonous gas.

1. Pressure problems: The exsolution of gas from pore water within the core liners can produce highly pressurized gas pockets. As the pressure builds, various things can happen. In some cases, gas pockets have caused material to shoot violently out of the end of the core liner. The Ocean Drilling Program (ODP) has had some sections of core liner explode on the deck and shoot fragments of the liner several meters away.

2. Hydrogen sulfide: Some sea-floor gas seeps are known to be associated with high concentrations of dissolved hydrogen sulfide, which will escape from the cores when they depressurize at the surface. Hydrogen sulfide is an extremely poisonous gas. Exposure to hydrogen sulfide at even modest levels can be fatal to humans. In small concentrations, the hydrogen sulfide smells like "rotten eggs." However, as the concentration increases, humans are no longer able to smell it. Thus, people are in most danger when they no longer smell hydrogen sulfide. Hydrogen sulfide is also a heavy gas; it settles into low areas; therefore, closed areas and areas on the lower decks of the ship are sites of greatest danger.

During this cruise, we will be coring in environments that are very similar to those in which other groups have experienced these problems.

Procedures:

1. Initial assessment of core gas hazards will be made by USGS watch leaders and IMAGES watch chiefs. Treat the core barrel and core liner like the barrel of a gun and never stand in its "fire path." The people inspecting the cores initially should wear eye protection. Holes may be drilled in the liner to release gas pressure. Please stay 10 m from the exposed core liner until the watch chiefs give an "all clear."

2. If initial contact with the core indicates a strong scent of hydrogen sulfide on deck, the deck chiefs will commence a sulfide caution.

   A. First step is to close off all the companionways and vents that could allow the sulfide to enter from the coring deck. Signs should be posted on the main companionways to indicate that they are closed to traffic. People should only use companionways on the upper decks.

   B. The bridge should be notified and, if possible, head into the wind and make enough way to generate a breeze.

   C. In a severe case, the bridge will announce that a gas hazard exists and request that all personnel seek refuge outside and as high as possible. Two areas are recommended, forward on the bow and on the helicopter deck. It could take several hours for the gas to vent from the core. Please stay outside and upwind until the bridge announces that it is "all clear."

Chapter 4

Physical Properties of Sediment Obtained During the IMAGES VIII/PAGE 127 Gas Hydrate and Paleoclimate Cruise on the RV *Marion Dufresne* in the Gulf of Mexico, 2–18 July 2002

William J. Winters[1], Ivana Novosel[2], Olya Boldina[3], William F. Waite[1], Sarah A. Kelsey[1], and Benjamin W. Hallett[1]

Physical properties of sediment obtained during the IMAGES VIII/PAGE 127 gas hydrate and paleoclimate cruise on the RV Marion Dufresne *in the Gulf of Mexico, 2–18 July 2002; chapter 4* in *Winters, W.J., Lorenson, T.D., and Paull, C.K., eds., 2007, Initial report of the IMAGES VIII/PAGE 127 gas hydrate and paleoclimate cruise on the RV* Marion Dufresne *in the Gulf of Mexico, 2–18 July 2002: U.S. Geological Survey Open-File Report 2004–1358.*

Abstract

This chapter summarizes the physical property measurements performed on sediment samples obtained in the northern Gulf of Mexico during July 2002. During this cruise on the RV *Marion Dufresne*, 17 giant piston cores up to 38-meters long, 4 giant box cores up to 10-meters long, and 8 gravity (heat flow) cores up to 9-meters long were recovered in widely different geologic environments in water depths ranging from about 580 to 2,260 meters. Gas hydrate was recovered in three cores at subbottom depths of about 3 to 9 meters, and gas bubbles indicative of gas hydrate dissociation were noticed in a fourth core. Numerous shipboard measurements were performed, including shear strength (mini-vane, Torvane, and pocket penetrometer) and electrical resistivity. Water content, grain-density, grain-size, and carbon content measurements were performed in a shore-based laboratory on samples collected at sea. Bulk density, porosity, and unit weight were determined from phase relations.

Introduction

Gas hydrate, an ice-like crystalline solid containing high concentrations of methane, is a potential energy resource. It is also a potential hazard to hydrocarbon exploration and production, and may influence global climate change. Although the amount of gas hydrate in the natural environment is inferred to be enormous, little is known about its distribution in shallow sediment or even exactly how it forms. Exploring these and other topics was among the goals of a July 2002 cruise conducted on board the research vessel (RV) *Marion Dufresne* within four continental slope regions of the northern Gulf of Mexico (Tunica Mound, Orca and Pigmy Basins, Bush Hill, and the Mississippi Canyon region) (fig. 1).

Determining physical properties of core sediment is a useful complement to sedimentologic studies (see Bout-Roumazeilles and Trentesaux, this volume, chapter 5), petrophysical analyses, and well-log interpretations. These measurements are important to relate the location of gas hydrate occurrences to the physical nature of the host material. These data also are used in a variety of modeling investigations, and similar data have been correlated with engineering behavior (Lambe and Whitman, 1969; Holtz and Kovacs, 1981).

Seventeen giant Calypso piston cores up to 38 meters (m) in length (500-m total recovery) and 2 box cores (designated either C2 or C[2]) (14-m total recovery) were collected for gas hydrate-related studies (Winters and others, this volume, chapter 3) (figs. 2–4). Eight gravity cores, rigged to measure

[1]U.S. Geological Survey, 384 Woods Hole Road, Woods Hole, MA 02543 USA.

[2]Rice University, Department of Earth Science, 6100 Main Street, Houston, TX 77005 USA.

[3]Moscow State University, Department of Geology, Chair of Geocryology, Moscow, Russia 119992.

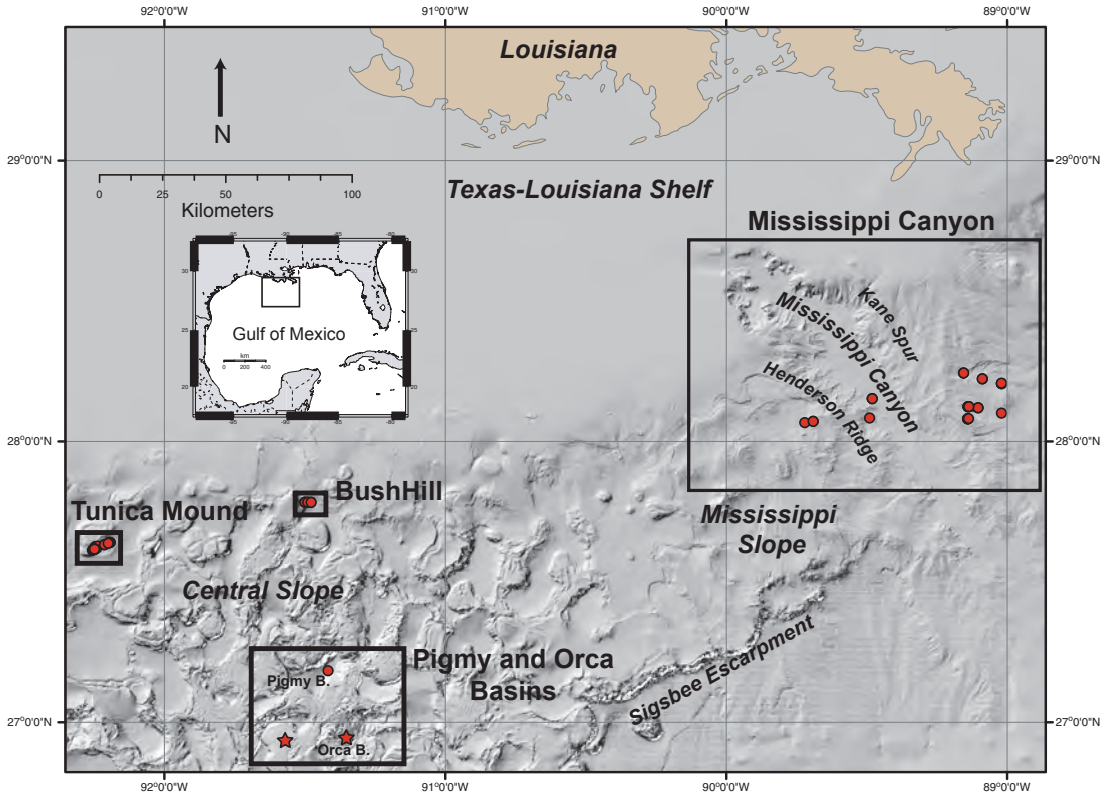

Figure 1. Northern Gulf of Mexico study areas.

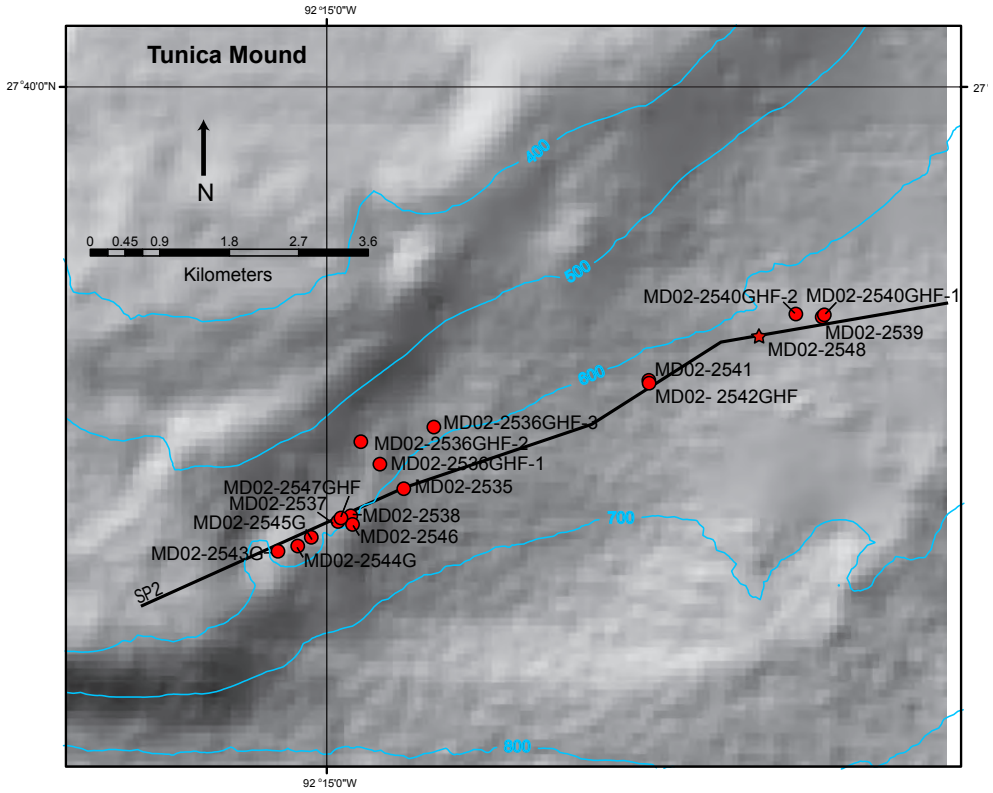

Figure 2. Core locations in Tunica Mound region.

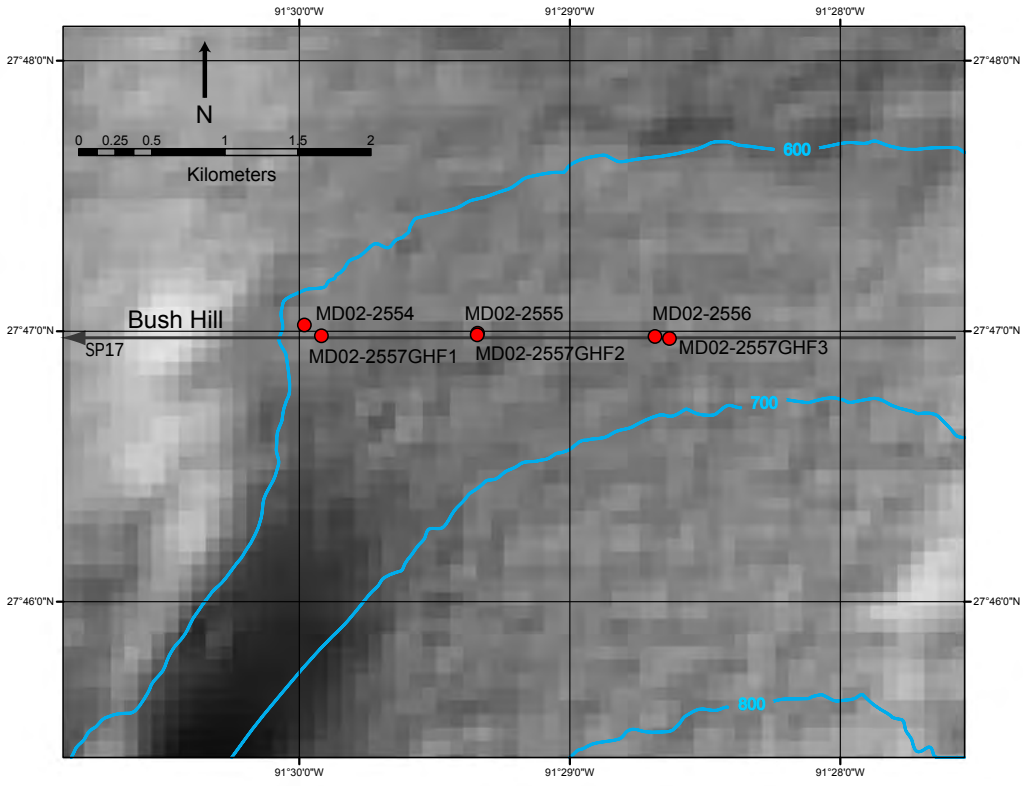

Figure 3. Core locations in Bush Hill region.

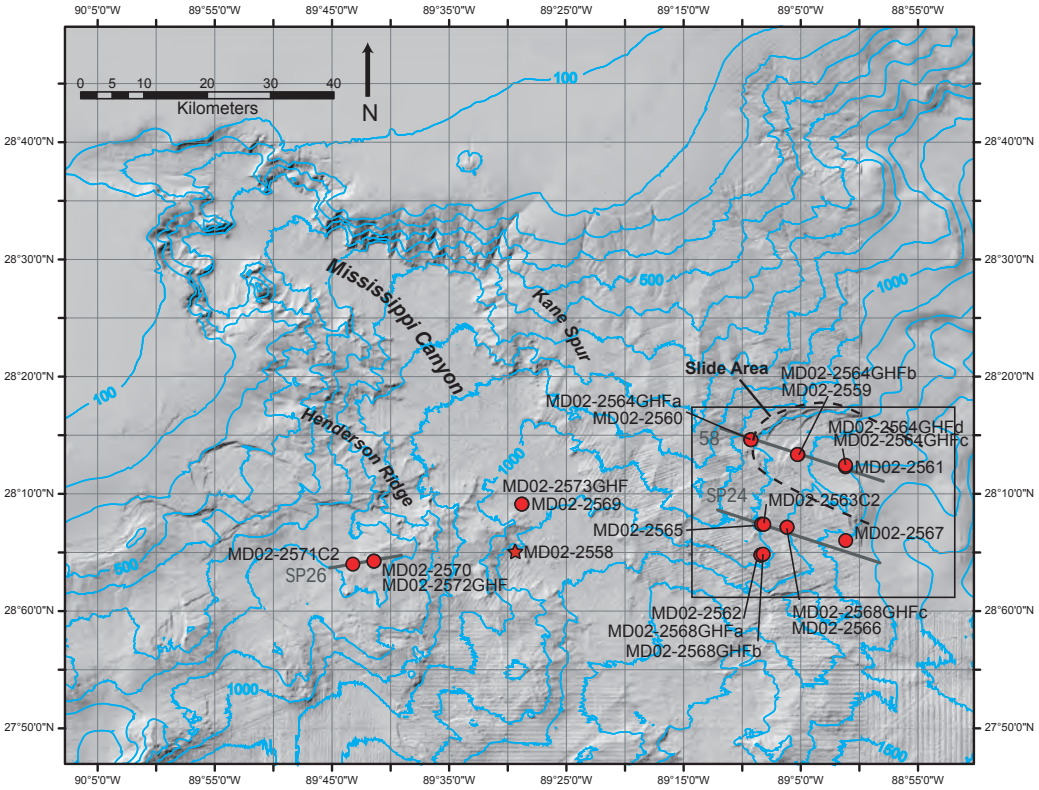

Figure 4. Core locations in Mississippi Canyon region.

in-place temperature, were also obtained as part of a heat-flow study (Labails and others, this volume, chapter 6). In addition, 9-m and 10-m-long box cores were taken from Orca and Pigmy Basins (fig. 5), respectively, for studies related to the International Marine Past Global Changes Study (IMAGES) program and Paleoceanography of the Atlantic and Geochemistry (PAGE) program, and for measuring anthropogenic contaminant input of Holocene age to the northern Gulf of Mexico from the Mississippi River (Flocks and Swarzenski, this volume, chapter 13).

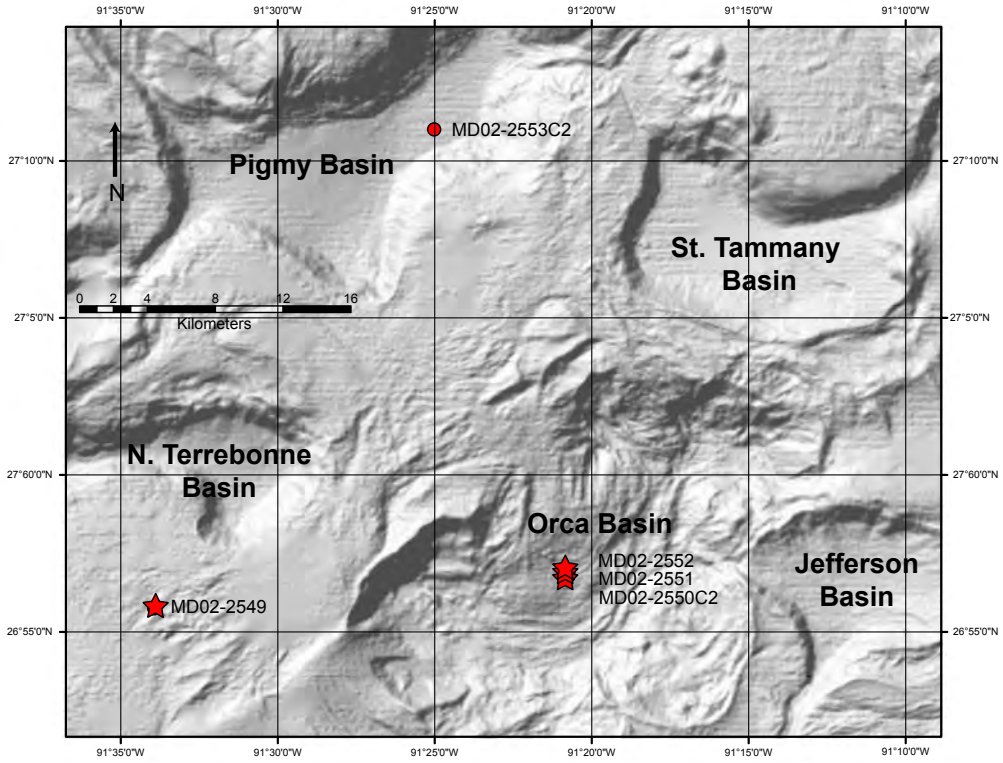

Figure 5. Core locations in Pigmy and Orca Basins region.

Numerous shipboard geotechnical measurements were performed on longitudinally split cores, including shear strength (mini-vane, Torvane, and pocket penetrometer) and electrical resistivity. Water content, grain-density, grain-size, and carbon content measurements were performed in shore-based laboratories on samples collected at sea. Bulk density, porosity, void ratio, and unit weight were determined from phase relations.

Geologic Setting and Gas Hydrate Presence

The northern Gulf of Mexico hosts numerous near-sea-floor (<7-m subbottom) occurrences of gas hydrate. The sea floor is dominated by salt-tectonic basin structures, high sedimentation rates, and complex stratigraphy with common sea-floor failures (Cooper and Hart, 2002). Natural oil and gas seeps are abundant, usually associated with fault conduits resulting in numerous hydrocarbon vents, often capped by gas hydrate when the seeps are within the hydrate stability zone. Whereas gas hydrate is relatively common at the sea floor, the lack of geophysical indicators on seismic records leaves the existence of deeper gas hydrates unresolved. Thus, it is unknown if there are significant gas hydrate accumulations in reservoir sediments away from structural conduits inferred to underlie the sea-floor mounds. Additional discussion of the geologic setting of the northern Gulf of Mexico is provided in Lorenson and others (this volume, chapter 2), and seismic reflection profiles for regional and core locations are presented in Appendix D.

Gas hydrate has been inferred from Bottom Simulating Reflections (BSR's) in many continental margins around the world (Kvenvolden and Lorenson, 2001). However, they are noticeably rare in the northern Gulf of Mexico. This may be in part because of the complicated geologic nature of the subsurface, including various geothermal gradients and hyper-saline pore waters that influence the formation of hydrate deposits.

Gas hydrate was recovered in three cores at subbottom depths of about 3 to 9 m, and gas bubbles indicative of gas hydrate dissociation were noticed in a fourth core. Because of safety concerns, however, entire cores containing gas hydrate typically were not split on board ship. Instead, subsectioned intervals surrounding gas hydrate occurrences in the cores were visually observed.

Methods and Equipment

Shipboard Measurements

Coring and procedures related to handling the giant piston cores, box cores, and gravity cores collected during this cruise are discussed in Winters and others (this volume, chapter 3). After thermal conductivity measurements were performed on whole-round core sections (Novosel and others, this volume, chapter 7), the cores were split longitudinally, and the working half-round cores were brought into the shipboard

physical properties laboratory for further analysis. After electrical resistivity measurements were completed, shear strength was determined using a mini-vane shear strength apparatus. Pocket penetrometer and Torvane shear strength measurements were then performed. Lastly, subsamples to be used for shore-based water content, grain-density, and grain-size measurements were obtained by removing sediment (typically with a spatula) from areas proximal to the previously performed shear strength measurements. The subsamples were placed into Whirl-Pak plastic bags and stored in a refrigerator at a temperature of approximately 4 degrees Celsius (°C) to minimize pore-water evaporation and biological effects.

Electrical Resistivity

To minimize evaporation and thereby preserve pore-water salinity, electrical resistivity measurements were performed on freshly split core sections. The measurements were typically performed every 1.5 m, in the vicinity of a thermal conductivity measurement. The measurements were omitted if the sediment was visibly altered during core recovery or if evidence of gas expansion was present.

The equipment was designed by D. Heffer, D. Mosher, and T. Hewitt of the Geological Survey of Canada (GSC). The measuring device consisted of a 4-pin Wenner array and a digital temperature probe. The pins were gold plated and approximately 3 millimeters (mm) in length, separated from each other by 2 mm. The outer two pins were connected to a circuit board with an AC voltage source acting through current-limiting resistors. The inner two pins were connected to a Fluke voltmeter. The entire instrument was connected to a PC through an RS-232 output, thus allowing all raw data processing and display to be automated.

Electrical resistivity, R, is defined by the following formula:

$$R = \frac{V}{I * C},$$

where

V is voltage,
I is current, and
C is a cell constant.

The cell constant was determined using seawater prior to each sediment measurement. Standard seawater has a known resistivity, R_W, which can be described by the following formula:

$$R_W = (2.8 + 0.1 * T)^{-1},$$

where T is the temperature, in degrees Celsius.

Measurement of the temperature, voltage, and current for a standard seawater sample allows the cell constant to be determined. The instrument is thus calibrated by adjusting the cell constant until R_W equals 0.209 ohm-meters for a temperature of 20 °C.

Sample resistivity, R_O, was derived using the following formula (Hewitt, 1998):

$$R_O = R * (1 + 0.025 * (T - 20)),$$

where

R is the measured sample resistivity, uncorrected for temperature; and
T is the temperature, in degrees Celsius.

A Labview data logging and processing program, written by T. Hewitt, calculated resistivity formation factor, F, using the following relation:

$$F = \frac{R_O}{R_W}.$$

Errors produced by small variations in the depth of the pin penetration into the sediment were assumed to be negligible.

Shear Strength

Shipboard miniature-vane shear tests were performed at approximately 1.5-m intervals down core with a 12.7-mm-diameter by 12.7-mm high four bladed vane. Vane shear strength tests were performed proximal to the sites of the thermal conductivity and electrical resistivity measurements. The vane was inserted so that the top of the vane was one vane height deep into the sediment and was turned by applying a constant rotation rate to the top of a calibrated spring. Because the sediment shear strengths throughout the study areas were similar, only one spring was used. Vane shear strength, Svs, was determined from:

$$Svs = \tau \gamma / K,$$

where

τ is a spring constant relating differential rotation across the spring to applied torque;
γ is the spring rotation required to reach maximum torque at failure, in degrees; and
K is the vane constant (Hewitt, 1998) relating shear strength to torque applied to the vane.

If cracking, which invalidates the measurement, was observed during shear, the measurement was not reported.

A pocket penetrometer (Hunt, 1984) was also used to determine shear strength. This device consists of a 6.35-mm diameter spring-loaded plunger that was pushed to a depth of 6.35 mm into the exposed sediment surface. A direct reading scale indicates the unconfined compressive strength (UCS) in kilograms per square centimeter. The maximum shear strength

that can be determined with this device is 220 kilopascals (kPa).

Pocket penetrometer shear strength, Spp, is determined from:

$$Spp\ (kPa) = UCS\ (kg/cm^2) * 49,$$

where UCS is the unconfined compressive strength reading from the pocket penetrometer strength scale.

If very soft sediment was tested, a 25.4-mm-diameter adapter was applied to the end of the plunger. The maximum shear strength that can be determined with the adapter is 13.8 kPa.

If this adapter was used, the shear strength, Spp, is determined from:

$$Spp\ (kPa) = UCS\ (kg/cm^2) * 3.1,$$

where UCS is the unconfined compressive strength reading from the pocket penetrometer strength scale.

A Torvane device (Hunt, 1984) was also used to measure the shear strength, Stv, near the exposed sediment surface of the longitudinally split cores. This device is operated by inserting a 25-mm-diameter eight-bladed adapter 5 mm into the exposed sediment surface. The top of the spring-loaded Torvane is rotated, thereby producing a torque that shears the sediment. A pointer records the maximum torque value, which is proportional to the shear strength. One full revolution of the Torvane top produces a shear strength value of approximately 100 kPa.

Shore-Based Measurements

Physical property index measurements, including water content, grain density, and grain size, were performed post-cruise at the U.S. Geological Survey, Woods Hole, MA. Other properties, such as porosity, wet and dry bulk density, void ratio, and unit weights, were calculated from the index properties. Carbon content of the sediment was also determined.

Water Content and Index Properties

Because sediment subsamples were irregular in shape, making volume difficult to measure, phase relations were back-calculated, assuming 100-percent water saturation of the pore voids. Visible drainage from the core sections at sea was not observed, primarily because of the fine-grained nature of the sediment.

The specimens were oven dried incrementally at temperatures between 50 and 110 °C for at least 24 hours at each temperature to obtain the amount of fresh water and solids present. Results for samples dried at the 110 °C temperature are presented in this report. The effect of drying at the lower temperatures will be made available in a subsequent report. After drying, the specimen was broken into finer-sized particles, and the volume of dried solids was determined with an automatic gas pycnometer, using helium as the purge and expansion gas (American Society for Testing and Materials, 1997). The grain density of the pycnometer specimen was calculated using the measured volume and the mass of solids that was determined immediately prior to insertion of the sample into the pycnometer. All mass determinations were made quickly and sealed containers were used to prevent moisture in the air from being adsorbed by clay minerals that may have been present.

All physical property calculations, except those specified, were corrected for the presence of residual salt left on the solid particles after driving off the pore fluid by oven drying. In the natural environment, salt and other particles that are dissolved in the pore fluid behave as part of the aqueous phase. The calculations remove the salt precipitate mass and volume from the solids and add it back to the fluid phase. A default 35 parts per thousand (ppt) value of pore-fluid salinity was assumed for samples without a nearby salinity measurement.

The following equations were used in calculating the physical property values:

$$\rho_d = M_S/V_t$$

where

ρ_d is the dry bulk density,
M_S is the mass of solid sediment grains, and
V_t is the calculated total specimen volume;

$$\rho_W = M_t/V_t$$

where

ρ_w is the wet bulk density,
M_t is the total mass of the specimen, and
V_t is the calculated total specimen volume;

$$\gamma_d = (M_S/ V_t)\ g$$

where

γ_d is the dry unit weight,
M_S is the mass of solid sediment grains,
V_t is the calculated total specimen volume, and
g is the constant of acceleration due to gravity;

$$\gamma_W = (M_t/ V_t)\ g$$

where

γ_w is the wet unit weight,
M_t is the total mass of the specimen,
V_t is the calculated total specimen volume, and
g is the constant of acceleration due to gravity;

$$\gamma_{sub} = [(M_t / V_t)\, g] - \gamma_{sw}$$

where

γ_{sub} is the submerged unit weight,
M_t is the total mass of the specimen,
V_t is the calculated total specimen volume,
g is the constant of acceleration due to gravity, and
γ_{sw} is the unit weight of seawater;

$$\rho_s = M_{ss}/V_{ss}$$

where

ρ_s is the uncorrected grain density,
M_{ss} is the mass of solid sediment grains plus mass of salt, and
V_{ss} is the volume of the sediment grains and salt measured with a gas pycnometer;

$$\rho_{sc} = M_s/V_s$$

where

ρ_{sc} is the corrected grain density,
M_s is the mass of solid sediment grains without salt, and
V_s is the volume of the sediment grains without salt measured with a gas pycnometer;

$$n = V_{sw}/(V_s + V_{sw})$$

where

n is the porosity based on calculated specimen volume,
V_{sw} is the volume of seawater, and
V_s is the volume of solid sediment grains;

$$e = V_v/V_s$$

where

e is the void ratio,
V_v is the volume of voids (assumed equal to volume of seawater), and
V_s is the volume of solid sediment grains;

$$WC_t = M_{fw}/M_t$$

where

WC_t is the uncorrected water content based on the total specimen mass,
M_{fw} is the mass of fresh water in the pore space, and
M_t is the total mass of the specimen;

$$WC_s = M_{fw}/M_{ss}$$

where

WC_s is the uncorrected water content based on the solid grain mass,
M_{fw} is the mass of fresh water in the pore space, and
M_{ss} is the mass of the solid sediment grains and residual salt;

$$WC_{tc} = M_{sw}/M_t$$

where

WC_{tc} is the corrected water content based on the total specimen mass,
M_{sw} is the mass of seawater in the void space, and
M_t is the total mass of the specimen;

$$WC_{sc} = M_{sw}/M_s$$

where

WC_{sc} is the corrected water content based on the solid grain mass,
M_{sw} is the mass of seawater in the void space, and
M_s is the mass of the solid sediment grains without residual salt.

Grain Size

A sediment subsample was dried in a convection oven at 90 °C to obtain the dry mass and water content of the sample. The dry mass was corrected for the salinity of the pore water. The sample was then wet-sieved through a number 230 sieve (0.062-mm opening) to separate the sand fraction from the silt and clay fraction. Because of the potential damage to the equipment caused by contamination from hydrocarbons, the typical Coulter Counter (Syvitski, 1991) analysis was not performed on these samples. Rather, the fine-grained material was further classified using a hydrometer technique (Syvitski, 1991). Most of the tests included enough readings to define the silt-clay boundary; however, some tests included additional readings to better define the entire grain-size distribution curve.

Carbon Analysis

The Carbon-Hydrogen-Nitrogen (CHN) Analyzer (Verardo and others, 1990) uses a combustion method to convert sample elements to simple gases, such as CO^2, H_2O, and N_2. The resulting gases are homogenized, depressurized, and quantified as a function of their thermal conductivities.

In order to measure the amount of organic carbon in sediment samples, the samples were first acidified to remove all inorganic carbonate matter by the addition of sulfurous acid. Using this method, only the organic material was further analyzed by the CHN Analyzer.

Multi-Sensor Core Logger

The Multi-Sensor Core Logger (MSCL) system is an automated apparatus that measures various properties remotely as a core section is conveyed by or through different sensors. During this cruise, P-wave velocity and amplitude, wet bulk density by gamma-ray attenuation, and magnetic susceptibility were measured. The MSCL is further discussed in this report in chapters by Bout-Roumazeilles and Trentesaux (this volume, chapter 5), and Winters and others (this volume, chapter 3). The MSCL operating manual is supplied in Appendix H.

Results and Discussion

The sedimentologic history of marine sediment is partly recorded in its physical characteristics. Additionally, knowing the relative quantity of and relation among the various components making up that sediment enable us to predict how the sediment will react to internal processes and external stresses. Many physical property measurements define those relations between solid sediment grains and occupied non-grain void space.

Water Content and Index Properties

Water content and porosity values are fundamental characteristics of sediment. These values also describe how much water is available to form gas hydrate in the pore space. Although porosity is important to the formation of gas hydrate, absolute values of porosity are not as important as individual pore sizes to the formation of gas hydrate (Winters and others, 1999).

A total of 35 cores were recovered from four different study areas in the northern Gulf of Mexico (table 1; fig. 1), including two cores dedicated for the IMAGES/PAGE program. Statistical information (table 2) and regression equations relating measured properties to subbottom depth (table 3) indicate that most properties fall within several fairly well-defined groups, even though they are from study areas that are considerable distances from each other. Bryant and Trabant (1972) were able to develop statistical relations between water content, shear strength, and bulk density, and subbottom depth in cores within two major areas in the northern Gulf of Mexico. Therefore, it is reasonable that we also are able to present properties that indicate fairly uniform distribution with subbottom depth of physical properties across the northern Gulf of Mexico (except for sediments with hyper-saline pore fluids located in Orca Basin).

Salt-corrected water contents, WCsc, determined for 420 sediment samples ranged from 47.8 to 800.7 percent, with a mean of 94.9 percent, and a median of 75.6 percent (tables 2; 4, p. 29). The higher water content values are from Orca Basin and are related to the presence of dense hyper-saline pore water. Pore-water salinities range from 21.3 to 305.9 ppt for all cores. Values of salinity used in making salt corrections were determined by linearly interpolating between other sediment samples with known salinity (Paull and others, 2005; W. Ussler, Monterey Bay Aquarium Research Institute, oral commun., 2003). Therefore, the salinity values reported in this chapter are to be treated as approximations only.

Table 1. Core information including location, water depth, recovered core length, and core type.

[ID, identification; deg, degrees; m, meters; PC, piston core; C2 (box), square box core; GHF, gravity core with heat-flow temperature sensors attached; Grav, gravity core without thermal sensors; **, denotes successful determination of geothermal gradient]

Core ID	Latitude (deg)	Longitude (deg)	Site name	Water depth (m)	Core length (m)	PC	C2 (box)	GHF	Grav	Comments
MD02-2535	27.6198	-92.2410	Tunica Mound	605	37.84	*				
MD02-2536GHF-1	27.6198	-92.2410	Tunica Mound	608	8.88			**		
MD02-2536GHF-2	27.6253	-92.2460	Tunica Mound	564	8.88			**		
MD02-2536GHF-3	27.6270	-92.2375	Tunica Mound	585	8.88			**		
MD02-2537	27.6160	-92.2487	Tunica Mound	600	33.58	*				
MD02-2538G	27.6167	-92.2472	Tunica Mound	599	7.76				*	
MD02-2539	27.6397	-92.1922	Tunica Mound	622	31.1	*				
MD02-2540GHF-1	27.6403	-92.1920	Tunica Mound	617	5.65			**		
MD02-2540GHF-2	27.6402	-92.1952	Tunica Mound	620	-			*		
MD02-2541	27.6325	-92.2123	Tunica Mound	615	35.34	*				
MD02-2542GHF	27.6322	-92.2120	Tunica Mound	617	7.7			**		
MD02-2543G	27.6123	-92.2555	Tunica Mound	579	0.15				*	
MD02-2544G	27.6130	-92.2535	Tunica Mound	584	0.1				*	
MD02-2545G	27.6140	-92.2517	Tunica Mound	588	9.27				*	

Table 1. Core information including location, water depth, recovered core length, and core type. — Continued

[ID, identification; deg, degrees; m, meters; PC, piston core; C2 (box), square box core; GHF, gravity core with heat-flow temperature sensors attached; Grav, gravity core without thermal sensors; **, denotes successful determination of geothermal gradient]

Core ID	Latitude (deg)	Longitude (deg)	Site name	Water depth (m)	Core length (m)	PC	C2 (box)	GHF	Grav	Comments
MD02-2546	27.6157	-92.2470	Tunica Mound	595	31.21	*				
MD02-2547GHF	27.6165	-92.2483	Tunica Mound	607	5.73			**		
MD02-2548	27.6375	-92.1995	Tunica Mound	610	32.92	*				
MD02-2550C2	26.9462	-91.3457	Orca Basin	2,249	9.09		*			
MD02-2553C2	27.1835	-91.4167	Pigmy Basin	2,259	10.03		*			
MD02-2554	27.7833	-91.4990	Bush Hill Basin	602	31.05	*				
MD02-2555	27.7832	-91.4892	Bush Hill Basin	636	35.68	*				
MD02-2556	27.7830	-91.4775	Bush Hill Basin	654	34.25	*				
MD02-2557GHF-1	27.7830	-91.4987	Bush Hill Basin	613	7.59			**		
MD02-2557GHF-2	27.7830	-91.4890	Bush Hill Basin	639	-			**		
MD02-2557GHF-3	27.7828	-91.4805	Bush Hill Basin	659	-			**		
MD02-2559	28.2225	-89.0882	Kane Spur	1,132	33.39	*				
MD02-2560	28.2433	-89.1550	Kane Spur	1,029	28.24	*				
MD02-2561	28.2052	-89.0202	Kane Spur	1,268	28.8	*				
MD02-2562	28.0798	-89.1402	Kane Spur	1,051	26.09	*				
MD02-2563C2	28.1233	-89.1363	MC853 Diapir	1,070	3.86		*			recovered hydrate (gas bubbles)
MD02-2564GHF-1	28.2433	-89.1545	Kane Spur	1,027	7.63			**		
MD02-2564GHF-2	28.2223	-89.0883	Kane Spur	1,261	-			**		
MD02-2564GHF-3	28.2052	-89.0200	Kane Spur	1,269	-			**		
MD02-2564GHF-4	28.2070	-89.0200	Kane Spur	1,269	-			**		
MD02-2565	28.1235	-89.1395	MC853 Diapir	1,068	22.5	*				recovered hydrate
MD02-2566	28.1192	-89.1032	Kane Spur	1,186	26.05	*				
MD02-2567	28.1002	-89.0198	Kane Spur	1,318	26.65	*				
MD02-2568GHF-1	28.0790	-89.1400	MC853 Diapir	1,049	6.96			**		
MD02-2568GHF-2	28.0810	-89.1370	MC853 Diapir	1,057	-			**		
MD02-2568GHF-3	28.1193	-89.1030	MC853 Diapir	1,190	-			**		
MD02-2568GHF-4	28.1233	-89.1395	MC853 Diapir	1,068	-			*		
MD02-2568GHF-5	28.1235	-89.1362	MC853 Diapir	1,049	-			*		
MD02-2569	28.1522	-89.4797	Mississippi Canyon	1,032	10.35	*				recovered hydrate
MD02-2570	28.0710	-89.6898	West Mississippi	631	28.35	*				
MD02-2571C2	28.0667	-89.7192	West Mississippi	664	10.38		*			
MD02-2572GHF	28.0710	-89.6897	West Mississippi	628	4.9			**		
MD02-2573GHF	28.1520	-89.4798	Mississippi Canyon	1,027	4.2			*		recovered hydrate
MD02-2574	28.6267	-88.2248	East Mississippi	1,963	32.28	*				

Note: Cores obtained during the cruise that are not listed in this table and cores MD02-2548 in Tunica Mound, MD02-2550C2 in Orca Basin, and MD02-2574 in East Mississippi region are IMAGES/PAGE cores, not dedicated USGS cores.

Table 2. Statistical information on sediment properties.

[ppt, parts per thousand; WCtc, water content based on total sample mass corrected for salinity; %, percent; WCsc, water content based on solids mass corrected for salinity; ρsc, grain density corrected for salinity; g/cm^3, grams per cubic centimeter; n, porosity; e, void ratio; ρw, wet bulk density; ρd, dry bulk density; γw, wet unit weight; kN/m^3, kiloNewton per cubic meter; γd, dry unit weight; γsub, submerged unit weight; min, minimum; max, maximum; stnd dev, standard deviation; Svs, vane shear strength; kPa, kilopascal; Spp, pocket penetrometer strength; Stv, Torvane strength; ER, electrical resistivity; FF, formation factor; TC, total carbon; H, hydrogen; N, nitrogen; OC, organic carbon; ON, organic nitrogen; IC, inorganic carbon; IN, inorganic nitrogen]

	Salinity (ppt)	WCtc (%)	WCsc (%)	ρsc (g/cm^3)	n (%)	e	ρw (g/cm^3)
min	21.3	32.4	47.8	2.36	55.7	1.26	1.31
max	305.9	88.9	800.7	3.52	95.7	22.34	1.77
range	284.6	56.6	752.9	1.16	40	21.08	0.46
mean	47.7	45.8	94.9	2.7	68.1	2.47	1.57
median	36.7	43.1	75.6	2.7	66.3	1.97	1.59
stnd dev	42.6	9.6	72.6	0.08	7.6	1.92	0.12

	ρd (g/cm^3)	γw (kN/m^3)	γd (kN/m^3)	γsub (kN/m^3)	Svs (kPa)	Spp (kPa)	Stv (kPa)
min	0.15	12.83	1.44	0.9	6.1	0	0
max	1.2	17.36	11.74	7.28	100	196	49
range	1.05	4.53	10.3	6.38	93.9	196	49
mean	0.86	15.37	8.43	5.2	34.5	15.1	17.1
median	0.91	15.63	8.91	5.5	30.2	8.2	15.7
stnd dev	0.21	1.2	2.03	1.28	19.4	23.9	10.9

	ER (ohm-m)	FF	Grain size				TC (%)
			Gravel (%)	Sand (%)	Silt (%)	Clay (%)	
min	0.26	1.22	0	0.01	5.17	53.81	0.92
max	1.06	5.08	15.18	6.54	40.02	94.71	5.83
range	0.81	3.86	15.18	6.53	34.85	40.9	4.91
mean	0.59	2.8	0.13	0.73	22.32	76.81	2.58
median	0.59	2.83	0	0.24	22.1	76.7	2.61
stnd dev	0.14	0.65	1.24	1.15	7.75	7.76	0.69

	H (%)	N (%)	OC (%)	ON (%)	IC (%)	IN (%)
min	0.22	0.04	0.49	0	0.15	-0.06
max	0.89	0.17	2.19	0.12	4.08	0.08
range	0.67	0.13	1.7	0.12	3.93	0.14
mean	0.56	0.08	1.17	0.07	1.42	0.01
median	0.57	0.07	1.19	0.07	1.41	0.01
stnd dev	0.12	0.03	0.33	0.02	0.56	0.03

Table 3. Equations for physical properties.

[WCsc, water content related to solid grains corrected for pore-water salinity; SD, subbottom depth (mbsf, meters below sea floor); n, porosity; ρw, wet bulk density; Svs, vane-shear strength; Spp, pocket penetrometer strength; Stv, Torvane strength; ER, electrical resistivity; FF, formation factor]

Parameter(s)	Core(s)/Comments	R	Equation
WCsc (%)	SD<15 mbsf; WCsc < 200 %	0.79	SD (mbsf) = 98897 * WCsc ^(-2.1134)
n (%)	SD < 15 mbsf	0.741	SD (mbsf) = 8.859e + 15 * n ^(-8.2159)
ρw (g/cm^3)	SD < 15 mbsf	0.736	SD (mbsf) = 7.3719e-05 * e^(7.4019ρw)
Svs (kPa)	All	0.831	Svs (kPa) = [SD (mbsf) - 0.55]/0.41
Spp (kPa)	0<Spp<18 kPa	0.761	Spp (kPa) = [SD (mbsf) - 0.31]/1.75
Stv (kPa)	All	0.868	Stv (kPa) = [SD (mbsf) - 1.61]/0.77
ER (ohm-m)	All cores (SD > 5 mbsf)	0.611	SD (mbsf) = 52.769 * ER^(3.0051)
FF	All cores (SD > 5 mbsf)	0.612	SD (mbsf) = 0.49145 * FF^(2.9831)

Both water content and porosity decrease significantly between the sea floor and about 10 meters below sea floor (mbsf) (figs. 6–8). Below about 10 mbsf, both properties decrease at a lower rate. The high water content and porosity values near the sea floor may be related to electro-chemical effects between fine-grained particles (with high specific surface) at subbottom depths too shallow for normal compaction to occur (Francisca and others, 2005). This probably is a more accurate explanation for the non-linear sediment behavior as opposed to subbottom depth than disturbance caused by the piston-coring technique for a number of reasons: (1) the sediment characteristics are widespread even in sediment obtained with other coring methods, (2) the grain size is too fine to allow quick changes in water content, (3) strength measurements do not exhibit a similar asymptotic decrease in strength near the sea floor, and (4) the stratigraphic descriptions do not indicate a pervasive disturbed region of sediment in the tops of cores. An exponential curve fit (table 3) for samples shallower than 15 mbsf is in contrast with the linear fit of Bryant and Trabant (1972).

Derived index properties, such as void ratio (fig. 9) and wet bulk density (fig. 10), show trends related to the normal

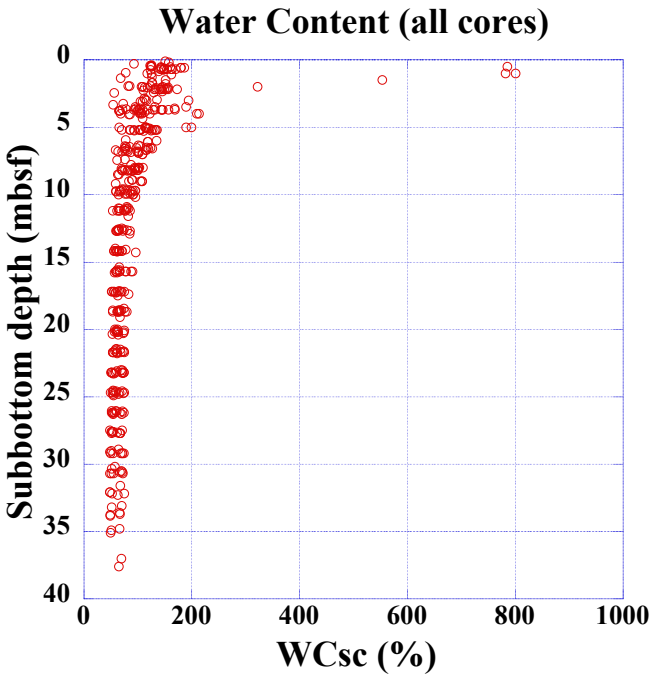

Figure 6. Water content, WCsc, for all cores in relation to subbottom depth.

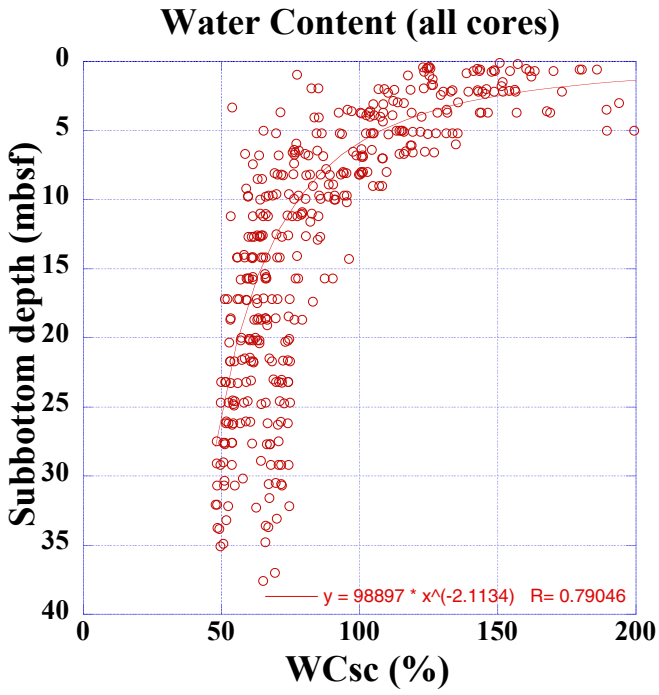

Figure 7. Water content, WCsc, (less than 200 percent) in relation to subbottom depth.

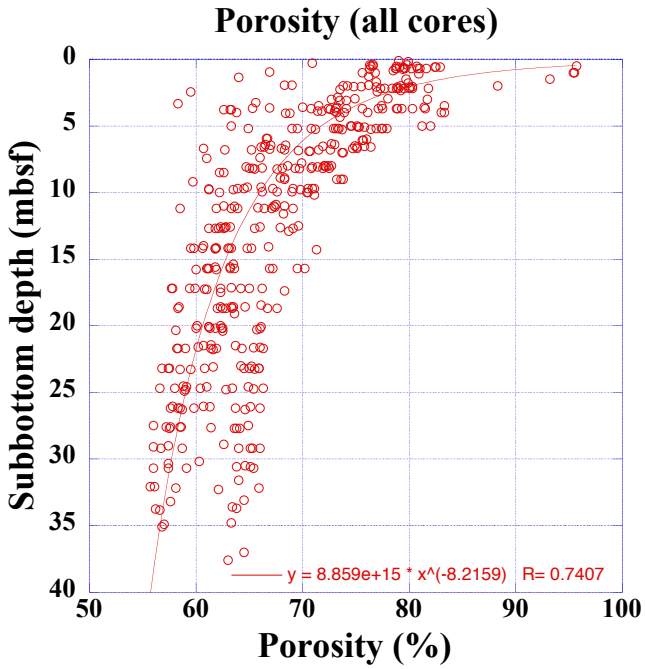

Figure 8. Porosity in relation to subbottom depth.

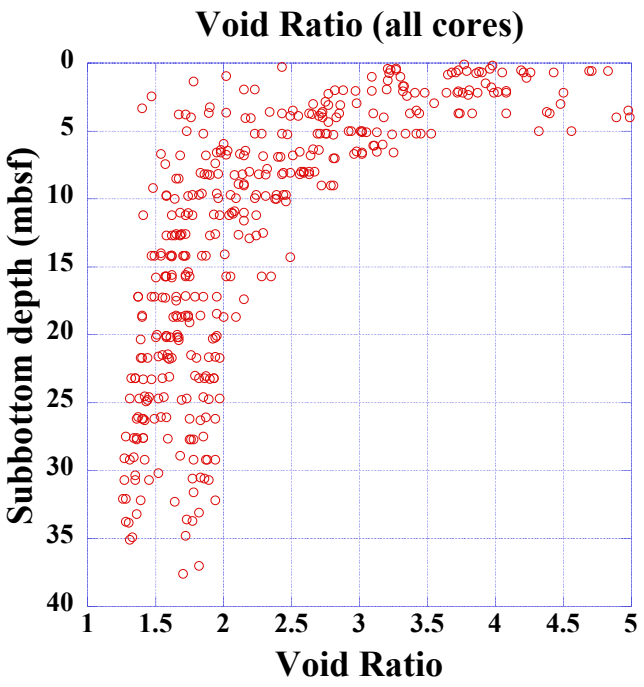

Figure 9. Void ratio in relation to subbottom depth.

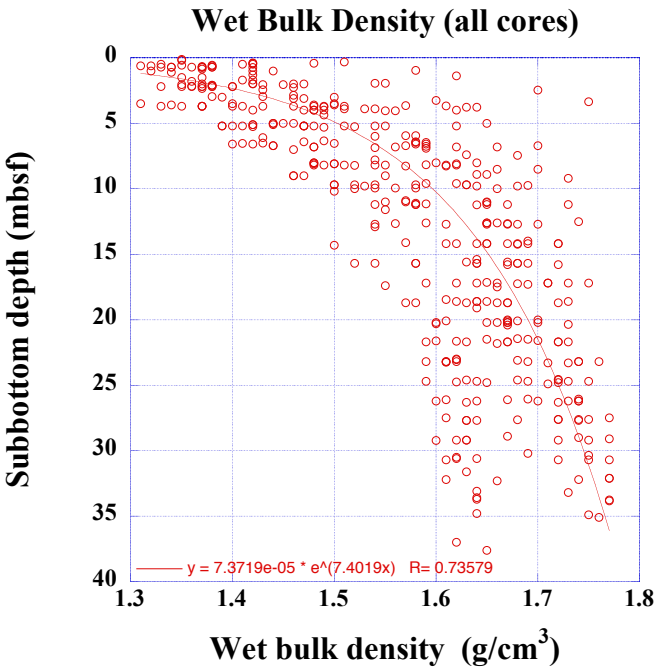

Figure 10. Wet bulk density in relation to subbottom depth.

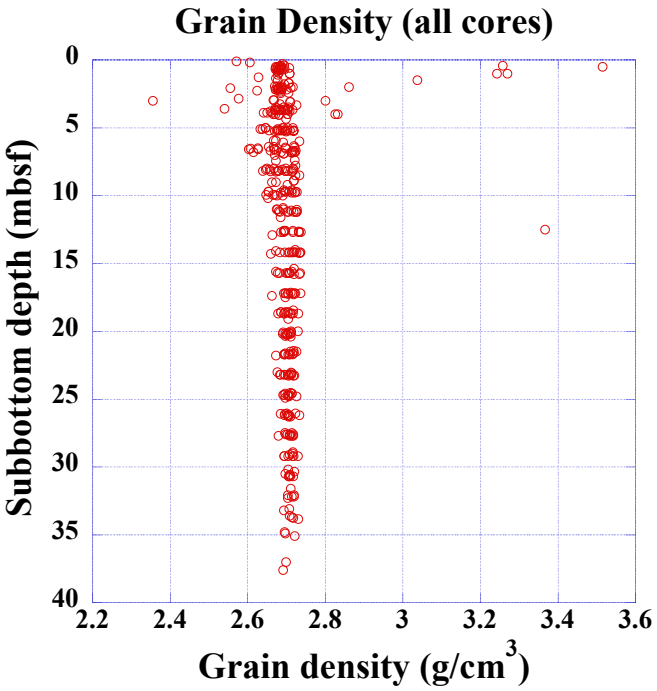

Figure 11. Grain density in relation to subbottom depth.

compaction process, as expected. Void ratio decreases and bulk density increases with depth below the sea floor. Grain density ranges from 2.36 to 3.53 grams per cubic centimeter (g/cm^3) (fig. 11), with a mean and median of 2.7 g/cm^3. Many of the outliers are related to the presence of hyper-saline pore water. At high salinity values, assumptions such as salt density (2.17 g/cm^3) have a much more pronounced effect and can produce considerable uncertainty in calculated values. These extreme values in grain density probably are not real, and caution should be exercised in using values from core MD02-2550C2 from Orca Basin. The values are only reported here because of the uniqueness of the environment from which the core was obtained.

To determine if regional variability occurs in physical properties, water content (figs. 12–17) and porosity (figs. 18–23) profiles from each study area were plotted individually. The change in slope of physical property profiles that occurs between 10 and 15 mbsf is nearly universal across the northern Gulf of Mexico and within each study area. Cores from Orca and Pigmy Basins were not long enough to determine if this sediment behavior is present at those locations. In the Mississippi Canyon, the effect of overburden removal is apparent in the low water content values of core MD02-2569 to a subbottom depth of 10 mbsf.

MSCL results (Appendix H) corroborate the same break in property slope between 10 and 15 mbsf in 9 of 13 of the longer cores. Magnetic susceptibility changes between 10 and 13 mbsf in 7 to 8 of the cores. However, because the indirectly measured values from the MSCL in most cases were not checked by independent physical tests, the data should be used with caution. For example, values of wet bulk density determined with the MSCL were routinely greater than 2.0 g/cm^3, whereas the maximum value determined by oven drying was 1.77 g/cm^3.

Shear Strength

Mini-vane shear strength values range from little or no strength close to the sea floor to as much as 100 kPa near the base of longer piston cores (tables 2; 5, p. 39). Each of the three methods—mini-vane, pocket penetrometer, and Torvane—produced strength values within fairly well-defined

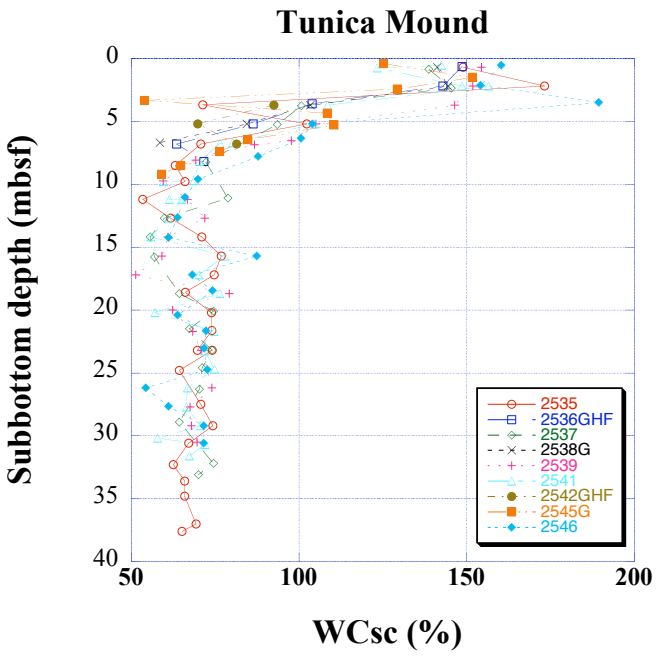

Figure 12. Water content, WCsc, in relation to subbottom depth in the Tunica Mound region.

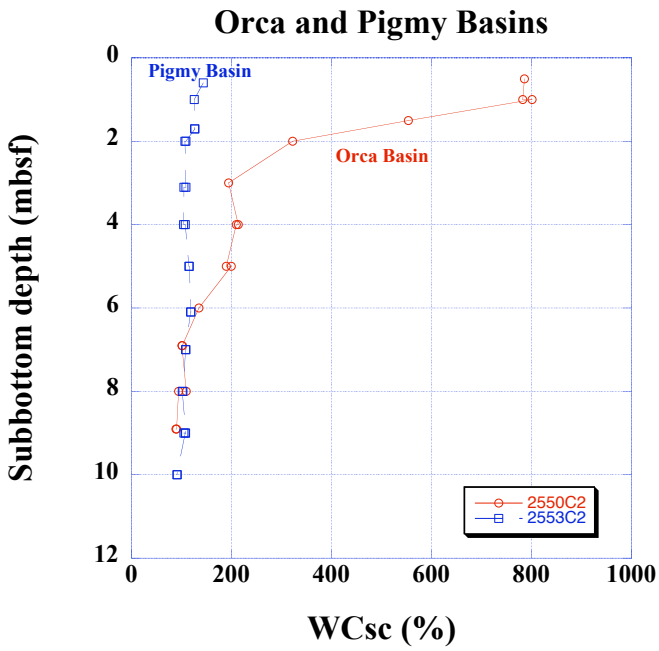

Figure 13. Water content, WCsc, in relation to subbottom depth in the Orca and Pigmy Basins region.

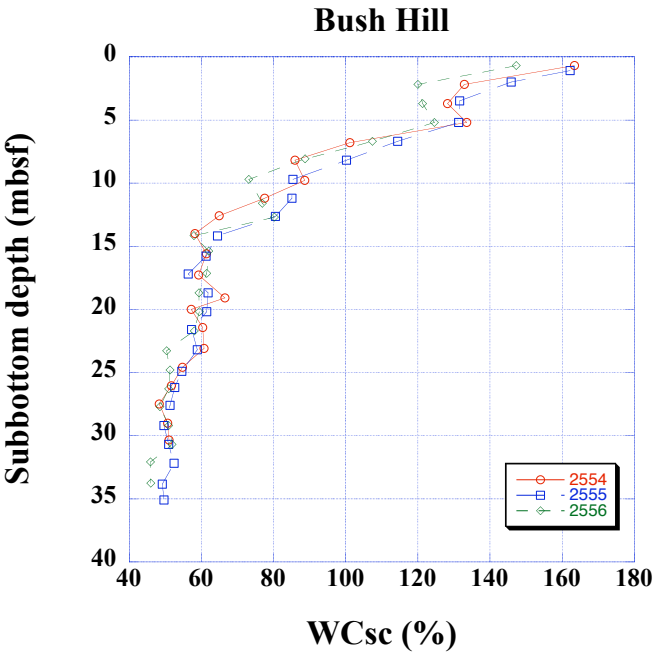

Figure 14. Water content, WCsc, in relation to subbottom depth in the Bush Hill region.

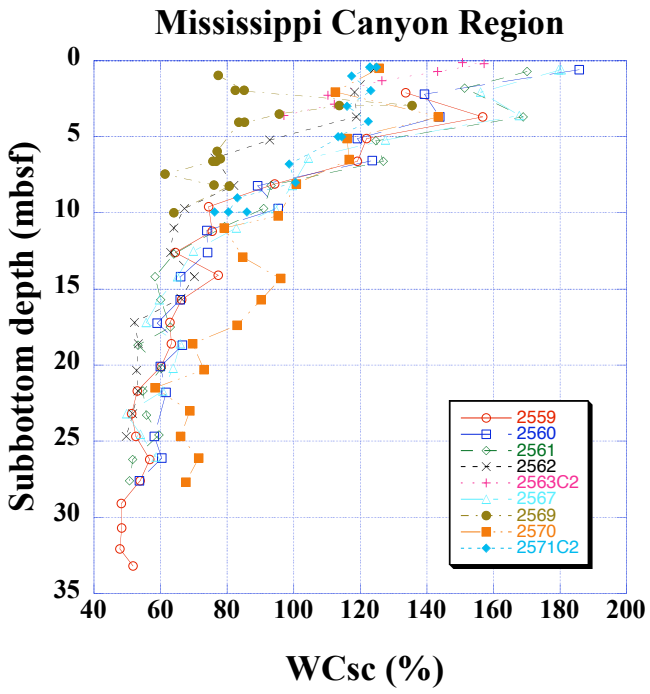

Figure 15. Water content, WCsc, in relation to subbottom depth in the overall Mississippi Canyon region.

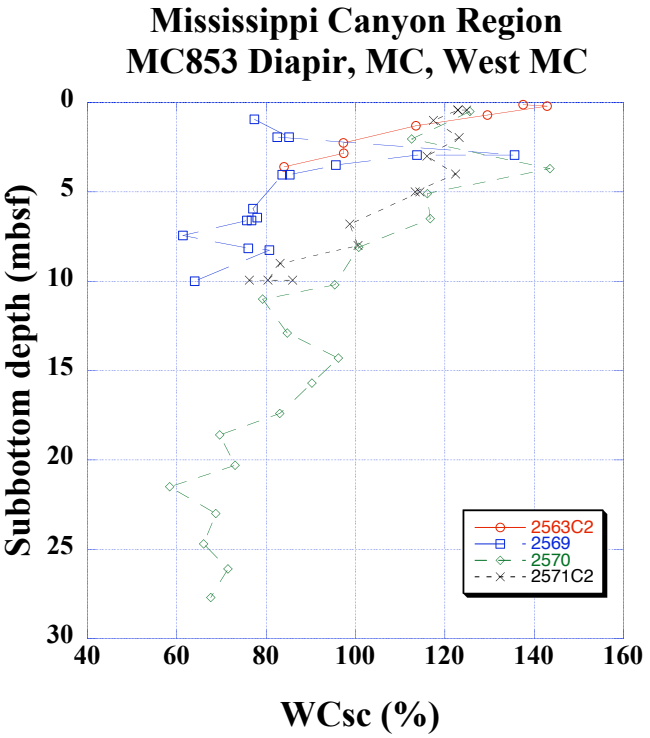

Figure 16. Water content, WCsc, in relation to subbottom depth in West of the Mississippi Canyon (MC), in the Mississippi Canyon, and at the MC853 diapir.

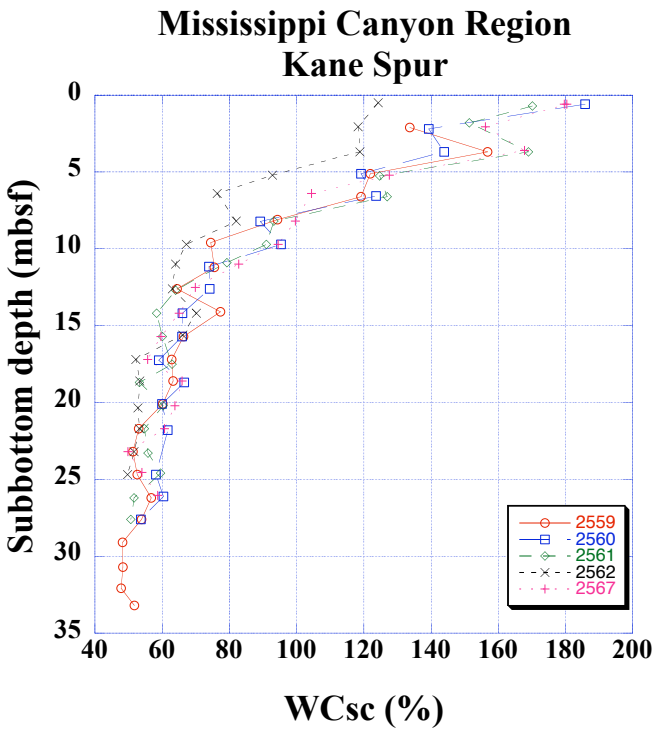

Figure 17. Water content, WCsc, in relation to subbottom depth in the Kane Spur region.

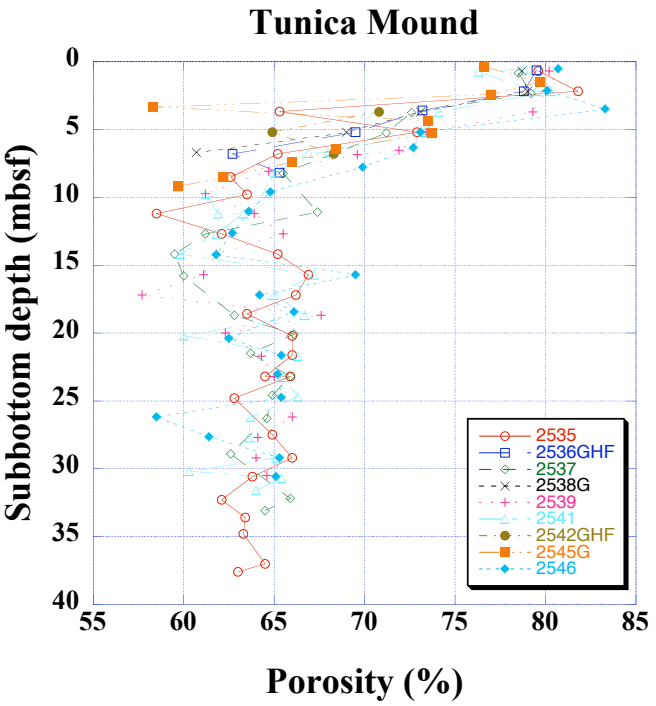

Figure 18. Porosity in relation to subbottom depth in the Tunica Mound region.

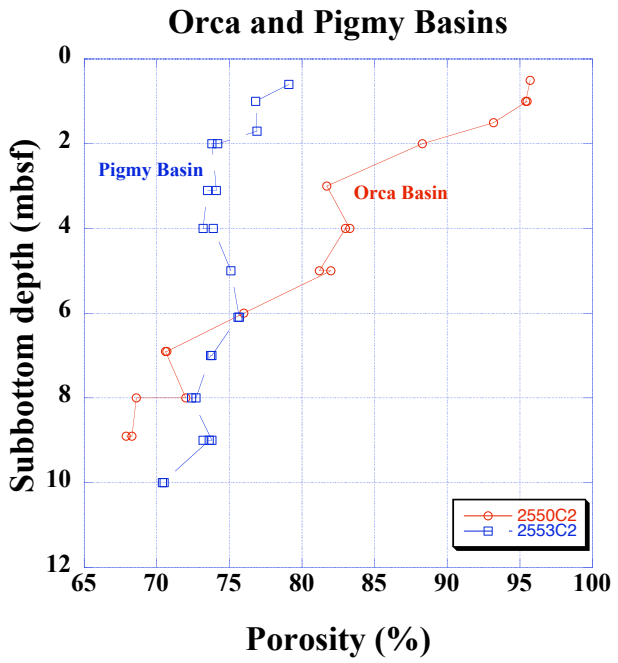

Figure 19. Porosity in relation to subbottom depth in the Orca and Pigmy Basins region.

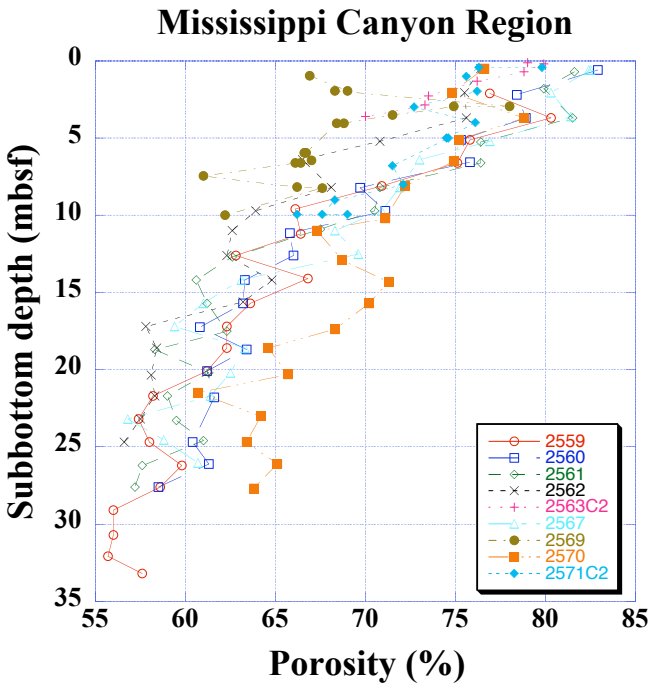

Figure 21. Porosity in relation to subbottom depth in the overall Mississippi Canyon region.

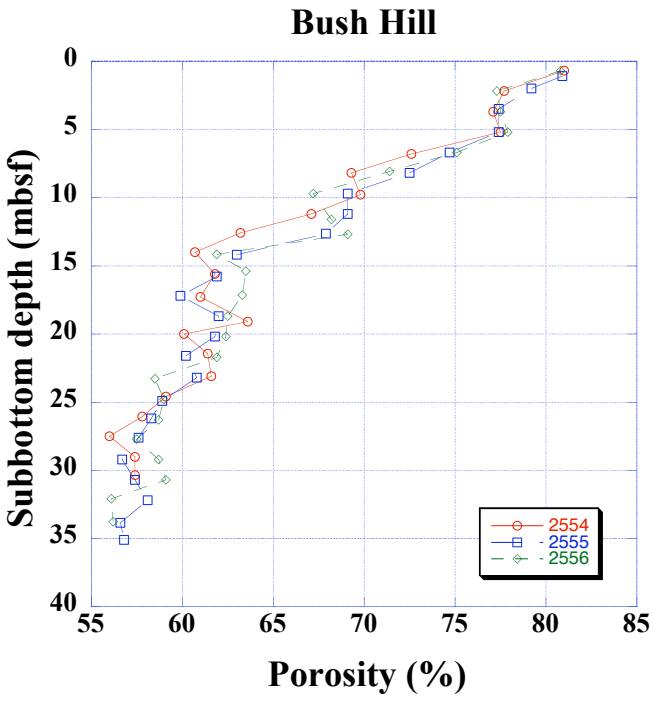

Figure 20. Porosity in relation to subbottom depth in the Bush Hill region.

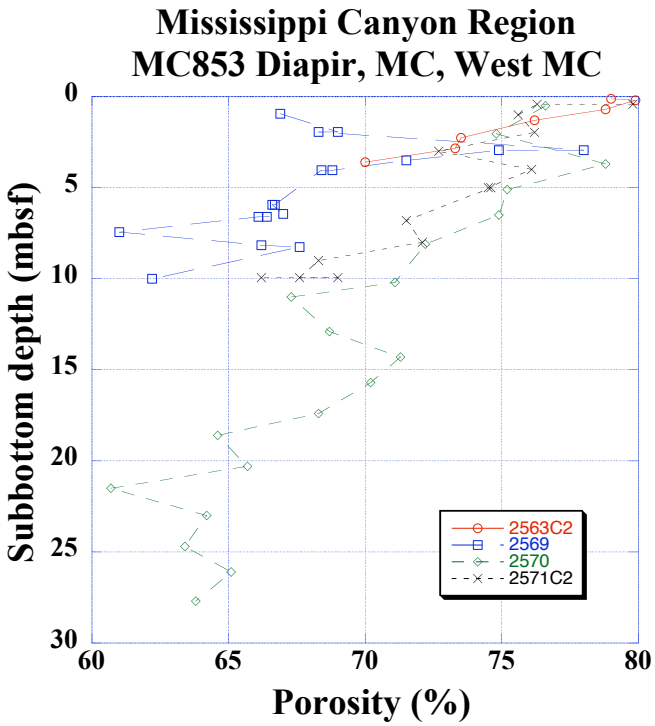

Figure 22. Porosity in relation to subbottom depth in West of the Mississippi Canyon (MC), in the Mississippi Canyon, and at the MC853 diapir.

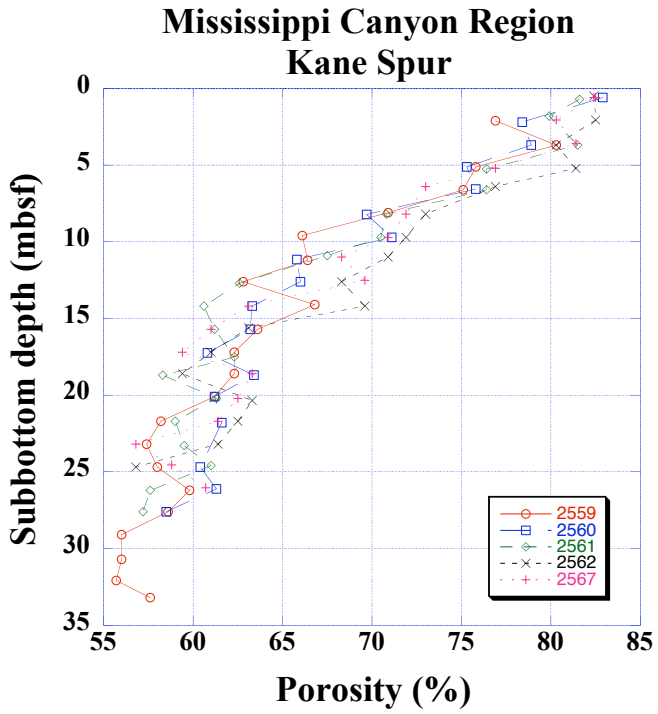

Figure 23. Porosity in relation to subbottom depth in the Kane Spur region.

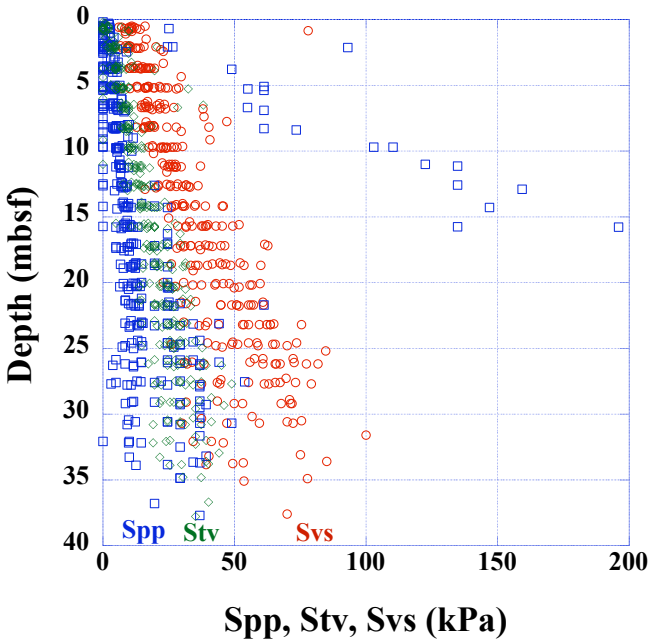

Figure 24. Shear strength results for all cores produced with a pocket penetrometer (Spp), Torvane (Stv), and a mini-vane (Svs), device in relation to subbottom depth.

zones related to subbottom depth (figs. 24–27). Except for some outlying values produced with the pocket penetrometer, the mini-vane strength test invariably produced higher strength results than the other methods. This may be due to its deeper penetration measuring the strength in zones away from the disturbed surface of the split core. We do not have any explanation for the occasional high strength values produced with the pocket penetrometer. Perhaps these values are related to the presence of carbonate or a diagenetic effect in the sediment. In some offshore areas, including the Gulf of Mexico, shear strength values can be related to sedimentation rate (Moore, 1964; Keller, 1974).

Linear regression analysis between the strength measurements and subbottom depth indicates that shear strength increases with subbottom depth likely are a result of the normal compaction process. Although we determined a linear fit for the strength data in a similar manner to Bryant and Trabant (1972), our strength values were lower near the sea floor and increased more rapidly with subbottom depth. The weaker zone near the sea floor may reflect the presence of higher water content.

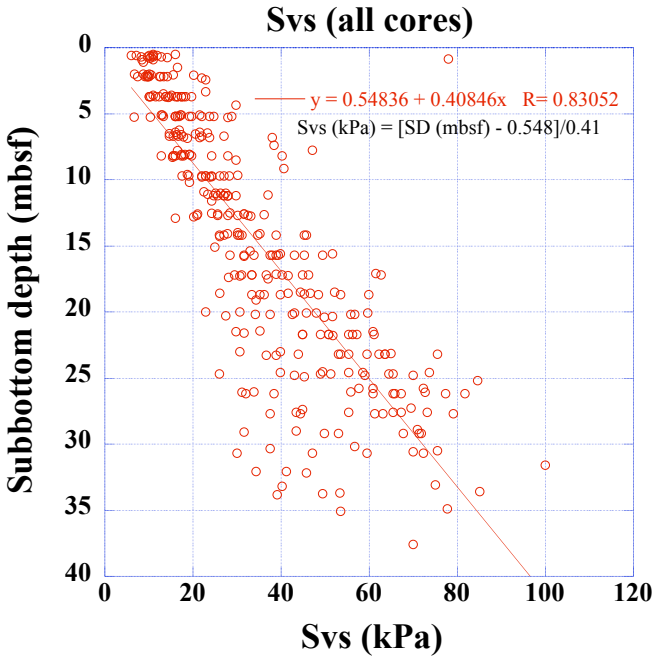

Figure 25. Vane-shear strength (Svs) in relation to subbottom depth for all cores.

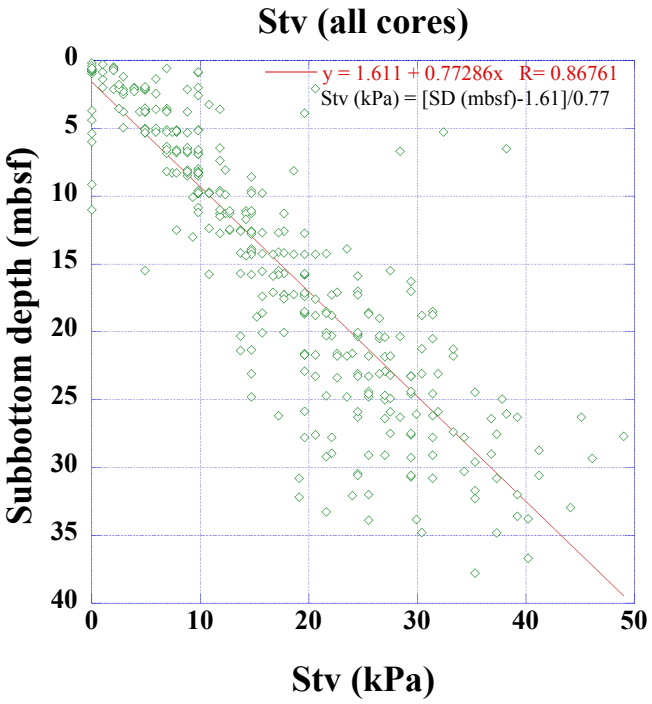

Figure 26. Torvane strength (Stv) in relation to subbottom depth for all cores.

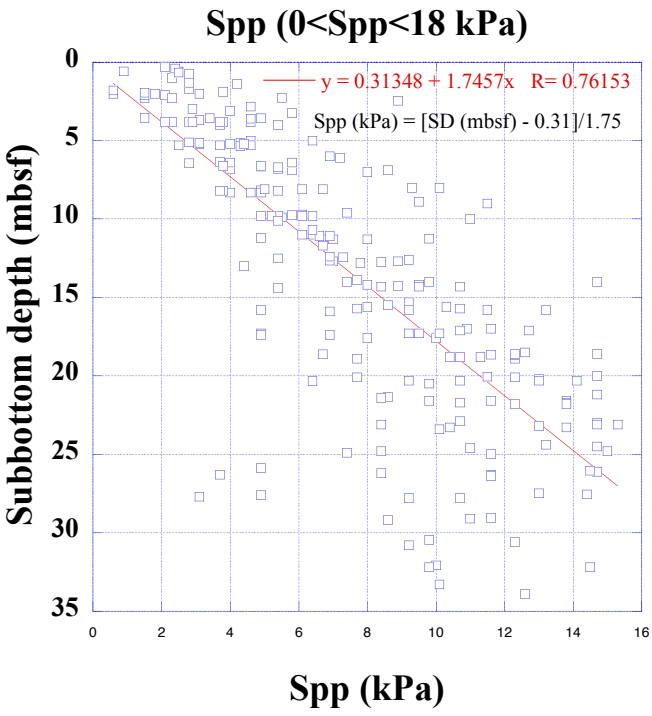

Figure 27. Pocket penetrometer strength (Spp) less than 18 kilopascals (kPa) in relation to subbottom depth.

Shear strength measurements were plotted for each of the main study areas (figs. 28–32). Because mini-vane tests were not possible with box cores, the pocket penetrometer strength was plotted for Orca Basin (fig. 29). The following shear strength characteristics were observed:

1. At Tunica Mound, the shear strength for core MD02-2545 (fig. 28), located near the crest of a mound at one end of the coring transect (fig. 2), is stronger than those of nearby cores.

2. Although Orca Basin has very high pore-water salinity, it does not appear to have pocket penetrometer strengths (fig. 29) significantly different from other cores (fig. 27).

3. Shear strengths are uniformly consistent at Bush Hill even though the cores were obtained at different water depths (fig. 3).

4. Core MD02-2570 on the western flank of the Mississippi Canyon is significantly weaker (fig. 31) than the uniform grouping of cores from Kane Spur located on the eastern side of the Mississippi Canyon (fig. 32).

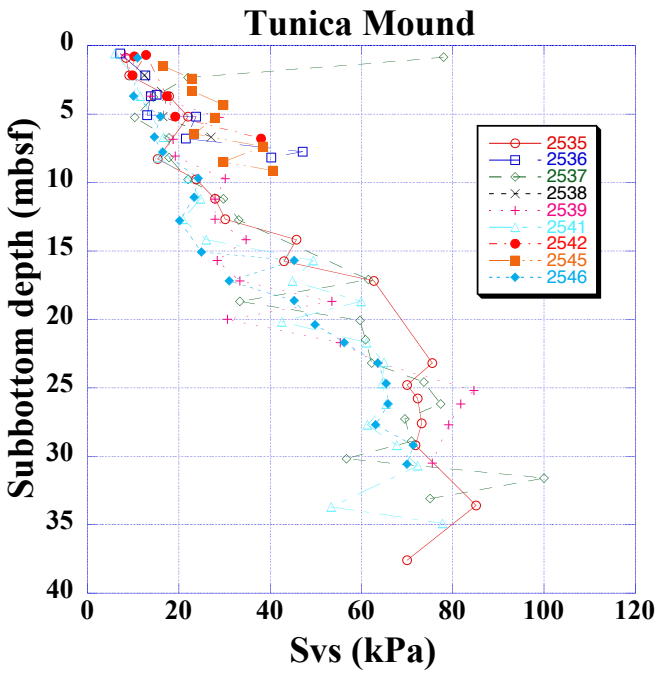

Figure 28. Vane-shear strength (Svs) in relation to subbottom depth for Tunica Mound.

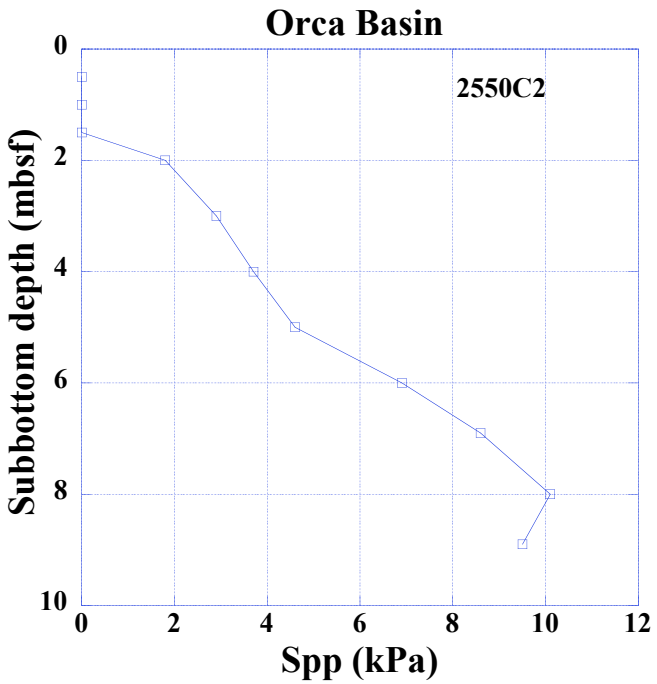

Figure 29. Pocket penetrometer strength (Spp) in relation to subbottom depth for Orca Basin.

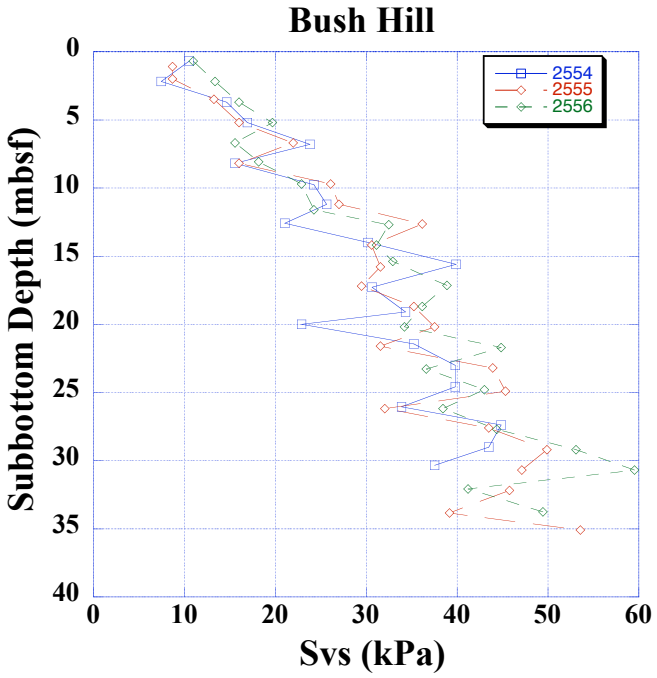

Figure 30. Vane-shear strength (Svs) in relation to subbottom depth for Bush Hill.

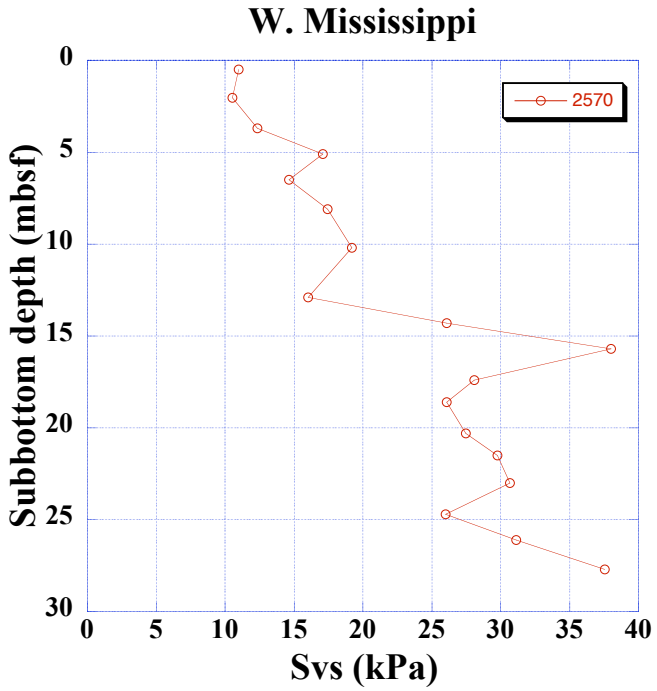

Figure 31. Vane-shear strength (Svs) in relation to subbottom depth for west of the Mississippi Canyon.

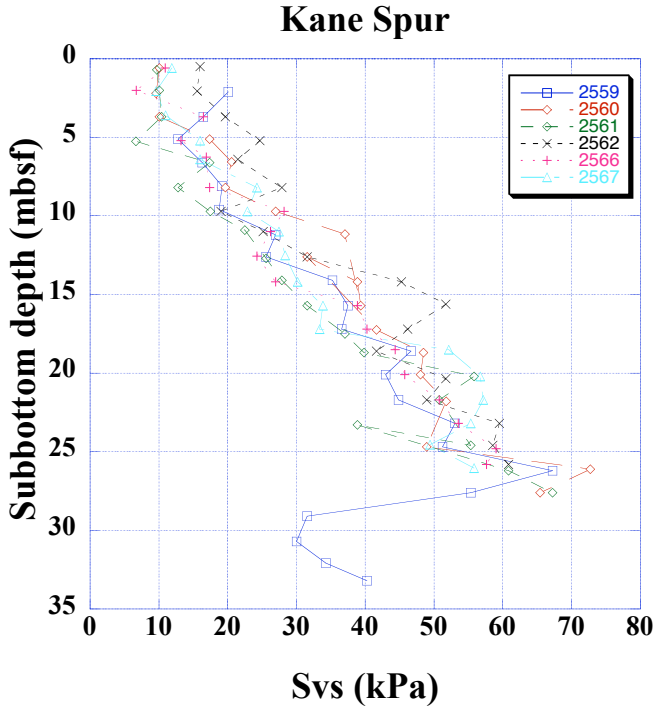

Figure 32. Vane-shear strength (Svs) in relation to subbottom depth for Kane Spur.

Electrical Resistivity

Although electrical resistivity for natural geologic materials ranges from close to that of seawater (0.18 to 0.24 ohm-m) to greater than 2,400 ohm-m (Hunt, 1984), the entire data set from the northern Gulf of Mexico only ranges from 0.26 to 1.06 ohm-m, with a mean value of 0.59 ohm-m (tables 2; 6, p. 49). As a result of higher water content, these values are somewhat lower than those reported for sediments rich in clay, which have resistivity values ranging from 3 to 100 ohm-m (Sharma, 1997) and from 3 to 15 ohm-m (Hunt, 1984). As anticipated, electrical resistivity and formation factor values increase with depth (figs. 33 and 34) because of the decrease in water content and porosity.

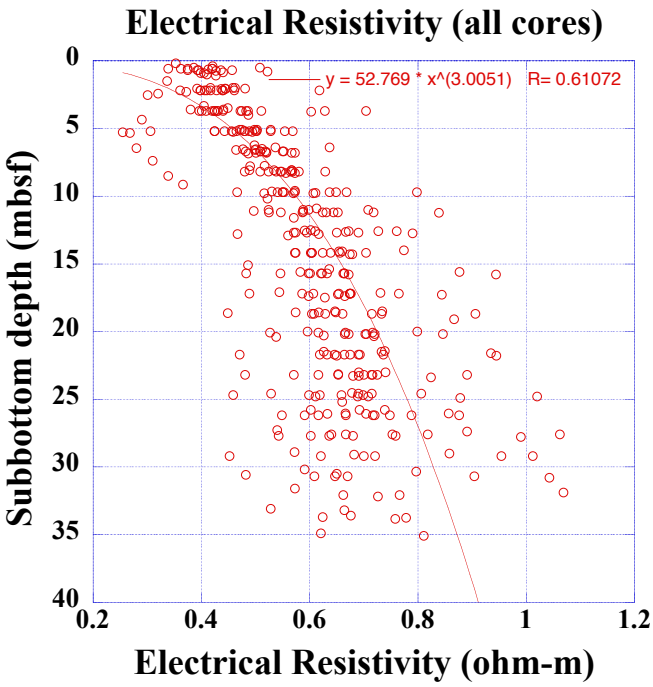

Figure 33. Electrical resistivity in relation to subbottom depth.

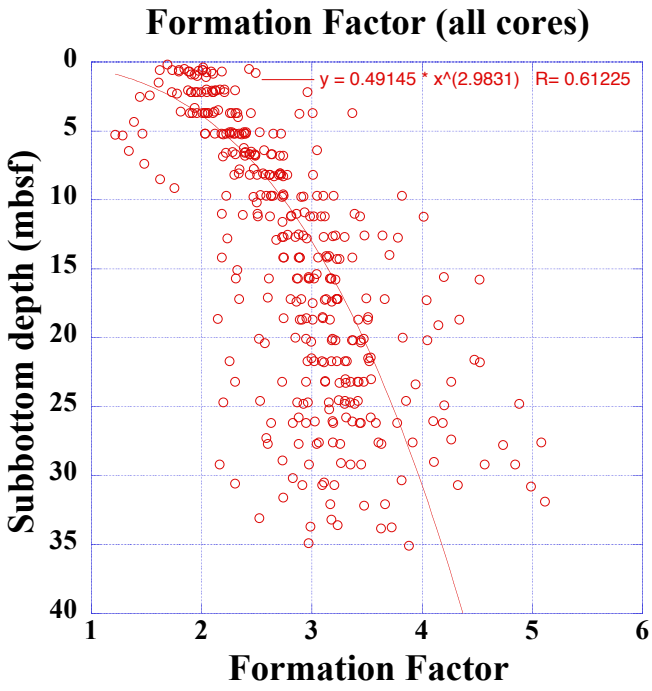

Figure 34. Formation factor in relation to subbottom depth.

Grain Size

Grain-size analyses were performed on 147 sediment samples from various subbottom depths in 29 cores (tables 7, p. 59, and 8). According to the Wentworth grade scale (Wentworth, 1929) and the Shepard classification scheme (Shepard, 1954), 56 percent of the samples classify as clay and the remaining classify as silty clay (figs. 35 and 36), with the exception of one sample that classifies as gravelly (Schlee, 1973). Full grain-size distribution curves are presented in figure 37 for six samples from throughout the northern Gulf of Mexico (table 8). Grain sizes (gravel, sand, silt, and clay) are distributed in wide, but uniform bands with subbottom depth (fig. 38) and are a byproduct of rapid sedimentation rates (Bouma and others, 1990). The uniform nature of the sediment texture is a contributing factor to the uniformity of physical properties across the northern Gulf of Mexico.

Visual observations indicate that the lithology of sediment containing gas hydrate was not substantially different from that of adjacent material. This is in contrast to other studies where hydrate was concentrated in coarser-grained sediment (for example, Winters and others (1999); Dallimore and others (2002); Matsumoto and others (2004)).

Table 8. Grain-size distributions.

[Values are in phi sizes. STDEV, standard deviation; SKEW, skewness; KURT, kurtosis; M1PHI, mode 1 phi size; M1FRQ, mode 1 frequency; Cfp3, cumulative frequency percent of 3 phi size class; Cfpm3, cumulative frequency percent of –3 phi size; Fp4, frequency percent of 4 phi size class; Fpm4, frequency percent of –4 phi size]

CORE	SUBBOT DEPTH (m)	WATER DEPTH (m)	GRVL (%)	SAND (%)	SILT (%)	CLAY (%)	SHEPARD CLASS	MEDIAN	MEAN	STDEV	SKEW
2537	5.2	600	0.00	0.50	15.89	83.60	CLAY	10.29	9.64	1.56	-1.14
2553	5.01	2,259	0.00	0.01	11.10	88.89	CLAY	10.28	9.80	1.24	-1.05
2554	5.18	602	0.00	0.16	5.17	94.67	CLAY	10.43	10.14	1.10	-2.01
2565	6.315	1,068	0.06	0.35	19.54	79.98	CLAY	10.2	9.47	1.58	-0.90
2569	4.215	1,032	0.00	1.57	24.96	73.49	SILTY CLAY	10.17	9.09	2.05	-0.63
2570	5.13	631	0.00	0.07	5.21	94.71	CLAY	10.31	9.99	0.96	-1.39

CORE	KURT	M1PHI	M1FRQ	M2PHI	M2FRQ	M3PHI	M3FRQ	Modes	Cfp11	Cfp10	Cfp9
2537	5.90	7.50	7.7	0.00	0.0	0.00	0.0	1.00	99.99	29.68	23.21
2553	3.62	0.00	0.0	0.00	0.0	0.00	0.0	0.00	100	30.45	20.17
2554	15.53	0.00	0.0	0.00	0.0	0.00	0.0	0.00	100	12.70	9.51
2565	4.03	6.50	8.8	0.00	0.0	0.00	0.0	1.00	100	37.40	28.30
2569	0.21	5.50	7.0	7.50	7.0	0.00	0.0	2.00	100.02	39.72	32.80
2570	9.35	0.00	0.0	0.00	0.0	0.00	0.0	0.00	100	27.01	16.07

CORE	Cfp8	Cfp7	Cfp6	Cfp5	Cfp4	Cfp3	Cfp2	Cfp1	Cfp0	Cfpm1	Cfpm2
2537	16.39	8.70	3.97	1.93	0.50	0.40	0.32	0.24	0.22	0.00	0.00
2553	11.11	5.24	2.17	0.59	0.01	0.01	0.01	0.00	0.00	0.00	0.00
2554	5.33	4.17	3.35	0.85	0.16	0.10	0.06	0.02	0.00	0.00	0.00
2565	20.02	11.67	2.89	0.55	0.48	0.42	0.39	0.26	0.09	0.06	0.00
2569	26.53	19.51	13.55	6.53	1.57	0.18	0.09	0.04	0.02	0.00	0.00
2570	5.29	1.34	0.99	0.33	0.08	0.05	0.03	0.02	0.00	0.00	0.00

CORE	Cfpm3	Cfpm4	Cfpm5	Fp11	Fp10	Fp9	Fp8	Fp7	Fp6	Fp5	Fp4
2537	0.00	0.00	0.00	70.31	6.47	6.82	7.69	4.73	2.04	1.43	0.10
2553	0.00	0.00	0.00	69.55	10.28	9.06	5.87	3.07	1.58	0.58	0.00
2554	0.00	0.00	0.00	87.30	3.19	4.18	1.16	0.82	2.50	0.69	0.06
2565	0.00	0.00	0.00	62.60	9.10	8.28	8.35	8.78	2.34	0.07	0.06
2569	0.00	0.00	0.00	60.30	6.92	6.27	7.02	5.96	7.02	4.96	1.39
2570	0.00	0.00	0.00	72.99	10.94	10.78	3.95	0.35	0.66	0.25	0.03

CORE	Fp3	Fp2	Fp1	Fp0	Fpm1	Fpm2	Fpm3	Fpm4	Fpm5
2537	0.08	0.08	0.02	0.22	0.00	0.00	0.00	0.00	0.00
2553	0.00	0.01	0.00	0.00	0.00	0.00	0.00	0.00	0.00
2554	0.04	0.04	0.02	0.00	0.00	0.00	0.00	0.00	0.00
2565	0.03	0.13	0.17	0.03	0.06	0.00	0.00	0.00	0.00
2569	0.09	0.05	0.02	0.02	0.00	0.00	0.00	0.00	0.00
2570	0.02	0.01	0.02	0.00	0.00	0.00	0.00	0.00	0.00

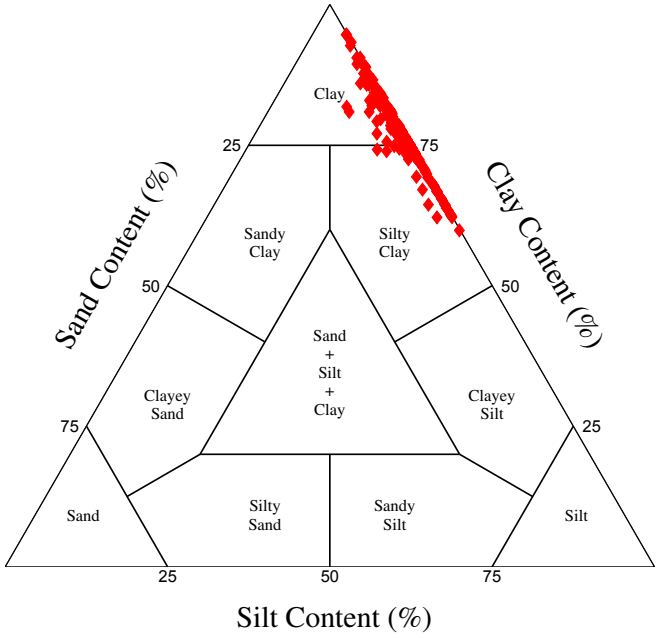

Figure 35. Grain sizes, including sand, silt, and clay.

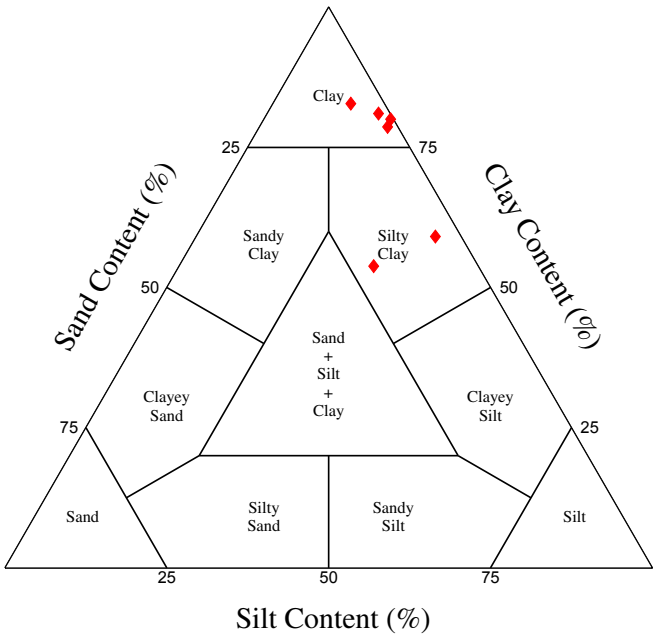

Figure 36. Grain sizes, including gravel, sand, silt, and clay. Gravel has been added to the sand quantity for these six samples (table 7).

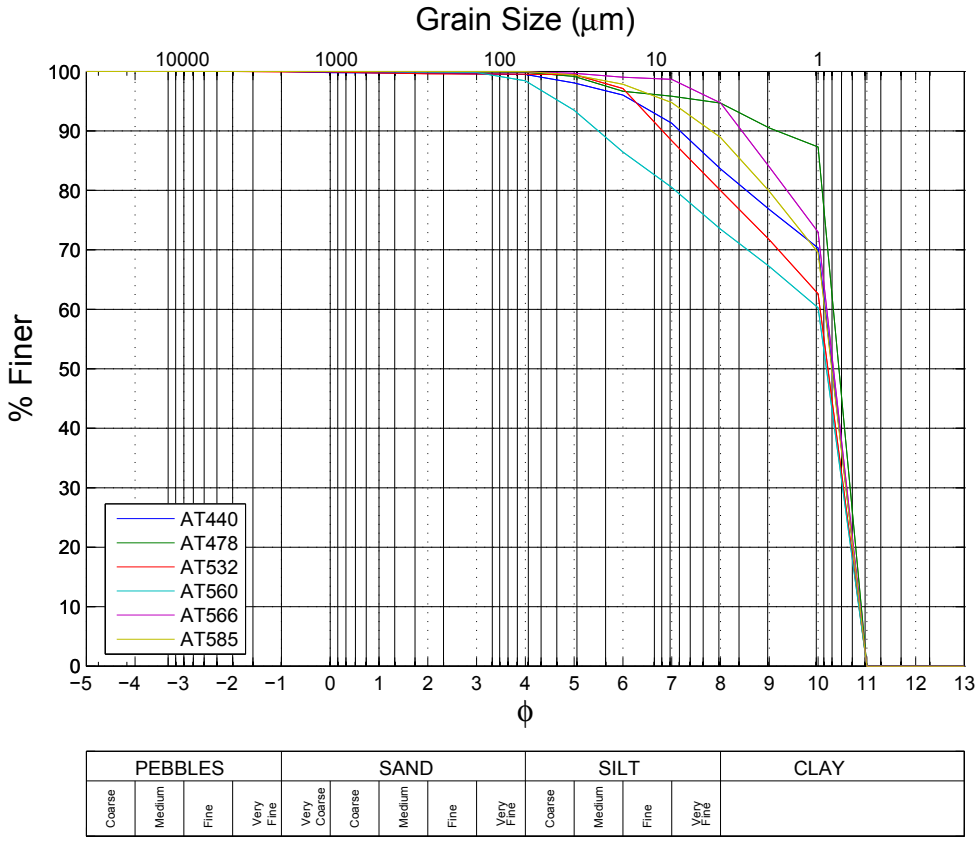

Figure 37. Grain-size distribution curves.

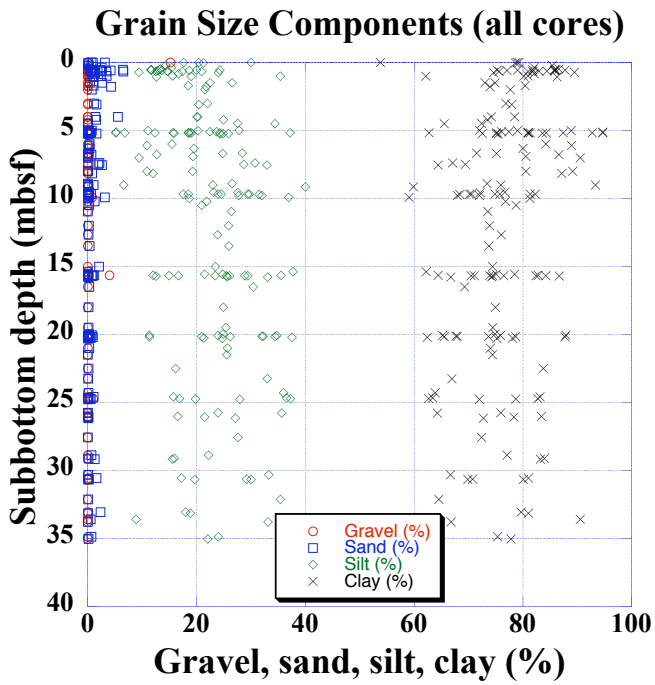

Figure 38. Grain size, including gravel, sand, silt, and clay in relation to subbottom depth.

Organic Carbon Content

Carbon and nitrogen content were determined in 144 sediment samples from 27 cores at various subbottom depths (table 9). All components are present in small quantities within the samples and are less than 5.8 percent of the total sample dry mass (table 2; fig. 39). Inorganic carbon, IC, (assumed to be carbonate) ranges from 0.15 to 2.8 percent (with a single measurement at 4.08 percent; fig. 40). The presence of carbonate must be geographically localized because unlike some samples retrieved from nearby MC852, which contained carbonate contents over 70 percent (Francisca and others, 2005), cores obtained during this cruise contained much smaller amounts. Organic carbon, OC, ranges from 0.5 to 2.2 percent (fig. 41). Considering the high sedimentation rates in the northern Gulf of Mexico (Bouma and others, 1990), this amount of organic carbon is sufficient to generate some biogenic methane gas (G. Claypool, oral commun., 2005). Of course, thermogenic gas seeps are responsible for many of the widely known gas hydrate outcrops that have been documented in the Gulf of Mexico (Brooks and others, 1984; MacDonald and others, 1994; Sassen, 2001).

Table 9. Geochemistry results.

[CHN ID, carbon, hydrogen, nitrogen identification number; TC, total carbon; %, percent; N, nitrogen; OC, organic carbon; IC, inorganic carbon]

CHN ID	Core	Subbottom depth (m)	TC (%)	N (%)	OC (%)	IC (%)
1	2535	0.67	3.7	0.08	1.28	2.42
4	2535	5.18	2.56	0.06	0.76	1.8
7	2535	9.78	3.51	0.05	1.76	1.75
11	2535	15.72	2.68	0.06	0.72	1.96
14	2535	20.19	1.81	0.06	0.54	1.27
17	2535	24.76	0.96	0.07	0.61	0.35
20	2535	29.19	1.99	0.08	0.63	1.36
23	2535	33.6	1.12	0.07	0.51	0.61
1	2536GHF	0.64	2.53	0.09	1	1.53
6	2536GHF	8.18	2.58	0.07	1.01	1.57
1	2537	0.83	2.46	0.09	0.55	1.91
4	2537	5.2	2.35	0.07	1.43	0.92
9	2537	12.67	3.21	0.05	0.87	2.34
11	2537	15.79	3.8	0.04	1.05	2.75
14	2537	20.07	2.55	0.07	1.14	1.41
17	2537	24.58	1.69	0.05	1.16	0.53
20	2537	28.87	1.04	0.07	0.89	0.15
23	2537	33.08	1.84	0.07	0.52	1.32
1	2538G	0.65	3.15	0.1	0.97	2.18
5	2538G	6.67	3.28	0.06	1.56	1.73

Table 9. Geochemistry results. — Continued

[CHN ID, carbon, hydrogen, nitrogen identification number; TC, total carbon; %, percent; N, nitrogen; OC, organic carbon; IC, inorganic carbon]

CHN ID	Core	Subbottom depth (m)	TC (%)	N (%)	OC (%)	IC (%)
1	2539	0.67	3.36	0.09	1.04	2.32
4	2539	5.17	2.69	0.07	1.06	1.63
7	2539	9.71	2.94	0.05	1.18	1.76
11	2539	15.68	3.51	0.05	1.31	2.2
14	2539	19.97	3.02	0.05	0.93	2.09
1	2540GHF	0.59	3.51	0.08	1	2.51
4	2540GHF	5.11	3.18	0.06	1.31	1.87
1	2541	0.55	3.7	0.08	1.02	2.68
4	2541	5.17	2.5	0.08	0.59	1.91
7	2541	9.67	2.92	0.07	1.17	1.76
11	2541	15.66	2.43	0.08	1.08	1.35
14	2541	20.18	2.93	0.07	0.75	2.18
20	2541	29.14	0.92	0.07	0.49	0.43
24	2541	34.88	1.06	0.08	0.57	0.49
5	2542GHF	6.77	2	0.07	0.61	1.39
1	2545G	0.37	3.68	0.1	0.99	2.69
6	2545G	5.27	2.02	0.07	0.86	1.16
10	2545G	9.16	3.2	0.06	1.8	1.4
1	2546	0.53	2.34	0.1	0.91	1.43
7	2546	9.58	2.79	0.07	0.52	2.27
11	2546	15.67	2.03	0.07	0.9	1.13
14	2546	20.28	3.31	0.05	1.49	1.82
17	2546	24.71	1.37	0.07	0.93	0.44
21	2546	30.57	1.79	0.08	0.49	1.3
1	2547GHF	0.72	2.24	0.1	0.83	1.41
4	2547GHF	4.98	2.74	0.07	1.09	1.65
1	2554	0.74	2.23	0.1	0.84	1.39
4	2554	5.18	2.34	0.12	1.54	0.8
7	2554	9.78	2.65	0.08	1.09	1.56
11	2554	15.58	2.32	0.07	0.83	1.49
14	2554	19.97	2.61	0.07	1.03	1.58
17	2554	24.29	2.6	0.07	1.12	1.48
21	2554	30.32	3.03	0.07	1.25	1.78
1	2555	1.08	2.54	0.1	1.42	1.12
4	2555	5.17	1.96	0.1	1.19	0.77
7	2555	9.67	2.65	0.08	1.52	1.13
11	2555	15.75	2.97	0.06	1.4	1.57
14	2555	20.21	2.52	0.06	1.55	0.97
18	2555	26.17	3.2	0.07	1.11	2.09
21	2555	30.67	3.09	0.07	1.24	1.85
22	2555	32.15	3.31	0.06	1.47	1.84
24	2555	35.05	3.22	0.06	1.3	1.92

Table 9. Geochemistry results. — Continued

[CHN ID, carbon, hydrogen, nitrogen identification number; TC, total carbon; %, percent; N, nitrogen; OC, organic carbon; IC, inorganic carbon]

CHN ID	Core	Subbottom depth (m)	TC (%)	N (%)	OC (%)	IC (%)
1	2556	0.67	2.61	0.1	0.94	1.67
4	2556	5.17	2.08	0.1	1.35	0.73
7	2556	9.68	3.14	0.07	1.5	1.64
11	2556	15.38	2.67	0.05	1.15	1.52
14	2556	20.18	2.82	0.06	1.34	1.48
16	2556	23.27	3	0.07	1.35	1.65
17	2556	24.78	3.01	0.06	1.19	1.82
21	2556	30.67	2.92	0.07	1.3	1.62
23	2556	33.78	3.26	0.06	1.27	1.99
1	2557GHF	0.6	1.74	0.08	0.76	0.98
1	2559	0.21	1.47	0.09	0.78	0.69
4	2559	5.11	2.52	0.08	1.65	0.87
7	2559	9.54	2.54	0.08	1.3	1.25
11	2559	15.68	2.55	0.06	1.14	1.41
14	2559	20.08	2.33	0.08	1.21	1.12
17	2559	24.67	2.8	0.07	1.25	1.55
21	2559	30.65	3.29	0.06	1.65	1.64
23	2559	33.15	3.28	0.06	1.64	1.64
1	2560	0.57	2.74	0.11	0.92	1.82
11	2560	15.67	2.68	0.07	1.22	1.46
14	2560	20.09	2.78	0.06	1.4	1.38
17	2560	24.72	2.71	0.07	1.28	1.43
1	2561	0.61	3.47	0.1	1.25	2.22
4	2561	5.23	2.03	0.07	1.15	0.88
7	2561	9.68	2.23	0.07	1.08	1.15
11	2561	15.66	2.87	0.07	1.34	1.53
14	2561	20.15	2.75	0.07	1.23	1.53
19	2561	27.57	2.74	0.06	1.28	1.46
1	2562	0.48	1.81	0.06	1.06	0.75
4	2562	5.18	2.34	0.07	1.21	1.13
8	2562	10.97	2.82	0.07	1.33	1.49
11	2562	15.58	2.59	0.07	1.18	1.41
14	2562	20.31	2.9	0.07	1.31	1.59
18	2562	25.77	2.93	0.06	1.35	1.58
1	2564GHF	0.99	3.63	0.17	1.38	2.25
5	2564GHF	6.69	2.78	0.07	1.33	1.45
1	2565	0.025	2.42	0.1	1.5	0.92
2	2565	1.51	2.83	0.1	1.68	1.15
3	2565	3.01	2.43	0.1	1.57	0.86
4	2565	4.525	2.97	0.08	1.77	1.2
5	2565	6.315	2.6	0.09	1.5	1.1
6	2565	7.515	2.59	0.08	1.45	1.14

Table 9. Geochemistry results. — Continued

[CHN ID, carbon, hydrogen, nitrogen identification number; TC, total carbon; %, percent; N, nitrogen; OC, organic carbon; IC, inorganic carbon]

CHN ID	Core	Subbottom depth (m)	TC (%)	N (%)	OC (%)	IC (%)
7	2565	9.015	2.47	0.1	1.37	1.1
8	2565	10.515	2.51	0.1	1.33	1.18
9	2565	12.015	2.59	0.09	1.45	1.14
10	2565	13.515	5.83	0.09	1.75	4.08
11	2565	15.015	2.46	0.1	1.44	1.02
12	2565	16.515	2.64	0.09	1.53	1.11
13	2565	18.015	2.75	0.08	1.41	1.34
14	2565	19.515	2.44	0.1	1.44	1
15	2565	21.015	2.54	0.09	1.4	1.14
16	2565	22.515	2.25	0.1	1.04	1.21
1	2566	0.57	2.79	0.14	1.01	1.79
4	2566	5.17	2	0.13	1.18	0.82
7	2566	9.68	2.81	0.14	1.61	1.2
11	2566	15.67	2.89	0.12	1.46	1.43
14	2566	20.15	3	0.12	1.48	1.52
18	2566	25.78	3.87	0.12	2.19	1.68
1	2567	0.53	3.09	0.14	1.03	2.06
4	2567	5.18	1.91	0.11	1.08	0.83
7	2567	9.68	2.3	0.11	1.16	1.14
11	2567	15.68	2.86	0.13	1.33	1.53
14	2567	20.18	2.5	0.12	1.33	1.17
18	2567	26.04	2.24	0.14	0.99	1.25
1	2568GHF	0.015	3.28	0.15	1.4	1.88
3	2568GHF	4.485	2.54	0.08	1.3	1.24
1	2569	0.015	1.46	0.1	0.9	0.56
2	2569	1.015	1.6	0.06	0.76	0.84
6	2569	4.215	1.22	0.07	0.74	0.48
7	2569	5.225	1.27	0.07	0.75	0.52
9	2569	7.385	1.39	0.07	0.84	0.55
10	2569	7.54	1.18	0.07	0.74	0.45
12	2569	9.935	1.25	0.07	0.71	0.54
1	2570	0.57	1.49	0.07	0.71	0.78
4	2570	5.13	2.2	0.07	1.15	1.05
7	2570	10.22	2.76	0.07	1.49	1.27
11	2570	15.69	2.17	0.08	1.3	0.87
15	2570	21.51	2.76	0.12	1.28	1.49
18	2570	26.1	2.64	0.14	1.21	1.43
1	2572GHF	0.015	2.27	0.17	0.92	1.35
2	2572GHF	1.515	3.25	0.16	1.4	1.85
3	2572GHF	1.805	3.35	0.16	1.98	1.37

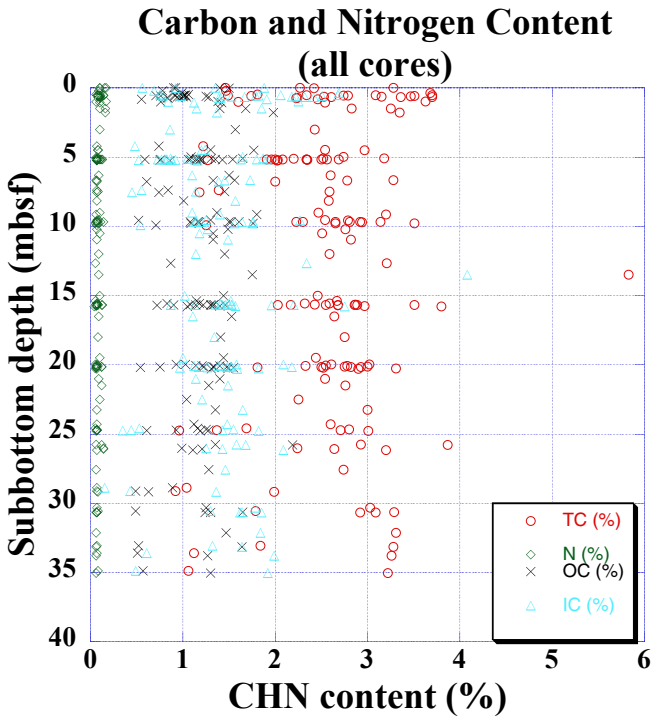

Figure 39. Carbon, hydrogen, and nitrogen content of sediment samples.

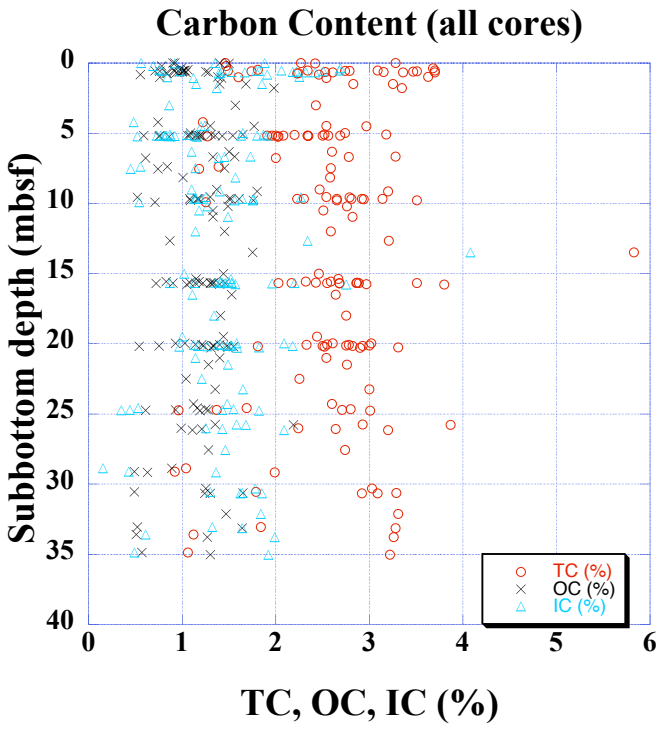

Figure 40. Carbon content of sediment samples.

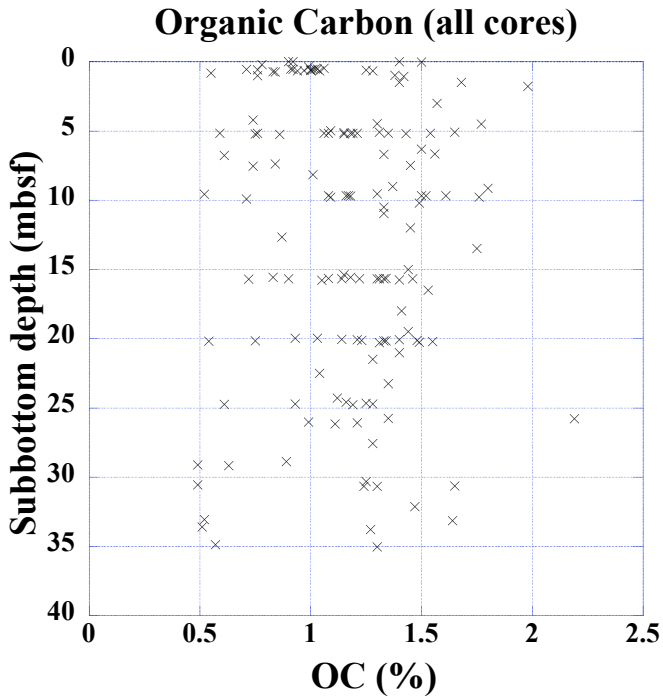

Figure 41. Organic carbon content of sediment samples.

Conclusions

Our results confirm that gas hydrates are present at discrete locations in the northern Gulf of Mexico, but they do not appear to be pervasive. In other terrestrial and marine regions, gas hydrate has been recovered in coarser-grained sediment. In the northern Gulf of Mexico, however, factors other than lithology, such as gas quantity and composition, pore-water salinity, and geothermal gradient, likely play a significant role in determining where and how much, if any, gas hydrate is present.

With the exception of a core from Orca Basin containing hyper-saline pore water, most cores possess physical properties that fall within wide, but predictable, bands. For example, almost all sediment classifies texturally as clay or silty clay. Such uniformity in properties is evidence of regionally pervasive depositional conditions. This is not to say that geologic conditions are currently uniform. Faulting, salt diapirs, directed fluid flow, and thermogenic gas seeps are all examples of localized processes occurring in the study region.

Nearly all texture samples were classified as clay or silty clay. In addition, the shipboard lithologic descriptions (Appendix F) indicate that few sandy layers were encountered during the cruise. Therefore, one of the challenges for developing gas hydrate in the Gulf of Mexico as a resource is to discover thick permeable coarse-grained layers containing substantial quantities of gas hydrate. However, from a hazards standpoint, the recovered pure hydrate layers would substantially increase pore pressure upon dissociation, thereby adversely affecting sea-floor stability.

Overall, physical properties show similar trends in the Tunica Mound, Bush Hill, and Mississippi Canyon regions. There is a pervasive break in slope of depth profiles of water content and related properties at 10 to 15 mbsf. This change in behavior is not believed to coincide with the last glacial maximum (Bout-Roumazeilles and Trentesaux, this volume, chapter 5) or with obvious textural changes.

The sedimentation rate, in conjunction with an ample amount of organic carbon, indicates that biogenic methane gas production is sufficient to form some gas hydrate at most locations. However, the fact that gas hydrate has not been pervasively observed indicates that other factors control hydrate formation and distribution.

Acknowledgments

Captain Jean-Michel Nicolas and the crew of the RV *Marion Dufresne* are thanked for their assistance in performing shipboard activities. Cruise logistical support was provided by the French Polar Institute [Institut Polaire Francais – Paul-Emile Victor (IPEV)].

Considerable at-sea help was provided by an international group of approximately 40 scientists under the IMAGES and PAGE programs. The IMAGES program is an international effort to understand the mechanisms and consequences of climatic changes using the oceanic sedimentary record.

The following people provided assistance with laboratory testing and technical assistance with data compilation: Sandy Milbert, Lauren Gilbert, Dave Mason, and Mario Santos.

Financial support of U.S. Geological Survey (USGS)-related activities was provided by the USGS Coastal and Marine Geology Program, the USGS Energy Program, and the U.S. Department of Energy's Gas Hydrate Program.

The U.S. Minerals Management Service provided information used to determine core locations and avoid existing sea-floor infrastructure.

The Integrated Ocean Drilling Program provided facilities to store and archive recovered cores.

References Cited

American Society for Testing and Materials, 1997, Standard test method for specific gravity of solids by gas pycnometer D5550-94, Annual Book of ASTM Standards, v. 04.09, Soil and Rock: West Conshohocken, PA, American Society for Testing and Materials, p. 380–383.

Bouma, A.H., Roberts, H.H., and Coleman, J.M., 1990, Acoustical and geological characteristics of near-surface sediments, upper continental slope of northern Gulf of Mexico: Geo-Marine Letters, v. 10, p. 200–208.

Brooks, J.M., Kennicutt, M.C., II, Fay, R.R., McDonald, T.J., and Sassen, R., 1984, Thermogenic gas hydrates in the Gulf of Mexico: Science, v. 25, p. 409–411.

Bryant, W., and Trabant, P., 1972, Statistical relationships between geotechnical properties and Gulf of Mexico sediments, *in* Offshore Technology Conference (OTC), Houston, TX, 1972, p. II/363–II/368.

Cooper, A.K., and Hart, P.E., 2002, High-resolution seismic-reflection investigation of the northern Gulf of Mexico gas-hydrate-stability zone: Marine and Petroleum Geology, v. 19, no. 10, p. 1275–1293.

Dallimore, S.R., Collett, T.S., Uchida, T., Weber, M., Takahashi, H., and Mallik Gas Hydrate Research Team, 2002, Overview of the 2002 Mallik gas hydrate production research well program: Fourth International Conference on Gas Hydrates, May 19–23, 2002, Yokohama, Japan, p. 36–39.

Francisca, F., Yun, T.-S., Ruppel, C., and Santamarina, J.C., 2005, Geophysical and geotechnical properties of near-seafloor sediments in the northern Gulf of Mexico gas hydrate province: Earth and Planetary Science Letters, v. 237, p. 924-939.

Hewitt, A.T., 1998, PGC sediment physical properties manual—compilation: Ocean Mapping Group, Geodesy & Geomatics Engineering, University of New Brunswick.

Holtz, R.D., and Kovacs, W.D., 1981, An introduction to geotechnical engineering: Englewood Cliffs, NJ, Prentice-Hall, Inc., 733 p.

Hunt, R.E., 1984, Geotechnical engineering investigation manual: New York, McGraw-Hill Book Co., 983 p.

Keller, G., 1974, Marine geotechnical properties—interrelationships and relationships to depth of burial, *in* Inderbitzen, A., ed., Deep sea sediments: New York, Plenum Publishing Corp., p. 77–100.

Kvenvolden, K.A., and Lorenson, T.D., 2001, The global occurrence of natural gas hydrate, *in* Paull, C.K., and Dillon, W.P., eds., Natural gas hydrates—occurrence, distribution, and detection: Washington, DC, American Geophysical Union, Geophysical Monograph 124, p. 3–18.

Lambe, T.W., and Whitman, R.V., 1969, Soil mechanics: New York, John Wiley & Sons, 553 p.

MacDonald, I.R., Guinasso, N.L., Jr., Sassen, R., Brooks, J.M., Lee, L., and Scott, K.T., 1994, Gas hydrate that breaches the sea floor on the continental slope of the Gulf of Mexico: Geology (Boulder), v. 22, no. 8, p. 699–702.

Matsumoto, R., Tomaru, H., and Lu, H., 2004, Detection and evaluation of gas hydrates in the Eastern Nankai Trough by geochemical and geophysical methods: Resource Geology, v. 54, no. 1, p. 53–67.

Moore, D., 1964, Shear strength and related properties of sediments from Experimental Mohole (Guadalupe Site): Journal of Geophysical Research, v. 69, no. 20, p. 4271–4291.

Paull, C.K., Ussler, W., III, Lorenson, T., Winters, W., and Dougherty, J., 2005, Geochemical constraints on the distribution of gas hydrates in the Gulf of Mexico: Geo-Marine Letters, DOI 10.1007/s00367–005–001–3.

Sassen, R., 2001, Gas hydrates in the Gulf of Mexico; a geochemical perspective—Outer Continental Shelf report: Minerals Management Service, Report MMS 2001-082, p. 92-105.

Schlee, J., 1973, Atlantic Continental Shelf and Slope of the United States—sediment texture of the Northeastern Part: U.S. Geological Survey Professional Paper 529–L, 64 p.

Sharma, P.V., 1997, Environmental and Engineering Geophysics: Cambridge, UK, Cambridge University Press, 475 p.

Shepard, F.P., 1954, Nomenclature based on sand-silt-clay ratios: Journal of Sedimentary Petrology, v. 24, p. 151–158.

Syvitski, J.P.M., ed., 1991, Principles, methods, and application of particle size analysis: New York, Cambridge University Press, 368 p.

Verardo, D.J., Froelich, P.N., and McIntyre, A., 1990, Determination of organic carbon and nitrogen in marine sediments using the Carlo Erba NA–1500 analyzer—Deep Sea Research Part A: Oceanographic Research Papers, v. 37, p. 157-165.

Wentworth, C.K., 1929, Method of computing mechanical composition of sediments: Geological Society of America Bulletin, v. 40, p. 771–790.

Winters, W.J., Dallimore, S.R., Collett, T.S., Katsube, T.J., Jenner, K.A., Cranston, R.E., Wright, J.F., Nixon, F.M., and Uchida, T., 1999, Physical properties of sediments from the JAPEX/JNOC/GSC Mallik 2L–38 gas hydrate research well: Bulletin, Geological Survey of Canada, Report 544, p. 95–100.

Table 4. Water content and index properties.

[m, meters; Sal Est, salinity estimated; ppt, parts per thousand; WCt, water content based on total sample mass not corrected for salinity; %, percent; WCs, water content based on solids mass not corrected for salinity; WCtc, water content based on total sample mass corrected for salinity; WCsc, water content based on solids mass corrected for salinity; ρs, grain density not corrected for salinity; g/cm^3, grams per cubic centimeter; ρsc, grain density corrected for salinity; n, porosity; e, void ratio; ρw, wet bulk density; ρd, dry bulk density; γw, wet unit weight; kN/m^3, kiloNewton per cubic meter; γd, dry unit weight; γsub, submerged unit weight]

Core no.	Section	Mid-depth (m)	Sal Est (ppt)	WCt (%)	WCs (%)	WCtc (%)	WCsc (%)	ρs (g/cm^3)	ρsc (g/cm^3)	n (%)	e	ρw (g/cm^3)	ρd (g/cm^3)	γw (kN/m^3)	γd (kN/m^3)	γsub (kN/m^3)
2535	1	0.7	36	57.7	136.3	59.8	149	2.66	2.69	79.6	3.9	1.37	0.55	13.4	5.38	3.33
2535	2	2.2	36.1	61.1	157.1	63.4	173.2	2.64	2.67	81.8	4.5	1.33	0.49	13.01	4.76	2.93
2535	3	3.68	36.1	40.1	67	41.6	71.3	2.7	2.72	65.3	1.89	1.61	0.94	15.81	9.23	5.74
2535	4	5.2	36.3	48.7	95.1	50.6	102.4	2.67	2.7	72.9	2.69	1.48	0.73	14.52	7.17	4.44
2535	5	6.8	36.8	39.9	66.4	41.4	70.7	2.71	2.72	65.2	1.87	1.62	0.95	15.87	9.29	5.78
2535	6	8.5	37	37.3	59.4	38.7	63.1	2.71	2.72	62.6	1.67	1.66	1.02	16.31	10	6.22
2535	7	9.8	36.9	38.3	62.1	39.8	66	2.7	2.71	63.5	1.74	1.64	0.99	16.11	9.71	6.03
2535	8	11.2	37.2	33.5	50.4	34.8	53.4	2.71	2.72	58.5	1.41	1.73	1.13	16.96	11.05	6.87
2535	8	11.2	37.2	33.5	50.4	34.8	53.4	2.71	2.72	58.5	1.41	1.73	1.13	16.96	11.05	6.87
2535	9	12.7	37.4	36.7	58.1	38.2	61.7	2.72	2.73	62.1	1.64	1.67	1.03	16.42	10.15	6.33
2535	10	14.2	37.5	40	66.6	41.5	71	2.7	2.71	65.2	1.87	1.61	0.94	15.84	9.26	5.75
2535	11	15.7	37.6	41.8	71.8	43.4	76.8	2.69	2.71	66.9	2.02	1.58	0.9	15.54	8.79	5.45
2535	12	17.2	37.6	41.1	69.9	42.8	74.7	2.68	2.69	66.2	1.95	1.59	0.91	15.61	8.94	5.52
2535	13	18.6	37.6	38.3	62	39.8	66.1	2.69	2.71	63.5	1.74	1.64	0.99	16.09	9.69	6.01
2535	14	20.22	37.9	40.9	69.2	42.5	74	2.68	2.7	66	1.94	1.6	0.92	15.66	9	5.57
2535	15	21.62	38.1	40.9	69.3	42.6	74.1	2.68	2.7	66	1.94	1.6	0.92	15.65	8.99	5.56
2535	16	23.2	38.2	39.5	65.4	41.1	69.8	2.67	2.68	64.5	1.82	1.62	0.95	15.85	9.33	5.75
2535	16	23.2	38.2	40.9	69.3	42.6	74.1	2.67	2.68	65.9	1.93	1.59	0.92	15.63	8.98	5.53
2535	17	24.8	38.4	37.7	60.4	39.2	64.4	2.69	2.71	62.8	1.69	1.65	1.01	16.2	9.86	6.11
2535	19	27.5	38.7	39.8	66.2	41.4	70.7	2.68	2.7	64.9	1.85	1.61	0.95	15.83	9.27	5.73
2535	19	27.5	38.7	39.8	66.2	41.4	70.7	2.68	2.7	64.9	1.85	1.61	0.95	15.83	9.27	5.73
2535	20	29.22	39	41	69.4	42.6	74.3	2.68	2.69	66	1.94	1.6	0.91	15.64	8.97	5.54
2535	21	30.6	38.8	38.6	62.9	40.2	67.1	2.69	2.71	63.8	1.77	1.64	0.98	16.05	9.6	5.95
2535	22	32.3	39.1	37	58.7	38.5	62.6	2.69	2.7	62.1	1.64	1.66	1.02	16.31	10.03	6.21
2535	23	33.6	39.6	38.2	61.8	39.8	66	2.69	2.71	63.4	1.73	1.64	0.99	16.12	9.71	6.02
2535	24	34.8	39.8	38.2	61.7	39.7	65.9	2.68	2.7	63.3	1.72	1.64	0.99	16.1	9.7	5.99
2535	25	37	39.9	39.3	64.8	40.9	69.3	2.68	2.7	64.5	1.82	1.62	0.96	15.92	9.4	5.81
2535	26	37.6	40.1	37.9	60.9	39.4	65.1	2.68	2.69	63	1.7	1.65	1	16.14	9.77	6.03
2536GHF	1	0.65	35	57.7	136.3	59.8	148.6	2.65	2.69	79.5	3.88	1.37	0.55	13.4	5.39	3.33
2536GHF	2	2.2	35	56.8	131.4	58.8	142.9	2.64	2.67	78.8	3.72	1.38	0.57	13.49	5.55	3.42
2536GHF	3	3.6	35	49.2	96.7	51	103.9	2.68	2.7	73.2	2.73	1.48	0.72	14.47	7.1	4.4
2536GHF	4	5.2	35	44.7	80.8	46.3	86.3	2.69	2.71	69.5	2.28	1.54	0.83	15.1	8.11	5.04
2536GHF	5	6.8	35	37.5	60	38.9	63.6	2.71	2.72	62.7	1.68	1.66	1.01	16.26	9.94	6.19
2536GHF	6	8.2	35	40.3	67.4	41.7	71.6	2.69	2.7	65.3	1.88	1.61	0.94	15.77	9.19	5.7
2537	1	0.85	21.3	56.9	131.9	58.1	138.7	2.66	2.68	78.5	3.65	1.37	0.58	13.46	5.64	3.5
2537	2	2.35	36.8	57.1	133	59.3	145.4	2.65	2.69	79.2	3.8	1.37	0.56	13.47	5.49	3.39
2537	3	3.75	37.7	48.3	93.4	50.2	100.7	2.68	2.71	72.6	2.65	1.49	0.74	14.6	7.27	4.51
2537	4	5.25	39.1	46.5	86.7	48.3	93.6	2.69	2.72	71.2	2.47	1.52	0.78	14.87	7.68	4.77
2537	6	8.25	42.8	40.1	67.1	41.9	72.2	2.69	2.71	65.5	1.9	1.61	0.94	15.81	9.18	5.69
2537	8	11.1	45.3	42.1	72.7	44.1	78.9	2.69	2.71	67.4	2.07	1.58	0.88	15.51	8.67	5.36
2537	9	12.7	47.4	35.7	55.4	37.4	59.8	2.72	2.74	61.2	1.58	1.7	1.06	16.63	10.4	6.46
2537	10	14.2	48.4	34	51.6	35.8	55.7	2.72	2.74	59.5	1.47	1.72	1.11	16.92	10.87	6.75
2537	11	15.8	48.3	34.5	52.7	36.3	56.9	2.72	2.73	60	1.5	1.72	1.09	16.82	10.72	6.65
2537	13	18.7	50.1	37.2	59.2	39.1	64.3	2.71	2.73	62.8	1.69	1.67	1.01	16.35	9.95	6.17
2537	14	20.1	50.6	40.6	68.2	42.7	74.6	2.69	2.71	66.1	1.95	1.61	0.92	15.75	9.02	5.57
2537	15	21.5	51.1	38.2	61.7	40.2	67.3	2.69	2.71	63.7	1.76	1.65	0.98	16.14	9.65	5.95
2537	16	23.2	52.2	40.4	67.7	42.6	74.2	2.69	2.71	65.9	1.93	1.61	0.92	15.79	9.06	5.59

Table 4. Water content and index properties. — Continued

[m, meters; Sal Est, salinity estimated; ppt, parts per thousand; WCt, water content based on total sample mass not corrected for salinity; %, percent; WCs, water content based on solids mass not corrected for salinity; WCtc, water content based on total sample mass corrected for salinity; WCsc, water content based on solids mass corrected for salinity; ρs, grain density not corrected for salinity; g/cm^3, grams per cubic centimeter; ρsc, grain density corrected for salinity; n, porosity; e, void ratio; ρw, wet bulk density; ρd, dry bulk density; γw, wet unit weight; kN/m^3, kiloNewton per cubic meter; γd, dry unit weight; γsub, submerged unit weight]

Core no.	Section	Mid-depth (m)	Sal Est (ppt)	WCt (%)	WCs (%)	WCtc (%)	WCsc (%)	ρs (g/cm^3)	ρsc (g/cm^3)	n (%)	e	ρw (g/cm^3)	ρd (g/cm^3)	γw (kN/m^3)	γd (kN/m^3)	γsub (kN/m^3)
2537	17	24.6	53.2	39.3	64.9	41.6	71.1	2.69	2.71	64.9	1.85	1.63	0.95	15.95	9.32	5.75
2537	18	26.3	54.7	39	64.1	41.3	70.4	2.68	2.71	64.6	1.83	1.63	0.96	15.99	9.38	5.77
2537	20	28.9	55.3	37	58.7	39.1	64.3	2.69	2.72	62.6	1.68	1.67	1.01	16.36	9.95	6.13
2537	22	32.2	57.1	40.3	67.4	42.7	74.5	2.69	2.71	65.9	1.94	1.61	0.92	15.81	9.06	5.57
2537	23	33.1	58.5	38.8	63.4	41.2	70.1	2.68	2.71	64.5	1.82	1.64	0.96	16.04	9.43	5.79
2538G	1	0.7	36.2	56.4	129.4	58.5	141.2	2.65	2.68	78.7	3.68	1.38	0.57	13.54	5.61	3.46
2538G	2	2.2	36.7	56.9	132.1	59.1	144.4	2.65	2.68	79	3.76	1.37	0.56	13.48	5.52	3.4
2538G	3	3.7	37.4	48.9	95.9	50.8	103.4	2.68	2.7	73.1	2.72	1.48	0.73	14.5	7.13	4.41
2538G	4	5.2	39.3	44	78.4	45.8	84.4	2.7	2.72	69	2.23	1.55	0.84	15.23	8.26	5.13
2538G	5	6.7	42.5	35.3	54.7	36.9	58.5	2.71	2.72	60.7	1.54	1.7	1.07	16.65	10.5	6.52
2539	1	0.7	36.3	58.5	140.9	60.7	154.4	2.66	2.7	80.2	4.05	1.36	0.53	13.32	5.23	3.24
2539	2	2.2	36.3	58.1	138.7	60.3	151.9	2.67	2.7	80	3.99	1.36	0.54	13.36	5.31	3.29
2539	3	3.7	36.2	57.3	134	59.4	146.4	2.65	2.69	79.3	3.83	1.37	0.56	13.45	5.46	3.37
2539	4	5.2	36.2	49.4	97.5	51.2	105	2.68	2.7	73.4	2.76	1.47	0.72	14.44	7.04	4.36
2539	5	6.55	36.3	47.6	90.9	49.4	97.7	2.68	2.7	71.9	2.56	1.5	0.76	14.67	7.42	4.6
2539	5	6.85	36.4	44.8	81.1	46.5	86.8	2.69	2.71	69.6	2.29	1.54	0.82	15.1	8.09	5.02
2539	6	8.1	36.4	39.4	65.1	40.9	69.3	2.7	2.72	64.7	1.83	1.62	0.96	15.93	9.41	5.85
2539	7	9.73	36.4	36	56.2	37.3	59.6	2.71	2.73	61.2	1.58	1.69	1.06	16.54	10.36	6.46
2539	8	11.22	36.5	38.6	62.8	40	66.8	2.71	2.73	63.9	1.77	1.64	0.98	16.09	9.65	6.01
2539	9	12.7	36.6	40.3	67.5	41.9	72	2.7	2.72	65.5	1.9	1.61	0.94	15.79	9.18	5.71
2539	10	14.2	36.5	36.5	57.4	37.9	60.9	2.71	2.73	61.8	1.61	1.68	1.04	16.45	10.22	6.37
2539	11	15.7	36.5	35.8	55.8	37.2	59.1	2.72	2.74	61.1	1.57	1.69	1.06	16.59	10.42	6.51
2539	12	17.2	36.8	32.7	48.5	33.9	51.3	2.72	2.74	57.7	1.37	1.75	1.16	17.16	11.35	7.08
2539	13	18.7	36.8	42.6	74.2	44.2	79.2	2.69	2.71	67.6	2.09	1.57	0.88	15.42	8.6	5.34
2539	14	20	36.7	37	58.7	38.4	62.4	2.71	2.73	62.3	1.66	1.67	1.03	16.36	10.08	6.28
2539	15	21.7	37.2	39.1	64.1	40.6	68.3	2.7	2.72	64.3	1.8	1.63	0.97	15.99	9.5	5.9
2539	16	23.2	37.3	39.9	66.4	41.4	70.8	2.69	2.7	65	1.86	1.61	0.95	15.83	9.27	5.74
2539	18	26.2	36.7	41	69.4	42.5	74	2.69	2.7	66	1.94	1.6	0.92	15.66	9	5.57
2539	19	27.7	37	38.8	63.4	40.3	67.5	2.7	2.71	64.1	1.78	1.63	0.98	16.02	9.57	5.94
2539	20	29.2	37.2	38.9	63.8	40.4	67.9	2.68	2.69	64	1.78	1.63	0.97	15.96	9.51	5.88
2539	21	30.5	37.8	39.5	65.3	41.1	69.6	2.68	2.7	64.6	1.83	1.62	0.95	15.88	9.36	5.79
2541	1	0.55	35.8	56.7	130.7	58.8	142.5	2.66	2.69	78.8	3.73	1.38	0.57	13.52	5.57	3.44
2541	1	0.75	35.8	53.3	113.9	55.2	123.3	2.65	2.68	76.3	3.22	1.42	0.64	13.92	6.23	3.84
2541	2	2.2	36	57.6	136	59.8	148.7	2.65	2.68	79.5	3.87	1.37	0.55	13.4	5.39	3.32
2541	2	2.2	36	58.8	142.8	61	156.5	2.65	2.68	80.3	4.08	1.35	0.53	13.26	5.17	3.19
2541	3	3.7	36.2	50.2	100.6	52	108.5	2.68	2.7	74.1	2.85	1.46	0.7	14.34	6.88	4.26
2541	4	5.2	36.2	49.3	97.3	51.2	104.8	2.67	2.7	73.3	2.75	1.47	0.72	14.44	7.05	4.36
2541	5	6.75	36.1	41.8	71.7	43.3	76.4	2.7	2.72	66.9	2.02	1.59	0.9	15.56	8.82	5.48
2541	5	6.7	36.1	42.9	75.2	44.5	80.2	2.7	2.72	68	2.12	1.57	0.87	15.39	8.54	5.31
2541	6	8.2	36.1	39.8	66.1	41.3	70.3	2.7	2.72	65	1.86	1.62	0.95	15.87	9.32	5.79
2541	7	9.7	36.8	39.2	64.5	40.7	68.6	2.71	2.72	64.5	1.82	1.63	0.97	15.98	9.48	5.9
2541	7	9.8	36.8	36	56.2	37.4	59.7	2.71	2.72	61.2	1.58	1.68	1.06	16.52	10.35	6.44
2541	8	11.2	37.3	36.6	57.7	38	61.3	2.71	2.72	61.9	1.62	1.67	1.04	16.42	10.18	6.34
2541	8	11.2	37.3	37.9	61.1	39.4	65.1	2.71	2.73	63.3	1.72	1.65	1	16.19	9.81	6.11
2541	9	12.7	37	36.5	57.5	37.9	61	2.72	2.73	61.8	1.62	1.68	1.04	16.46	10.22	6.38
2541	10	14.2	36.9	34.5	52.7	35.8	55.8	2.72	2.74	59.8	1.49	1.72	1.1	16.82	10.79	6.74

Table 4. Water content and index properties. — Continued

[m, meters; Sal Est, salinity estimated; ppt, parts per thousand; WCt, water content based on total sample mass not corrected for salinity; %, percent; WCs, water content based on solids mass not corrected for salinity; WCtc, water content based on total sample mass corrected for salinity; WCsc, water content based on solids mass corrected for salinity; ρs, grain density not corrected for salinity; g/cm^3, grams per cubic centimeter; ρsc, grain density corrected for salinity; n, porosity; e, void ratio; ρw, wet bulk density; ρd, dry bulk density; γw, wet unit weight; kN/m^3, kiloNewton per cubic meter; γd, dry unit weight; γsub, submerged unit weight]

Core no.	Section	Mid-depth (m)	Sal Est (ppt)	WCt (%)	WCs (%)	WCtc (%)	WCsc (%)	ρs (g/cm^3)	ρsc (g/cm^3)	n (%)	e	ρw (g/cm^3)	ρd (g/cm^3)	γw (kN/m^3)	γd (kN/m^3)	γsub (kN/m^3)
2541	11	15.7	37	42.1	72.8	43.8	77.8	2.69	2.71	67.2	2.05	1.58	0.89	15.49	8.71	5.4
2541	12	17.2	37.1	39.7	65.9	41.3	70.2	2.7	2.72	65	1.85	1.62	0.95	15.88	9.33	5.8
2541	13	18.7	36.9	41.7	71.5	43.3	76.4	2.68	2.69	66.7	2	1.58	0.9	15.53	8.8	5.44
2541	14	20.2	36.8	35	53.8	36.3	57	2.7	2.71	60	1.5	1.7	1.08	16.68	10.63	6.6
2541	15	21.7	36.9	41.2	70.1	42.8	74.8	2.69	2.71	66.3	1.97	1.59	0.91	15.63	8.95	5.55
2541	16	23.25	37	40.3	67.4	41.8	71.9	2.7	2.72	65.5	1.9	1.61	0.94	15.8	9.19	5.72
2541	17	24.7	36.9	41.2	70.2	42.8	74.9	2.69	2.71	66.3	1.97	1.59	0.91	15.63	8.94	5.54
2541	18	26.2	36.9	38.5	62.7	40	66.7	2.69	2.7	63.7	1.75	1.64	0.98	16.05	9.63	5.96
2541	19	27.7	37.2	38.4	62.4	39.9	66.4	2.69	2.71	63.6	1.75	1.64	0.99	16.08	9.66	5.99
2541	20	29.2	37.7	39.8	66.2	41.4	70.7	2.7	2.72	65.1	1.87	1.62	0.95	15.87	9.3	5.78
2541	21	30.2	37.7	35.2	54.4	36.6	57.8	2.69	2.7	60.3	1.52	1.69	1.07	16.61	10.53	6.52
2541	21	30.7	37.4	40.3	67.4	41.8	71.9	2.69	2.71	65.4	1.89	1.61	0.94	15.77	9.18	5.69
2541	22	31.6	37.1	38.8	63.3	40.2	67.3	2.7	2.71	64	1.78	1.63	0.98	16.03	9.58	5.95
2541	23	33.7	37.8	38.6	62.8	40.1	66.9	2.7	2.71	63.8	1.77	1.64	0.98	16.06	9.62	5.97
2541	24	34.9	38.5	32.3	47.8	33.6	50.7	2.68	2.7	57	1.33	1.75	1.16	17.12	11.36	7.02
2542GHF	3	3.7	35	46.4	86.4	48	92.5	2.68	2.7	70.8	2.43	1.51	0.79	14.84	7.71	4.78
2542GHF	4	5.2	35	39.7	65.8	41.1	69.8	2.7	2.72	64.9	1.85	1.62	0.95	15.89	9.36	5.82
2542GHF	5	6.8	35	43.3	76.4	44.9	81.5	2.69	2.71	68.3	2.15	1.56	0.86	15.31	8.44	5.24
2545G	1	0.4	42.4	53.2	113.9	55.6	125.2	2.66	2.69	76.6	3.27	1.42	0.63	13.94	6.19	3.82
2545G	2	1.5	43.3	57.7	136.2	60.3	151.8	2.64	2.68	79.7	3.93	1.37	0.54	13.4	5.32	3.27
2545G	3	2.43	57.4	53.2	113.5	56.4	129.3	2.66	2.71	77	3.35	1.43	0.62	13.98	6.1	3.74
2545G	4	3.35	67	32.7	48.5	35	53.9	2.7	2.73	58.3	1.4	1.75	1.14	17.16	11.15	6.85
2545G	5	4.35	75.1	48.1	92.8	52	108.5	2.65	2.7	73.5	2.77	1.49	0.72	14.64	7.02	4.27
2545G	6	5.3	80.8	48.2	93.2	52.5	110.4	2.65	2.7	73.7	2.81	1.49	0.71	14.63	6.95	4.22
2545G	7	6.46	86.1	41.9	72.2	45.9	84.7	2.67	2.72	68.4	2.16	1.59	0.86	15.59	8.44	5.13
2545G	8	7.4	91.8	39.3	64.8	43.3	76.3	2.68	2.72	66	1.94	1.63	0.93	16	9.08	5.51
2545G	9	8.5	95.5	35.5	55.1	39.3	64.7	2.69	2.73	62.2	1.65	1.7	1.03	16.67	10.12	6.15
2545G	10	9.2	99.6	33.4	50.2	37.1	59	2.67	2.7	59.7	1.48	1.73	1.09	16.98	10.68	6.43
2546	1	0.55	35.8	59.4	146.2	61.6	160.3	2.65	2.69	80.7	4.19	1.35	0.52	13.21	5.07	3.13
2546	2	2.15	35.9	58.5	140.8	60.7	154.1	2.65	2.68	80.1	4.02	1.36	0.53	13.3	5.23	3.23
2546	3	3.5	36.1	63.1	170.9	65.4	189.4	2.66	2.71	83.3	4.98	1.31	0.45	12.83	4.43	2.75
2546	4	5.2	36.8	49.1	96.5	51	104	2.66	2.68	73.1	2.71	1.47	0.72	14.45	7.08	4.36
2546	5	6.35	37.6	48.3	93.4	50.2	100.7	2.7	2.72	72.7	2.66	1.49	0.74	14.62	7.28	4.53
2546	6	7.8	39.2	44.9	81.6	46.8	87.8	2.7	2.72	69.9	2.32	1.54	0.82	15.1	8.04	5
2546	7	9.6	40.2	39.5	65.3	41.2	69.9	2.7	2.71	64.8	1.84	1.62	0.96	15.92	9.37	5.81
2546	8	11.05	43	38.1	61.5	39.8	66.1	2.71	2.73	63.6	1.74	1.65	0.99	16.18	9.75	6.06
2546	9	12.65	44.4	37.2	59.3	38.9	63.8	2.71	2.73	62.7	1.68	1.67	1.02	16.34	9.98	6.2
2546	10	14.25	45.6	36.2	56.8	38	61.2	2.71	2.73	61.8	1.62	1.68	1.05	16.52	10.25	6.37
2546	11	15.7	46.5	44.5	80.1	46.6	87.4	2.68	2.71	69.5	2.28	1.54	0.82	15.14	8.08	4.99
2546	12	17.2	47.4	38.6	63	40.6	68.2	2.7	2.72	64.2	1.79	1.64	0.97	16.08	9.56	5.92
2546	13	18.45	47.9	40.6	68.3	42.6	74.3	2.69	2.72	66.1	1.95	1.61	0.92	15.76	9.04	5.59
2546	14	20.4	48.6	37	58.8	38.9	63.8	2.69	2.71	62.5	1.67	1.67	1.02	16.33	9.97	6.16
2546	15	21.65	50.6	39.9	66.3	42	72.4	2.69	2.72	65.4	1.89	1.62	0.94	15.87	9.21	5.69
2546	16	23.05	49.8	39.7	65.8	41.8	71.7	2.69	2.71	65.2	1.87	1.62	0.94	15.89	9.26	5.71
2546	17	24.75	52.9	39.9	66.3	42.1	72.7	2.68	2.71	65.4	1.89	1.62	0.94	15.85	9.18	5.65
2546	18	26.2	53.7	33.3	49.9	35.2	54.3	2.69	2.71	58.5	1.41	1.73	1.12	16.98	11.01	6.77

Table 4. Water content and index properties. — Continued

[m, meters; Sal Est, salinity estimated; ppt, parts per thousand; WCt, water content based on total sample mass not corrected for salinity; %, percent; WCs, water content based on solids mass not corrected for salinity; WCtc, water content based on total sample mass corrected for salinity; WCsc, water content based on solids mass corrected for salinity; ρs, grain density not corrected for salinity; g/cm^3, grams per cubic centimeter; ρsc, grain density corrected for salinity; n, porosity; e, void ratio; ρw, wet bulk density; ρd, dry bulk density; γw, wet unit weight; kN/m^3, kiloNewton per cubic meter; γd, dry unit weight; γsub, submerged unit weight]

Core no.	Section	Mid-depth (m)	Sal Est (ppt)	WCt (%)	WCs (%)	WCtc (%)	WCsc (%)	ρs (g/cm^3)	ρsc (g/cm^3)	n (%)	e	ρw (g/cm^3)	ρd (g/cm^3)	γw (kN/m^3)	γd (kN/m^3)	γsub (kN/m^3)
2546	19	27.65	52.5	36	56.2	38	61.2	2.69	2.71	61.4	1.59	1.68	1.05	16.52	10.25	6.31
2546	20	29.2	53.1	39.5	65.4	41.7	71.6	2.7	2.73	65.3	1.88	1.63	0.95	15.96	9.3	5.75
2546	21	30.6	54.4	39.5	65.2	41.7	71.6	2.68	2.71	65.1	1.86	1.62	0.95	15.93	9.28	5.71
2547GHF	1	0.74	35	57.5	135.5	59.6	147.7	2.65	2.69	79.4	3.86	1.37	0.55	13.41	5.41	3.34
2547GHF	2	2.1	35	56.8	131.2	58.8	142.7	2.66	2.69	78.9	3.73	1.38	0.57	13.51	5.56	3.44
2547GHF	3	3.7	35	48.3	93.4	50.1	100.2	2.67	2.69	72.4	2.63	1.49	0.74	14.57	7.28	4.5
2547GHF	4	5	35	38.1	61.6	39.5	65.3	2.7	2.72	63.3	1.73	1.65	1	16.14	9.77	6.08
2550C2	1	0.5	305.9	61.6	160.2	88.7	785.2	2.45	3.52	95.7	22.34	1.33	0.15	13.07	1.48	0.96
2550C2	2	1	299.8	62.1	163.8	88.7	782.2	2.41	3.24	95.4	20.61	1.32	0.15	12.98	1.47	0.91
2550C2	2	1	299.8	62.3	164.9	88.9	800.7	2.41	3.27	95.5	21.27	1.32	0.15	12.97	1.44	0.9
2550C2	3	1.5	297.1	59.5	147.1	84.7	553.6	2.43	3.04	93.2	13.69	1.35	0.21	13.26	2.03	1.21
2550C2	4	2	292.2	54	117.5	76.3	322.4	2.48	2.86	88.3	7.53	1.42	0.34	13.89	3.29	1.88
2550C2	5	3	275.5	47.8	91.6	66	193.9	2.54	2.8	81.7	4.48	1.5	0.51	14.73	5.01	2.84
2550C2	6	4	275.4	49.4	97.5	68.1	213.7	2.55	2.83	83.3	4.99	1.48	0.47	14.54	4.63	2.65
2550C2	6	4	275.4	49.1	96.3	67.7	209.6	2.55	2.83	83	4.89	1.49	0.48	14.57	4.71	2.69
2550C2	7	5	234.4	50.1	100.5	65.5	189.5	2.51	2.69	81.2	4.32	1.46	0.51	14.36	4.96	2.78
2550C2	7	5	234.4	51	104	66.6	199.4	2.51	2.7	82	4.56	1.45	0.49	14.26	4.76	2.68
2550C2	8	6	209.9	45.4	83	57.4	134.8	2.59	2.73	76	3.17	1.54	0.65	15.08	6.42	3.69
2550C2	9	6.9	167.8	41.9	72.1	50.3	101.3	2.6	2.69	70.7	2.42	1.59	0.79	15.56	7.73	4.49
2550C2	9	6.9	167.8	41.8	71.7	50.2	100.7	2.6	2.69	70.6	2.4	1.59	0.79	15.58	7.76	4.51
2550C2	10	8	207.8	41.5	70.8	52.3	109.8	2.6	2.72	72	2.57	1.6	0.76	15.65	7.46	4.27
2550C2	10	8	207.8	38.4	62.3	48.4	94	2.6	2.7	68.6	2.19	1.64	0.85	16.11	8.31	4.74
2550C2	11	8.9	183.9	38.8	63.3	47.5	90.4	2.63	2.72	68.3	2.15	1.64	0.86	16.1	8.46	4.91
2550C2	11	8.9	183.9	38.4	62.3	47	88.8	2.63	2.72	67.9	2.11	1.65	0.87	16.16	8.56	4.96
2553C2	1	0.6	35.7	56.9	131.8	59	143.7	2.67	2.71	79.1	3.79	1.38	0.57	13.52	5.55	3.44
2553C2	2	1	35.7	53.6	115.6	55.6	125.3	2.68	2.71	76.8	3.3	1.42	0.63	13.91	6.17	3.83
2553C2	2	1	35.7	53.6	115.6	55.6	125.2	2.68	2.71	76.8	3.3	1.42	0.63	13.91	6.17	3.83
2553C2	3	1.7	35.9	53.8	116.3	55.8	126.1	2.68	2.71	76.9	3.32	1.42	0.63	13.88	6.14	3.81
2553C2	3	1.7	35.9	53.9	116.7	55.9	126.6	2.68	2.71	76.9	3.33	1.41	0.62	13.87	6.12	3.8
2553C2	4	2	38	50.2	100.7	52.2	109	2.69	2.72	74.2	2.88	1.46	0.7	14.36	6.87	4.27
2553C2	4	2	38	49.7	98.8	51.7	106.8	2.69	2.72	73.8	2.82	1.47	0.71	14.42	6.97	4.33
2553C2	5	3.1	36.1	50.2	100.7	52.1	108.5	2.69	2.71	74.1	2.86	1.46	0.7	14.35	6.88	4.27
2553C2	5	3.1	36.1	49.4	97.5	51.2	105	2.69	2.71	73.5	2.77	1.47	0.72	14.45	7.05	4.38
2553C2	6	4	36.2	49.1	96.4	50.9	103.8	2.68	2.7	73.2	2.73	1.48	0.72	14.48	7.11	4.4
2553C2	6	4	36.2	49.9	99.8	51.8	107.5	2.68	2.7	73.9	2.83	1.47	0.71	14.37	6.92	4.29
2553C2	7	5	36.3	51.6	106.5	53.5	115.1	2.66	2.69	75.1	3.01	1.44	0.67	14.14	6.57	4.06
2553C2	7	5	36.3	51.7	106.9	53.6	115.5	2.66	2.69	75.1	3.02	1.44	0.67	14.13	6.56	4.05
2553C2	8	6.1	36.5	52.3	109.7	54.3	118.8	2.66	2.69	75.7	3.11	1.43	0.65	14.05	6.42	3.97
2553C2	8	6.1	36.5	52.2	109.3	54.2	118.4	2.66	2.69	75.6	3.1	1.43	0.66	14.06	6.44	3.98
2553C2	9	7	36.6	50.1	100.5	52	108.4	2.65	2.67	73.8	2.82	1.46	0.7	14.3	6.86	4.22
2553C2	9	7	36.6	50.1	100.2	52	108.1	2.65	2.67	73.7	2.81	1.46	0.7	14.31	6.88	4.23
2553C2	10	8	36.7	48.8	95.4	50.7	102.8	2.65	2.67	72.7	2.67	1.48	0.73	14.47	7.13	4.39
2553C2	10	8	36.7	48.5	94	50.3	101.2	2.65	2.67	72.4	2.63	1.48	0.74	14.52	7.21	4.43
2553C2	11	9	36.8	50	100.2	52	108.1	2.65	2.67	73.8	2.81	1.46	0.7	14.32	6.88	4.23
2553C2	11	9	36.8	49.3	97.2	51.2	104.8	2.65	2.67	73.2	2.72	1.47	0.72	14.41	7.04	4.33
2553C2	11	9	36.8	49.8	99.3	51.7	107.2	2.65	2.67	73.6	2.79	1.46	0.71	14.34	6.92	4.26

Table 4. Water content and index properties. — Continued

[m, meters; Sal Est, salinity estimated; ppt, parts per thousand; WCt, water content based on total sample mass not corrected for salinity; %, percent; WCs, water content based on solids mass not corrected for salinity; WCtc, water content based on total sample mass corrected for salinity; WCsc, water content based on solids mass corrected for salinity; ρs, grain density not corrected for salinity; g/cm^3, grams per cubic centimeter; ρsc, grain density corrected for salinity; n, porosity; e, void ratio; ρw, wet bulk density; ρd, dry bulk density; γw, wet unit weight; kN/m^3, kiloNewton per cubic meter; γd, dry unit weight; γsub, submerged unit weight]

Core no.	Section	Mid-depth (m)	Sal Est (ppt)	WCt (%)	WCs (%)	WCtc (%)	WCsc (%)	ρs (g/cm^3)	ρsc (g/cm^3)	n (%)	e	ρw (g/cm^3)	ρd (g/cm^3)	γw (kN/m^3)	γd (kN/m^3)	γsub (kN/m^3)
2553C2	12	10	36.8	45.9	84.7	47.6	90.9	2.67	2.69	70.4	2.38	1.52	0.8	14.91	7.81	4.82
2553C2	12	10	36.8	45.9	85	47.7	91.2	2.67	2.69	70.5	2.39	1.52	0.79	14.9	7.79	4.81
2554	1	0.7	36	59.8	148.8	62	163.4	2.64	2.68	81	4.26	1.34	0.51	13.16	4.99	3.08
2554	2	2.2	35.9	55	122.3	57.1	132.9	2.66	2.69	77.7	3.48	1.4	0.6	13.71	5.89	3.64
2554	3	3.7	35.6	54.2	118.2	56.2	128.2	2.67	2.7	77.1	3.37	1.41	0.62	13.82	6.06	3.75
2554	4	5.2	35.5	55.2	123	57.2	133.6	2.63	2.66	77.5	3.45	1.39	0.6	13.66	5.85	3.59
2554	5	6.8	35.8	48.5	94.1	50.3	101.1	2.66	2.69	72.6	2.64	1.48	0.74	14.54	7.23	4.46
2554	6	8.2	36.1	44.6	80.4	46.2	86	2.68	2.7	69.3	2.26	1.54	0.83	15.11	8.12	5.03
2554	7	9.8	36.5	45.3	82.7	47	88.6	2.66	2.68	69.8	2.31	1.53	0.81	14.98	7.94	4.9
2554	8	11.2	36.5	42.1	72.7	43.7	77.6	2.69	2.71	67.1	2.04	1.58	0.89	15.49	8.72	5.41
2554	9	12.6	36.4	37.9	61.1	39.4	65	2.7	2.72	63.2	1.72	1.65	1	16.17	9.81	6.09
2554	10	14	36.6	35.5	54.9	36.8	58.2	2.71	2.72	60.7	1.54	1.69	1.07	16.62	10.5	6.54
2554	11	15.6	37	36.6	57.8	38	61.4	2.7	2.71	61.8	1.62	1.67	1.04	16.39	10.15	6.31
2554	12	17.3	37.4	35.8	55.8	37.2	59.2	2.7	2.72	61	1.57	1.69	1.06	16.55	10.39	6.46
2554	13	19.1	37.2	38.5	62.5	40	66.5	2.69	2.7	63.6	1.75	1.64	0.98	16.06	9.64	5.98
2554	14	20	36.7	35.1	54	36.4	57.2	2.7	2.71	60.1	1.51	1.7	1.08	16.66	10.6	6.58
2554	15	21.45	40.2	36.1	56.6	37.6	60.3	2.7	2.72	61.4	1.59	1.68	1.05	16.49	10.29	6.39
2554	16	23.1	37.2	36.4	57.2	37.8	60.8	2.7	2.71	61.6	1.6	1.68	1.04	16.43	10.22	6.35
2554	17	24.6	37	34.1	51.7	35.4	54.8	2.7	2.71	59.1	1.45	1.72	1.11	16.84	10.88	6.76
2554	18	26.05	36.3	32.8	48.9	34.1	51.7	2.71	2.72	57.8	1.37	1.74	1.15	17.1	11.27	7.02
2554	19	27.5	36.7	31.4	45.7	32.6	48.3	2.7	2.71	56	1.28	1.77	1.19	17.35	11.69	7.26
2554	20	29	30.9	32.6	48.4	33.6	50.7	2.7	2.72	57.4	1.34	1.74	1.16	17.11	11.35	7.07
2554	21	30.35	37.1	32.5	48.2	33.8	51	2.71	2.72	57.4	1.35	1.75	1.16	17.14	11.35	7.06
2555	1	1.1	35.8	59.7	147.8	61.9	162.2	2.64	2.68	80.9	4.23	1.34	0.51	13.17	5.02	3.1
2555	2	2	35.8	57.2	133.6	59.3	145.8	2.65	2.68	79.2	3.81	1.37	0.56	13.45	5.47	3.38
2555	3	3.5	35.9	54.8	121.1	56.8	131.6	2.65	2.67	77.4	3.42	1.4	0.6	13.72	5.93	3.65
2555	4	5.2	36	54.7	120.9	56.8	131.3	2.65	2.68	77.4	3.42	1.4	0.61	13.73	5.94	3.66
2555	5	6.7	36.1	51.4	105.9	53.4	114.4	2.63	2.66	74.7	2.96	1.44	0.67	14.12	6.59	4.04
2555	6	8.2	36.1	48.2	93.2	50.1	100.2	2.67	2.7	72.5	2.63	1.49	0.74	14.59	7.29	4.51
2555	7	9.7	36.3	44.4	79.8	46.1	85.3	2.68	2.7	69.1	2.24	1.54	0.83	15.13	8.16	5.05
2555	8	11.2	36.4	44.3	79.6	46	85.1	2.68	2.7	69.1	2.24	1.54	0.83	15.15	8.18	5.07
2555	9	12.65	36.3	43	75.4	44.6	80.5	2.68	2.7	67.9	2.11	1.56	0.87	15.33	8.49	5.25
2555	10	14.2	36.4	37.8	60.7	39.2	64.4	2.7	2.72	63	1.7	1.65	1.01	16.21	9.86	6.13
2555	11	15.8	36.4	36.6	57.8	38	61.3	2.7	2.72	61.9	1.62	1.67	1.04	16.4	10.17	6.32
2555	12	17.2	36.2	34.8	53.3	36.1	56.4	2.71	2.72	59.9	1.49	1.71	1.09	16.74	10.7	6.66
2555	13	18.7	36.4	36.8	58.3	38.2	61.8	2.7	2.71	62	1.63	1.67	1.03	16.36	10.11	6.28
2555	14	20.2	36.7	36.7	57.9	38.1	61.5	2.69	2.7	61.8	1.61	1.67	1.03	16.36	10.13	6.28
2555	15	21.6	36.6	35.1	54.1	36.4	57.3	2.71	2.72	60.2	1.52	1.7	1.08	16.67	10.6	6.59
2555	16	23.2	36.5	35.7	55.6	37.1	58.9	2.69	2.71	60.8	1.55	1.69	1.06	16.54	10.41	6.46
2555	17	24.9	36.3	34	51.6	35.3	54.6	2.68	2.7	58.9	1.43	1.71	1.11	16.81	10.87	6.73
2555	18	26.2	36.3	33.2	49.8	34.5	52.6	2.72	2.73	58.3	1.4	1.74	1.14	17.05	11.17	6.97
2555	19	27.6	36.4	32.7	48.5	33.9	51.3	2.7	2.72	57.6	1.36	1.74	1.15	17.11	11.31	7.03
2555	20	29.2	36.4	32	47	33.2	49.7	2.69	2.7	56.7	1.31	1.75	1.17	17.2	11.49	7.12
2555	21	30.7	36.3	32.5	48.2	33.7	50.9	2.71	2.72	57.4	1.35	1.75	1.16	17.14	11.36	7.06
2555	22	32.2	36.2	33.1	49.6	34.4	52.4	2.71	2.72	58.1	1.39	1.74	1.14	17.03	11.17	6.95
2555	23	33.85	36.7	31.7	46.5	33	49.2	2.72	2.73	56.6	1.3	1.77	1.18	17.32	11.61	7.24
2555	24	35.1	36.1	32	47	33.2	49.6	2.71	2.72	56.8	1.31	1.76	1.18	17.25	11.53	7.18

Table 4. Water content and index properties. — Continued

[m, meters; Sal Est, salinity estimated; ppt, parts per thousand; WCt, water content based on total sample mass not corrected for salinity; %, percent; WCs, water content based on solids mass not corrected for salinity; WCtc, water content based on total sample mass corrected for salinity; WCsc, water content based on solids mass corrected for salinity; ρs, grain density not corrected for salinity; g/cm^3, grams per cubic centimeter; ρsc, grain density corrected for salinity; n, porosity; e, void ratio; ρw, wet bulk density; ρd, dry bulk density; γw, wet unit weight; kN/m^3, kiloNewton per cubic meter; γd, dry unit weight; γsub, submerged unit weight]

Core no.	Section	Mid-depth (m)	Sal Est (ppt)	WCt (%)	WCs (%)	WCtc (%)	WCsc (%)	ρs (g/cm^3)	ρsc (g/cm^3)	n (%)	e	ρw (g/cm^3)	ρd (g/cm^3)	γw (kN/m^3)	γd (kN/m^3)	γsub (kN/m^3)
2556	1	0.7	35.5	59.6	147.3	61.8	161.5	2.65	2.68	80.8	4.21	1.34	0.51	13.18	5.04	3.11
2556	2	2.2	35.6	54.6	120	56.6	130.2	2.66	2.69	77.3	3.41	1.4	0.61	13.77	5.98	3.69
2556	3	3.7	35.9	54.8	121.3	56.9	131.8	2.66	2.69	77.5	3.44	1.4	0.6	13.73	5.93	3.66
2556	4	5.2	36	55.5	124.5	57.5	135.5	2.65	2.68	77.9	3.53	1.39	0.59	13.64	5.79	3.57
2556	5	6.7	36	51.8	107.4	53.7	116.1	2.65	2.67	75.1	3.02	1.44	0.67	14.09	6.52	4.02
2556	6	8.1	35.9	47	88.8	48.8	95.2	2.67	2.69	71.4	2.49	1.5	0.77	14.74	7.55	4.66
2556	7	9.7	35.8	42.2	73.1	43.8	77.9	2.68	2.7	67.2	2.05	1.58	0.89	15.45	8.69	5.38
2556	8	11.6	35.6	43.5	76.9	45.1	82.1	2.67	2.68	68.2	2.15	1.55	0.85	15.24	8.37	5.17
2556	9	12.7	35.5	44.5	80.2	46.2	85.7	2.67	2.69	69.1	2.24	1.54	0.83	15.09	8.13	5.02
2556	10	14.17	35.5	36.7	57.9	38	61.4	2.71	2.72	61.9	1.62	1.67	1.04	16.4	10.16	6.32
2556	11	15.4	35.5	38.3	62	39.7	65.8	2.7	2.72	63.5	1.74	1.64	0.99	16.12	9.73	6.05
2556	12	17.15	35.9	38.1	61.5	39.5	65.2	2.7	2.71	63.3	1.72	1.65	1	16.14	9.77	6.07
2556	13	18.7	36.1	37.2	59.3	38.6	62.9	2.7	2.72	62.5	1.66	1.66	1.02	16.29	10	6.22
2556	14	20.2	36.3	37.3	59.4	38.7	63	2.69	2.71	62.4	1.66	1.66	1.02	16.27	9.98	6.19
2556	15	21.7	36.3	36.7	58	38.1	61.6	2.69	2.71	61.9	1.62	1.67	1.03	16.36	10.13	6.28
2556	16	23.3	36.4	33.5	50.4	34.8	53.3	2.7	2.72	58.5	1.41	1.73	1.13	16.95	11.06	6.87
2556	17	24.8	36.2	33.9	51.3	35.2	54.3	2.71	2.73	59	1.44	1.72	1.12	16.9	10.96	6.83
2556	18	26.3	36.1	33.7	50.9	35	53.9	2.7	2.71	58.7	1.42	1.72	1.12	16.89	10.98	6.82
2556	19	27.7	36.1	32.7	48.5	33.9	51.3	2.7	2.72	57.5	1.36	1.74	1.15	17.11	11.31	7.03
2556	20	29.2	36.1	33.7	50.9	35	53.8	2.7	2.72	58.7	1.42	1.72	1.12	16.91	10.99	6.83
2556	21	30.7	36.2	34.1	51.8	35.4	54.8	2.7	2.71	59.1	1.45	1.72	1.11	16.82	10.86	6.74
2556	22	32.1	36.3	31.4	45.8	32.6	48.4	2.71	2.72	56.1	1.28	1.77	1.19	17.35	11.69	7.27
2556	23	33.75	36.1	31.5	46	32.7	48.6	2.71	2.72	56.2	1.28	1.77	1.19	17.33	11.67	7.25
2559	2	2.1	36.3	55.1	122.8	57.2	133.6	2.53	2.56	76.9	3.32	1.38	0.59	13.54	5.8	3.46
2559	3	3.7	36.2	58.9	143	61.1	156.8	2.64	2.67	80.3	4.08	1.35	0.53	13.25	5.16	3.18
2559	4	5.1	36.1	53	112.6	55	122	2.62	2.64	75.8	3.13	1.42	0.64	13.9	6.26	3.82
2559	5	6.6	36	52.4	110.2	54.4	119.2	2.58	2.6	75.1	3.02	1.42	0.65	13.92	6.35	3.84
2559	6	8.1	36.1	46.8	87.9	48.5	94.3	2.64	2.66	70.9	2.44	1.5	0.77	14.73	7.58	4.65
2559	7	9.6	36.3	41.1	69.9	42.7	74.5	2.68	2.69	66.1	1.95	1.59	0.91	15.61	8.95	5.53
2559	8	11.2	36.2	41.5	70.9	43	75.6	2.67	2.68	66.4	1.97	1.58	0.9	15.54	8.85	5.46
2559	9	12.6	36.1	37.8	60.7	39.2	64.5	2.68	2.7	62.8	1.69	1.65	1	16.16	9.83	6.08
2559	10	14.1	36.1	42	72.5	43.6	77.3	2.66	2.67	66.8	2.01	1.57	0.89	15.43	8.7	5.36
2559	11	15.7	36.1	38.4	62.4	39.9	66.3	2.69	2.71	63.6	1.75	1.64	0.99	16.07	9.66	5.99
2559	12	17.2	36.2	37.2	59.2	38.6	62.8	2.68	2.7	62.3	1.65	1.66	1.02	16.26	9.99	6.18
2559	13	18.6	36.3	37.4	59.6	38.8	63.3	2.67	2.69	62.3	1.65	1.65	1.01	16.2	9.92	6.13
2559	14	20.1	36.4	36.2	56.8	37.6	60.2	2.68	2.69	61.2	1.58	1.67	1.04	16.41	10.24	6.33
2559	15	21.7	36.6	33.4	50.2	34.7	53.1	2.68	2.7	58.2	1.39	1.73	1.13	16.92	11.05	6.84
2559	16	23.2	36.7	32.7	48.5	33.9	51.3	2.69	2.7	57.4	1.35	1.74	1.15	17.06	11.27	6.97
2559	17	24.7	36.5	33.2	49.7	34.5	52.6	2.69	2.71	58	1.38	1.73	1.13	16.98	11.13	6.9
2559	18	26.2	36.2	34.9	53.6	36.2	56.8	2.68	2.7	59.8	1.49	1.7	1.08	16.65	10.62	6.57
2559	19	27.6	36.2	33.7	50.9	35	53.9	2.69	2.7	58.6	1.41	1.72	1.12	16.86	10.96	6.79
2559	20	29.1	36.3	31.4	45.7	32.6	48.3	2.7	2.71	56	1.27	1.77	1.19	17.33	11.69	7.25
2559	21	30.7	36.4	31.4	45.8	32.6	48.3	2.7	2.71	56	1.27	1.77	1.19	17.32	11.68	7.24
2559	22	32.1	36.6	31.2	45.3	32.4	47.8	2.69	2.7	55.7	1.26	1.77	1.2	17.36	11.74	7.28
2559	23	33.2	36.4	32.9	48.9	34.1	51.8	2.68	2.69	57.6	1.36	1.73	1.14	17.01	11.21	6.93
2560	1	0.6	35.6	62.7	168.1	65	185.9	2.63	2.67	82.9	4.83	1.31	0.46	12.84	4.49	2.76

Table 4. Water content and index properties. — Continued

[m, meters; Sal Est, salinity estimated; ppt, parts per thousand; WCt, water content based on total sample mass not corrected for salinity; %, percent; WCs, water content based on solids mass not corrected for salinity; WCtc, water content based on total sample mass corrected for salinity; WCsc, water content based on solids mass corrected for salinity; ρs, grain density not corrected for salinity; g/cm^3, grams per cubic centimeter; ρsc, grain density corrected for salinity; n, porosity; e, void ratio; ρw, wet bulk density; ρd, dry bulk density; γw, wet unit weight; kN/m^3, kiloNewton per cubic meter; γd, dry unit weight; γsub, submerged unit weight]

Core no.	Section	Mid-depth (m)	Sal Est (ppt)	WCt (%)	WCs (%)	WCtc (%)	WCsc (%)	ρs (g/cm^3)	ρsc (g/cm^3)	n (%)	e	ρw (g/cm^3)	ρd (g/cm^3)	γw (kN/m^3)	γd (kN/m^3)	γsub (kN/m^3)
2560	2	2.2	35.9	56.1	128	58.2	139.4	2.65	2.68	78.4	3.64	1.38	0.58	13.57	5.67	3.5
2560	3	3.7	36.2	56.9	131.9	59	143.9	2.64	2.67	78.9	3.74	1.37	0.56	13.48	5.53	3.4
2560	4	5.1	36.4	52.4	110.1	54.4	119.2	2.61	2.63	75.3	3.05	1.42	0.65	13.96	6.37	3.88
2560	5	6.55	36.7	53.3	113.9	55.3	123.6	2.58	2.61	75.8	3.13	1.41	0.63	13.83	6.18	3.74
2560	6	8.22	36.7	45.4	83.2	47.1	89.2	2.64	2.66	69.7	2.31	1.52	0.8	14.92	7.88	4.83
2560	7	9.7	36.7	47	88.8	48.8	95.4	2.63	2.65	71.1	2.46	1.5	0.77	14.69	7.52	4.61
2560	8	11.15	36.7	40.9	69.3	42.5	73.9	2.66	2.68	65.8	1.93	1.59	0.92	15.62	8.98	5.53
2560	9	12.6	36.8	41	69.5	42.6	74.2	2.68	2.69	66	1.94	1.59	0.92	15.63	8.98	5.55
2560	10	14.2	36.7	38.3	62.1	39.8	66	2.67	2.68	63.3	1.72	1.64	0.99	16.04	9.66	5.96
2560	11	15.7	36.7	38.3	62	39.7	65.9	2.67	2.68	63.2	1.72	1.64	0.99	16.04	9.67	5.96
2560	12	17.25	36.7	35.7	55.6	37.1	59	2.69	2.7	60.8	1.55	1.68	1.06	16.52	10.39	6.44
2560	13	18.7	36.9	38.5	62.6	40	66.6	2.66	2.68	63.4	1.74	1.63	0.98	16	9.6	5.92
2560	14	20.1	37	36.1	56.5	37.5	59.9	2.69	2.71	61.2	1.58	1.68	1.05	16.47	10.3	6.38
2560	15	21.8	36.6	36.7	58.1	38.1	61.6	2.66	2.67	61.6	1.6	1.66	1.03	16.28	10.07	6.2
2560	17	24.7	36.6	35.4	54.9	36.8	58.2	2.68	2.69	60.4	1.52	1.69	1.07	16.55	10.46	6.47
2560	18	26.1	36.5	36.3	56.9	37.7	60.4	2.68	2.7	61.3	1.58	1.67	1.04	16.41	10.23	6.33
2560	19	27.6	36.3	33.7	50.8	34.9	53.7	2.69	2.7	58.5	1.41	1.72	1.12	16.89	10.99	6.81
2561	1	0.7	35.4	60.8	154.8	63	170.2	2.64	2.67	81.6	4.43	1.33	0.49	13.04	4.83	2.97
2561	2	1.8	35.5	58.1	138.6	60.2	151.4	2.66	2.69	79.9	3.97	1.36	0.54	13.36	5.31	3.29
2561	3	3.7	35.9	60.6	153.6	62.8	169	2.64	2.68	81.5	4.4	1.33	0.5	13.07	4.86	2.99
2561	4	5.25	36.1	53.5	115	55.5	124.7	2.64	2.67	76.4	3.24	1.42	0.63	13.88	6.18	3.8
2561	5	6.6	36.2	53.9	117	55.9	127	2.6	2.63	76.4	3.25	1.4	0.62	13.77	6.07	3.69
2561	6	8.2	36.6	46.5	86.9	48.3	93.3	2.66	2.68	70.8	2.43	1.51	0.78	14.8	7.66	4.71
2561	7	9.7	36.8	45.9	84.8	47.6	91	2.68	2.7	70.5	2.39	1.52	0.8	14.91	7.81	4.83
2561	8	10.9	36.8	42.6	74.2	44.2	79.3	2.67	2.69	67.5	2.08	1.57	0.87	15.38	8.58	5.3
2561	9	12.7	36.8	37.6	60.2	39	64	2.68	2.69	62.6	1.68	1.65	1.01	16.18	9.86	6.1
2561	10	14.2	36.8	35.5	55.1	36.9	58.4	2.69	2.71	60.6	1.54	1.69	1.07	16.57	10.46	6.49
2561	11	15.7	36.9	36.2	56.6	37.5	60.1	2.69	2.7	61.2	1.58	1.68	1.05	16.45	10.27	6.36
2561	12	17.5	37	37.2	59.2	38.6	62.9	2.68	2.7	62.3	1.65	1.66	1.02	16.26	9.98	6.17
2561	13	18.7	36.9	33.5	50.3	34.8	53.3	2.68	2.69	58.3	1.4	1.72	1.12	16.9	11.03	6.82
2561	14	20.2	36.9	36.2	56.8	37.6	60.3	2.68	2.7	61.3	1.58	1.67	1.04	16.42	10.25	6.34
2561	15	21.7	36.8	34.1	51.7	35.4	54.7	2.69	2.7	59	1.44	1.72	1.11	16.82	10.87	6.74
2561	16	23.3	36.7	34.5	52.7	35.8	55.8	2.69	2.71	59.5	1.47	1.71	1.1	16.74	10.75	6.66
2561	17	24.6	36.7	35.9	56.1	37.3	59.5	2.68	2.7	61	1.56	1.68	1.05	16.47	10.33	6.39
2561	18	26.2	36.6	32.8	48.8	34.1	51.6	2.7	2.71	57.6	1.36	1.74	1.15	17.06	11.25	6.98
2561	19	27.6	36.3	32.4	48	33.7	50.7	2.7	2.71	57.2	1.34	1.75	1.16	17.13	11.37	7.05
2562	1	0.5	35.7	53.4	114.7	55.4	124.3	2.65	2.67	76.4	3.23	1.42	0.63	13.88	6.19	3.81
2562	2	2.05	35.6	52.3	109.6	54.2	118.4	2.65	2.68	75.5	3.09	1.43	0.66	14.04	6.43	3.96
2562	3	3.7	35.6	52.4	109.9	54.3	118.8	2.66	2.68	75.6	3.1	1.43	0.65	14.03	6.41	3.95
2562	4	5.2	36	46.4	86.6	48.2	92.9	2.66	2.68	70.8	2.43	1.51	0.78	14.82	7.68	4.74
2562	5	6.4	36.2	41.7	71.6	43.3	76.3	2.65	2.67	66.5	1.98	1.58	0.89	15.47	8.77	5.39
2562	6	8.2	36.5	43.4	76.7	45.1	82	2.66	2.68	68.1	2.14	1.55	0.85	15.24	8.37	5.16
2562	7	9.7	36.7	38.7	63.1	40.2	67.2	2.69	2.71	63.9	1.77	1.63	0.98	16.03	9.59	5.95
2562	8	11	36.7	37.6	60.3	39	64.1	2.68	2.69	62.6	1.68	1.65	1.01	16.18	9.86	6.09
2562	9	12.6	36.6	37.2	59.3	38.7	63	2.68	2.7	62.3	1.65	1.66	1.02	16.25	9.97	6.17
2562	10	14.2	36.6	39.7	65.9	41.3	70.2	2.68	2.7	64.8	1.84	1.62	0.95	15.84	9.31	5.76
2562	11	15.6	36.5	38.4	62.2	39.8	66.2	2.66	2.67	63.2	1.72	1.63	0.98	16.01	9.64	5.93

Table 4. Water content and index properties. — Continued

[m, meters; Sal Est, salinity estimated; ppt, parts per thousand; WCt, water content based on total sample mass not corrected for salinity; %, percent; WCs, water content based on solids mass not corrected for salinity; WCtc, water content based on total sample mass corrected for salinity; WCsc, water content based on solids mass corrected for salinity; ρs, grain density not corrected for salinity; g/cm^3, grams per cubic centimeter; ρsc, grain density corrected for salinity; n, porosity; e, void ratio; ρw, wet bulk density; ρd, dry bulk density; γw, wet unit weight; kN/m^3, kiloNewton per cubic meter; γd, dry unit weight; γsub, submerged unit weight]

Core no.	Section	Mid-depth (m)	Sal Est (ppt)	WCt (%)	WCs (%)	WCtc (%)	WCsc (%)	ρs (g/cm^3)	ρsc (g/cm^3)	n (%)	e	ρw (g/cm^3)	ρd (g/cm^3)	γw (kN/m^3)	γd (kN/m^3)	γsub (kN/m^3)
2562	12	17.2	36.4	33	49.4	34.3	52.2	2.69	2.7	57.8	1.37	1.73	1.14	16.99	11.16	6.91
2562	13	18.6	36.5	33.5	50.4	34.8	53.3	2.69	2.7	58.4	1.4	1.73	1.13	16.92	11.03	6.84
2562	14	20.35	36.4	33.3	50	34.6	52.8	2.68	2.7	58.1	1.39	1.73	1.13	16.94	11.08	6.86
2562	15	21.7	36.4	33.5	50.4	34.8	53.3	2.68	2.69	58.3	1.4	1.72	1.12	16.89	11.02	6.82
2562	16	23.2	36.4	32.8	48.8	34	51.6	2.68	2.69	57.5	1.35	1.74	1.14	17.02	11.23	6.94
2562	17	24.7	36.5	32	47.1	33.2	49.7	2.69	2.7	56.6	1.31	1.75	1.17	17.2	11.49	7.12
2563C2	1	0.12	36.9	57.9	137.5	60.1	150.7	2.55	2.57	79	3.77	1.35	0.54	13.26	5.29	3.17
2563C2	1.5	0.2	37.6	58.8	142.9	61.1	157.2	2.58	2.61	79.9	3.98	1.35	0.52	13.19	5.13	3.1
2563C2	2	0.7	41.8	56.4	129.5	58.9	143.3	2.64	2.68	78.8	3.71	1.38	0.57	13.54	5.56	3.42
2563C2	3	1.3	48.1	53.2	113.5	55.9	126.5	2.6	2.63	76.2	3.21	1.42	0.62	13.88	6.13	3.71
2563C2	4	2.27	60.1	49.3	97.3	52.5	110.4	2.59	2.62	73.5	2.77	1.46	0.7	14.36	6.83	4.11
2563C2	5	2.85	66.8	49.3	97.4	52.9	112.2	2.54	2.58	73.3	2.75	1.46	0.69	14.3	6.74	3.99
2563C2	6	3.6	73.5	45.7	84	49.3	97.1	2.51	2.54	70	2.34	1.5	0.76	14.72	7.47	4.36
2565	3	3.9	122.1	46.4	86.4	52.8	111.9	2.57	2.64	73	2.7	1.51	0.71	14.83	7	4.1
2565	3.1	3.9	122.1	45	81.9	51.3	105.2	2.59	2.65	71.8	2.55	1.53	0.75	15.03	7.32	4.3
2565	3.2	3.9	122.1	44.4	80	50.6	102.5	2.6	2.66	71.4	2.49	1.54	0.76	15.13	7.47	4.4
2567	1	0.6	36	61.9	162.7	64.2	179.7	2.65	2.68	82.4	4.69	1.32	0.47	12.93	4.62	2.85
2567	1	0.6	36	62	163.3	64.3	180.4	2.65	2.68	82.5	4.71	1.32	0.47	12.92	4.61	2.84
2567	2	2.05	36.2	58.8	142.5	61	156.2	2.65	2.69	80.3	4.08	1.35	0.53	13.28	5.18	3.2
2567	3	3.6	36.4	60.4	152.4	62.7	167.8	2.65	2.68	81.4	4.38	1.34	0.5	13.1	4.89	3.02
2567	4	5.2	36.6	54	117.5	56.1	127.6	2.66	2.69	76.9	3.34	1.41	0.62	13.84	6.08	3.75
2567	5	6.4	36.7	49.2	96.9	51.1	104.5	2.63	2.65	73	2.7	1.47	0.72	14.39	7.04	4.31
2567	6	8.2	36.7	48.1	92.7	49.9	99.7	2.62	2.64	71.9	2.56	1.48	0.74	14.52	7.27	4.44
2567	7	9.7	36.8	46.8	88	48.6	94.5	2.63	2.65	70.9	2.44	1.5	0.77	14.72	7.57	4.63
2567	8	11	36.9	43.6	77.3	45.3	82.8	2.66	2.68	68.3	2.15	1.55	0.85	15.21	8.32	5.12
2567	9	12.5	37	39.6	65.6	41.1	69.9	3.32	3.37	69.6	2.29	1.74	1.02	17.06	10.04	6.97
2567	10	14.2	36.8	38	61.2	39.4	65.1	2.69	2.71	63.1	1.71	1.65	1	16.14	9.78	6.06
2567	11	15.7	36.8	36	56.2	37.4	59.7	2.69	2.7	61	1.57	1.68	1.05	16.47	10.31	6.39
2567	12	17.2	37	34.5	52.6	35.8	55.8	2.69	2.7	59.4	1.47	1.71	1.1	16.75	10.75	6.66
2567	13	18.6	37	38.3	62	39.7	65.9	2.67	2.69	63.3	1.72	1.64	0.99	16.06	9.68	5.97
2567	14	20.2	36.9	37.5	60	39	63.8	2.68	2.69	62.5	1.67	1.65	1.01	16.19	9.88	6.11
2567	15	21.7	37	36.4	57.2	37.8	60.7	2.68	2.7	61.4	1.59	1.67	1.04	16.39	10.2	6.31
2567	16	23.2	37	32	47.2	33.3	49.9	2.7	2.71	56.8	1.32	1.76	1.17	17.22	11.49	7.13
2567	17	24.55	36.8	33.8	51.1	35.1	54.1	2.7	2.71	58.8	1.42	1.72	1.12	16.88	10.96	6.8
2567	18	26.05	36.6	35.7	55.4	37	58.7	2.69	2.7	60.7	1.54	1.69	1.06	16.53	10.41	6.45
2569	1	0.95	35.8	42.1	72.6	43.6	77.4	2.66	2.68	66.9	2.02	1.58	0.89	15.45	8.71	5.37
2569	2	1.95	35.7	44.3	79.6	46	85.1	2.67	2.69	69	2.23	1.54	0.83	15.12	8.17	5.05
2569	2	1.95	35.7	43.6	77.3	45.2	82.5	2.66	2.68	68.3	2.15	1.55	0.85	15.21	8.33	5.13
2569	3	2.95	23.9	56.2	128.2	57.6	135.6	2.65	2.67	78	3.55	1.38	0.59	13.54	5.75	3.55
2569	3	2.95	23.9	51.9	108.1	53.2	113.7	2.65	2.67	74.9	2.98	1.43	0.67	14.05	6.57	4.06
2569	1?	3.5	32.4	47.3	89.8	48.9	95.7	2.67	2.69	71.5	2.51	1.5	0.77	14.7	7.52	4.65
2569	4	4.05	48.3	43.8	78	46	85.3	2.66	2.68	68.8	2.2	1.55	0.84	15.2	8.2	5.03
2569	4	4.05	48.3	43.3	76.5	45.5	83.6	2.66	2.68	68.4	2.16	1.56	0.85	15.27	8.32	5.1
2569	5	5.95	37	41.9	72.2	43.5	77.1	2.66	2.67	66.7	2	1.58	0.89	15.45	8.73	5.37
2569	5	5.95	37	41.9	72.1	43.5	77	2.65	2.67	66.6	2	1.57	0.89	15.45	8.72	5.36

Table 4. Water content and index properties. — Continued

[m, meters; Sal Est, salinity estimated; ppt, parts per thousand; WCt, water content based on total sample mass not corrected for salinity; %, percent; WCs, water content based on solids mass not corrected for salinity; WCtc, water content based on total sample mass corrected for salinity; WCsc, water content based on solids mass corrected for salinity; ρs, grain density not corrected for salinity; g/cm^3, grams per cubic centimeter; ρsc, grain density corrected for salinity; n, porosity; e, void ratio; ρw, wet bulk density; ρd, dry bulk density; γw, wet unit weight; kN/m^3, kiloNewton per cubic meter; γd, dry unit weight; γsub, submerged unit weight]

Core no.	Section	Mid-depth (m)	Sal Est (ppt)	WCt (%)	WCs (%)	WCtc (%)	WCsc (%)	ρs (g/cm^3)	ρsc (g/cm^3)	n (%)	e	ρw (g/cm^3)	ρd (g/cm^3)	γw (kN/m^3)	γd (kN/m^3)	γsub (kN/m^3)
2569	2?	6.45	44.8	41.9	72	43.8	78	2.68	2.7	67	2.03	1.58	0.89	15.52	8.72	5.38
2569	6	6.6	47.1	41.4	70.6	43.4	76.7	2.65	2.67	66.4	1.98	1.58	0.9	15.54	8.79	5.38
2569	6	6.6	47.1	41.1	69.7	43.1	75.7	2.65	2.67	66.1	1.95	1.59	0.9	15.59	8.87	5.43
2569	7	7.45	60.4	35.7	55.6	38	61.4	2.65	2.67	61	1.57	1.68	1.04	16.47	10.21	6.21
2569	3	8.16	49.5	41	69.6	43.2	76	2.66	2.68	66.2	1.96	1.59	0.9	15.61	8.87	5.44
2569	8	8.25	46.6	42.6	74.2	44.7	80.7	2.65	2.67	67.6	2.08	1.57	0.87	15.36	8.5	5.21
2569	9	10	54.6	36.9	58.4	39	64	2.65	2.68	62.2	1.64	1.66	1.01	16.28	9.93	6.06
2570	1	0.5	35.8	53.7	115.9	55.7	125.6	2.65	2.68	76.6	3.27	1.41	0.63	13.86	6.14	3.79
2570	2	2.05	35.9	51.1	104.3	53	112.6	2.69	2.71	74.8	2.97	1.45	0.68	14.23	6.7	4.16
2570	3	3.7	36.1	56.8	131.5	58.9	143.5	2.64	2.67	78.8	3.73	1.37	0.56	13.48	5.54	3.4
2570	4	5.1	36	51.8	107.4	53.7	116.1	2.65	2.68	75.2	3.02	1.44	0.67	14.1	6.52	4.02
2570	5	6.5	36.2	51.9	108	53.9	116.8	2.6	2.63	74.9	2.98	1.43	0.66	14.01	6.46	3.93
2570	6	8.1	36.4	48.4	93.7	50.2	100.8	2.63	2.65	72.2	2.59	1.48	0.74	14.49	7.22	4.41
2570	7	10.2	36.4	47	88.8	48.8	95.3	2.63	2.65	71.1	2.46	1.5	0.77	14.68	7.52	4.6
2570	8	11	36.7	42.6	74.2	44.2	79.2	2.66	2.67	67.3	2.06	1.57	0.87	15.36	8.57	5.27
2570	9	12.9	37.1	44.2	79.1	45.9	84.8	2.64	2.66	68.7	2.19	1.54	0.83	15.1	8.17	5.02
2570	10	14.3	36.8	47.2	89.4	49	96.1	2.64	2.66	71.3	2.49	1.5	0.76	14.67	7.48	4.59
2570	11	15.7	36.6	45.7	84.2	47.4	90.3	2.66	2.68	70.2	2.35	1.52	0.8	14.91	7.84	4.83
2570	12	17.4	36.7	43.7	77.6	45.4	83.1	2.64	2.66	68.3	2.15	1.55	0.84	15.17	8.29	5.09
2570	13	18.6	36.7	39.6	65.4	41.1	69.7	2.68	2.7	64.6	1.83	1.62	0.95	15.87	9.35	5.79
2570	14	20.3	36.7	40.7	68.5	42.2	73.1	2.68	2.7	65.7	1.92	1.6	0.93	15.7	9.07	5.62
2570	15	21.5	36.7	35.5	55.1	36.9	58.4	2.71	2.73	60.7	1.55	1.69	1.07	16.62	10.49	6.53
2570	16	23	36.7	39.3	64.6	40.8	68.8	2.66	2.68	64.2	1.79	1.62	0.96	15.87	9.4	5.79
2570	17	24.7	36.7	38.3	62.1	39.8	66.1	2.68	2.69	63.4	1.73	1.64	0.99	16.06	9.67	5.98
2570	18	26.1	36.6	40.2	67.1	41.7	71.5	2.67	2.69	65.1	1.87	1.61	0.94	15.75	9.18	5.67
2570	19	27.7	36.6	38.9	63.6	40.4	67.6	2.66	2.68	63.8	1.76	1.63	0.97	15.94	9.51	5.86
2571C2	1	0.42	36.2	53.5	115.2	55.5	124.9	3.19	3.26	79.8	3.96	1.48	0.66	14.49	6.44	4.41
2571C2	1	0.42	36.2	53.1	113.4	55.1	122.9	2.66	2.69	76.3	3.21	1.42	0.64	13.94	6.25	3.86
2571C2	1	0.42	36.2	53.2	113.5	55.2	123	2.66	2.69	76.3	3.21	1.42	0.64	13.93	6.25	3.86
2571C2	2	1	35.8	52.1	108.7	54	117.4	2.68	2.71	75.6	3.09	1.44	0.66	14.1	6.48	4.02
2571C2	3	1.96	36	53.2	113.8	55.2	123.2	2.64	2.67	76.2	3.2	1.42	0.64	13.91	6.23	3.83
2571C2	4	3	37.1	51.7	107.1	53.7	116.1	2.35	2.36	72.7	2.66	1.39	0.64	13.64	6.31	3.56
2571C2	5	5	37.2	51.2	104.7	53.1	113.4	2.62	2.65	74.5	2.92	1.44	0.68	14.13	6.62	4.05
2571C2	5	5	37.2	51.4	105.7	53.4	114.4	2.62	2.65	74.6	2.94	1.44	0.67	14.11	6.58	4.02
2571C2	6	4	36.7	53	112.9	55.1	122.5	2.64	2.67	76.1	3.18	1.42	0.64	13.93	6.26	3.85
2571C2	7	6.8	35.7	47.9	92	49.7	98.7	2.6	2.62	71.5	2.51	1.48	0.74	14.5	7.3	4.43
2571C2	8	8	37.8	48.3	93.2	50.1	100.6	2.63	2.65	72.1	2.59	1.48	0.74	14.52	7.24	4.43
2571C2	9	9.95	37.7	42.9	75.1	44.6	80.4	2.65	2.67	67.6	2.09	1.56	0.86	15.3	8.48	5.21
2571C2	9	9.95	37.7	44.5	80.1	46.2	86	2.65	2.67	69	2.23	1.54	0.83	15.06	8.1	4.97
2571C2	9	9.95	37.7	41.6	71.4	43.3	76.3	2.63	2.65	66.2	1.96	1.58	0.89	15.45	8.76	5.36
2571C2	9	9	37.9	43.7	77.5	45.4	83.1	2.64	2.66	68.3	2.15	1.55	0.84	15.17	8.29	5.08
2573GHF	2	0.3	35	46.5	86.8	48.2	92.9	2.67	2.69	70.9	2.43	1.51	0.78	14.82	7.68	4.75
2573GHF	5	1.37	35	39.2	64.5	40.6	68.4	2.66	2.67	64	1.78	1.62	0.96	15.87	9.42	5.8
2573GHF	3	2.45	35	34.7	53.2	36	56.2	2.67	2.68	59.5	1.47	1.7	1.09	16.65	10.66	6.58
2573GHF	4	3.25	35	40.7	68.6	42.2	72.9	2.67	2.68	65.6	1.9	1.6	0.92	15.66	9.06	5.59
2573GHF	6	3.65	35	42.2	73.1	43.8	77.8	2.65	2.67	66.9	2.02	1.57	0.88	15.4	8.66	5.33

Table 4. Water content and index properties. — Continued

[m, meters; Sal Est, salinity estimated; ppt, parts per thousand; WCt, water content based on total sample mass not corrected for salinity; %, percent; WCs, water content based on solids mass not corrected for salinity; WCtc, water content based on total sample mass corrected for salinity; WCsc, water content based on solids mass corrected for salinity; ρs, grain density not corrected for salinity; g/cm^3, grams per cubic centimeter; ρsc, grain density corrected for salinity; n, porosity; e, void ratio; ρw, wet bulk density; ρd, dry bulk density; γw, wet unit weight; kN/m^3, kiloNewton per cubic meter; γd, dry unit weight; γsub, submerged unit weight]

Core no.	Section	Mid-depth (m)	Sal Est (ppt)	WCt (%)	WCs (%)	WCtc (%)	WCsc (%)	ρs (g/cm^3)	ρsc (g/cm^3)	n (%)	e	ρw (g/cm^3)	ρd (g/cm^3)	γw (kN/m^3)	γd (kN/m^3)	γsub (kN/m^3)
2573GHF	9	3.78	35	38.6	62.7	40	66.5	2.65	2.66	63.3	1.72	1.63	0.98	15.95	9.58	5.88
2573GHF	9	3.78	35	38.5	62.5	39.9	66.3	2.65	2.66	63.2	1.72	1.63	0.98	15.96	9.6	5.89
2573GHF	9	3.78	35	37.9	60.9	39.2	64.5	2.65	2.66	62.6	1.67	1.64	1	16.06	9.76	5.99
2573GHF	7	4	35	39	63.9	40.4	67.8	2.65	2.67	63.8	1.76	1.62	0.97	15.89	9.48	5.83

Table 5. Shear strength results.

[mbsf, meters below sea floor; Svs, vane shear strength; kPa, kilopascal; Spp, pocket penetrometer strength; Stv, Torvane strength]

Core	Sub-bottom depth (mbsf)	Svs (kPa)	Core	Sub-bottom depth (mbsf)	Spp (kPa)	Core	Sub-bottom depth (mbsf)	Stv (kPa)
2535	0.9	8.41	2535	0.8	0	2535	0.9	9.8
2535	2.2	9.15	2535	2.1	24.5	2535	2	9.8
2535	3.7	17.85	2535	3.8	49	2535	3.9	19.6
2535	5.2	21.97	2535	5.4	61.3	2535	5.3	32.4
2535	8.3	15.41	2535	6.7	54.9	2535	6.5	38.2
2535	9.8	23.8	2535	8.4	73.5	2535	8.5	9.8
2535	11.2	27.92	2535	9.7	102.9	2535	9.6	9.8
2535	12.7	30.21	2535	11	122.5	2535	11.3	12.3
2535	14.2	45.77	2535	12.6	134.8	2535	12.5	13.7
2535	15.7	43.02	2535	14	14.7	2535	13.9	23.5
2535	17.2	62.7	2535	15.8	196	2535	15.9	24.5
2535	23.2	75.51	2535	17.1	24.5	2535	17	29.4
2535	24.8	70.02	2535	18.6	14.7	2535	18.5	31.4
2535	25.8	72.31	2535	20.4	25	2535	20.5	31.4
2535	27.6	73.23	2535	21.2	14.7	2535	21.25	30.4
2535	29.2	71.85	2535	21.5	25	2535	21.8	33.3
2535	33.6	85.13	2535	23	14.7	2535	22.9	27
2535	37.6	70.02	2535	24.6	24.5	2535	24.4	25.5
2536	0.6	7.15	2535	26.1	14.7	2535	26.2	31.4
2536	2.2	12.64	2535	27.5	29.4	2535	27.4	33.3
2536	3.6	15.18	2535	29.5	36.8	2535	29	36.8
2536	3.7	13.87	2535	30.7	36.8	2535	29.6	35.3
2536	5.1	13.04	2535	32.5	29.4	2535	30.8	31.4
2536	5.2	23.8	2535	33.7	36.8	2535	32	39.2
2536	6.8	21.51	2535	34.88	29.4	2535	33.8	40.2
2536	7.75	47.14	2535	36.8	19.6	2535	34.8	30.4
2536	8.2	40.27	2535	37.7	36.8	2535	36.7	40.2
2537	0.85	78.03	2536	0.67	0	2535	37.8	35.3
2537	2.3	21.97	2536	2.15	0	2536	0.69	2
2537	3.75	14.42	2536	3.55	0	2536	2.13	3.9
2537	5.25	10.35	2536	5.15	0	2536	3.55	6.9
2537	6.75	17.85	2536	6.75	0	2536	5.13	6.9
2537	8.2	17.87	2536	8.18	4.9	2536	6.75	9.8
2537	9.8	21.97	2537	0.8	0	2536	8.15	18.6
2537	11.2	29.75	2537	2.45	0	2537	0.95	0
2537	12.75	33.18	2537	5.1	61.3	2537	2.5	2.9
2537	17.1	61.56	2537	8.3	61.3	2537	3.6	4.9
2537	18.7	33.41	2537	12.9	159.3	2537	5	4.9
2537	20.1	59.72	2537	14.3	147	2537	12.6	13.7

Table 5. Shear strength results. — Continued

[mbsf, meters below sea floor; Svs, vane shear strength; kPa, kilopascal; Spp, pocket penetrometer strength; Stv, Torvane strength]

Core	Sub-bottom depth (mbsf)	Svs (kPa)	Core	Sub-bottom depth (mbsf)	Spp (kPa)	Core	Sub-bottom depth (mbsf)	Stv (kPa)
2537	21.5	60.87	2537	15.75	134.8	2537	14.15	17.2
2537	23.2	62.24	2537	17	24.5	2537	15.75	10.8
2537	24.6	73.68	2537	18.9	12.3	2537	17	24.5
2537	26.2	77.35	2537	20	24.5	2537	19	26.5
2537	27.3	69.57	2537	21.6	29.4	2537	20.2	24.5
2537	28.9	70.94	2537	23.1	24.5	2537	21.3	33.3
2537	30.2	56.75	2537	24.4	36.8	2537	23.1	31.9
2537	31.6	100	2537	26.2	36.8	2537	24.45	35.3
2537	33.1	75.06	2537	27.93	36.8	2537	26.4	36.8
2538	2.2	12.44	2537	29	36.8	2537	28.75	41.2
2538	3.7	17.39	2537	32.1	0	2537	32.3	35.3
2538	5.2	16.48	2537	33.2	39.2	2537	32.95	44.1
2538	6.7	27	2538	0.6	0	2538	0.75	0
2539	0.7	8.24	2538	2.15	0	2538	2.13	4.9
2539	2.2	9.61	2538	3.7	0	2538	3.7	6.9
2539	3.7	13.73	2538	5.15	0	2538	5.15	7.8
2539	5.2	28.83	2538	6.42	0	2538	6.45	11.8
2539	6.85	18.76	2539	0.6	0	2539	0.62	0
2539	8.1	19.22	2539	2.1	0	2539	2.15	2
2539	9.65	30.21	2539	5.3	0	2539	5.25	7.8
2539	11.23	27.92	2539	6.6	0	2539	6.5	8.8
2539	12.7	27.92	2539	6.8	0	2539	6.9	9.8
2539	14.2	34.78	2539	9.77	4.9	2539	8.5	8.8
2539	15.7	28.38	2539	11.25	9.8	2539	9.8	15.7
2539	17.2	33.41	2539	12.63	19.6	2539	11.3	17.7
2539	18.7	53.55	2539	14.2	19.6	2539	12.6	17.7
2539	20	30.66	2539	15.73	0	2539	14.26	21.6
2539	21.7	55.38	2539	17.2	19.6	2539	15.7	17.7
2539	23.2	63.62	2539	20	14.7	2539	17.25	19.6
2539	25.2	84.67	2539	21.6	9.8	2539	18.75	31.4
2539	26.2	81.79	2539	23.15	34.3	2539	20.05	17.7
2539	27.7	79.18	2539	26.3	36.8	2539	21.6	22.6
2539	30.5	75.51	2539	27.8	24.5	2539	23.25	29.4
2541	0.6	6.06	2539	29.3	39.2	2539	26.3	39.2
2541	2.2	10.03	2539	30.6	24.5	2539	27.8	31.4
2541	3.7	11.52	2541	0.53	0	2539	29.35	46.1
2541	6.7	16.61	2541	0.7	25	2539	30.6	41.2
2541	8.2	15.56	2541	2.15	93.1	2541	0.51	2
2541	9.7	21.97	2541	2.15	0	2541	0.85	9.8

Table 5. Shear strength results. — Continued

[mbsf, meters below sea floor; Svs, vane shear strength; kPa, kilopascal; Spp, pocket penetrometer strength; Stv, Torvane strength]

Core	Sub-bottom depth (mbsf)	Svs (kPa)	Core	Sub-bottom depth (mbsf)	Spp (kPa)	Core	Sub-bottom depth (mbsf)	Stv (kPa)
2541	11.2	24.7	2541	3.62	0	2541	2.1	20.6
2541	12.7	20.93	2541	3.8	2.3	2541	2.13	2.9
2541	14.2	26.02	2541	5.15	0	2541	3.65	4.9
2541	15.7	49.43	2541	5.3	55.1	2541	3.8	4.9
2541	17.2	44.85	2541	6.65	4.9	2541	5.15	7.8
2541	18.7	59.95	2541	6.8	4	2541	5.35	4.9
2541	20.2	42.56	2541	6.9	61.3	2541	6.7	28.4
2541	21.7	61.1	2541	8.3	4.6	2541	6.8	7.8
2541	23.15	64.99	2541	9.65	0	2541	6.85	6.9
2541	24.7	64.53	2541	9.7	110.3	2541	8.3	9.8
2541	26.2	65.45	2541	11.15	134.8	2541	9.6	14.7
2541	27.7	61.33	2541	11.3	6.7	2541	9.6	11.8
2541	29.2	67.73	2541	12.65	0	2541	11.1	14.2
2541	30.7	72.31	2541	14.3	24.5	2541	11.3	11.8
2541	33.7	53.4	2541	15.8	13.2	2541	12.75	11.8
2541	34.9	77.8	2541	17.3	4.9	2541	14.3	18.6
2542	0.8	10.26	2541	18.8	24.5	2541	15.8	19.6
2542	2.2	9.89	2541	20.3	24.5	2541	17.3	24.5
2542	0.7	12.81	2541	21.8	27	2541	18.8	30.4
2542	3.7	17.41	2541	23.15	24.5	2541	20.35	28.4
2542	5.2	19.22	2541	24.75	29.4	2541	21.85	27
2542	5.2	19.22	2541	26.15	29.4	2541	23.1	24.5
2542	6.8	37.99	2541	27.6	19.6	2541	24.8	25.5
2545	1.5	16.48	2541	29.3	29.4	2541	26.3	28.4
2545	2.43	22.88	2541	30.25	36.8	2541	27.6	29.4
2545	3.35	22.88	2541	30.8	29.4	2541	29.3	29.4
2545	4.35	29.75	2541	31.65	36.8	2541	30.3	34.3
2545	5.3	27.92	2541	33.65	34.3	2541	30.8	37.3
2545	6.45	23.3	2541	34.85	29.4	2541	31.7	35.3
2545	7.4	38.44	2545	0.5	0	2541	33.6	39.2
2545	8.5	29.75	2545	1.4	0	2541	34.83	37.3
2545	9.15	40.62	2545	2.27	0	2545	0.5	2
2546	0.9	10.98	2545	2.57	0	2545	1.4	1
2546	3.7	10.07	2545	4.4	0	2545	2.15	8.8
2546	5.2	16.02	2545	5.4	0	2545	2.6	9.8
2546	6.7	14.65	2545	6.6	0	2545	4.4	0
2546	7.8	16.48	2545	7.53	0	2545	5.4	0
2546	9.7	24.26	2545	8.57	0	2545	6	0
2546	11.1	23.34	2545	9.1	0	2545	7.4	11.8

Table 5. Shear strength results. — Continued

[mbsf, meters below sea floor; Svs, vane shear strength; kPa, kilopascal; Spp, pocket penetrometer strength; Stv, Torvane strength]

Core	Sub-bottom depth (mbsf)	Svs (kPa)	Core	Sub-bottom depth (mbsf)	Spp (kPa)	Core	Sub-bottom depth (mbsf)	Stv (kPa)
2546	12.8	20.14	2546	0.5	0	2545	8.6	14.7
2546	15.1	24.99	2546	2.24	0	2545	9.15	0
2546	15.7	45.31	2546	3.63	0	2546	0.6	2
2546	17.2	31.08	2546	5.1	0	2546	2.2	4.9
2546	18.65	45.31	2546	6.4	0	2546	3.63	4.9
2546	20.4	49.89	2546	8	0	2546	5.1	4.9
2546	21.7	56.29	2546	9.72	0	2546	6.42	8.8
2546	23.2	63.62	2546	11.4	0	2546	8	9.8
2546	24.7	65.45	2546	12.5	0	2546	9.75	11.8
2546	26.2	65.9	2546	14.23	0	2546	11.5	11.8
2546	27.7	63.16	2546	15.8	4.9	2546	12.55	12.7
2546	29.2	71.4	2546	16.3	24.5	2546	14.2	13.7
2546	30.6	70.02	2546	17.4	4.9	2546	15.8	14.7
2547	0.75	14.19	2546	18.55	19.6	2546	16.3	29.4
2547	2.2	14.19	2546	20.5	9.8	2546	17.4	19.6
2547	3.7	18.31	2546	21.7	24.5	2546	18.6	25.5
2547	5.1	21.51	2546	23.13	44.1	2546	20.5	26.5
2554	0.7	10.53	2546	24.5	34.3	2546	21.7	19.6
2554	2.2	7.43	2546	27.8	36.8	2546	23.1	30.4
2554	3.7	14.65	2546	29.16	29.4	2546	24.56	31.4
2554	5.2	16.93	2546	30.7	49	2546	27.8	34.3
2554	6.8	23.8	2547	0.8	0	2546	29.1	31.4
2554	8.2	15.56	2547	2.04	0	2546	30.7	29.4
2554	9.75	24.26	2547	3.84	0	2547	0.85	1
2554	11.2	25.63	2547	5.08	0	2547	2	3.9
2554	12.6	21.05	2550	0.5	0	2547	3.8	8.8
2554	14	30.21	2550	1	0	2547	5.14	9.8
2554	15.6	39.88	2550	1.5	0	2554	0.8	0
2554	17.3	30.66	2550	2	1.8	2554	2.3	2.9
2554	19.1	34.32	2550	3	2.9	2554	3.8	6.9
2554	20	22.88	2550	4	3.7	2554	5.3	7.8
2554	21.45	35.24	2550	5	4.6	2554	6.9	9.8
2554	23	39.82	2550	6	6.9	2554	8.3	7.4
2554	24.6	39.82	2550	6.9	8.6	2554	9.9	12.3
2554	26.05	33.87	2550	8	10.1	2554	11.3	14.7
2554	27.4	44.85	2550	8.9	9.5	2554	12.5	7.8
2554	29	43.48	2552	0.6	0.9	2554	13.9	14.7
2554	30.35	37.53	2552	1	2.3	2554	15.5	4.9
2555	1.1	8.7	2552	1.7	2.8	2554	17.4	15.7

Table 5. Shear strength results. — Continued

[mbsf, meters below sea floor; Svs, vane shear strength; kPa, kilopascal; Spp, pocket penetrometer strength; Stv, Torvane strength]

Core	Sub-bottom depth (mbsf)	Svs (kPa)	Core	Sub-bottom depth (mbsf)	Spp (kPa)	Core	Sub-bottom depth (mbsf)	Stv (kPa)
2555	2	8.7	2552	2	3.1	2554	18.9	15.2
2555	3.5	13.27	2552	3.1	4	2554	20.1	15.7
2555	5.2	16.02	2552	4	5.4	2554	21.35	14.7
2555	6.7	21.97	2552	5	6.4	2554	22.9	19.6
2555	8.2	16.02	2552	6.1	7.2	2554	24.73	21.6
2555	9.7	26.09	2552	7	8	2554	25.87	19.6
2555	11.2	27	2552	8	9.3	2554	27.6	20.6
2555	12.65	36.16	2552	9	11.5	2554	29.1	27
2555	14.2	30.6	2552	10	11	2554	30.45	24.5
2555	15.8	31.58	2554	0.8	0	2555	1.2	2.9
2555	17.2	29.48	2554	2.3	1.5	2555	2.1	3.9
2555	18.7	35.24	2554	3.8	4.6	2555	3.6	11.8
2555	20.2	37.53	2554	5.3	4.6	2555	5.3	7.4
2555	21.6	31.58	2554	6.9	5.8	2555	6.8	8.8
2555	23.2	43.94	2554	8.3	4.6	2555	8.3	7.8
2555	24.9	45.31	2554	9.9	5.5	2555	9.8	9.8
2555	26.2	32.04	2554	11.3	7	2555	11.3	14.2
2555	27.6	43.48	2554	12.5	5.4	2555	12.75	19.6
2555	29.2	49.89	2554	13.9	7.7	2555	14.2	14.7
2555	30.7	47.14	2554	15.5	8.6	2555	15.7	13.7
2555	32.2	45.77	2554	17.4	6.9	2555	17.3	17.7
2555	33.85	39.17	2554	18.9	7.7	2555	18.8	22.1
2555	35.1	53.55	2554	20.1	7.7	2555	20.3	22.1
2556	0.7	10.98	2554	21.35	8.6	2555	21.7	20.6
2556	2.2	13.38	2554	22.9	10.7	2555	23.3	20.6
2556	3.7	16	2554	24.5	14.7	2555	25	27
2556	5.2	19.68	2554	25.87	4.9	2555	26.3	24.5
2556	6.7	15.56	2554	27.6	4.9	2555	27.5	27.5
2556	8.1	18.18	2554	29.1	19.6	2555	29.1	25.5
2556	9.7	22.88	2554	30.45	9.8	2555	30.6	24.5
2556	11.6	24.26	2555	1.2	0	2555	32.1	24
2556	12.7	32.49	2555	2.1	2.1	2555	33.9	25.5
2556	14.2	31.15	2555	3.6	4.6	2556	0.8	0
2556	15.4	32.95	2555	5.3	4.6	2556	2.3	3.9
2556	17.15	38.9	2555	6.8	5.4	2556	3.8	4.9
2556	18.7	36.16	2555	8.3	4	2556	5.3	6.9
2556	20.2	34.19	2555	9.8	5.4	2556	6.6	7.8
2556	21.7	44.85	2555	11.3	8	2556	8.2	6.9
2556	23.3	36.61	2555	12.75	8.4	2556	9.8	10.8

Table 5. Shear strength results. — Continued

[mbsf, meters below sea floor; Svs, vane shear strength; kPa, kilopascal; Spp, pocket penetrometer strength; Stv, Torvane strength]

Core	Sub-bottom depth (mbsf)	Svs (kPa)	Core	Sub-bottom depth (mbsf)	Spp (kPa)	Core	Sub-bottom depth (mbsf)	Stv (kPa)
2556	24.8	43.02	2555	14.2	8	2556	11.7	14.2
2556	26.2	38.44	2555	15.7	7.7	2556	12.6	14.7
2556	27.7	44.39	2555	17.3	9.2	2556	14.3	20.6
2556	29.2	53.09	2555	18.8	10.4	2556	15.5	17.2
2556	30.7	59.5	2555	20.3	9.2	2556	17.25	18.6
2556	32.1	41.19	2555	21.7	10.7	2556	18.5	21.6
2556	33.75	49.43	2555	23.3	10.4	2556	20.35	24.5
2559	2.1	20.14	2555	25	11.6	2556	21.6	19.6
2559	3.7	16.48	2555	26.3	11.6	2556	23.4	22.6
2559	5.1	12.81	2555	27.5	13	2556	24.95	37.8
2559	6.6	16.32	2555	29.1	11	2556	26.4	27
2559	8.1	19.22	2555	30.6	12.3	2556	27.8	22.1
2559	9.6	18.76	2555	32.1	10	2556	28.95	22.1
2559	11.2	27	2555	33.9	12.6	2556	30.6	29.4
2559	12.6	25.63	2556	0.8	0	2556	32	25.5
2559	14.1	35.24	2556	2.3	0	2556	33.85	29.9
2559	15.7	37.52	2556	3.8	3.8	2559	0.2	0
2559	17.2	36.61	2556	5.3	3.7	2559	2	1
2559	18.6	46.68	2556	6.6	4.9	2559	3.8	4.4
2559	20.1	43.02	2556	8.2	3.8	2559	5.2	5.9
2559	21.7	44.85	2556	9.8	6.4	2559	6.7	7.8
2559	23.2	53.09	2556	11.7	6.7	2559	8.2	9.8
2559	24.7	51.26	2556	12.6	9.2	2559	9.7	10.8
2559	26.2	67.28	2556	14	7.4	2559	11.3	12.7
2559	27.6	55.38	2556	15.3	9.2	2559	12.7	15.7
2559	29.1	31.58	2556	17	10.9	2559	14.2	17.7
2559	30.7	30.04	2556	18.8	10.7	2559	15.8	19.6
2559	32.1	34.32	2556	20.3	10.7	2559	17.1	16.7
2559	33.2	40.27	2556	21.6	11.6	2559	18.7	19.6
2560	0.6	10.07	2556	23.4	10.1	2559	20.2	24.5
2560	2.2	9.61	2556	24.9	7.4	2559	21.6	24
2560	3.7	10.07	2556	26.4	11.6	2559	23.1	26.5
2560	5.1	17.39	2556	27.8	10.7	2559	24.6	29.4
2560	6.55	20.59	2556	29.05	11.6	2559	26.1	29.9
2560	8.2	19.68	2556	30.6	24.5	2559	27.5	29.4
2560	9.7	27	2556	32.2	14.5	2559	29.2	21.6
2560	11.15	37.07	2556	33.85	24.5	2559	30.8	19.1
2560	15.7	39.36	2559	0.2	0	2559	32.2	19.1
2560	14.2	38.9	2559	2	0.6	2559	33.3	21.6

Table 5. Shear strength results. — Continued

[mbsf, meters below sea floor; Svs, vane shear strength; kPa, kilopascal; Spp, pocket penetrometer strength; Stv, Torvane strength]

Core	Sub-bottom depth (mbsf)	Svs (kPa)	Core	Sub-bottom depth (mbsf)	Spp (kPa)	Core	Sub-bottom depth (mbsf)	Stv (kPa)
2560	12.6	31.58	2559	3.8	2.8	2560	0.7	0
2560	17.25	41.65	2559	5.2	3.1	2560	2	4.9
2560	18.7	48.51	2559	6.7	5.4	2560	3.6	5.9
2560	20.1	48.05	2559	8.2	5.4	2560	5	5.9
2560	21.8	51.78	2559	9.7	6.1	2560	6.6	9.8
2560	24.7	48.97	2559	11.3	7	2560	8.3	9.8
2560	26.1	72.77	2559	12.7	8.9	2560	9.8	14.7
2560	27.6	65.45	2559	14.2	9.5	2560	11.03	0
2561	0.7	9.7	2559	15.8	9.2	2560	12.45	12.7
2561	2	10.07	2559	17.1	10.7	2560	14.05	14.7
2561	3.7	10.43	2559	18.7	12.3	2560	15.5	27.5
2561	5.25	6.69	2559	20.2	13	2560	17.15	19.6
2561	6.6	17.39	2559	21.6	13.8	2560	18.65	21.6
2561	8.2	12.81	2559	23.1	14.7	2560	20.05	24.5
2561	9.7	17.53	2559	23.1	15.3	2560	21.7	19.6
2561	10.9	22.5	2559	24.6	24.5	2560	24.6	25.5
2561	12.7	25.63	2559	26.1	24.5	2560	26.05	38.2
2561	14.1	27.9	2559	27.5	22.1	2560	27.55	37.3
2561	15.7	31.58	2559	29.2	8.6	2561	0.6	6.9
2561	17.5	37.07	2559	30.8	9.2	2561	3.7	0
2561	18.7	39.82	2559	32.2	9.8	2561	5.35	4.9
2561	20.2	55.84	2559	33.3	10.1	2561	6.7	8.8
2561	21.7	50.8	2560	0.75	2.8	2561	8.3	8.8
2561	24.6	55.38	2560	2.3	2.3	2561	9.8	9.8
2561	23.3	38.9	2560	3.8	3.7	2561	11	11.8
2561	26.2	60.87	2560	5.2	4	2561	12.8	14.7
2561	27.6	67.28	2560	6.4	5.8	2561	14.3	14.7
2562	0.5	16.02	2560	8.1	6.1	2561	15.8	19.6
2562	2.05	15.56	2560	9.6	7.4	2561	17.6	20.6
2562	3.7	19.68	2560	11	6.4	2561	18.8	20.6
2562	5.2	24.71	2560	12.45	7.3	2561	20.3	26.5
2562	6.4	21.51	2560	14	9.8	2561	21.8	22.6
2562	8.2	27.92	2560	15.6	10.3	2561	23.2	27.5
2562	9.7	19.04	2560	17	11.6	2561	24.8	23.5
2562	11	25.17	2560	18.65	11.6	2561	26.3	45.1
2562	12.6	31.58	2560	20.05	11.5	2561	27.7	49
2562	14.2	45.31	2560	21.7	61.3	2562	0.4	0
2562	15.6	51.72	2560	21.7	13.8	2562	2.1	4.9
2562	17.2	46.22	2560	24.6	11	2562	3.53	4.9

Table 5. Shear strength results. — Continued

[mbsf, meters below sea floor; Svs, vane shear strength; kPa, kilopascal; Spp, pocket penetrometer strength; Stv, Torvane strength]

Core	Sub-bottom depth (mbsf)	Svs (kPa)	Core	Sub-bottom depth (mbsf)	Spp (kPa)	Core	Sub-bottom depth (mbsf)	Stv (kPa)
2562	18.6	41.65	2560	26.05	44.1	2562	5.17	9.8
2562	20.35	51.72	2560	26.05	14.5	2562	5.33	8.8
2562	21.7	48.97	2560	27.55	53.9	2562	8.1	12.3
2562	23.2	59.5	2560	27.55	14.4	2562	9.8	10.8
2562	24.6	58.58	2561	0.6	2.5	2562	11.1	12.7
2562	25.8	60.87	2561	1.9	3.8	2562	12.7	17.2
2566	0.6	10.95	2561	3.7	3.1	2562	14.3	19.6
2566	2	6.72	2561	5.15	3.1	2562	15.7	19.6
2566	3.7	16.48	2561	6.4	4	2562	17.1	22.6
2566	5.2	13.27	2561	8.3	4.9	2562	18.7	25.5
2566	6.25	16.93	2561	9.8	4.9	2562	20.4	27
2566	8.2	17.39	2561	11	6.1	2562	21.8	27.5
2566	9.7	28.22	2561	12.8	7.8	2562	23.3	29.4
2566	11	26.24	2561	14.3	9.5	2562	24.7	27
2566	12.55	24.26	2561	15.8	11.5	2562	25.9	31.9
2566	14.2	27	2561	17.6	10	2566	0.7	0
2566	15.7	38.9	2561	18.8	11.3	2566	2.1	2.5
2566	17.2	40.27	2561	20.3	13	2566	3.8	2.9
2566	18.5	44.39	2561	21.8	12.3	2566	5.3	5.9
2566	20.1	45.77	2561	23.2	13	2566	6.35	6.9
2566	21.7	50.8	2561	24.8	15	2566	8.3	9.8
2566	23.2	53.55	2561	26.3	3.7	2566	9.8	9.8
2566	24.8	59.04	2561	27.7	3.1	2566	11.1	14.7
2566	25.8	57.67	2562	0.4	2.4	2566	12.65	14.7
2567	0.6	11.9	2562	2.1	26.6	2566	14.3	16.7
2567	2.05	9.61	2562	3.57	3.4	2566	15.8	17.2
2567	3.6	10.98	2562	5.17	4.3	2566	17.3	17.7
2567	5.2	16.02	2562	5.35	4.3	2566	18.6	19.6
2567	6.4	16.02	2562	8.1	6.7	2566	20.1	21.6
2567	8.2	24.26	2562	9.8	5.2	2566	21.8	25.5
2567	9.7	22.88	2562	11.1	6.9	2566	23.3	25.5
2567	11	27.46	2562	12.7	7	2566	24.9	27.5
2567	12.5	28.38	2562	14.3	10.7	2566	25.9	24.5
2567	14.2	30.21	2562	15.7	10.7	2567	0.75	2
2567	15.7	33.87	2562	17.1	12.7	2567	1.8	2.5
2567	17.2	33.41	2562	18.7	19.6	2567	3.55	2.5
2567	18.5	52.17	2562	20.4	24.5	2567	4.95	2.9
2567	20.2	56.75	2562	21.8	24.5	2567	8.1	8.8
2567	21.7	57.21	2562	23.3	29.4	2567	9.75	9.8

Table 5. Shear strength results. — Continued

[mbsf, meters below sea floor; Svs, vane shear strength; kPa, kilopascal; Spp, pocket penetrometer strength; Stv, Torvane strength]

Core	Sub-bottom depth (mbsf)	Svs (kPa)	Core	Sub-bottom depth (mbsf)	Spp (kPa)	Core	Sub-bottom depth (mbsf)	Stv (kPa)
2567	23.2	55.38	2562	24.7	29.4	2567	10.85	9.8
2567	24.55	49.43	2562	25.9	29.4	2567	12.37	10.8
2567	26.05	55.84	2563	0.65	2.5	2567	14.25	15.7
2570	0.5	10.98	2563	1.3	2.8	2567	15.55	15.7
2570	2.05	10.53	2563	2.27	5.5	2567	17.3	22.1
2570	3.7	12.35	2563	2.82	4.6	2567	18.5	19.6
2570	5.1	17.1	2563	3.58	4.9	2567	20.3	21.6
2570	6.5	14.65	2566	0.7	0	2567	21.8	23.5
2570	8.1	17.44	2566	2.1	1.5	2567	23.3	24.5
2570	10.2	19.22	2566	3.8	2.1	2567	24.4	29.4
2570	12.9	16.04	2566	5.3	2.5	2567	25.9	27.5
2570	14.3	26.09	2566	6.35	3.7	2570	0.6	0
2570	15.7	37.99	2566	8.3	4.9	2570	1.95	4.9
2570	17.4	28.1	2566	9.8	6.1	2570	3.8	4.9
2570	18.6	26.09	2566	11.1	6.6	2570	5.2	7.8
2570	20.3	27.46	2566	12.65	6.9	2570	6.6	6.9
2570	21.5	29.75	2566	14.3	8.4	2570	8.2	8.8
2570	23	30.66	2566	15.8	9.2	2570	10.1	9.3
2570	24.7	26.02	2566	17.3	10.1	2570	11.2	9.8
2570	26.1	31.12	2566	18.6	12.3	2570	13	9.3
2570	27.7	37.54	2566	20.1	12.3	2570	14.4	14.2
			2566	21.8	19.6	2570	15.9	16.7
			2566	23.3	19.6	2570	17.58	17.7
			2566	24.9	27	2570	18.62	15.7
			2566	25.9	24.5	2570	20.33	13.7
			2567	0.75	0	2570	21.4	13.7
			2567	1.8	0.6	2570	23.1	14.7
			2567	3.55	1.5	2570	24.8	14.7
			2567	5.1	2.8	2570	26.2	17.2
			2567	6.45	2.8	2570	27.8	19.6
			2567	8.1	5	2573	0.3	1
			2567	9.75	5.8	2573	1.37	5.9
			2567	10.7	6.4	2573	2.45	5.9
			2567	12.4	6.9	2573	3.25	10.8
			2567	14.25	8.9			
			2567	15.6	8			
			2567	17.3	9.5			
			2567	18.5	12.6			
			2567	20.3	14.1			

Table 5. Shear strength results. — Continued

[mbsf, meters below sea floor; Svs, vane shear strength; kPa, kilopascal; Spp, pocket penetrometer strength; Stv, Torvane strength]

Core	Sub-bottom depth (mbsf)	Svs (kPa)	Core	Sub-bottom depth (mbsf)	Spp (kPa)	Core	Sub-bottom depth (mbsf)	Stv (kPa)
			2567	21.8	13.8			
			2567	23.3	13.8			
			2567	24.4	13.2			
			2567	25.9	34.3			
			2570	0.6	0			
			2570	1.95	1.5			
			2570	3.8	2.9			
			2570	5.2	4.4			
			2570	6.6	3.8			
			2570	8.2	3.7			
			2570	10.1	5.4			
			2570	11.2	4.9			
			2570	13	4.4			
			2570	14.4	5.4			
			2570	15.9	6.9			
			2570	17.58	8			
			2570	18.62	6.7			
			2570	20.33	6.4			
			2570	21.4	8.4			
			2570	23.1	8.4			
			2570	24.8	8.4			
			2570	26.2	8.4			
			2570	27.8	9.2			
			2573	0.3	2.1			
			2573	1.37	4.2			
			2573	2.45	8.9			
			2573	3.25	5.8			

Table 6. Electrical resistivity and formation factor results.

[mbsf, meters below sea floor; cm, centimeters]

Core	Section	Sub-bottom depth (mbsf)	Resistivity (ohm-m)	Formation factor	Comments
2535	1	0.9	0.399	1.908	soupy sediments
2535	2	2.2	0.399	1.907	
2535	3	3.7	0.704	3.367	
2535	4	5.2	0.306	1.463	
2535	5	6.8	0.567	2.711	
2535	6	8.3	0.573	2.741	
2535	7	9.8	0.57	2.729	
2535	8	11.2	0.718	3.437	
2535	9	12.7	0.595	2.849	
2535	10	14.2	0.573	2.74	
2535	11	15.7	0.664	3.175	vane shear measurement taken @ 1575
2535	12	17.2	0.654	3.13	
2535	16	23.2	0.616	2.946	
2535	17	24.8	0.611	2.923	
2535	18	25.8	0.602	2.88	
2535	19	27.6	0.818	3.915	
2535	20	29.2	0.621	2.973	
2535	23	33.6	0.676	3.236	
2535	26	37.6	?		
2536	1	0.6	0.375	1.795	soupy
2536	2	2.2	0.398	1.904	
2536	3	3.6	0.441	2.117	
2536	3	3.7	0.44	2.103	
2536	4	5.1	0.471	2.255	
2536	4	5.2	0.481	2.302	
2536	5	6.8	0.52	2.488	
2536	6	7.75	0.517	2.475	light brown
2536	6	8.2	0.548	2.622	dark brown
2537	1	0.85	0.44	2.105	
2537	2	2.3	0.372	1.779	vane shear at 235 cm, soupy
2537	3	3.75	0.603	2.887	
2537	4	5.25	0.459	2.198	fairly soupy for this depth
2537	5	6.75	0.52	2.488	
2537	6	8.2	0.48	2.298	fairly soupy for this depth
2537	7	9.8	0.516	2.469	
2537	8	11.2	0.525	2.512	
2537	9	12.75	0.79	3.781	

Table 6. Electrical resistivity and formation factor results. — Continued

[mbsf, meters below sea floor; cm, centimeters]

Core	Section	Sub-bottom depth (mbsf)	Resistivity (ohm-m)	Formation factor	Comments
2537	12	17.1	0.544	2.602	
2537	13	18.7	0.715	3.421	gas crack 10 cm away on each side
2537	14	20.1	0.527	2.519	gas crack 10 cm away from thermal conductivity
2537	15	21.5	0.626	2.998	gas crack @ 2166 close to thermal conductivity measurement
2537	16	23.2	0.571	2.73	
2537	17	24.6	0.529	2.532	
2537	18	26.2	0.591	2.829	
2537	19	27.3	0.54	2.586	
2537	20	28.9	0.572	2.735	
2537	21	30.2	0.591	2.827	small gas cracks
2537	22	31.6	0.573	2.741	too large for spring
2537	23	33.1	0.528	2.525	
2538	2	2.2	0.417	1.997	
2538	3	3.7	0.483	2.309	
2538	4	5.2	0.502	2.402	TO DATE: no significant sediment drying observed (IN) (July 08, 04:30)
2538	5	6.7	0.55	2.63	
2539	1	0.65	0.413	1.976	
2539	1	0.7	0.436	2.087	
2539	2	2.2	0.406	1.942	
2539	3	3.7	0.424	2.029	
2539	4	5.2	0.479	2.29	vane shear @ 525 cm
2539	5	6.55	0.501	2.397	
2539	5	6.85	0.487	2.193	
2539	6	8.1	0.567	2.715	
2539	7	9.65	0.53	2.535	vane shear @ 973 cm
2539	7	9.7	0.668	3.198	
2539	8	11.23	0.839	4.013	
2539	9	12.7	0.69	3.299	
2539	10	14.2	0.604	2.889	
2539	11	15.7	0.598	2.863	
2539	12	17.2	0.674	3.223	
2539	13	18.7	0.608	2.91	
2539	14	20	0.596	2.852	
2539	15	21.7	0.736	3.521	
2539	16	23.2	0.653	3.122	
2539	17	25.2	0.66	3.158	
2539	18	26.2	0.616	2.946	

Table 6. Electrical resistivity and formation factor results. — Continued

[mbsf, meters below sea floor; cm, centimeters]

Core	Section	Sub-bottom depth (mbsf)	Resistivity (ohm-m)	Formation factor	Comments
2539	19	27.7	0.636	3.044	
2539	21	30.5	0.65	3.111	
2541	1	0.6	0.42	2.01	
2541	2	2.2	0.361	1.73	
2541	3	3.7	0.472	2.258	
2541	4	5.2	0.489	2.34	
2541	5	6.7	0.518	2.48	
2541	6	8.2	0.568	2.719	
2541	7	9.7	0.637	3.046	
2541	8	11.2	0.652	3.118	
2541	9	12.7	0.571	2.731	
2541	10	14.2	0.574	2.747	
2541	11	15.7	0.601	2.873	
2541	12	17.2	0.586	2.806	
2541	13	18.7	0.604	2.889	
2541	14	20.2	0.72	3.444	
2541	15	21.7	0.664	3.177	
2541	16	23.15	0.653	3.122	
2541	17	24.7	0.599	2.868	
2541	18	26.2	0.72	3.445	
2541	19	27.7	0.602	2.881	
2541	20	29.2	0.721	3.448	
2541	21	30.7	0.609	2.915	
2541	23	33.7	0.624	2.988	
2541	24	34.9	0.621	2.97	
2542	1	0.8	0.522	2.49	
2542	2	2.2	0.618	2.959	
2542	1	0.7	0.457	2.185	
2542	3	3.7	0.511	2.447	
2542	4	5.2	0.528	2.256	repeated resistivity
2542	4	5.2	0.554	2.65	
2542	5	6.8	0.573	2.74	
2545	1	0.4	0.421	2.013	
2545	2	1.5	0.337	1.612	
2545	2	2.43	0.32	1.53	
2545	2	2.53	0.301	1.44	

Table 6. Electrical resistivity and formation factor results. — Continued

[mbsf, meters below sea floor; cm, centimeters]

Core	Section	Sub-bottom depth (mbsf)	Resistivity (ohm-m)	Formation factor	Comments
2545	4	3.35	0.405	1.938	
2545	5	4.35	0.29	1.388	gas cracks - not sure if resistivity is meaningful
2545	6	5.3	0.255	1.218	
2545	6	5.35	0.268	1.283	strong smell of H2S; lots of large gas cracks throughout the core
2545	7	6.45	0.28	1.341	small air pockets
2545	8	7.4	0.31	1.482	
2545	9	8.5	0.339	1.623	
2545	10	9.15	0.366	1.753	
2546	1	0.9	0.405	1.938	
2546	2	2.2	0.428	2.047	
2546	3	3.7	0.401	1.918	
2546	4	5.2	0.424	2.03	
2546	5	6.7	0.509	2.437	
2546	6	7.8	0.49	2.343	
2546	7	9.7	0.541	2.588	
2546	8	11.1	0.497	2.374	
2546	9	12.8	0.467	2.235	gas cracks on each side
2546	10	15.1	0.486	2.325	
2546	11	15.7	0.483	2.31	
2546	12	17.2	0.489	2.34	
2546	13	18.65	0.449	2.147	gas crack next to thermal conductivity measurement, many small gas cracks
2546	14	20.4	0.538	2.574	
2546	15	21.7	0.471	2.253	gas cracks on each side
2546	16	23.2	0.481	2.302	
2546	17	24.7	0.459	2.196	
2546	18	26.2	0.549	2.629	
2546	19	27.7	0.543	2.6	
2546	20	29.2	0.452	2.164	
2546	21	30.6	0.482	2.305	
2547	1	0.75	0.427	2.043	
2547	2	2.2	0.44	2.105	
2547	3	3.7	0.486	2.324	
2547	4	5.1	0.528	2.526	
2554	1	0.7	0.393	1.88	
2554	2	2.2	0.41	1.962	
2554	3	3.7	0.425	2.033	

Table 6. Electrical resistivity and formation factor results. — Continued

[mbsf, meters below sea floor; cm, centimeters]

Core	Section	Sub-bottom depth (mbsf)	Resistivity (ohm-m)	Formation factor	Comments
2554	4	5.2	0.443	2.122	
2554	5	6.8	0.501	2.395	
2554	6	8.2	0.546	2.615	
2554	7	9.75	0.611	2.924	
2554	8	11.2	0.644	3.083	
2554	9	12.6	0.761	3.64	
2554	10	14	0.774	3.704	
2554	11	15.6	0.877	4.198	
2554	12	17.3	0.844	4.04	
2554	13	19.1	0.867	4.148	large gas crack @ ~1720
2554	14	20	0.799	3.823	
2554	15	21.45	0.739	3.534	
2554	16	23	0.74	3.539	
2554	17	24.6	0.806	3.856	banding pull downs 2340–2432 cm?
2554	18	26.05	0.857	4.099	
2554	19	27.4	0.891	4.264	
2554	20	29	0.858	4.107	
2554	21	30.35	0.797	3.814	
2555	1	1.1	0.427	2.041	
2555	2	2	0.462	2.208	
2555	3	3.5	0.449	2.149	
2555	4	5.2	0.5	2.391	
2555	5	6.7	0.552	2.64	
2555	6	8.2	0.565	2.702	
2555	7	9.7	0.649	3.104	
2555	8	11.2	0.624	2.983	
2555	9	12.65	0.667	3.19	
2555	10	14.2	0.704	3.367	
2555	11	15.8	0.944	4.519	
2555	12	17.2	0.765	3.661	
2555	13	18.7	0.906	4.336	
2555	14	20.2	0.846	4.047	
2555	15	21.6	0.935	4.476	
2555	16	23.2	0.891	4.265	
2555	17	24.9	0.878	4.201	
2555	18	26.2	0.876	4.189	
2555	19	27.6	1.062	5.081	
2555	20	29.2	0.954	4.566	

Table 6. Electrical resistivity and formation factor results. — Continued

[mbsf, meters below sea floor; cm, centimeters]

Core	Section	Sub-bottom depth (mbsf)	Resistivity (ohm-m)	Formation factor	Comments
2555	21	30.7	0.904	4.324	
2555	22	32.2	0.726	3.476	
2555	23	33.85	0.758	3.628	
2555	24	35.1	0.811	3.879	
2556	1	0.7	0.375	1.792	
2556	2	2.2	0.461	2.207	
2556	3	3.7	0.429	2.054	
2556	4	5.2	0.456	2.18	
2556	5	6.7	0.482	2.307	
2556	6	8.1	0.534	2.556	
2556	7	9.7	0.573	2.743	
2556	8	11.6	0.571	2.733	
2556	9	12.7	0.574	2.746	
2556	10	14.2	0.624	2.184	
2556	11	15.4	0.636	3.045	
2556	12	17.15	0.731	3.496	
2556	13	18.7	0.661	3.164	
2556	14	20.2	0.672	3.213	
2556	15	21.7	0.646	3.089	
2556	16	23.3	0.68	3.252	
2556	17	24.8	0.689	3.297	
2556	18	26.2	0.717	3.432	
2556	19	27.7	0.759	3.629	
2556	20	29.2	0.7	3.349	
2556	21	30.7	0.67	3.204	
2556	22	32.1	0.766	3.665	
2556	23	33.75	0.778	3.725	
2559	1	0.2	0.353	1.69	
2559	2	2.1	0.445	2.129	
2559	3	3.7	0.431	2.06	
2559	4	5.1	0.475	2.274	
2559	5	6.6	0.499	2.39	
2559	6	8.1	0.489	2.338	
2559	7	9.6	0.573	2.742	
2559	8	11.2	0.631	3.018	
2559	9	12.6	0.672	3.214	
2559	10	14.1	0.654	3.13	

Table 6. Electrical resistivity and formation factor results. — Continued

[mbsf, meters below sea floor; cm, centimeters]

Core	Section	Sub-bottom depth (mbsf)	Resistivity (ohm-m)	Formation factor	Comments
2559	11	15.7	0.546	2.612	
2559	12	17.2	0.607	2.903	
2559	13	18.6	0.574	2.746	
2559	14	20.1	0.616	2.948	
2559	15	21.7	0.632	3.022	
2559	16	23.2	0.716	3.425	
2559	17	24.7	0.619	2.963	
2559	18	26.2	0.667	3.193	
2559	19	27.6	0.667	3.191	
2559	20	29.1	0.682	3.264	
2559	21	30.7	0.647	3.093	
2559	22	32.1	0.662	3.167	
2559	23	33.2	0.664	3.178	
2560	1	0.6	0.42	2.008	
2560	2	2.2	0.439	2.103	
2560	3	3.7	0.409	1.957	
2560	4	5.1	0.498	2.383	
2560	5	6.55	0.477	2.282	
2560	6	8.2	0.538	2.576	
2560	7	9.7	0.55	2.629	
2560	8	11.15	0.588	2.815	
2560	11	15.7	0.662	3.165	
2560	10	14.2	0.639	3.059	
2560	9	12.6	0.61	2.92	
2560	12	17.25	0.652	3.118	
2560	13	18.7	0.629	3.008	
2560	14	20.1	0.666	3.186	
2560	15	21.8	0.65	3.109	
2560	17	24.7	0.659	3.154	
2560	18	26.1	0.633	3.027	
2560	19	27.6	0.64	3.062	
2561	1	0.7	0.395	1.892	
2561	2	2	0.458	2.168	
2561	3	3.7	0.42	2.008	
2561	4	5.25	0.494	2.364	
2561	5	6.6	0.464	2.219	
2561	6	8.2	0.524	2.505	

Table 6. Electrical resistivity and formation factor results. — Continued

[mbsf, meters below sea floor; cm, centimeters]

Core	Section	Sub-bottom depth (mbsf)	Resistivity (ohm-m)	Formation factor	Comments
2561	7	9.7	0.553	2.646	
2561	8	10.9	0.613	2.933	
2561	9	12.7	0.65	3.108	
2561	10	14.1	0.66	3.159	
2561	11	15.7	0.664	3.177	
2561	12	17.5	0.628	3.006	
2561	13	18.7	0.733	3.507	
2561	14	20.2	0.705	3.374	
2561	15	21.7	0.693	3.316	
2561	16	24.6	0.69	3.3	
2561	17	23.3	0.691	3.307	
2561	18	26.2	0.748	3.581	
2561	19	27.6	0.753	3.603	
2562	1	0.5	0.508	2.43	
2562	2	2.05	0.481	2.303	
2562	3	3.7	0.628	3.006	
2562	4	5.2	0.569	2.721	
2562	5	6.4	0.637	3.049	
2562	6	8.2	0.629	3.011	
2562	7	9.7	0.798	3.817	
2562	8	11	0.708	3.387	
2562	9	12.6	0.727	3.478	
2562	10	14.2	0.656	3.14	
2562	11	15.6	0.583	2.97	
2562	12	17.2	0.676	3.233	
2562	13	18.6	0.648	3.1	
2562	14	20.35	0.719	3.442	
2562	15	21.7	0.675	3.228	
2562	16	23.2	0.714	3.415	
2562	17	24.6	0.715	3.419	
2562	18	25.8	0.692	3.311	
2566	1	0.6	0.362	1.734	
2566	2	2	0.417	2.045	
2566	3	3.7	0.396	1.894	
2566	4	5.2	0.425	2.033	
2566	5	6.25	0.498	2.384	
2566	6	8.2	0.58	2.776	

Table 6. Electrical resistivity and formation factor results. — Continued

[mbsf, meters below sea floor; cm, centimeters]

Core	Section	Sub-bottom depth (mbsf)	Resistivity (ohm-m)	Formation factor	Comments
2566	7	9.7	0.466	2.223	
2566	8	11	0.598	2.859	
2566	9	12.55	0.591	2.78	
2566	10	14.2	0.602	2.879	
2566	11	15.7	0.623	2.981	
2566	12	17.2	0.675	3.23	
2566	13	18.5	0.647	3.096	
2566	14	20.1	0.716	3.472	
2566	15	21.7	0.69	3.301	
2566	16	23.2	0.7	3.35	
2566	17	24.8	0.708	3.387	
2566	18	25.8	0.739	3.534	
2567	1	0.6	0.339	1.621	
2567	2	2.05	0.392	1.875	
2567	3	3.6	0.38	1.81	
2567	4	5.2	0.465	2.224	
2567	5	6.4	0.537	2.569	
2567	6	8.2	0.509	2.436	
2567	7	9.7	0.55	2.632	
2567	8	11	0.524	2.506	
2567	9	12.5	0.602	2.882	
2567	10	14.2	0.604	2.891	
2567	11	15.7	0.621	2.97	
2567	12	17.2	0.674	3.224	
2567	13	18.5	0.734	3.511	
2567	14	20.2	0.703	3.365	
2567	15	21.7	0.619	2.961	
2567	16	23.2	0.725	3.469	
2567	17	24.55	0.678	3.246	
2567	18	26.05	0.666	3.187	
2570	1	0.5	0.386	1.845	
2570	2	2.05	0.444	2.123	
2570	3	3.7	0.475	2.274	highly gas cracked sediment throughout the core
2570	4	5.1	0.503	2.405	
2570	5	6.5	0.512	2.452	
2570	6	8.1	0.567	2.712	
2570	7	10.2	0.522	2.499	

Table 6. Electrical resistivity and formation factor results. — Continued

[mbsf, meters below sea floor; cm, centimeters]

Core	Section	Sub-bottom depth (mbsf)	Resistivity (ohm-m)	Formation factor	Comments
2570	8	11	0.588	2.184	
2570	9	12.9	0.56	2.679	
2570	10	14.3	0.679	3.251	
2570	11	15.7	0.632	3.022	
2570	12	17.4	0.598	2.862	
2570	13	18.6	0.617	2.951	
2570	14	20.3	0.626	2.996	
2570	15	21.5	0.733	3.509	
2570	16	23	0.691	3.304	
2570	17	24.7	0.699	3.346	
2570	18	26.1	0.704	3.368	
2570	19	27.7	0.68	3.256	
2574	1	1	0.41	1.962	French core - no vane shear measurements
2574	2	2.1	0.437	2.093	
2574	3	4	0.487	2.332	
2574	5	6.7	0.509	2.435	
2574	6	8.3	0.556	2.659	
2574	7	9.8	0.607	2.904	
2574	8	11.2	0.587	2.81	
2574	8	11.2	0.547	2.619	
2574	9	12.8	0.617	2.953	
2574	10	14.3	0.674	3.227	
2574	11	15.8	0.672	3.214	
2574	12	17.4	0.665	3.18	
2574	13	20.2	0.665	3.181	
2574	15	21.8	0.945	4.523	
2574	16	23.4	0.824	3.941	
2574	17	24.8	1.02	4.879	
2574	18	26.2	0.788	3.773	
2574	19	27.8	0.99	4.736	
2574	20	29.2	1.012	4.843	
2574	21	30.8	1.043	4.987	
2574	22	31.9	1.069	5.115	

Table 7. Grain size results.

[m, meters; %, percent]

Core	Section	Sub-bottom depth (m)	Gravel (%)	Sand (%)	Silt (%)	Clay (%)	Gravel notes	SHEPARD CLASS	Comments
2535	1	0.67	0	6.54	12.51	80.95		CLAY	
2535	4	5.18	0	0.56	18.44	81		CLAY	
2535	7	9.78	0	0.1	31.98	67.92		SILTY CLAY	
2535	11	15.72	0	0.75	12.55	86.7		CLAY	
2535	14	20.19	0	0.92	11.32	87.76		CLAY	
2535	17	24.76	1.03	0.53	19.78	78.66	wood fragments	CLAY	
2535	20	29.19	0	1.25	15.55	83.2		CLAY	
2535	23	33.6	0	0.57	8.86	90.57		CLAY	
2536	1	0.64	0	0.95	14.67	84.39		CLAY	
2536	6	8.18	0	0.82	12.03	87.15		CLAY	
2537	1	0.83	0	1.25	16.7	82.05		CLAY	
2537	4	5.2	0	0.5	15.89	83.6		CLAY	full pipette analysis performed
2537	9	12.67	0	0.11	23.87	76.02		CLAY	
2537	11	15.79	0	0.15	33.09	66.76		SILTY CLAY	
2537	14	20.07	0	0.76	11.38	87.86		CLAY	
2537	17	24.58	0	1.06	15.78	83.16		CLAY	
2537	20	28.87	0	0.69	22.23	77.08		CLAY	
2537	23	33.08	0	2.34	17.99	79.67		CLAY	
2538	1	0.65	0	2.4	14.63	82.97		CLAY	
2538	5	6.67	0	0.13	28.42	71.45		SILTY CLAY	
2539	1	0.67	0	3.43	20.95	75.61		CLAY	
2539	4	5.17	0	0.56	24.28	75.16		CLAY	
2539	7	9.71	0	0.09	31.49	68.42		SILTY CLAY	
2539	11	15.68	0	0.09	29.43	70.48		SILTY CLAY	
2539	14	19.97	0	0.18	24.91	74.91		SILTY CLAY	
2540	1	0.59	0	4.21	18.7	77.09		CLAY	
2540	4	5.11	0	0.24	23.69	76.06		CLAY	
2541	1	0.55	0	6.49	11.67	81.84		CLAY	
2541	4	5.17	0	0.21	18.79	80.99		CLAY	
2541	7	9.67	0	0.24	23.98	75.78		CLAY	
2541	11	15.66	4	1.18	12.01	82.8	nodules	CLAY	

Table 7. Grain size results. — Continued

[m, meters; %, percent]

Core	Section	Sub-bottom depth (m)	Gravel (%)	Sand (%)	Silt (%)	Clay (%)	Gravel notes	SHEPARD CLASS	Comments
2541	14	20.18	0	0.38	20.96	78.66		CLAY	
2541	20	29.14	0	0.13	15.91	83.95		CLAY	
2541	24	34.88	0	0.66	24.03	75.31		CLAY	
2542	5	6.77	0	0.69	12.7	86.62		CLAY	
2545	1	0.37	0	2.5	15.44	82.07		CLAY	
2545	6	5.27	0	0.17	24.35	75.48		CLAY	
2545	10	9.16	0	0.11	40.02	59.87		SILTY CLAY	
2546	1	0.53	0	1.05	13.15	85.8		CLAY	
2546	7	9.58	0	0.25	27.63	72.13		SILTY CLAY	
2546	11	15.67	0	0.78	14.97	84.24		CLAY	
2546	14	20.28	0	0.57	21.34	78.09		CLAY	
2546	17	24.71	0	0.35	16.9	82.74		CLAY	
2546	21	30.57	0.17	1.61	17.19	81.03	shell fragments	CLAY	
2547	1	0.72	0	1.1	9.43	89.47		CLAY	
2547	4	4.98	0	0.19	27.82	71.99		SILTY CLAY	
2550	1	4.01	0	1.42	20.08	78.5		CLAY	
2550	2	5.01	0	0.74	20.28	78.99		CLAY	
2550	3	6.01	0	0.34	15.47	84.19		CLAY	
2550	4	6.91	0	0.12	19.33	80.56		CLAY	
2550	5	8.01	0	0.1	19.31	80.58		CLAY	
2550	6	8.91	0	0.04	26.53	73.42		SILTY CLAY	
2553	1	1.01	0	0.85	19.01	80.14		CLAY	
2553	2	1.71	0	1.07	18.51	80.43		CLAY	
2553	3	2.01	0	0.72	21.58	77.7		CLAY	
2553	4	3.11	0	1.64	20.43	77.92		CLAY	
2553	5	4.01	0	5.58	20.19	74.23		SILTY CLAY	
2553	6	5.01	0	0.01	11.1	88.89		CLAY	full pipette analysis performed
2553	7	6.11	0	0.19	10.89	88.92		CLAY	
2553	8	7.01	0	0.03	9.41	90.56		CLAY	
2553	9	8.01	0	0.03	10.84	89.13		CLAY	
2553	10	9.01	0	0.03	6.63	93.34		CLAY	

Table 7. Grain size results. — Continued

[m, meters; %, percent]

Core	Section	Sub-bottom depth (m)	Gravel (%)	Sand (%)	Silt (%)	Clay (%)	Gravel notes	SHEPARD CLASS	Comments
2553	11	10.01	0	0.03	18.71	81.26		CLAY	
2554	1	0.74	0	1.38	24.04	74.58		SILTY CLAY	
2554	4	5.18	0	0.16	5.17	94.67		CLAY	full pipette analysis performed
2554	14	5.18	0	0.09	37.19	62.72		SILTY CLAY	
2554	7	9.78	0	0.26	27.74	72		SILTY CLAY	
2554	11	15.58	0	0.08	24.84	75.07		CLAY	
2554	17	24.29	0	0.15	36.01	63.84		SILTY CLAY	
2554	21	30.32	0	0.07	33.28	66.65		SILTY CLAY	
2555	1	1.08	0	1.07	12.65	86.28		CLAY	
2555	4	5.17	0	0.48	6.78	92.74		CLAY	
2555	7	9.67	0	0.59	24.53	74.88		SILTY CLAY	
2555	11	15.75	0	0.08	25.64	74.28		SILTY CLAY	
2555	14	20.21	0	0.07	37.52	62.41		SILTY CLAY	
2555	18	26.17	0	0.08	27.16	72.76		SILTY CLAY	
2555	21	30.67	0	0.1	30.01	69.89		SILTY CLAY	
2555	22	32.15	0	0.06	35.4	64.54		SILTY CLAY	
2555	24	35.05	0	0.11	22.1	77.79		CLAY	
2556	1	0.67	0	0.77	17.42	81.81		CLAY	
2556	4	5.17	0	0.21	12.35	87.43		CLAY	
2556	7	9.68	0	0.14	29.68	70.18		SILTY CLAY	
2556	11	15.38	0	0.05	37.73	62.22		SILTY CLAY	
2556	14	20.18	0	0.09	26.21	73.7		SILTY CLAY	
2556	16	23.27	0	0.08	33	66.92		SILTY CLAY	
2556	17	24.78	0	0.09	27.93	71.98		SILTY CLAY	
2556	21	30.67	0	0.24	19.7	80.06		CLAY	
2556	23	33.78	0	0.05	33.15	66.8		SILTY CLAY	
2557	1	0.6	0	0.52	13.59	85.89		CLAY	
2559	1	0.21	0	0.25	14.36	85.39		CLAY	
2559	4	5.11	0	0.08	22.49	77.43		CLAY	
2559	7	9.54	0	0.18	23.13	76.7		CLAY	
2559	11	15.68	0	0.06	23.43	76.51		CLAY	
2559	14	20.08	0	0.15	23.95	75.89		CLAY	
2559	17	24.67	0	0.04	36.57	63.39		SILTY CLAY	

Table 7. Grain size results. — Continued

[m, meters; %, percent]

Core	Section	Sub-bottom depth (m)	Gravel (%)	Sand (%)	Silt (%)	Clay (%)	Gravel notes	SHEPARD CLASS	Comments
2559	21	30.65	0	0.07	29.18	70.75		SILTY CLAY	
2559	23	33.15	0	0.08	18.9	81.01		CLAY	
2560	1	0.57	0	0.61	11.63	87.75		CLAY	
2560	11	15.67	0	0.07	28.87	71.06		SILTY CLAY	
2560	14	20.09	0	0.04	34.77	65.19		SILTY CLAY	
2560	17	24.72	0	0.03	37.31	62.66		SILTY CLAY	
2561	1	0.61	0	1.42	12.8	85.79		CLAY	
2561	4	5.23	0	0.05	24.88	75.08		CLAY	
2561	7	9.68	0	0.19	17.53	82.28		CLAY	
2561	11	15.66	0	0.04	35.52	64.43		SILTY CLAY	
2561	14	20.15	0	0.05	32.03	67.91		SILTY CLAY	
2561	19	27.57	0	0.03	27.58	72.38		SILTY CLAY	
2562	1	0.48	0	0.04	13.33	86.63		CLAY	
2562	4	5.18	0	0.03	19.09	80.87		CLAY	
2562	8	10.97	0	0.04	26.39	73.56		SILTY CLAY	
2562	11	15.58	0	0.06	21.48	78.46		CLAY	
2562	14	20.31	0	0.04	24.77	75.19		CLAY	
2562	18	25.77	0	0.05	23.97	75.97		CLAY	
2564	1	0.99	0	3.46	15.59	80.95		CLAY	
2564	5	6.69	0	0.04	24.79	75.16		CLAY	
2565	1	0.025	0	0.09	21.31	78.6		CLAY	
2565	2	1.51	0	0.43	26.58	73		SILTY CLAY	
2565	3	3.01	0	1.16	21.98	76.86		CLAY	
2565	4	4.51	0	0.06	34.4	65.53		SILTY CLAY	
2565	5	6.315	0.06	0.35	19.54	79.98		CLAY	full pipette analysis performed
2565	6	7.515	0	1.95	28.65	69.4		SILTY CLAY	
2565	7	9.015	0	1.07	23	75.93		CLAY	
2565	8	10.515	0	0.3	20.94	78.76		CLAY	
2565	9	12.015	0	0.24	25.86	73.9		SILTY CLAY	
2565	10	13.515	0	0.31	25.97	73.72		SILTY CLAY	
2565	11	15.015	0	2.1	23.5	74.4		SILTY CLAY	
2565	12	16.515	0	0.3	30.43	69.27		SILTY CLAY	
2565	13	18.015	0	0.12	24.94	74.94		SILTY CLAY	

Table 7. Grain size results. — Continued

[m, meters; %, percent]

Core	Section	Sub-bottom depth (m)	Gravel (%)	Sand (%)	Silt (%)	Clay (%)	Gravel notes	SHEPARD CLASS	Comments
2565	14	19.515	0	0.13	25.42	74.45		SILTY CLAY	
2565	15	21.015	0	0.27	25.7	74.03		SILTY CLAY	
2565	16	22.515	0	0.11	16.15	83.73		CLAY	
2566	1	0.57	0	1.02	19.99	78.99		CLAY	
2566	4	5.17	0	0.06	18.58	81.36		CLAY	
2566	7	9.68	0	0.2	18.47	81.33		CLAY	
2566	11	15.67	0	0.06	26.1	73.84		SILTY CLAY	
2566	14	20.15	0	0.04	32.28	67.68		SILTY CLAY	
2566	18	25.78	0	0.04	35.7	64.26		SILTY CLAY	
2567	1	0.53	0	2.29	11.68	86.03		CLAY	
2567	4	5.18	0	0.05	15.66	84.28		CLAY	
2567	7	9.68	0	0.04	29.38	70.58		SILTY CLAY	
2567	11	15.68	0	0.06	25.46	74.49		SILTY CLAY	
2567	14	20.18	0	0.05	34.43	65.52		SILTY CLAY	
2567	18	26.04	0	0.03	16.54	83.43		CLAY	
2568	1	0.015	0	3.15	17.6	79.25		CLAY	
2568	3	4.485	0	0.03	27.53	72.43		SILTY CLAY	
2569	1	0.015	15.18	0.97	30.05	53.81	bricks/ nod-ules?	GRAVELLY SEDIMENT	
2569	2	1.015	0	2.41	35.42	62.17		SILTY CLAY	
2569	6	4.215	0	1.57	24.96	73.49		SILTY CLAY	full pipette analysis performed
2569	7	5.225	0	1.63	25.86	72.5		SILTY CLAY	
2569	9	7.385	0	2.17	30.73	67.1		SILTY CLAY	
2569	10	7.54	0	2.59	32.97	64.44		SILTY CLAY	
2569	12	9.935	0.8	3.15	36.94	59.11	coral/nod-ule?	SILTY CLAY	
2570	1	0.57	0	0.43	24.31	75.27		CLAY	
2570	4	5.13	0	0.07	5.21	94.71		CLAY	full pipette analysis performed
2570	7	10.22	0	1.27	21.9	76.82		CLAY	
2570	11	15.69	0	0.91	16.71	82.38		CLAY	
2570	15	21.51	0	0.03	25.56	74.41		SILTY CLAY	
2570	18	26.1	0	0.15	21.47	78.38		CLAY	

Table 7. Grain size results. — Continued

[m, meters; %, percent]

Core	Section	Sub-bottom depth (m)	Gravel (%)	Sand (%)	Silt (%)	Clay (%)	Gravel notes	SHEPARD CLASS	Comments
2572	1	0.015	0	0.68	20.38	78.94		CLAY	
2572	2	1.515	0	2.64	22.48	74.88		SILTY CLAY	
2572	3	1.805	0	4.27	21.76	73.97		SILTY CLAY	

Chapter 5

Sedimentologic Analysis of Cores Recovered from the RV *Marion Dufresne* Cruise in the Gulf of Mexico, 2–18 July 2002

Viviane Bout-Roumazeilles[1] and Alain Trentesaux[1]

Sedimentologic analysis of cores recovered from the RV Marion Dufresne *cruise in the Gulf of Mexico, 2–18 July 2002; chapter 5* in *Winters, W.J., Lorenson, T.D., and Paull, C.K., eds., 2007, Initial report of the IMAGES VIII/PAGE 127 gas hydrate and paleoclimate cruise on the RV* Marion Dufresne *in the Gulf of Mexico, 2–18 July 2002: U.S. Geological Survey Open-File Report 2004–1358.*

Introduction

The Gulf of Mexico is a small ocean basin surrounded by land masses. It is connected to the Atlantic Ocean through the Florida Strait to the east and to the Caribbean Sea through the Yucatan channel (fig. 1). Numerous topics have been studied in the Gulf of Mexico, including sediment transport (Coleman and others, 1991), mineralogy (Griffen, 1962), grain size (Mazzullo and Bates, 1985; Mazzulo, 1986), and more recently, sea-floor sediment distribution (Balsam and Beeson, 2003). These studies confirm the major influence of sediment supplied by the Mississippi River on the composition of the Gulf of Mexico sediments. In fact, sediments transported by the Mississippi River spread out over the Texas, Louisiana, and Mississippi shelves, and reach the Mississippi deep-sea fan and the Sigsbee abyssal plain (Bouma and others, 1985; Davies and Moore, 1970).

The Gulf of Mexico is divided into two morphological and sedimentological provinces (fig. 1), separated by the De Soto Canyon to the northeast and the Campeche Canyon to the southwest (Burk and Drake, 1974; Nairm and Stehli, 1975):

– a northwestern terrigenous province—the Mississippi Delta, the abyssal plain, and the northern, western, and southern continental shelves; and
– a southeastern calcareous province—the Campeche bank and the Florida bank.

Much of the sea floor is dominated by salt-tectonic basin structures, high sedimentation rates, and complex stratigraphy with common sea-floor failures (Cooper and Hart, 2002). Natural oil and gas seeps are abundant, usually associated with fault conduits resulting in numerous hydrocarbon vents, often capped by gas hydrate when the seeps are within the hydrate stability zone. While gas hydrate is relatively common at the sea floor (Sassen and others, 1999), the lack of geophysical indicators on seismic records leaves the existence of deeper gas hydrates unresolved. Thus, it is unknown if there are significant gas hydrate accumulations in reservoir sediments away from structural conduits inferred to underlie the sea-floor mounds. The geologic setting and its influence on site

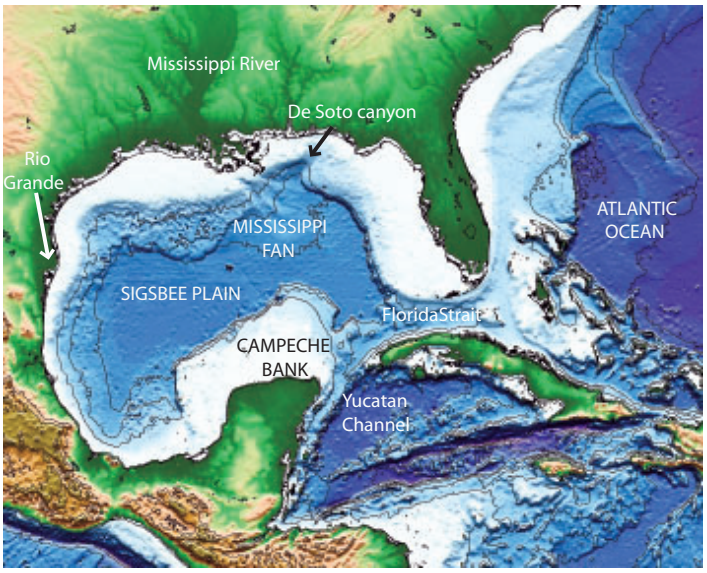

Figure 1. Bathymetry and morphology of the Gulf of Mexico.

[1]1UMR8110 CNRS Processus et Bilans des Domaines SŽdimentaires PBDS University of Lille I, 59655 Villeneuve d'Ascq, France.

selection for this cruise are further discussed by Lorenson and others (this volume, chapter 2).

Methods

Seventeen giant Calypso piston cores, up to 38 meters (m) long, four Calypso square box (CASQ, C2 or C^2) cores up to 10 m long, and four gravity cores up to 9 m long (Winters and others, this volume, chapter 3) were recovered along chirp seismic-reflection transects in widely different geologic environments (fig. 2; Appendix A) in water depths ranging from 580 to 2,260 m. For each core, a corresponding track-line map and 3.5 kilohertz (kHz) seismic profile are presented in Appendix D. Note that the arrows labeled "Carotte" in the figures in Appendix D represent piston-core locations.

Core Handling and Sampling Procedures

As soon as the core arrived onboard, sediment from the core cutter and catcher was bagged. The core liner was then pulled out of the barrel and the ends were capped. A meter tape was used to measure the length of the core and to mark precisely each 1.5-m-long section. Using the predefined orientation line as a guide, the starboard side of each core was identified as the "working" half and the port side as the "archive" half. Each section was identified with the core number (Arabic number), section number (Roman numeral), and the depth of the section top and bottom. The sections were then cut with a core cutter, capped, and transported to the Thermal Conductivity Laboratory to warm up. When necessary, holes were drilled in the core lining to relieve excess gas pressure. After thermal conductivity measurements were performed, each section was split along its orientation line by using two rotating saws mounted on a moving track. Both archive and working halves were scraped and cleaned. The archive half was used for description while the working half was subsampled. After sedimentological descriptions were recorded, the archive half was photographed and analyzed with a spectrophotometer. Both halves were then wrapped in thin plastic, packed in specially designed rectangular D-tubes, and stored in a refrigerated container. Additional details related to core handling are described in Winters and others (this volume, chapter 3).

Multi-Sensor Core Logger (MSCL)

Measurements of high-resolution sediment physical properties were obtained at 2-centimeter (cm) intervals by using a Geotek Multi-Sensor Core Logger (MSCL). These measurements comprise P-wave velocity, bulk density, and magnetic susceptibility. A summary description of the MSCL system is presented below, and a detailed description of the system and software can be found in the Geotek MSCL Manual (available in Appendix H). The MSCL consists of a conveyor system, a central unit assembly, a microprocessor, and a personal computer (PC). The conveyor system has a two-track section,

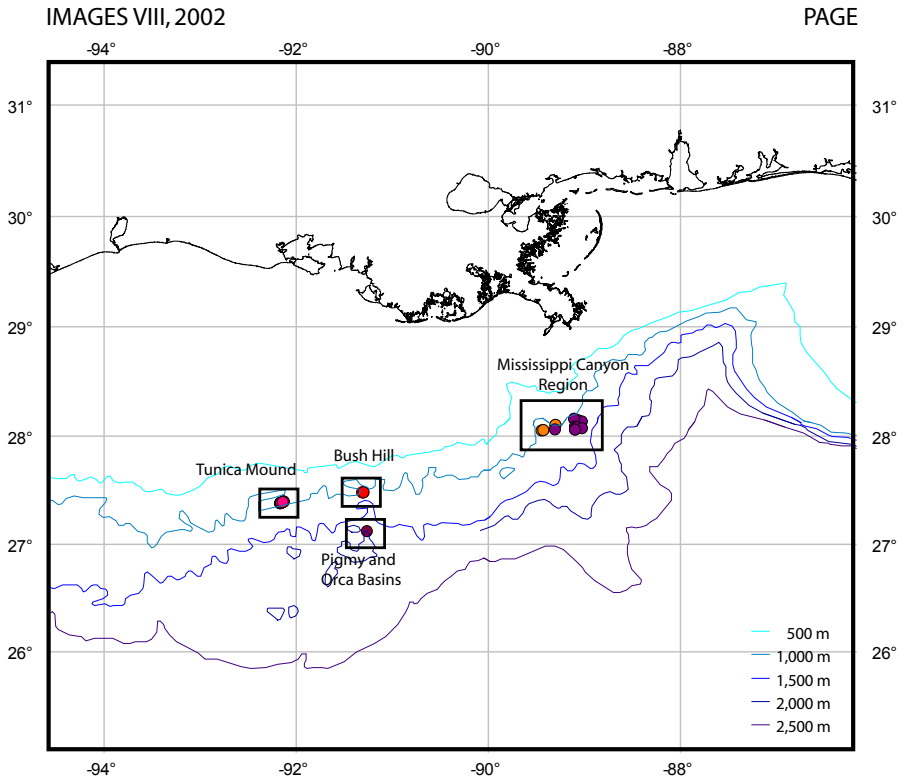

Figure 2. General map of the IMAGES VIII/PAGE 127 cruise.

mounted and aligned on either side of the central unit, and a belt-driven pusher block, which is driven in either direction by a stepper motor and gear box assembly. The central unit assembly incorporates a compressional wave (P-wave) logger, a gamma ray attenuation logger, and a magnetic susceptibility loop. A reference position is located 12 cm to the right of the P-wave logger. The gamma ray attenuation logger and magnetic susceptibility loop were offset to the left of a reference position 26 cm and 44 cm, respectively. The 1.5-m-long sections of split core were brought into the Geotek container and allowed to equilibrate to ambient temperature to reduce drift of the magnetic susceptibility measurements. The core section was then placed on the track to the right of the P-wave transducer, and the top of the core section was aligned with the reference zero position. A temperature probe was inserted in the core section to record core temperature. To ensure good acoustic coupling for the P-wave velocity measurements, the section liner was wiped down with a wet sponge, and distilled water was sprayed on the P-wave transducers. Each 1.5-m-long core section was placed on the right-hand track with the top located at the reference position and traveled incrementally past the P-wave logger, gamma ray attenuation logger, and through the magnetic susceptibility loop. After each increment of travel, a reading from each sensor was recorded. The MSCL measurements are presented in Appendix H (this volume).

Lithologic Description

Split sections were scraped to expose fresh sediment. Texture then was estimated through analysis of smear slides, tactile sensations, and taste. Grain-size results determined in a shore-based laboratory are presented in Winters and others (this volume, chapter 4).

Textural components are described as clay (<2 micrometer (μm), silt (2–63 μm)), or sand (>63 μm).

Sediment textural names are:

– *Clay* (>80-percent clay);

– *Silt* (>80-percent silt);

– *Sand* (>80-percent sand);

– *Silty clay* (clay > silt; <80-percent silt or clay, <10-percent sand);

– *Clayey silt* (silt > clay; <80-percent clay or silt; <10-percent sand);

– *Sandy mud* (<80-percent silt or clay; 10- to 50-percent sand);

– *Muddy sand* (<80-percent silt or clay or sand; 50- to 80-percent sand).

Multimodal mixtures span a range of size classes. Both unimodal and multimodal sediment names and associated patterns are summarized in figure 3. Symbols for biogenic or genetically significant sediment components are displayed where this component exceeds 10 to 20 percent. In such cases, no vertical line separates the terrigenous textural symbol from the biogenic one. This implies that the components are intimately mixed in the sediment. Sediment with significant biogenic content has a name that indicates fossils are more abundant (for example, nannofossil silty clay). If the biogenic component exceeds 50 percent of the sediments, the sediment is called an ooze. Very thinly laminated sediments, with laminations too small to be differentiated, are indicated by using a split lithologic column with a vertical dividing line. Sedimentary structures, contacts, and grading are indicated by using the symbols in figure 3. Coring disturbances also are indicated by symbols in figure 3, and colors are designed using the Munsell classification. The sedimentological descriptions are presented in Appendix F.

Digital Photography

Digital core photographs, in 50-cm intervals, were taken with a Minolta/Agfa system (courtesy of Laboratoire des Sciences du Climat et de l'Environnement (LSCE), Gif-sur-Yvette, France). Adobe Photoshop and Actioncam were used to edit the photographs of the archive cores. If the working half of a core was photographed, a "W" suffix was placed after the section number of the saved file. The photos were saved in the highest quality JPEG format. Photographs of entire cores are presented in Appendix G. Individual photographs are available on CD by request to V. Bout-Roumazeilles, (UMR 8110 CNRS, University of Lille I, 59655 Villeneuve d'Ascq, France) or email: Bout@univ-lille1.fr.

Spectrophotometry

A Minolta CM-2002 handheld spectrophotometer with an 8-millimeter (mm)-diameter optical sensor (courtesy of University of Aix-Marseille, France) was used to measure properties of the reflected light from split sediment cores. Spectral reflectance is measured in the frequency band near 40,000 nanometers (nm) and divided into 31 channels, each 10 nm in length. Reflectance was measured after the core was split, described, and photographed (an elapsed time of about 40 minutes). Measurements were made every 5 cm down the length of the core, wherever possible, and a white calibration was performed at the end of each section. The reflectance measurement also provides an estimate of the sediment color in the L*a*b Colour-Difference System and in Munsell notation. The estimation of the color should be used with care because the actual value is an average of an 8-mm-diameter section of sediment. The spectral reflectance in the longer wavelengths is useful in distinguishing layers of detrital carbonate (light color) that occurred in several cores. Color reflectance diagrams are presented in Appendix I.

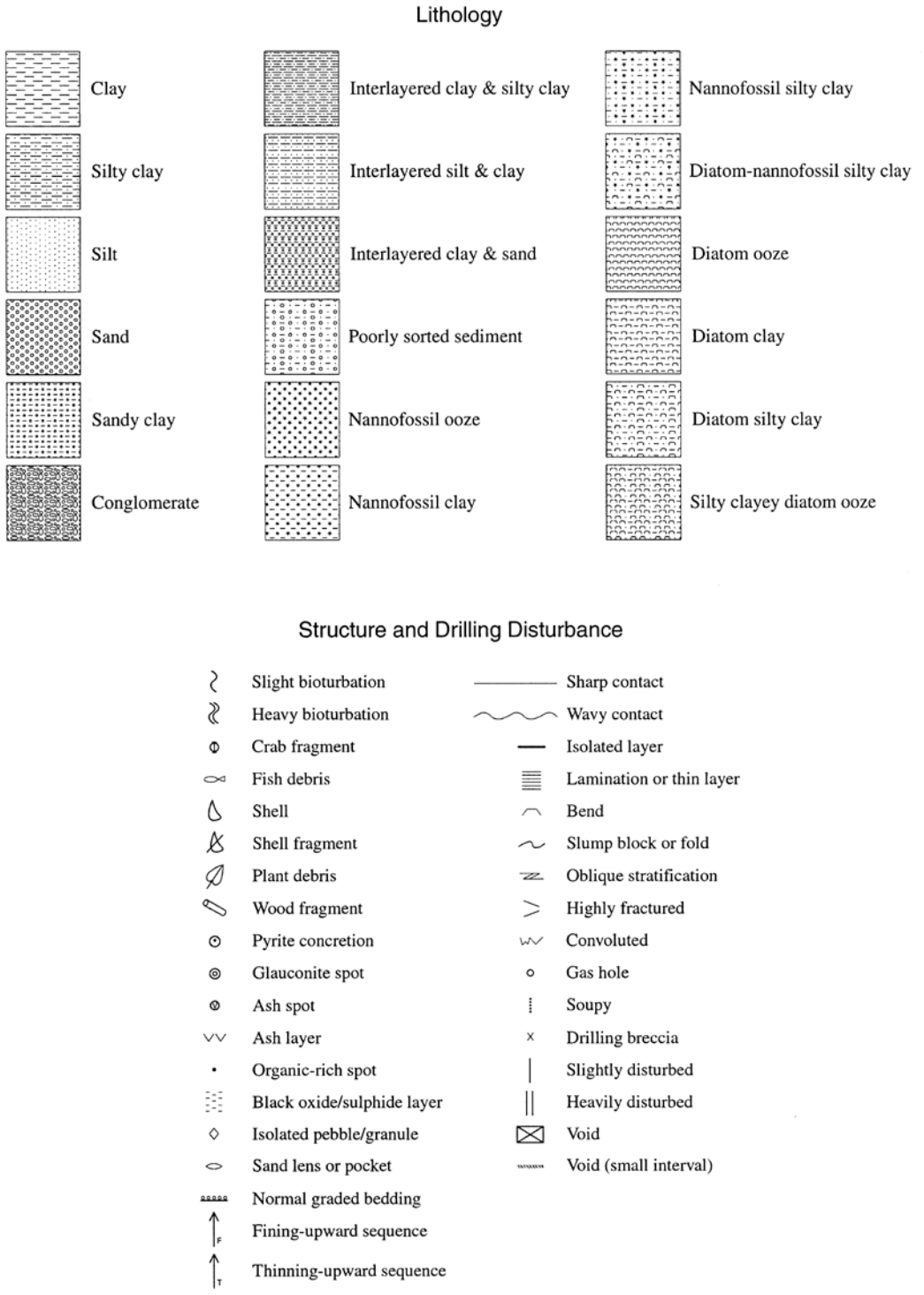

Figure 3. Legend for core descriptions.

Sedimentological Summary

The analysis of both sedimentological observations and spectral reflectance data provides preliminary interpretations on the dominant sedimentary processes occurring in each of the five geographical study areas: Tunica Mound, Bush Hill, Pigmy Basin, west of the Mississippi Canyon, and east of the Mississippi Canyon (Kane Spur) (fig. 2). The complete sedimentologic description of each core is contained in Appendix F, and a summary of the description is presented in this chapter and in Appendix E (this volume).

Tunica Mound

A number of cores were recovered in water depths of about 600 m adjacent to Tunica Mound along a 7-kilometer (km) transect (fig. 4). The principal cores that were sedimentologically described (from west to east) are labeled: MD02-2545G, MD02-2537, MD02-2546, MD02-2535, MD02-2541, MD02-2548, and MD02-2539. Visual and smear-slide observations indicate that the sediment mostly consists of silty clay and clay, and that the amount of foraminifers decreases with subbottom depth. Within cores MD02-2541 and MD02-2539, a clear transition is observed in the upper few meters (0 to 4.5 meters below sea floor (mbsf) and 0 to 6 mbsf, respectively). This transition corresponds to a down core progressive decrease in the nannofossil and foraminifer content, and is reflected in a darkening color progression (fig. 5A, B).

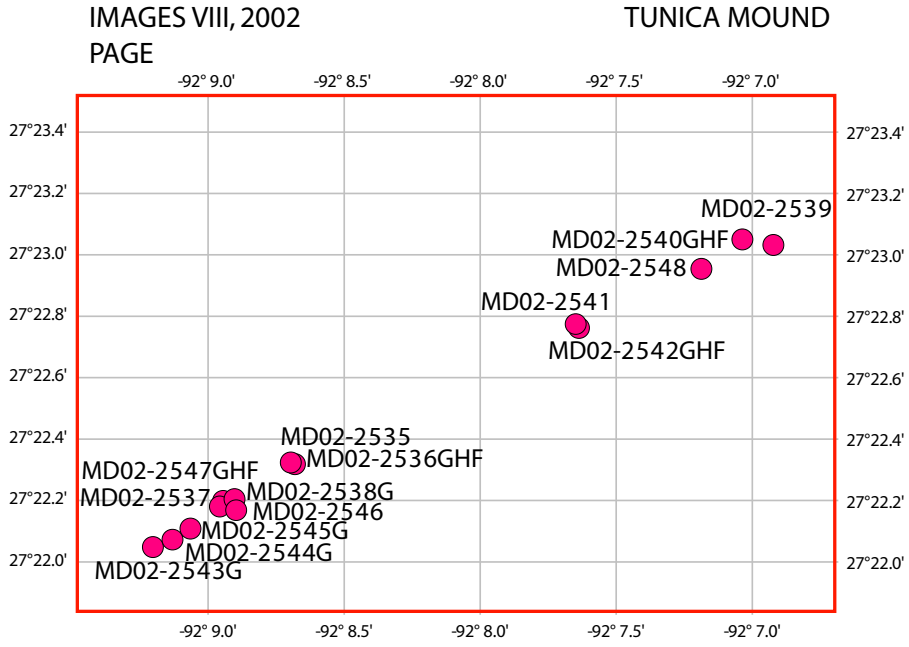

Figure 4. Tunica Mound core locations.

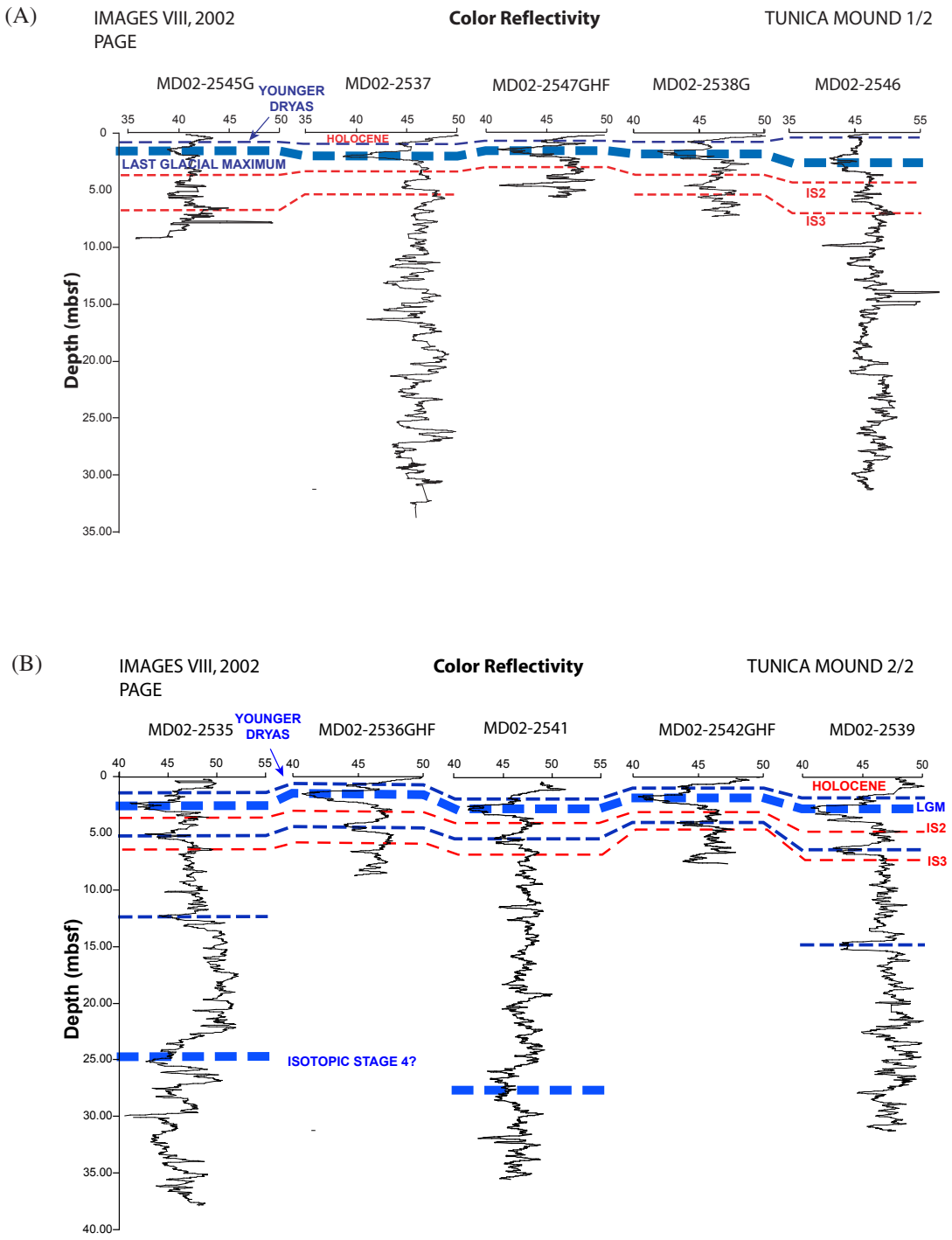

Figure 5. Color reflectivity for (A) cores located in the southwestern Tunica Mound study area and (B) cores located in the northeastern Tunica Mound study area.

Sedimentological Description Summary

MD02-2535 (37.84 m long)

Dominant lithologies:

0 to 9 mbsf: greenish gray to brown silty clay with nannofossils and in some intervals rich in foraminifera, bioturbated.

9 to 13.50 mbsf: layered dark gray silty clay, not bioturbated.

13.50 to 37.84 mbsf: brownish dark gray nannofossil clay with rare to common foraminifera, bioturbated.

Minor lithologies:

common organic-rich layers with black streaks, pyrite layers.

MD02-2537 (33.58 m long)

Dominant lithologies:

dark gray nannofossil clay with rare foraminifera.

18.7 to 23 mbsf: partially layered.

> 9 mbsf are disturbed by gas holes and voids.

Minor lithologies:

33.50 to 33.53 mbsf: ash layer.

MD02-2539 (31.10 m long)

Dominant lithologies:

0 to 6 mbsf: greenish gray to dark greenish gray sandy silt rich in foraminifera (upper 2 m) to greenish gray to dark greenish gray silty clay with foraminifera.

6 to 31.10 mbsf: dark gray clay, mostly contain faint layering; bioturbated.

Minor lithologies:

black organic-rich streaks are common.

MD02-2541 (35.34 m long)

Dominant lithologies:

0 to 4.5 mbsf: greenish gray to dark greenish gray silty clay with abundant foraminifera (upper 2.2 m) to greenish gray to dark greenish gray silty clay.

4.5 to 35.34 mbsf: dark gray clay with foraminifera, mostly contain faint layering; bioturbated.

Minor lithologies:

black organic-rich streaks common, several pyrite concretions.

MD02-2545G (9.27 m long)

Dominant lithologies:

greenish gray silty clay to dark gray clay with foraminifera, bioturbated, homogenous, gas voids common below 4.20 m, layered below 8.18 m.

Minor lithologies:

carbonate nodules, black streaks common.

MD02-2546 (31.21 m long)

Dominant lithologies:

0 to 21.00 mbsf: dark gray to greenish gray frequently layered clay with nannofossils and various amount of forams; bioturbation common to abundant.

10.50 to 18.00 mbsf: gas voids abundant

21.00 to 31.20 mbsf: greenish gray laminated silty clay with decreasing downward foram content, slightly bioturbated.

Minor lithologies:

Diagenetically modified sediments have formed some nodules (26.70 m) or are increasing the hardness of the sediment below 27.95 m.

MD02-2548 (32.93 m long)

Dominant lithologies:

0 to 18.00 mbsf: light greenish to greenish and brownish gray clay with some layers enriched in silt. Forams are present in some intervals. Layering occurs in most of this interval. Bioturbation is limited.

18.00 to 32.92 mbsf: greenish to dark greenish gray silty clay. Black streaks are common, slight bioturbation is present in most of the interval. Forams are not observed.

Minor lithologies:

28.28 to 28.30 mbsf: very light greenish gray ash layer with sharp contacts.

Preliminary Interpretations

Because the textural analyses were widely spaced within each core, they could not be used to compare different cores. However, the continuous spectrophotometer data (fig. 5A b) proved to be a useful proxy for carbonate content. However, chemical analyses are needed to confirm this relation. Although the spectrophotometer data were useful, some problems were encountered. For example, the color reflectivity value displays systematically higher values along core MD02-2535 that could be due to poor calibration. The color of core MD02-2548 was not measured. The Holocene is clearly visible and displays a constant increase of color reflectivity from the last glacial with a noticeable drop in the middle of

the curve, corresponding to the Younger Dryas cooling event (Broecker and others, 1988). Further interpretation is more difficult but seems to be possible between the eastern cores. Some high-frequency oscillations characterize the color reflectivity record before the last glacial maximum (fig. 5A, B). These oscillations mimic the stadials/interstadial oscillations of the last glacial cycle, the so-called Dansgaard/Oeschger oscillations (Johnsen and others, 1992; Bond and others, 1993; Dansgaard and others, 1993). Lower values of the color reflectivity characterizing the lower part of core MD02-2535 (below 23.00 m) may correspond to the Marine Isotopic Stage 4 (fig. 5A). Using only this approach, it seems the sedimentation rate increases to the east.

Tunica Mound Special Features

The seven cores sampled in the Tunica Mound area display special features that do not correlate well with depth or age:

- Diagenetic nodules occur in core MD02-2537 within the interval 30.57 to 30.70 mbsf. However, the nodules appear in core MD02-2546 near 26.70 mbsf.
- Hardness increases below 27.95 mbsf in core MD02-2546.
- Some core intervals display iron (?) sulfide traces, most often in the lower sections. For example, core MD02-2537 at about 27.00 m, core MD02-2541 below 28.00 m, and in the lower end of core MD02-2539. Even if pyrite is not observed, the presence of iron sulfide may be responsible for the black streaks in cores MD02-2535, MD02-2539, MD02-2541, MD02-2545G, and MD02-2548. These intervals may be enriched in organic matter.
- Some cores display voids that may have been caused by the escape of gas.

Bush Hill

Four cores were collected at Bush Hill along a 2.2-km-long profile in water depths ranging from 602 to 654 m (fig. 6). Visual and smear-slide observations indicate that the upper sediment (to a depth of 8.0 mbsf) mostly consists of clay and silty clay containing foraminifera. The upper part of cores MD02-2554 and MD02-2555 display similar color trends with decreasing color reflectivity (related to decreasing foraminifer content) down core, followed by increasing reflectivity (fig. 7).

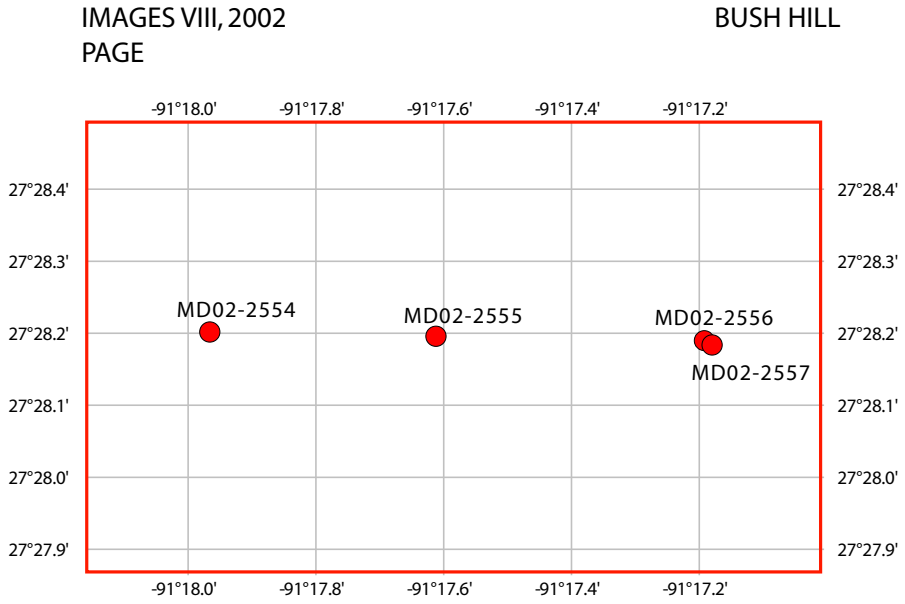

Figure 6. Bush Hill core locations.

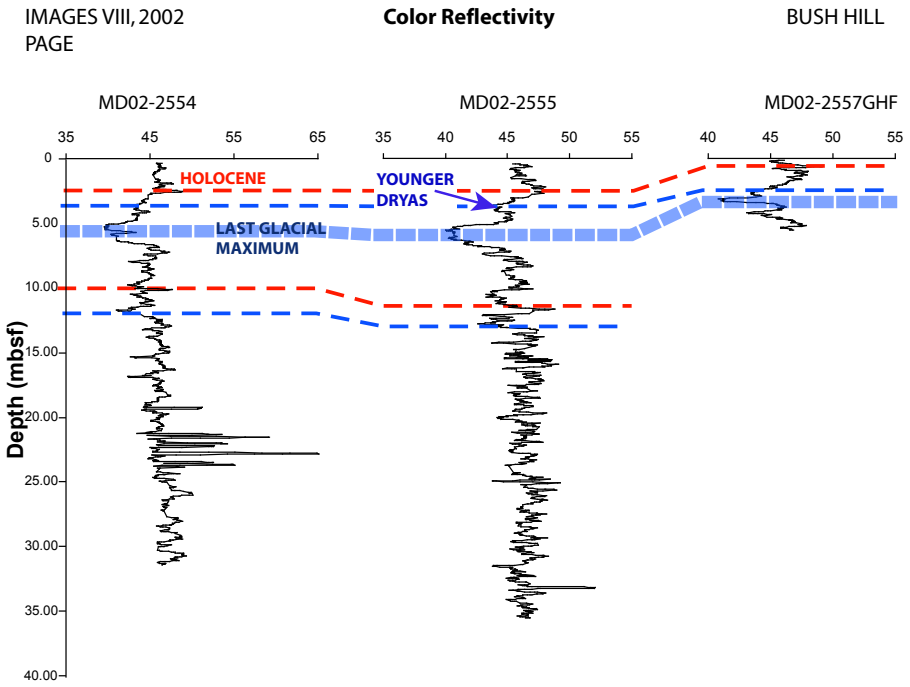

Figure 7. Color reflectivity for Bush Hill cores MD02-2554 to MD02-2557GHF.

Sedimentological Description Summary

MD02-2554 (31.05 m long)

Dominant lithologies:

0 to 6.00 mbsf: greenish to dark greenish gray silty clay with coccoliths and foraminifers. Bioturbation slight, black streaks common along some intervals.

6.00 to 12.00 mbsf: dark greenish to brownish clay without visible foraminifer.

12.00 to 31.05 mbsf: laminated dark greenish gray clay with little bioturbation. Numerous voids caused by gas expansion and gas pockets. Rare to absent foraminifers.

Minor lithologies: None.

MD02-2555 (35.68 m long)

Dominant lithologies:

0 to 9.00 mbsf: greenish gray bioturbated clay with common foraminifers.

9.00 to 35.68 mbsf: light to dark greenish gray layered clay with bioturbation.

Minor lithologies:

19.63 to 19.65 mbsf and 21.60 to 21.63 mbsf: silty, organic-rich layers.

MD02-2556 (34.25 m long)

Dominant lithologies:

dark greenish to dark brownish gray clay with some foraminifers. Gas pockets are present throughout the core.

Preliminary Interpretations

The color reflectivity records (fig. 7) provide good correlations among the cores of the Bush Hill area (fig. 6). The Holocene is clearly characterized on all cores by the highest values of the color reflectivity. These high values may correspond to an increased carbonate content of the sediment deposited during the Holocene. A darker interval in the color reflectivity record near 4.50 mbsf in cores MD02-2554 and MD02-2555 (fig. 7) and around 2.50 mbsf in core MD02-2557GHF (fig. 7) could correspond to the cold Younger Dryas event (Broecker and others, 1988). The last glacial maximum (LGM) may be marked by the lowest values (between 5.00 mbsf and 6.00 mbsf in cores MD02-2554 and MD02-2555) of the color reflectivity (that is, the lowest carbonate content and highest detrital content), reflecting the general decrease of the primary productivity in the Gulf of Mexico during this period. Correlations are less evident between cores MD02-2554/55 and core MD02-2557GHF.

Bush Hill Special Features

–The lower half of core MD02-2554 contains numerous voids caused by gas expansion. These voids are only observed in laminated to faint layered clay, usually without foraminifera. These voids are not observed in cores MD02-2555 or MD02-2556 (except along a few intervals), but sulfide traces or black organic-rich lenses are observed at similar depths.

–Pyrite cubes or dispersed iron (?) sulphides as black spots or streaks are more common in the lower half of the cores.

Pigmy Basin

One giant square box core (CASQ; C2 or C^2) (MD02-2553C2) was sampled in Pigmy Basin (figs. 2, 8). The sediment consists of sandy to silty clay with foraminifers and coccoliths to 1.55-m subbottom depth. The rest of the core (1.55 to 10.32 mbsf) consists of bioturbated clay with foraminifers.

Sedimentological Descriptions Summary

MD02- 2553C2 (10.03 m long)

Dominant lithologies:

0 to 1.55 mbsf: sandy to silty clay with foraminifers and coccoliths.

1.55 to 10.32 mbsf: greenish to dark greenish gray bioturbated clay with foraminifers.

Minor lithologies and special features:

0.58 to 0.60 mbsf, 3.00 to 3.02 mbsf, 4.00 to 4.02 mbsf, 4.20 to 4.22 mbsf, 5.81 to 5.95 mbsf, and 9.70 to 9.81 mbsf: foraminifer-rich intervals interpreted as turbidites, some with clearly defined upward fining texture.

Mississippi Canyon and Kane Spur

A series of piston and giant square box (CASQ; C2 or C^2) cores were obtained in the Mississippi Canyon area in three distinct sub-areas (fig. 9). Note that cores MD02-2565 and MD02-2569 were not opened onboard.

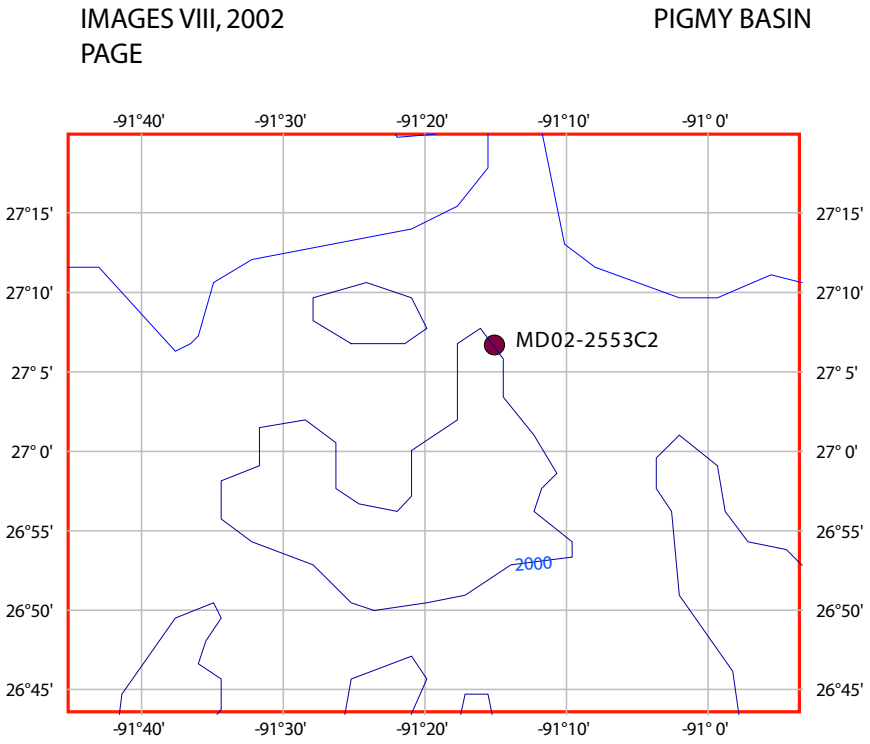

Figure 8. Location of Pigmy Basin core MD02-2553C2.

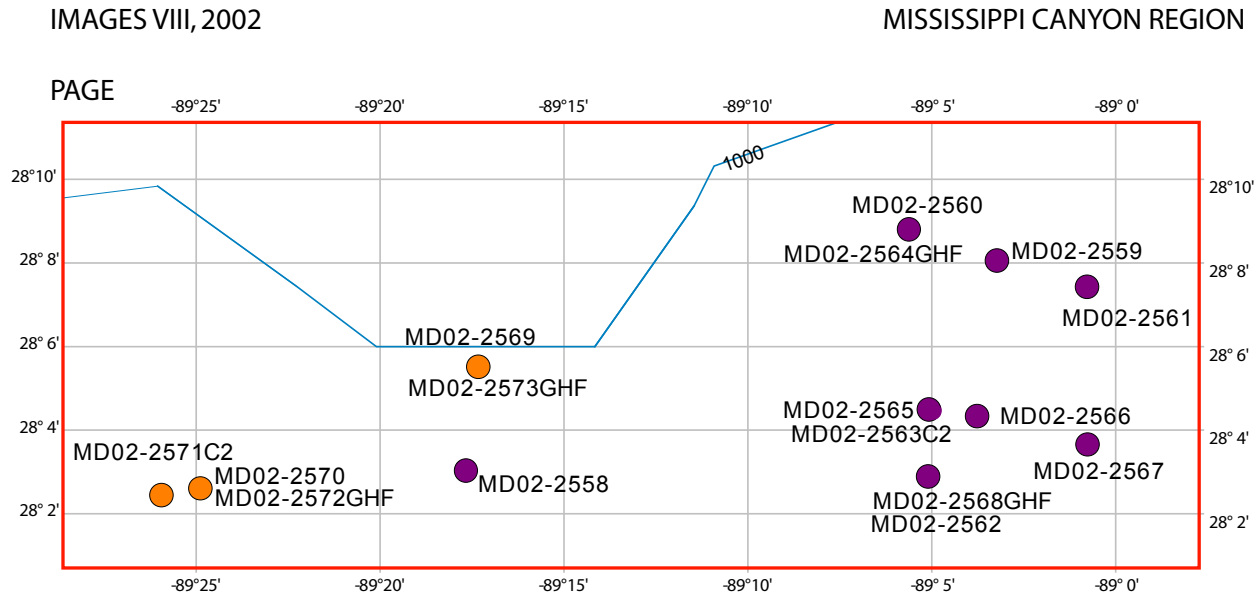

Figure 9. Core sites west of the Mississippi Canyon (MD02-2570, -2571C2, and -2572GHF), in the Mississippi Canyon (MD02-2558 (not a USGS core), -2569, -2573GHF), and east of the Mississippi Canyon (Kane Spur) (MD02-2559 to -2568GHF).

Sedimentological Description Summary

MD02-2559 (33.39 m long)

Dominant lithologies:

0 to 3.50 mbsf: light to dark greenish grey bioturbated silty clay with some foraminifers.

3.50 to 28.80 mbsf: laminated, then layered light to dark greenish gray silty clay with few bioturbated intervals and no foraminifer visible.

Below 8.33 mbsf: sand or silts layers or pockets throughout the core.

Minor lithologies:

thin layers and pockets of sand and silt.

MD02-2561 (28.8 m long)

Dominant lithologies:

0 to 4.50 mbsf: light to dark greenish gray silty clay with moderate bioturbation and some foraminifers with decreasing content down core.

4.50 to 9.00 mbsf: dark greenish gray laminated silty clay. No foraminifer visible.

9.00 to 28.80 mbsf: clay, then silty clay, slightly bioturbated.

Minor lithologies:

Numerous silt layers at the bottom of the core, for example, at 14.30 mbsf.

MD02-2562 (26.09 m long)

Dominant lithologies:

greenish to light greenish gray layered silty clay. Some bioturbation. Rare to absent foraminifers. Some layers are composed of upward fining silty clay.

Minor lithologies: None.

MD02-2563C2 (3.86 m long)

Dominant lithologies:

light to dark greenish gray with common tar (bitumen) spots and sandy layers. Forams are rare except in the upper part of the core.

Minor lithologies: None.

MD02-2566 (26.05 m long)

Dominant lithologies:

light to dark greenish gray silty clay with some layering. Foraminifers visible in the upper 2.60 m of the core with coccoliths. Silt layers occur from 14.00 mbsf to the bottom of the core.

Minor lithologies: None.

MD02-2567 (26.65 m long)

Dominant lithologies:

0 to 13.15 mbsf: greenish gray clay with subtle laminations. Foraminifers abundant to 3.85 mbsf.

13.15 to 26.65 mbsf: layered greenish gray silty clay. Increase of bioturbation.

below 18.50 mbsf: increased bioturbation. Silty layers at several depths including 10.74 m.

Minor lithologies: None.

MD02-2570 (28.50 m long)

Dominant lithologies:

0 to 6.50 mbsf: greenish to dark greenish gray silty clay with strong H_2S smell below 1.50 mbsf.

6.50 to 18.00 mbsf: dark greenish gray to dark gray silty clay with numerous gas bubbles or voids.

18.00 to 21.00 mbsf: clay.

below 24.00 mbsf: greenish to light greenish gray silty clay with gas bubbles and voids. Some organic-rich layers and spots. Most of the core is slightly bioturbated.

Minor lithologies: None.

Preliminary Interpretations

Only the Kane Spur cores and one from the west Mississippi Canyon area were split. Therefore, only these cores will be sedimentologically described. In every core, visual and smear-slide observations indicate that the sediment mainly consists of dark greenish silty clay with a common two-fold system: an upper interval with some foraminifers and a lower interval with rare to absent foraminifers. The transition depth varies from core to core. In some cores, the lowermost section of the core consists of coarser material containing sand and silt layers. The color reflectivity records of the Kane Spur cores are used for correlation purposes (fig. 10A, B). The upper part (0 to 3.00 mbsf) of cores MD02-2558, MD02-2560, MD02-2561, MD02-2562, MD02-2564GHF, MD02-2566, and MD02-2568GHF is characterized by high color reflectivity related to a high carbonate content, which was observed in the smear slides. This interval is believed to be Holocene in age. The Younger Dryas cold event (Broecker and others, 1988) is also tentatively identified in most of the cores by slightly lower values of color reflectivity when compared to Holocene sediments (less carbonate content and increased detrital content). The last glacial maximum is characterized by a decrease of the carbonate content as shown by the color reflectivity. Drastic cold climatic conditions prevented the development of primary nannofossil production during that time. Some high-frequency oscillations characterize the color reflectivity record before the last glacial maximum (fig. 10A, B). These oscillations mimic the stadials/interstadial oscillations of the last glacial cycle, the so-called Dansgaard/Oeschger oscillations (Johnsen and others, 1992; Bond and others, 1993; Dansgaard and others, 1993).

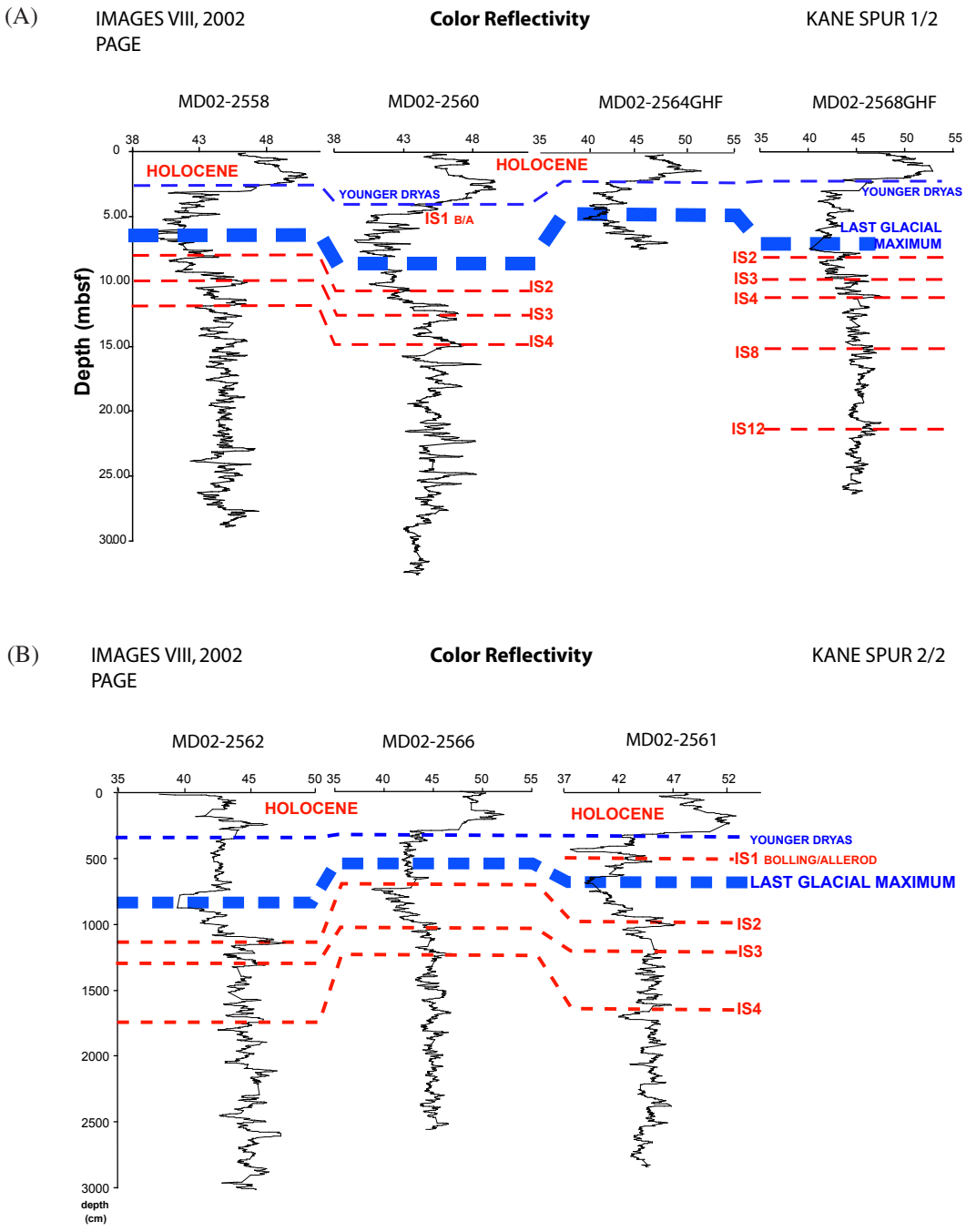

Figure 10. Color reflectivity for (A) Mississippi Canyon cores MD02-2558 (not a USGS core) to MD02-2568GHF and (B) Mississippi Canyon (Kane Spur) cores MD02-2562 to MD02-2561.

References

Balsam, W.L., and Beeson, J.P., 2003, Sea-floor sediment distribution in the Gulf of Mexico: Deep-Sea Research I, v. 50, p. 1421–1444.

Bond, G., Broecker, W., Johnsen, S.J., McManus, J., Labeyrie, L., Jouzel, J., and Bonami, G., 1993, Correlations between climate records from North Atlantic sediments and Greenland ice: Nature, v. 365, p. 143–147.

Bouma, A.H., Normark, W.R., and Barnes, N.E., eds., 1985, Submarine fans and related turbidite systems: New York, Springer, 351 p.

Broecker, W.S., Andree, M., Wolfli, W., Oeschger, H., Bonami, G., Kennett, J., and Peteet, D., 1988, The chronology of the last deglaciation—implications to the cause of the Younger Dryas event: Paleoceanography, v. 3, no. 1, p. 1–19.

Burk, C.A., and Drake, C.L., eds., 1974, The geology of continental margins: Berlin, Springer-Verlag.

Coleman, J.M., Roberts, H.H., and Bryant, W.R., 1991, Late Quaternary sedimentation, *in* Salvador, A., ed., The Gulf of Mexico basin: Geological Society of America, p. 325–352.

Cooper, A.K., and Hart, P.E., 2002, High-resolution seismic-reflection investigation of the northern Gulf of Mexico gas-hydrate-stability zone: Marine and Petroleum Geology, v. 19, no. 10, p. 1275–1293.

Dansgaard, W., Johnsen, S.J., Clausen, H.B., Dahl-Jensen, D., Gundestrup, N.S., Hammer, C.U., Hvidberg, C.S., Steffensen, J.P., Sveinbjšrnsdottir, A.E., Jouzel, J., and Bond, G., 1993, Evidence for general instability of climate from a 250-kyr ice-core record: Nature, v. 364, p. 218–220.

Davies, D.K., and Moore, W.R., 1970, Dispersal of Mississippi sediment in the Gulf of Mexico: Journal of Sedimentary Petrology, v. 40, p. 339–353.

Griffen, G.M., 1962, Regional clay-mineral facies-product of weathering intensity and current distribution in the northeastern Gulf of Mexico: Geological Society of America Bulletin, v. 73, p. 737–768.

Johnsen, S.J., Clausen, H.B., Dansgaard, W., Fuhrer, K., Gundestrup, N.S., Hammer, C.U., Kersen, P., Jouzel, J., Stauffer, B., and Steffensen, J.P., 1992, Irregular glacial interstadials recorded in a new Greenland ice core: Nature, v. 359, p. 311–313.

Mazzullo, J., 1986, Sources and provinces of late Quaternary sand on the East Texas-Louisiana continental shelf: Geological Society of America Bulletin, v. 97, p. 638–647.

Mazzullo, J., and Bates, C., 1985, Source of sand for the northeast Gulf of Mexico shelf and the Mississippi fan: Gulf Coast Association of Geological Societies Transactions, v. 35, p. 457–466.

Nairm, A.E.M., and Stehli, F.G., 1975, The Gulf of Mexico and the Caribbean: The Ocean Basins and Margins, 3, New York, Plenum Press, 706 p.

Sassen, R., Sweet, S.T., Milkov, A.V., DeFreitas, D.A., Salata, G.G., and McDade, E.C., 1999, Geology and geochemistry of gas hydrates, central Gulf of Mexico continental slope: Gulf Coast Association of Geological Societies Transactions, v. 49, p. 462–468.

Chapter 6

Thermal Measurements from the Gulf of Mexico Continental Slope: Results from the PAGE Cruise

Cinthia Labails[1], Louis Géli[1], Nabil Sultan[1], Ivana Novosel[2], and William J. Winters[3]

Thermal measurements from the Gulf of Mexico continental slope: Results from the PAGE cruise; chapter 6 in *Winters, W.J., Lorenson, T.D., and Paull, C.K., eds., 2007, Initial report of the IMAGES VIII/PAGE 127 gas hydrate and paleoclimate cruise on the RV* Marion Dufresne *in the Gulf of Mexico, 2–18 July 2002: U.S. Geological Survey Open-File Report 2004–1358.*

Abstract

In July 2002, the French Polar Institute (Institut Polaire Francais – Paul-Emile Victor (IPEV)) and the U.S. Geological Survey jointly conducted a cruise aboard the research vessel (RV) *Marion Dufresne* to collect giant piston cores to determine the distribution of gas hydrate in the northern Gulf of Mexico. Thermal measurements (made by Ifremer, using autonomous digital temperature probes fitted on gravity-core barrels) were successfully used to calculate a geothermal gradient at 17 sites. Geothermal gradients varied from 20 to 38 degrees Celsius per kilometer.

Introduction

To determine the thermodynamic conditions (temperature and pressure) at which gas hydrate is stable in reservoir sediments at depth and to assess the potential amount of gas hydrate in the Gulf of Mexico, heat-flow measurements were made in three areas: Tunica Mound (fig. 1), Bush Hill (fig. 2), and proximally to the Mississippi Canyon (fig. 3). Because the main objective of the cruise was the acquisition of giant piston cores, only a limited number of thermal measurements were made at each site by using autonomous digital temperature probes (fig. 4) fitted onto gravity-core barrels. A total of 21 deployments were made (table 1), resulting in the calculation of 17 geothermal gradients. Four deployments were unsuccessful because of bent barrels or inadequate penetration.

[1]Department of Marine Geosciences, Ifremer, BP 70, 29280, Plouzané, France.

[2]Rice University, Department of Earth Sciences, 6100 Main Street, MS-126, Houston, TX 77005-1892 USA.

[3]U.S. Geological Survey, 384 Woods Hole Road, Woods Hole, MA 02543 USA.

Equipment, Data Reduction, and Processing

Equipment. Temperature measurements were made using autonomous temperature probes welded onto gravity-core barrels. The probes incorporate an energy source and are able to record a total of 26,280 acquisitions. Most measurements were made in water depths ranging between about 600 and 1,200 meters (m). Because temperatures in the few upper meters of sediments could be affected by seasonal changes in bottom water temperatures, the thermal sensors were placed so as to record temperatures deeper than this transitional shallow subbottom zone. The sensors were fitted onto 17- to 21-m-long gravity core barrels (except at one site, where a 12-m-long barrel was used). The inclination of the barrel was measured using a tiltmeter installed on the corer weight stand. Mud recovered on the corer weight stand typically indicated that full penetration of the gravity corer was achieved at most sites (except for sites where barrels were bent). Thermal gradients were computed using probe depths calculated from the tilt measurements and the probe relative spacing.

Probe Intercalibration. Before each core-barrel penetration, temperature probes were intercalibrated for 3 minutes in the water column by measuring temperature for each sensor as the core barrel was suspended 150 m and 100 m above the sea floor. With these two intercalibrations, it is possible to calculate the temperature difference measured by two different sensors placed at the same water depth. After each core penetration, temperatures were again measured for 3 minutes

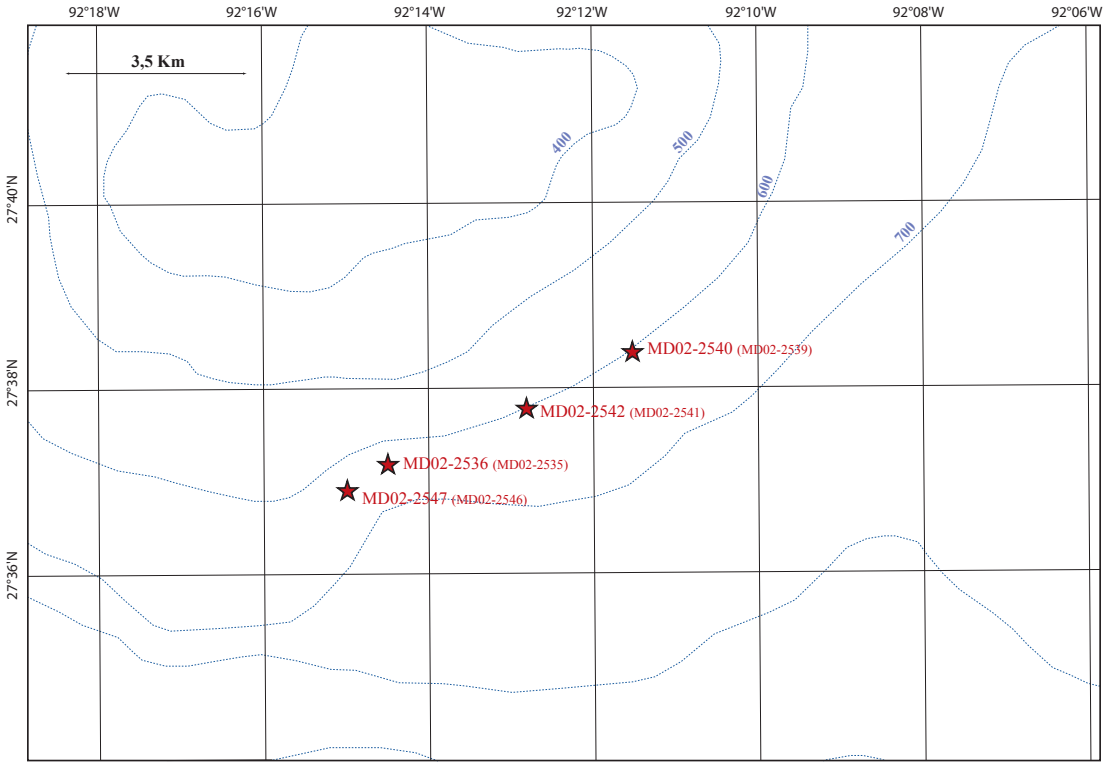

Figure 1. Tunica Mound sites for thermal measurements. The closest Calypso cores that were used for conductivity measurements and heat-flow calculations are in parentheses.

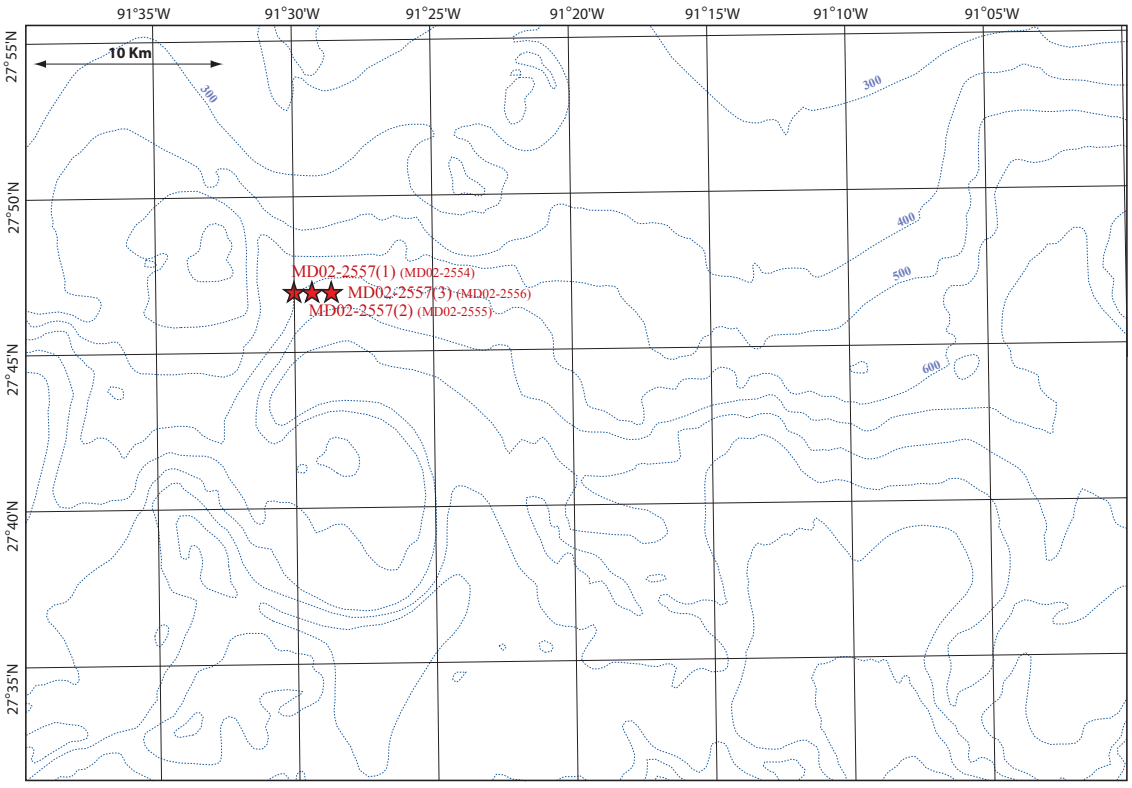

Figure 2. Bush Hill sites for thermal measurements. The closest Calypso cores that were used for conductivity measurements and heat-flow calculations are in parentheses.

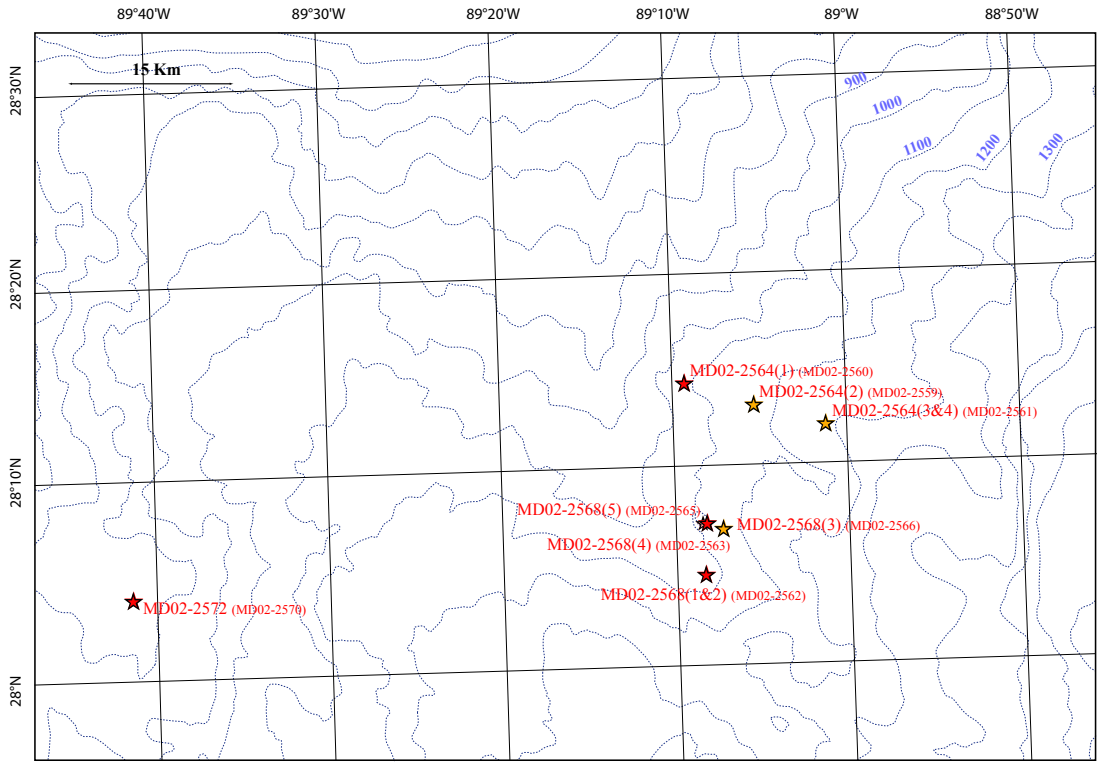

Figure 3. Mississippi Canyon region sites for thermal measurements. The closest Calypso cores that were used for conductivity measurements and heat-flow calculations are in parentheses.

Figure 4A. Gravity corer of RV *Marion Dufresne* equipped with autonomous temperature probes. Thermal sensors are rotated along the core barrel to avoid disturbing effects from one sensor to the other during penetration.

Figure 4B. A Micrel autonomous temperature sensor welded onto a gravity-core barrel. Because the sensor is fully self contained, there is no connector and no power switch. Dialog is performed using a reading pen connected to the serial port of a personal computer. Batteries and a data logger are contained in a 172-millimeter (mm)- long, 28-mm-diameter titanium cylinder. Two temperature probes are contained in a 130-mm-long, 4-mm-diameter titanium needle. The probe is located 60 mm from the core barrel. This distance ensures that it will take 1 hour for the heat generated by the friction of penetration to reach the needle probe. Probe temperature range: –2 to 35 degrees Celsius (°C); linearity: ±2 milli-degrees Celsius (m°C); resolution: 0.6 m°C; stability: 20 m°C/year; repeatability: ±0.6 m°C; total measurement range: –2 to 75 °C ; maximum water depth: 6,000 meters (m).

Table 1. Summary of thermal measurements.

[m, meters; N, north; W, west; °C/km, degrees Celsius per kilometer; k_a, average thermal conductivity; $Wm^{-1}K^{-1}$, watt per meter Kelvin; mW/m^2, milliwatt per meter squared; mfbc, meters from bottom of corer; TM, Tunica Mound; POGO, multiple pogo-like penetrations; BH, Bush Hill; MC, Mississippi Canyon. "Average" conductivity and "average" heat flow are defined in the text. Because gravity core recovery ratios typically did not exceed 50 to 70 percent, the nearest giant (Calypso) piston core was used to estimate thermal conductivity over a depth of 35 meters, while temperature measurements were collected only over the length of the gravity corer (~17 to 20 meters long)]

Area	Nearest giant piston (Calypso) core MD02-	Length of Calypso piston core (m)	Name of heat-flow measurement MD02-	Latitude (N)	Longitude (W)	Water depth (m)	Thermal gradient (°C/km)	Average thermal conductivity k_a ($Wm^{-1}K^{-1}$)	Heat flow (Bullard) (mW/m^2)	Average heat flow (mW/m^2)	Core length (m)	Observations (mfbc)
TM	2535	37.6	2536(1)	27°37.19'	92°14.46'	608	23 ± 2	0.99 ± 0.07	23 ± 2	22 ±4	8.88	
TM			2536(2)	27°37.52'	92°14.76'	564	26 ± 2			26 ± 4		POGO (natural drift).
TM			2536(3)	27°37.62'	92°14.25'	585	26 ± 2			26 ± 4		POGO (natural drift).
TM	2539	30.7	2540(1)	27°38.42'	92°11.52'	617	38 ± 5	1.01 ± 0.08	39 ± 5	36 ± 8	5.65	Uncertainty in inclination.
TM			2540(2)	27°38.41'	92°11.71'	620						Corer bent 15 mfbc; no measurements.
TM	2541	35.7	2542	27°37.93'	92°12.72'	617	25 ± 1	1.01 ± 0.09	27 ± 2	26 ± 3	7.70	
TM	2546	30.6	2547	27°36.99'	92°14.90'	607	29 ± 1	0.92 ± 0.07	25 ± 1	27 ± 3	5.69	Corer bent 12 mfbc; data OK.
BH	2554	30.3	2557(1)	27°46.98'	91°29.92'	613	29 ± 1	0.91 ± 0.16	28 ± 3	27 ± 6	7.59	
BH	2555	24.9	2557(2)	27°46.98'	91°29.34'	639	25 ± 1	0.98 ± 0.09	23 ± 1	25 ± 3		
BH	2556	23.3	2557(3)	27°46.97'	91°28.83'	659	25 ± 1	0.97 ± 0.08	24 ± 1	24 ± 3		
MC	2560	22.6	2564(1)	28°14.60'	89°9.27'	1,027	32 ± 1	0.94 ± 0.13	30 ± 1	30 ± 5	7.63	
MC	2559	23.7	2564(2)	28°13.34'	89°05.30'	1,261	35 ± 1	1.02 ± 0.14	32 ± 1	35 ± 6		
MC	2561	28.7	2564(3)	28°12.31'	89°01.20'	1,269	38 ± 1	0.96 ± 0.18	36 ± 1	37 ± 8		
MC			2564(4)	28°12.42'	89°01.20'	1,269	38 ± 1	0.96 ± 0.18		37 ± 8		POGO (natural drift).
MC	2562	25.8	2568(1)	28°04.74'	89°08.40'	1,049	22 ± 1	1.03 ± 0.09	23 ± 1	23 ± 3	6.96	
MC			2568(2)	28°04.86'	89°08.22'	1,057	20 ± 2	1.03 ± 0.09		21 ± 3		POGO (natural drift).
MC	2566	25.8	2568(3)	28°07.16'	89°06.18'	1,190	33 ± 1	0.99 ± 0.08	32 ± 1	32 ± 4		
MC	2565		2568(4)	28°07.40'	89°08.37'	1,068						Bad penetration; no measurements.
MC	2563		2568(5)	28°07.41'	89°08.17'	1,049						Corer bent 9 mfbc; bad penetration; no measurements.
MC	2570	20.9	2572	28°04'.26'	89°41.39'	628	36 ± 3	0.79 ± 0.11	26 ± 3	28 ± 5	4.9	Full penetration; mud on core weight.
MC	2569		2573	28°9.11'	89°28.79'	1,027					4.2	Corer bent 9 mfbc; bad penetration; no measurements.

in the water column, 100 m above sea floor. This second check ensured that all sensors were functioning properly after penetration.

Thermal Gradients. To reduce the effect of frictional heating produced by the penetration of probes into the sea floor (Bullard, 1954; Jaeger, 1965), the core remained embedded in the sea floor for more than 6 minutes to allow collection of baseline data. The exact duration of the measurements was a function of the behavior of the corer cable. The cable tension was measured in real time to ensure that no tension was applied during the measurement period. Temperature and time plots were produced to estimate the background sediment temperature [for example, (Lister, 1970; Hyndman and others, 1979; Villinger and Davis, 1987)].

Thermal Conductivity. Even when full penetration of the gravity corer was achieved (providing sediment temperatures over the full corer length), simultaneously recovered sediment cores generally were shorter than 6 to 9 m long. For this reason, thermal measurements (except multiple POGO-like penetrations were made as close as possible to Calypso piston core sites, and thermal conductivities were measured on the piston cores by using a needle probe technique (such as Von Herzen and Maxwell, 1959). Measurements were made every 1.5 m (one measurement per core section) after thermal equilibrium of the core was reached. In one single piston core, the variability typically was greater than about 20 to 25 percent. We, therefore, computed different mean values of thermal conductivity (Novosel and others, this volume, chapter 7) :

– equivalent mean conductivity (k_e):

$$k_e = \frac{\Delta Z}{\sum \frac{\Delta Z_i}{k_i}} \tag{1}$$

– harmonic mean conductivity (k_h):

$$k_h = \frac{n}{\sum \frac{1}{k_i}} \tag{2}$$

– arithmetic mean conductivity (k_a):

$$k_a = \frac{1}{n} \sum k_i \tag{3}$$

where Δz_i and ki are the spacing and the thermal conductivity, respectively, between probes I and I+1.

Heat-Flow Measurements. Two heat-flow values (q_e and q_a) were computed (table 1) :

– the Bullard heat flow (q_e) was obtained by plotting temperature (T) with integrated thermal resistance at depth (z) (Bullard, 1954) :

$$q_e = \frac{dT}{d\xi} \tag{4}$$

where

$$\xi = \sum_{i=0}^{N} R_i \Delta Z_i \quad with \quad R_i = \frac{1}{k_i} \tag{5}$$

and k_i is the measured conductivity at a given core section number (i).

– the average heat flow (q_a) was determined from:

$$q_a = G \times k_a \tag{6}$$

where G is the average thermal gradient estimated by linear regression on the (T, z) plot; and k_a is the arithmetic mean conductivity.

– the error for q_a can be determined from:

$$\frac{\Delta q_a}{q_a} = \frac{\Delta k_a}{k_a} + \frac{\Delta G}{G} \tag{7}$$

Summary of Results and General Remarks

At a number of sites, several heat-flow measurements (POGO-like) were made by reentering the corer into the sea floor several times during the same lowering (reentries were made after the ship drifted for about 15 to 20 minutes). This procedure provided additional information on local variability but used little ship time. Previous experience indicates that the corer can easily penetrate several times into the sea floor and that this typically does not adversely affect the core sampled during the first penetration. Results are summarized in table 1 and figures 5 and 6. Thermal measurements are presented in table 2. Thermal conductivities are reported separately by Novosel and others (this volume, chapter 7).

(1) In the Tunica Mound and Bush Hill areas (figs. 1 and 2), water depths ranged between 564 and 659 m. Except for the bottom two temperature readings at site MD02-2540 GHF, the temperature and depth profiles all were relatively linear. The measured thermal gradients (obtained by fitting a regression line to the temperature and depth plots for depths >2 m) ranged between 23 and 29 degrees Celsius per kilometer (°C/km), except at site MD02-2540 GHF, where a value of 38 °C/km was determined.

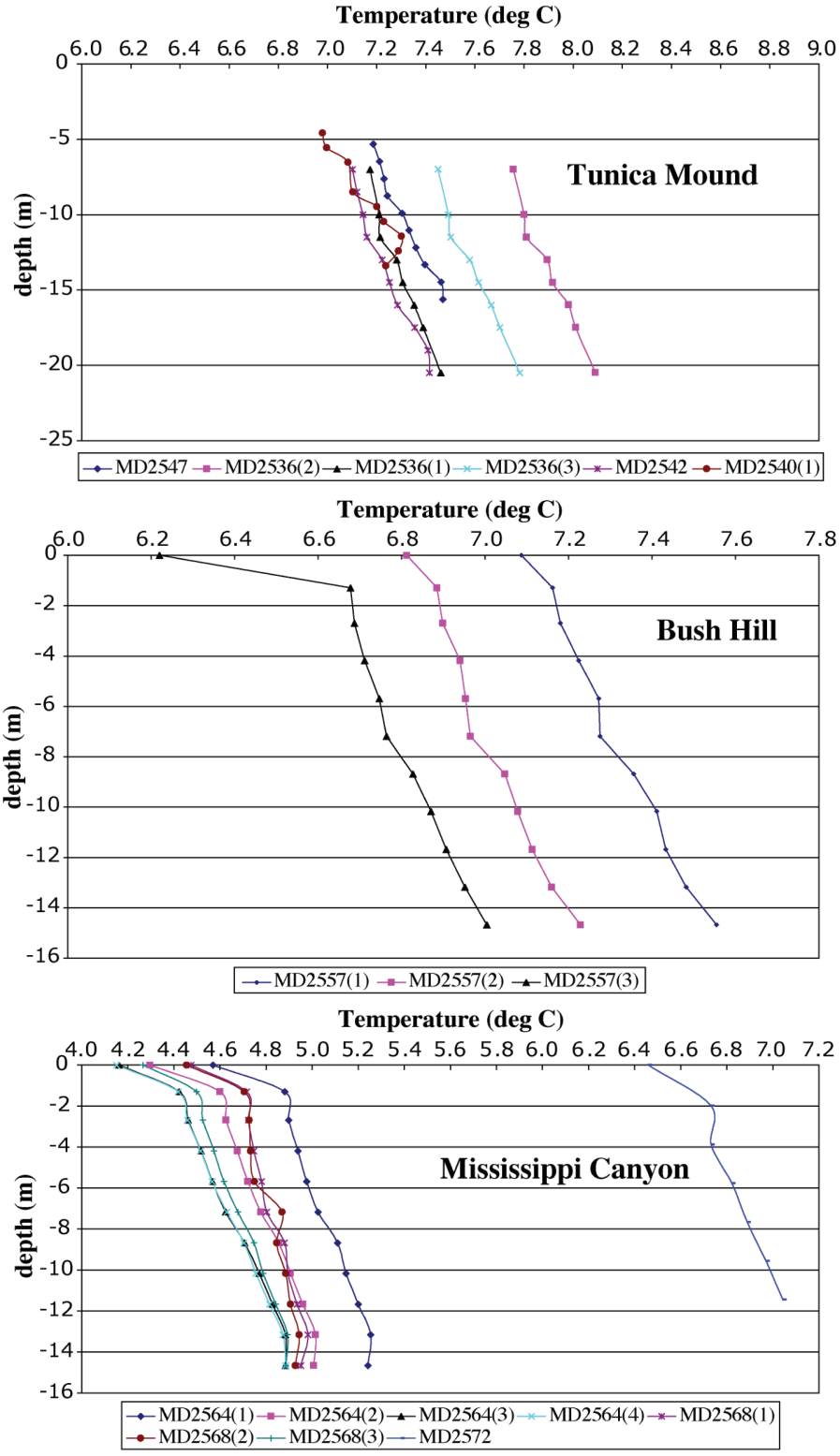

Figure 5. Temperature versus depth profiles for each study area.

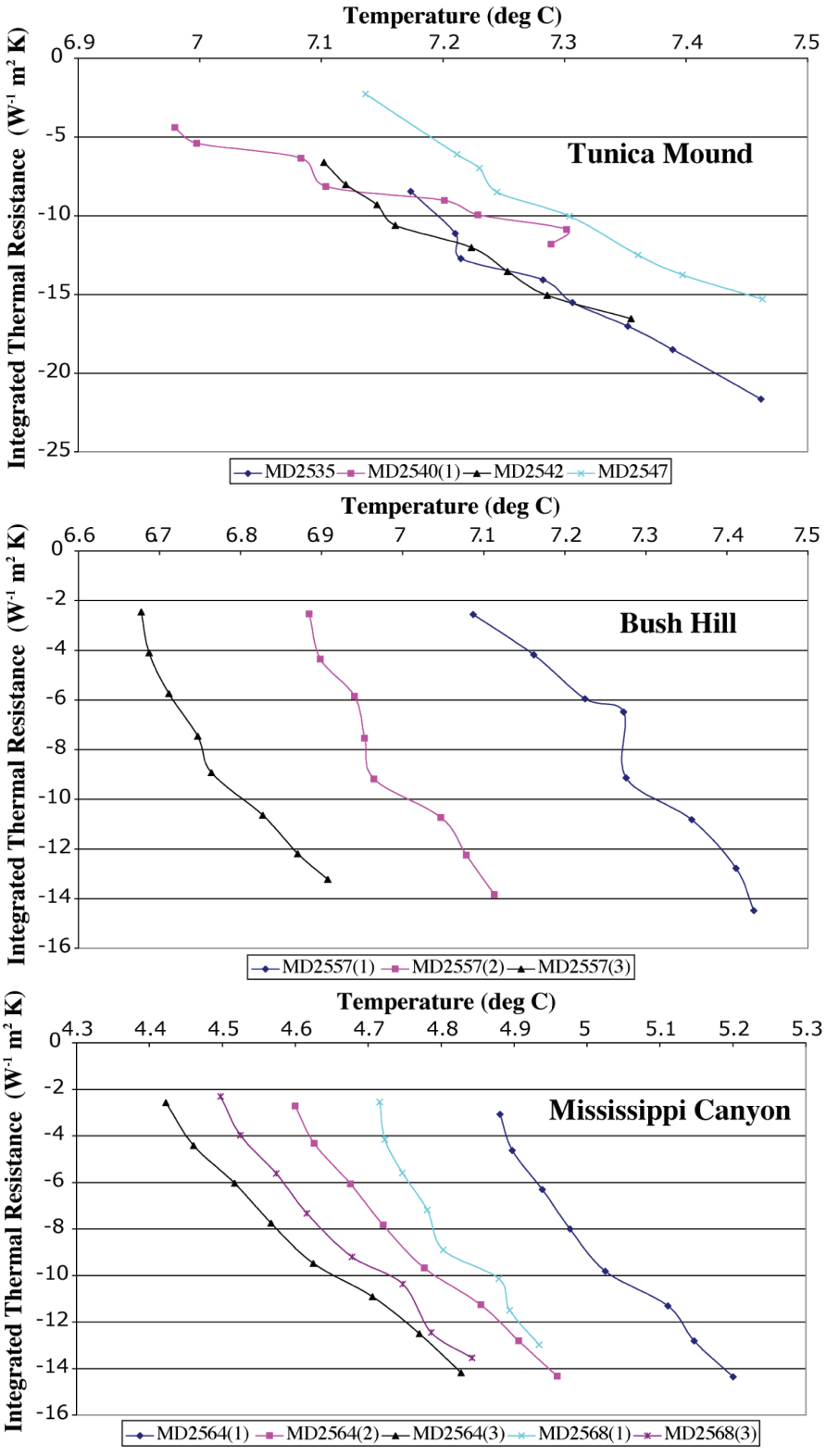

Figure 6. Temperature versus integrated thermal resistance curves for each study area. At a number of sites, several heat-flow measurements were made (POGO-like) by reentering the corer into the sea floor several times during the same lowering. Thus, there are fewer plots here than in figure 5, and there is no one-to-one correspondence between symbols in both figures. At the site of the first penetration of the gravity core, one Calypso piston core was collected, generally with 100% recovery. Because the core recovery ratio of the gravity cores hardly exceeded 70%, shipboard thermal conductivity measurements were performed on the Calypso giant piston core rather than on the gravity core.

Table 2. Temperature measurements.

[N, north; W, west; T_0, bottom water temperature; m, meters; C, degrees Celsius; GB-GC, Garden Banks-Green Canyon (Tunica Mound); NaN, not a valid number; BH, Bush Hill; MC, Mississippi Canyon]

Area	Name of Calypso core MD02-	Name of heat-flow measurement MD02-	Latitude (N)	Longitude (W)	Depth (m)	T_0	Depth											Temperature										
							d1 (m)	d2 (m)	d3 (m)	d4 (m)	d5 (m)	d6 (m)	d7 (m)	d8 (m)	d9 (m)	d10 (m)	d11 (m)	T1 (°C)	T2 (°C)	T3 (°C)	T4 (°C)	T5 (°C)	T6 (°C)	T7 (°C)	T8 (°C)	T9 (°C)	T10 (°C)	T11 (°C)
GB -GC	2535	2536(1)	27°37.19'	092°14.46'	608	8.266	7	10	11.5	13	14.5	16	17.5	20.5				7.173	7.210	7.215	7.282	7.306	7.352	7.389	7.462			
GB -GC		2536(2)	27°37.52'	092°14.76'	564	8.692	7	10	11.5	13	14.5	16	17.5	20.5				7.757	7.780	7.809	7.895	7.916	7.981	8.001	8.089			
GB -GC		2536(3)	27°37.62'	092°14.25'	585	8.692	7	10	11.5	13	14.5	16	17.5	20.5				7.451	7.491	7.502	7.579	7.616	7.667	7.702	7.783			
GB -GC	2539	2540(1)	27°38.42'	092°11.52'	617	6.570	4.58	5.56	8.5	10.46	11.44	12.42	13.4					6.979	6.997	7.104	7.229	7.302	7.289	7.238				
GB -GC		2540(2)	27°38.41'	092°11.71'	620	NaN	NaN	NaN	NaN	NaN	NaN	NaN	NaN					NaN	NaN	NaN	NaN	NaN	NaN	NaN				
GB -GC	2541	2542	27°37.93'	092°12.72'	617	6.401	7	8.5	10	11.5	13	14.5	16	17.5	19.0	20.5		7.102	7.120	7.146	7.161	7.223	7.253	7.286	7.355	7.409	7.416	
GB -GC	2546	2547	27°36.99'	092°14.90'	607	7.111	5.33	6.48	7.62	8.76	9.90	11.05	12.19	13.33	14.47	15.62		7.186	7.212	7.230	7.244	7.304	7.332	7.360	7.397	7.463	7.470	
BH	2554	2557(1)	27°46.98'	091°29.92'	613	7.087	1.3	2.7	4.2	5.7	7.2	8.7	10.2	11.7	13.2	14.7	16.2	7.162	7.181	7.225	7.272	7.276	7.356	7.411	7.433	7.482	7.555	7.578
BH	2555	2557(2)	27°46.98'	091°29.34'	639	6.812	1.3	2.7	4.2	5.7	7.2	8.7	10.2	11.7	13.2	14.7	16.2	6.885	6.898	6.941	6.953	6.964	7.047	7.079	7.113	7.160	7.229	7.232
BH	2556	2557(3)	27°46.97'	091°28.83'	659	6.220	1.3	2.7	4.2	5.7	7.2	8.7	10.2	11.7	13.2	14.7	16.2	6.677	6.687	6.711	6.747	6.764	6.827	6.870	6.907	6.952	7.005	7.014
MC	2560	2564(1)	28°14.60'	089°09.27'	1,027	4.570	1.3	2.7	4.2	5.7	7.2	8.7	10.2	11.7	13.2	14.7	16.2	4.881	4.897	4.939	4.977	5.025	5.111	5.147	5.200	5.254	5.242	5.350
MC	2559	2564(2)	28°13.34'	089°05.30'	1,261	4.296	1.3	2.7	4.2	5.7	7.2	8.7	10.2	11.7	13.2	14.7	16.2	4.599	4.626	4.676	4.721	4.777	4.855	4.907	4.959	5.014	5.006	5.111
MC	2561	2564(3)	28°12.31'	089°01.20'	1,269	4.162	1.3	2.7	4.2	5.7	7.2	8.7	10.2	11.7	13.2	14.7	16.2	4.423	4.461	4.517	4.567	4.625	4.706	4.770	4.827	4.883	4.884	4.987
MC		2564(4)	28°12.42'	089°01.20'	1,269	4.151	1.3	2.7	4.2	5.7	7.2	8.7	10.2	11.7	13.2	14.7	16.2	4.419	4.459	4.516	4.565	4.629	4.704	4.756	4.814	4.873	4.885	4.995
MC	2562	2568(1)	28°04.74'	89°08.40'	1,049	4.474	1.3	2.7	4.2	5.7	7.2	8.7	10.2	11.7	13.2	14.7	16.2	4.716	4.723	4.747	4.781	4.803	4.879	4.984	4.934	4.981	4.952	5.039
MC		2568(2)	28°04.86'	89°08.22'	1,057	4.455	1.3	2.7	4.2	5.7	7.2	8.7	10.2	11.7	13.2	14.7	16.2	4.705	4.726	4.733	4.750	4.870	4.846	4.884	4.907	4.943	4.927	5.016
MC	2566	2568(3)	28°07.16'	89°06.18'	1,190	4.265	1.3	2.7	4.2	5.7	7.2	8.7	10.2	11.7	13.2	14.7	16.2	4.498	4.525	4.574	4.616	4.678	4.747	4.787	4.843	4.893	4.885	4.989
MC	2565	2568(4)	28°07.40'	89°08.37'	1,068		NaN	NaN	NaN	NaN	NaN	NaN	NaN	NaN	NaN	NaN	NaN	NaN	NaN	NaN	NaN	NaN	NaN	NaN	NaN	NaN	NaN	NaN
MC	2563	2568(5)	28°07.41'	89°08.17'	1,049		NaN	NaN	NaN	NaN	NaN	NaN	NaN	NaN	NaN	NaN	NaN	NaN	NaN	NaN	NaN	NaN	NaN	NaN	NaN	NaN	NaN	NaN
MC	2570	2572	28°04'.26'	89°41.39'	628	6.459	2.0	3.9	5.8	7.7	9.6	11.5						6.730	6.732	6.822	6.888	6.971	7.044					
MC	2569	2573	28°09.11'	89°28.79'	1,027		NaN	NaN	NaN	NaN	NaN	NaN						NaN	NaN	NaN	NaN	NaN	NaN					

Note: Values of bottom water temperature (T_0) measured at sites M02-2536 (1 to 3) are uncertain, possibly due to the heat capacity of the corer weight stand.

(2) In the Mississippi Canyon area (fig. 3), one successful measurement (MD02-2572 GHF) was obtained on the western side of the canyon. Seven measurements were obtained on the eastern side of the canyon: two (MD02-2568 GHF-1 and GHF-2) were made on a small apron, at water depths of about 1,050 m; the other five measurements were made in a valley adjacent to the main canyon. At all sites, recent changes in bottom water temperature affected the temperature of the uppermost sediment layer (at depths <1.5 m). Temperature and depth profiles all were relatively linear, except for MD02-2568 GHF-1 and GHF-2. At these sites, the temperature and depth profiles were less linear in the T-z (fig. 5) and T-R spaces (fig. 6) than at all other sites.

Measured thermal gradients (obtained by fitting a regression line to the temperature and depth plots for depths >1.5 m) ranged between 32 and 38 °C/km, except for MD02-2568 GHF-1 and GHF-2, where low values of 22 and 20 °C/km, respectively, were determined. Except for these two values, gradients were relatively uniform, with an average of about 35 ± 3 °C/km.

Conclusions

The data reported here provide robust, first-order estimations of the geothermal gradient in the northern Gulf of Mexico. These results are critical for determining the thermodynamic conditions related to gas hydrate stability. Further studies are needed to understand the observed variability and the processes that affect the measured temperature-depth profiles, such as variations in bottom water temperature, small-scale heterogeneities within the sediments, and vertical advection of pore water.

Acknowledgments

At-sea help was provided by the IMAGES (International Marine Past Global Changes Study) and PAGE (Paleoceanography of the Atlantic and Geochemistry) programs, and by IPEV personnel onboard the RV *Marion Dufresne*. Funding was provided by the U.S. Department of Energy Gas Hydrate Program.

References

Bullard, E.C., 1954, The flow of heat through the floor of the Atlantic Ocean: Proceedings of the Royal Society of London, v. 222, p. 408–429.

Hyndman, R.D., Davis, E.E., and Wright, J.A., 1979, The measurement of marine geothermal heat flow by a multipenetration probe with digital acoustic telemetry and in-situ thermal conductivity: Marine Geophysical Research, v. 4, p. 181–205.

Jaeger, J.C., 1965, Application of the theory of heat conduction to geothermal measurements, *in* Smith, W.E., ed., Terrestrial heat flow: American Geophysical Union, Geophysical Monograph, v. 8, p. 7–21.

Lister, C.R.B., 1970, Heat flow west of the Juan de Fuca Ridge: Journal of Geophysical Research, v. 75, p. 2648–2654.

Villinger, H., and Davis, E.E., 1987, A new reduction algorithm for marine heat flow measurements: Journal of Geophysical Research, v. 92, p. 12846–12856.

Von Herzen, R.P., and Maxwell, A.E., 1959, The measurement of thermal conductivity of deep- sea sediments by a needle-probe method: Journal of Geophysical Research, v. 64, p. 1557–1563.

Chapter 7

Thermal Conductivity of Sediment Recovered from the IMAGES VIII/PAGE 127 Gas Hydrate and Paleoclimate Cruise on the RV Marion Dufresne in the Gulf of Mexico, 2–18 July 2002

Ivana Novosel[1,2], William J. Winters[3], Olya M. Boldina[4], Cinthia Labails[5], and Louis Géli[5]

Thermal conductivity of sediment recovered from the IMAGES VIII/PAGE 127 gas hydrate and paleoclimate cruise on the RV Marion Dufresne *in the Gulf of Mexico, 2–18 July 2002; chapter 7* in *Winters, W.J., Lorenson, T.D., and Paull, C.K., eds., 2007, Initial report of the IMAGES VIII/PAGE 127 gas hydrate and paleoclimate cruise on the RV* Marion Dufresne *in the Gulf of Mexico, 2–18 July 2002: U.S. Geological Survey Open-File Report 2004–1358.*

Introduction

A scientific piston-coring cruise aimed at studying the distribution of shallow gas hydrate deposits was conducted aboard the RV *Marion Dufresne* in July 2002. Thermal conductivity, a property related to the rate of heat transport through a medium and used to determine heat flow, was measured on a total of 23 cores. Ten cores were from Tunica Mound, four were from Bush Hill, and nine were from the Mississippi Canyon area. Only one core containing gas hydrate, MD02-2565, from the Mississippi Canyon 853 diapir was tested for thermal conductivity. Core information, including water depth, is presented in Appendix A, and maps of core locations are in Appendix B of this report.

Methods

When a core became accessible on the ship's deck, it was labeled and cut into 1.5-meter (m)-long sections for ease in handling (Winters and others, this volume, chapter 3). The sections then were brought into thermal equilibrium with ambient temperature in the laboratory in preparation for thermal conductivity measurements. In this study, two separate instruments using the pulsed-needle probe transient method (Lister, 1979) were used to determine thermal conductivities. The system used for the first half of the cruise was provided by T. Lewis (Geological Survey of Canada – Pacific Geoscience Center, GSC–PGC), and a more automated 'black-box' type system provided by L. Geli (French Research Institute for Exploitation of the Sea, IFRAMER) was used for the second half of the cruise. It is believed that the change in equipment had minimal, if any, effect on results because both systems produced nearly identical data during a transition period when multiple tests were performed on the same sediment.

The measuring equipment consisted of (1) an ~2-millimeter (mm) diameter and 70-mm-long needle probe with a constant calibration resistance of 40.3 ohm, (2) a programmable power supply producing 2.6 joules of total energy per 10-mm length of probe, (3) a multi-meter that measured the resistance of the thermistor every 0.5 second(s), and (4) a computer for logging and calculations. Each system had one needle probe, and each probe was calibrated once using food-grade clear gelatin, which was assumed to have thermal conductivity properties similar to water. Measurements were repeated occasionally to check for variability. The uncertainty range for the measurements is less than 10 percent.

[1]University of Victoria, School of Earth and Ocean Sciences, Victoria, BC, V8W 3P6 Canada.

[2]Currently at: Rice University, Department of Earth Science, 6100 Main Street, Houston, TX 77005 USA.

[3]U.S. Geological Survey, 384 Woods Hole Road, Woods Hole, MA 02543 USA.

[4]Moscow State University, Department of Geocryology, Moscow, Russia 119992.

[5]Marine Geosciences Department, IFRAMER, BP 70, 29280, Plouzané, France.

The change in the temperature inside a probe can be described by the following relation (Lewis and others, 1993):

$$T(t)=Q/(4\pi\kappa t),$$

where

- Q is the total heat input per unit length of the probe;
- κ is the thermal conductivity;
- t is the time since the start of the heat pulse; and
- T is the temperature change, in degrees Kelvin.

The thermal conductivity is obtained by defining the slope of the temperature decay curve on a T versus 1/t graph.

Thermal conductivities were measured approximately once per standard 1.5-m core section. A small hole was hand-drilled (to avoid excessive heat generation) into the core liner through which the needle probe was immediately inserted. For the first system, the temperature drift was measured, and a heat pulse was applied only if the drift was less than 0.0003 degrees Kelvin per second (K/s). The decay of temperature with time was measured and displayed on a graph to check the quality of the data and to visually choose the proper time window based on test duration and system response for the determination of the conductivity. In this study, the window was commonly set to 30 to 70 s after the heat pulse. These steps were omitted while using the second, more automated system.

Results

Thermal conductivities of all core samples (table 1) range from 0.00 (in the presence of gas) to 2.64 W/m•K (watt per meter times degrees Kelvin) with a mean of 0.93 W/m•K and a median of 0.95 W/m•K (table 2). Values were plotted with subbottom depth for the three different study areas—Tunica Mound (fig. 1), Bush Hill (fig. 2), and Mississippi Canyon region (figs. 3, 4). Thermal conductivity values typically increase with depth from approximately 0.8 to 1.0 W/m•K, with a greater rate of increase within the top 10 to 15 m of sediment than deeper in the core.

Conclusions

Thermal conductivity increases more rapidly in the upper 10 to 15 m of sediment than below that depth where values decrease at a more gradual rate or are nearly constant with depth. This change in behavior coincides with water content and porosity trends noted in Winters and others (this volume, chapter 4). This is reasonable considering the relation between thermal conductivity and water content. Thermal conductivity in sediments collected offshore Vancouver Island on the Cascadia accretionary prism also changed more abruptly in shallow subbottom sediment (Novosel, 2002).

Except for a few outlying points, the thermal conductivities presented for Tunica Mound (fig. 1) and Bush Hill (fig. 2) have much less scatter in relation to depth than at the Mississippi Canyon region (fig. 4), where almost all the low values are present in only two cores—MD02-2565 and MD02-2570. If results are plotted without data from those two cores, the scatter is equivalent to or better than at Tunica Mound and Bush Hill (fig. 5). The upper linear trend of thermal conductivity in relation to depth of the Mississippi Canyon sediment as shown in figure 5 extends to about 15 meters below sea floor (mbsf), deeper than at either Tunica Mound or Bush Hill.

Because gas hydrate was recovered in core MD02-2565, the likely cause of the low thermal conductivities is the presence of free gas caused by hydrate dissociation. Similar gas expansion effects on thermal conductivity values of shallow gas hydrate-bearing sediments is also observed on the Cascadia margin (Novosel, 2002; Riedel and others, 2005). Thermal conductivities are also low in core MD02-2570, suggesting free gas may have been present in that core as well. This interpretation is supported by core photographs showing numerous expansion cracks in core MD02-2570 (Appendix G). These cracks were not observable during thermal conductivity

Table 1. Summary of thermal conductivity measurements.

[Note: Core MD02-2548 is not a USGS core. Thermal conductivitiy values (W/m•K) for core MD02-2548 are presented in this table for information purposes only. The values for core MD02-2548 are not plotted in figure 1]

Depth (cm)	Thermal Conductivity (W/m•K)
MD022535	
70	0.82
90	0.85
220	0.79
380	0.92
520	0.95
680	1.02
830	1.06
980	1.05
1110	1.11
1270	1.09
1420	1.02
1570	1.04
1720	0.98
1880	1.07
2000	0.97
2160	0.94
2320	0.98
2480	1.02
2620	0.99
2760	1.00
2920	0.99
3060	0.99
3220	1.02
3360	1.00
3500	1.01
3640	0.98
3760	0.96
MD022537	
75	0.84
225	0.85
375	0.92
520	0.92
675	0.92
820	0.97
980	1.05
1120	1.00
1275	0.98
1420	1.00
1580	0.95
1710	0.92
1870	1.00
2020	0.96
2170	0.98
2320	0.95
2475	0.95
2620	0.97
2770	0.96
2895	0.91
3005	0.96
3165	0.87
3310	0.96
MD022538	
70	0.85
220	0.85
370	0.91
570	0.96
670	0.95
765	0.95
MD022539	
60	0.82
220	0.83
370	0.85
520	0.92
670	1.00
820	1.06
970	1.13
1120	1.10
1270	1.03
1420	1.06
1570	1.07
1720	1.06
1870	0.98
2020	1.03
2170	0.99
2320	0.95
2470	1.07
2620	0.97
2770	0.97
2920	1.08
3070	0.99
MD022541	
60	0.88
220	0.90
370	0.91
520	0.91
670	1.00
820	1.07
970	1.04
1120	1.23
1270	1.14
1420	1.02
1570	0.97
1720	1.01
1870	0.99
2020	1.13
2170	0.96
2320	0.98
2470	0.96
2620	0.99
2770	0.95
2920	0.97
3070	0.99
3220	0.97
3370	0.99
3570	1.19
MD022542	
80	0.84
220	0.83
370	0.95
530	1.05
680	0.97
760	1.02
MD022545	
40	0.84
145	0.81
250	0.85
345	1.02
445	0.47
545	0.54
650	0.88
740	0.91
850	0.83
915	0.86
MD022546	
70	0.81
220	0.73
370	0.88
520	0.91
670	0.98
780	0.94
860	0.97
970	0.94
1110	0.92
1280	0.99
1410	0.79
1570	0.90
1720	0.95
1870	0.73
1960	0.90
2040	0.97
2170	0.94
2320	0.95
2450	0.94
2620	0.99
2770	0.98
2920	0.92
3060	0.97
MD022547	
75	0.81
220	0.85
370	0.90
510	0.90
MD022548	
80	0.82
220	0.84
370	0.88
520	0.86
680	0.99
780	0.94
940	1.02
1020	0.98
1130	0.98
1280	1.03
1420	0.93
1570	0.99
1730	0.95
1880	1.07
1960	0.90
2030	0.94
2180	0.95
2330	0.99
2470	1.01
2620	1.00
2780	1.02
2925	0.95
3075	1.00
3220	1.00
MD022554	
70	0.76
220	0.85
370	0.87
520	0.86
680	0.85
825	0.92
925	0.95
1115	0.92
1265	0.90
1415	0.33
1565	1.01
1725	1.08
1830	0.90
2000	0.88
2145	0.79
2300	1.00
2450	1.06
2595	1.08
2745	1.07
2895	0.96
3030	1.02
MD022555	
70	0.80
185	0.84
370	0.86
520	0.90
670	0.87
820	0.91
970	1.00
1120	0.96
1260	0.96
1420	0.87
1680	1.02
1720	1.02
1870	1.09
2020	1.03
2160	1.00
2320	1.06
2480	1.15
2620	1.06
2770	1.10
2920	1.03
3070	0.90
3220	0.99
3380	1.06
3510	1.08
MD022556	
70	0.86
220	0.90
380	0.83
520	0.83
670	0.89
810	1.12
970	0.98
1160	0.96
1270	0.82
1420	0.99
1540	1.00
1720	0.99
1870	0.95
2020	0.99
2170	0.98
2340	1.03
2480	1.05
2620	1.08
2770	0.98
2920	0.88
3070	1.06
3210	1.02
3370	1.01
MD022557	
70	0.85
220	0.86
375	1.02
510	1.04
MD022559	
60	0.83
220	0.84
370	0.81
520	0.88
660	0.79
820	0.91
970	0.90
1120	0.96
1260	0.96
1420	1.08
1570	0.95
1720	1.07
1870	0.99
2010	1.03
2170	1.13
2320	1.18
2470	1.12
2620	1.01
2770	1.16
2910	1.25
3070	1.29
3210	1.16
3320	1.22
MD022560	
60	0.49
220	0.90
370	0.82
520	0.91
655	0.84
820	0.93
970	0.93
1115	0.99
1262	1.01
1420	1.02
1570	1.00
1725	0.99
1870	0.96
2010	1.09
2180	0.96
2320	0.93
2470	1.03
2610	0.99
2760	1.08
MD022561	
70	0.73
200	0.87
370	0.80
520	0.84
660	0.88
820	0.96

Table 1. Summary of thermal conductivity measurements. — Continued

[Note: Core MD02-2548 is not a USGS core. Thermal conductivitiy values (W/m•K) for core MD02-2548 are presented in this table for information purposes only. The values for core MD02-2548 are not plotted in figure 1]

Depth (cm)	Thermal Conductivity (W/m•K)	Depth (cm)	Thermal Conductivity (W/m•K)	Depth (cm)	Thermal Conductivity (W/m•K)	Depth (cm)	Thermal Conductivity (W/m•K)	Depth (cm)	Thermal Conductivity (W/m•K)
970	0.90	480	0.03	565	0.86	485	0.77	240	0.86
1090	1.00	530	0.66	625	0.93	520	0.92	320	0.85
1270	1.01	625	0.75	660	0.95	565	0.87	370	0.83
1420	1.08	675	0.75	775	0.87	620	0.93	420	0.25
1570	1.03	725	0.75	820	0.93	660	0.90	470	0.81
1730	1.04	775	0.69	865	0.92	775	0.96	510	0.82
1870	1.05	810	0.60	925	1.93	820	0.97	550	0.77
2020	1.09	850	0.65	970	0.96	865	0.84	620	0.84
2170	0.98	925	0.72	1015	0.94	920	0.90	650	0.80
2330	1.16	985	0.66	1145	1.05	970	0.96	690	0.91
2470	1.13	1075	0.81	1080	0.88	1020	1.64	780	0.84
2620	1.12	1120	0.71	1220	0.93	1070	0.98	820	0.85
2760	1.00	1160	0.72	1255	1.07	1130	1.06	860	0.83
2870	0.32	1310	0.76	1290	1.00	1225	0.92	980	0.74
MD022562		1225	0.70	1375	1.03	1290	1.01	1020	0.81
60	0.87	1270	0.77	1420	1.04	1370	0.97	1080	0.86
205	0.90	1450	0.77	1465	0.92	1420	0.90	1140	0.88
370	0.86	1410	0.71	1525	1.04	1465	1.06	1260	0.98
520	0.93	1370	0.77	1570	1.02	1520	1.08	1320	0.84
640	0.99	1520	0.83	1615	0.99	1570	1.04	1380	0.87
820	0.97	1570	0.62	1665	0.90	1620	1.09	1420	0.63
970	1.10	1610	0.71	1720	1.03	1670	1.01	1460	0.84
1110	1.06	1670	0.72	1765	1.08	1720	1.13	1540	0.76
1260	1.08	1700	0.76	1820	0.93	1770	1.07	1580	0.80
1420	1.12	1760	0.73	1855	1.19	1825	1.09	1620	0.71
1560	1.05	1680	0.80	1890	0.00	1890	1.13	1680	0.81
1720	1.13	1840	0.73	1975	1.13	1970	1.09	1740	0.81
1860	1.13	1880	0.81	2020	1.11	2020	1.07	1820	0.82
2035	1.15	1980	0.65	2065	1.07	2070	1.08	1880	0.66
2170	1.01	2020	0.77	2125	0.99	2120	1.18	1920	0.67
2320	1.11	2060	0.71	2170	1.16	2170	1.00	1980	0.70
2460	1.07	2120	0.67	2215	1.09	2220	1.12	2020	0.69
2580	1.00	2170	0.73	2275	1.05	2275	1.11	2060	0.87
MD022564		2215	0.83	2320	1.11	2320	1.18	2120	0.86
80	0.83	2280	0.63	2365	0.00	2365	1.03	2180	0.84
220	0.81	2320	0.75	2430	1.02	2420	1.04	2210	0.79
370	0.87	**MD022566**		2480	1.04	2455	1.09	2260	0.76
530	0.91	20	0.82	2580	1.06	2490	1.00	2340	0.69
670	0.99	60	0.80	**MD022567**		2570	0.93	2420	0.83
755	0.95	90	0.78	20	0.78	2605	1.00	2490	0.77
MD022565		235	0.86	60	0.85	2640	1.00	2510	0.78
40	0.67	175	0.78	90	0.88	**MD022570**		2570	0.93
85	2.64	325	0.81	175	0.85	20	0.49	2620	0.75
180	0.69	370	0.80	225	0.83	55	0.90	2670	0.87
220	0.73	415	0.86	325	0.79	90	0.88	2720	0.83
260	0.69	475	0.84	380	0.83	170	0.87	2760	0.91
340	0.72	520	0.84	420	0.90	205	0.89	2810	0.67

Table 2. Statistical values for the thermal conductivity (W/m•K) measurements.

	Tunica Mound	Bush Hill	Mississippi Canyon region	Mississippi Canyon region without MD02-2565 and MD02-2570	All regions
Minimum	0.47	0.33	0	0	0
Maximum	1.23	1.15	2.64	1.93	2.64
Range	0.76	0.82	2.64	1.93	2.64
Mean	0.95	0.95	0.91	0.97	0.93
Median	0.97	0.98	0.9	0.99	0.95
Standard deviation	0.10	0.12	0.22	0.18	0.18

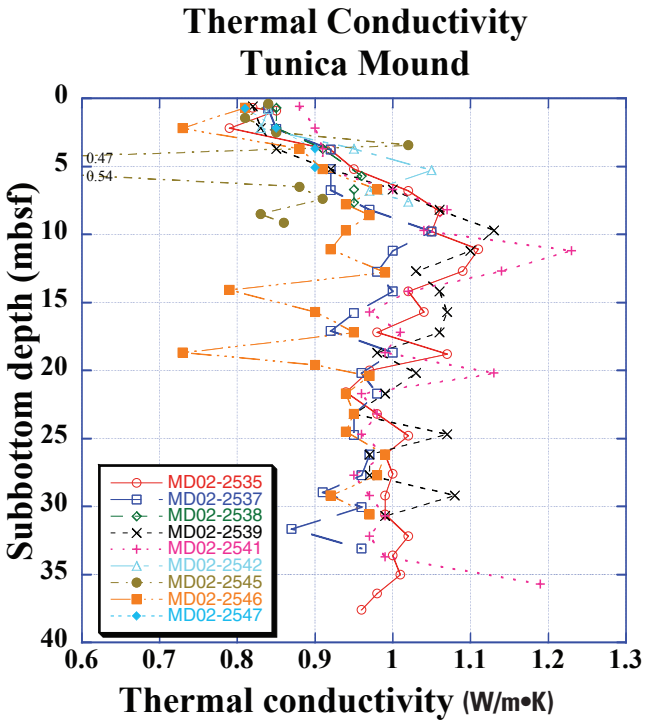

Figure 1. Thermal conductivity values (0.6 to 1.3 W/m•K) in relation to subbottom depth for Tunica Mound.

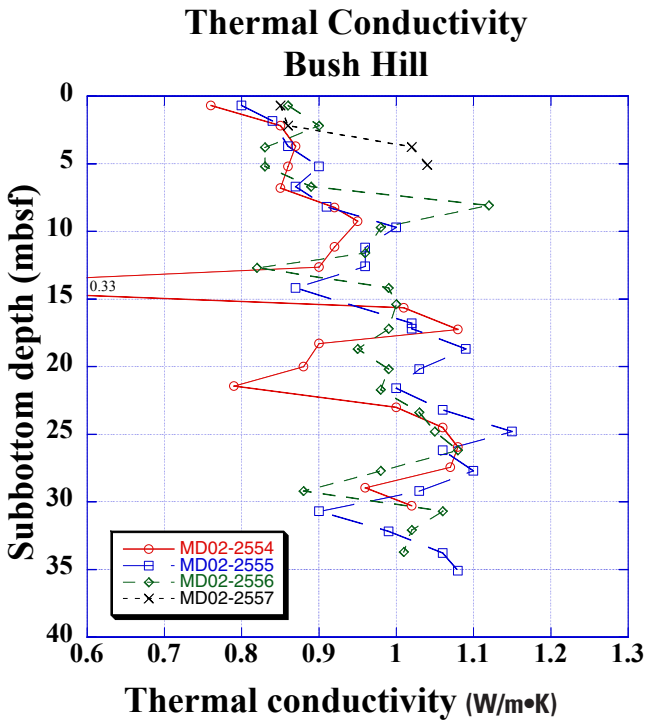

Figure 2. Thermal conductivity values (0.6 to 1.3 W/m•K) in relation to subbottom depth for Bush Hill.

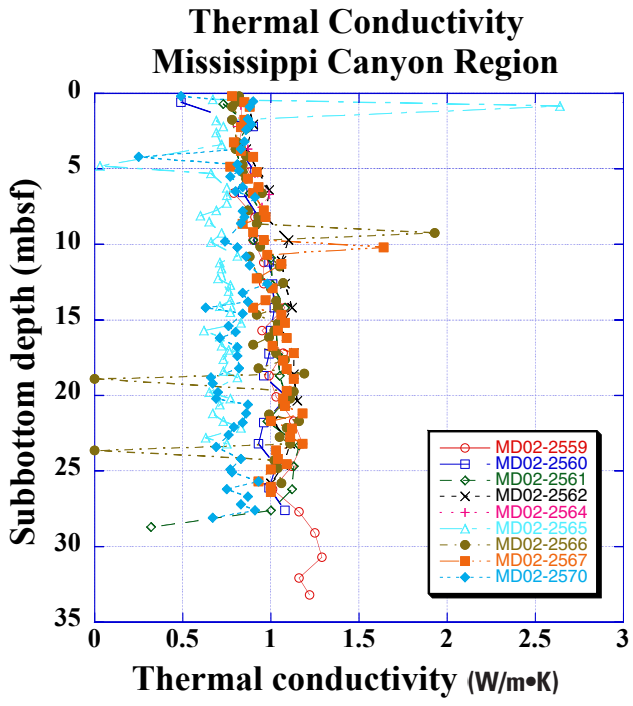

Figure 3. Thermal conductivity values (0 to 3 W/m•K) in relation to subbottom depth for the Mississippi Canyon region.

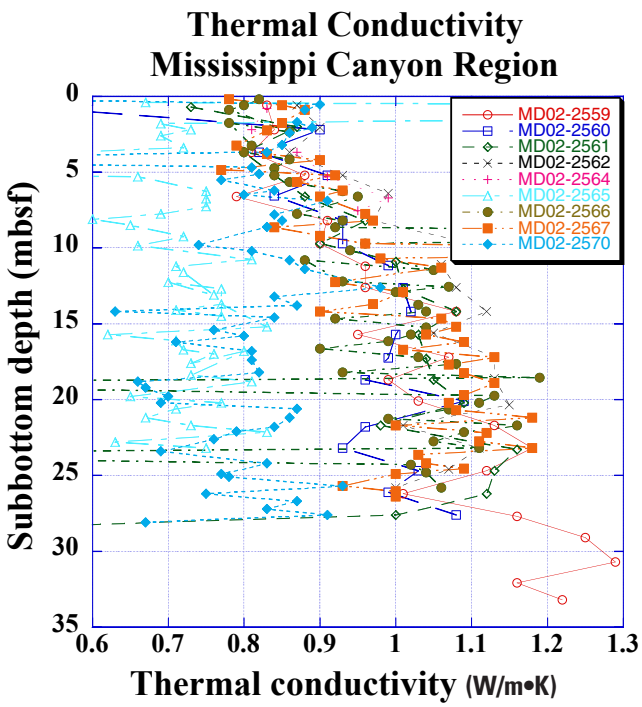

Figure 4. Thermal conductivity values (0.6 to 1.3 W/m•K) in relation to subbottom depth for the Mississippi Canyon region.

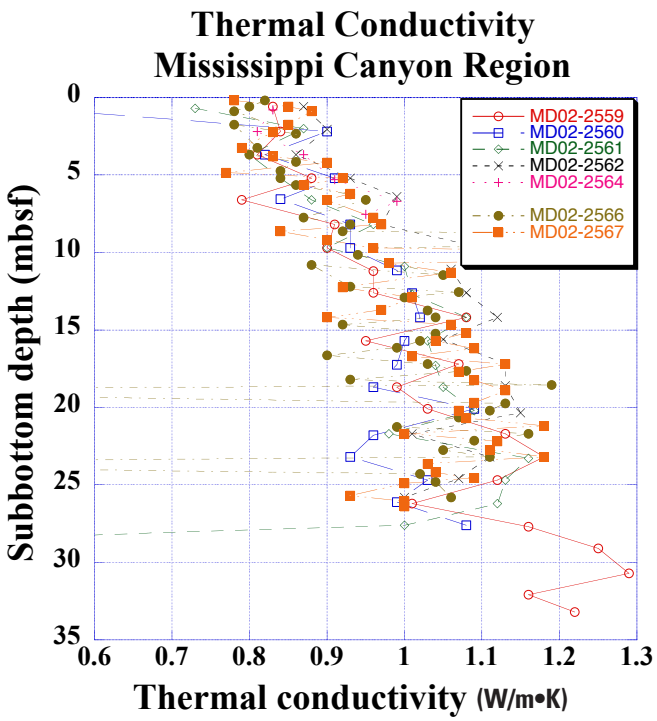

Figure 5. Thermal conductivity values (0.6 to 1.3 W/m•K) without data from cores MD02-2565 and MD02-2570 in relation to subbottom depth for the Mississippi Canyon region.

measurements (because of the opaque core liner) and were discovered subsequently when the cores were split for conducting additional physical property analyses.

References Cited

Lewis, T.J., Villinger, H., and Davis, E.E., 1993, Thermal conductivity measurement of rock fragments using a pulsed needle probe: Canadian Journal of Earth Sciences, v. 30, no. 3, p. 480–485.

Lister, C.R.B., 1979, The pulse-probe method of conductivity measurement: Geophysical Journal, v. 57, p. 451–461.

Novosel, I., 2002, Physical properties of gas hydrate related sediments offshore Vancouver Island, M.S. Thesis, University of Victoria, Canada.

Riedel, M., Novosel, I., Spence, G.D., Hyndman, R.D., Chapman, R.N., Solem, R.C., and Lewis, T., in press, Geophysical and geochemical signatures associated with gas hydrate related venting at the North Cascadia Margin: Geological Society of America Bulletin.

Chapter 8

Pore-Water Gradients in Giant Piston Cores from the Northern Gulf of Mexico

William Ussler III[1] and Charles K. Paull[1]

Pore-water gradients in giant piston cores from the northern Gulf of Mexico; chapter 8 in *Winters, W.J., Lorenson, T.D., and Paull, C.K., eds., 2007, Initial report of the IMAGES VIII/PAGE 127 gas hydrate and paleoclimate cruise on the RV* Marion Dufresne *in the Gulf of Mexico, 2–18 July 2002: U.S. Geological Survey Open-File Report 2004–1358.*

Abstract

Chloride, sulfate, and methane concentration data for pore waters from 483 sediment samples obtained at Tunica Mound, Bush Hill, Kane Spur, and the Mississippi Canyon areas of the Gulf of Mexico indicate that wide ranges in these geochemical species occur in methane-rich and methane-gas-hydrate-bearing sediments. Chloride concentration gradients increase with depth and proximity to salt-cored diapirs and are inversely correlated with the depth to the sulfate-methane interface. Except for six cores from the Kane Spur area, the cores crossed the SMI at depths ranging from 0.4 to 13 meters below sea floor. The sulfate gradients for cores containing a shallow SMI were linear with respect to depth, and sulfate was not found in pore waters below the SMI.

Introduction

In July 2002, giant Calypso piston cores, gravity cores, and box cores were obtained aboard the research vessel (RV) *Marion Dufresne* from four study areas (Tunica Mound, Bush Hill, Kane Spur, and the Mississippi Canyon) and a few surrounding sites in the northern Gulf of Mexico as part of the International Marine Past Global Changes Study (IMAGES VIII)/Paleoceanography of the Atlantic and Geochemistry (PAGE 127) research programs (fig. 1). One of the primary goals of this coring effort was to characterize the pore-water geochemistry of sediments associated with gas hydrate. The target areas were chosen because they were known from previous investigations to contain gas hydrate at or near the sea floor, and high resolution seismic data previously collected by the U.S. Geological Survey (USGS) were available for these areas (Cooper and Hart, 2003).

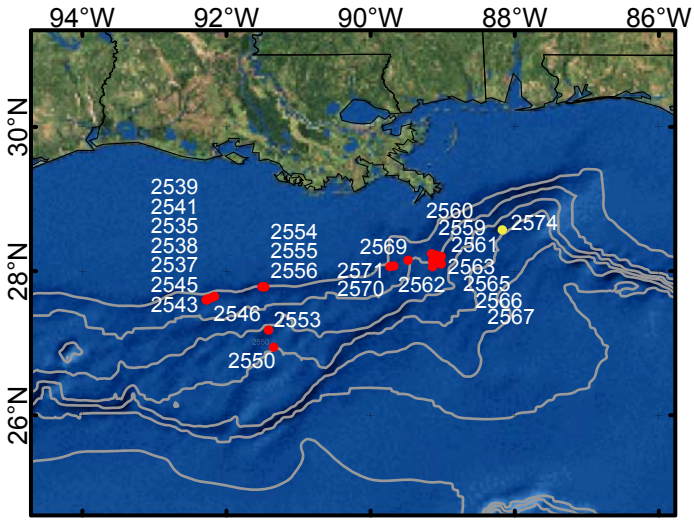

Figure 1. Map of the Gulf of Mexico showing locations of cores analyzed (red filled circles). Cores collected at Tunica Mound include 2535, 2537, 2538, 2539, 2541, 2543, 2545, and 2546; Orca Basin include 2550; Pygmy Basin 2553; Bush Hill include 2554, 2555, and 2556; Kane Spur include 2559, 2560, 2561, 2562, 2566, and 2567; MC-853 Diapir site include 2563 and 2565; West Mississippi Canyon include 2569, 2570, and 2571; and a background site 2574 (yellow filled circle). Contours start at 500 meters water depth, and the intervals are 500 meters. Refer to Appendix B of this report for large-scale station location maps.

This report summarizes the pore-water geochemical data collected shipboard during the cruise, including chloride, sulfate, and methane concentration measurements. Shore-based

[1]Monterey Bay Aquarium Research Institute, 7700 Sandholdt Road, Moss Landing, CA 95039 USA.

measurements of other chemical species are in progress at the time of publication of this report.

Methods

Sediment cores were sampled on deck, typically within 3 hours after recovery. Ten-cm-long whole-round sections of core were removed at regularly spaced (typically ~1.5 m) intervals down the core or at locations of special interest and taken immediately to the shipboard geochemistry laboratory. Pore waters were extracted using either Reeburgh-style (Reeburgh, 1967) or Manheim-style (Manheim, 1966) sediment squeezers. The Reeburgh-style squeezer was preferred because the pore-water extraction and collection process is essentially gas tight. The Manheim-style squeezer was used for firm sediments that could not be processed in the Reeburgh-style squeezer. Generally, sediment samples from greater than 25 meters below sea floor (mbsf) required use of the Manheim-style squeezer.

Sediment pore-water samples were collected in either 60-cubic centimeter (cc) (Reeburgh-style squeezer) or 10-cc (Manheim-style squeezer) plastic syringes. Pore-water subsamples for (1) sulfide concentration, (2) $\delta^{34}S$ measurements of sulfide, (3) $\delta^{34}S$ measurements of sulfate, (4) dissolved inorganic carbon (DIC) concentration and $\delta^{13}C$ measurements, and (5) pore water $\delta^{18}O$ and δD measurements were obtained from the 60-cc syringes prior to headspace gas extraction. The water for these subsamples was filtered through a 0.2-micrometer (μm) sterile syringe filter (Gelman Acrodisc) into a clean scintillation vial prior to sample splitting. From the above subsamples, two separate 2-milliliter (mL) aliquots were placed without chemical preservation in 5-mL glass ampoules and flame-sealed for DIC and water isotopic measurements. Three additional 2-mL aliquots were placed into clean scintillation vials. A 1-mL aliquot of saturated zinc acetate solution was added to two of the vials to precipitate sulfide for concentration and $\delta^{34}S$ measurements, and a 1-mL aliquot of saturated barium chloride solution was added to the third vial to precipitate sulfate for $\delta^{34}S$ measurements.

Headspace gases were extracted from the remaining pore water in the 60-cc syringe samples by adding an equivalent volume of ultra high-purity (UHP, 99.999%+) nitrogen gas to the pore water in the syringe and shaking for 2 minutes. The remaining pore water subsequently was filtered through a 0.2-μm sterile syringe filter (Gelman Acrodisc) and combined with the previously filtered pore samples stored in scintillation vials. These water samples were archived in flame-sealed 5-mL glass ampoules prior to the end of the coring cruise.

Methane concentrations in the headspace gas samples were measured in our shipboard chemical laboratory van using a Shimadzu mini-2 gas chromatograph equipped with a flame-ionization detector (FID). Methane was separated isothermally from other gases by using a 5-foot by 1/8-inch OD(outside diameter) stainless steel chromatographic column packed with 60/80 mesh Carbosieve G (Supelco, Bellefonte, PA). Gas samples were injected into the gas chromatograph by a small volume magnesium perchlorate drying trap in series with a 1-mL stainless steel sample loop. Retention time was approximately 1 minute. Methane samples were run in batches of approximately 50 samples. Primary methane gas standards (9.93 parts per million (ppm) and 98.6 ppm in nitrogen) were run in triplicate at the beginning, end, and nominally every 27th sample of each batch. Measurement time between each sample was approximately 1.5 minutes. High concentration methane samples were identified by their relatively low sulfate concentrations (<5 millimole (mM) sulfate) and segregated before analysis. Lab air was used to purge residual methane from the gas chromatographic sample loop between high concentration samples. The detection limit for methane using this method is 0.01 μm.

Sulfate and chloride concentrations in pore-water samples were measured shipboard using a Dionex DX-100 ion chromatograph equipped with a 4-millimeter (mm) AS-9HC column and an AS-40 autosampler. The eluent was 9-mM sodium bicarbonate and flowed at 1 milliliter per minute. Pore-water samples were diluted 1:100 by using deionized water so that sulfate and chloride could be resolved during one chromatographic run. A 1:100 bulk dilution of International Association for the Physical Sciences of the Oceans (IAPSO) standard seawater was run every sixth sample for calibration purposes. A deionized water blank and a seven-anion standard (Dionex, Sunnyvale, CA) were analyzed at the beginning and end of each nightly chromatographic run to detect contamination and peak center drift. Samples with significantly greater than seawater chloride concentrations were diluted up to 1:1,000 and run with more dilute IAPSO seawater calibration standards. Detection limits for chloride and sulfate measurements using this method are 0.05 mM.

Results and Discussion

A total of 483 sediment pore-water samples was obtained from 25 cores recovered during this cruise; 375 pore-water samples were extracted from sediment samples by using Reeburgh-style squeezers and the remaining 108 samples were extracted using Manheim-style squeezers. Sulfate, chloride, and methane concentration measurements of these pore waters are listed in table 1 (p. 11) and are summarized in figures 2 through 19 according to geographical area and chemical species.

Chloride Concentrations and Gas Hydrate Occurrence

A wide range of chloride concentrations was observed in the sediment pore-water samples. At Tunica Mound, chloride concentrations increase systematically towards the mound and with depth, and reach values as high as about 2,200 mM

in core MD02-2543G at the sea floor on top of the mound (fig. 2). In contrast, chloride concentrations remain near seawater-like values (~560 mM) across the coring transect at Bush Hill and do not increase significantly with depth (fig. 5). Except for three cores (MC-853 Diapir site—MD02-2563C2 and MD02-2565, and the Mississippi Canyon—MD02-2569; figs. 8, 9, and 13; table 2), Kane Spur and West Mississippi Canyon cores also have seawater-like chloride concentration profiles that do not increase significantly with depth. The core from the Orca Basin (MD02-2550) has very high chloride concentrations (up to 4,800 mM) that decrease with depth (fig. 16). These elevated concentrations are the result of chloride diffusing downward into the sediments from a dense brine ponded on the sea floor within the closed basin. In contrast, the Pigmy Basin core (MD02-2553C2) has seawater-like chloride values (fig. 16) as does the "background" core (MD02-2574) collected for paleoceanographic purposes by the PAGE 127 shipboard scientists (figs. 16 and 17).

Table 2. Summary of maximum chloride concentrations and depth to the SMI grouped by coring site in the Gulf of Mexico.

[mM, millimole; SMI, surfate-methane interface; m, meter; G, gravity core; C2, jumbo box core; <, less than]

Core number	Maximum chloride (mM)	Depth to SMI (m)
Tunica Mound		
2535	625	12
2537	900	6
2538G	700	5
2539	560	12
2541	600	13
2543G	2,100	0.4
2545G	1,500	2
2546	850	9
Bush Hill		
2554	600	5
2555	575	11
2556	575	9
Kane Spur		
2559	560	no SMI
2560	560	no SMI
2561	560	no SMI
2562	560	no SMI
2566	560	no SMI
2567	560	no SMI
MC-853 Diapir		
2563C2	1,200	1
2565	2,000	<1
West Mississippi Canyon		
2569	750	2
2570	560	4
2571C2	600	3
Orca Basin		
2550	4,000	~22
Pigmy Basin		
2553C2	575	~62
Background site		
2574	560	28

The primary control on the chloride gradients at Tunica Mound and the MC-853 Diapir site is in proximity to salt-cored diapirs that formed the mounds on the sea floor. The primary effect on the distribution of gas hydrate within these sedimentary sections is the reduction of the thickness of the gas hydrate stability zone caused by the presence of dissolved salts in the pore water.

Nodular pieces of gas hydrate were recovered in two cores from the MC-853 Diapir (MD02-2565) and Mississippi Canyon (MD02-2569) areas. Chloride concentration anomalies were not detected in the MD02-2565 core; however, core MD02-2569 from the floor of the Mississippi Canyon had chloride anomalies superimposed on a rapidly increasing chloride concentration gradient. These data indicate that gas hydrate can occur in sediments containing high salinity pore water (up to ~750-mM chloride).

Sulfate and Methane Concentrations

In methane-rich sedimentary sections on continental margins, sulfate gradients are controlled primarily by the upward flux of methane toward the sea floor rather than by sulfate reduction of sedimentary organic matter (for example, Borowski and others, 1999). Pore-water geochemical data, including sulfate, methane, bisulfide (HS^-), DIC concentrations, and methane and DIC $\delta^{13}C$ values, indicate that anaerobic oxidation of methane (AOM; Reeburgh, 1976) occurs at an interface between upward rising methane and downward diffusing sulfate that has been termed the sulfate-methane interface (SMI; Borowski and others, 1997). High rates of AOM focused at the SMI produce linear sulfate gradients within the overlying sediments. These linear gradients indicate that sulfate reduction of sedimentary organic matter is less important than AOM for producing sulfate depletion in methane-rich sediments with a well-defined SMI. Linear sulfate gradients are a reflection of the upward rate of methane transport by fluid advection and(or) diffusion. Steep sulfate gradients indicate relatively high fluxes, and shallower gradients indicate lower fluxes (Borowski and others, 1996).

Available data suggest that the zone of AOM at the SMI has a vertical thickness that is relatively thin (on the order of a few meters or less) and sharply defined. One core from the west side of the Mississippi Canyon (MD02-2571C2) was subsampled for high-resolution geochemical, microbiological, and genomic analysis. Preliminary results of this shore-based

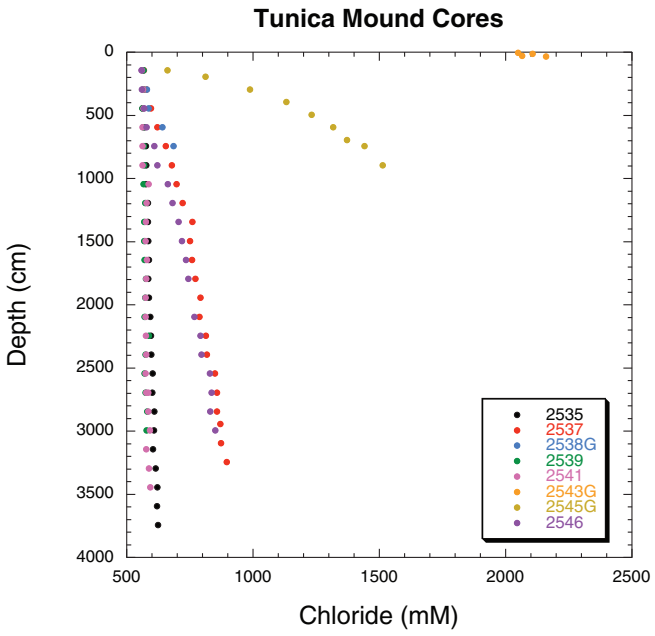

Figure 2. Chloride concentration in relation to depth for cores from Tunica Mound.

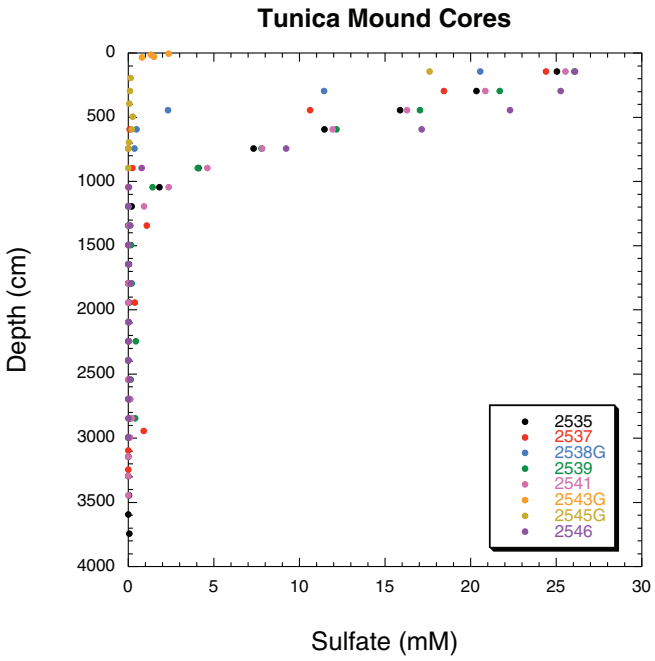

Figure 3. Sulfate concentration in relation to depth for cores from Tunica Mound.

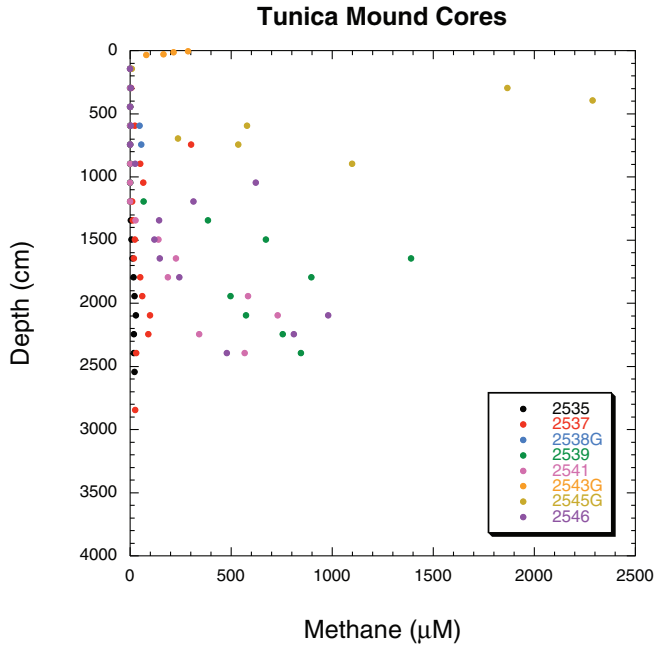

Figure 4. Methane concentration in relation to depth for cores from Tunica Mound.

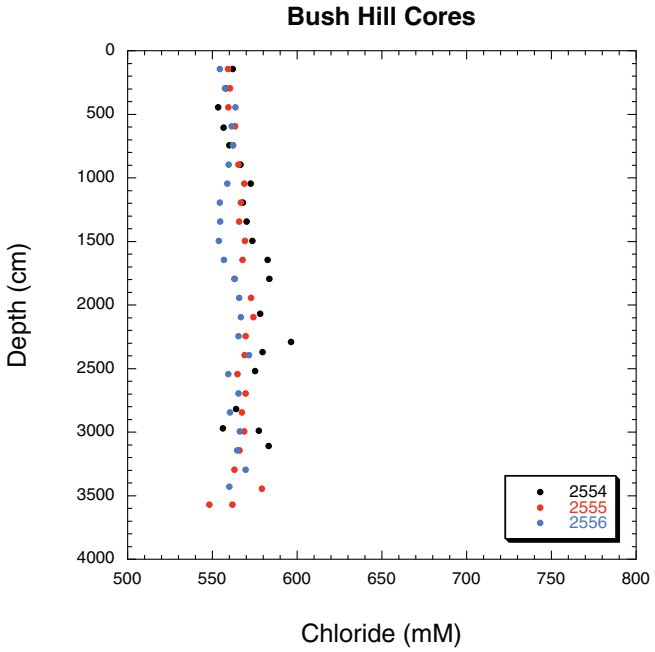

Figure 5. Chloride concentration in relation to depth for cores from Bush Hill.

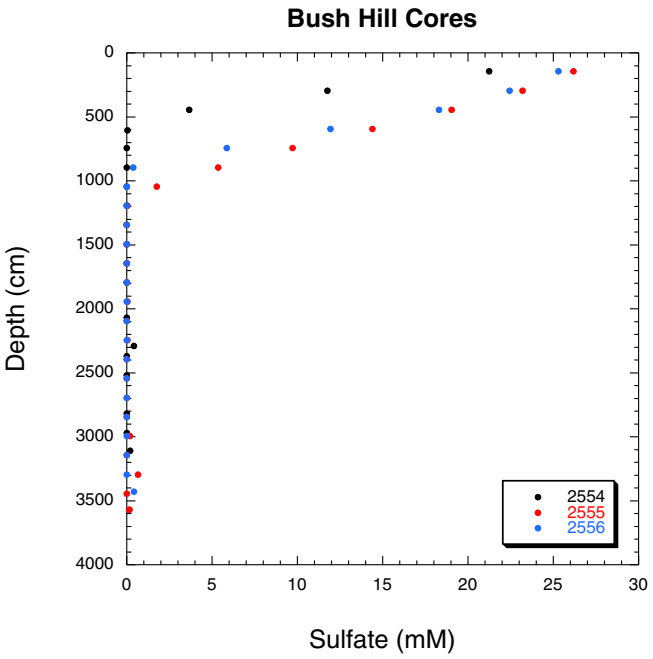

Figure 6. Sulfate concentration in relation to depth for cores from Bush Hill.

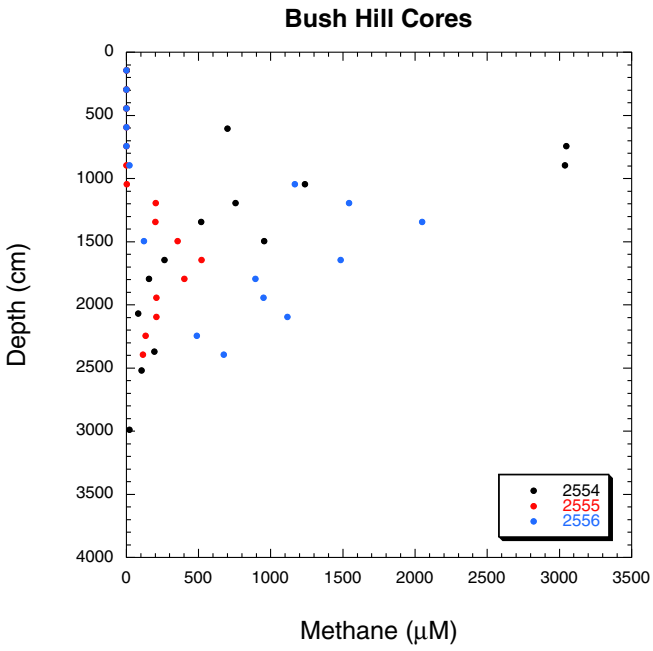

Figure 7. Methane concentration in relation to depth for cores from Bush Hill.

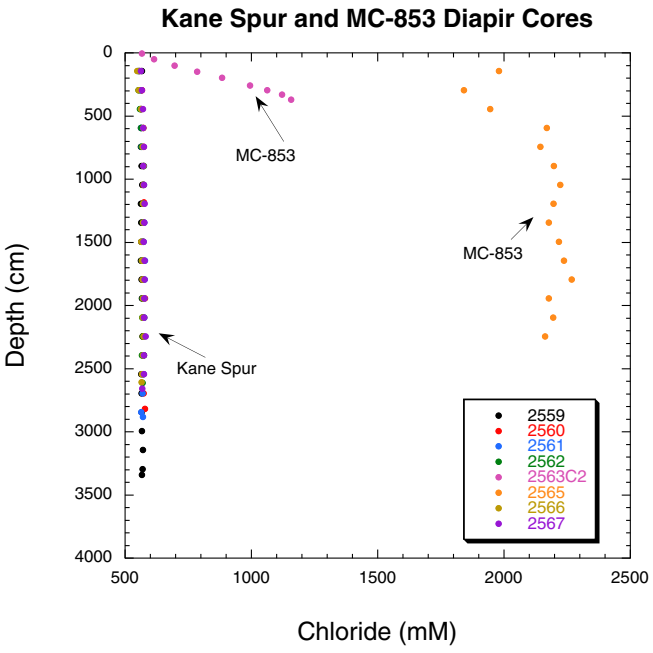

Figure 8. Chloride concentration in relation to depth for cores from Kane Spur and the MC-853 Diapir site.

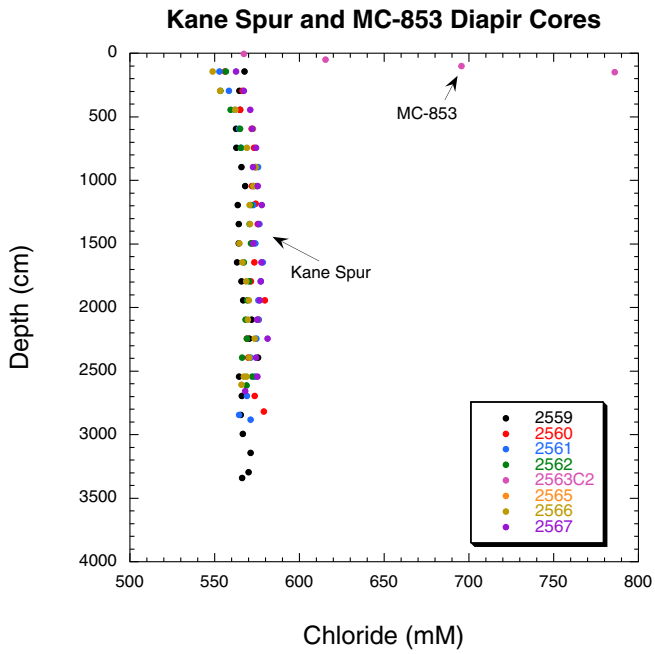

Figure 9. An expanded plot of chloride concentration in relation to depth for cores from Kane Spur and the MC-853 Diapir site.

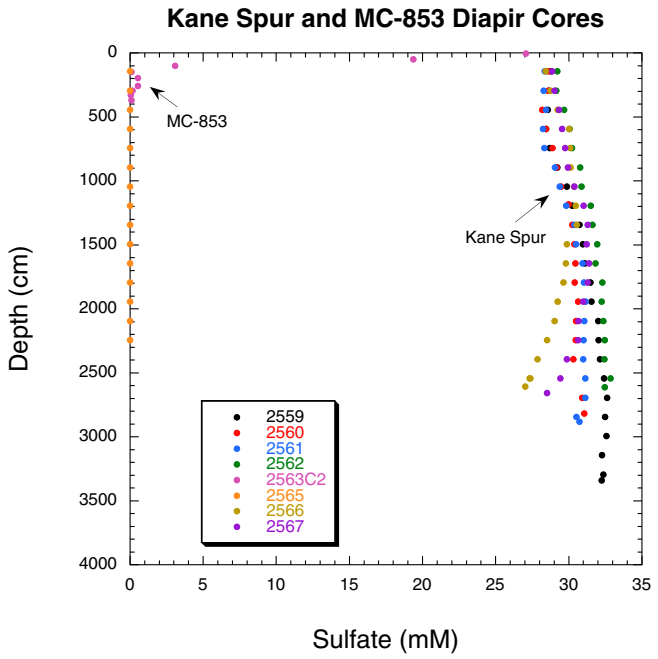

Figure 10. Sulfate concentration in relation to depth for cores from Kane Spur and the MC-853 Diapir site.

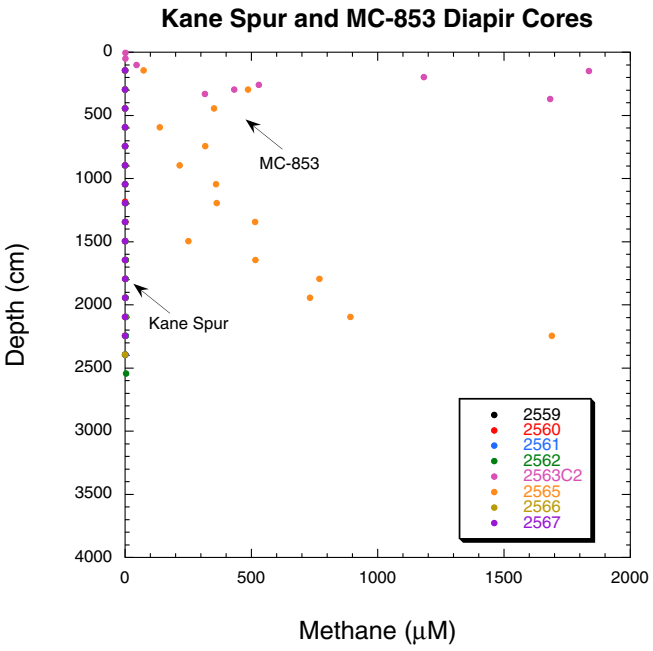

Figure 11. Methane concentration in relation to depth for cores from Kane Spur and the MC-853 Diapir site.

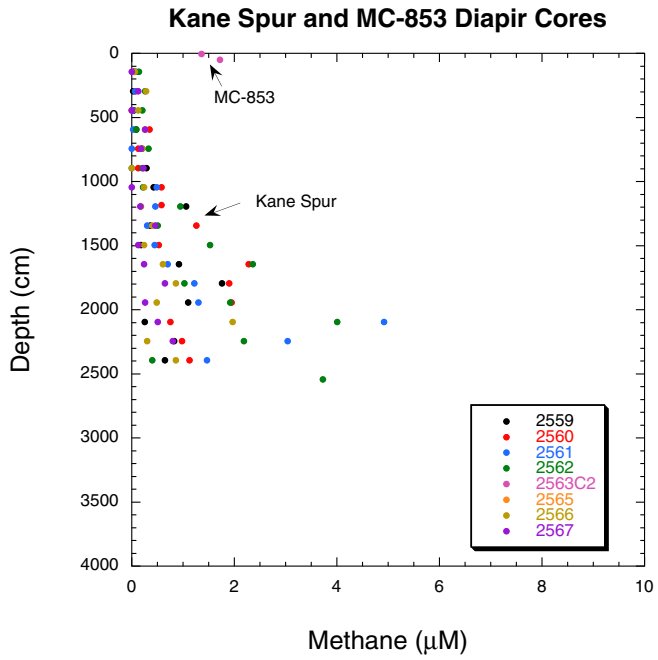

Figure 12. An expanded plot of methane concentration in relation to depth for cores from Kane Spur and the MC-853 Diapir site.

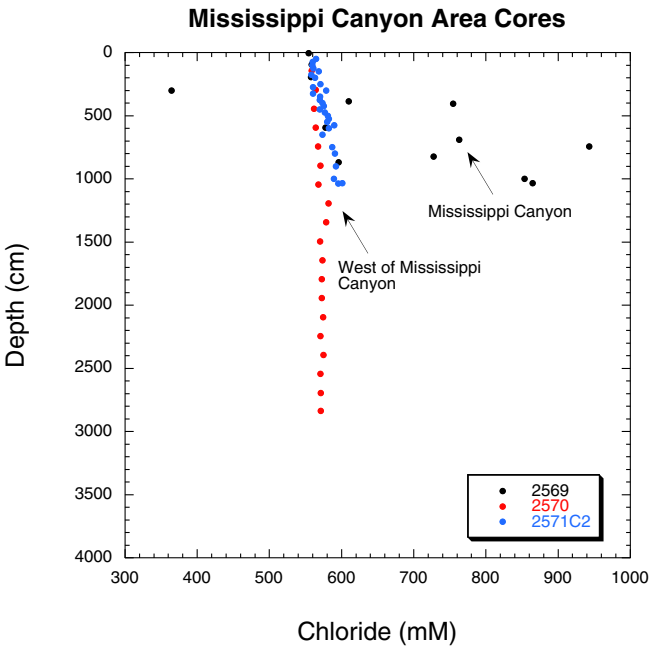

Figure 13. Plot of chloride concentration in relation to depth for cores from the Mississippi Canyon (MD02-2569) and west of the Mississippi Canyon.

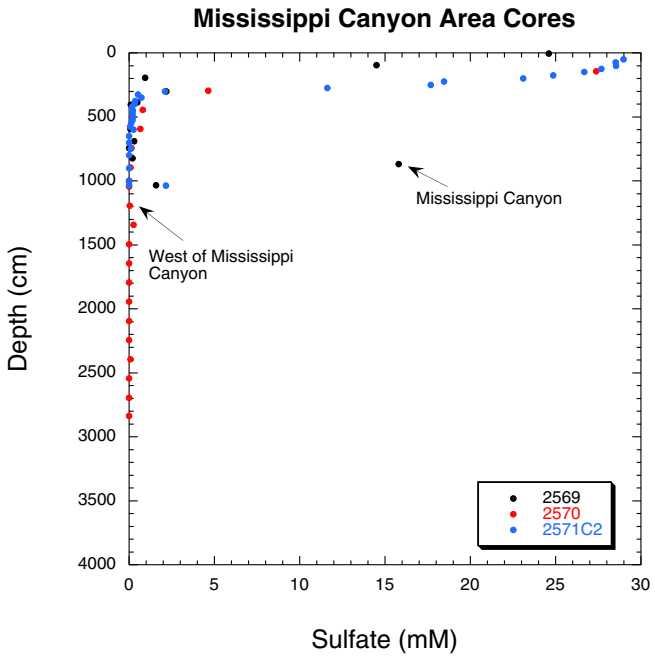

Figure 14. Sulfate concentration in relation to depth for cores from the Mississippi Canyon (MD02-2569) and west of the Mississippi Canyon.

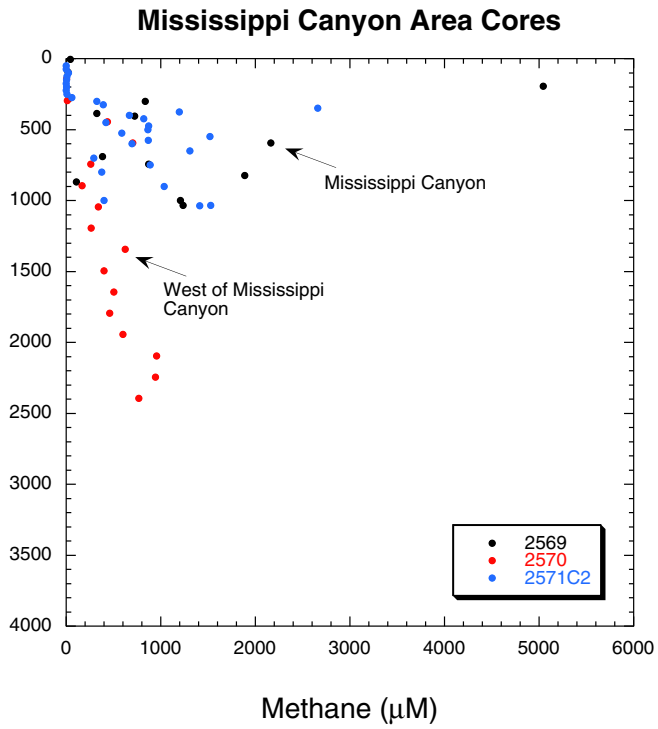

Figure 15. Methane concentration in relation to depth for cores from the Mississippi Canyon (MD02-2569) and west of the Mississippi Canyon.

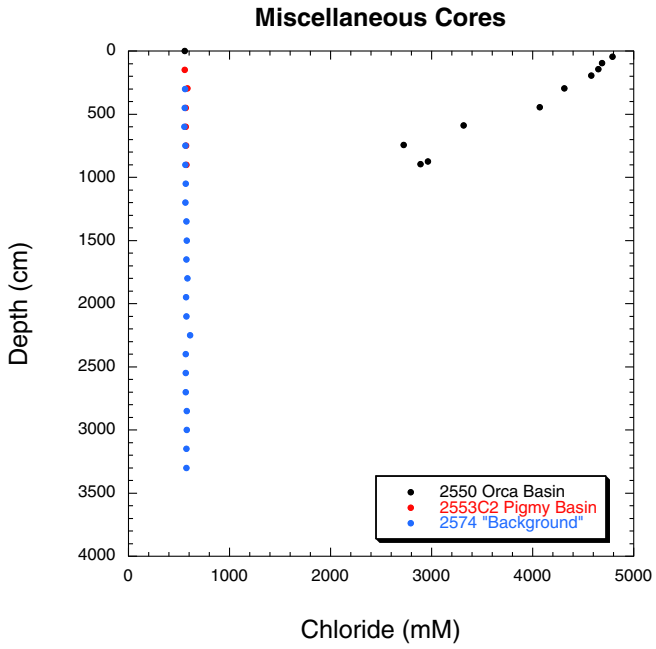

Figure 16. Chloride concentration in relation to depth for miscellaneous cores collected during the MD-02 cruise.

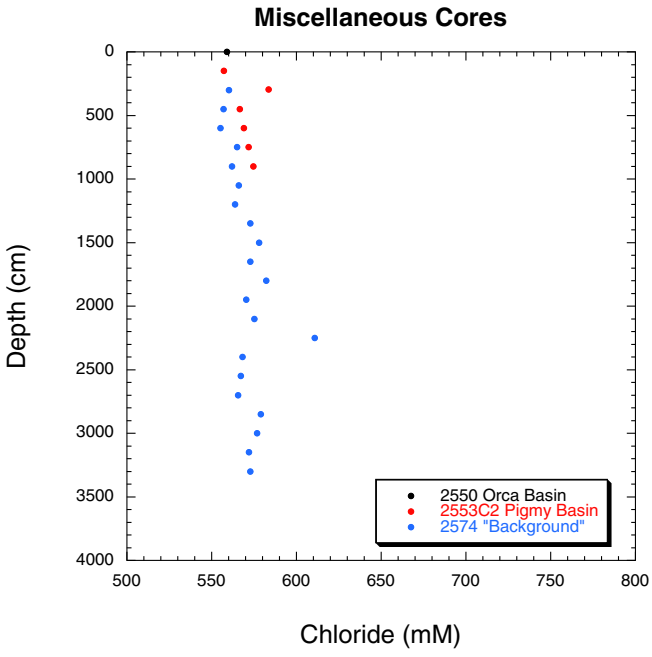

Figure 17. An expanded plot of chloride concentration in relation to depth for miscellaneous cores collected during the MD-02 cruise.

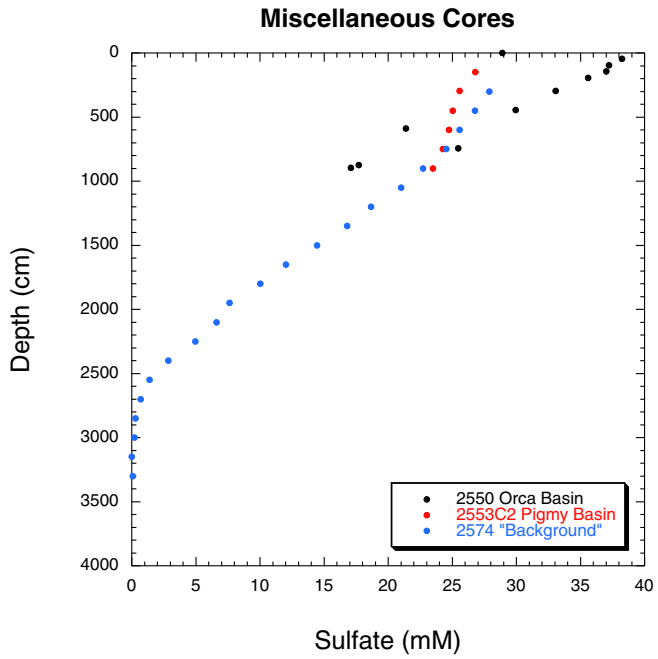

Figure 18. Sulfate concentration in relation to depth for miscellaneous cores collected during the MD-02 cruise.

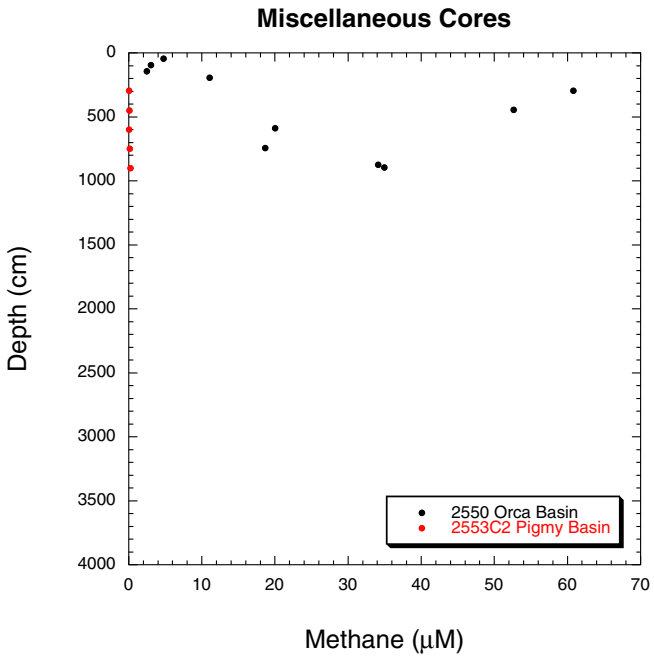

Figure 19. Methane concentration in relation to depth for miscellaneous cores collected during the MD-02 cruise.

work appear in an accompanying chapter (Hallam and others, this volume, chapter 10).

Well-defined linear sulfate gradients occur at Tunica Mound (fig. 3), Bush Hill (fig. 6), the MC-853 Diapir site (fig. 10), and west of the Mississippi Canyon (fig. 14) cores. These linear sulfate gradients indicate that substantial amounts of methane are present in the near subsurface either as dissolved methane and(or) methane gas hydrate (for example, Borowski and others, 1996).

The depth to the SMI for all cores is summarized in table 2. As with the chloride profiles obtained along the coring transect at Tunica Mound, the depth to the SMI systematically changes toward Tunica Mound and is shallowest on the top of the mound. An inverse correlation exists between maximum chloride concentrations and depth to the SMI at Tunica Mound (fig. 20). This indicates that the methane flux also increases toward the salt diapir, resulting in the observed shoaling of the SMI.

In contrast with the linear sulfate gradients mentioned above, cores at Kane Spur have sulfate concentration profiles that increase slightly with depth, reaching values of 33 mM (fig. 10) before decreasing to values of 26 mM. This increase in sulfate concentration above seawater-like values (~28 mM) cannot be explained by proximity to dissolving salt deposits because the corresponding chloride concentration profiles (fig. 9) do not vary with depth from seawater concentrations (~560 mM). Alternative explanations include (1) advection of seawater down into the sedimentary section or (2) the addition of sulfate to the pore water by dissolution of barite or gypsum. Shore-based geochemical measurements, especially strontium isotopes, may provide a better understanding of the processes controlling pore-water gradients in the Kane Spur sediments.

In all cores with linear sulfate gradients, methane concentrations remain low (typically <2 µm) until below the SMI and then increase sharply to values commonly about 1 mM (see fig. 21 for an illustration of this relation). Because most of the methane dissolved in methane-rich sediments is lost by degassing during core recovery (Paull and Ussler, 2001), methane concentrations in pore-water samples obtained from below the SMI (figs. 4, 7, 11, 15, and 19) generally are less than Earth surface saturation concentrations (~1.2 mM; Yamamoto and others, 1976). In contrast, in situ methane saturation concentrations calculated using the methane solubility model of Duan and others (1992) range from 81 mM on the top of Tunica Mound (~580-m water depth) to 150 mM in the Kane Spur area for core MD02-2567 (~1,320-m water depth).

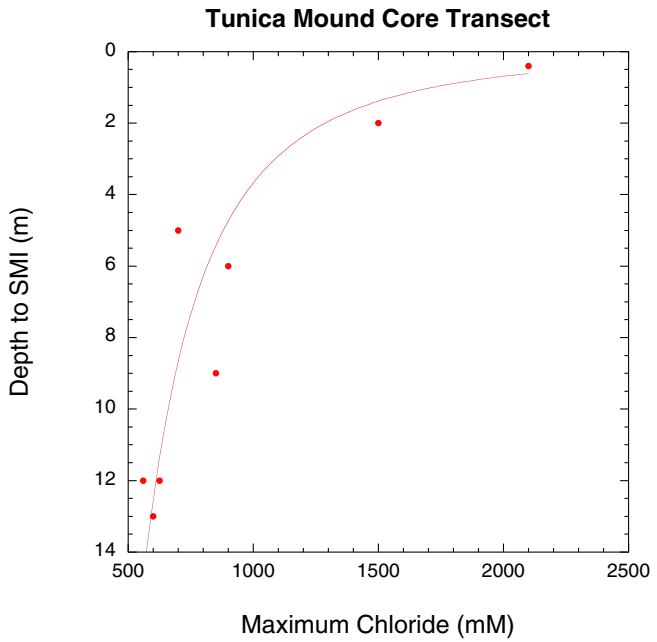

Figure 20. Maximum chloride concentration and an inverse correlation with depth to the SMI for cores collected along the Tunica Mound transect.

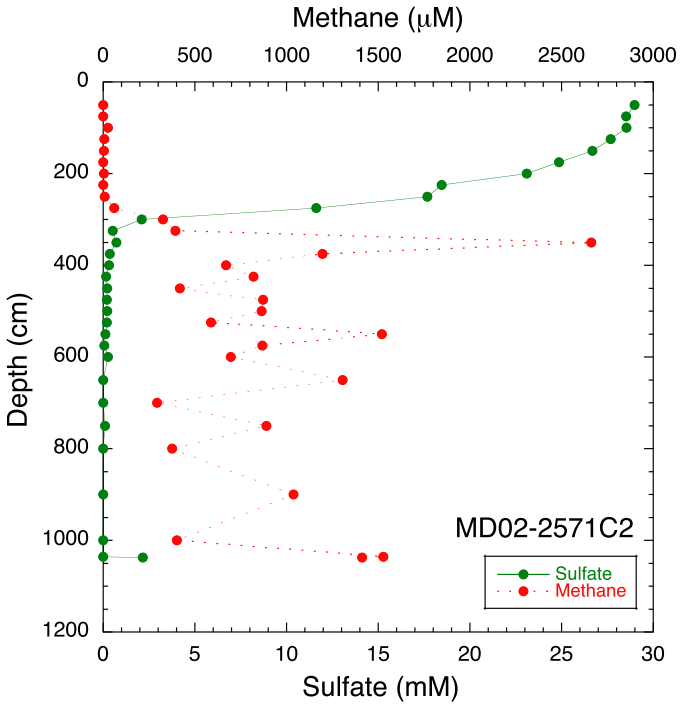

Figure 21. Sulfate and methane concentrations in relation to depth for MD02-2571C2. The SMI is centered at about 300 centimeters below the sea floor.

Conclusions

Pore-water geochemical profiles collected during shipboard operations indicate the following:

1. Chloride concentrations span a wide range of values (360 mM to more than 4,800 mM).
2. Chloride concentrations increase with depth and proximity to salt-cored diapirs at Tunica Mound and the MC-853 Diapir site.
3. The depth to the SMI decreases in proximity to diapiric structures forming Tunica Mound, Bush Hill, and the MC-853 Diapir site. This suggests that methane fluxes are higher over and around these diapiric structures.
4. Chloride concentration and the depth to the SMI are inversely correlated.

Acknowledgments

Financial support for this research was provided by the USGS through Cooperative Agreement 02WRAG0021, and the David and Lucile Packard Foundation. We thank Patrick Mitts, Rendy Keaten, Steve Hallam, John Pohlman, Yifeng Chen, and Bill Waite for their help with sediment-core processing and pore-water extraction. We thank the crew and scientific party of the RV *Marion Dufresne* for their assistance with coring and sample processing.

References Cited

Borowski, W.S., Paull, C.K., and Ussler, W., III, 1996, Marine pore-water sulfate profiles indicate in situ methane flux from underlying gas hydrate: Geology, v. 24, p. 655–658.

Borowski, W.S., Paull, C.K., and Ussler, W., III, 1997, Methane and CO_2 from piston cores over the Blake Ridge gas hydrate field—isotopic evidence for carbon fractionation via coupled metabolic pathways: Marine Chemistry, v. 57, p. 299–311.

Borowski, W.S., Paull, C.K., and Ussler, W., III, 1999, Global and local variations of interstitial sulfate gradients in deep-water, continental margin sediments—sensitivity to underlying gas hydrates: Marine Geology, v. 159, p. 131–154.

Cooper, A.K., and Hart, P.E., 2003, High-resolution seismic-reflection investigation of the northern Gulf of Mexico gas hydrate stability zone: Marine and Petroleum Geology, v. 19, p. 1275–1293.

Duan, Z., Moller, N., Greenberg, J., and Weare, J.H., 1992, The prediction of methane solubility in natural waters to high ionic strength from 0 to 250 °C and from 0 to 1600 bar: Geochimica et Cosmochimica Acta, v. 56, p. 1451–1460.

Manheim, F.T., 1966, A hydraulic squeezer for obtaining interstitial water from consolidated and unconsolidated sediments: U.S. Geological Survey Professional Paper 550-C, p. C256–C261.

Paull, C.K., and Ussler, W., III, 2001, History and significance of gas sampling during DSDP and ODP drilling associated with gas hydrates, *in* Paull, C.K., and Dillon, W.P., eds., Natural gas hydrates—occurrence, distribution, and detection: American Geophysical Union Geophysical Monograph 124, p. 53–66.

Reeburgh, W.S., 1967, An improved interstitial water sampler: Limnology and Oceanography, v. 12, p. 163–165.

Reeburgh, W.S., 1976, Methane consumption in Cariaco Trench waters and sediments: Earth and Planetary Science Letters, v. 28, p. 337–344.

Yamamoto, S., Alcauskas, J.B., and Croxier, T.E., 1976, Solubility of methane in distilled water and seawater: Journal of Chemical Engineering Data, v. 21, no. 1, p. 78–80.

Table 1. Summary of shipboard pore-water geochemical measurements.

[cm, centimeter; mL, milliliter; mM, millimole; µM, micromole; C.C., core catcher; >, greater than]

Core	Interval (cm)	Mid depth (cm)	Syringe number	Fluid volume (mL)	Chloride (mM)	Sulfate (mM)	Methane (µM)
MD02-2535	140–150	145	1	28	562.5	25.05	0.03
MDD2-2535	290–300	295	2	26	565.6	20.34	0.02
MD02-2535	440–450	445	3	24	563.4	15.88	0.00
MD02-2535	590–600	595	4	19	571.2	11.46	0.00
MDD2-2535	740–750	745	5	18	576.6	7.33	0.00
MD02-2535	890–900	895	6	14	577.3	4.10	0.00
MD02-2535	1,040–1,050	1,045	7	15	576.6	1.82	0.00
MD02-2535	1,190–1,200	1,195	8	15	583.8	0.20	0.38
MD02-2535	1,340–1,350	1,345	9	12	583.6	0.00	3.77
MD02-2535	1,490–1,500	1,495	10	12	585.9	0.00	7.02
MD02-2535	1,640–1,650	1,645	12	13	587.5	0.05	16.75
MD02-2535	1,790–1,800	1,795	11	10	585.4	0.00	12.04
MD02-2535	1,940–1,950	1,945	13	10	588.7	0.04	21.68
MD02-2535	2,090–2,100	2,095	14	10	594.1	0.00	29.64
MD02-2535	2,240–2,250	2,245	16	7	596.0	0.00	19.25
MD02-2535	2,390–2,400	2,395	17	8	597.6	0.00	21.35
MD02-2535	2,540–2,550	2,545	15	7	602.3	0.00	19.54
MD02-2535	2,690–2,700	2,695	M1	4.6	601.7	0.08	gas not collected
MD02-2535	2,840–2,850	2,845	M2	5.9	609.4	0.10	gas not collected
MD02-2535	2,990–3,000	2,995	M3	8	608.3	0.00	gas not collected
MD02-2535	3,140–3,150	3,145	M4	8	604.2	0.00	gas not collected
MD02-2535	3,290–3,300	3,295	M5	6	614.6	0.00	gas not collected
MD02-2535	3,440–3,450	3,445	M6	8.2	622.2	0.05	gas not collected
MD02-2535	3,590–3,600	3,595	M7	8.1	620.1	0.00	gas not collected
MD02-2535	3,740–3,750	3,745	M8	8.7	623.8	0.06	gas not collected
MD02-2537	140–150	145	18	38	567.7	24.41	0.78
MD02-2537	290–300	295	19	31	579.2	18.45	6.06
MD02-2537	440–450	445	20	27	596.3	10.62	0.23
MD02-2537	590–600	595	21	21	622.1	0.09	22.73
MD02-2537	740–750	745	22	25	654.3	0.00	301.94
MD02-2537	890–900	895	23	21	679.3	0.24	49.53
MD02-2537	1,040–1,050	1,045	24	18	697.9	0.00	65.08
MD02-2537	1,190–1,200	1,195	25	15	720.9	0.00	10.79
MD02-2537	1,340–1,350	1,345	26	16	760.3	1.09	13.52
MD02-2537	1,490–1,500	1,495	27	17	750.8	0.06	23.33
MD02-2537	1640–1650	1,645	28	16	758.3	0.00	17.95
MD02-2537	1,790–1,800	1,795	29	14	772.4	0.00	50.52
MD02-2537	1,940–1,950	1,945	30	17	791.8	0.38	61.13
MD02-2537	2,090–2,100	2,095	31	18	787.9	0.00	98.87

Table 1. Summary of shipboard pore-water geochemical measurements. — Continued

[cm, centimeter; mL, milliliter; mM, millimole; µM, micromole; C.C., core catcher; >, greater than]

Core	Interval (cm)	Mid depth (cm)	Syringe number	Fluid volume (mL)	Chloride (mM)	Sulfate (mM)	Methane (µM)
MD02-2537	2,240–2,250	2,245	32	10	813.9	0.05	89.86
MD02-2537	2,390–2,400	2,395	34	9	816.7	0.00	30.70
MD02-2537	2,540–2,550	2,545	M13	9.2	849.7	0.07	gas not collected
MD02-2537	2,690–2,700	2,695	M12	9	858.1	0.00	gas not collected
MD02-2537	2,840–2,850	2,845	33	8	857.8	0.10	25.33
MD02-2537	2,940–2,950	2,945	M11	10	870.7	0.90	gas not collected
MD02-2537	3,090–3,100	3,095	M10	7.5	873.6	0.00	gas not collected
MD02-2537	3,240–3,250	3,245	M9	6.9	896.0	0.00	gas not collected
MD02-2538G	140–150	145	35	34	565.9	20.57	0.02
MD02-2538G	290–300	295	36	31	579.9	11.45	0.06
MD02-2538G	440–450	445	37	26	587.3	2.33	0.19
MD02-2538G	590–600	595	38	21	641.2	0.48	46.76
MD02-2538G	740–750	745	39	14	685.8	0.36	55.85
MD02-2539	140–150	145	40	33	567.1	26.06	0.07
MD02-2539	290–300	295	41	26	566.0	21.70	0.19
MD02-2539	440–450	445	42	30	563.3	17.05	0.17
MD02-2539	590–600	595	43	26	565.6	12.17	0.15
MD02-2539	740–750	745	44	25	568.1	7.79	0.15
MD02-2539	890–900	895	45	23	569.2	4.06	0.60
MD02-2539	1,040–1,050	1,045	46	22	567.3	1.43	0.20
MD02-2539	1,190–1,200	1,195	47	22	573.2	0.00	67.54
MD02-2539	1,340–1,350	1,345	48	21	569.8	0.00	384.88
MD02-2539	1,490–1,500	1,495	49	20	569.9	0.16	671.33
MD02-2539	1,640–1,650	1,645	50	21	571.3	0.00	1,390.38
MD02-2539	1,790–1,800	1,795	51	23	576.8	0.21	897.27
MD02-2539	1,940–1,950	1,945	52	20	573.8	0.00	497.86
MD02-2539	2,090–2,100	2,095	53	22	571.6	0.00	572.86
MD02-2539	2,240–2,250	2,245	54	19	588.8	0.44	755.16
MD02-2539	2,390–2,400	2,395	55	19	575.7	0.00	845.63
MD02-2539	2,540–2,550	2,545	M14	7.8	570.8	0.15	gas not collected
MD02-2539	2,690–2,700	2,695	M15	8.7	574.7	0.00	gas not collected
MD02-2539	2,840–2,850	2,845	M16	9.7	580.9	0.41	gas not collected
MD02-2539	2,990–3,000	2,995	M17	8.8	579.6	0.00	gas not collected
MD02-2541	130–140	135	M19	C-14 sample			gas not collected
MD02-2541	140–150	145	56	38	559.7	25.55	0.51
MD02-2541	290–300	295	57	35	565.4	20.86	0.29
MD02-2541	440–450	445	58	30	566.5	16.29	0.32

Table 1. Summary of shipboard pore-water geochemical measurements. — Continued

[cm, centimeter; mL, milliliter; mM, millimole; µM, micromole; C.C., core catcher; >, greater than]

Core	Interval (cm)	Mid depth (cm)	Syringe number	Fluid volume (mL)	Chloride (mM)	Sulfate (mM)	Methane (µM)
MD02-2541	580–590	585	M20	C-14 sample			gas not collected
MD02-2541	590–600	595	59	29	563.6	11.94	0.37
MD02-2541	740–750	745	60	26	563.0	7.82	0.40
MD02-2541	890–900	895	61	30	563.3	4.63	0.33
MD02-2541	1,030–1,040	1,035	M21	C-14 sample			gas not collected
MD02-2541	1,040–1,050	1,045	62	23	587.0	2.37	0.50
MD02-2541	1,190–1,200	1,195	63	24	578.6	0.93	0.36
MD02-2541	1,340–1,350	1,345	64	29	575.8	0.05	26.62
MD02-2541	1,480–1,490	1,485	M22	C-14 sample			gas not collected
MD02-2541	1,490–1,500	1,495	65	25	575.6	0.00	140.96
MD02-2541	1,640–1,650	1,645	66	28	580.6	0.00	227.82
MD02-2541	1,790–1,800	1,795	67	20	577.3	0.00	187.04
MD02-2541	1,940–1,950	1,945	68	25	574.9	0.00	584.40
MD02-2541	2,090–2,100	2,095	69	20	575.0	0.00	729.21
MD02-2541	2,240–2,250	2,245	70	17	575.9	0.00	341.32
MD02-2541	2,390–2,400	2,395	71	14	578.0	0.00	566.74
MD02-2541	2,540–2,550	2,545	M22	8.5	574.5	0.00	gas not collected
MD02-2541	2,690–2,700	2,695	M23+M24	7.2	577.0	0.00	gas not collected
MD02-2541	2,840–2,850	2,845	M25	>10.0	586.0	0.20	gas not collected
MD02-2541	2,990–3,000	2,995	M26	8.5	591.5	0.10	gas not collected
MD02-2541	3,140–3,150	3,145	M27	9	577.6	0.00	gas not collected
MD02-2541	3,290–3,300	3,295	M28	8.8	587.4	0.00	gas not collected
MD02-2541	3,440–3,450	3,445	M29	8.8	593.0	0.00	gas not collected
MD02-2543G	C.C.TOP	5	72	20	2,050	2.61	286.34
MD02-2543G	C.C.TOP	15	73	18	2,107	1.40	214.87
MD02-2543G	C.C.BOTTOM	35	74	12	2,161	0.81	80.92
MD02-2543G	C.C.BOTTOM	30	75	18	2,066	1.50	165.70
MD02-2545G	140-150	145	76	25	661.8	17.60	9.32
MD02-2545G	190-200	195	77	24	812.7	0.15	
MD02-2545G	200-210	205	M30	25			gas not collected
MD02-2545G	290-300	295	78	25	988.4	0.11	1,866.61
MD02-2545G	390-400	395	79	23	1,133	0.06	2,287.89
MD02-2545G	490-500	495	80	20	1,232	0.26	
MD02-2545G	500–510	505	M31	30			gas not collected
MD02-2545G	590–600	595	81	23	1,318	0.21	578.72
MD02-2545G	690–700	695	82	22	1,372	0.05	237.52
MD02-2545G	740–750	745	83	20	1,441	0.00	535.61
MD02-2545G	890–900	895	84	14	1,514	0.00	1,099.70

Table 1. Summary of shipboard pore-water geochemical measurements. — Continued

[cm, centimeter; mL, milliliter; mM, millimole; µM, micromole; C.C., core catcher; >, greater than]

Core	Interval (cm)	Mid depth (cm)	Syringe number	Fluid volume (mL)	Chloride (mM)	Sulfate (mM)	Methane (µM)
MD02-2546	140–150	145	87	30	559.1	26.11	1.12
MD02-2546	150–160	155	M32	20			gas not collected
MD02-2546	290–300	295	88	28	560.8	25.25	3.60
MD02-2546	440–450	445	89	23	569.2	22.30	0.87
MD02-2546	590–600	595	90	30	579.0	17.14	3.26
MD02-2546	740–750	745	91	25	610.0	9.22	1.07
MD02-2546	890–900	895	92	24	621.6	0.78	25.45
MD02-2546	1,040–1,050	1,045	93	24	663.0	0.04	622.87
MD02-2546	1,190–1,200	1,195	94	24	682.3	0.00	312.99
MD02-2546	1,340–1,350	1,345	95	19	705.8	0.13	143.31
MD02-2546	1,490–1,500	1,495	96	19	718.9	0.00	120.95
MD02-2546	1,640–1,650	1,645	97	14	734.4	0.00	146.51
MD02-2546	1,790–1,800	1,795	98	18	744.6	0.15	243.49
MD02-2546	2,090–2,100	2,095	99	19	768.5	0.05	980.93
MD02-2546	2,240–2,250	2,245	100	19	792.4	0.00	810.05
MD02-2546	2,390–2,400	2,395	101	17	796.9	0.00	478.75
MD02-2546	2,540–2,550	2,545	M34	8.5	829.8	0.11	gas not collected
MD02-2546	2,690–2,700	2,695	M35	7.8	835.9	0.00	gas not collected
MD02-2546	2,840–2,850	2,845	M36	8.2	830.4	0.00	gas not collected
MD02-2546	2,990–3,000	2,995	M37	9	850.1	0.00	gas not collected
MD02-2550	40–50	45	102	55	4,790	38.25	4.74
MD02-2550	90–100	95	103	50	4,688	37.23	3.04
MD02-2550	140–150	145	104	57	4,650	37.00	2.51
MD02-2550	190–200	195	105	35	4,580	35.61	11.08
MD02-2550	290–300	295	106	26	4,313	33.08	60.84
MD02-2550	440–450	445	107	23	4,070	29.96	52.65
MD02-2550	590–600	590	109	28	3,318	21.39	18.69
MD02-2550	740–750	745	108	16	2,724	25.47	20.04
MD02-2550	870–880	875	111	22	2,965	17.71	34.12
MD02-2550	890–900	895	110	26	2,890	17.10	34.96
MD02-2553C2	145–155	150	112	30	557.3	26.81	LOST
MD02-2553C2	290–300	295	113	26	583.6	25.59	0.06
MD02-2553C2	445–455	450	114	21	566.6	25.06	0.10
MD02-2553C2	595–605	600	115	21	569.1	24.74	0.07
MD02-2553C2	745–755	750	116	13	571.8	24.28	0.14
MD02-2553C2	895–905	900	117	12	574.8	23.49	0.24

Table 1. Summary of shipboard pore-water geochemical measurements. — Continued

[cm, centimeter; mL, milliliter; mM, millimole; µM, micromole; C.C., core catcher; >, greater than]

Core	Interval (cm)	Mid depth (cm)	Syringe number	Fluid volume (mL)	Chloride (mM)	Sulfate (mM)	Methane (µM)
MD02-2554	140–150	145	120	28	562.1	21.24	2.54
MD02-2554	280–290	285	M38	C-14 sample			gas not collected
MD02-2554	290–300	295	121	21	558.0	11.77	0.97
MD02-2554	440–450	445	122	23	553.4	3.67	0.24
MD02-2554	600–610	605	123	20	556.7	0.05	700.25
MD02-2554	740–750	745	124	24	560.1	0.00	3,048.58
MD02-2554	890–900	895	125	28	566.6	0.00	3,037.65
MD02-2554	910–920	915	M40	C-14 sample			gas not collected
MD02-2554	1,040–1,050	1,045	126	17	572.6	0.00	1,237.80
MD02-2554	1,190–1,200	1,195	127	19	568.0	0.00	755.83
MD02-2554	1,340–1,350	1,345	128	19	570.3	0.00	518.47
MD02-2554	1,490–1,500	1,495	129	19	573.6	0.00	955.72
MD02-2554	1,640–1,650	1,645	130	18	582.6	0.00	265.05
MD02-2554	1,790–1,800	1,795	131	21	583.7	0.00	157.68
MD02-2554	2,065–2,075	2,070	132	17	578.1	0.00	82.93
MD02-2554	2,285–2,295	2,290	133	17	596.5	0.43	LOST
MD02-2554	2,365–2,375	2,370	134	13	579.7	0.00	194.76
MD02-2554	2,515–2,525	2,520	135	15	575.2	0.00	106.70
MD02-2554	2,665–2,675	2,670	M41	7.8	567.5	0.00	gas not collected
MD02-2554	2,815–2,825	2,820	M42+M43	9.6+10	567.5	0.00	gas not collected
MD02-2554	2,965–2,975	2,970	M44	~11.5	556.2	0.00	gas not collected
MD02-2554	0–7 FROM BOTTOM	2,990	118	7	577.5	0.06	21.79
MD02-2554	C.C.TOP	3,109	119	0.5	583.2	0.20	LOST
MD02-2555	140–150	145	136	24	559.3	26.19	0.10
MD02-2555	280–290	285	M47	C-14 sample			gas not collected
MD02-2555	290–300	295	137	23	560.4	23.21	0.14
MD02-2555	440–450	445	138	24	559.4	19.05	0.98
MD02-2555	580–590	585	M48	C-14 sample			gas not collected
MD02-2555	590–600	595	139	17	563.6	14.40	0.15
MD02-2555	740–750	745	140	20	562.3	9.72	0.35
MD02-2555	880–890	885	M49	C-14 sample			gas not collected
MD02-2555	890–900	895	141	17	565.4	5.37	0.16
MD02-2555	1,040–1,050	1,045	142	15	568.9	1.75	3.52
MD02-2555	1,190–1,200	1,195	143	16	566.8	0.05	203.45
MD02-2555	1,340–1,350	1,345	144	16	565.8	0.00	201.58
MD02-2555	1,490–1,500	1,495	145	14	569.3	0.00	355.23
MD02-2555	1,640–1,650	1,645	146	11	567.8	0.00	522.00
MD02-2555	1,790–1,800	1,795	147	13	563.2	0.00	401.01

Table 1. Summary of shipboard pore-water geochemical measurements. — Continued

[cm, centimeter; mL, milliliter; mM, millimole; µM, micromole; C.C., core catcher; >, greater than]

Core	Interval (cm)	Mid depth (cm)	Syringe number	Fluid volume (mL)	Chloride (mM)	Sulfate (mM)	Methane (µM)
MD02-2555	1,940–1,950	1,945	148	13	572.9	0.04	208.22
MD02-2555	2,090–2,100	2,095	149	12	574.2	0.00	209.17
MD02-2555	2,240–2,250	2,245	150	13	569.6	0.04	132.59
MD02-2555	2,390–2,400	2,395	151	9	569.1	0.00	115.29
MD02-2555	2,540–2,550	2,545	M50	9	564.9	0.00	gas not collected
MD02-2555	2,690–2,700	2,695	M51	8.2	569.6	0.00	gas not collected
MD02-2555	2,840–2,850	2,845	M52	7.2	567.5	0.00	gas not collected
MD02-2555	2,990–3,000	2,995	M53	8.1	568.9	0.18	gas not collected
MD02-2555	3,140–3,150	3,145	M54	9.2	565.9	0.00	gas not collected
MD02-2555	3,290–3,300	3,295	M55	8.2	563.0	0.67	gas not collected
MD02-2555	3,440–3,450	3,445	M56	8	579.3	0.00	gas not collected
MD02-2555	C.C.	3,572	M45+M46	9.8	548.3	0.15	gas not collected
MD02-2556	140–150	145	152	23	554.4	25.31	0.19
MD02-2556	290–300	295	153	22	557.5	22.45	0.57
MD02-2556	440–450	445	154	23	563.6	18.30	0.59
MD02-2556	590–600	595	155	24	561.5	11.95	0.68
MD02-2556	740–750	745	156	21	562.2	5.87	0.54
MD02-2556	890–900	895	157	21	559.7	0.39	22.53
MD02-2556	1,040–1,050	1,045	158	22	558.9	0.00	1,167.46
MD02-2556	1,190–1,200	1,195	159	22	554.3	0.00	1,542.92
MD02-2556	1,340–1,350	1,345	160	24	554.6	0.00	2,048.93
MD02-2556	1,490–1,500	1,495	161	22	553.7	0.00	121.01
MD02-2556	1,640–1,650	1,645	162	22	557.0	0.00	1,484.94
MD02-2556	1,790–1,800	1,795	163	22	563.0	0.00	893.87
MD02-2556	1,940–1,950	1,945	164	21	565.8	0.00	950.55
MD02-2556	2,090–2,100	2,095	165	23	566.8	0.00	1,116.74
MD02-2556	2,240–2,250	2,245	166	21	565.4	0.00	487.75
MD02-2556	2,390–2,400	2,395	167	19	571.6	0.00	674.42
MD02-2556	2,540–2,550	2,545	M58	8	559.5	0.00	gas not collected
MD02-2556	2,690–2,700	2,695	M59	8	565.5	0.00	gas not collected
MD02-2556	2,840–2,850	2,845	M60	9.4	560.5	0.00	gas not collected
MD02-2556	2,990–3,000	2,995	M61	10	566.2	0.00	gas not collected
MD02-2556	3,140–3,150	3,145	M62	>10	564.6	0.00	gas not collected
MD02-2556	3,290–3,300	3,295	M63	>10	569.6	0.00	gas not collected
MD02-2556	C.C. TOP	3,429	M57	9.4	560.0	0.43	gas not collected
MD02-2559	140–150	145	168	30	567.6	28.80	0.05
MD02-2559	280–290	285	M65	C-14 sample			gas not collected
MD02-2559	290–300	295	169	27	564.7	28.65	0.03

Table 1. Summary of shipboard pore-water geochemical measurements. — Continued

[cm, centimeter; mL, milliliter; mM, millimole; µM, micromole; C.C., core catcher; >, greater than]

Core	Interval (cm)	Mid depth (cm)	Syringe number	Fluid volume (mL)	Chloride (mM)	Sulfate (mM)	Methane (µM)
MD02-2559	440–450	445	170	22	564.9	28.57	0.04
MD02-2559	580–590	585	M66	C-14 sample			gas not collected
MD02-2559	590–600	595	171	29	562.6	28.44	0.09
MD02-2559	740–750	745	172	19	562.9	28.71	0.20
MD02-2559	880–890	885	M67	C-14 sample			gas not collected
MD02-2559	890–900	895	173	22	565.9	29.21	0.29
MD02-2559	1,040–1,050	1,045	174	19	568.1	29.87	0.43
MD02-2559	1,190–1,200	1,195	175	14	563.6	30.25	1.06
MD02-2559	1,340–1,350	1,345	176	14	564.2	30.74	0.36
MD02-2559	1,490–1,500	1,495	177	13	564.3	30.96	0.18
MD02-2559	1,640–1,650	1,645	178	14	563.2	31.11	0.92
MD02-2559	1,790–1,800	1,795	179	16	565.8	31.49	1.76
MD02-2559	1,940–1,950	1,945	180	13	566.8	31.54	1.10
MD02-2559	2,090–2,100	2,095	181	14	571.9	32.02	0.25
MD02-2559	2,240–2,250	2,245	182	13	570.4	32.04	0.83
MD02-2559	2,390–2,400	2,395	183	12	575.6	32.13	0.65
MD02-2559	2,540–2,550	2,545	M68	10.1	564.4	32.42	gas not collected
MD02-2559	2,690–2,700	2,695	M69	8.3	566.0	32.62	gas not collected
MD02-2559	2,840–2,850	2,845	M70	9	565.5	32.49	gas not collected
MD02-2559	2,990–3,000	2,995	M71	10.2	566.6	32.58	gas not collected
MD02-2559	3,140–3,150	3,145	M72	9.2	571.2	32.28	gas not collected
MD02-2559	3,290–3,300	3,295	M73	9.7	570.1	32.36	gas not collected
MD02-2559	C.C.	3,343	M64	>10	566.2	32.26	gas not collected
MD02-2560	140–150	145	184	24	556.0	28.61	0.04
MD02-2560	280–290	285	M74	C-14 sample			gas not collected
MD02-2560	290–300	295	185	25	566.4	28.59	0.07
MD02-2560	440–450	445	186	22	565.0	28.20	0.00
MD02-2560	590–600	595	187	20	572.0	28.45	0.35
MD02-2560	730–740	735	M75	C-14 sample			gas not collected
MD02-2560	740–750	745	188	21	573.1	28.90	0.13
MD02-2560	890–900	895	189	20	574.2	29.18	0.13
MD02-2560	1,040–1,050	1,045	190	22	572.0	29.48	0.58
MD02-2560	1,180–1,190	1,185	191	20	574.3	29.99	0.58
MD02-2560	1,190–1,200	1,195	M76	C-14 sample			gas not collected
MD02-2560	1,340–1,350	1,345	192	18	575.5	30.24	1.26
MD02-2560	1,490–1,500	1,495	193	15	571.8	30.39	0.53
MD02-2560	1,640–1,650	1,645	194	13	573.5	30.45	2.28
MD02-2560	1,790–1,800	1,795	195	17	571.5	30.42	1.90
MD02-2560	1,940–1,950	1,945	196	16	579.8	30.65	1.95

Table 1. Summary of shipboard pore-water geochemical measurements. — Continued

[cm, centimeter; mL, milliliter; mM, millimole; µM, micromole; C.C., core catcher; >, greater than]

Core	Interval (cm)	Mid depth (cm)	Syringe number	Fluid volume (mL)	Chloride (mM)	Sulfate (mM)	Methane (µM)
MD02-2560	2,090–2,100	2,095	197	13	576.1	30.51	0.75
MD02-2560	2,240–2,250	2,245	198	13	569.1	30.48	0.98
MD02-2560	2,390–2,400	2,395	199	13	569.8	30.31	1.13
MD02-2560	2,540–2,550	2,545	M78	10.2	LOST	LOST	gas not collected
MD02-2560	2,690–2,700	2,695	M79	9.6	573.6	30.91	gas not collected
MD02-2560	2,814–2,824	2,819	M77	10	579.0	31.06	gas not collected
MD02-2561	140–150	145	200	35	552.9	28.35	0.09
MD02-2561	250–280	265	242+243+244 IODINE	50			gas not collected
MD02-2561	280–290	285	M82	C-14 sample			gas not collected
MD02-2561	290–300	295	201	29	558.4	28.29	0.07
MD02-2561	440–450	445	202	25	562.0	28.44	0.03
MD02-2561	590–600	595	203	22	564.3	28.23	0.03
MD02-2561	700–730	715	245+246+247 IODINE	50			gas not collected
MD02-2561	730–740	735	M81	C-14 sample			gas not collected
MD02-2561	740–750	745	204	20	565.7	28.34	0.00
MD02-2561	890–900	895	205	19	575.7	29.06	0.00
MD02-2561	1,040–1,050	1,045	206	20	574.9	29.39	0.49
MD02-2561	1,150–1,180	1,165	248+249+250+251 IODINE	50			gas not collected
MD02-2561	1,180–1,190	1,185	M83	C-14 sample			gas not collected
MD02-2561	1,190–1,200	1,195	207	19	572.9	29.83	0.46
MD02-2561	1,340–1,350	1,345	208	16	576.4	30.39	0.33
MD02-2561	1,490–1,500	1,495	209	16	574.0	30.50	0.45
MD02-2561	1,640–1,650	1,645	210	15	578.5	30.95	0.70
MD02-2561	1,790–1,800	1,795	211	13	577.2	31.03	1.22
MD02-2561	1,940–1,950	1,945	212	15	575.8	31.16	1.30
MD02-2561	2,090–2,100	2,095	213	14	575.8	31.05	4.92
MD02-2561	2,240–2,250	2,245	214	15	574.6	31.01	3.04
MD02-2561	2,390–2,400	2,395	215	11	571.2	31.00	1.47
MD02-2561	2,540–2,550	2,545	M84	8.9	573.8	31.14	gas not collected
MD02-2561	2,690–2,700	2,695	M85	8.8	569.1	31.12	gas not collected
MD02-2561	2,840–2,850	2,845	M86	9.2	564.5	30.52	gas not collected
MD02-2561	C.C.	2,884	M80	>10	571.2	30.74	gas not collected
MD02-2562	140–150	145	216	21	556.7	29.21	0.14
MD02-2562	250–280	265	414+415+434+435 IODINE	18+30			gas not collected
MD02-2562	290–300	295	217	23	553.4	29.15	0.26

Table 1. Summary of shipboard pore-water geochemical measurements. — Continued

[cm, centimeter; mL, milliliter; mM, millimole; µM, micromole; C.C., core catcher; >, greater than]

Core	Interval (cm)	Mid depth (cm)	Syringe number	Fluid volume (mL)	Chloride (mM)	Sulfate (mM)	Methane (µM)
MD02-2562	440–450	445	218	22	559.5	29.69	0.21
MD02-2562	590–600	595	219	22	565.1	30.05	0.09
MD02-2562	700–730	715	252+253+254 IODINE	50			gas not collected
MD02-2562	740–750	745	220	24	565.4	30.21	0.33
MD02-2562	890–900	895	221	22	574.1	30.77	0.21
MD02-2562	1,040–1,050	1,045	222	17	573.1	30.89	0.22
MD02-2562	1,150–1,180	1,165	259+260+261 IODINE	50			gas not collected
MD02-2562	1,190–1,200	1,195	223	20	571.5	31.50	0.95
MD02-2562	1,340–1,350	1,345	224	16	570.6	31.61	0.51
MD02-2562	1,490–1,500	1,495	225	16	571.5	31.94	1.53
MD02-2562	1,640–1,650	1,645	226	16	567.3	31.83	2.36
MD02-2562	1,790–1,800	1,795	227	14	570.4	32.30	1.03
MD02-2562	1,940–1,950	1,945	228	13	569.2	32.26	1.92
MD02-2562	1,950–1,980	1,965	255+256+257+258 IODINE	50			gas not collected
MD02-2562	2,090–2,100	2,095	229	12	568.3	32.36	4.01
MD02-2562	2,240–2,250	2,245	230	13	569.0	32.47	2.19
MD02-2562	2,390–2,400	2,395	231	12	566.3	32.43	0.40
MD02-2562	2,540–2,550	2,545	232	14	572.2	32.85	3.73
MD02-2562	C.C.	2,613	M87	9.6	568.7	32.47	gas not collected
MD02-2563C2	0–10	5	240	31	567.1	27.07	1.36
MD02-2563C2	97–107	102	241	28	695.6	3.08	46.21
MD02-2563C2	45–55	50	238	26	615.5	19.38	1.72
MD02-2563C2	145–155	150	239	26	786.0	0.10	1,836.01
MD02-2563C2	192–202	197	236	27	884.0	0.54	1,182.65
MD02-2563C2	253–263	258	234	28	995.0	0.54	529.57
MD02-2563C2	292–302	297	237	20	1,064	0.16	431.96
MD02-2563C2	327–337	332	235	21	1,121	0.06	315.68
MD02-2563C2	365–375	370	233	22	1,157	0.10	1,682.70
MD02-2565	140–150	145	272	12	1,981	0.00	73.79
MD02-2565	280–290	285	M89	C-14 sample			gas not collected
MD02-2565	290–300	295	273	18	1,842	0.00	486.88
MD02-2565	390–400	395	263+264	31			496.67
MD02-2565	440–450	445	274	22	1,946	0.00	652.52
MD02-2565	580–590	585	M88	C-14 sample			gas not collected
MD02-2565	590–600	595	275	20	2,169	0.00	137.25
MD02-2565	740–750	745	276	24	2,144	0.00	316.87

Table 1. Summary of shipboard pore-water geochemical measurements. — Continued

[cm, centimeter; mL, milliliter; mM, millimole; µM, micromole; C.C., core catcher; >, greater than]

Core	Interval (cm)	Mid depth (cm)	Syringe number	Fluid volume (mL)	Chloride (mM)	Sulfate (mM)	Methane (µM)
MD02-2565	880–890	885	M90	C-14 sample			gas not collected
MD02-2565	890–900	895	277	20	2,198	0.00	216.19
MD02-2565	1,040–1,050	1,045	278	25	2,223	0.00	359.64
MD02-2565	1,190–1,200	1,195	279	23	2,197	0.00	363.20
MD02-2565	1,340–1,350	1,345	280	24	2,178	0.00	514.66
MD02-2565	1,490–1,500	1,495	281	21	2,218	0.00	250.59
MD02-2565	1,640–1,650	1,645	282	19	2,238	0.00	516.06
MD02-2565	1,790–1,800	1,795	283	15	2,268	0.00	769.54
MD02-2565	1,940–1,950	1,945	284	19	2,177	0.00	732.47
MD02-2565	2,090–2,100	2,095	285	18	2,195	0.00	892.21
MD02-2565	2,240–2,250	2,245	286	20	2,163	0.00	1,689.21
MDO2-2566	140–150	145	287	31	548.8	28.42	0.06
MDO2-2566	260–290	275	416+417 IODINE	32			gas not collected
MDO2-2566	290–300	295	288	22	553.3	28.75	0.28
MDO2-2566	440–450	445	289	18	562.2	29.24	0.13
MDO2-2566	590–600	595	290	18	572.6	30.03	0.26
MDO2-2566	710–740	725	438+439+440 IODINE	50			gas not collected
MDO2-2566	740–750	745	291	18	569.1	30.11	0.20
MDO2-2566	890–900	895	292	21	574.2	30.13	0.00
MDO2-2566	1,040–1,050	1,045	293	23	572.9	30.36	0.24
MDO2-2566	1,160–1,190	1,175	400+401+402+403 IODINE	50			gas not collected
MDO2-2566	1,190–1,200	1,195	294	20	570.7	30.47	0.18
MDO2-2566	1,340–1,350	1,345	295	18	570.9	30.54	0.40
MDO2-2566	1,490–1,500	1,495	296	16	564.7	29.88	0.24
MDO2-2566	1,640–1,650	1,645	297	15	566.5	29.81	0.61
MDO2-2566	1,790–1,800	1,795	298	12	568.7	29.63	0.86
MDO2-2566	1,940–1,950	1,945	299	12	570.3	29.23	0.49
MDO2-2566	2,090–2,100	2,095	300	13	569.6	29.03	1.97
MDO2-2566	2,240–2,250	2,245	301	9.5	573.6	28.51	0.30
MDO2-2566	2,390–2,400	2,395	302	10	570.3	27.86	0.86
MDO2-2566	2,540–2,550	2,545	M92+M94	12.3	567.2	27.33	gas not collected
MDO2-2566	C.C.	2,609	M91	>10	565.9	27.03	gas not collected
MD02-2567	140–150	145	303	27	562.6	28.87	0.00
MD02-2567	250–280	265	436+437 IODINE	60			gas not collected
MD02-2567	280–290	285	M94	C-14 sample	568.9	27.37	gas not collected
MD02-2567	290–300	295	304	18	567.1	29.03	0.13

Table 1. Summary of shipboard pore-water geochemical measurements. — Continued

[cm, centimeter; mL, milliliter; mM, millimole; µM, micromole; C.C., core catcher; >, greater than]

Core	Interval (cm)	Mid depth (cm)	Syringe number	Fluid volume (mL)	Chloride (mM)	Sulfate (mM)	Methane (µM)
MD02-2567	440–450	445	305	16	571.3	29.33	0.00
MD02-2567	590–600	595	306	13	572.3	29.53	0.26
MD02-2567	700–730	715	322+323+324+325 IODINE	50			gas not collected
MD02-2567	740–750	745	307	12	574.5	29.76	0.18
MD02-2567	890–900	895	308	13	572.6	29.94	0.23
MD02-2567	1,040–1,050	1,045	309	14	575.5	30.37	0.00
MD02-2567	1,150–1,180	1,165	318+319+320+321 IODINE	>50			gas not collected
MD02-2567	1,190–1,200	1,195	310	15	577.8	31.02	0.17
MD02-2567	1,340–1,350	1,345	311	15	575.9	31.23	0.46
MD02-2567	1,490–1,500	1,495	312	16	572.9	31.22	0.13
MD02-2567	1,640–1,650	1,645	313	18	577.6	31.40	0.24
MD02-2567	1,790–1,800	1,795	314	15	577.3	31.28	0.65
MD02-2567	1,940–1,950	1,945	315	14	576.6	31.00	0.26
MD02-2567	2,090–2,100	2,095	316	14	575.1	30.66	0.51
MD02-2567	2,240–2,250	2,245	317	13	581.3	30.63	0.80
MD02-2567	2,390–2,400	2,395	M99	9.2	574.3	29.88	gas not collected
MD02-2567	2,540–2,550	2,545	M98	9.8	575.2	29.43	gas not collected
MD02-2567	C.C.	2,659	M93	9.7	568.1	28.53	gas not collected
MD02-2569	0–10	5	328	21	554.7	24.60	43.62
MD02-2569	90–100	95	341	17	558.8	14.50	20.18
MD02-2569	190–200	195	342	17	557.7	0.94	5,045.27
MD02-2569	200–210	205	M102	C-14 sample			gas not collected
MD02-2569	290–310	300	343+351	28+25	364.5	2.18	835.84
MD02-2569	374–400	387	340	20	609.7	0.49	327.23
MD02-2569	400–410	405	344	17	754.7	0.11	725.32
MD02-2569	410–420	415	M101	C-14 sample			gas not collected
MD02-2569	590–600	595	345	20	577.7	0.09	2163.42
MD02-2569	740–750	745	347	11	943.4	0.00	873.54
MD02-2569	816–820	818	330	17	763.0	0.31	386.01
MD02-2569	820–830	825	348	15	727.3	0.21	1,889.44
MD02-2569	865–875	870	346+350+M100 DOC IODINE	41+33			106.91
MD02-2569	995–1,005	1,000	349	13	853.5	0.00	1,208.77
MD02-2569	C.C.	1,036	327	17	864.9	1.58	1,237.49
MD02-2570	140–150	145	352	22	558.9	27.39	4.26
MD02-2570	260–290	275	412+413 IODINE	32			gas not collected

Table 1. Summary of shipboard pore-water geochemical measurements. — Continued

[cm, centimeter; mL, milliliter; mM, millimole; µM, micromole; C.C., core catcher; >, greater than]

Core	Interval (cm)	Mid depth (cm)	Syringe number	Fluid volume (mL)	Chloride (mM)	Sulfate (mM)	Methane (µM)
MD02-2570	290–300	295	353	15	564.0	4.64	14.29
MD02-2570	440–450	445	354	17	561.9	0.81	435.14
MD02-2570	590–600	595	355	14	564.0	0.66	704.93
MD02-2570	710–740	725	409+410 IODINE	45			gas not collected
MD02-2570	740–750	745	356	11	567.6	0.15	260.43
MD02-2570	890–900	895	357	11	570.5	0.08	170.22
MD02-2570	1,040–1,050	1,045	358	11	568.1	0.00	341.01
MD02-2570	1,160–1,190	1,175	405+406 IODINE	25			gas not collected
MD02-2570	1,190–1,200	1,195	359	9	581.8	0.04	263.39
MD02-2570	1,340–1,350	1,345	360	11	578.6	0.25	624.60
MD02-2570	1,490–1,500	1,495	361	21	570.4	0.00	400.70
MD02-2570	1,640–1,650	1,645	362	19	573.8	0.00	503.60
MD02-2570	1,790–1,800	1,795	363	20	572.6	0.00	461.43
MD02-2570	1,940–1,950	1,945	364	18	572.4	0.00	600.61
MD02-2570	2,090–2,100	2,095	365	16	574.6	0.00	956.55
MD02-2570	2,240–2,250	2,245	366	15	570.8	0.00	945.86
MD02-2570	2,390–2,400	2,395	367	18	575.0	0.08	768.28
MD02-2570	2,540–2,550	2,545	M104	10	571.1	0.00	gas not collected
MD02-2570	2,690–2,700	2,695	M105	>10	571.1	0.00	gas not collected
MD02-2570	C.C.	2,839	M103	7.8	570.5	0.00	gas not collected
MD02-2571C2	45–55	50	371	-	564.8	28.99	0.67
MD02-2571C2	70–80	75	396	32	560.1	28.53	1.33
MD02-2571C2	95–105	100	372	15	559.4	28.55	26.97
MD02-2571C2	120–130	125	395	29	561.1	27.69	7.23
MD02-2571C2	145–155	150	373	-	568.4	26.69	3.78
MD02-2571C2	170–180	175	397	29	558.0	24.86	1.43
MD02-2571C2	195–205	200	374	-	563.3	23.10	3.47
MD02-2571C2	216–223	219.5	M107	C-14 sample			gas not collected
MD02-2571C2	220–230	225	387	28	523.1	18.47	1.33
MD02-2571C2	245–255	250	375	14	570.6	17.68	8.73
MD02-2571C2	270–280	275	388	27	560.5	11.63	59.49
MD02-2571C2	295–305	300	376	16	578.7	2.09	325.44
MD02-2571C2	320–330	325	389	22	560.4	0.52	394.46
MD02-2571C2	345–355	350	377	14	570.1	0.72	2,662.02
MD02-2571C2	370–380	375	390	13+26	569.7	0.37	1,196.65
MD02-2571C2	377–390	383.5	M108	C-14 sample			gas not collected
MD02-2571C2	395–405	400	378	12	573.5	0.32	670.28

Table 1. Summary of shipboard pore-water geochemical measurements. — Continued

[cm, centimeter; mL, milliliter; mM, millimole; µM, micromole; C.C., core catcher; >, greater than]

Core	Interval (cm)	Mid depth (cm)	Syringe number	Fluid volume (mL)	Chloride (mM)	Sulfate (mM)	Methane (µM)
MD02-2571C2	420–430	425	391	27	575.3	0.17	820.52
MD02-2571C2	445–455	450	379	25	569.8	0.22	419.58
MD02-2571C2	470–480	475	392	25	576.7	0.20	873.46
MD02-2571C2	495–505	500	380	13	581.0	0.22	865.15
MD02-2571C2	520–530	525	393	25	582.2	0.20	587.66
MD02-2571C2	545–555	550	381	19	580.0	0.13	1,520.42
MD02-2571C2	570–580	575	394	27	589.7	0.06	867.66
MD02-2571C2	582–597	589.5	M109	C-14 sample			gas not collected
MD02-2571C2	595–605	600	382	16	582.6	0.26	696.80
MD02-2571C2	645–655	650	383	15	573.7	0.00	1,306.22
MD02-2571C2	695–705	700	384	23	545.9	0.00	295.22
MD02-2571C2	745–755	750	398	-	587.0	0.11	890.34
MD02-2571C2	754–771	762.5	M106	C-14 sample			gas not collected
MD02-2571C2	795–805	800	385	22	590.7	0.00	375.66
MD02-2571C2	895–905	900	386	-	592.2	0.00	1,038
MD02-2571C2	995–1,005	1,000	399	-	589.5	0.00	401.55
MD02-2571C2	TOP OF C.C.	1,036	370	-	601.3	0.00	1,527.47
MD02-2571C2	C.C.	1,037	369	24	595.2	2.17	1,411.59
MD02-2574	295–305	300	418	17	560.3	27.89	gas not collected
MD02-2574	445–455	450	419	17	557.0	26.78	gas not collected
MD02-2574	595–605	600	420	18	555.2	25.57	gas not collected
MD02-2574	745–755	750	421	15	565.1	24.55	gas not collected
MD02-2574	895–905	900	422	13	562.0	22.72	gas not collected
MD02-2574	1,045–1,055	1,050	423	9.5	566.0	21.03	gas not collected
MD02-2574	1,195–1,205	1,200	424	8	563.8	18.67	gas not collected
MD02-2574	1,345–1,355	1,350	425	7	572.9	16.80	gas not collected
MD02-2574	1,495–1,505	1,500	426	6	578.0	14.47	gas not collected
MD02-2574	1,645–1,655	1,650	427	6	572.8	12.04	gas not collected
MD02-2574	1,795–1,805	1,800	428	6	582.3	10.04	gas not collected
MD02-2574	1,945–1,955	1,950	429	6	570.3	7.62	gas not collected
MD02-2574	2,095–2,105	2,100	430	6	575.2	6.63	gas not collected
MD02-2574	2,245–2,255	2,250	431	-	610.8	4.95	gas not collected
MD02-2574	2,395–2,405	2,400	432	-	568.2	2.85	gas not collected
MD02-2574	2,545–2,555	2,550	433	-	567.1	1.39	gas not collected
MD02-2574	2,695–2,705	2,700	M110	>10	565.7	0.69	gas not collected
MD02-2574	2,845–2,855	2,850	M118	9.8	579.0	0.29	gas not collected
MD02-2574	2,995–3,005	3,000	M111	7.8	576.8	0.21	gas not collected
MD02-2574	3,145–3,155	3,150	M112	-	572.1	0.00	gas not collected
MD02-2574	3,295–3,305	3,300	M113	6.9	572.9	0.09	gas not collected

Table 1. Summary of shipboard pore-water geochemical measurements. — Continued

[cm, centimeter; mL, milliliter; mM, millimole; µM, micromole; C.C., core catcher; >, greater than]

Core	Interval (cm)	Mid depth (cm)	Syringe number	Fluid volume (mL)	Chloride (mM)	Sulfate (mM)	Methane (µM)

NOTES:
0.00 entry indicates an amount below detection limit
M prefix for syringe number indicates Manheim-style squeezer sample; all others were Reeburgh-style squeezers
"+" sign in Syringe Number column indicates syringes combined; the volume of each prior to combining is indicated in the Fluid Volume column.
"C-14 sample" indicates samples collected by J. Pohlman for DIC and(or) DOC 14C AMS analysis.
Iodine isotope samples were obtained by combining the syringes listed in Syringe Number column; total volume is indicated in the Fluid Volume column.

Chapter 9

Hydrocarbon Gases from Giant Piston Cores in the Northern Gulf of Mexico: Results from the IMAGES VIII/ PAGE 127 cruise of the RV Marion Dufresne, July 2002

Thomas D. Lorenson[1], Jennifer A. Dougherty[1], and James G. Flocks[2]

Hydrocarbon gases from giant piston cores in the northern Gulf of Mexico: Results from the IMAGES VIII/PAGE 127 cruise of the RV Marion Dufresne*, July 2002; chapter 9* in *Winters, W.J., Lorenson, T.D., and Paull, C.K., eds., 2007, Initial report of the IMAGES VIII/PAGE 127 gas hydrate and paleoclimate cruise on the RV* Marion Dufresne *in the Gulf of Mexico, 2–18 July 2002: U.S. Geological Survey Open-File Report 2004–1358.*

Abstract

Hydrocarbon gases and carbon dioxide (CO_2) extracted from sediment cores from the northern Gulf of Mexico in four distinct regions were studied to constrain the possible occurrence and source of gas that may form gas hydrate. Three sample types were analyzed: gas from dissociated gas hydrate, dissolved gas in sediment, and free gas evolved from sediment collected from gas voids in the core liner.

Gas hydrate was recovered in four cores from previously known venting sites about 3 to 9 meters below the sea floor but was not found in adjacent basins. Gas hydrate samples were preserved for analysis from only one core—MD02-2569 in the thalweg of Mississippi Canyon within lease area MC802. The quality of the gas hydrate recovered was poor because the time for core recovery and sampling approached 2 hours. Methane, ranging from 95.0 to 99.5 percent, is the principal gas in the gas hydrate with concentrations of CO_2 ranging from 0.16 to 4.0 percent. Higher molecular weight hydrocarbon gases—ethane, propane, and isobutane—are found in concentrations exceeding 1,000 parts per million, suggesting that both structure I and structure II gas hydrate are present.

Sediment collected near the summit of a 1- to 1.5-kilometer-diameter sea-floor mound on Kane Spur within lease area MC853 (34 kilometers east of MC802) contained visible oil and hydrocarbon gases of thermogenic origin. Sediment from MC802 contained some proportion of hydrocarbon gases of likely thermogenic origin but at much lower concentrations than at MC853. Free gas from sediment at MC853 also was composed of mainly thermogenic hydrocarbons. Sediment gases from other areas (Tunica Mound, Bush Hill, and areas in and flanking Mississippi Canyon) were composed mainly of microbial methane with traces of thermogenic hydrocarbons.

Introduction

The northern Gulf of Mexico hosts numerous sea-floor (<7-meter (m) subbottom) occurrences of gas hydrate. The sea floor is dominated by salt-tectonic basin structures, high sedimentation rates (about 40 centimeters per thousand years (cm/k.y.)), and complex late Neogene stratigraphy with common sea-floor failures. Natural oil and gas seeps are abundant, usually associated with fault conduits that often are capped by gas hydrate when the seeps are within the hydrate stability zone. While gas hydrate is relatively common at the sea floor, the lack of bottom simulating reflections (BSR) on seismic records suggests that gas hydrate at depth is largely absent. Thus, it is unknown if there are significant gas hydrate accumulations in reservoir sediments away from faults. To address this question, a cruise was conducted with the International Marine Past Global Changes Study (IMAGES) and Paleoceanography of the Atlantic and Geochemistry (PAGE) programs aboard the research vessel (RV) *Marion Dufresne* in July 2002 (Lorenson and others, 2002).

Eighteen giant piston cores up to 38 m long and four giant box cores up to 9 m long were recovered along seismic-reflection transects in widely different geologic environments

[1]U.S. Geological Survey, 345 Middlefield Road, MS-999, Menlo Park, CA 94025 USA (tlorenson@usgs.gov).

[2]U.S. Geological Survey, 600 4th Street S., St. Petersburg, FL 33701 USA.

in water depths ranging from 600 to 1,300 m (table 1). The transects were designed to extend from known sea-floor gas hydrate occurrences across the adjacent basin to background sediments away from any gas-venting sites.

The type of dissolved and free hydrocarbon gas in marine sediments that is trapped in gas hydrate determines the hydrate structure and, hence, the pressure and temperature conditions under which it is stable. To this end, we measured the hydrocarbon gas content of sediments and used the data as proxies for methane and other hydrocarbon gas source discrimination, the general gas contents of the sediment, and the likely type of gas hydrate that may have dissociated during the core recovery process.

Table 1. Locations of cores measured for gas composition.

[G, gravity core; GHF, gravity heat-flow core; C2, box core]

Core ID	Latitude	Longitude	Area name
MD02-2535	27.61983	92.24100	Tunica Mound
MD02-2537	27.61600	92.24867	Tunica Mound
MD02-2538GHF	27.61667	92.24717	Tunica Mound
MD02-2539	27.63967	92.19217	Tunica Mound
MD02-2541	27.63250	92.21233	Tunica Mound
MD02-2542GHF	27.63217	92.21200	Tunica Mound
MD02-2543G	27.61233	92.25550	Tunica Mound
MD02-2545G	27.61400	92.25167	Tunica Mound
MD02-2546	27.61567	92.24700	Tunica Mound
MD02-2548	27.63750	92.19950	Tunica Mound
MD02-2553C2	27.18350	91.41667	Pigmy Basin
MD02-2554	27.78333	91.49900	Bush Hill Basin
MD02-2555	27.78317	91.48917	Bush Hill Basin
MD02-2556	27.78300	91.47750	Bush Hill Basin
MD02-2559	28.22250	89.08817	Kane Spur
MD02-2560	28.24333	89.15500	Kane Spur
MD02-2561	28.20517	89.02017	Kane Spur
MD02-2562	28.07983	89.14017	Kane Spur
MD02-2563	28.12333	89.13633	Kane Spur
MD02-2565	28.12350	89.13950	Kane Spur
MD02-2566	28.11917	89.10317	Kane Spur
MD02-2567	28.10017	89.01983	Kane Spur
MD02-2569	28.15217	89.47967	West Mississippi
MD02-2570	29.57100	89.68983	West Mississippi
MD02-2572GHF	28.07100	89.68967	West Mississippi
MD02-2573GHF	28.15200	89.47983	West Mississippi

Methods

Field Sampling

A variety of gas sample types were collected for this study: (1) cored sediment, (2) free gas, and (3) gas produced by controlled dissociation of gas hydrate samples.

Sediment samples destined for gas analysis were prepared using a procedure modified from Kvenvolden and Redden (1980). Cored sediment in a 5-centimeter (cm) interval was cut out, extruded from the core liner, sealed in a 500-milliliter (mL) metal can equipped with a septum, and weighed. The sample can was filled with water to the rim, and 100 mL of water was removed. After 2 to 3 grams of sodium chloride salt was added as a bacterial growth inhibitor, the can was sealed, frozen in the upside-down position, and shipped to the U.S. Geological Survey (USGS) laboratory in Menlo Park, California, for hydrocarbon gas analyses.

In the shore-based laboratory, the frozen samples were thawed in cans until they reached a temperature of about 20 degrees Celsius (°C). They were then placed into a high-speed shaker for 5 minutes. The partitioned hydrocarbon headspace gases were analyzed using a gas chromatograph. Other gas subsamples were withdrawn from the can by using a syringe and were injected into a pre-evacuated 30-mL serum vial for subsequent carbon isotopic analyses.

Free Gas

Free-gas samples were taken when visible signs of sediment extrusion were noticed during routine drilling of gas-venting holes in the core liner. In such instances, “mud-worms” commonly were seen extruding from the holes. Gas was sampled by inserting a valve-tipped plastic syringe into the hole and allowing the gas to expand into the syringe. The gas in the syringe was injected into an evacuated 30-mL serum vial for transport to the laboratory and then analyzed by direct injection onto a gas chromatograph as described below.

Gas Hydrate Analyses

The system for measuring the gas and water content of dissociating gas hydrate consisted of a sample holder, a gauge block, a pressure gauge, and a manifold. The manifold had an interchangeable gas-sampling port with septum or a quick-connection to vacuum, a steel cylinder for collection of gas, and a pressure gauge. The device was first used on Deep Sea Drilling Program Leg 76, and a more complete description of the device can be found in Kvenvolden and others (1984). For each experiment, gas hydrate that was temporarily stored in liquid nitrogen was placed on aluminum foil and broken into smaller sizes. Pieces with minimal sediment were placed into the sample device previously cooled by liquid nitrogen. The system was sealed and the lower portion of the device was placed into a water bath. As the gas hydrate dissociated, pressure inside the device increased, then stabilized. After about

10 minutes of stable pressure, the pressure and the temperature of the water bath were recorded. A valve was opened on the manifold, which allowed the dissociated gas to expand into the sample manifold and the pre-evacuated cylinder. Gas was sampled from the manifold and analyzed by gas chromatography. After gas sampling, the residual water and any sediment were weighed and their respective volumes calculated and subtracted from the volume of the reaction chamber. Gas volumes were calculated according to the ideal gas law at standard temperature and pressure (STP). Residual water was decanted after centrifugation, then sealed, and refrigerated pending chlorinity measurements and isotopic analyses of the water.

Hydrocarbon Gas Composition Determination

A Shimadzu GC-14A gas chromatograph equipped with a Chemipack C-18, 1.8-m x 3.2-millimeter (mm) 80/100 mesh stainless steel column was used to measure C_1-C_8 hydrocarbon gases. The GC-14A is configured with a 1-mL, valve-actuated, sample loop for injection, and a flame ionization detector (FID) for gas detection. Samples were introduced by syringe at atmospheric pressure, and a minimum of 10 mL of gas was used to flush the injection loop. Run conditions were 35 °C for 1.5 minutes increasing at 20 degrees per minute to a constant 150 °C. Helium was used as the carrier gas at a constant mass flow rate of 3 kilograms per square centimeter (kg/cm^2). FID temperature was held at 150 °C.

Results are reported relative to the volume of cuttings or weight of core material from which the gases were extracted, that is, microliters of gas per liter of wet sediment (microliter per liter (µL/L). Gas concentration data are reported for a series of hydrocarbons given in order of elution (table 2, p. 28): methane (C_1), ethane (C_2), propane (C_3), isobutane (iC_4), normal butane (nC_4), neopentane ($neoC_5$), isopentane (iC_5), normal pentane (nC_5), 2,2 dimethylbutane ($2,2MC_4$), 2methylpentane ($2MC_5$), 3methylpentane ($3MC_5$), normal hexane (nC_6), normal heptane (nC_7), and methylcyclohexane (McC_6). Approximate detection limits for all hydrocarbon compounds are 0.05 parts per million (ppm) by volume corresponding to about 0.02 µL/L.

CO_2 Determination

Carbon dioxide (CO_2) concentrations were determined in the laboratory with a Hewlett-Packard P-200 micro-gas chromatograph equipped with an 8-m-long by 0.32-mm-diameter PoraPlot U column. Run conditions were isothermal at 60 °C with a run time of 2 minutes. Helium carrier gas column head pressure was maintained at 1.25 bar. Compounds were detected with a micro-machined thermal conductivity detector. The approximate detection limit for CO_2 is about 0.5 µL/L. Concentrations of primary gases (nitrogen, oxygen, and argon) were not determined because the samples were exposed to air during recovery and packaging.

Hydrocarbon Gas Isotopic Composition Determination

Stable carbon isotope ratio determinations of C_1, C_2, C_3, iC_4, nC_4, nC_5, and CO_2 were made on a Continuous Flow-Isotope Ratio Mass Spectrometer (Finnigan MAT 252 GC-CF-IRMS) at the School of Earth and Ocean Sciences (SEOS), University of Victoria, Canada.

Samples were introduced by syringe into a Stanford Research Instruments gas chromatograph (GC) by way of a gas sample valve (loop volumes: 10, 100, or 200 µL). Analytes were separated at 40 °C on a 30-m GS-Q column (0.32 mm ID (inner diameter)) with a carrier gas flow of 1.8 milliliter per minute (mL/min) ultra-high purity helium. After gas partitioning on the GC, the gas passed through a CuO/Pt microcombustion oven at 850 °C. This oven quantitatively converts the hydrocarbon gases to carbon dioxide and water. The combusted sample products were then passed through a Nafion™ tube to remove water from the combustion and any that may have been in the carrier gas. The purified CO_2/He pulse was scaled by an open-split interface and then transferred into the GC-C-IRMS. Isotope ratios are referenced to the conventional PeeDee Belemnite (PDB) standard through a known CO_2 isotope standard that is added at the open split to the sample runs several times during the analysis.

For stable carbon isotope ratio measurements on the sample CO_2, the gas was partitioned on the GC as discussed above. The microcombustion oven was bypassed for the CO_2 measurements, but the gas stream was dried, split, and measured by CF-IRMS in a manner similar to the light hydrocarbons.

Regional Descriptions

Sediment cores from the northern Gulf of Mexico in four distinct regions (fig. 1) were analyzed in this study: Tunica Mound, Pigmy Basin, Bush Hill, and the Mississippi Canyon area (Kane Spur and West Mississippi Canyon). Table 1 lists core locations that were analyzed for sediment gas concentration.

Tunica Mound

Garden Banks and Green Canyon are known for locally high sedimentation rates from 7 to 11 meters per thousand years (m/k.y.) for the upper sedimentary section, extensive late Neogene salt deformation, and slope failures with mass-wasting along over-steepened parts of the continental slope (Rowan and Weimer, 1998). Sediment ages in the upper 600–700 meters below sea floor (mbsf) likely are no older than 0.5 million years (m.y.) in the study area (Berryhill and others, 1987; Weimer and others, 1998). This region includes the Tunica Mound and Bush Hill coring sites.

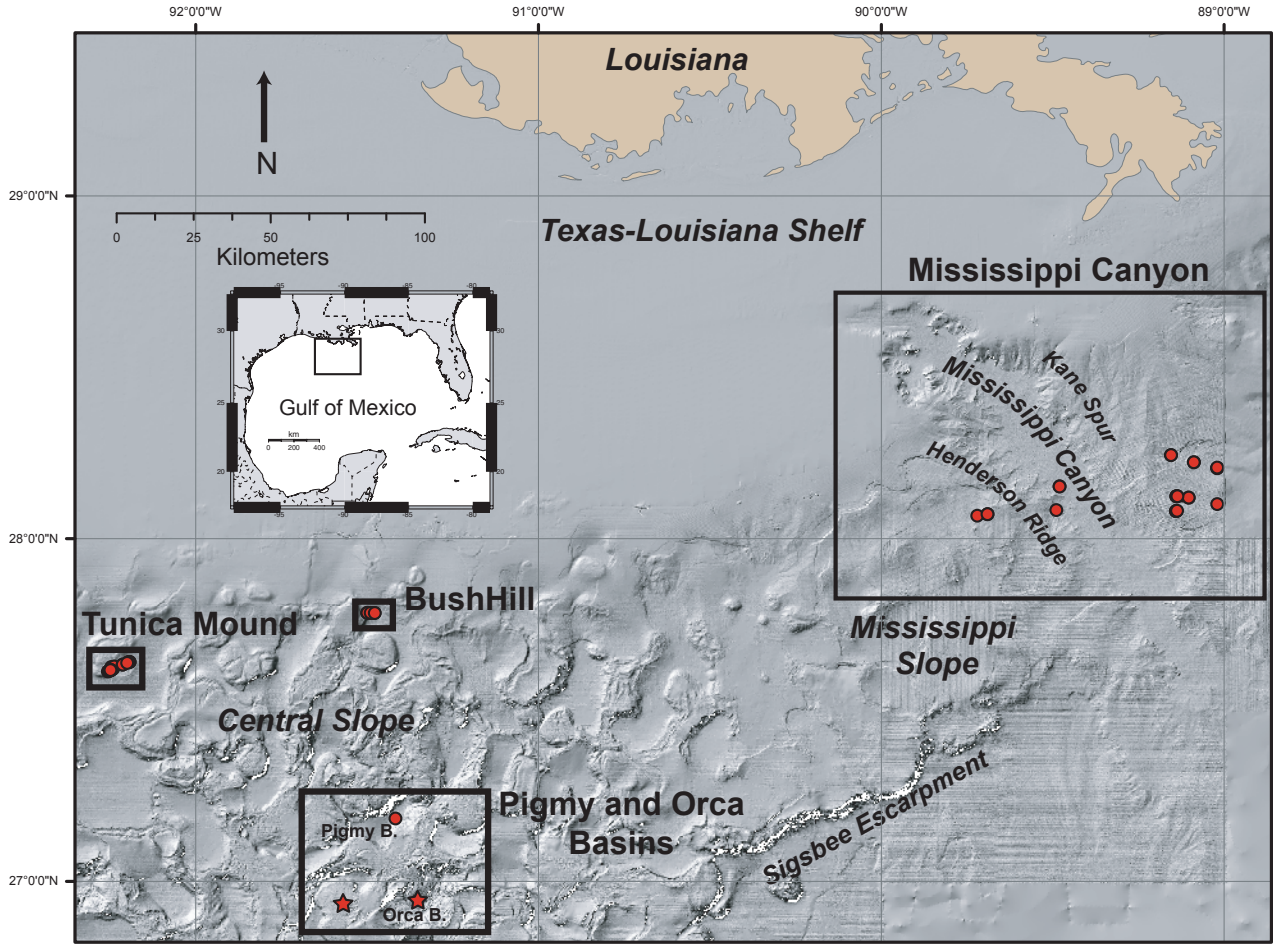

Figure 1. Index map of locations in this report.

The upper sedimentary section of the continental slope, including Tunica Mound, is characterized by layered and chaotic units that are faulted near basin edges and by slope failures on basin flanks. Deformation is greater near salt structures and on over-steepened slopes.

Downslope, well-layered sediments within 300 m of the sea floor have many vertical acoustic "chimney" features, likely small faults, and are bounded by chaotic units directly below and above. The underlying chaotic unit has high reflectivity zones (HRZs) that are dispersed within chaotic stratal units and similar to those in other slope basins at about the same depth (Cooper and Hart, 2003). These gas chimney features extend up from this chaotic unit to the overlying disrupted unit, which has low seismic amplitudes and evidence of faulting and sliding.

Nine gravity and piston cores were taken along a transect along the southern flank of Tunica Mound verging toward but not entering the basin to the east (fig. 2). Tunica Mound is about 14 square kilometers (km^2) in area with a fault running through the southwest to northeast corners. The northwest side of the mound is uplifted in contrast to the southeast corner. The coring transect is about 7 kilometers (km) long at a subparallel angle to the fault in the southeast quadrant. Water depths along the transect range from 580 to 620 m. All sites on the transect remain within the confines of the dome; however, the site to the northeast enters the basin between Tunica Mound and Caddo Mound located to the east of Tunica Mound. Most of the gravity cores were taken on or near a subsidiary mound with seismic features indicative of active fluid flow, including authigenic carbonate, sea-floor relief, and gas. Piston cores were taken away from the submound.

Pigmy and Orca Basins

Cores in Pigmy and Orca Basins were obtained to conduct paleoceanographic research (fig. 3). The basins presumably have similar depositional histories; however, Orca Basin has been covered by a seawater brine for some time causing an anoxic environment and preservation of organic matter. In contrast, Pigmy Basin has been subject to oxic conditions. One sample was analyzed from Pigmy Basin and none from Orca Basin.

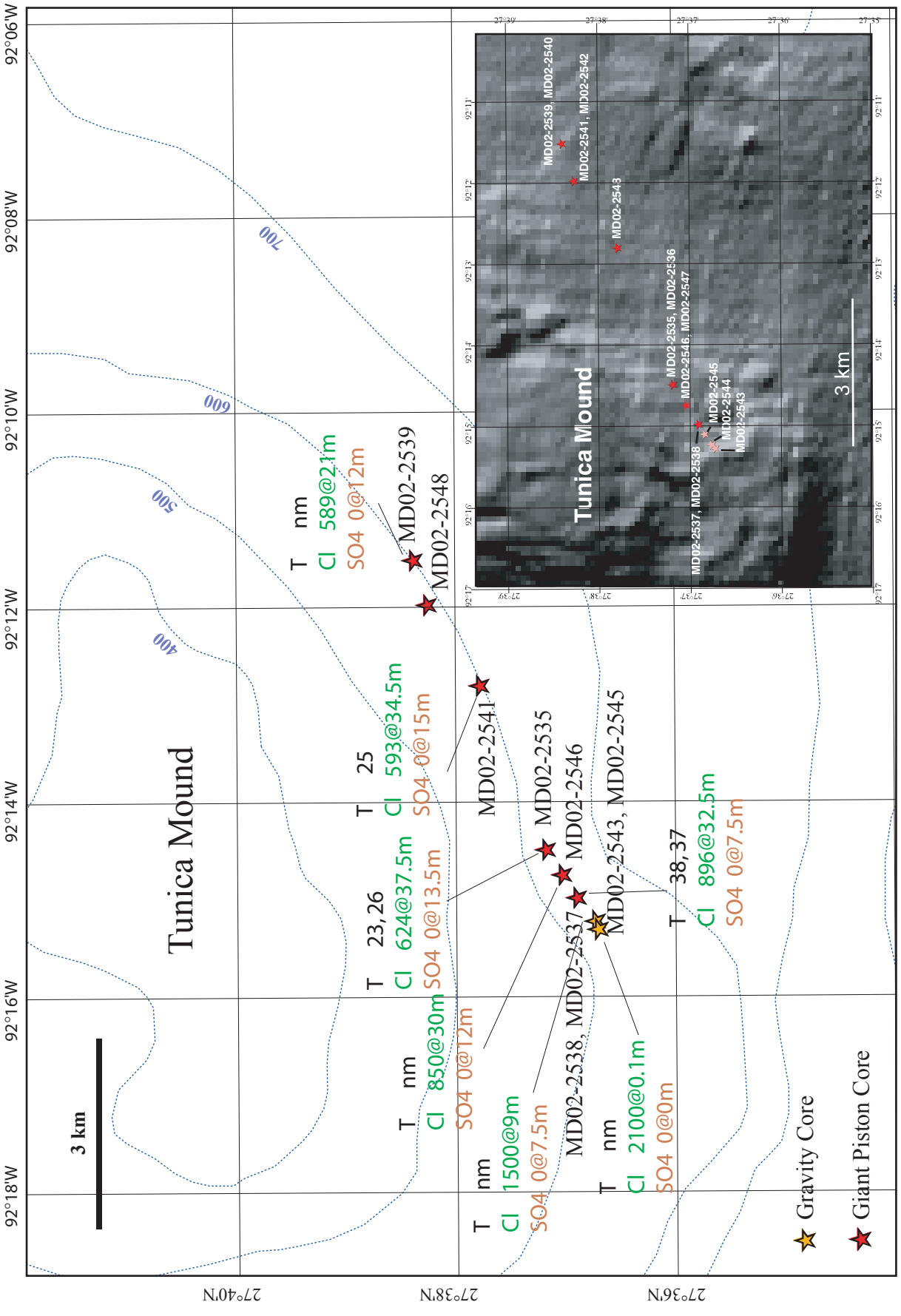

Figure 2. Core sites adjacent to Tunica Mound. Gravity and giant piston cores noted with yellow and red stars, respectively. Other core observations are indicated as follows: T = measured geothermal gradient (degrees Celsius per kilometer); Cl = chloride ion concentration (μM) maximum at the corresponding depth (meters below sea floor); SO_4 = sulfate ion concentration (μM) minimum at the corresponding depth (meters below sea floor) indicates the depth to the sulfate-methane interface (SMI); nm = not measured.

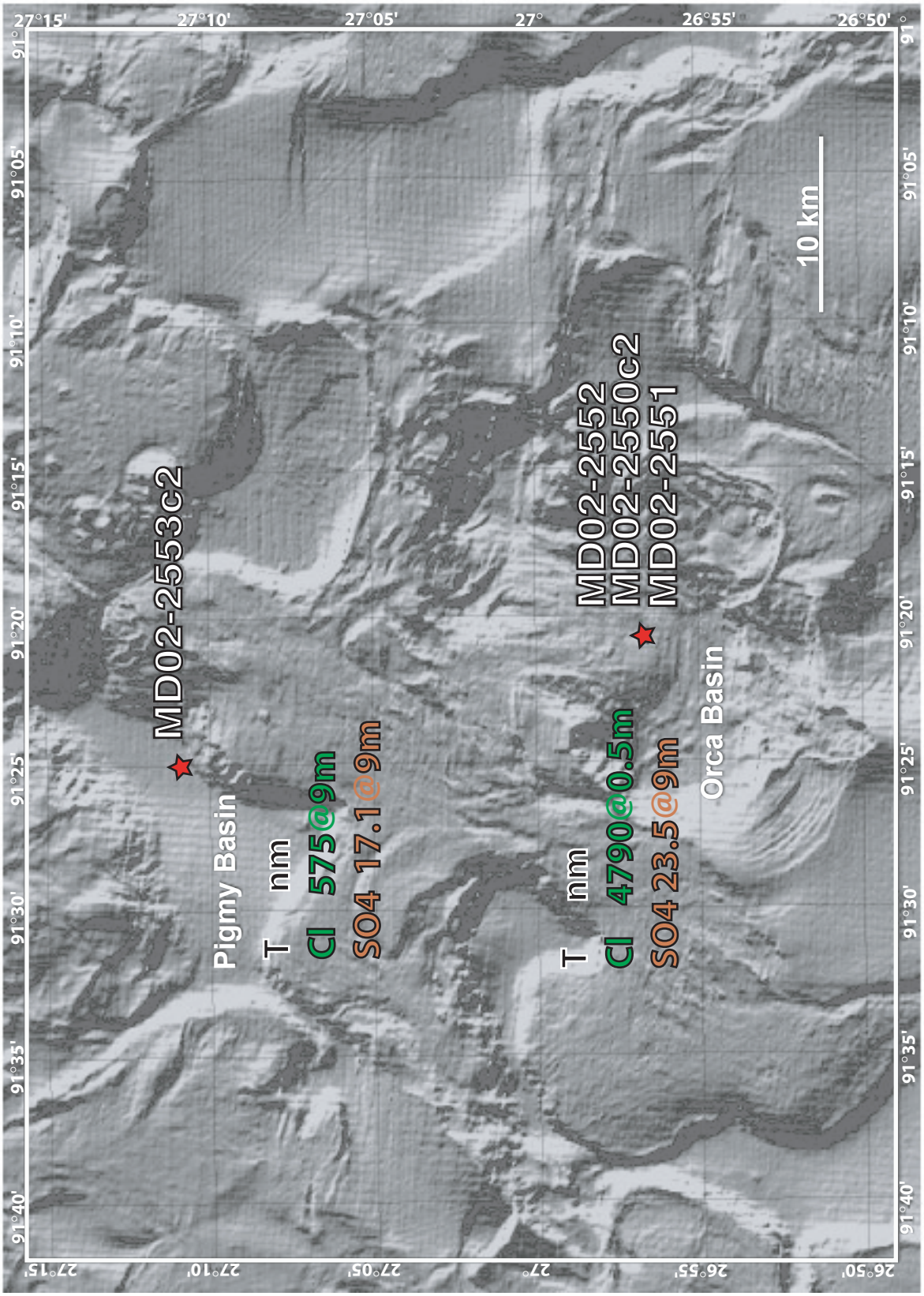

Figure 3. Core sites adjacent to Tunica Mound. Gravity and giant piston cores noted with yellow and red stars, respectively. Other core observations: T = measured geothermal gradient (nm = not measured); Cl = chloride ion concentration (µM) maximum at the corresponding depth (meters below sea floor); SO_4 = sulfate ion concentration (µM) minimum at the corresponding depth (meters below sea floor) indicates the depth to the sulfate-methane interface (SMI).

Bush Hill

The small basin just east of Bush Hill (fig. 4) was cored at a 2-kilometer (km) spacing along an east-west transect. Bush Hill itself has been extensively surveyed by numerous groups focusing on vent gas, gas hydrate, and chemosynthetic communities (MacDonald and others, 1989, 1994, 1996; Sassen and others, 1993, 1998; Roberts and Carney, 1997; Sassen, Sweet, and others 1999; Sassen, Joye, and others, 1999; Roberts, 2001; Sassen, Sweet, and others 2001a, b). The Bush Hill sea-floor feature is a fault-related seep mound at a water depth of about 540 m that may have seismic attributes of a mud diapir. An antithetic fault at Bush Hill is structurally related to nearby growth faults that constitute the structural trap at Jolliet Field just a few kilometers to the south (Cook and D'Onfro, 1991). The oil and gas at the Bush Hill site correlate with reservoirs at approximately 2 to 3 km depth in the Jolliet Field (for example, Kennicutt and others, 1988; Sassen, Losh, and others, 2001). Shallow sediment is underconsolidated hemipelagic mud with near-normal salinity (about 38 parts per thousand (ppt)), high concentration of H_2S (as much as 20.3 micromoles per liter (μM/L)), and high pH (8.3–9.0) (Aharon and Fu, 2000). Mounds of structure II gas hydrate outcrop on the sea floor and have been observed persistently since 1991 (Sassen and others, 2003).

Mississippi Canyon Region—

Kane Spur

Cooper and Hart (2003) recorded high-resolution seismic-reflection profiles across the east and west sides of the Mississippi Canyon. These areas are characterized by extreme sedimentation rates up to 15 to 20 m/k.y., with pelagic drape and mass-wasting (Coleman and others, 1983) over the last 20 thousand years (ka). The age of the sedimentary sections in the upper 600 to 700 m likely is no older than late Pleistocene age (Goodwin and Prior, 1989).

The most prominent feature on the east side of Kane Spur (fig. 5) is a large sea-floor slide that is about 15 km wide and at least 15 km long, covering more than 225 km^2. Extensional faults are found at the head of the slide, and a 1- to 2-km-wide shear zone appears along the southwest edge of the slide. The slide exhibits many features common to large-scale active slope failures in the Mississippi Canyon area resulting from several causes, including salt withdrawal and diapirism, deep- and shallow-extensional faulting, and gravity sliding (Cooper and Hart, 2003).

The subbottom is cut by two categories of faults: a suite of high-angle faults that converge with depth and extend off the bottom of the seismic-reflection record, and a set of faults that appear to be related to stratigraphic sliding within the upper sedimentary section. Cooper and Hart (2003) infer that the high-angle faults are rooted in deep-seated salt that is the principal driving mechanism for the sea-floor slide. The shallow faults that sole out within a chaotic unit partly accommodate the slide motion that includes extension near the slide's head and compression near the toe.

Within the boundaries of the extensional subsidence zone, Cooper and Hart (2003) observed a chaotic stratigraphic unit that occurs with disrupted reflections and high reflectivity. The gas hydrate stability field terminates within the high-reflectivity zone (HRZ). The top of the HRZ under the slide lies at about 440 to 480 mbsf, is about 90 to130 m thick, and generally mimics the sea floor. The high reflectivity occurs mostly where reflections are discontinuous and chaotic. The unit can be traced regionally, but reflectivity is greatest under the slide and near large fault zones. During development of the Ursa Field, drilling along the southwest side of the slide encountered wet sands with overpressured shallow water flows and some gas from about 300 to 550 mbsf (Eaton, 1999). Such features are common in the northern Gulf of Mexico (Minerals Management Service, 2001).

Mississippi Canyon Region—

MC853 Lease Block Diapiric Structure

An oblong sea-floor mound, perhaps a diapir, (1 to 1.5 km across) overlies a shallow salt body at the boundary of Mississippi Canyon lease blocks 852 and 853 referred to in this report as MC853. The MC853 sea-floor mound is on a structural high along the extensional boundary of a salt withdrawal basin on the western flank of Kane Spur (fig. 5). Allochthonous salt bodies occur at shallow depth in the sediment and have initiated major growth faults believed to serve as conduits for fluid migration to the sea floor from the subsurface petroleum system within salt withdrawal basins (Sassen, Sweet, and others, 1999). An acoustic wipeout zone typical of fluid expulsion occurs below the mound on multichannel seismic lines (Sager and Kennicutt, 2000). Intact gas hydrate has been recovered from MC 852/853 at water depths of 1,050 to 1,060 m by numerous researchers on several cruises, suggesting that the gas hydrates are persistent at the site (Sassen, Sweet, and others, 1999). Here, gas hydrate occurs within gassy sediments containing biodegraded crude oil, contains C_1–C_5 hydrocarbon gases, and is inferred to be structure II.

The estimated maximum thickness of the gas hydrate stability zone (GHSZ) is about 780 m (Appendix L). Salt is present in the near surface as evidenced by high chloride concentrations (Ussler and Paull, this volume, chapter 8). Core descriptions indicate relatively high hydrate concentration in shallow sediments with up to 90 to 100 volume percent saturation in some intervals (Sassen, Losh, and others, 2001).

Thick, relatively unfaulted sediments overlie the reservoir section of the Ursa Field. A lack of hydrocarbon seeps directly over the Ursa Field suggests that the unfaulted section is relatively impermeable. Part of the subregional fluid flow is channeled laterally along sand carrier beds out of the basin

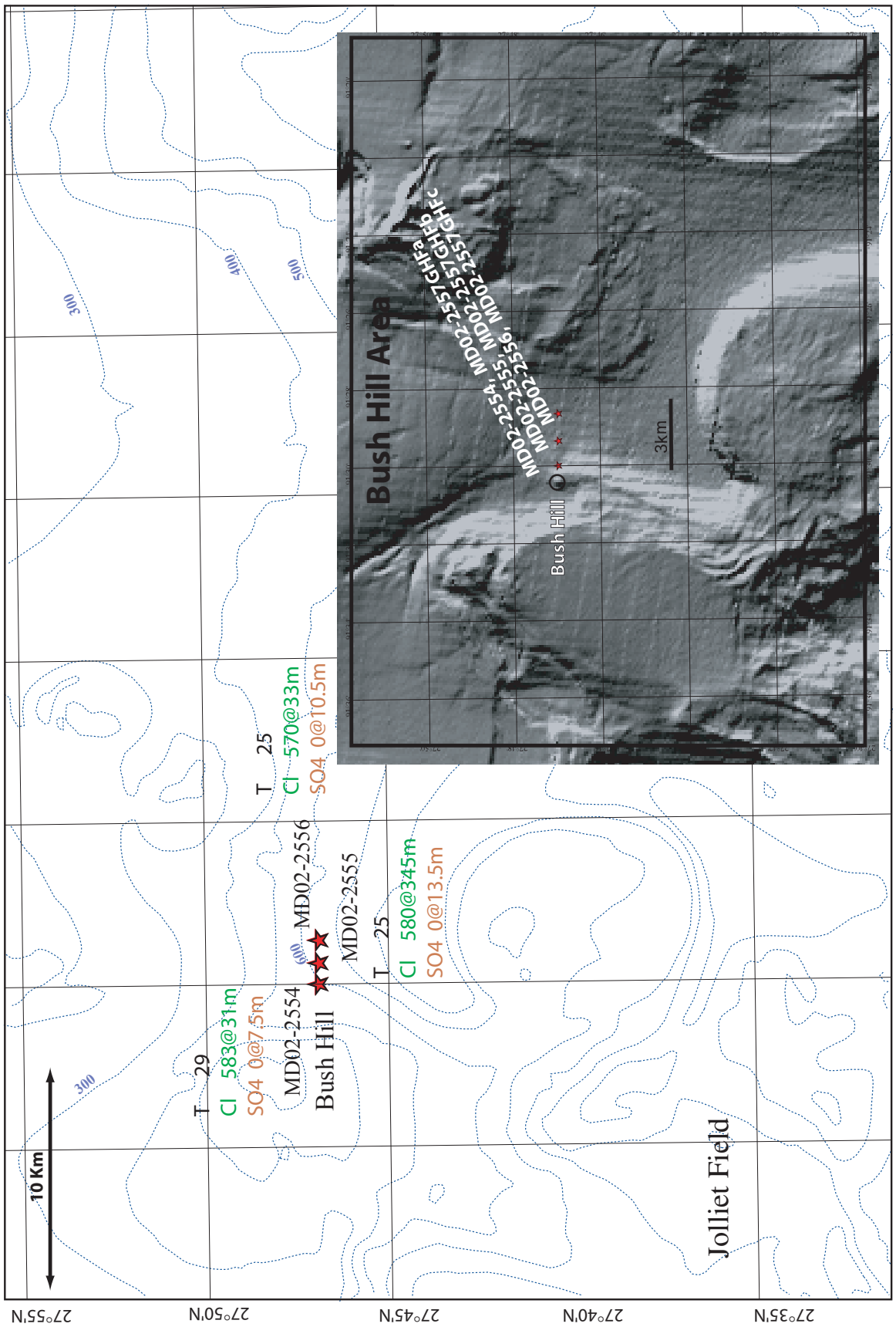

Figure 4. Giant piston core sites adjacent to Bush Hill. Core measurements: T = geothermal gradient (degrees Celsius per kilometer); Cl = chloride ion concentration (micrometers) maximum at the corresponding depth (meters below sea floor); SO_4 = sulfate ion concentration (micrometers) minimum at the corresponding depth (meters below sea floor) indicative of the depth to the sulfate-methane interface (SMI).

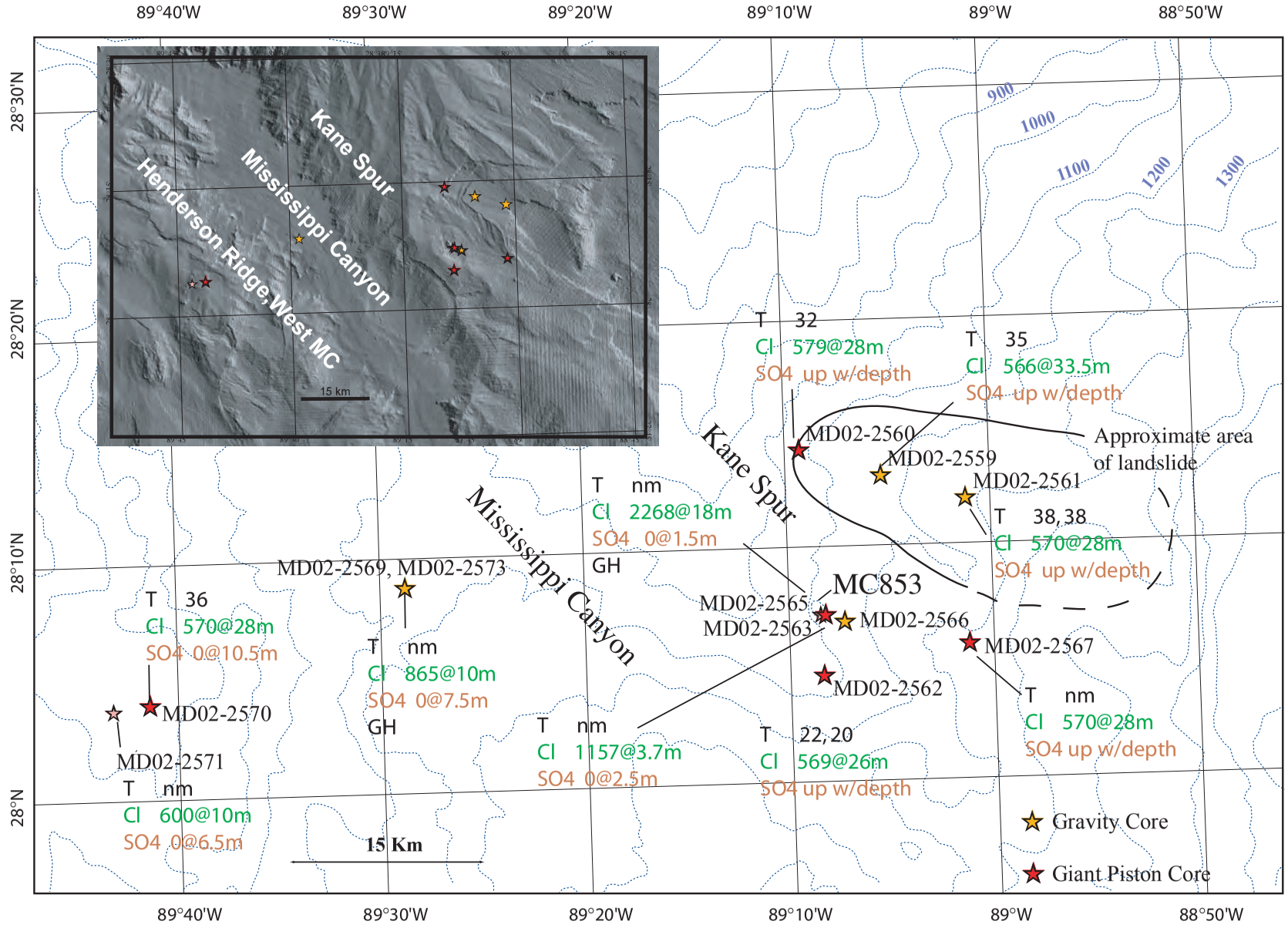

Figure 5. Core sites in the Mississippi Canyon region. Contours are in meters. Gravity and giant piston cores are noted with yellow and red stars, respectively. Core measurements: T = measured geothermal gradient (degrees Celsius per kilometer); Cl = chloride ion concentration (micrometers) maximum at the corresponding depth (meters below sea floor); SO_4 = sulfate ion concentration (micrometers) minimum at the corresponding depth (meters below sea floor) indicative of the depth to the sulfate-methane interface (SMI), up w/depth = SO_4 concentration increases with depth; nm = not measured.

to a major fluid-flow release point over the shallow salt on MC853 (Sassen, Losh, and others, 2001).

West Mississippi Canyon

West Mississippi Canyon is an area with widespread sea-floor deformation, shallow structures, and gas hydrate (fig. 5). Cooper and Hart (2003) found irregular and diffuse HRZs above diapiric structures, along high angle fault zones, laterally within layered and chaotic stratal units bounded by faults, and adjacent to acoustic wipeout zones. Gas is the likely cause of the high reflectivity; thus, localized concentrations of upward migrating gas are moving into shallow reservoirs adjacent to faults potentially forming gas hydrate. In other areas of the Gulf of Mexico's upper continental slope where acoustic wipeout zones and diffuse HRZs are seen, massive deformation, flow units, gas hydrate, and diagenetic carbonates are found within the near-sea-floor sediments (Roberts, 2001).

Results and Discussion

Sediment gas extracted from 99 samples from 23 holes was classified according to the origin of the gas (table 2): microbial (M), mainly microbial methane with some thermogenic hydrocarbons (X), and mainly thermal hydrocarbons with some microbial methane (TX). Sample depths ranged from 90 to 3,740 cm below the sea floor. Eight free-gas samples were collected and analyzed.

Tunica Mound

Gas concentrations measured on the flank of Tunica Mound (fig. 2) were highest very near the crest of a subsidiary diapir-like structure characterized by signs of active fluid flow. Methane concentrations in the nine-hole transect ranged from 24,000 μL/L in core MD02-2535 to 6 μL/L in core MD02-2538 (figs. 6–9; table 2). Methane's carbon isotopic composition ranged from –98.30 ppt PDB in core MD02-2545 to –61.20 ppt in core MD02-2543; thus, all values fall within the range expected of microbially sourced methane. Ethane and higher molecular weight hydrocarbon gas concentrations were low along the transect with the highest concentration found at a depth of about 27 m in core MD02-2535. The gas near the mound is interpreted to be from mainly microbial sources with some mixture of microbial and thermal sources (table 2). Likely input of thermogenic gases are limited to within the mound (not successfully cored because of armoring by carbonate) and very near the mound. In general, the isotopic signature of methane was found to be lighter than expected for the entire study area. Sassen and others (2003) have speculated that a deep-seated source of microbial gas exists in the north-

Table 3. Composition of hydrocarbon gas and carbon dioxide of free gas normalized to methane. Free gas was collected by drilling a hole into the core liner and inserting a syringe to collect gas.

[cm, centimeters; ppm, parts per million]

Sample ID core/depth (cm)	CO_2	C_1	C_2	C_3	iC_4	nC_4	neo-C_5	iC_5	n-C_5	c C_5	2,2MC_4	2MC_5
	ppm											
2537	6,261	993,343	360.93	7.75	0.63	0.74	3.01	0.04	0.06	0.00	0.00	0.68
2546 1600	2,259	997,076	591.85	2.33	0.64	0.64	5.02	0.00	0.00	0.02	0.00	2.24
2554 1642	8,326	991,287	352.42	4.08	0.11	0.17	2.31	0.00	0.04	0.01	0.00	1.11
2555 423	6,314	993,620	16.42	2.45	0.21	0.44	3.87	0.00	0.04	0.01	0.00	1.57
2565	24,872	919,972	24,646	23,540	3,508.43	2,524.31	31.68	560.12	123.51	37.96	16.89	34.69
2570 1500	7,072	992,217	290.34	292.62	61.86	45.38	2.96	10.68	2.43	0.43	0.25	0.66
2570 1800	5,074	994,809	84.64	6.31	0.55	0.48	1.69	0.12	0.06	0.00	0.00	0.53
2570 2000	6,099	993,769	85.89	6.01	0.44	0.00	2.96	0.00	0.00	0.00	0.00	1.97

Sample ID core/depth (cm)	3MC_5	n-C_6	McC_5	n-C_7	McC_6	C_1/C_2+C_3	iC_4/nC_4	iC_5/nC_5	C_1	CO_2	C_2	C_3
	ppm								$\delta^{13}C$	$\delta^{13}C$	$\delta^{13}C$	$\delta^{13}C$
2537	0.68	6.28	15.22	0.99	0.00	0.00	0.85	0.66	-82.19			
2546 1600	2.24	20.67	39.29	2.86	0.00	0.00	1.00		-72.24			
2554 1642	1.11	8.85	16.99	1.17	0.12	0.00	0.62	0.00	-84.24			
2555 423	1.57	13.59	25.33	2.04	0.00	0.00	0.48	0.00	-88.27			
2565	34.69	54.66	37.89	20.29	14.20	4.58	1.39	4.53	-61.83	-13.54	-29.79	-26.5
2570 1500	0.66	2.11	1.21	0.46	0.21	0.00	1.36	4.40	-70.11			
2570 1800	0.53	5.90	14.81	1.37	0.53	0.00	1.14	2.13	-70.61			
2570 2000	1.97	14.11	20.17	1.10	0.15	0.00			-70.28			

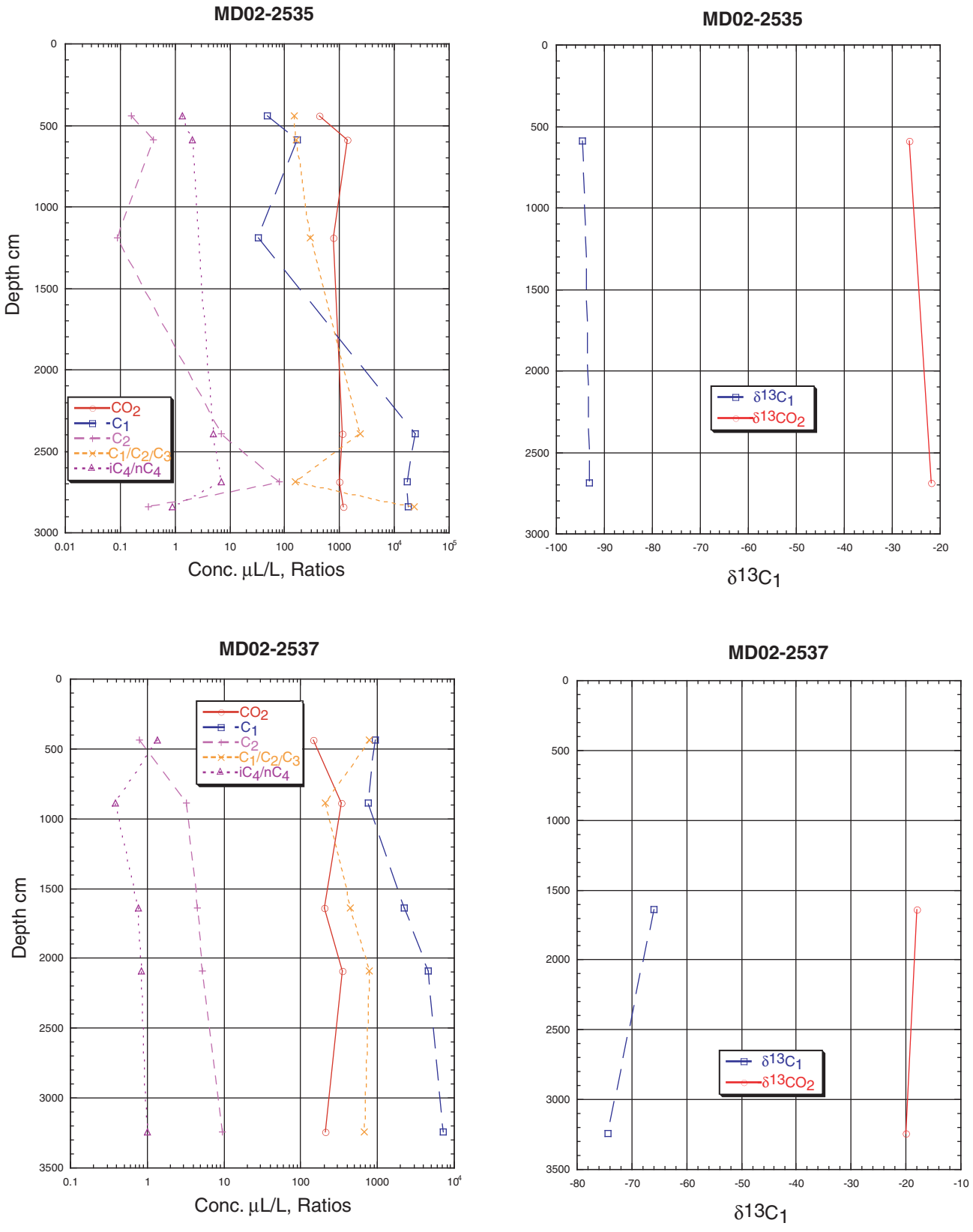

Figure 6. Plots of diagnostic sediment gas molecular composition and hydrocarbon ratios for cores MD02-2535 and MD02-2537. Core locations are shown in figure 2.

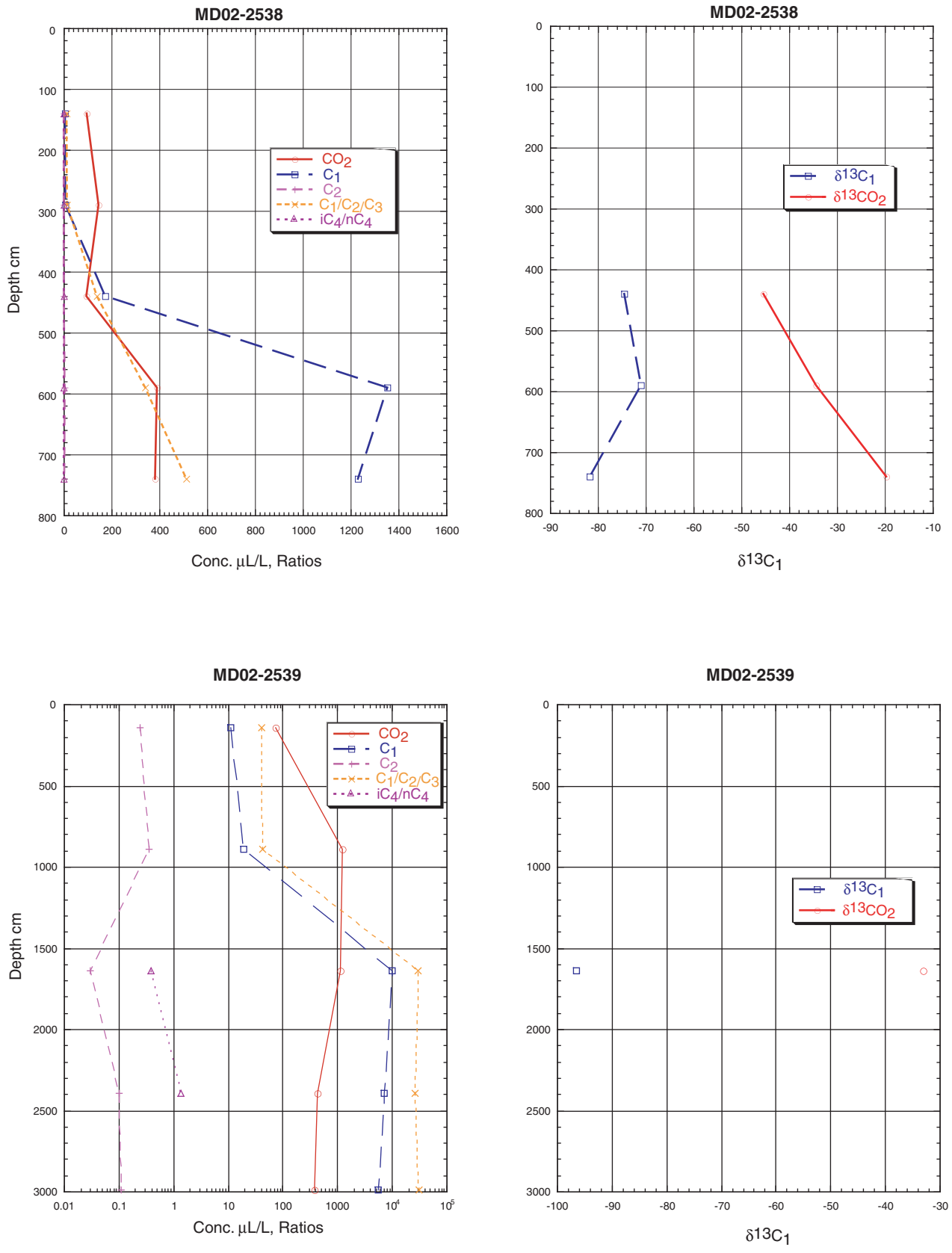

Figure 7. Plots of diagnostic sediment gas molecular composition and hydrocarbon ratios for cores MD02-2538 and MD02-2539. Core locations are shown in figure 2.

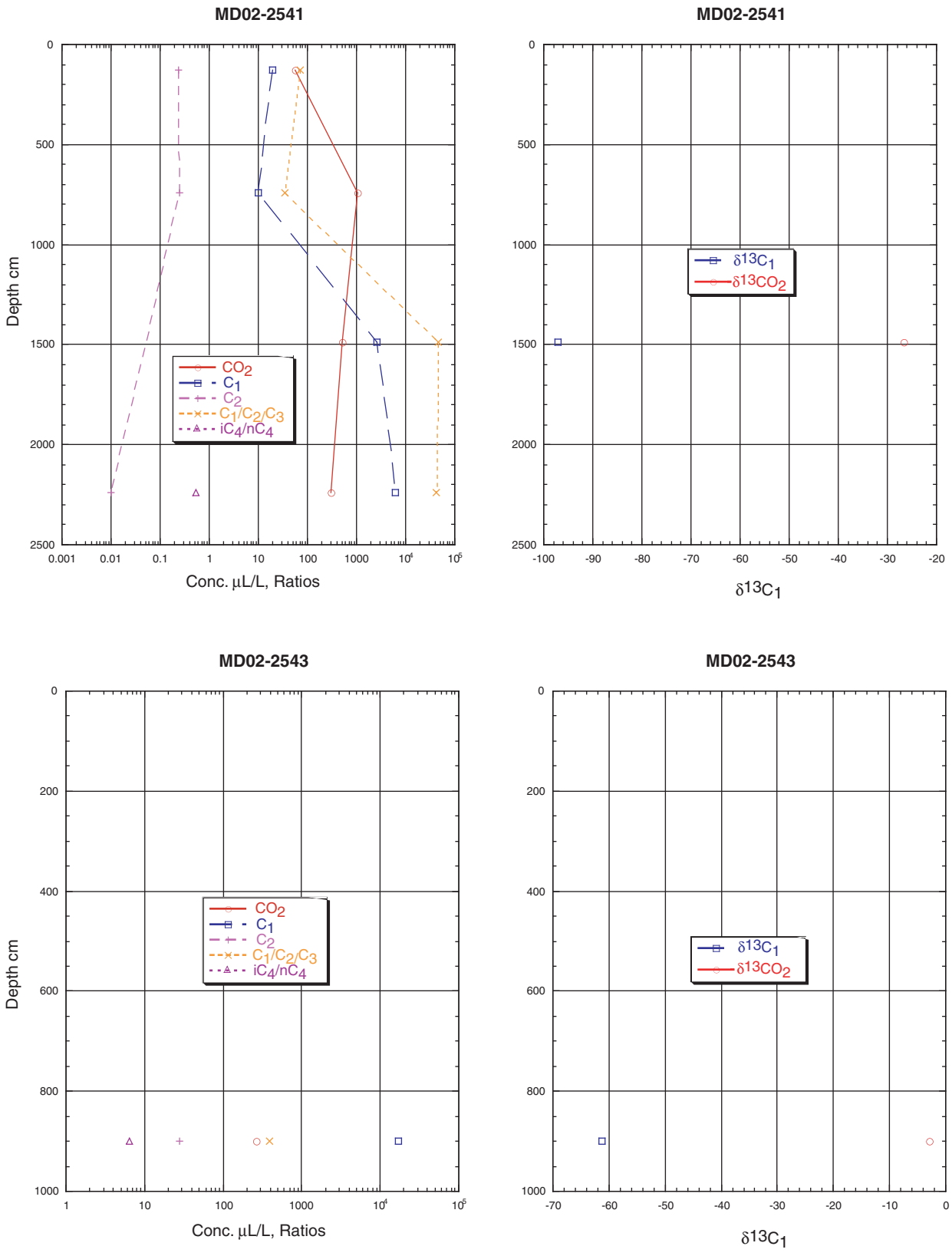

Figure 8. Plots of diagnostic sediment gas molecular composition and hydrocarbon ratios for cores MD02-2541 and MD02-2543. Core locations are shown in figure 2.

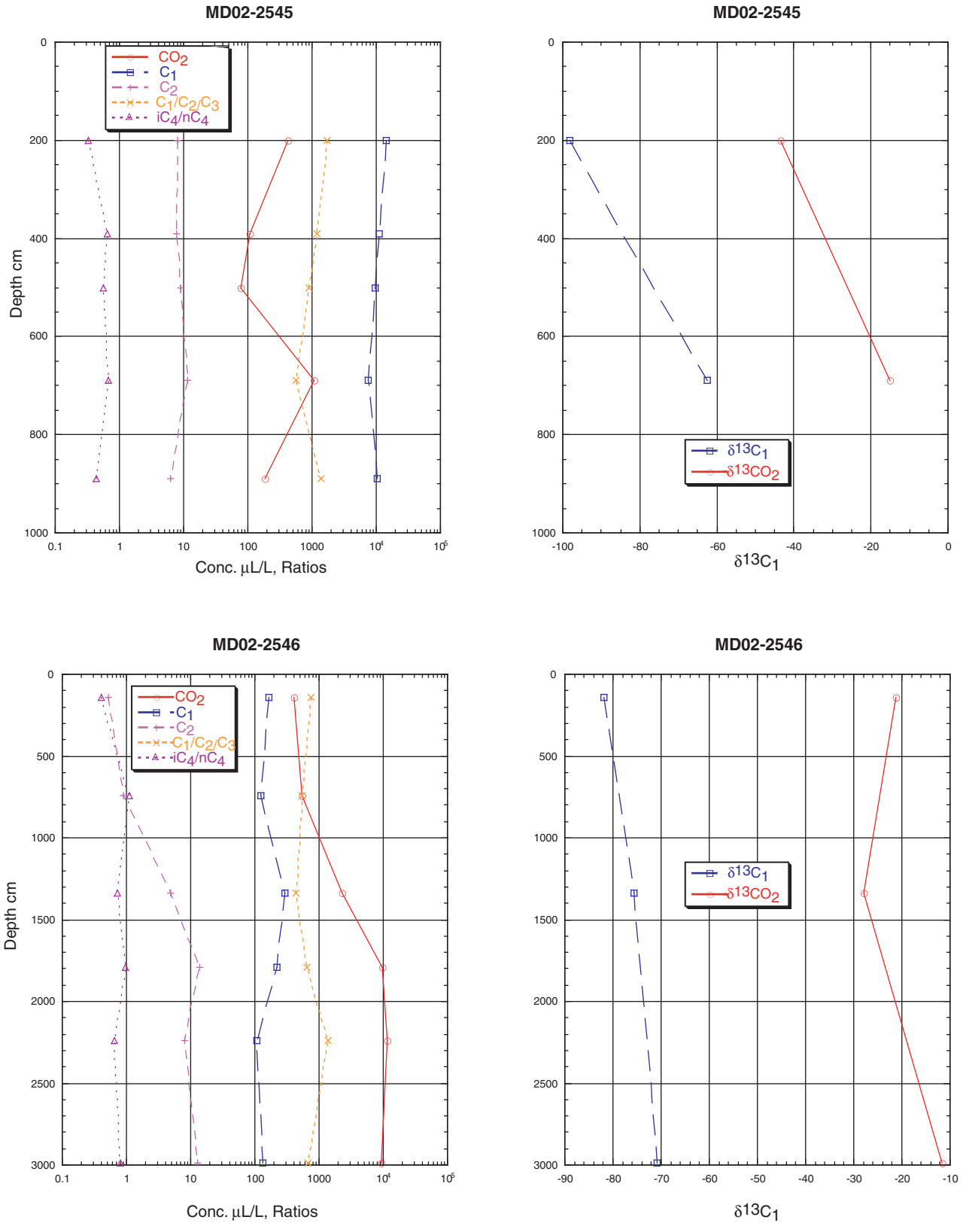

Figure 9. Plots of diagnostic sediment gas molecular composition and hydrocarbon ratios for cores MD02-2545 and MD02-2546. Core locations are shown in figure 2.

ern Gulf of Mexico, and this may be the case here and at other cored locations.

Free-gas samples were collected from cores MD02-2537 and 2546 (table 3). Gas concentrations were normalized to recovered methane values to eliminate the dilution effect of atmospheric gases that are considered artifacts of the sampling technique. Free-gas concentrations indicate that the gas is of microbial origin with greater than 99-percent methane, less than 0.1-percent ethane, and up to about 8-ppm propane. The methane is of microbial carbon isotopic composition ranging from –82.2 ppt to –72.2 ppt. The above data and the presence of high chloride concentrations (up to 2,100 mM) and shallow sulfate-methane interface (SMI, 0 to 13.5 mbsf) (Ussler and Paull, this volume, chapter 8) are consistent with fluid flow along high-angle faults flanking diapers. All indications of active fluid flow are near background levels approximately 4 km from the mound. The SMI ranges from 12 to 15 mbsf here with chloride concentrations very near those of seawater (about 560 millimoles (mM)), and the hydrocarbon gas composition is indicative of strictly a microbial source of methane.

Pigmy Basin

One gas sample was collected and analyzed from core MD02-2553 (fig. 3) within Pigmy Basin. The methane concentration was low, 136 μL/L, with a carbon isotopic composition of –45.7 and a similar carbon isotopic composition in CO_2 of –23.8‰. This thermogenic $\delta^{13}C$ coupled with a low concentration of methane indicate that the methane pool likely has been oxidized by methanotrophs (fig. 10; table 2). Higher hydrocarbons are at very low concentrations, and it is concluded that Pigmy Basin may be characterized by microbial sources of methane.

Bush Hill

Beginning on the eastern flank of Bush Hill, three cores were taken at 2-km intervals into the adjoining basin (fig. 4). Methane concentrations in the three-core transect ranged from 19,800 μL /L in core MD02-2554 to 195 μL /L in core MD02-2555 (figs. 10 and 11; table 2). The carbon isotopic composition of methane ranges from –91.1 ppt PDB in core MD02-2545 to –72.8 ppt in core MD02-2543; thus, all values fall within the isotopic range expected of microbially sourced methane. The highest concentration of ethane and higher molecular weight hydrocarbon gases were found in core MD02-2554 at a depth of about 3 m. Elsewhere, concentrations were low.

Free-gas samples were collected from cores MD02-2554 and MD02-2555 (table 3). Gases from these samples are of microbial origin with greater than 99-percent methane, less than 0.05-percent ethane, and up to about 4-ppm propane. The microbial-sourced methane has carbon isotopic composition ranging from –88.3 to –84.2 ppt.

Chloride concentrations are nearly those of seawater but increase to 583 mM in core MD02-2554, indicating the slight presence of fluid flow associated with salt dissolution. Shallow SMI's range from about 7.5 to 13.5 mbsf (Ussler and Paull, this volume, chapter 8) indicative of a substantial methane flux (Borowski and others, 1996). It is concluded that the hydrocarbon gases here are of microbial origin.

Because a number of experiments were being conducted in situ, Bush Hill itself was not cored where gas hydrate previously has been sampled. Structure II gas hydrate is abundant at Bush Hill (Sassen, Sweet, and others, 2001a) and indicates some spatial and temporal variation in composition and isotopic properties. Vein-filling gas hydrate has been discovered at Bush Hill, and this may be indicative of rapid fluid flow (Ginsburg and Soloviev, 1998). It appears that such fluid flow is bringing thermogenic hydrocarbon gases to a small venting area on the sea floor.

Two vent-gas samples collected from Bush Hill in 1998 (Sassen and others, 1998) contained thermogenic methane (90.4 to 95.9 percent) and individual C2–C5 hydrocarbons decreasing in concentration with increasing molecular weight. The $\delta^{13}C$ of this vent methane varies between –44.1 ppt and –46.0 ppt, and the δD varies between –198 ppt and –200 ppt standard mean ocean water (SMOW). The $\delta^{13}C$ of the CO_2 of the vent gas ranges from –4.9 ppt to –5.4 ppt and is consistent with a thermogenic origin of the gas. The $\delta^{13}C$ of Bush Hill gas hydrate methane had isotopic values similar to the vent gas with $\delta^{13}C$ and δD of methane at –43.6 ppt and –167 ppt, respectively, and CO_2 $\delta^{13}C$ of +17.5 ppt. Relative to the vent gases from which it likely precipitated, the gas hydrate-bound gases, including methane, occur in lower concentrations (72.1 percent), and the higher molecular-weight hydrocarbons occur in higher amounts (Sassen, Sweet, and others, 2001a).

Mississippi Canyon Region

Kane Spur

Methane concentrations in five cores ranged from 1,670 μL/L (core MD02-2559) to 6 μL/L (core MD02-2555) (figs. 12, 13, 14, and 15; table 2). The $\delta^{13}C$ of methane ranged from –93.6 ppt PDB in core MD02-2560 to –62.6 ppt in core MD02-2561, with all values falling within the isotopic range expected of microbially sourced methane. Ethane and higher molecular weight hydrocarbon gas concentrations were low in each of the five cores with the highest concentration of ethane found in core MD02-2567 (5.14 μL/L) at a depth of 13.4 m. It is concluded that the minor volumes of gas present in the upper 35 m of sediment on Kane Spur are of microbial origin.

Chloride concentrations are the same as seawater, between 566 to 579 micromoles (μM), indicative of the lack of fluid flow associated with salt dissolution within the upper 35 m of sediment. The SMI in this area is deeper than the cores and could not be penetrated. In addition, the sulfate con-

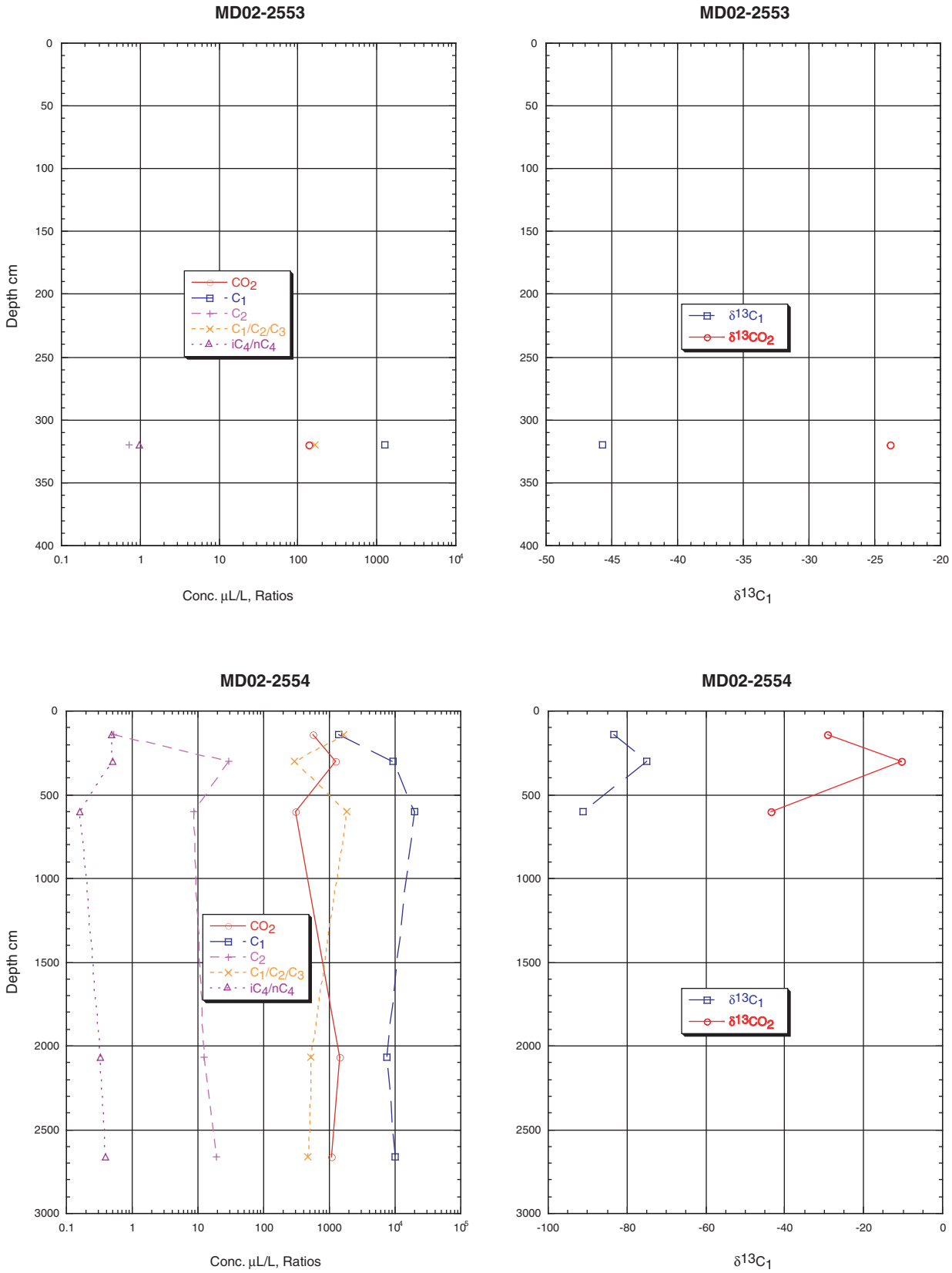

Figure 10. Plots of diagnostic sediment gas molecular composition and hydrocarbon ratios for cores MD02-2553 and MD02-2554. Core locations are shown in figures 3 and 4.

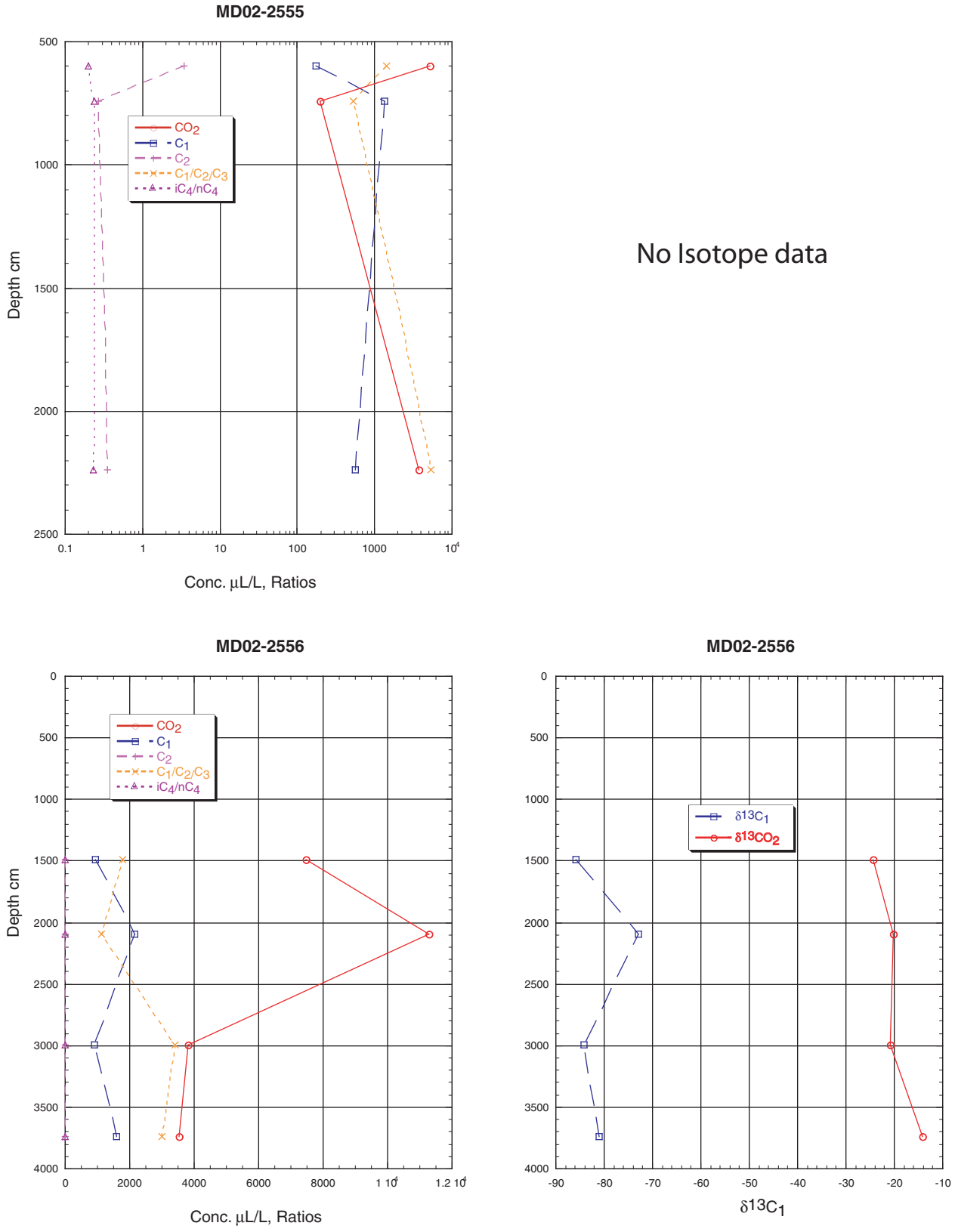

Figure 11. Plots of diagnostic sediment gas molecular composition and hydrocarbon ratios for cores MD02-2555 and MD02-2556. Core locations are shown in figure 4.

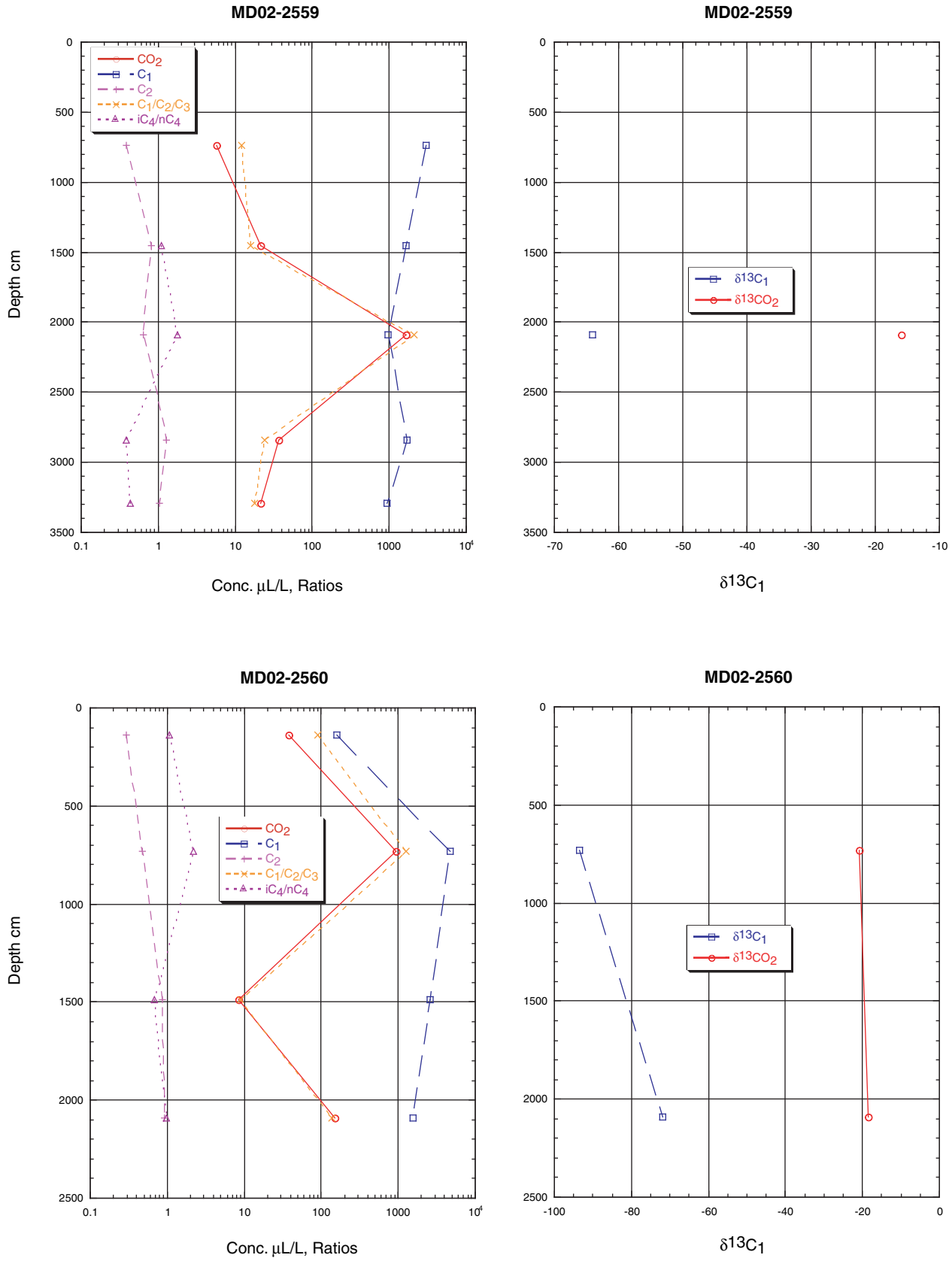

Figure 12. Plots of diagnostic sediment gas molecular composition and hydrocarbon ratios for cores MD02-2559 and MD02-2560. Core locations are shown in figure 5.

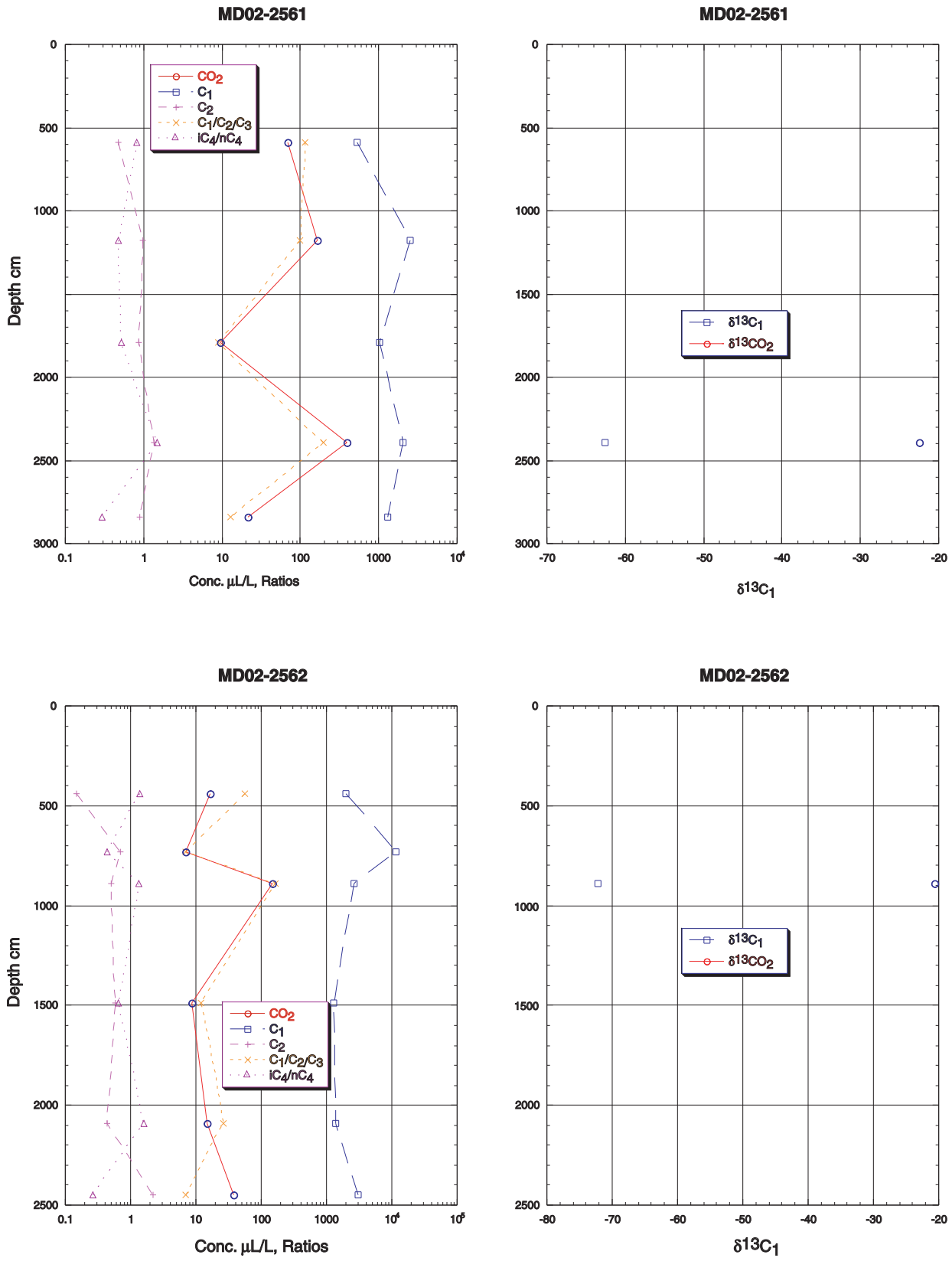

Figure 13. Plots of diagnostic sediment gas molecular composition and hydrocarbon ratios for cores MD02-2561 and MD02-2562. Core locations are shown in figure 5.

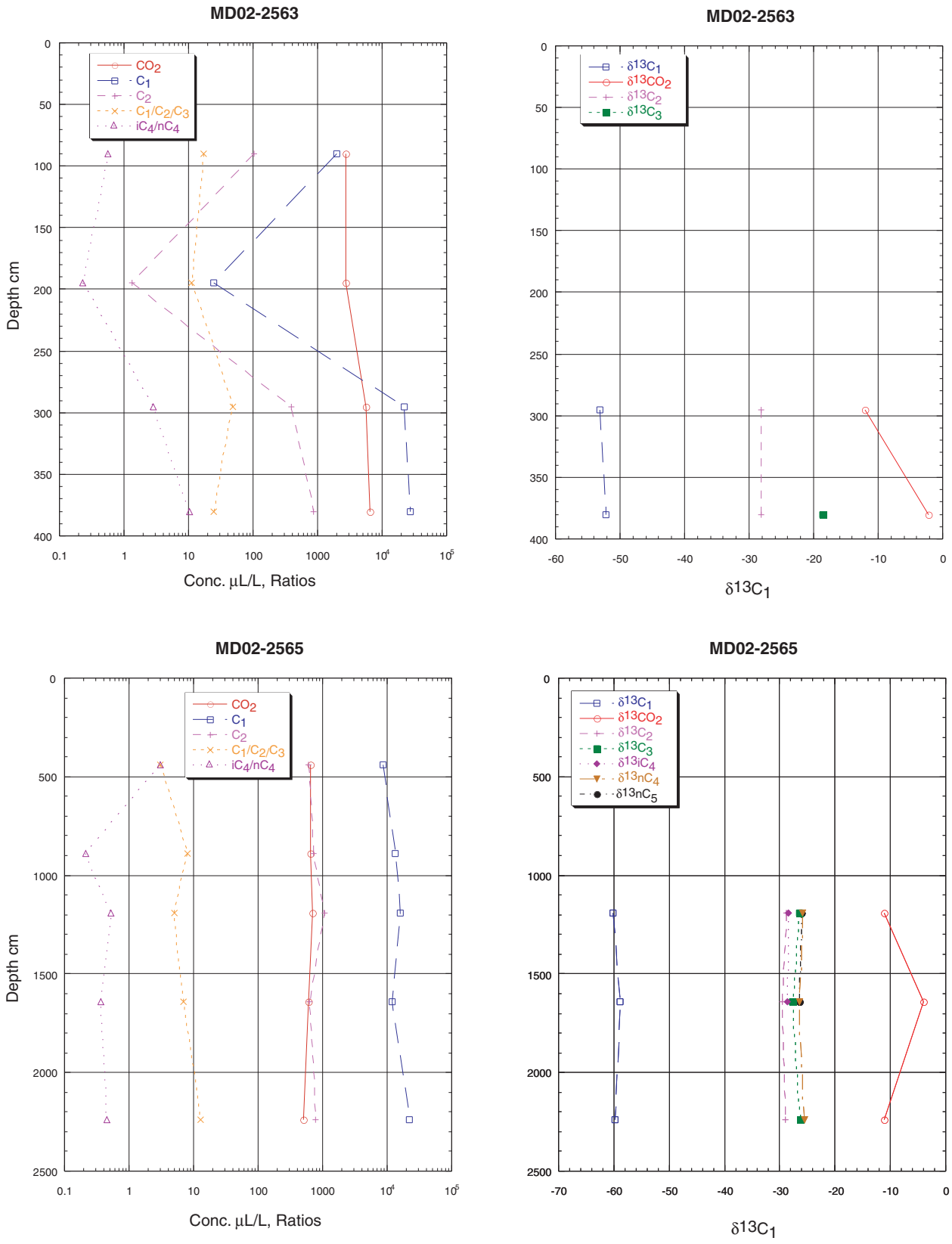

Figure 14. Plots of diagnostic sediment gas molecular composition and hydrocarbon ratios for cores MD02-2563 and MD02-2565. Core locations are shown in figure 5.

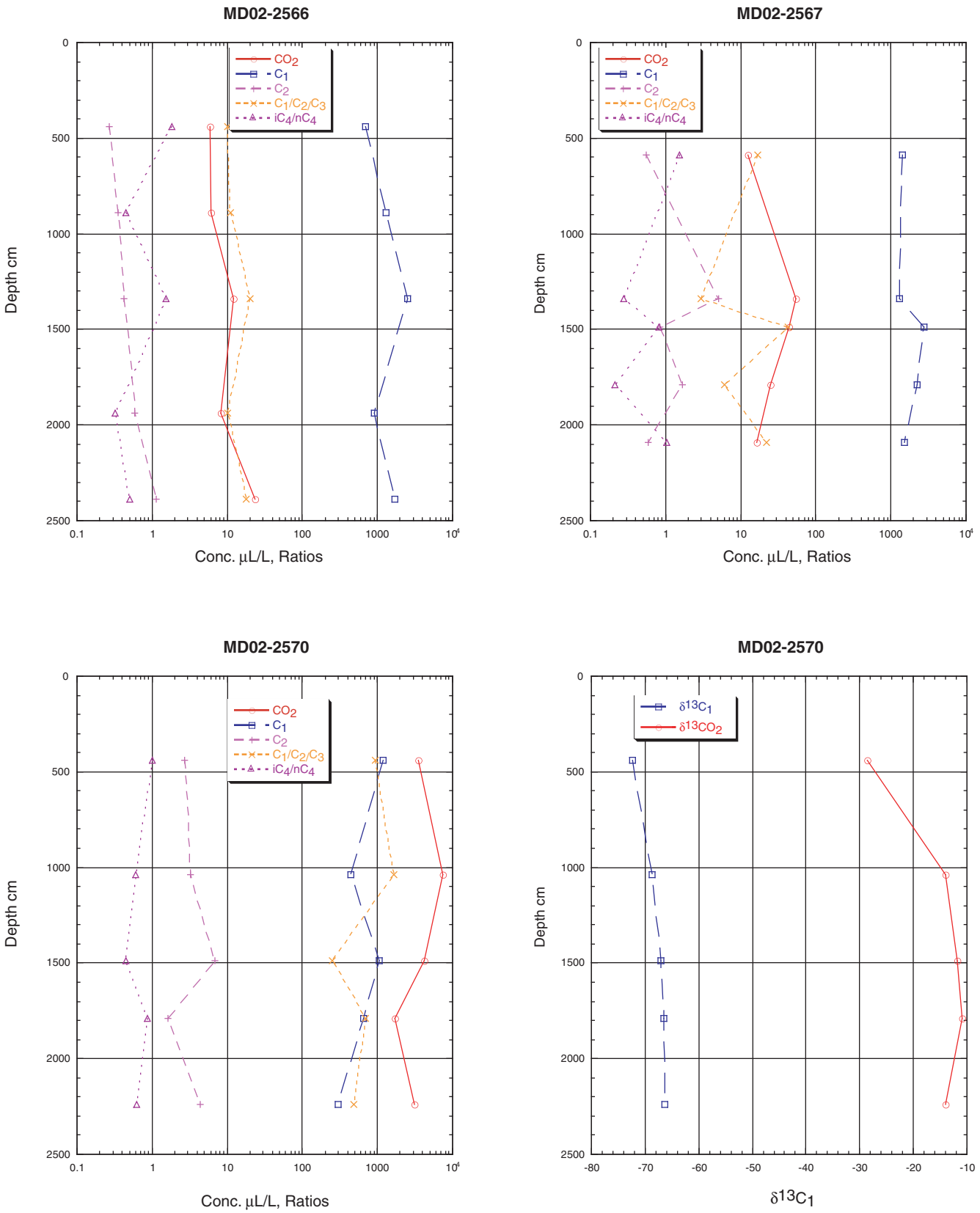

Figure 15. Plots of diagnostic sediment gas molecular composition and hydrocarbon ratios for cores MD02-2566, MD02-2567, and MD02-2570. Core locations are shown in figure 5.

centrations increase slightly with depth (Ussler and Paull, this volume, chapter 8), indicative of very little methane flux. It is concluded that the minor volumes of gas present in the upper 35 m of sediment on Kane Spur are of microbial origin.

MC853

A three-hole transect beginning near the MC853 diapir was cored. Core MD02-2566, notable for the lack of hydrocarbon gases, was taken on the southeast flank of the diapir. Two cores were taken on the summit of the diapir (MD02-2563 and MD02-2565) (fig. 5). These cores were noted for the presence of visible oil and gas of clearly thermogenic origin. Both cores contained disseminated gas hydrate, with the majority found in core MD02-2565 as indicated by over-pressuring that resulted in the upper 3 to 4 m of core exploding out of the core barrel and into the ocean. Although gas hydrate was not preserved or analyzed from this core, vigorous bubbling in the water adjacent to the ship confirmed the presence of gas hydrate (Lorenson and others, 2002).

Methane concentrations in the three-hole transect ranged from 27,300 µL/L in core MD02-2563 to 6 µL/L in core MD02-2566 (figs. 14 and 15; table 2). The $\delta^{13}C$ of methane spans from –52.2 ppt in core MD02-2563 to –60.1 ppt in core MD02-2565. These values fall within the isotopic range expected of microbially sourced methane; however, the visible presence of oil and higher molecular weight hydrocarbon gases in the core clearly confirm the presence of thermogenic hydrocarbons. Ethane and higher molecular weight hydrocarbon gas concentrations were higher near and on the diapir, with the highest ethane concentration of 1,060 µL/L found in core MD02-2565 at a depth of 12 m. The carbon isotopic composition of ethane was –28.8 ppt, indicative of a thermal origin.

In addition to ethane, higher molecular weight hydrocarbons up to normal pentane were analyzed for $\delta^{13}\mathbf{C}$. Typically the carbon isotopic composition of hydrocarbon gas becomes heavier with increasing carbon number; however, isobutane $\delta^{13}\mathbf{C}$ is lighter (–28.5 ppt) than propane (–27.6 ppt) or normal butane (–26.5 ppt). Typically, this result is an indication of either multiple sources or that some fractionation is occurring between the sediment gas and gas hydrate. Because there is no compelling evidence of multiple thermogenic sources of gas, the isotopic fractionation of isobutane into Structure II gas hydrate is likely. Gas hydrate gas composition from this diapir has been described previously by Sassen, Sweet, and others (1999) and by Sassen and others (2001b). Because they measured about 75-percent methane in four samples with a mean $\delta^{13}\mathbf{C}$ of –46.6 ppt, a thermal source of methane and other hydrocarbon gases was suggested. The carbon isotopic composition of higher molecular weight hydrocarbons also showed the same trend described above for sediment gases. Thus, it is concluded that the sediment gas reflects the composition of gas hydrate here with the notable exception of methane. Methane is preferentially excluded by gas hydrate formation in favor of higher molecular weight hydrocarbons and is isotopically heavier (Sassen, Sweet, and others, 2001a).

Free gas collected from core MD02-2565 (table 3) is of mixed microbial and thermal origin. Gas measured from this core is composed of 92-percent methane, 2.5-percent ethane, 2.3-percent propane, and other higher weight hydrocarbon gases. The carbon isotopic composition of methane is –61.8 ppt, suggesting a microbial origin and indicating that there is a significant contribution of methane from microbial sources in addition to the obvious presence of thermogenic higher molecular weight hydrocarbons.

Chloride concentrations in core MD02-2566 are nearly those of seawater, indicating little fluid flow; however, the chloride concentrations are much higher (up to 2,270 µM in core MD02-2565) on the diapir, suggesting rapid fluid flow. Sulfate concentrations are higher than seawater values in core MD02-2566, similar to those on Kane Spur (Ussler and Paull, this volume, chapter 8). On the diapir, the SMI is shallow and ranges from about 1.5 to 2.5 mbsf (Ussler and Paull, this volume, chapter 8), indicative of a substantial methane flux. It is concluded that the hydrocarbon gases here are mainly thermogenic with a component of microbially sourced methane.

West Mississippi Canyon

In this region, gas chimneys and shallow faults were observed very near the sea floor by Cooper and Hart (2003) and in the thalweg of Mississippi Canyon on lease block MC802 where gas hydrate previously had been observed (Sassen and others, 1994). Gas hydrate was recovered within MC802 in cores MD02-2569 and 2573, both taken on top of the same sea-floor mound, but only in adequate amounts to obtain gas analyses from core MD02-2569. Heat-flow measurements were planned for core MD02-2573, but the core barrel was bent during recovery, making those measurements impossible. However, visible gas hydrate was found in the core-catcher. It is assumed the core met refusal at a gas hydrate layer or an authigenic carbonate layer, which caused the barrel to bend.

Methane concentrations measured in three cores from this area ranged from 19,900 µL/L (core MD02-2573) to 1,410 µL/L (core MD02-2569) (figs. 15 and 16; table 2). The methane $\delta^{13}\mathbf{C}$ values ranged from –72.4 ppt PDB in core MD02-2570 to –59.5 ppt in core MD02-2569, therefore, all values fall within the isotopic range expected of microbially sourced methane. Ethane and higher molecular weight hydrocarbon gas concentrations generally were low with the highest ethane concentration of 70.7 µL/L found in core MD02-2573 at a depth of 2.6 m.

Three free-gas samples were collected from core MD02-2570 at depths of 15, 18, and 20 m (table 3). These samples were composed primarily of methane (99 percent) with smaller amounts of ethane (0.03 percent) and propane (300 ppm), indicating mainly a microbial origin. A modest amount of thermogenic hydrocarbons was found in the shallowest sample (15 m) while the lower samples had much less, suggesting some vertical heterogeneity or lateral gas migration

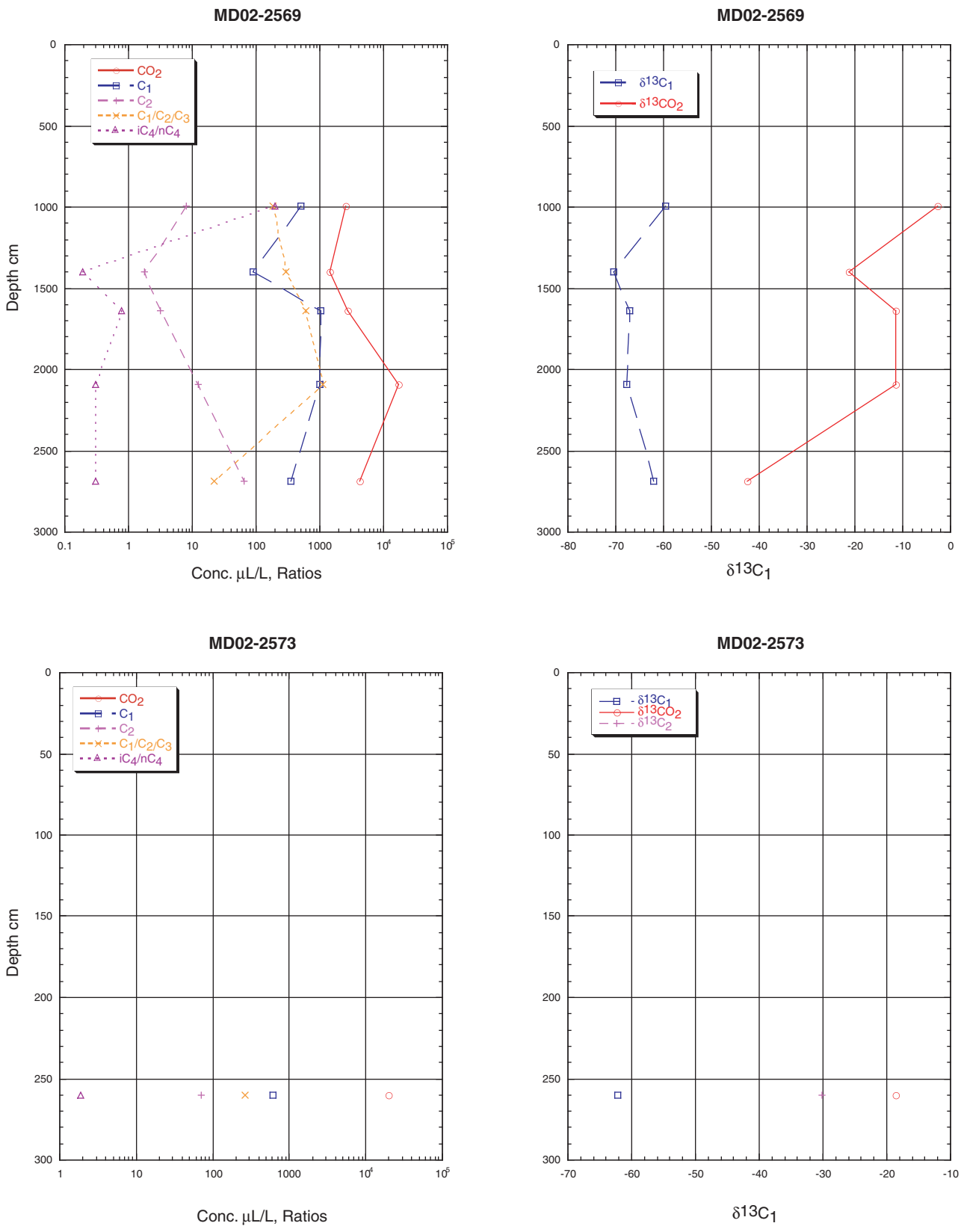

Figure 16. Plots of diagnostic sediment gas molecular composition and hydrocarbon ratios for cores MD02-2569 and MD02-2573. Core locations are shown in figure 5.

pathways. The mean $\delta^{13}C$ of methane (–70.3 ppt) suggests a microbial origin.

Lenticular bodies of gas hydrate were sampled in core MD02-2569 at two depths—3.8 and 7.0 mbsf. Results of controlled gas hydrate dissociation are presented in table 4. The quality of the gas hydrate recovered was poor because of core recovery time approaching 2 hours. Low gas-to-water ratios from dissociated samples with a maximum of 33 (170 for a fully saturated gas hydrate; Lorenson, 2000) confirmed that the samples had previously decomposed.

The composition of gas hydrate principally is methane, 95.0 to 99.5 percent, followed by CO_2 concentrations ranging from 0.16 to 4.0 percent. Higher molecular weight hydrocarbon gases—ethane, propane, and isobutane—are found in concentrations exceeding 1,000 ppm, suggesting that both structure I and structure II gas hydrate are present. The lack of normal butane suggests that gas hydrate formation here is from lean thermogenic gas (for example, the free-gas composition) selectively incorporating isobutane. A similar effect has been noted by Lorenson and others (1999) in Arctic gas hydrate accumulations.

Chloride concentrations are nearly equal to those of seawater in core MD02-2570, indicating little fluid flow associated with diapirism; however, the presence of gas and shallow faults in the seismic records (this volume, Appendix D) indicate the flow of gas without salt. Chloride concentrations are much higher (865 mM) in core MD02-2569, suggesting fluid flow associated with salt. Unpublished industry 3–D seismic records suggest the MD02-2569 site is likely a diapiric structure. The SMI is shallow and ranges from 10.5 to 7.5 mbsf (Ussler and Paull, this volume, chapter 8), indicating substantial methane flux. In conclusion, the hydrocarbon gases here are of mainly microbial origin with a component of thermogenic hydrocarbons at site MD02-2569.

Summary of Gas Origins

The majority of hydrocarbon gases encountered in this study are of microbial origin. Sassen and others (2003) have speculated that there is a deep-seated source of microbial gas in the northern Gulf of Mexico, and this observation agrees with our data.

Thermogenic gases are present in cores that are on or very near sea-floor features that exhibit active fluid venting. These areas typically are along the rims of salt withdrawal basins and

Table 4. Composition of hydrocarbon gas and carbon dioxide of gas hydrate gas normalized to methane. Gas was collected in syringes after controlled dissociation.

[ppm, parts per million; cm, centimeter; mL, milliliter]

Sample	CO_2	C_1	C_2	C_3	iC_4	nC_4	neo-C_5	iC_5	n-C_5	c C_5	2,2MC_4	2MC_5
	ppm											
2569 380 cm Vial 2	2,700	994,890	1,843.87	460.30	43.50	0.00	29.22	14.42	1.77	0.00	3.02	9.10
2569 380 cm Vial 3	40,202	949,767	7,590.37	1,079.97	1,084.72	6.42	107.47	29.03	0.00	0.00	7.33	26.31
2569 380 cm Vial 4	1,570	992,052	1,861.08	2,175.54	2,245.43	0.00	56.40	16.40	0.00	0.00	3.42	12.51
2569 700 cm Vial 3	11,407	980,376	4,093.25	1,757.19	2,208.34	0.00	61.42	12.27	0.00	0.00	2.75	10.09

Sample	3MC_5	n-C_6	McC$_5$	n-C_7	McC$_6$	Gas-to-water ratio (mL gas/mL water)	C_1/C_2+C_3	iC_4/nC_4	C_1 $\delta^{13}C$	CO_2 $\delta^{13}C$
	ppm									
2569 380 cm Vial 2	1.22	3.88	0.00	0.40	0.00	6.56	432	>1,000	-63.26	
2569 380 cm Vial 3	19.37	70.47	0.00	9.64	0.00	6.56	110	169	-62.12	-14.99
2569 380 cm Vial 4	1.85	4.27	0.00	1.74	0.00	6.56	246	>1,000	-63.11	
2569 700 cm Vial 3	8.87	51.85	0.00	11.26	0.00	33.14	168	>1,000	-54.62	

Note: Gas concentrations normalized to methane. Hydrogen and helium not measured.

active diapirism. In the northern Gulf of Mexico, this diapirism commonly is associated with saline fluids that limit the extent of the gas hydrate stability field to the near surface. Methane carbon isotopic composition in relation to the gas wetness ratio C_1/C_2+C_3 for core gas is plotted in figures 17 and 18. Primary fields representing accepted values for microbial and thermogenic sourced methane gas are noted. Most of the data fall outside these boundaries, likely reflecting mixing of microbial methane with thermogenic methane.

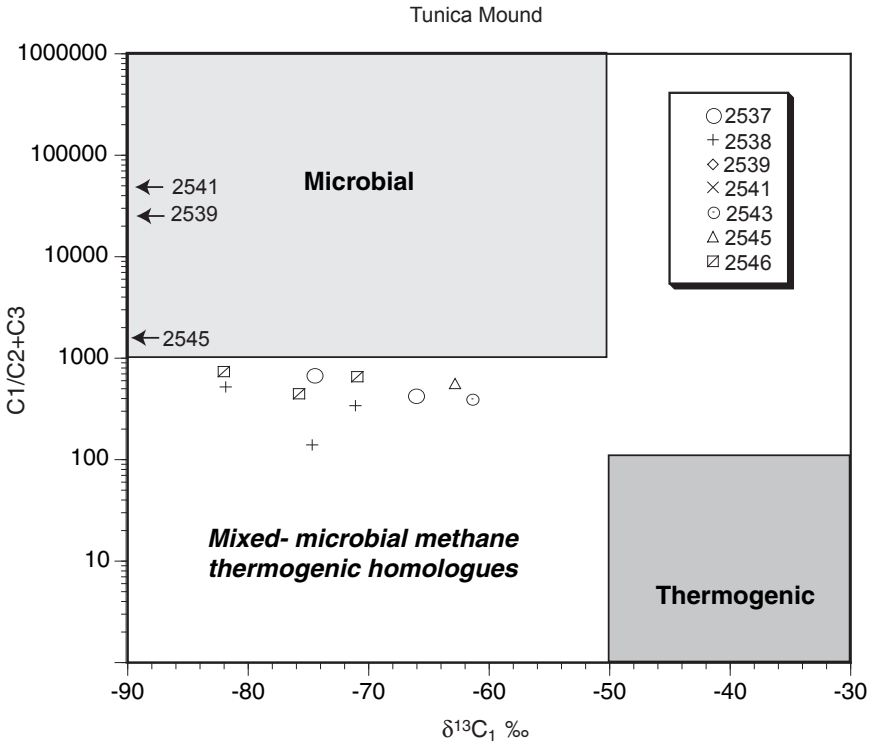

Figure 17. Plot of methane carbon isotopic composition in relation to the gas wetness ratio C_1/C_2+C_3 for Tunica Mound core gas. Primary fields representing accepted values for microbial and thermogenic-sourced methane gas are noted. Carbon isotopic compositions less than –90 are not plotted but are noted by core number with relative gas wetness ratios indicated by position on the y-axis.

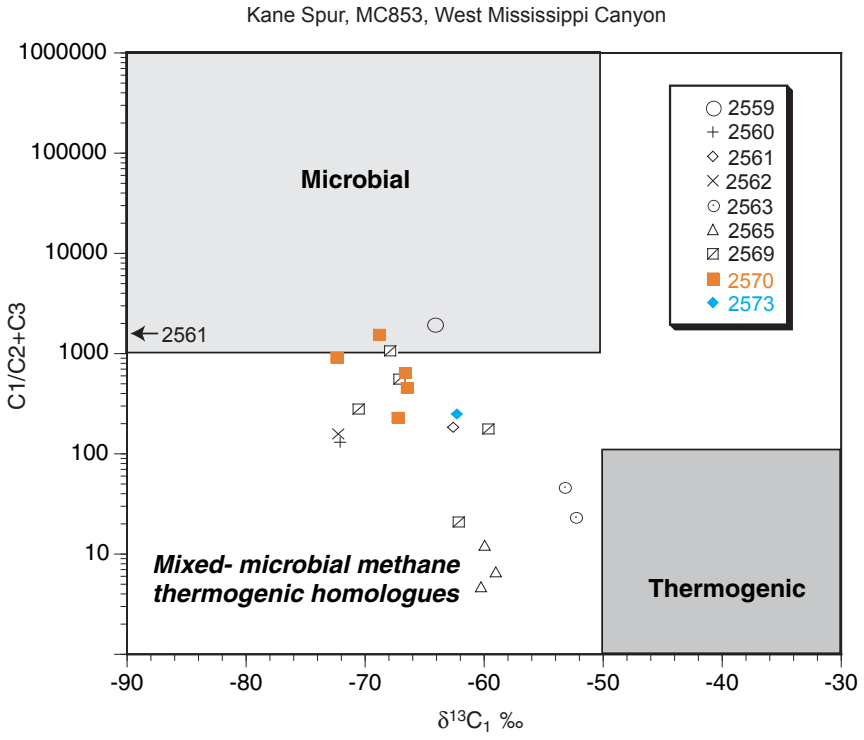

Figure 18. Plot of methane carbon isotopic composition in relation to the gas wetness ratio C_1/C_2+C_3 for Kane Spur (2559, 2560, 2561, and 2562), MC853 (2563 and 2565), and West Mississippi Canyon (2569, 2570, and 2573) core gas. Primary fields representing accepted values for microbial and thermogenic-sourced methane gas are noted. Carbon isotopic compositions less than –90 are not plotted but are noted by core number with relative gas wetness ratios indicated by position on the y-axis.

References

Aharon, P., and Fu, B., 2000, Microbial sulfate reduction rates and sulfur and oxygen isotope fractionations at oil and gas seeps in deepwater Gulf of Mexico: Geochimica et Cosmochimica Acta, v. 64, no. 2, p. 233–246.

Berryhill, H.L., Suter, J.R., and Hardin, N.S., 1987, Late Quaternary facies and structure, northern Gulf of Mexico: AAPG Studies in Geology, no. 23, 289 p.

Borowski, W.S., Paull, C.K., and Ussler, W., III, 1996, Marine pore-water sulfate profiles indicate in situ methane flux from underlying gas hydrate: Geology, v. 24, no. 7, p. 655–658.

Coleman, J.M., Prior, D.B., and Lindsay, J.F., 1983, Deltaic influences on shelf edge instability processes: SEPM Special Publication 33, p. 121–137.

Cook, D., and D'Onfro, P., 1991, Jolliet Field thrust structure and stratigraphy, Green Canyon Block 184, offshore Louisiana: Trans. —Gulf Coast Assoc. Geol. Soc., v. 41, p. 100–121.

Cooper, A.K., and Hart, P.E., 2003, High resolution seismic-reflection investigation of the northern Gulf of Mexico gas-hydrate-stability zone: Marine and Petroleum Geology, v. 19, p. 1275–1293.

Eaton, L.F., 1999, Drilling through deepwater shallow water flow zones at Ursa: Conference Proceedings Shallow Water Flows, October 6–8, 1999, Penn Well, Tulsa, OK, 600 p.

Ginsburg, G.D., and Soloviev, V.A., 1998, Submarine gas hydrates: St. Petersburg, Russia, VNII Okeangeologia, 216 p.

Goodwin, R.H., and Prior, D.B., 1989, Geometry and depositional sequences of the Mississippi Canyon, Gulf of Mexico: Journal of Sedimentary Petrologists, v. 59, no. 2, p. 318–329.

Kennicutt, M.C., II, Brooks, J.M., and Denoux, G.J., 1988, Leakage of deep, reservoired petroleum to the near surface of the Gulf of Mexico continental slope: Marine Chemistry, v. 24, p. 39–59.

Kvenvolden, K.A., Claypool, G.E., Threlkeld, C.N., and Sloan, D.E., 1984, Geochemistry of a naturally occurring massive marine gas hydrate, *in* Schenck, P.A., deLeeuw, J.W., and Lijmbach, G.W.M., eds., Advances in organic geochemistry 1983: Org. Geochem., v. 6, p. 703–713.

Kvenvolden, K.A., and Redden G.D., 1980, Hydrocarbon gas in sediment from the shelf, slope, and basin of the Bering Sea: Geochim. Cosmochim. Acta, v. 44, p. 1145–1150.

Lorenson, T.D., and Collett, T.C., 2000, Gas content and composition of gas hydrates from sediments of the southeastern North American continental margin, *in* Paull, C.K., Matsumoto, R., Wallace, P.J., and Dillon, W.P., eds., Proceedings of the Ocean Drilling Program, Scientific Results, v. 164: College Station, TX, p. 37–46.

Lorenson, T.D., Whiticar, M., Waseda, A., Dallimore, S.R., and Collett, T.S., 1999, Gas composition and isotopic geochemistry of cuttings, core, and gas hydrate from the JAPEX/JNOC/GSC Mallik 2L-38 gas hydrate research well: Geological Survey of Canada Bulletin 544, p. 143–163.

Lorenson, T.D., Winters, W., Hart, P.E., and Paull, C.K., 2002, Gas hydrate occurrence in the Northern Gulf of Mexico studied with giant piston cores: EOS, Transactions, American Geophysical Union, v. 83, no. 51 p. 601 and 607.

MacDonald, I.R., Boland, G.S., Baker, J.S., Brooks, J.M., Kennicutt, M.C., II, and Bidigare, R.R., 1989, Gulf of Mexico hydrocarbon seep communities—II. Spatial distribution of seep organisms and hydrocarbons at Bush Hill: Marine Biology, v. 101, p. 235–247.

MacDonald, I.R., Guinasso, N.L., Jr., Sassen, R., Brooks, J.M., Lee, L., and Scott, K.T., 1994, Gas hydrate that breaches the sea floor on the continental slope of the Gulf of Mexico: Geology, v. 22, p. 699–702.

MacDonald, I.R., Reilly, J.F., Jr., Best, S.E., Venkataramaiah, R., Sassen, R., Amos, J., and Guinasso, N.L., Jr., 1996, A remote-sensing inventory of active oil seeps and chemosynthetic communities in the northern Gulf of Mexico, *in* Schumacher, D., and Abrams, M.A., eds., Hydrocarbon migration and its near-surface expression: AAPG Memoir 66, p. 27–37.

Minerals Management Service, 2001, Shallow water flows in the northern Gulf of Mexico; accessed October 13, 2006, at *http://www.gomr.mms.gov/homepg/offshore/safety/wtrflow.html*

Roberts, H.H., 2001, Fluid and gas expulsion on the northern Gulf of Mexico continental slope—mud-prone to mineral-prone responses, *in* Paull, C.K., and Dillon, W.P., eds., Natural gas hydrate—occurrence, distribution, and dynamics: AGU Monograph Series, v. 24, p. 145–161.

Roberts, H.H., and Carney, R., 1997, Evidence of episodic fluid, gas and sediment venting on the northern Gulf of Mexico continental slope: Economic Geology, v. 92, p. 863–879.

Rowan, M.G., and Weimer, P., 1998, Salt-sediment interaction, northern Green Canyon and Ewing Bank (Offshore Louisiana), northern Gulf of Mexico: AAPG Bulletin, v. 82, p. 1055–1082.

Sager, W.W., and Kennicutt, M.C., 2000, Proposal for ocean drilling program research on gas hydrate in the Gulf of Mexico: Proceedings Offshore Technology Conference, 1, OTC 12111.

Sassen, R., Joye, S., Sweet, S.T., DeFreitas, D.A., Milkov, A.V., and MacDonald, I.R., 1999, Thermogenic gas hydrates and hydrocarbon gases in complex chemosynthetic communities, Gulf of Mexico continental slope: Organic Geochemistry, v. 30, p. 485–497.

Sassen, R., Losh, S.L., Cathles, L., III, Roberts, H.H., Whelan, J.K., Milkov, A.V., Sweet, S.T., and DeFreitas, D.A., 2001, Massive vein-filling gas hydrate—relation to ongoing gas migration from the deep subsurface of the Gulf of Mexico: Marine and Petroleum Geology, v. 18, no. 5, p. 551–560.

Sassen, R., MacDonald, I.R., Guinasso, N.L., Joye, S., Requejo, A.G., Sweet, S.T., Alcala-Herrera, J., DeFreitas, D.A., and Schink, D.R., 1998, Bacterial methane oxidation in sea-floor gas hydrate, Significance to life in extreme environments: Geology, v. 26, p. 289–293.

Sassen, R., MacDonald, I.R., Requejo, A.G., Guinasso, N.L., Kennicutt, M.C., II, Sweet, S.T., and Brooks, J.M., 1994, Organic geochemistry of sediments from chemosynthetic communities, Gulf of Mexico slope: Geo-Marine Letters, v. 14, p. 110–119.

Sassen, R., Milkov, A.V., Ozgul, E., Roberts, H.H., Hunt, J.L., Beeunas, M.A., and others, 2003, Gas venting and subsurface charge in the Green Canyon area, Gulf of Mexico continental slope; evidence of a deep bacterial methane source? Organic Geochemistry, v. 34, no. 10, p. 1455–1464.

Sassen, R., Roberts, H.H., Aharon, A., Larkin, J., Chinn, E.W., and Carney, R., 1993, Chemosynthetic bacterial mats at cold hydrocarbon seeps, Gulf of Mexico continental slope: Organic Geochemistry, v. 20, p. 77– 89.

Sassen, R., Sweet, S.T., Milkov, A.V., DeFreitas, D.A., and Kennicutt, M.C., II, 2001a, Thermogenic vent gas and gas hydrate in the Gulf of Mexico slope—is gas hydrate decomposition significant: Geology, v. 29, p. 107–110.

Sassen, R., Sweet, S.T., Milkov, A.V., DeFreitas, D.A., and Kennicutt, M.C., II, 2001b, Stability of thermogenic gas hydrate in the Gulf of Mexico—constraints on models of climate change, *in*, Paull, C.K., and Dillon, W.P., eds., Natural gas hydrates—occurrence, distribution, and detection: Washington, DC, American Geophysical Union, p. 131–143.

Sassen, R., Sweet, S.T., Milkov, A.V., DeFreitas, D.A., Salata, G.G., and McDade, E.C., 1999, Geology and geochemistry of gas hydrates, central Gulf of Mexico continental slope: Trans. Gulf Coast Assoc. Geol. Soc., v. 49, p. 462–468.

Weimer, P., Crews, J.R., Crow, R.S., and Varnai, P., 1998, Atlas of petroleum fields and discoveries, northern Green Canyon, Ewing Bank, and Southern Ship Shoal northern Gulf of Mexico: AAPG Bulletin, v. 82, p. 878–917.

Table 2. Composition of hydrocarbon gas and carbon dioxide of core samples.

[c, centimeter; µL/L, microliter per liter; CO_2, carbon dioxide; C_1, methane; C_2, ethane; C_3, propane; iC_4, isobutane; nC_4, normal butane; $neoC_5$, neopentane; iC_5, isopentane; nC_5, normal pentane; cC_5, cyclopentane; M, microbial; X, mainly microbial methane with some thermogenic hydrocarbons; TX, mainly thermal hydrocarbons with some microbial methane]

Core	Depth (cm)	CO_2 µL/L	C_1 µL/L	C_2 µL/L	C_3 µL/L	iC_4 µL/L	nC_4 µL/L	$neoC_5$ µL/L	iC_5 µL/L	nC_5 µL/L	cC_5 µL/L
2535	440	435	49	0.16	0.17	0.14	0.10	0.00	0.09	0.11	0.00
2535	590	1,404	166	0.40	0.61	0.53	0.25	0.00	0.20	0.06	0.24
2535	1,190	774	33	0.09	0.02	0.00	0.00	0.00	0.00	0.18	0.00
2535	2,,390	1,115	23,847	6.97	3.07	1.33	0.27	4.43	0.36	0.06	0.30
2535	2690	1,004	17,240	80.57	31.19	9.32	1.31	42.04	1.23	0.00	0.00
2535	2,840	1,191	17,750	0.33	0.43	0.16	0.18	0.04	0.10	0.06	0.16
2537	440	144	938	0.80	0.41	0.23	0.17	0.02	0.13	0.06	0.26
2537	890	337	748	3.20	0.34	0.02	0.05	0.00	0.01	0.00	0.00
2537	1,640	205	2,242	4.56	0.57	0.14	0.19	0.11	0.29	0.08	0.31
2537	2,090	350	4,587	5.29	0.57	0.18	0.22	0.02	0.11	0.05	0.14
2537	3,240	209	7,089	9.49	0.96	0.34	0.33	0.03	0.40	0.09	0.34
2538	140	96	6	0.39	0.07	0.00	0.01	0.02	0.01	0.00	0.00
2538	290	145	7	0.43	0.07	0.06	0.06	0.07	0.17	0.07	0.21
2538	440	94	174	0.51	0.75	0.71	0.50	0.02	0.40	0.16	0.62
2538	590	390	1,353	3.73	0.24	0.01	0.04	0.02	0.01	0.01	0.00
2538	740	382	1,231	2.19	0.21	0.02	0.06	0.02	0.02	0.00	0.00
2539	140	75	11	0.24	0.04	0.00	0.00	0.00	0.00	0.00	0.00
2539	890	1,221	19	0.36	0.08	0.00	0.02	0.01	0.00	0.00	0.00
2539	1,640	1,130	10,105	0.03	0.30	0.02	0.05	0.01	0.00	0.00	0.00
2539	2,390	431	7,233	0.10	0.18	0.17	0.12	0.13	0.34	0.11	0.43
2539	2,990	381	5,434	0.11	0.07	0.00	0.02	0.01	0.01	0.00	0.00
2541	130	56	20	0.24	0.03	0.01	0.00	0.02	0.04	0.00	0.05
2541	740	1,027	10	0.25	0.04	0.00	0.01	0.01	0.00	0.00	0.00
2541	1,490	504	2,637	0.00	0.06	0.00	0.02	0.01	0.01	0.00	0.00
2541	2,240	298	6,107	0.01	0.13	0.03	0.05	0.04	0.09	0.04	0.11
2543	900	266	16,881	27.60	15.15	8.82	1.39	3.49	2.40	0.11	0.20
2545	200	419	14,481	8.19	0.40	0.02	0.06	0.03	0.01	0.01	0.00
2545	390	109	10,943	7.81	1.39	0.18	0.27	0.04	0.04	0.01	0.00
2545	500	77	9,581	9.07	1.49	0.17	0.30	0.06	0.05	0.01	0.00
2545	690	1,072	7,444	11.45	1.76	0.23	0.34	0.14	0.23	0.05	0.21
2545	890	186	10,353	6.28	1.22	0.12	0.27	0.18	0.07	0.02	0.00
2546	140	167	404	0.52	0.02	0.01	0.01	0.01	0.03	0.01	0.02
2546	740	124	551	0.90	0.12	0.07	0.06	0.06	0.17	0.04	0.17
2546	1,340	291	2,277	4.92	0.27	0.05	0.07	0.00	0.02	0.01	0.00
2546	1,790	220	9,625	14.07	0.63	0.29	0.29	0.11	0.27	0.08	0.25
2546	2,240	107	11,391	8.01	0.30	0.07	0.12	0.02	0.04	0.02	0.00

Table 2. Composition of hydrocarbon gas and carbon dioxide of core samples. — Continued

[c, centimeter; µL/L, microliter per liter; CO_2, carbon dioxide; C_1, methane; C_2, ethane; C_3, propane; iC_4, isobutane; nC_4, normal butane; $neoC_5$, neopentane; iC_5, isopentane; nC_5, normal pentane; cC_5, cyclopentane; M, microbial; X, mainly microbial methane with some thermogenic hydrocarbons; TX, mainly thermal hydrocarbons with some microbial methane]

Core	Depth (cm)	CO_2 µL/L	C_1 µL/L	C_2 µL/L	C_3 µL/L	iC_4 µL/L	nC_4 µL/L	$neoC_5$ µL/L	iC_5 µL/L	nC_5 µL/L	cC_5 µL/L
2546	2,990	131	9,308	12.65	1.27	0.21	0.26	0.07	0.14	0.04	0.00
2553	2,814	1,246	136	0.72	0.10	0.04	0.04	0.01	0.03	0.10	0.03
2554	140	556	1,386	0.53	0.29	0.16	0.34	0.05	0.20	0.18	0.10
2554	300	1,241	9,399	29.09	2.88	0.12	0.24	0.02	0.05	0.00	0.00
2554	600	309	19,750	8.70	2.10	0.02	0.10	0.03	0.02	0.02	0.00
2554	2,065	1,437	7,574	12.39	1.98	0.39	1.21	0.05	0.91	0.47	0.20
2554	2,665	1,061	10,081	19.30	1.89	0.08	0.19	0.02	0.04	0.02	0.00
2555	600	177	5,148	3.42	0.17	0.02	0.08	0.04	0.01	0.01	0.00
2555	740	1,353	195	0.27	0.10	0.01	0.03	0.03	0.01	0.01	0.00
2555	2,240	556	3,690	0.35	0.34	0.02	0.09	0.01	0.01	0.01	0.00
2556	1,490	923	7,476	3.42	0.81	0.39	0.89	2.74	0.67	0.28	0.15
2556	2,090	2,143	11,283	2.05	7.99	1.78	9.45	0.06	5.04	2.51	0.62
2556	2,990	894	3,818	0.40	0.72	0.12	0.35	0.03	0.16	0.00	0.10
2556	3,740	1,587	3,535	0.38	0.80	0.13	0.23	0.03	0.07	0.00	0.07
2559	740	3,043	6	0.39	0.09	0.00	0.03	0.05	0.01	0.80	0.00
2559	1,450	1,660	21	0.82	0.55	0.46	0.42	0.03	0.39	0.21	0.00
2559	2,090	977	1,673	0.64	0.16	0.18	0.10	0.00	0.07	0.05	0.12
2559	2,840	1,681	37	1.26	0.27	0.14	0.36	0.03	0.33	0.12	0.08
2559	3,290	948	21	1.03	0.18	0.06	0.14	0.02	0.12	0.05	0.03
2560	140	158	38	0.29	0.14	0.07	0.07	0.03	0.08	0.03	0.07
2560	730	4,742	944	0.47	0.27	0.23	0.10	0.00	0.06	0.03	0.00
2560	1,490	2,611	8	0.87	0.10	0.02	0.02	0.03	0.02	0.05	0.00
2560	2,090	1,543	150	0.92	0.16	0.08	0.08	0.02	0.09	0.03	0.08
2561	590	525	68	0.47	0.12	0.03	0.03	0.00	0.01	0.03	0.00
2561	1,180	2,555	166	0.99	0.67	0.33	0.70	0.49	0.35	0.30	0.16
2561	1,790	1,017	9	0.87	0.21	0.13	0.26	0.02	0.11	0.02	0.05
2561	2,390	2,067	393	1.37	0.64	0.56	0.37	0.02	0.29	0.10	0.00
2561	2,840	1,311	22	0.89	0.73	0.26	0.89	0.04	0.75	0.37	0.16
2562	440	1,959	17	0.15	0.15	0.11	0.08	0.00	0.06	0.00	0.09
2562	730	11,387	7	0.71	0.23	0.09	0.20	0.05	0.21	0.09	0.07
2562	890	2,596	147	0.51	0.38	0.29	0.22	0.02	0.14	0.05	0.18
2562	1,490	1,280	9	0.59	0.13	0.08	0.11	0.02	0.11	0.05	0.06
2562	2,090	1,376	15	0.44	0.13	0.11	0.07	0.01	0.05	0.01	0.06
2562	2,450	3,082	37	2.21	3.25	1.42	5.52	0.02	2.76	3.54	0.00
2563	90	2,695	1,976	104.48	13.65	2.37	4.14	11.65	3.63	1.92	0.27

Table 2. Composition of hydrocarbon gas and carbon dioxide of core samples. — Continued

[c, centimeter; µL/L, microliter per liter; CO_2, carbon dioxide; C_1, methane; C_2, ethane; C_3, propane; iC_4, isobutane; nC_4, normal butane; $neoC_5$, neopentane; iC_5, isopentane; nC_5, normal pentane; cC_5, cyclopentane; M, microbial; X, mainly microbial methane with some thermogenic hydrocarbons; TX, mainly thermal hydrocarbons with some microbial methane]

Core	Depth (cm)	CO_2 µL/L	C_1 µL/L	C_2 µL/L	C_3 µL/L	iC_4 µL/L	nC_4 µL/L	$neoC_5$ µL/L	iC_5 µL/L	nC_5 µL/L	cC_5 µL/L
2563	295	5,530	22,293	393.82	56.87	21.15	7.58	164.83	5.24	0.79	0.05
2563	380	6,460	27,274	858.40	247.02	107.69	10.41	409.68	13.17	0.62	4.35
2565	440	653	8,719	615.00	2322.47	1,995.15	655.05	22.44	413.87	87.31	227.44
2565	890	651	13,464	710.72	914.68	281.99	1,359.92	3.74	1,041.04	245.11	26.80
2565	1,190	708	16,191	1057.77	2038.86	602.47	1,150.62	8.41	445.62	238.69	54.40
2565	1,640	595	12,137	633.55	1175.73	383.08	1,066.64	3.70	417.06	254.99	30.38
2565	2,240	501	22,370	773.56	1006.22	28.86	62.15	1.78	196.04	153.67	29.53
2566	440	702	6	0.27	0.30	0.27	0.14	0.01	0.12	0.09	0.20
2566	890	1,300	6	0.35	0.18	0.08	0.18	0.02	0.09	0.12	0.04
2566	1,340	2,481	12	0.42	0.19	0.16	0.10	0.01	0.08	0.06	0.12
2566	1,940	898	8	0.58	0.21	0.08	0.24	0.00	0.11	0.02	0.05
2566	2,390	1,702	23	1.13	0.16	0.08	0.16	0.03	0.10	0.03	0.06
2567	590	1,413	12	0.55	0.17	0.17	0.11	0.01	0.09	0.05	0.15
2567	1,340	1,297	55	5.14	12.77	5.18	18.34	0.04	8.09	8.69	0.00
2567	1,490	2,766	44	0.84	0.18	0.13	0.16	0.00	0.10	0.02	0.06
2567	1,790	2,208	25	1.70	2.33	0.79	3.73	0.02	1.85	2.36	0.50
2567	2,090	1,535	16	0.58	0.15	0.09	0.09	0.02	0.12	0.01	0.09
2569	995	504	2,589	8.14	5.90	10.48	0.05	4.19	0.74	0.13	0.00
2569	1,400	89	1,412	1.77	3.01	0.91	4.84	0.10	3.27	2.02	0.24
2569	1,640	1,029	2,692	3.16	1.34	0.33	0.43	0.76	0.16	0.12	0.00
2569	2,090	997	17,223	12.31	3.21	0.41	1.31	0.48	0.91	0.50	0.19
2569	2,690	347	4,191	65.10	129.30	34.71	114.95	1.16	37.60	19.77	2.07
2570	440	1,177	3,507	2.67	1.02	0.50	0.50	0.05	0.30	0.14	0.00
2570	1,040	447	7,441	3.27	1.26	0.39	0.63	0.08	0.27	0.38	0.00
2570	1,490	1,056	4,197	6.89	9.94	3.01	6.75	0.36	5.01	1.90	0.55
2570	1,790	660	1,727	1.63	0.85	0.11	0.13	0.38	0.07	0.10	0.00
2570	2,240	295	3,116	4.38	2.12	0.56	0.90	0.33	0.72	0.30	0.15
2573	260	611	19,870	70.66	5.37	2.56	1.37	55.16	2.21	0.55	0.17

Table 2. Composition of hydrocarbon gas and carbon dioxide of core samples. — Continued

[c, centimeter; µL/L, microliter per liter; M, microbial; X, mainly microbial methane with some thermogenic hydrocarbons; TX, mainly thermal hydrocarbons with some microbial methane]

Core	Depth (cm)	2,2MC$_4$ µL/L	2MC$_5$ µL/L	3MC$_5$ µL/L	n-C$_6$ µL/L	McC$_5$ µL/L	n-C$_7$ µL/L	McC$_6$ µL/L	C$_1$/C$_2$+C$_3$	iC$_4$/nC$_4$	iC$_5$/nC$_5$
2535	440	0.00	0.01	0.05	0.16	0.00	0.15	0.50	150	1.33	0.83
2535	590	0.01	0.03	0.08	0.20	0.05	0.36	0.46	164	2.10	3.54
2535	1,190	0.00	0.02	0.00	0.00	0.00	0.00	0.00	292		
2535	2,390	0.75	1.15	0.29	0.46	0.37	0.09	0.30	2,376	4.90	5.94
2535	2,690	5.03	6.50	0.49	0.42	2.49	0.00	0.00	154	7.11	
2535	2,840	0.00	0.04	0.08	0.20	0.00	0.45	0.49	23,318	0.89	1.61
2537	440	0.00	0.02	0.09	0.32	0.04	0.41	0.49	775	1.37	2.17
2537	890	0.00	0.00	0.00	0.00	0.00	0.00	0.00	211	0.39	
2537	1,640	0.03	0.19	0.41	0.00	1.03	0.84	1.17	436	0.76	3.69
2537	2,090	0.00	0.01	0.05	0.12	0.00	0.15	0.28	783	0.84	2.06
2537	3,240	0.00	0.10	0.46	0.50	0.86	0.58	0.87	678	1.01	4.48
2538	140	0.00	0.00	0.00	0.00	0.00	0.00	0.00	12	0.00	
2538	290	0.02	0.08	0.21	0.33	0.77	0.82	1.10	14	0.94	2.36
2538	440	0.05	0.06	0.17	0.42	0.12	0.73	0.98	139	1.44	2.54
2538	590	0.00	0.00	0.09	0.22	0.00	0.00	0.00	341	0.30	1.50
2538	740	0.00	0.00	0.00	0.00	0.00	0.00	0.00	513	0.37	
2539	140	0.00	0.00	0.00	0.08	0.00	0.00	0.00	40		
2539	890	0.00	0.00	0.00	0.07	0.00	0.00	0.00	42	0.00	
2539	1,640	0.00	0.00	0.00	0.07	0.00	0.00	0.00	30,118	0.39	
2539	2,390	0.06	0.08	0.30	0.00	1.25	0.94	1.60	26,064	1.35	3.10
2539	2,990	0.00	0.00	0.00	0.04	0.00	0.00	0.00	30,561	0.00	
2541	130	0.00	0.00	0.06	0.11	0.21	0.22	0.25	72		
2541	740	0.00	0.00	0.00	0.03	0.00	0.00	0.00	35	0.00	0.00
2541	1,490	0.00	0.00	0.00	0.00	0.44	0.00	0.00	46,354	0.00	1.57
2541	2,240	0.00	0.03	0.12	0.23	0.44	0.49	0.52	41,208	0.54	2.32
2543	900	1.64	5.84	1.81	0.18	0.62	1.03	0.38	395	6.34	21.42
2545	200	0.00	0.00	0.00	0.10	0.00	0.00	0.00	1,686	0.33	0.95
2545	390	0.00	0.00	0.00	0.06	0.00	0.00	0.00	1,190	0.66	4.12
2545	500	0.00	0.00	0.02	0.05	0.00	0.00	0.00	908	0.56	6.33
2545	690	0.03	0.08	0.24	0.31	0.64	0.60	0.75	564	0.67	4.71
2545	890	0.00	0.02	0.06	0.14	0.00	0.00	0.00	1,379	0.44	3.55
2546	140	0.00	0.00	0.00	0.30	0.16	0.19	0.14	747	0.40	2.81
2546	740	0.02	0.08	0.19	0.26	0.47	0.53	0.73	542	1.10	4.63
2546	1,340	0.00	0.02	0.00	0.03	0.00	0.00	0.00	438	0.73	2.57
2546	1,790	0.04	0.13	0.48	0.50	0.77	0.70	0.87	655	0.98	3.31
2546	2,240	0.01	0.00	0.00	0.12	0.00	0.00	0.00	1,371	0.64	1.72
2546	2,990	0.04	0.05	0.00	0.04	0.00	0.03	0.00	669	0.81	3.27

Table 2. Composition of hydrocarbon gas and carbon dioxide of core samples. — Continued

[c, centimeter; µL/L, microliter per liter; M, microbial; X, mainly microbial methane with some thermogenic hydrocarbons; TX, mainly thermal hydrocarbons with some microbial methane]

Core	Depth (cm)	$2,2MC_4$ µL/L	$2MC_5$ µL/L	$3MC_5$ µL/L	$n\text{-}C_6$ µL/L	McC_5 µL/L	$n\text{-}C_7$ µL/L	McC_6 µL/L	C_1/C_2+C_3	iC_4/nC_4	iC_5/nC_5
2553	2,814	0.00	0.00	0.02	0.14	0.00	0.08	0.05	166	0.97	0.26
2554	140	0.02	0.01	0.17	0.44	0.10	0.44	0.72	1,680	0.48	1.11
2554	300	0.00	0.00	0.04	0.21	0.00	0.00	0.00	294	0.50	
2554	600	0.00	0.00	0.11	0.50	0.00	0.00	0.00	1,828	0.16	0.95
2554	2,065	0.07	0.22	0.57	0.70	0.75	0.95	0.98	527	0.33	1.94
2554	2,665	0.00	0.01	0.05	0.15	0.00	0.00	0.00	476	0.39	1.94
2555	600	0.00	0.00	0.05	0.32	0.00	0.00	0.00	1,434	0.20	1.19
2555	740	0.00	0.00	0.04	0.21	0.00	0.00	0.00	528	0.24	0.62
2555	2,240	0.00	0.00	0.05	0.15	0.00	0.00	0.00	5,339	0.23	1.19
2556	1,490	0.17	0.26	0.42	0.47	0.45	0.31	0.49	1,769	0.44	2.39
2556	2,090	0.44	1.72	2.74	4.33	0.72	5.36	7.88	1,123	0.19	2.01
2556	2,990	0.01	0.03	0.07	0.22	0.04	0.36	0.52	3,410	0.35	
2556	3,740	0.00	0.00	0.09	0.27	0.28	0.10	0.23	3,008	0.54	
2559	740	0.00	0.00	0.00	0.00	0.00	0.00	0.00	12	0.00	0.02
2559	1,450	0.05	0.07	0.18	0.29	0.12	0.50	0.61	16	1.10	1.88
2559	2,090	0.00	0.01	0.06	0.15	0.00	0.28	0.47	2,081	1.76	1.43
2559	2,840	0.01	0.06	0.20	0.36	0.31	0.26	0.30	24	0.38	2.85
2559	3,290	0.00	0.02	0.12	0.22	0.14	0.11	0.14	18	0.44	2.50
2560	140	0.00	0.02	0.12	0.24	0.21	0.16	0.24	89	1.08	2.42
2560	730	0.00	0.00	0.02	0.08	0.00	0.18	0.11	1,281	2.22	1.92
2560	1,490	0.00	0.00	0.00	0.11	0.00	0.00	0.00	9	0.68	0.40
2560	2,090	0.00	0.03	0.12	0.20	0.23	0.13	0.22	139	0.99	2.72
2561	590	0.00	0.00	0.00	0.08	0.00	0.00	0.00	116	0.81	0.44
2561	1,180	0.06	0.05	0.11	0.38	0.55	0.83	0.81	100	0.47	1.16
2561	1,790	0.00	0.01	0.03	0.12	0.01	0.18	0.29	9	0.52	5.67
2561	2,390	0.02	0.03	0.13	0.32	0.08	0.40	0.61	196	1.50	2.94
2561	2,840	0.04	0.19	0.71	0.59	0.62	0.78	0.93	13	0.29	2.00
2562	440	0.00	0.01	0.04	0.11	0.00	0.20	0.35	56	1.37	
2562	730	0.00	0.06	0.23	0.39	0.32	0.25	0.43	7	0.44	2.42
2562	890	0.00	0.05	0.11	0.28	0.05	0.50	0.82	165	1.32	2.51
2562	1,490	0.00	0.02	0.11	0.00	0.20	0.23	0.24	12	0.66	2.20
2562	2,090	0.00	0.01	0.03	0.00	0.02	0.16	0.30	26	1.57	5.50
2562	2,450	0.16	1.22	1.11	2.91	0.28	1.87	1.31	7	0.26	0.78
2563	90	0.77	1.25	1.93	2.19	1.62	3.79	2.75	17	0.57	1.90
2563	295	9.00	4.88	0.52	0.46	0.33	0.00	0.25	49	2.79	6.64
2563	380	35.11	71.64	5.46	2.77	1.92	0.00	1.20	25	10.34	21.16

Table 2. Composition of hydrocarbon gas and carbon dioxide of core samples. — Continued

[c, centimeter; µL/L, microliter per liter; M, microbial; X, mainly microbial methane with some thermogenic hydrocarbons; TX, mainly thermal hydrocarbons with some microbial methane]

Core	Depth (cm)	2,2MC$_4$ µL/L	2MC$_5$ µL/L	3MC$_5$ µL/L	n-C$_6$ µL/L	McC$_5$ µL/L	n-C$_7$ µL/L	McC$_6$ µL/L	C$_1$/C$_2$+C$_3$	iC$_4$/nC$_4$	iC$_5$/nC$_5$
2565	440	44.02	95.65	113.69	104.27	39.05	97.70	83.87	3	3.05	4.74
2565	890	58.43	143.10	285.10	159.20	133.63	181.45	151.53	8	0.21	4.25
2565	1,190	35.53	116.88	109.62	108.42	24.83	87.76	88.52	5	0.52	1.87
2565	1,640	27.65	119.26	106.27	122.31	25.16	112.58	67.31	7	0.36	1.64
2565	2,240	6.28	28.60	26.23	32.55	2.95	14.61	8.53	13	0.46	1.28
2566	440	0.01	0.02	0.06	0.19	0.02	0.31	0.38	10	1.84	1.28
2566	890	0.00	0.01	0.04	0.19	0.00	0.11	0.18	11	0.45	0.69
2566	1,340	0.00	0.01	0.05	0.16	0.02	0.29	0.48	20	1.51	1.43
2566	1,940	0.00	0.01	0.03	0.13	0.01	0.19	0.24	10	0.32	7.07
2566	2,390	0.00	0.01	0.05	0.24	0.02	0.20	0.49	18	0.50	3.88
2567	590	0.00	0.01	0.06	0.18	0.03	0.33	0.58	17	1.54	1.73
2567	1,340	0.43	2.70	2.28	5.13	0.35	2.33	2.06	3	0.28	0.93
2567	1,490	0.00	0.03	0.07	0.19	0.00	0.28	0.47	43	0.82	5.00
2567	1,790	0.11	0.90	0.76	2.15	0.23	1.63	1.02	6	0.21	0.78
2567	2,090	0.00	0.03	0.16	0.26	0.26	0.16	0.29	22	1.04	9.50
2569	995	0.17	0.89	0.02	8.03	8.01	0.37	0.00	184	201.08	5.77
2569	1,400	0.13	0.74	2.49	1.79	1.00	1.37	1.43	296	0.19	1.62
2569	1,640	0.00	0.00	0.00	0.18	0.00	0.00	0.00	597	0.77	1.31
2569	2,090	0.04	0.23	0.82	0.72	0.63	0.75	0.76	1,110	0.31	1.82
2569	2,690	2.39	10.46	9.95	10.81	2.32	10.86	7.32	22	0.30	1.90
2570	440	0.02	0.05	0.16	0.32	0.07	0.56	0.71	950	1.02	2.14
2570	1,040	0.00	0.10	0.07	0.12	0.00	0.41	0.45	1,644	0.61	0.70
2570	1,490	0.27	0.76	1.85	1.45	1.56	1.79	2.25	249	0.45	2.64
2570	1,790	0.00	0.00	0.00	0.11	0.00	0.33	0.00	695	0.86	0.72
2570	2,240	0.04	0.16	0.64	0.66	0.57	0.74	1.01	479	0.62	2.41
2573	260	2.90	1.94	0.37	0.84	0.89	0.00	0.45	261	1.87	3.99

Table 2. Composition of hydrocarbon gas and carbon dioxide of core samples. — Continued

[c, centimeter; µL/L, microliter per liter; M, microbial; X, mainly microbial methane with some thermogenic hydrocarbons; TX, mainly thermal hydrocarbons with some microbial methane]

Core	Depth (cm)	C_1 $\delta^{13}C$	CO_2 $\delta^{13}C$	C_2 $\delta^{13}C$	C_3 $\delta^{13}C$	i-C_4 $\delta^{13}C$	n-C_4 $\delta^{13}C$	C_5 $\delta^{13}C$	Source
2535	440								M
2535	590	-94.62	-26.52						M
2535	1,190								M
2535	2,390								M
2535	2,690	-93.11	-21.87						X
2535	2,840								M
2537	440								M
2537	890								M
2537	1,640	-66.00	-18.00						M
2537	2,090								M
2537	3,240	-74.30	-20.11						M
2538	140								M
2538	290								M
2538	440	-74.50	-45.40						M
2538	590	-71.00	-34.40						M
2538	740	-81.70	-19.70						M
2539	140								M
2539	890								M
2539	1,640	-96.60	-33.10						M
2539	2,390								M
2539	2,990								M
2541	130								M
2541	740								M
2541	1,490	-97.10	-26.70						M
2541	2,240								M
2543	900	-61.20	-3.00						X
2545	200	-98.30	-43.40						X
2545	390								X
2545	500								X
2545	690	-62.60	-15.20						X
2545	890								X
2546	140	-81.90	-21.20						M
2546	740								M
2546	1,340	-75.60	-27.90						X
2546	1,790								X
2546	2,240								X
2546	2,990	-70.80	-11.70						X

Table 2. Composition of hydrocarbon gas and carbon dioxide of core samples. — Continued

[c, centimeter; µL/L, microliter per liter; M, microbial; X, mainly microbial methane with some thermogenic hydrocarbons; TX, mainly thermal hydrocarbons with some microbial methane]

Core	Depth (cm)	C_1 $\delta^{13}C$	CO_2 $\delta^{13}C$	C_2 $\delta^{13}C$	C_3 $\delta^{13}C$	i-C_4 $\delta^{13}C$	n-C_4 $\delta^{13}C$	C_5 $\delta^{13}C$	Source
2553	2,814	-45.67	-23.81						M
2554	140	-83.24	-29.22						M
2554	300	-75.00	-10.40						X
2554	600	-91.10	-43.40						X
2554	2,065								X
2554	2,665								X
2555	600								X
2555	740								M
2555	2,240								M
2556	1,490	-85.89	-24.38						X
2556	2,090	-72.82	-20.19						X
2556	2,990	-84.08	-20.78						M
2556	3,740	-81.01	-14.22						M
2559	740								M
2559	1,450								M
2559	2,090	-64.09	-15.94						M
2559	2,840								M
2559	3,290								M
2560	140								M
2560	730	-93.59	-20.88						M
2560	1,490								M
2560	2,090	-72.00	-18.57						M
2561	590								M
2561	1,180								M
2561	1,790								M
2561	2,390	-62.56	-22.51						M
2561	2,840								M
2562	440								M
2562	730								M
2562	890	-72.12	-20.61						M
2562	1,490								M
2562	2,090								M
2562	2,450								M
2563	90								TX
2563	295	-53.11	-12.07	-28.15					TX
2563	380	-52.22	-2.23	-28.18	-18.53				TX

Table 2. Composition of hydrocarbon gas and carbon dioxide of core samples. — Continued

[c, centimeter; µL/L, microliter per liter; M, microbial; X, mainly microbial methane with some thermogenic hydrocarbons; TX, mainly thermal hydrocarbons with some microbial methane]

Core	Depth (cm)	C_1 $\delta^{13}C$	CO_2 $\delta^{13}C$	C_2 $\delta^{13}C$	C_3 $\delta^{13}C$	i-C_4 $\delta^{13}C$	n-C_4 $\delta^{13}C$	C_5 $\delta^{13}C$	Source
2565	440								TX
2565	890								TX
2565	1,190	-60.10	-11.10	-28.83	-26.40	-28.44	-25.94	-26.01	TX
2565	1,640	-58.87	-3.93	-29.48	-27.63	-28.55	-26.45	-26.51	TX
2565	2,240	-59.88	-11.15	-28.96	-26.18		-25.49		TX
2566	440								M
2566	890								M
2566	1,340								M
2566	1,940								M
2566	2,390								M
2567	590								M
2567	1,340								M
2567	1,490								M
2567	1,790								M
2567	2,090								M
2569	995	-59.52	-2.71						X
2569	1,400	-70.52	-21.33						X
2569	1,640	-67.02	-11.40						X
2569	2,090	-67.81	-11.55						X
2569	2,690	-62.02	-42.48						X
2570	440	-72.35	-28.58						X
2570	1,040	-68.74	-13.98						X
2570	1,490	-67.14	-11.76						X
2570	1,790	-66.55	-10.85						M
2570	2,240	-66.38	-14.03						X
2573	260	-62.11	-18.66	-30.08					X

Chapter 10

Methanogenic and Methanotrophic Archaeal Diversity in Northern Gulf of Mexico Sediments

Steven J. Hallam[1], Edward F. DeLong[1], William Ussler III[1], and Charles K. Paull[1]

Methanogenic and methanotrophic archaeal diversity in northern Gulf of Mexico sediments; chapter 10 in *Winters, W.J., Lorenson, T.D., and Paull, C.K., eds., 2007, Initial report of the IMAGES VIII/PAGE 127 gas hydrate and paleoclimate cruise on the RV* Marion Dufresne *in the Gulf of Mexico, 2–18 July 2002: U.S. Geological Survey Open-File Report 2004–1358.*

Abstract

Archaeal small subunit (SSU) ribosomal Ribonucleic acid (rRNA) gene diversity was surveyed in sediment samples obtained at 50-, 100-, 150-, 300-, 400-, and 600-centimeter depths below the sea floor in core MD02-2571_c2 located above a gas chimney at a water depth of 647 meters in the West Mississippi Canyon area. The distribution of methanogenic and methanotrophic archaea was compared to pore-water chemical profiles indicative of methane and sulfate consumption. SSU rRNA sequences corresponding to the methane-oxidizing archaeal (MOA) groups ANME-1 and ANME-2 were recovered at 100 centimeters below the sediment surface concomitant with a localized increase in dissolved methane concentration and again at 300 and 400 centimeters below the sediment surface in close proximity to the sulfate-methane interface (SMI). Methanogen-related SSU rRNA sequences spanning the genus Methanosarcinales were recovered at 50, 100, 300, 400, and 600 centimeters below the sea floor. The distribution of SSU rRNA sequences associated with additional archaeal orders, *Thermoplasmales* and *Crenarchaeota,* appeared to vary inversely with MOA groups across sediment horizons. These results are consistent with a broad distribution and complex community structure of methane cycling archaea across multiple sediment horizons in samples associated with core MD02-2571_c2.

Introduction

In July 2002, the research vessel (RV) *Marion Dufresne* obtained the box core MD02-2571_c2 from the West Mississippi Canyon area in the Gulf of Mexico as part of the International Marine Past Global Changes Study (IMAGES) VIII and Paleoceanography of the Atlantic and Geochemistry (PAGE) 127 research programs. One of the goals of this coring effort was to characterize the microbial ecology associated with gas hydrates and deep zones of active anaerobic methane oxidation (AOM) in continental margin sediments. Previous studies in the Gulf of Mexico using lipid biomarker (Zhang and others, 2002) or molecular phylogenetic approaches (Lanoil and others, 2001) have identified microbial groups associated with gas hydrates and superficial sediments from several subsurface environments, including but not limited to Green Canyon, Mississippi Canyon, Atwater Valley, and the edge of the Sigsbee Escarpment. The latter two locations were found to contain assemblages of bacteria and archaea physically associated with gas hydrates, including members of the methane-oxidizing archaeal groups ANME-1 and ANME-2 (Lanoil and others, 2001).

These observations suggest that microbial activity may play an important role in the formation and stability of marine gas hydrates. While these studies provide a useful foundation for identifying the microbial community structure physically associated with gas hydrates in the Gulf of Mexico, ecological and evolutionary questions relating to the distribution, relatedness, and activity of community members within and beyond the gas hydrate stability zone as a function of sediment depth and geochemical profile remain. Specifically, little is known about the disposition of methane-oxidizing archaea associated with subsurface AOM in sediment intervals below 15–20 centimeters (cm). This report summarizes archaeal diversity data determined for MD02-2571_c2, spanning a zone

[1]Monterey Bay Aquarium Research Institute, 7700 Sandholdt Road, Moss Landing, CA 95039 USA.

of active AOM at 300 cm. The analysis is based on SSU rRNA sequence analysis in conjunction with pore-water sulfate and methane concentration measurements (Ussler and Paull, this volume, chapter 8).

Methods

Between 25 and 50 grams (g) of sediment was subsampled from MD02-2571_c2 at 25-cm intervals to correspond directly in depth with pore-water samples collected approximately 2 hours after recovery of the core. Samples were collected serially from top to bottom only in regions of intact core that could be cut away with a spatula using sterile techniques. This approach excluded the most superficial layers of the core down to 25 cm. In order to avoid cross contamination with adjacent layers and the sidewalls of the box core, samples were collected from a central and internal portion of each interval by using a clean spatula. The last 50 cm of core was excluded from analysis because of the likelihood of contamination with superficial layers when the box core first penetrated the sea floor. In addition to the 25-cm intervals along the 1,038-cm length of the entire core, 15 g of sediment were subsampled at 2-cm intervals between 100 and 400 cm for subsequent vertical mapping of the microbial community structure across the SMI. Sediment samples were immediately frozen at –80 degrees Celsius (°C) and thawed only for subsequent shore-based deoxyribonucleic acid (DNA) extraction. Sediment pore-water samples were collected and analyzed according to methods described in an accompanying chapter by Ussler and Paull (this volume, chapter 8). For DNA extraction, 0.5-g sediment was removed from the central portion of selected intervals by using sterile techniques and processed using a Fast soil prep kit (MoBio, San Diego, CA) following the manufacturer's protocol. Final elution volumes varied between 30 and 50 micro-liter (μL) TE buffer (Tris-EDTA buffer [trishydroxymethylaminomethane ethylenediaminetetraacetic acid]) (10 millimoles (mM) Tris, 1 mM EDTA, pH 7.5).

Archaeal SSU rRNA sequences were amplified by the Polymerase Chain Reaction (PCR) from sediment extracts by using archaeal-specific primers (A20_F 5' TTCCGGTTGATCCYGCCRG and A958_R 5' YCCGGCGTTGAMTCCAATT). Amplification reaction mixtures contained 1 μL template DNA, 41.5 μL 1X buffer, 1 μL each 10 micrometer (μM) forward and reverse primer, 2.5 units TaqPlus Precision polymerase (Stratagene, La Jolla, CA), 5 μL 10 mM stock dNTP (deoxyribonucleotide triphosphate) mixture in a total reaction volume of 50 μL. Amplifications were carried out using the following profile: 94 °C/3 minutes, X36 cycles 94 °C/40 seconds, 55 °C/1.5 minutes, and 72 °C/2 minutes, followed by a final extension at 72 °C/10 minutes.

SSU rRNA were visualized on 1-percent agarose gels in 1XTBE buffer (50 mM Tris, 50 mM boric acid, 1 mM EDTA, pH 8.3) and purified directly using Qiaquick PCR purification kit (Giagen, Valencia, CA). Purified SSU rRNA amplicons were cloned into pCR4-TOPO vector by using a TOPO TA cloning kit for sequencing (Invitrogen, Carlsbad, CA) and transformed by chemical transformation into TOP10 one-shot cells according to the manufacturer's instructions. Transformants were transferred to 96-well plates containing 180 μL Lb_{kan50} and 7-percent glycerol and stored at –80 °C. Plasmid DNA was purified from glycerol stocks by using the Montage Plasmid $Miniprep_{96}$ kit (Millipore, Bedford, MA) following the manufacturer's protocol and stored at –20 °C. Plasmid insert sequence data were collected on an ABI Prism 3100 DNA sequencer (Applied Biosystems, Inc., Foster, CA) by using Big Dye™ chemistry (PE Biosystems, Foster, CA) according to manufacturer's instructions. Plasmids were sequenced bidirectionally with M13F and M13R primers. Sequences were edited manually from traces by using Sequencher software V4.1.2 (Gene Codes Corporation, Ann Arbor, MI).

Representative euryarchaeal SSU rRNA ribotypes were selected for phylogenetic analysis. SSU rRNA sequence data were compiled with ARB software (*http://www.arb-home.de*) and aligned with sequences from the Genbank database by using the FastAligner program. Aligned sequences were visually inspected for conservation of secondary structure features and manually edited when necessary. SSU rRNA trees were based on comparison of 675 nucleotides. The SSU rRNA phylogenetic tree was generated using distance and parsimony methods implemented in PAUP* version 4.0b10 (Swafford, 2000). SSU rRNA sequence distances were estimated using the Kimura two-parameter model with the evolutionary rate adjusted according to a gamma distribution (alpha = 0.5). Bootstrapping for distance and parsimony was accomplished with 1,000 replicates per tree by using heuristic search methods.

Results

A total of 68 euryarchaeal and 87 crenarchaeal SSU rRNA sequences were obtained from sediment intervals 50, 100, 150, 300, 400, and 600 cm below the sea floor in box core MD02-2571_c2. Euryarchaeal sequences corresponding to Thermoplasmales, methanogens spanning the genus Methanosarcinales, and the MOA groups ANME-1 and ANME-2, in addition to crenarchaeal sequences corresponding to various group I subdivisions were found to partition phylogenetically by depth (fig. 1B). For comparison, pore-water sulfate and methane concentration data are listed in relation to archaeal SSU rRNA sequence recovery by depth interval (fig. 1). Consistent with a methanotrophic lifestyle, ANME ribotypes were recovered from the 300- and 400-cm intervals in close proximity to the chemically defined SMI. ANME ribotypes also were recovered from the 100-cm interval in sediments containing relatively high sulfate (~25 mM) and methane (~27 μM) concentrations (fig. 1A). Methanogen-

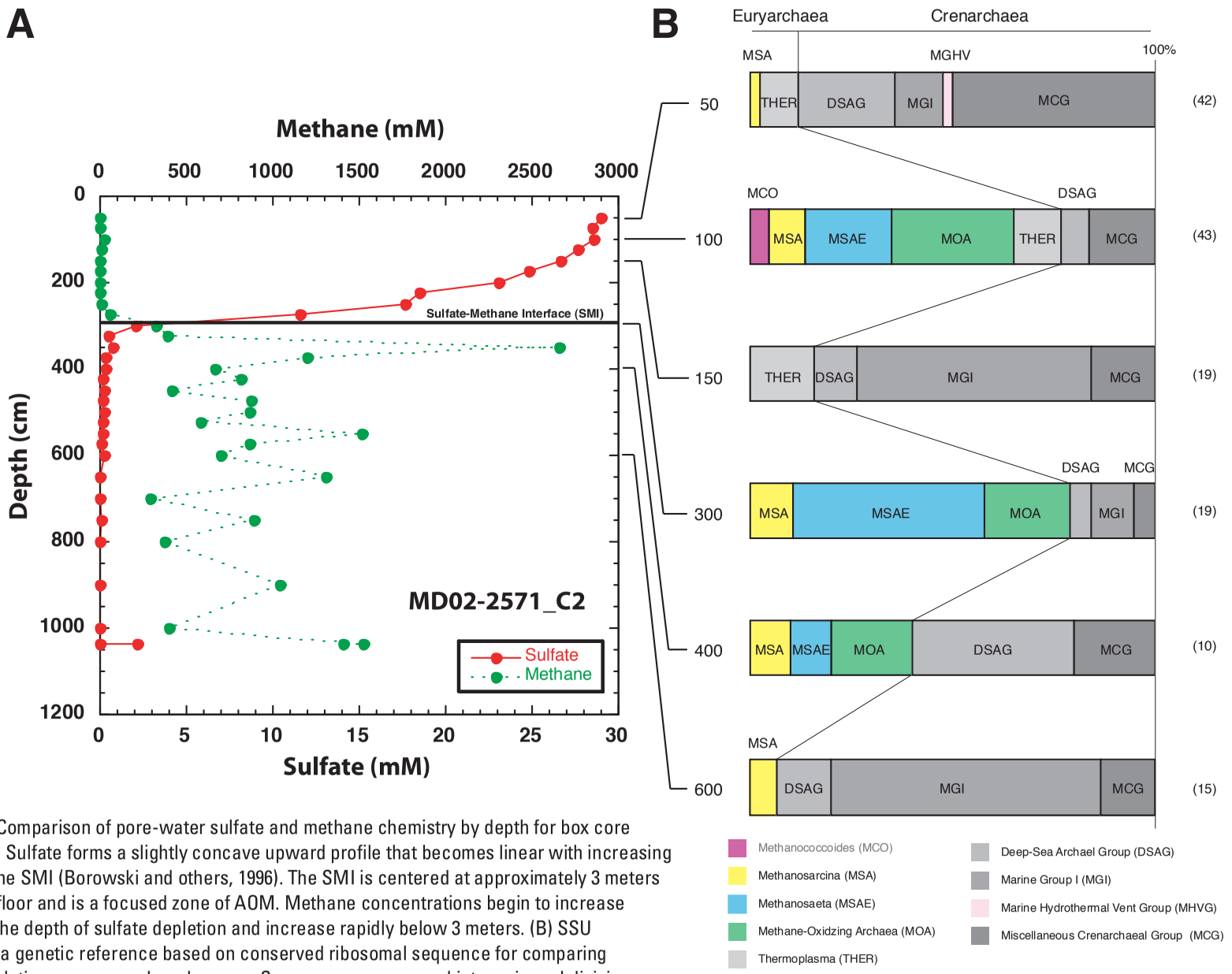

Figure 1. (A) Comparison of pore-water sulfate and methane chemistry by depth for box core MD02-2571_c2. Sulfate forms a slightly concave upward profile that becomes linear with increasing depth toward the SMI (Borowski and others, 1996). The SMI is centered at approximately 3 meters below the sea floor and is a focused zone of AOM. Methane concentrations begin to increase slightly above the depth of sulfate depletion and increase rapidly below 3 meters. (B) SSU rRNA provides a genetic reference based on conserved ribosomal sequence for comparing phylogenetic relations among archaeal groups. Sequences are grouped into major subdivisions with the Euryarchaeota and Crenarchaeota and represented as a percentage of total recovered sequences. Numbers in parentheses to the right of each sampling interval contain the total number of sequenced archaeal SSU rRNA clones for that interval. Methane-oxidizing archaeal groups are highlighted in green.

related sequences affiliated with the order Methanosarcinales were recovered from all sampling intervals with the exception of 150 cm. Phylogenetic affiliation of methanogenic and methanotropic archaeal SSU rRNA sequences recovered in this study are represented in figure 2. SSU rRNA sequences spanning the order Thermoplasmales were recovered from the 50- and 150-cm intervals. Crenarchaeal SSU rRNA sequences were recovered from all sampling intervals. Overall, the abundance of thermoplasma and crenarchaeal ribotypes diminished in the presence of MOA with SSU rRNA sequences associated with the order Thermoplasmales disappearing in samples from below 150 cm.

Discussion

Archaeal Diversity Associated with MD02-2571_c2

Previous phylogenetic studies from a wide range of geological settings (Hinrichs and others, 1999; Boetius and others, 2000; Orphan, Hinrichs, and others, 2001; Orphan and others, 2002; Teske and others, 2002) and coupled fluorescent in situ hybridization and isotopic analysis (FISH-SIMS) (Orphan, House, and others, 2001) have identified the MOA groups ANME-1 and ANME-2 as mediators of anaerobic methane oxidation (AOM). The molecular and phylogenetic evidence described in this study indicates the presence of ANME groups in close proximity to the chemically determined SMI of MD02-2571_c2. The identification of ANME-1 near the SMI of MD02-2571_c2 is consistent with a methanotrophic lifestyle and provides a glimpse at MOA community composition in the high flux, methane-hydrate rich sediments of the Gulf of Mexico. However, the identification of ANME ribotypes at 100 cm in the absence of a SMI suggests that MOA groups may have the potential to utilize alternative metabolic subsystems to derive cellular energy and carbon. Likewise, the presence of methanogen-related SSU rRNA sequences well above the SMI of MD02-2571_c2 suggests that high levels of primary productivity at the SMI coupled to high rates of fluid advection and(or) diffusion could fuel hydrogen-based alternatives to the methanogenic lifestyle at higher elevations in the substrata. MOA groups living in syntrophic association with methanogens could harness a local methane cycle far removed from the chemically defined SMI. The punctuated increase in dissolved methane concentration at 100 cm and the presence of a diverse assemblage of methanogen and MOA ribotypes appears to be consistent with this latter hypothesis. However, it remains formally possible, given the limited sample number and sensitivity of amplification-based approaches used in this study, that MOA ribotypes recovered from the 100-cm horizon could represent the decomposing remains of dead cells, a remnant population of metabolically inactive cells, or a founder population recently transported upward by fluid advection. Future deep-core chemotaxonomic studies, including lipid biomarker analysis, in the Gulf of Mexico and beyond will be required to ascertain the generality of this phenomenon. Due to the limited number of SSU rRNA sequences analyzed in this study, the observed patterns of vertical stratification should be considered a preliminary finding. A more comprehensive treatment of the data, including an expanded sequence set across additional sampling intervals and concomitant statistical analysis, will be required to more accurately describe the anatomy of this core.

Geochemical studies indicate that AOM occurs at an interface between upward-rising methane and downward-diffusing sulfate termed the SMI (Barnes and Goldberg, 1976; Reeburgh, 1976; Whiticar and others, 1986; Borowski and others, 1996; Reeburgh, 1996; Joye and others, 1999; Martens and others, 1999). AOM produces linear sulfate gradients that reflect the rate of methane transport by fluid advection and(or) diffusion toward the surface with steeper gradients exhibiting higher flux (Borowski and others, 1996). At present, little is known about the vertical thickness of the SMI, although current models suggest a sharp boundary over several meters. Given the well-defined linear pore-water chemistry profile available for MD02-2571_c2, future studies aimed at higher resolution mapping of microbial diversity have the potential

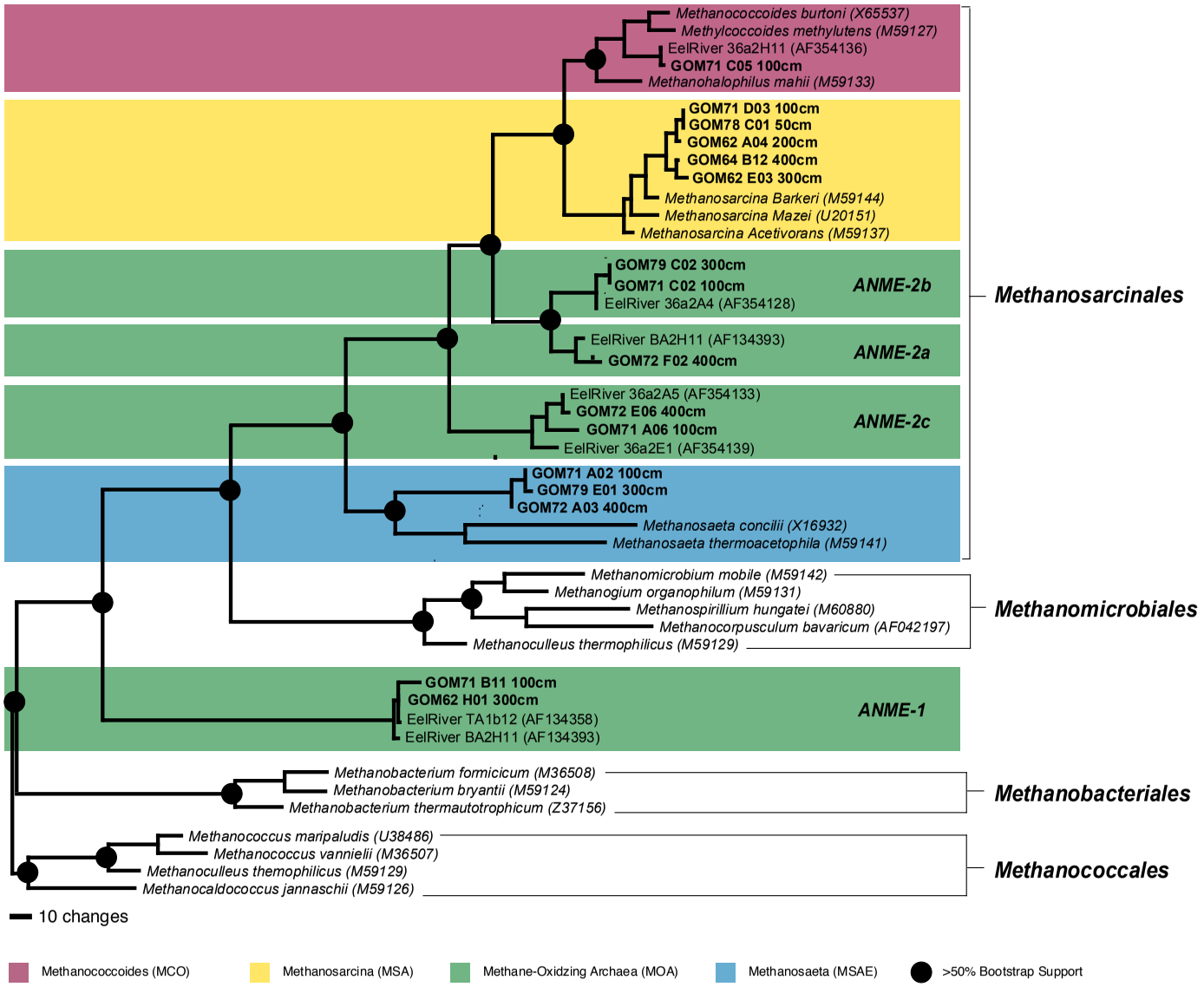

Figure 2. Phylogenetic tree comparing representative methanogen and methanotroph SSU rRNA sequences recovered from box core MD02 2571_c2. Bootstrap values are based on 1,000 replicates (neighbor-joining and parsimony). Scale bar represents 10-percent estimated sequence divergence. Sequences recovered in this study begin with GOM (Gulf of Mexico) followed by a clone number and the sampling interval. Methane-oxidizing archaeal groups are highlighted in green. Genbank accession numbers follow clone names when available.

to more closely bracket the chemically determined SMI with both qualitative and quantitative genetic information.

Conclusions

Archaeal SSU rRNA sequences obtained from 50-, 100-, 150-, 300-, 400-, and 600-cm intervals of MD02-2571_c2 suggest the following:

1. The anaerobic methanotrophic groups ANME-1 and ANME-2, identified at 300 and 400 cm, likely mediate AOM in MD02-2571_c2 sediments.
2. In addition to ANME-1 and ANME-2 groups, methanogen-related sequences most similar to *Methanosarcinales spp.* were identified throughout the core, suggesting a potential role for methanogenesis at this site. SSU rRNA sequence analysis suggests that methanogenenic archaeal groups exhibit a vertical distribution spanning the sediment matrix 3 m above and at least 1 meter below the SMI.
3. More comprehensive analyses of MD02-2571_c2 intervals and clone libraries will be required to accurately determine archaeal community structure across the SMI. Future work using quantitative PCR approaches could provide more accurate analyses of microbes and microbial processes that coincide with pore-water chemical profiles to better define the dynamic biogeochemistry in the Gulf of Mexico subsea-floor system.

Acknowledgments

Financial support for this research was provided by the U.S. Geological Survey (USGS) through Cooperative Agreement 02WRAG0021, and by the David and Lucile Packard Foundation. The authors thank Patrick Mitts, Rendy Keaten, John Pohlman, and Yi Feng Cheng for their help with sediment-core processing and pore-water extraction. The authors also thank the crew and scientific party of the RV *Marion Dufresne* for their assistance with coring and sample processing.

References Cited

Barnes, R.O., and Goldberg, E.D., 1976, Methane production and consumption in anaerobic marine sediments: Geology, v. 4 , p. 297–300.

Boetius, A., Ravenschlag, K., Schubert, C.J., Rickert, D., Widdel, F., Gieseke, A., Jorgensen, B.B., Witte, U., and Pfannkuche, O., 2000, A marine microbial consortium apparently mediating anaerobic oxidation of methane: Nature, v. 407, no. 6804, p. 623–626.

Borowski, W.S., Paull, C.K., and Ussler, W., III, 1996, Marine pore-water sulfate profiles indicate in situ methane flux from underlying gas hydrate: Geology, v. 24, p. 655–658.

Hinrichs, K.U., Hayes J.M., Sylva, S.P., Brewer, P.G., and DeLong, E.F., 1999, Methane-consuming archaebacteria in marine sediments: Nature, v. 398, no. 6730, p. 802–805.

Joye, S.B., Connell, T.L., Miller, L.G., Oremland, R.S., and Jellison, R.S., 1999, Oxidation of ammonia and methane in an alkaline, saline lake: Limnology and Oceanography, v. 44, p. 178–188.

Lanoil, B.D., Sassen, R., La Duc, M.T., Sweet, S.T., and Nealson, K.H., 2001, Bacteria and archaea physically associated with Gulf of Mexico gas hydrates: Applied and Environmental Microbiology, v. 67, no. 11, p. 5143–5153.

Martens, C.S., Albert, D.B., and Alperin, M.J., 1999, Stable isotope tracing of anaerobic methane oxidation in the gassy sediments of Eckernforde Bay, German Baltic Sea: American Journal of Science, v. 299, p. 589–610.

Orphan, V.J., Hinrichs, K.U., Ussler, W., III, Paull, C.K., Taylor, L.T., Sylva, S.P., Hayes J.M., and DeLong, E.F., 2001, Comparative analysis of methane-oxidizing archaea and sulfate-reducing bacteria in anoxic marine sediments: Applied and Environmental Microbiology, v. 67, no. 4, p. 1922–1934.

Orphan, V.J., House, C.H., Hinrichs, K.U., McKeegan, K.D., and Delong, E.F., 2001, Methane-consuming archaea revealed by directly coupled isotopic and phylogenetic analysis: Science, v. 293, no. 5529, p. 484–487.

Orphan, V.J., House, C.H., Hinrichs, K.U., McKeegan, K.D., and Delong, E.F., 2002, Multiple archaeal groups mediate methane oxidation in anoxic cold seep sediments: Proceedings of the National Academy of Science USA, v. 99, no. 11, p. 7663–7668.

Reeburgh, W.S., 1976, Methane consumption in Caraico Trench waters and sediments: Earth and Planetary Science Letters, v. 28, p. 337–344.

Reeburgh, W.S., 1996, Microbial growth on C1 compounds: Dordrecht, Kluwer Academic Publishers.

Swafford, D.L., 2000, Pylogenetic analysis using parsimony (and other methods): Sunderland, Massachusetts, Sinauer Associates.

Teske, A., Hinrichs, K.U., Edgcomb, V., de vera Gomez, A., Kysela, D., Sylva, S.P., Sogin, M.L., and Jannasch, H.W., 2002, Microbial diversity of hydrothermal sediments in the Guaymas Basin—evidence for anaerobic methanotrophic communities: Applied Environmental Microbiology, v. 68, no. 4, p. 1994–2007.

Whiticar, M.J., Faber, E., and Schoell, M., 1986, Biogenic methane formation in marine and freshwater environments—CO_2 reduction vs. acetate fermentation-isotope evidence: Geochim Cosmochim Acta, v. 50, p. 693–709.

Zhang, C.L., Wall, J.D., Larsen, L., Sassen, R., Huang, Y., Wang, Y., Peacock, A., White, D.C., Horita, J., and Cole, D.R., 2002, Lipid and carbon isotopic evidence of methane-oxidizing and sulfate-reducing bacteria in association with gas hydrates from the Gulf of Mexico: Geological Society of America, v. 30, no. 3, p. 239–242.

Chapter 11

Qualitative Planktonic Foraminiferal Biostratigraphy of Core MD02-2570, of Late Quaternary age, from the Northern Gulf of Mexico

Charlotte A. Brunner

Qualitative planktonic foraminiferal biostratigraphy of core MD02-2570, of late Quaternary age, from the northern Gulf of Mexico; chapter 11 in *Winters, W.J., Lorenson, T.D., and Paull, C.K., eds., 2007, Initial report of the IMAGES VIII/PAGE 127 gas hydrate and paleoclimate cruise on the RV* Marion Dufresne *in the Gulf of Mexico, 2–18 July 2002: U.S. Geological Survey Open-File Report 2004–1358.*

Abstract

Preliminary age models were developed for the RV *Marion Dufresne* Calipso piston core, MD02-2570, based on datum levels defined from the regional biostratigraphic zonation of planktonic foraminifers. Two datum levels were recognized, the base of the Z Zone, which is ~9.8 thousand years (ka) in the Gulf of Mexico, and the top of the Y2 Subzone, which is ~14 ka. The sedimentation rate in the Z Zone was 26 centimeters per thousand years (cm/k.y.), a rate somewhat slower than that found in other ponded basins in the northern Gulf of Mexico but faster than rates on the open slope and abyssal plain. In contrast, the rate of the Y1 Subzone was >200 cm/k.y., exceeding rates in local ponded basins. The fast rate may be related to "overbank" deposition from the Mississippi Canyon during deglaciation and possibly during slumping that formed the canyon.

Introduction

A 28-meter (m)-long Calipso core, MD02-2570, was recovered at Station 18 in the northern Gulf of Mexico during the research vessel (RV) *Marion Dufresne* cruise, International Marine Past Global Changes Study (IMAGES) VIII in 2002. IMAGES is a program of Paleoceanography of the Atlantic and Geochemistry (PAGES). The core site lies in a minibasin on the west flank of the Mississippi Canyon at 28° 4.26' N, 89° 41.39' W, in 631 m of water. The site is adjacent to a field of mud volcanoes associated with methane gas emissions (Carol Lutken, oral. commun., Center for Marine Resources and Environmental Technology, Mississippi Mineral Resources Institute, University of Mississippi, 2003).

Sediments in core MD02-2570 were divided into two units: (1) a bioturbated, silty clay with biogenic sand from the top to 3.8 meters below the sea floor (mbsf), and (2) a laminated silty clay below. The laminations of the second unit typically have sharp contacts with some cross beds and cut-and-fill structures. The second unit also contains several stringers and laminae of well-sorted silt, minor amounts (<2 percent by weight) of mineral sand from 9 to 18 mbsf, and an interval of particularly clay-rich sediment from 18 to 21 mbsf. The entire core is affected by gas expansion expressed in a continuum from reduced wet bulk density and small molds of apparent gas bubbles to large gaps that occur below 4 mbsf.

Methods

Thirty large samples of ~40 cubic centimeters (cm^3) were taken at 1-m intervals and prepared for microscopic examination of the sand-size fraction. Samples were dried in a forced-air oven at 40 °C, weighed, and soaked in a 1-percent (by weight) solution of Calgon® for no more than 3 hours in order to disaggregate the clay-rich sediment. The dispersed sediment was poured into a 9-inch sieve with 63-micrometer (μm) openings and rinsed with tap water until all of the silt and clay was removed. The sand-size residue was dried, weighed to determine the weight percent of sand, and vialed for microscopic examination.

[1]Department of Marine Science, University of Southern Mississippi, 1020 Balch Blvd., Stennis Space Center, MS 39529 USA.

Dry sand samples were sieved in a 3-inch sieve with 150-µm openings, and the sands were examined under a dissecting microscope at magnifications up to 63X. The qualitative abundance of planktonic foraminifers relative to other constituents of the sand-size fraction, preservation state, and relative frequency of species of planktonic foraminifers was tabulated. Other constituents of the sand fraction were identified to general type and ranked by abundance.

The biostratigraphy of Ericson and Wollin (1968) was applied, as modified for use in the Gulf of Mexico by Kennett and Huddlestun (1972) and Kennett and others (1985). Ages of biostratigraphic horizons are from Flower and Kennett (1990) and Poore and others (2003).

Results

Dry bulk sediment samples range in weight from ~20 grams (g) at the top of the section to 60 to 120 g below 4 mbsf (fig. 1; table 1). The large samples contain an average of ~1-percent sand-size material by weight after sieving to remove silt and clay (fig. 2; table 1). Relatively coarse samples with more than 0.5-percent sand are limited to three intervals: above 4 mbsf, between 7 and 18 mbsf, and at 21 mbsf. The coarsest two samples at 3.04 and 9.00 mbsf have anomalously heavy sand-size fractions of 11 and 4 percent, respectively. These values are more than one standard deviation heavier than the mean weight percent of all samples.

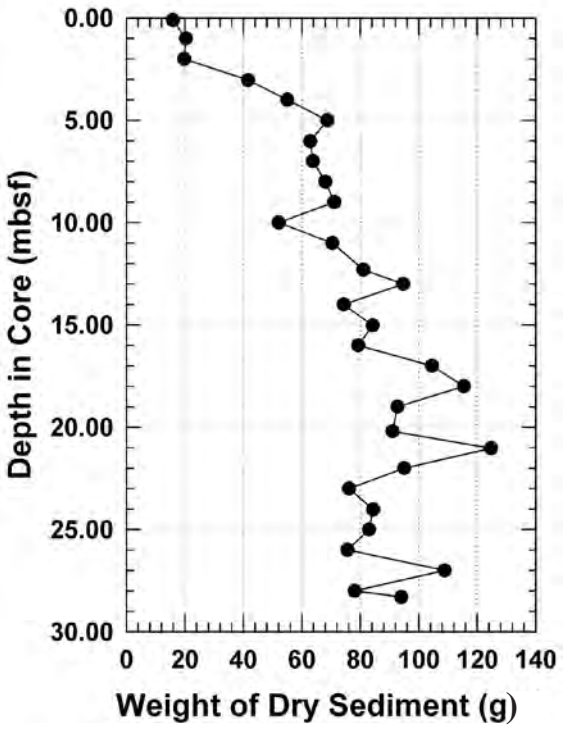

Figure 1. Weight of total dry bulk sediment in samples from core MD02-2570.

Table 1. Sample depths, dry sediment weight (grams, g), sand content (g), and sand content as weight percent for core MD02-2570.

[mbsf, meters below sea floor; g, grams; %, percent]

Depth (mbsf)	Dry bulk sediment weight (g)	Sand (g)	Sand (%)
0.10	15.888	0.400	2.5
1.00	20.355	0.226	1.1
2.00	19.736	0.141	0.7
3.04	41.600	4.725	11.4
4.00	55.030	0.228	0.4
5.00	68.719	0.052	0.1
6.03	62.892	0.036	0.1
7.00	63.779	0.123	0.2
8.00	68.047	0.389	0.6
9.00	71.111	3.121	4.4
10.00	52.070	1.108	2.1
11.00	70.445	0.382	0.5
12.31	81.064	1.676	2.1
13.00	94.653	0.144	0.2
14.00	74.339	1.458	2.0
15.03	84.215	0.807	1.0
16.00	79.254	1.392	1.8
17.00	104.513	1.004	1.0
18.00	115.362	0.136	0.1
19.00	92.679	0.023	0.0
20.20	91.057	0.381	0.4
21.03	124.678	1.035	0.8
22.00	95.010	0.031	0.0
23.00	76.166	0.127	0.2
24.03	84.377	0.053	0.1
25.00	83.019	0.067	0.1
26.00	75.576	0.156	0.2
27.00	108.830	0.060	0.1
28.00	78.109	0.029	0.0
28.30	93.997	0.013	0.0
		Average	1.1
		StDev	2.2

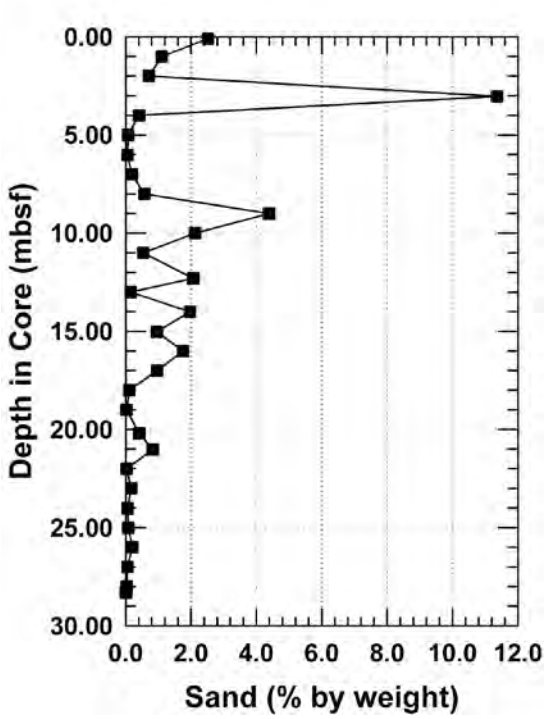

Figure 2. Sand content measured as weight percent in samples from core MD02-2570.

Microscopic assessment of the >150-μm fraction (table 2) shows that planktonic foraminifers dominate samples from the top of the core to <3 mbsf, framboidal pyrite or benthic foraminifers dominate from <3 to <9 mbsf, and mineral grains dominate from <9 to <18 mbsf. Below 17 to 18 mbsf, the cored section contains various amounts of siderite (?), unidentified organic disks, and foraminifers. Trace amounts of ostracodes and radiolarians occur sporadically throughout the core. The unusually heavy sand sample at 3.04 mbsf contains carbonate nodules, and the sample at 9.00 mbsf contains several large pieces of framboidal pyrite.

A total of 28 species of planktonic foraminifers were identified in the core (table 2). The tropical to subtropical foraminifer, *Globigerinoides ruber*, both the pink and the white form, which are likely different species (Darling and others, 1997), is the most abundant plexus, composing about half of the specimens. Two end-member foraminiferal assemblages occur in the core: (1) a tropical assemblage with abundant warm-water forms, such as *Globorotalia cultrata, Globorotalia tumida*, other members of the "*menardii*" plexus (Ericson and Wollin, 1968), and *Pulleniatina obliquiloculata;* and (2) a cool subtropical assemblage with reduced numbers of warm-water species and greater numbers of cool-tolerant species, such as *Globorotalia inflata, Globigerina falconensis,* and *Globigerina bulloides*. The tropical assemblage with the "*menardii*" plexus occurs in samples from the top of the core to <3 mbsf. The cool subtropical assemblage occurs in samples below 11 mbsf. An intermediate assemblage with neither the *"menardii"* plexus nor *Globorotalia inflata* bridges the interval between <3 and <12 mbsf.

A single planktonic foraminifer of late Paleocene to middle Eocene age, *Pseudohastigerina wilcoxensis*, was found mixed into the sand fraction at 11 mbsf. However, no fossils of Pliocene or Miocene age were observed (Kohl and Roberts, 1994). Reworking of material of pre-Quaternary age, presumably from the adjacent mud volcanoes, does not significantly affect the planktonic foraminifers in the >150-μm fraction (Kohl and Roberts, 1994; 1995) of this core.

Table 2. Biostratigraphy of core MD02-2570.

Tabulated are the sample depths; mbsf, meters below sea floor; assigned biostratigraphic zone; quality of planktonic foraminifer preservation; overall abundance of planktonic foraminifers relative to other constituents in the sand-size fraction; qualitative frequency of planktonic foraminifer species of Quaternary age (a=abundant, c=common, f=frequent, r=rare, vr=very rare); and listing of common constituents of the >150-micrometer (μm) fraction ranked in order of abundance.

Depth (mbsf)	Zone	Preservation	Abundance	*Beella digitata*	*Globigerina bulloides*	*Globigerina calida*	*Globigerina falconensis*	*Globigerina rubescens*	*Globigerinella aequilateralis*	*Globigerinita glutinata*	*Globigerinoides conglobatus*	*Globigerinoides quadrilobatus*	*Globigerinoides ruber (white)*	*Globigerinoides ruber (pink)*	*Globigerinoides tenellus*	*Globorotalia crassaformis*	*Globorotalia cultrata*	*Globorotalia hirsuta*	*Globorotalia inflata*	*Globorotalia scitula*	*Globorotalia truncatulinoides (right)*	*Globorotalia truncatulinoides (left)*	*Globorotalia tumida*	*Globorotalia ungulata*	*Hastigerina pelagica*	*Neogloboquadrina dutertrei*	*Neogloboquadrina pachyderma (right)*	*Neogloboquadrina pachyderma (left)*	*Orbulina universa*	*Pulleniatina obliquiloculata*	*Sphaeroidinella dehiscens*	Constituents of the >150-μm sand fraction
0.10	Z1	good	abundant			vr					r	f	c	r			c				f		f			f			r	r		Mostly planktonic foraminifers, rare benthics, a few pieces of iron oxide.
1.00	Z1 or Z2	good	abundant			vr				r		f	f	r			r				f		r			f			r	f	vr	Mostly planktonic foraminifers, few benthics, pyritized tubes, urchin spines.
2.00	Z2	mod	abundant			vr	r			r		f	r	r		f			r?		r		r			f			f	r		Mostly planktonic foraminifers, benthics, trace of pyrite in tests .
3.04	Y1	poor	common				r		r			f	f	vr		f					r				vr	r	r		f	vr		Mostly carbonate nodules, planktonic foraminifers, benthics, ostracodes, pyrite, plant fibers.
4.00	Y1	mod	rare			vr				vr		r	r	r												r						Mostly pyrite with benthic foraminifers, planktonics.
5.00	Y1	mod	rare		vr	vr				vr			r	r	vr						r					r						Mostly pyrite with planktonic foraminifers, benthics.
6.03	Y1	mod	few		vr	vr			r	vr		r	r	r	vr	r					r	vr				r	r		vr	vr		Mostly benthic foraminifers, planktonics, pyrite, radiolarians.
7.00	Y1	mod	rare		vr	vr	vr			vr			r	r			1									r			r			Mostly pyrite, benthic foraminifers, planktonics.
8.00	Y1	mod	rare		vr				r	vr		vr	r	r		r					vr	r				r			r			Mostly pyrite (slightly crystalline), benthic foraminifers, planktonics, quartz grains, ostracodes.
9.00	Y1	mod	rare		r	r	r	r		r			r	r		c				vr						r			r			Mostly mineral grains, benthic foraminifers, planktonics, ostracodes, >1-millimeter chunks of pyrite.
10.00	Y1	mod	common		r	r	r		r	r	vr	r	c	f		f				vr						r			r			Mostly mineral grains, benthic foraminifers, planktonics, trace of pyrite.

Table 2. Biostratigraphy of core MD02-2570. — Continued

Tabulated are the sample depths; mbsf, meters below sea floor; assigned biostratigraphic zone; quality of planktonic foraminifer preservation; overall abundance of planktonic foraminifers relative to other constituents in the sand-size fraction; qualitative frequency of planktonic foraminifer species of Quaternary age (a=abundant, c=common, f=frequent, r=rare, vr=very rare); and listing of common constituents of the >150-micrometer (μm) fraction ranked in order of abundance.

Depth (mbsf)	Zone	Preservation	Abundance	*Beella digitata*	*Globigerina bulloides*	*Globigerina calida*	*Globigerina falconensis*	*Globigerina rubescens*	*Globigerinella aequilateralis*	*Globigerinita glutinata*	*Globigerinoides conglobatus*	*Globigerinoides quadrilobatus*	*Globigerinoides ruber (white)*	*Globigerinoides ruber (pink)*	*Globigerinoides tenellus*	*Globorotalia crassaformis*	*Globorotalia cultrata*	*Globorotalia hirsuta*	*Globorotalia inflata*	*Globorotalia scitula*	*Globorotalia truncatulinoides (right)*	*Globorotalia truncatulinoides (left)*	*Globorotalia tumida*	*Globorotalia ungulata*	*Hastigerina pelagica*	*Neogloboquadrina dutertrei*	*Neogloboquadrina pachyderma (right)*	*Neogloboquadrina pachyderma (left)*	*Orbulina universa*	*Pulleniatina obliquiloculata*	*Sphaeroidinella dehiscens*	Constituents of the >150-μm sand fraction
11.00	Y1	good	very rare		vr	vr	vr		vr	vr		vr	vr	vr	vr		1									vr	vr		vr			Mostly mineral grains, benthic foraminifers, planktonics, ostracodes, trace of pyrite.
12.30	Y2	mod	common		r	f	r	vr		r		r	c	f		c			vr							vr	r		r			Mostly mineral grains, benthic foraminifers, planktonics, trace of pyrite.
13.00	Y	good	rare	vr	r			vr	vr			r	c	c	r	r		r	vr		r						vr					Mostly mineral grains, benthic foraminifers, planktonics, ostracodes, trace of pyrite.
14.00	Y	good	rare		r	r			r	r		r	c	c		r			c	r	r						r		r			Mostly mineral grains, benthic foraminifers, planktonics, ostracodes, trace of pyrite.
15.03	Y	good	common		r	r	r						c	c		f			r		r					r			r			Mostly mineral grains, benthic foraminifers, planktonics, pyrite, ostracodes.
16.00	Y	good	common			r	r		r	r	vr		c	c		f			r		r								r			Mostly mineral grains, benthic foraminifers, planktonics, pyrite, ostracodes.
17.00	Y	good	common		r				r	r		r	c			f			r	vr	r	r		vr		r			r			Mostly mineral grains, with equal amounts of benthic foraminifers, planktonics, and pyrite; ostracodes.
18.00	Y	good	common		r				r	r			c	c		r			r		r	r				r	r		r			Mostly siderite(?), organic discs?, with equal amounts of benthic foraminifers and planktonics; mineral grains, ostracodes.
19.00	Y	good	rare			r	r		r	r		vr	c	c	r	r					r					r			r			Mostly organic discs, planktonic foraminifers, benthics, siderite(?), ostracodes, mineral grains.

Table 2. Biostratigraphy of core MD02-2570. — Continued

Tabulated are the sample depths; mbsf, meters below sea floor; assigned biostratigraphic zone; quality of planktonic foraminifer preservation; overall abundance of planktonic foraminifers relative to other constituents in the sand-size fraction; qualitative frequency of planktonic foraminifer species of Quaternary age (a=abundant, c=common, f=frequent, r=rare, vr=very rare); and listing of common constituents of the >150-micrometer (μm) fraction ranked in order of abundance.

Depth (mbsf)	Zone	Preservation	Abundance	*Beella digitata*	*Globigerina bulloides*	*Globigerina calida*	*Globigerina falconensis*	*Globigerina rubescens*	*Globigerinella aequilateralis*	*Globigerinita glutinata*	*Globigerinoides conglobatus*	*Globigerinoides quadrilobatus*	*Globigerinoides ruber (white)*	*Globigerinoides ruber (pink)*	*Globigerinoides tenellus*	*Globorotalia crassaformis*	*Globorotalia cultrata*	*Globorotalia hirsuta*	*Globorotalia inflata*	*Globorotalia scitula*	*Globorotalia truncatulinoides (right)*	*Globorotalia truncatulinoides (left)*	*Globorotalia tumida*	*Globorotalia ungulata*	*Hastigerina pelagica*	*Neogloboquadrina dutertrei*	*Neogloboquadrina pachyderma (right)*	*Neogloboquadrina pachyderma (left)*	*Orbulina universa*	*Pulleniatina obliquiloculata*	*Sphaeroidinella dehiscens*	Constituents of the >150-μm sand fraction
20.00	Y	mod	rare	vr			r		r	r		r	c	c	r	r		vr	r		r				r	r		r			Mostly siderite(?), organic discs, planktonic foraminifers, benthics, mineral grains.
21.03	Y	mod	very rare				r					r	r	r															r			Mostly siderite(?) and mica; rare organic discs, benthic foraminifers, very rare planktonics.
22.00	Y	mod	rare			r	r		r	r			r						r							r	r		r			Mostly organic discs, benthic foraminifers, planktonics, mineral grains.
23.00	Y	good	common		r	r	r		r	r		r	c	c		r				r	vr	r				r	r		r			Mostly organic discs, benthic foraminifers, planktonics, mineral grains.
24.00	Y	good	very rare					vr	vr				vr	vr	vr																	Mostly siderite(?), with rare benthic foraminifers, planktonics, organic discs.
25.00	Y	good	very rare			vr			vr	vr			vr	vr		vr						vr				vr	vr		vr			Mostly siderite(?), with organic discs, rare benthic foraminifers, planktonics.
26.00	Y	mod	common			r	r		r		vr	r	c	c	r	r			r		r	r				r			r			Equal parts organic discs, planktonic foraminfiers, benthics; rare siderite(?).
27.00	Y	mod	rare			r	r		r	r		r	c	c	r	r			r		r	vr				r	r		r			Organic discs with benthic foraminifers and rare planktonic foraminifers.
28.00	Y	mod	rare			r	r	r	r	r			c		r	r			r		r	vr							r			Organic discs with benthic foraminifers and rare planktonic foraminifers.
28.30	Y	good	very rare	r	r				r				r	r	r	r					r						r	r	r			Organic discs with benthic foraminifers and very rare planktonic foraminifers.

Discussion

Zonation

The sequence of planktonic foraminiferal assemblages is consistent with the results of Kennett and others (1985), Flower and Kennett (1990), and Poore and others (2003) (fig. 3; table 2). The tropical assemblage at the top of the core correlates with the Z Zone of Ericson and Wollin (1968), which is equivalent to all but the bottom of the Holocene and Marine Isotope Stage (MIS) 1. This interval is tentatively subdivided into Subzones Z1 and Z2 of Kennett and Huddlestun (1972) with the boundary falling near 1 mbsf. Subzone Z2 is recognized based on the greater abundance of *Globorotalia crassaformis* and lesser abundance of *Globorotalia cultrata* compared to Subzone Z1, a pattern reaffirmed by the results of Poore and others (2003). However, Kennett and Huddlestun (1972) used census data, whereas this tentative assessment is based on qualitative frequency estimates. Although the core may contain sediment from Subzone Z1, it remains unresolved whether or not the core successfully sampled the topmost sediment of the subzone (for example, Dowsett and others, 2003).

The lower section of the core below 2 mbsf is assigned to the Y Zone of Ericson and Wollin (1968). This section can be further subdivided with confidence into Subzones Y1 and Y2 of Kennett and Huddlestun (1972), the boundary of which lies between 11.00 and 12.30 mbsf. Subzone Y1 is recognized based on the absence of both *Globorotalia cultrata* and *Globorotalia inflata*, whereas the top of Y2 is based on the occurrence of *Globorotalia inflata* without members of the *Gt. menardii* plexus. Subzone Y1 is equivalent to the Wisconsinan deglaciation in the upper part of MIS 2. The deglaciation is expressed in the Gulf of Mexico as a period of warming and rising sea level punctuated by events of low surface-water salinities, which caused excessively light values of oxygen-18 ($\delta^{18}O$). Subzone Y1A (Kennett and others, 1985; Flower and Kennett, 1990), which is equivalent to the Younger Dryas cooling, was not

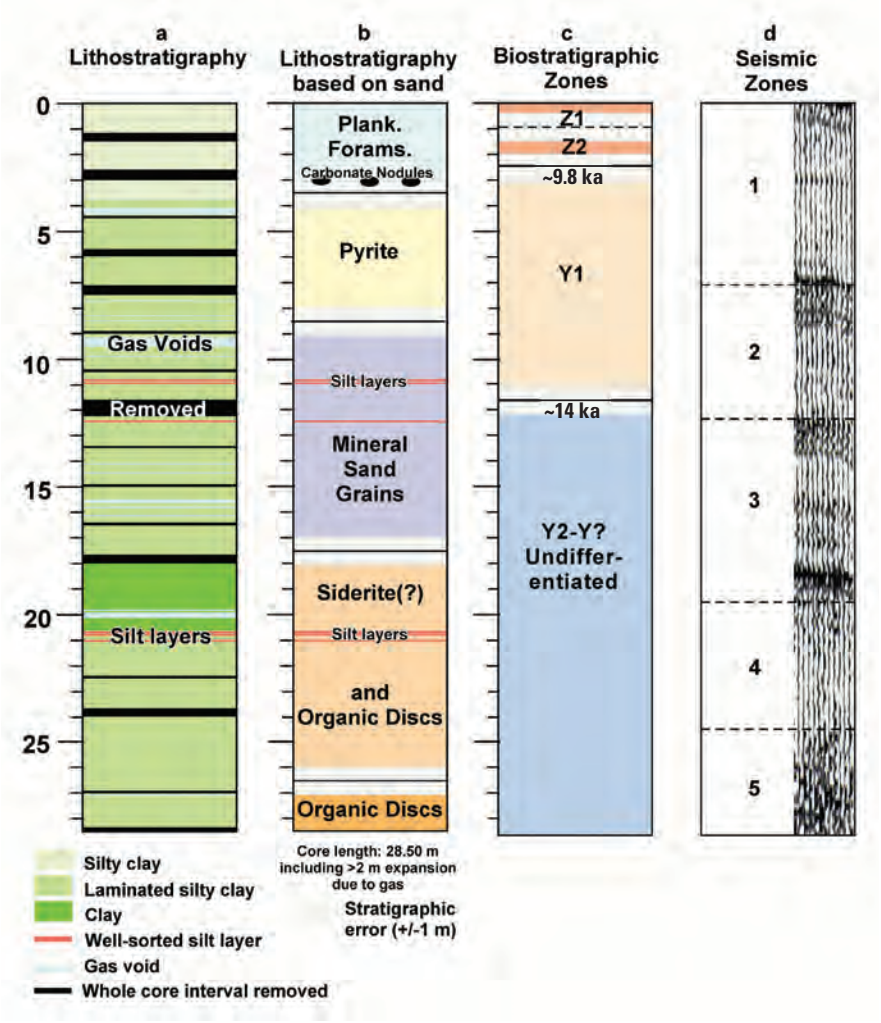

Figure 3. (a) Lithology of core MD02-2570. The core was described onboard the RV *Marion Dufresne* by cruise scientists. (b) Microscopic assessment of the >150-micrometer-size class shows that planktonic foraminifers dominate samples from the top of the core to ~3 meters below sea floor (mbsf), framboidal pyrite or benthic foraminifers dominate from ~3 to 9 mbsf, and mineral grains dominate from ~9 to 18 mbsf. Below 17 to 18 mbsf, the section contains various amounts of siderite (?), spore-like organic disks, and foraminifers. Trace amounts of ostracodes and radiolarians occur sporadically throughout the core. Carbonate nodules were observed at 3 mbsf. Several of these sand-size constituents are authigenic byproducts of anoxic bacterial respiration and methanogenesis. (c) The core is divided into four biostratigraphic zones based on qualitative assessment of assemblages of planktonic foraminifers (Kennett and others, 1985; Flower and Kennett, 1990). Zones include the Z1 and Z2 Subzones, which span most of the Holocene from 0–9.8 ka, Subzone Y1, which covers most of the glacial termination from 9.8–14 ka, and an as yet undifferentiated Y Zone. Extrapolation of the sedimentation rate in Zone Y1 (220 centimeters per thousand years (cm/k.y.)) suggests that the base of the core is no younger than ~22 ka. (d) The biostratigraphy of core MD02-2570 can be loosely correlated to the seismic stratigraphy of Lutken and others (2003). The core penetrated apparently to the top of Seismic Unit 5; however, there is uncertainty in correlation for several reasons, including gas expansion in the core.

recognized, perhaps because the sampling interval is too coarse (the 1-m sample interval corresponds to a period of ~500 years on average in Subzone Y1).

The Y Zone below the Y1–Y2 boundary cannot be further subdivided based on qualitative estimates of species frequencies; however, the age of the bottom can be constrained. Two volcanic ashes occur in the northeastern Gulf of Mexico in the Y Zone: (1) a distinctive ash layer within Subzone Y8 and (2) a dispersed ash in Y6 (Kennett and Huddlestun, 1972; Ledbetter, 1986). No volcanic ash was reported in the core description, so the base of the core may lie above Y6 and below the top of Y2. The base of the core, without question, lies above the top of the X Zone, which is near the MIS 5.1–MIS 5.2 boundary, which is ~86 ka (Williams, 1984; Martinson and others, 1987).

Age Models

Two datum levels that were clearly recognized from the biostratigraphy were combined with two inferred datum levels to develop age models of the core. The ages of the two well-controlled biostratigraphic levels are known from radiocarbon dating in the Gulf of Mexico. The base of the Z Zone is 9.8 ka, and the base of Y1 is 14 ka (Flower and Kennett, 1990; Poore and others, 2003). These ages are not calibrated to calendar years. The two inferred datum levels are the present-day and the top of Subzone Y6. The top of the core may or may not be present-day, but it is tentatively assumed to be 0 ka. The bottom of the core may be younger or older than Y6, the top of which is equivalent to the top of MIS 4 (Kennett and Huddlestun, 1972; Williams and Kohl, 1986). The top of MIS 4 is 59 ka based on astronomical tuning of the Spectral Analysis and Mapping Project (SPECMAP) composite oxygen isotope curve (Martinson and others, 1987).

Two age models were formulated to embrace the likely minimum and maximum ages of the base of the core (fig. 4). The tops of both models are the same and estimate sedimentation rates of 26 cm/k.y. in the Z Zone and 217 cm/k.y. in the deglacial Subzone Y1 interval. Below the deglacial Y1 Subzone, model 1 is based on the assumption that the age of the base of the core is 59 ka, equivalent to the top of the Y6 Subzone. Model 1 implies that the sedimentation rate of this interval is 37 cm/k.y., not much faster than the interglacial interval. In model 2, the sedimentation rate of the deglacial Y1 interval is extrapolated to the base of the core. The age of the base of the core in model 2 is ~22 ka. The two models indicate that the age of the base of core MD02-2570 is between 22 and 59 ka. The actual age of the base of the core cannot be younger than 14 ka nor older than 86 ka, the respective ages of the base of Subzone Y1 and the top of Zone X.

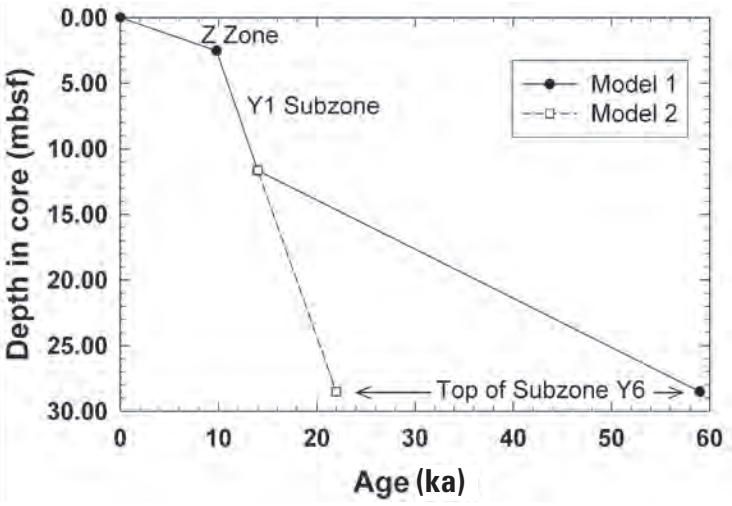

Figure 4. Age models 1 and 2 for core MD02-2570. Age model 1 is based on the assumption that the base of the core lies at the top of Subzone Y6, and age model 2 is based on the assumption that the rate of sedimentation in Subzone Y1 extends to the base of the core.

Comparisons to Other Sections From Gulf of Mexico Ponded Basins

Core MD02-2570 is comparable to other cores from two ponded basins in the northern Gulf of Mexico—the Pigmy and Orca Basins (fig. 5a, b). DSDP Site 618 in the Pigmy Basin recovered an orderly sequence to 74 mbsf, reaching the W Zone of Ericson and Wollin (1968; Kohl, 1986). The base of the Z Zone is 5 mbsf, and the base of the Y Zone is 147 mbsf, with the Y8 ash layer at 142 mbsf (85 Ka, Ledbetter, 1986; Williams and Kohl, 1986). Core EN32-PC6 in the south section of the Orca Basin recovered a continuous section to 11 mbsf, reaching the Y2 Subzone of Kennett and Huddlestun (1972). The base of the Z Zone lies at 4 mbsf, and the base of the Y1 Subzone lies at 6.4 mbsf. The age of the base of the core is ~29 ka based on extrapolation from radiocarbon ages in the section.

Sedimentation rates in the Z Zone are 26, 51, and 41 cm/k.y. at the MD02-2570 site, DSDP Site 618, and EN32-PC6, respectively. For comparison, the sedimentation rate in the Z Zone for several cores outside ponded basins in the northern Gulf of Mexico are <20 cm/k.y. (Poore and others, 2003).

Sedimentation rates for the Y1 Subzone are 217, 89, and 57 cm/k.y. (fig. 5a) at the MD02-2570 site, DSDP Site 619, and EN32-PC6, respectively. The rate at the MD02-2570 site is substantially faster than those at the other locales and may be related to formation of the Mississippi Canyon by mega-slumping event(s) culminating ~20 ka (Coleman and others, 1983). Alternatively, the sands may be overbank deposits derived from the already-formed Mississippi Canyon, which channelized debris from low-stand coastal deposits drowned by rising sea level.

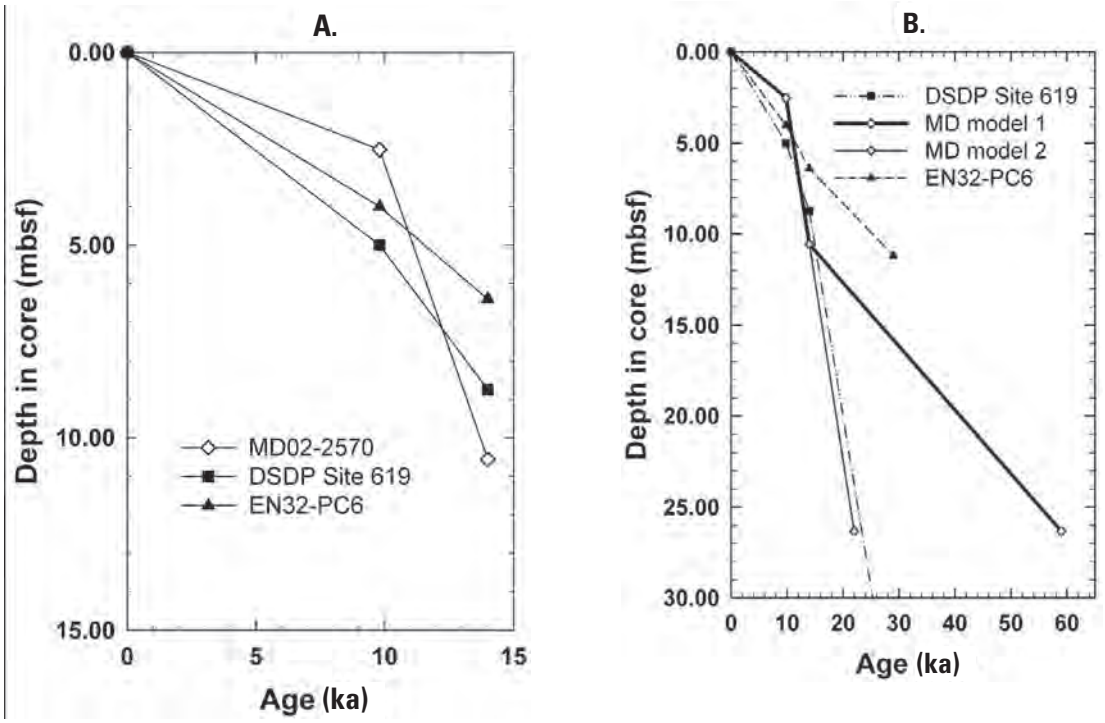

Figure 5. (A) Comparison of age model 1 for core MD02-2570 (diamond symbols) with two cores from other ponded basins in the northern Gulf of Mexico, DSDP Site 619 (squares) and piston core EN32-PC6 (triangles). (B) Comparison of age model 2 for core MD02-2570 (diamond symbols) with two cores from other ponded basins in the northern Gulf of Mexico, DSDP Site 619 (squares) and piston core EN32-PC6 (triangles).

Mean sedimentation rates in the lower Y Zone range between 205 and 32 cm/k.y. at DSDP Site 619 and EN32-PC6, respectively (fig. 5b). These rates bracket the rates of the MD02-2570 site for the two age models, which estimate rates of 37 and 217 cm/k.y. below the Y1 Subzone.

Conclusion

Core MD02-2570 of late Quaternary age contains sediments from the Z and upper Y Zones of Ericson and Wollin (1968). The sedimentary record spans the Wisconsinan deglaciation and the Holocene interglacial period with quite high average rates of sedimentation, 217 and 26 cm/k.y., respectively, although the continuity of the record cannot be reliably established based on these data. The fossils remain in excellent condition based on visual inspection; however, the presence of free gas, possibly gas hydrate, and abundant alteration products, such as carbonate nodules, pyrite, and siderite(?), raises some questions regarding the potential use of either carbon or oxygen isotopes in fossil tests for high-resolution biostratigraphy, geochronology, and paleoclimate analysis. The effects of possible density-current activity must be assessed below 3.8 mbsf prior to further faunal analysis. The cored section may contain the depositional signature associated with excavation of the Mississippi Canyon and(or) subsequent drowning of lowstand coastal deposits during the last Wisconsinan transgression of the sea.

Acknowledgments

The reported work was funded by a contract from the Mississippi Mineral Resources Institute as part of the Gulf of Mexico Hydrates Research Consortium. The author heartily thanks Carol Lutken for making available the samples and data and for assistance in the laboratory. The author also thanks Bill Winters for making available logger data and core descriptions. Many thanks also to the reviewers, C. Wylie Poag and C. Paull, who offered constructive suggestions.

References Cited

Coleman, J.M., Prior, D.B., and Lindsay, J.F., 1983, Deltaic influences on shelfedge instability processes: SEPM, Sp. Pub., no. 33, p. 121–137.

Darling, K.F., Wade, C.M., Kroon, D., and Leigh-Brown, A.J., 1997, Planktic foraminiferal molecular evolution and their polyphyletic origins from benthic taxa: Marine Micropaleontology, v. 30, no. 4, p. 251–266.

Dowsett, H., Brunner, C.A., Verardo, S., and Poore, R.Z., 2003, Gulf of Mexico planktic foraminifer core-top calibration data set—raw data: U.S. Geological Survey Open-File Report 03–8, 11 p.

Ericson, D.B., and Wollin, G., 1968, Pleistocene climates and chronology in deep-sea sediments: Science, v. 162, p. 1227–1234.

Flower, B.P., and Kennett, J.P., 1990, The younger Dryas cool episode in the Gulf of Mexico: Paleoceanography, v. 5, no. 6, p. 949–961.

Kennett, J.P., Elmstrom, K., and Penrose, N., 1985, The last deglaciation in Orca Basin, Gulf of Mexico—high resolution planktonic foraminiferal changes: Palaeogeo. Palaeocl., Palaeoeco., v. 50, p. 189–216.

Kennett, J.P., and Huddlestun, P., 1972, Late Pleistocene paleoclimatology, foraminiferal biostratigraphy and tephrochronology, Western Gulf of Mexico: Quaternary Research, v. 2, p. 38–69.

Kohl, B., 1986, Late Quaternary planktonic foraminifers from the Pigmy Basin, Gulf of Mexico, Site 619, Deep Sea Drilling Project Leg 96, *in* Bouma, A.H., Coleman, J.M., Meyer, A.W., and others, Initial reports of the deep sea drilling project, v. 96: Washington, D.C., U.S. Government Printing Office, p. 657–670.

Kohl, B., and Roberts, H.H., 1994, Fossil foraminifera from four active mud volcanoes in the Gulf of Mexico: Geo-Marine Letters, v. 14, no. 2–3, p. 126–134.

Kohl, B., and Roberts, H.H., 1995, Mud volcanoes in the Gulf of Mexico; a mechanism for mixing sediments of different ages in slope environments [abs.]: AAPG Bulletin, v. 79, no. 10, p. 1561.

Ledbetter, M.T., 1986, Late Pleistocene tephrochronology of Pigmy Basin, Deep Sea Drilling Project Site 619, Leg 96, *in* Bouma, A.H., Coleman, J.M., Meyer, A.W., and others, Initial reports of the deep sea drilling project, v. 96: Washington, D.C., U.S. Government Printing Office, p. 685–688.

Lutken, C., Lowrie, A., Geresi, E., Bennett, R., Faas, R., Battista, B., and McGee, T., 2003, Interpretation of high resolution seismic data from a geologically complex continental margin, northern Gulf of Mexico: Transactions of the Gulf Coast Association of Geological Societies, v. 53, p. 504–516.

Martinson, D.G., Pisias, N.G., Hays, J.D., Imbrie, J., Moore, T.C., and Shackleton, N.J., 1987, Age dating and the orbital theory of the ice ages—development of a high-resolution 0 to 300,000-year chronostratigraphy: Quaternary Research, v. 27, no. 1, p. 1–29.

Poore, R.Z., Dowsett, J.J., and Verardo, S., 2003, Millennial- to century-scale variability in Gulf of Mexico Holocene climate records: Paleoceanography, v. 18, no. 2, p. 1048, doi: 10.1029/2002PA000868.

Williams, D.F., 1984, Correlation of Pleistocene marine sediments of the Gulf of Mexico and other basins using oxygen isotope stratigraphy, *in* Healy-Williams, N., Principles of Pleistocene stratigraphy applied to the Gulf of Mexico: Boston, MA, Int. Hum. Resour. Dev. Corp., p. 65–118.

Williams, D.F., and Kohl, B., 1986, Isotope chronostratigraphy and carbonate record for Quaternary Site 619, Pigmy Basin, Louisiana continental slope, *in* Bouma, A.H., Coleman, J.M., Meyer, A.W., and others, Initial reports of the deep sea drilling project, v. 96: Washington, D.C., U.S. Government Printing Office, p. 671–676.

Chapter 12

Grain and Pore Structure Imaging of Gas Hydrate From Core MD02-2569 (Mississippi Canyon, Gulf of Mexico): A First Look by Scanning Electron Microscopy (SEM)

Laura A. Stern[1] and Stephen H. Kirby[1]

Grain and pore structure imaging of gas hydrate from core MD02-2569 (Mississippi Canyon, Gulf of Mexico): A first look by Scanning Electron Microscopy (SEM); chapter 12 in *Winters, W.J., Lorenson, T.D., and Paull, C.K., eds., 2007, Initial report of the IMAGES VIII/PAGE 127 gas hydrate and paleoclimate cruise on the RV* Marion Dufresne *in the Gulf of Mexico, 2–18 July 2002: U.S. Geological Survey Open-File Report 2004–1358.*

Abstract

Natural gas hydrate nodules from core MD02-2569, Gulf of Mexico/Mississippi Canyon site, were imaged by Scanning Electron Microscopy and compared to similar features observed in lab-synthesized gas hydrates of known composition, grain texture, and pressure-temperature histories.

Introduction

One of the challenges of investigating both natural and laboratory-made gas hydrates involves evaluation of their grain and pore structures, characteristics that are revealing guides to the physics and chemistry of hydrate formation, and the effects of changes in environmental conditions. Such structural and textural details also influence the specific effects of gas hydrates on sediment properties.

Scanning Electron Microscopy (SEM) offers significant potential for obtaining such textural information because of its versatility in detection capabilities, its resolution, and its large depth of focus. When applied to gas hydrates, however, numerous technical challenges must be considered: avoiding condensation of atmospheric water on samples during cold transfer, coating samples with an electrically conductive layer without introducing heat or damage to the sample surface, maintaining the hydrate sample material at conditions that avoid spontaneous decomposition or substantial sublimation under vacuum, and either avoiding electron beam damage of the imaging area or properly identifying it when it occurs. Distinguishing handling-induced surface artifacts from the intrinsic sample surface morphology also can be difficult, as well as distinguishing hydrate from water ice. Few SEM images of gas hydrates have been published; work by Kuhs and his coworkers being notable exceptions (Kuhs and others, 2000; Techmer and others, 2001, 2005; Suess and others, 2002; Klapproth and others, 2003; Staykova and others, 2003; Genov and others, 2004), as well as work from our own laboratory (Stern and others, 2002, 2003, 2004; Circone and others, 2003; Stern, Circone, and others, 2005; Stern, Kirby, and others, 2005).

For the study of natural (as opposed to lab-synthesized) gas hydrates, these challenges are greatly amplified by such additional unknowns as the complex in situ environmental conditions controlling the original growth textures or the effects of subsequent recrystallization, annealing, secondary growth, dissociation, dissolution, or chemical exchange processes. The indeterminate extent of sample damage or alteration incurred during retrieval and subsequent storage or handling of the hydrate presents additional unknowns. Without a wider sampling archive and additional experience with assessing these issues, most interpretations of SEM images of natural gas hydrates, therefore, should be regarded as speculative. Nonetheless, useful information about grain structure, pore characteristics, phase composition, and phase distribution may still be gleaned from even preliminary work, particularly if the natural hydrates can be compared to other materials with well-known histories, including lab-synthesized samples.

Here, we present a suite of images offering a “first look” at some natural gas hydrate nodules recovered from research

[1]U.S. Geological Survey, Menlo Park, CA 94025 USA.

vessel (RV) *Marion Dufresne* core MD02-2569 (Mississippi Canyon, Gulf of Mexico), and compare the observed features to those previously documented (Stern and others, 2002, 2003, 2004) in lab-synthesized gas hydrates of known composition, grain structure, and pressure-temperature processing histories. These results are purely qualitative, as we are unable to obtain direct compositional information on the MD02 hydrates at this time. We offer preliminary interpretations drawn from comparison with our SEM image archive of a wide variety of other gas hydrate samples, including pure end-member gas hydrates grown in our laboratory, samples used in compaction and deformation experiments, samples from dissolution experiments, samples of varying (and known) porosity, samples with known fractions of ice and hydrate, and samples used in surface sublimation or partial decomposition tests to help distinguish hydrate from ice.

Experimental Methods

The RV *Marion Dufresne* samples were sent by air freight from St. Petersburg, FL, to the USGS in Menlo Park, CA, in liquid-nitrogen-cooled "dry shippers" approximately 2 months after sample recovery. Upon arrival, the samples were transferred to deep-freezer storage at –90 degrees Celsius (°C). The bulk samples included fine-grained white nodules that were sometimes surrounded by translucent ice or sometimes interspersed with fine-grained sediments. Several samples arrived in small pieces. The white material from both the nodules and fragments actively degassed when warmed and appeared to be composed primarily of hydrate. Information on gas hydrate specimens present in the Gulf of Mexico can be found in Lorenson and others (this volume, chapters 2 and 9) and Winters and others (this volume, chapter 3). Prior to SEM imaging, each sample was immersed in liquid nitrogen while a small section of hydrate, typically 0.75 x 0.75 x 0.5 centimeter (cm), was cleaved for imaging. The section was then attached to a specially designed sample holder.

Surfaces of the sections were prepared and imaged with a LEO 982 field emission SEM equipped with a Gatan Alto 2100 cryo-preparation and coating station, and cryo-imaging stage. The samples, initially in liquid nitrogen, were quickly transferred to the evacuated and pre-chilled (to below –178 °C) preparation chamber, then fractured by cold blade to produce fresh surfaces for viewing. While still in the preparation chamber, the samples were coated with AuPd using a non-heat-emitting sputter head. Samples were then inserted directly through the back of the preparation chamber onto the auxiliary cryo-imaging stage in the SEM column. Imaging was conducted at temperatures below –168 °C and vacuum below 10^{-5} millibar (mbar), using low voltage ($\leq$2 kilovolt (kV)) to minimize sample alteration or beam damage of the sample surface. Several imaged areas were re-examined later in the session to monitor vacuum effects or changes in surface topology over time, a procedure routinely used during SEM imaging of any hydrate- or ice-bearing materials (see Stern and others, 2004, for further technical description of SEM procedures). A companion sample of methane hydrate was also imaged uncoated to ensure that surface topology was not altered by the coating process. Upon subsequent removal from the SEM, all samples actively degassed upon warming, as evidenced by vigorous bubble formation on the specimen surfaces.

Phase identification was not part of this imaging study because our SEM port requirements necessitate removal of the back-scattered electron detector when the cryosystem is in use. Use of energy dispersive x-ray (EDX) capabilities also was problematic because of the long focal distance needed for that technique combined with the low accelerating voltage needed to ensure minimal damage of hydrate. While EDX detection of carbon can permit distinction of hydrocarbon hydrates from ice in some cases where the hydrate has nearly complete guest-molecule site occupancy (Stern and others, 2004; Stern, Kirby, and others, 2005), this method did not yield convincing results on the partially decomposed MD02 samples.

Results and Discussion

Figures 1 and 2 show low-to-high resolution mosaics of the interiors of hydrate nodules from core MD02-2569, and figure 3 shows characteristic textures from near the outer surface and from the mixed hydrate + sediment ± ice sections. Interpretation of the images remains somewhat uncertain given the many unknowns involving bulk sample composition, phase distribution, partial alteration of original textures and(or) composition during the recovery process, and other factors already discussed above. These mosaics, therefore, are presented primarily to give the reader a general sense of the appearance of the as-received sample texture, pore structure, and pore connectivity.

Without more information for definitive interpretation, our best option is to compare the imaged textures with those of known materials having well-characterized composition, grain structure, and known pressure-temperature histories. Figure 4 shows both low- and high-resolution features from the natural hydrate (left column) compared to those of pure methane hydrate used in partial dissolution and(or) dissociation experiments (right column). The samples shown in the right column initially were synthesized in our laboratory by previously published methods (Stern and others, 1996, 2000) that produce pure methane hydrate of composition $CH_4 \cdot 5.9H_2O$. Two samples were compacted hydrostatically (while maintained within their equilibrium stability field) from 30-percent to less than 3-percent porosity, then transported under pressure to an ocean floor test site at 1,030-meter (m) water depth for observation and measurement (see Stern and others, 2003, and Rehder and others, 2004, for further details). Two samples of uncompacted methane hydrate were also sent down in the experiment. Those samples that did not fully dissolve after 26 hours were successfully retrieved for SEM imaging (fig. 4B, D, F, and H).

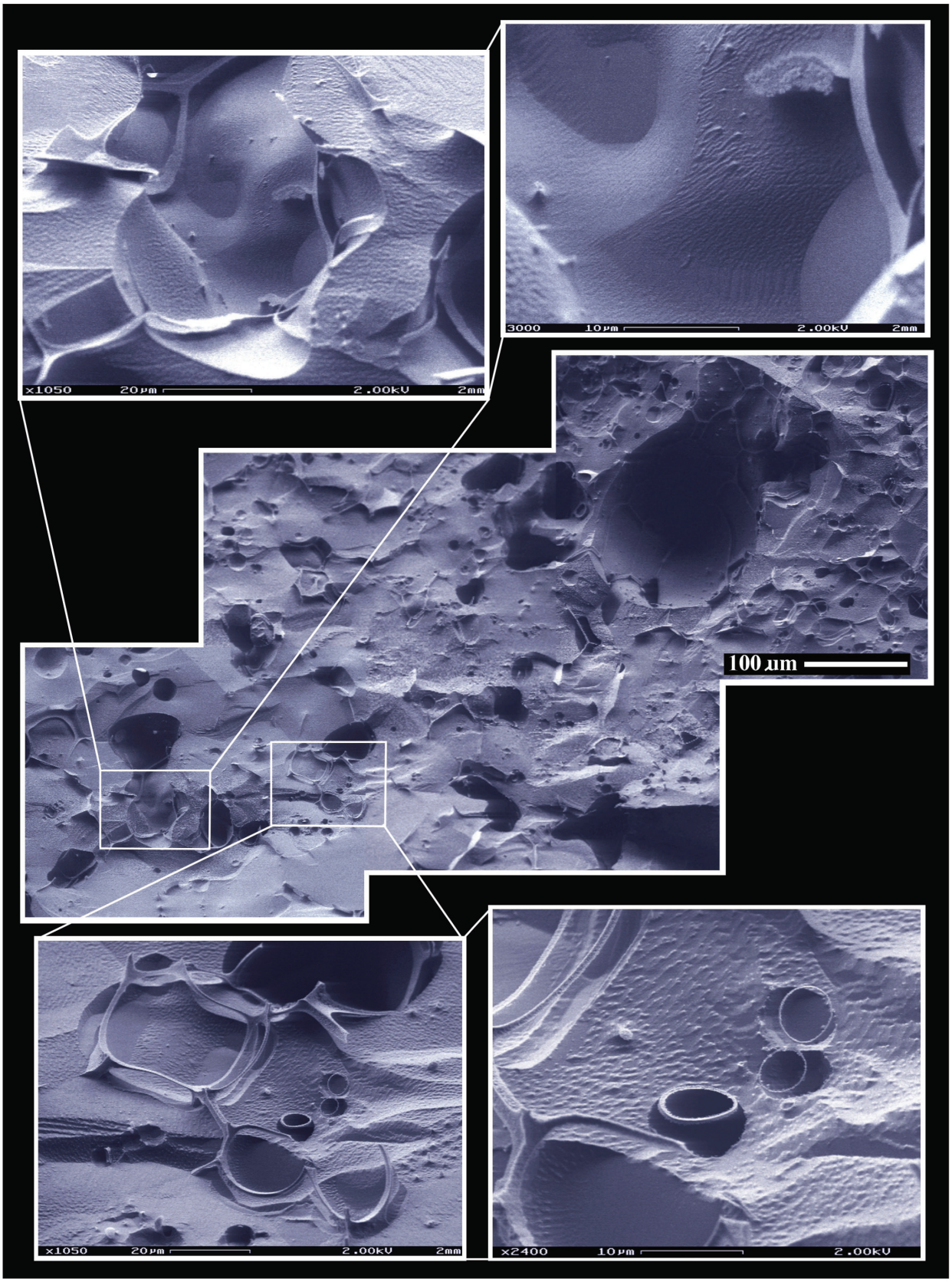

Figure 1. Scanning Electron Microscopy (SEM) mosaic showing a typical section within a gas hydrate "nodule" from core MD02-2569.

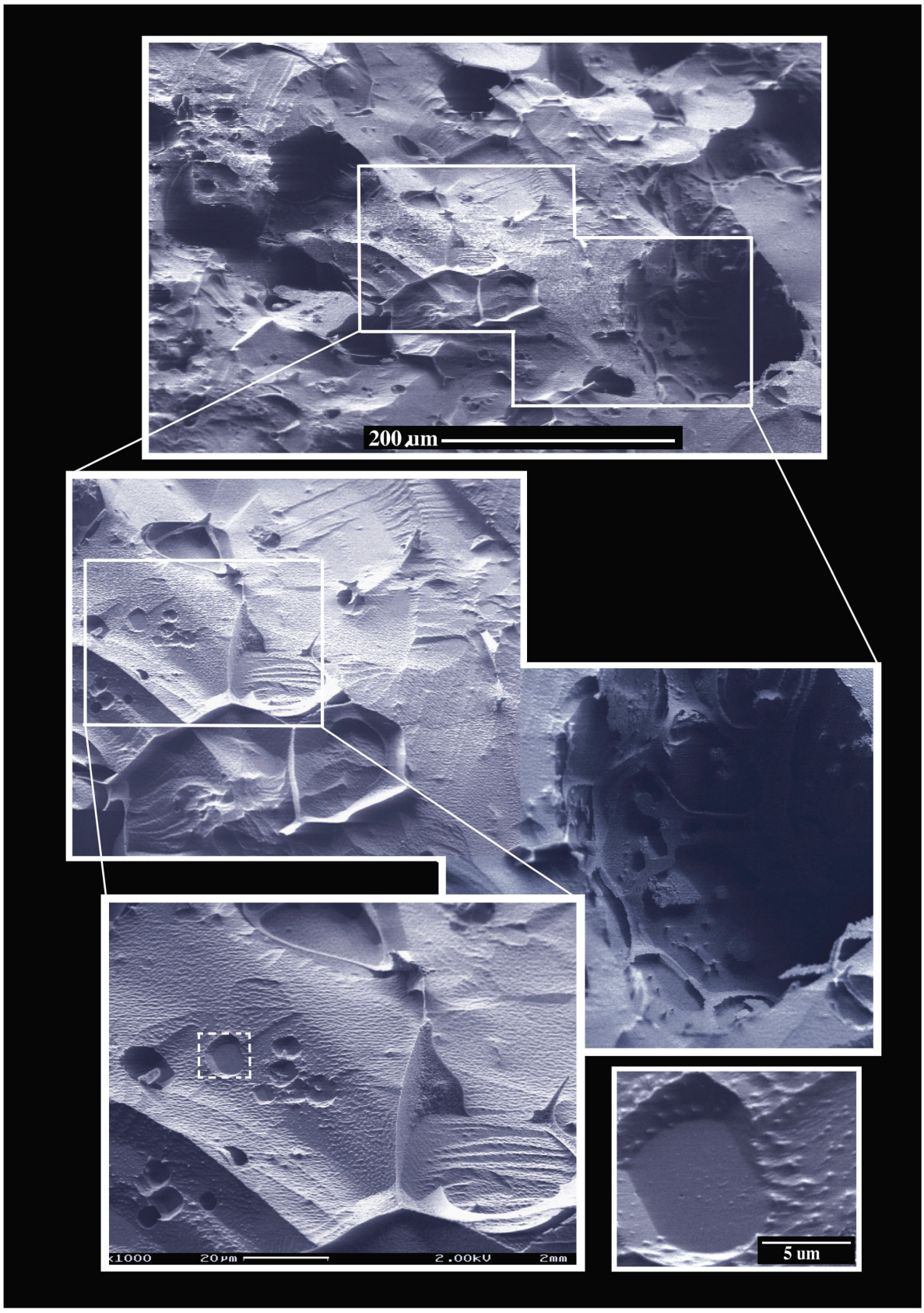

Figure 2. Low-to-high resolution Scanning Electron Microscopy (SEM) mosaic showing textural features within a second subsection of the gas hydrate nodule shown in figure 1.

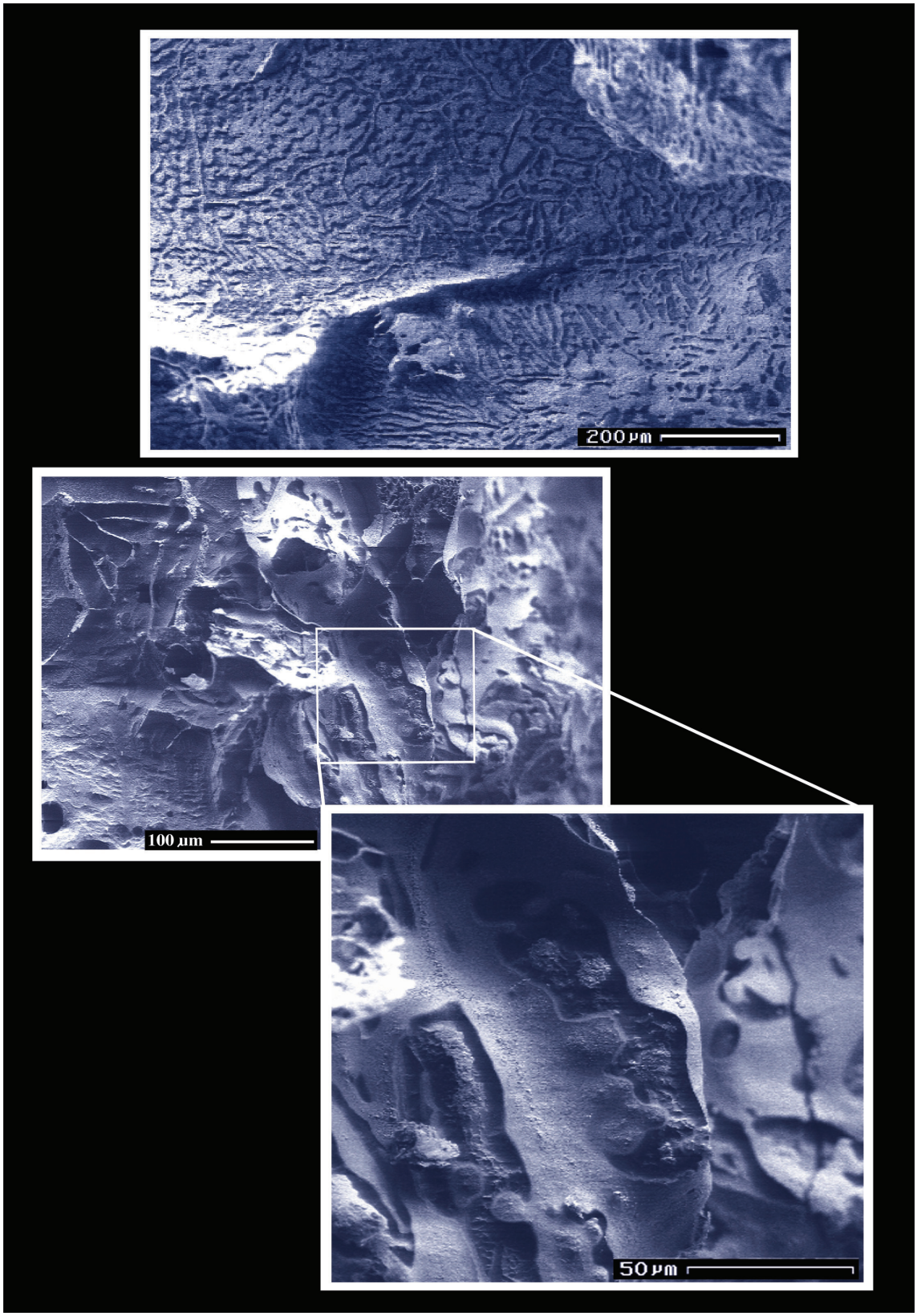

Figure 3. Images from a near-surface section from core MD02-2569 (top photograph) showing what may be partial dissolution textures (compare with figure 4B) and a section through the hydrate/sediment portion of the sample (lower two photographs).

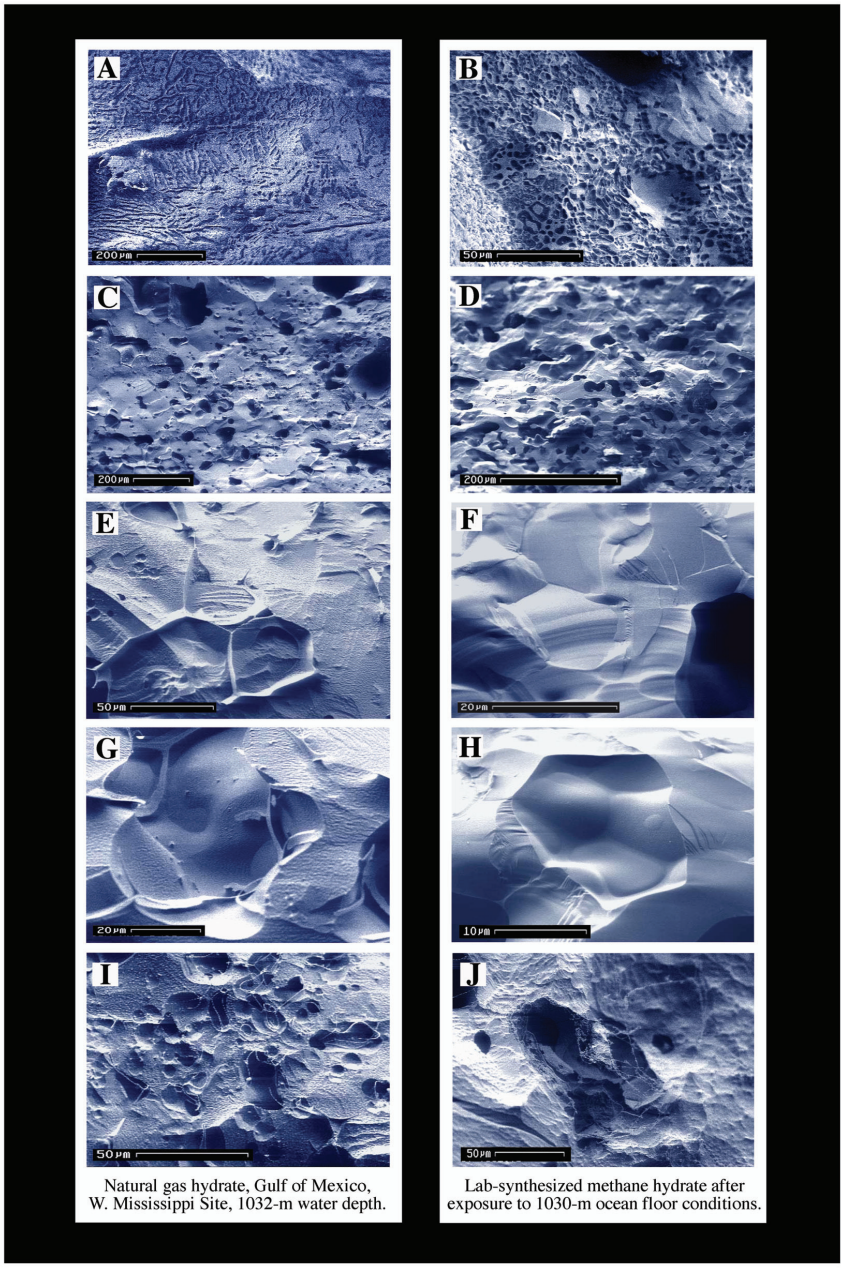

Figure 4. Comparison of Gulf hydrate (left column) to lab-synthesized methane hydrate used in partial dissolution or dissociation experiments (right column). A and B show similarities in grain boundary and pore "cast" textures. A is from a near-surface section of the natural hydrate, and B is a 30-percent porous methane hydrate sample that underwent partial dissolution before subsequent retrieval (see text for further discussion). C and D show similar cavity size, distribution, and cavity connectivity in partially compacted sections of samples. The lab-synthesized sample shown in D was compacted to < 3-percent porosity, although the remaining porosity is not homogeneously distributed throughout the sample. E and F show similarities in grain size, material "density," and clean fracture surfaces. Neither the natural or lab-synthesized material appears to be mesoporous, in contrast with some synthetic and natural methane hydrates discussed in Kuhs and others (2000), Techmer and others (2001), and Suess and others (2002). See also Stern and others (2004, 2005a, 2005b) for further discussion of porous microstructural development. The grain size of the pure methane hydrate sample shown in F is several 10's of microns, which is typical of our synthetic hydrate despite growth conditions from initially larger (~200 micrometers (µm)) ice grains. G and H show minimal-surface-area grain textures along cavity walls that we interpret (based on comparison to features observed in low temperature experiments) as grain growth or annealing at the relatively warm conditions (above 0 degrees Celsius) of marine environments. I and J show similar "frothy" or sponge-like textural development indicative either of partial dissociation of gas hydrate to ice, or to hydrate dissociation to water followed by rapid quenching in liquid nitrogen. The sample shown in J was used in controlled low-temperature (< 0 degrees Celsius) partial dissociation experiment discussed more fully in Stern and others (2003), and its surface is known to be composed of both hydrate and the dissociated ice product.

The test site essentially was the same depth from which core MD02-2569 samples were retrieved, hence offering a basis for comparison.

Despite the relatively short duration of the ocean-floor experiment, the interiors of both the compacted and uncompacted hydrates showed surprisingly different grain and pore structure than the original densely crystalline material (compare to figs. 6, 7, and 10 in Stern and others, 2004, for example). Even more surprising was the striking similarity in textural and structural development displayed by core MD02-2569 material compared with the synthetic samples. For instance, the highly faceted and finely crystalline grain morphology pervasive in many of our as-grown gas hydrate materials (Stern and others 2004, figs. 6, 7, 8) is conspicuously absent from all ocean-floor or sub-ocean-floor samples that we have imaged to date. Instead, those samples exposed to deep marine conditions developed minimal-surface-area grain structures, as shown in figures 1 and 4. Unusual relic grain "skeletal" features also are commonly found lining cavity walls (fig. 2), although we cannot rule out the possibility that some of these features may be artifacts of hydrate breakdown followed by quenching (for instance, as shown in fig. 4I, J). Cavity and(or) pore geometry also tends to be rounder or more regularly shaped in marine samples than in our lab-grown hydrates formed from gas-reaction with ice, and do not appear to be highly connected in the samples imaged here, except for in near-surface sections of the nodules. All seawater-exposed hydrate samples that we have imaged to date exhibit dense hydrate interspersed with micro- to macro-sized pores, with no observed mesoporosity at the intragranular scale. Further comparison is given in the caption for figure 4.

Conclusion

While the results presented here are clearly preliminary, our initial success with gas hydrate imaging by low-temperature SEM persuades us that it will be an extremely useful tool for further resolving the wide range of grain characteristics and microstructures that develop within both natural and lab-made gas hydrates. Such comparisons also should help us decide how accurately we emulate gas hydrates in nature and should greatly aid in the interpretation of physical property measurements made on these materials.

Acknowledgments

Funding was provided by the U.S. Geological Survey (USGS) Gas Hydrate Project and the Methane Hydrate R&D Program of the U.S. Department of Energy, National Energy and Technology Laboratory. Samples from ocean-floor dissolution tests described in the text and shown in figure 4B, D, F, and H were obtained in collaborative work with Monterey Bay Aquarium Research Institute researchers P. Brewer and E. Peltzer. The authors thank W. Waite and R. Kayen of the USGS for helpful reviews of this manuscript, and R. Oscarson, J. Pinkston, S. Circone (all USGS) and W. Durham (Lawrence Livermore National Laboratory) for their technical assistance.

References

Circone, S., Stern, L.A., Kirby, S.H., Durham, W.B., Chakoumakos, B., Rawn, C., Rondinone, A., and Ishii, Y., 2003, CO_2 hydrate—synthesis, composition, dissociation behavior, and a comparison to structure I CH_4 hydrate: Journal of Physical Chemistry B, v. 107, no. 23, p. 5529–5539.

Genov, G., Kuhs, W., Staykova, D., Goreshnik, E., and Salamatin, A., 2004, Experimental studies of the formation of porous gas hydrates: American Mineralogist, v. 89, no. 8–9, p. 1228–1239.

Klapproth, A., Goreshnik, E., Staykova, D., Klein, H., and Kuhs, W., 2003, Structural studies of gas hydrates: Canadian Journal of Physics, v. 81, no. 1–2, p. 503–518.

Kuhs, W., Klapproth, A., Gotthardt, F., Techmer, K., and Heinrichs, T., 2000, The formation of meso- and macroporous gas hydrates: Geophysical Research Letters, v. 27, no. 18, p. 2929–2932.

Rehder, G., Kirby, S.H., Durham, W.B., Stern, L.A., Peltzer, E.T., Pinkston, J., and Brewer, P., 2004, Dissolution rates of pure methane hydrate and carbon dioxide hydrate in undersaturated seawater at 1000 m depth: Geochimica Cosmochimica Acta, v. 68, no. 2, p. 285–292.

Staykova, D., Kuhs, W., Salamatin, A., and Hansen, T., 2003, Formation of porous gas hydrate from ice powders—diffraction experiments and multi-stage model: Journal of Physical Chemistry B, v. 107, p. 10299–10311.

Stern, L.A., Circone, S., Kirby, S.H., and Durham, W.B., 2003, Temperature, pressure, and compositional effects on anomalous or "self" preservation of gas hydrates: Canadian Journal of Physics, v. 81, no. 1–2, p. 271–283.

Stern, L.A., Circone, S., Kirby, S.H., and Durham, W.B., 2004, Application of Scanning Electron Microscopy (SEM) to investigate growth and annealing of gas clathrate hydrates formed from melting ice: American Mineralogist, v. 89, no. 8–9, p. 1162–1175.

Stern, L.A., Circone, S., Kirby, S.H., and Durham, W.B., 2005, SEM imaging of gas hydrate formation processes and growth textures, and comparison to natural hydrates of marine and permafrost origin, Paper 1046, *in* Proceedings of the 5th International Conference on Gas Hydrates, Trondheim, Norway, v. 1, p. 300–309.

Stern, L.A., Kirby, S.H., and Durham, W.B., 1996, Peculiarities of methane clathrate hydrate formation and solid-state deformation, including possible superheating of water ice: Science, v. 273, p. 1843–1848.

Stern, L.A., Kirby, S.H., and Durham, W.B., 2005, SEM imaging of grain structure and phase distribution within hydrate-bearing intervals from JAPEX/JNOC/GSC et al. Mallik 5L-38—What can we learn from comparisons with laboratory-synthesized samples? *in* Dallimore, S.R., and Collett, T.S., eds., Scientific results from the Mallik 2002 gas hydrate production research well program, Mackenzie Delta, Northwest Territories, Canada: Geological Survey of Canada, Bulletin 585.

Stern, L.A., Kirby, S.H., Durham, W.B., Circone, S., and Waite, W., 2000, Synthesis of pure methane hydrate suitable for measurement of physical properties and decomposition behavior, chap. 25, *in* Max, M.D., ed., Natural gas hydrate—in oceanic and polar subaerial environments: Dordrecht, Kluwer publ., p. 323–349.

Stern, L.A., Peltzer, E., Durham, W.B., Kirby, S.H., Brewer, P., Circone, S., and Rehder, G., 2002, Dissolution of hydrocarbon gas hydrates in seawater at 1030 meters; effects of porosity, structure, and compositional variation as determined by high-definition video and SEM imaging: EOS, Transactions of the American Geophysical Union, v. 83, no. 47, Abstract OS21B-0216.

Suess, E., Borhmann, G., Rickert, D., Kuhs, W.F., Torres, M.E., Trehu, A., and Linke, P., 2002, Properties and fabric of near-surface methane hydrates at Hydrate Ridge, Cascadia Margin, *in* Proceedings of the 4th International Conference on Gas Hydrates, Yokohama, Japan, v. 2, p. 740–744.

Techmer, K., Heinrichs, T., and Kuhs, W., 2005, Cryo-electron microscopic studies of structures and composition of Mallik gas-hydrate-bearing samples, *in* Dallimore, S.R., and Collett, T.S., eds., Scientific results from the Mallik 2002 gas hydrate production research well program, Mackenzie Delta, Northwest Territories, Canada: Geological Survey of Canada, Bulletin 585, 12 p.

Techmer, K., Kuhs, W., Heinrichs, T., and Bohrmann, G., 2001, Scanning Electron Microscopic investigations on natural and synthetic gas hydrates—new insights into the formation process: EOS, Transactions of the American Geophysical Union, v. 82, no. 47, Abstract B21D-01.

Chapter 13

Cruise Report: Sediment Collection from Orca and Pigmy Basins, Gulf of Mexico, and Analyses for Texture and Trace-Metal Concentrations, July 2002, PAGE 127 Campaign

James Flocks[1] and Peter Swarzenski[1]

Cruise report: Sediment collection from Orca and Pigmy Basins, Gulf of Mexico, and analyses for texture and trace-metal concentrations, July 2002, PAGE 127 campaign; chapter 13 in *Winters, W.J., Lorenson, T.D., and Paull, C.K., eds., 2007, Initial report of the IMAGES VIII/PAGE 127 gas hydrate and paleoclimate cruise on the RV* Marion Dufresne *in the Gulf of Mexico, 2–18 July 2002: U.S. Geological Survey Open-File Report 2004–1358.*

Introduction

The Mississippi River system, which drains almost half of the conterminous United States, ranks seventh among rivers worldwide for water discharge (580 cubic kilometers per year (km^3/yr)) and sixth for suspended-sediment discharge ($200x10^6$ metric tons per year (mt/yr)). Together, the Mississippi and Atchafalaya Rivers provide almost all of the freshwater influx to the Gulf of Mexico. The suspended-sediment load is composed predominantly of terrigenous clays and silts. A 3-year record of suspended-sediment load north of the Mississippi River Delta indicates that usually much more than 70 percent of the suspended load consists of particles that are less than 62 micrometers (μm) (4 phi (φ)) in size (Swarzenski, 2001). The silts are deposited along the periphery of the Mississippi River Delta, whereas the clays are transported offshore (Flocks and others, 2002; Walker and others, 2002). Fine particles, such as clay, are a primary transport mechanism for trace metals that adhere to the particle surface or are included interstitially within the silicate structure (Horowitz, 1991).

Trace-metal distribution in the Mississippi River Delta has been the subject of many research efforts (for example, DiMarco and others, 1986; Landrum, 1995; Trefry and others, 1995; Grant and Middleton, 1998). The extent to which the clay fraction distributes trace-metal constituents across the Gulf of Mexico is not entirely understood. During the Paleoceanography of the Atlantic and Geochemistry (PAGE) 127 campaign onboard the RV *Marion Dufresne*, sediment samples were collected along the continental slope several hundred miles southwest of the Mississippi River Delta. On July 8 and 9, 2002, two 11-meter-long box cores were deployed in two intraslope basins (Orca and Pigmy Basins) situated along the continental shelf in roughly 2,000 meters of water (fig. 1). Box core MD02-2550 was collected from Orca Basin and box core MD02-2553 from Pigmy Basin. The basins provide a sediment trap for pelagic and hemipelagic material and have been used in studies that address fluvial influence from the Mississippi River (Stearns and others, 1986; Raiswell and Canfield, 1998; Flower and others, 2004). Brine (in Orca Basin) and low-oxygen concentrations in the bottom waters provide a high preservation potential for organic material accumulating in the sediments. One objective of the survey was to collect and compare grain-size and trace-metal constituents from the basins with samples collected from the Mississippi and Atchafalaya River Deltas.

Methods

Coring and Sampling

Sediments were collected in a continuous, undisturbed 11-meter (m)-long core using the "Calypso3" box core developed for use on the research vessel (RV) *Marion Dufresne*. A

[1]USGS Center for Coastal and Watershed Studies, 600 4th St. South, St. Petersburg, FL 33701.

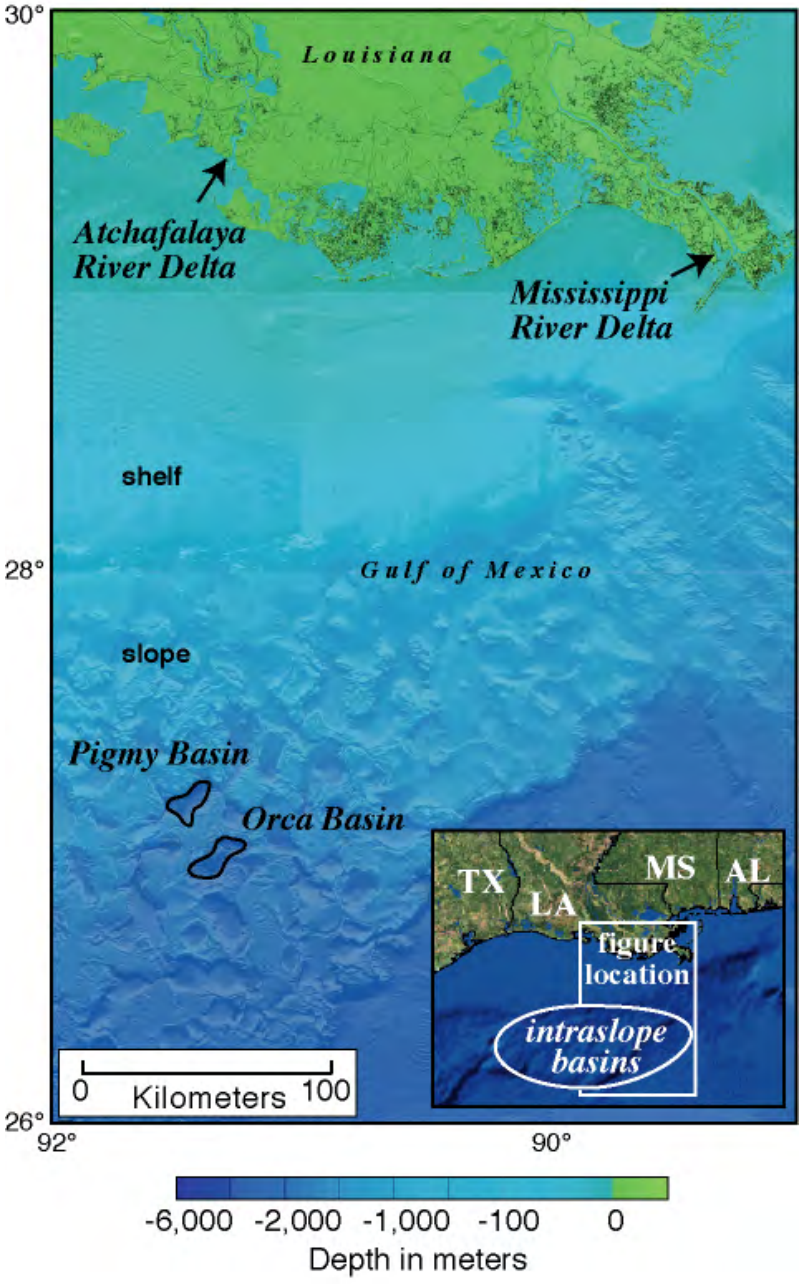

Figure 1. Locations of Orca and Pigmy intraslope basins and the Mississippi and Atchafalaya River Deltas, Gulf of Mexico. Bathymetric data from the National Geophysical Data Center (NGDC).

0.0625-square-meter (m^2) by 11-m-long steel box corer was attached to 2,400 kilograms (kg) of lead weight and lowered to the sea floor. Upon retrieval, one side of the box was removed to reveal the core. Plastic liners (8x13x155 centimeters (cm) were inserted longitudinally into the box core to subsample the sediment into four identical sections (fig. 2). For the purpose of this study, the first 2 m of one subcore was immediately sampled into 2.5-cm sections; each section was transferred to an individual plastic sampling cup and frozen.

Trace Metals

The subsamples were soaked in a 50-percent acetone-dH_2O mixture to remove organic material and facilitate wet sieving through a 63-μm screen. The resulting coarse and fine fractions were dried and weighed. The fine fraction was ground by mortar and pestle, and the coarse fraction was described and archived.

The fine fraction was further pulverized and analyzed using an inductively coupled plasma-optical emission spectrometer (ICP-OES) at a commercial laboratory (ACTLABS, Tucson, AZ). Elements measured by this method include aluminum (Al), calcium (Ca), cobalt (Co), copper (Cu), iron (Fe), potassium (K), magnesium (Mg), manganese (Mn), sodium (Na), phosphorous (P), nickel (Ni), lead (Pb), strontium (Sr), sulfur (S), titanium (Ti), yttrium (Y), vanadium (V) and zinc (Zn). Prior to analysis, the sediment samples were dissolved in acid to mobilize the trace metals into solution. "Near total" digestion employs HF, $HClO_4$, HNO_3, and HCl to get as much of the sample into solution as possible without fusing the sample (ACTLABS, written commun., 2002). Triplicates of two samples were analyzed to determine standard analytical error.

Grain Size

Textural analysis of sediment samples was performed at the U.S. Geological Survey (USGS) Center for Coastal Geology using a Coulter LS 200 particle-size analyzer. The LS 200 utilizes laser diffraction to measure size distribution of sedimentary particles between 0.4 μm and 2 millimeters (mm). Grain-size analyses were conducted by simulating the sizes that would be determined from standard ASTM 11-E sieves. For more information on this technique, see Kindinger and others (2001).

Scanning Electron Microscope (SEM)

The fine fraction of wet samples was pipetted into a micro-analysis vacuum filter and support assembly onto 0.2-mm polycarbonate filter pads. The filters were air-dried, mounted on aluminum stubs, and sputter coated with gold-palladium. The samples were then placed in a Hitachi 3500N

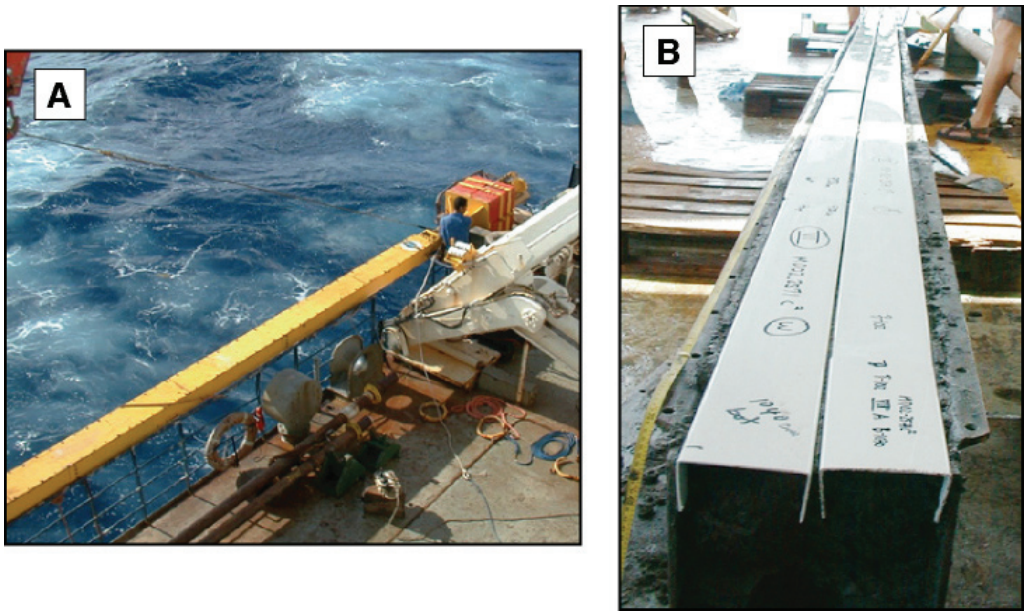

Figure 2. (A) Eleven-meter Calypso3 box core being deployed from the RV *Marion Dufresne*. (B) Opened box corer showing placement of subsampling tubes.

variable pressure scanning electron microscope (SEM) equipped with energy-dispersive spectroscopy (EDS). Samples were imaged using both secondary electron and backscatter electron detectors (atomic number differences). EDS was performed on several particles within each sample to determine relative elemental compositions.

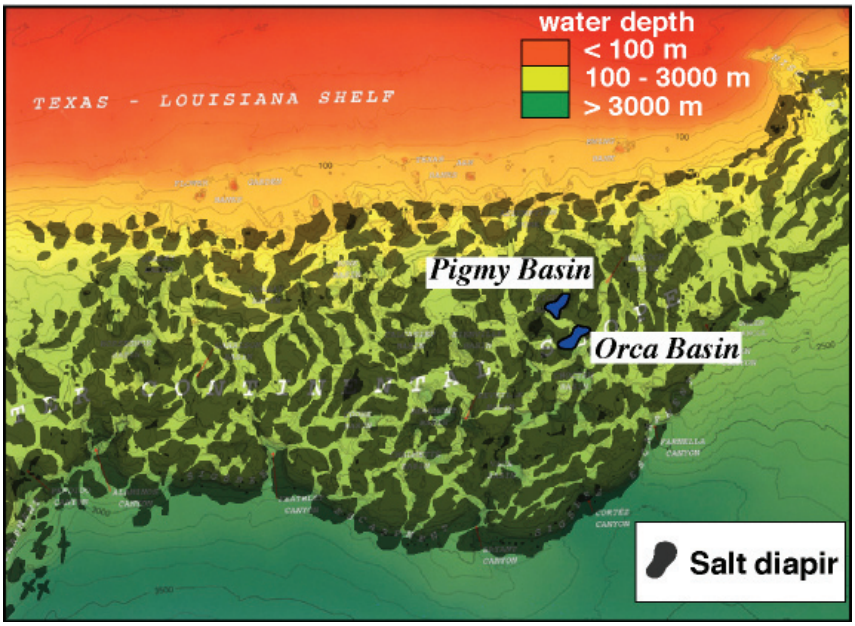

Figure 3. Bathymetric map showing positions of salt diapirs, northern Gulf of Mexico continental slope. Bathymetric data from NGDC, salt structure map from Bouma and others (1980). See figure 1 for locations of basins.

Discussion

Geology

The structure and topography of the slope that includes Pigmy and Orca Basins are controlled by salt diapirs (Bouma, 1981). Intrusion of these giant salt domes into the surficial sediments produced a topography similar to the Basin and Range Province of the Midwest of the United States (fig. 3), with dome rims protruding several hundred meters from the interdiapiric sea floor. The salt originates from Jurassic time and is overlain by shales of Tertiary age (Bouma and others, 1980). The shales are then overlain by a thick sequence of pelagic deposits and hemipelagic sediments of Pleistocene age associated with Mississippi River deposition.

Bouma and Coleman (1986) characterize several intraslope basin types relative to their previous geomorphology and subsequent diapiric construction: blocked-canyon, interdomal, and collapse basins. Pigmy Basin is an example of a blocked-canyon intraslope basin, which is defined as a former channel that has become blocked by upward or laterally moving diapirs. The channel effectively becomes dammed by the diapirs, terminating any basin infilling by bottom transport. Subsequent deposition in the basin is either by slumping along the periphery of the basin or through pelagic and hemipelagic accumulation. Orca Basin may not have started as a

blocked canyon but is entirely isolated from outside currents by upward-moving diapirs. As a result, this example of an interdomal basin exhibits hypersaline and anoxic bottom waters, which preserve carbonate and organic material in the sediments (Tompkins and Shephard, 1979; Flower and others, 2004). Previous coring and seismic-profiling activities indicate that both basins contain a thick surficial sequence of sediments of Holocene to late Wisconsinan age (Bouma and Coleman, 1986; Jasper and Gagosian, 1990). Previous studies determined that the primary clay constituent in the top 3 m of sediment within Orca Basin is smectite, with lesser amounts of illite and kaolinite (Tompkins and Shephard, 1979).

Orca Basin Sediments (box core MD02-2550)

Box core MD02-2550 was acquired from the central portion of Orca Basin, in 2,249 m of water (fig. 4). A photomosaic of the core (fig. 5) shows over 6 m of light gray, faintly laminated clays, overlain by 2.5 m of black, laminated clay. The black color of the highly fluid surficial sediments represents FeS present in the hypersaline, anoxic muds that exist within the basin. The transition from gray to black muds presumably represents the beginning of anoxic conditions within the basin about 8,000 year before present (BP) (Trefry

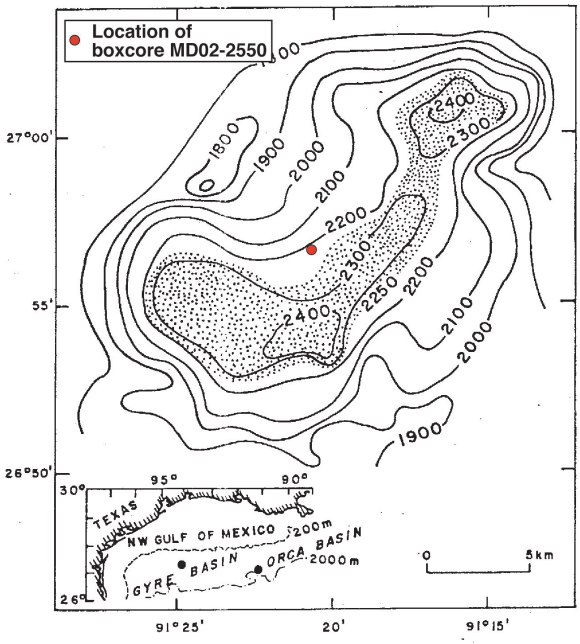

Figure 4. Bathymetric map of Orca Basin, from Bouma (1981), showing location of box core MD02-2550 (red dot).

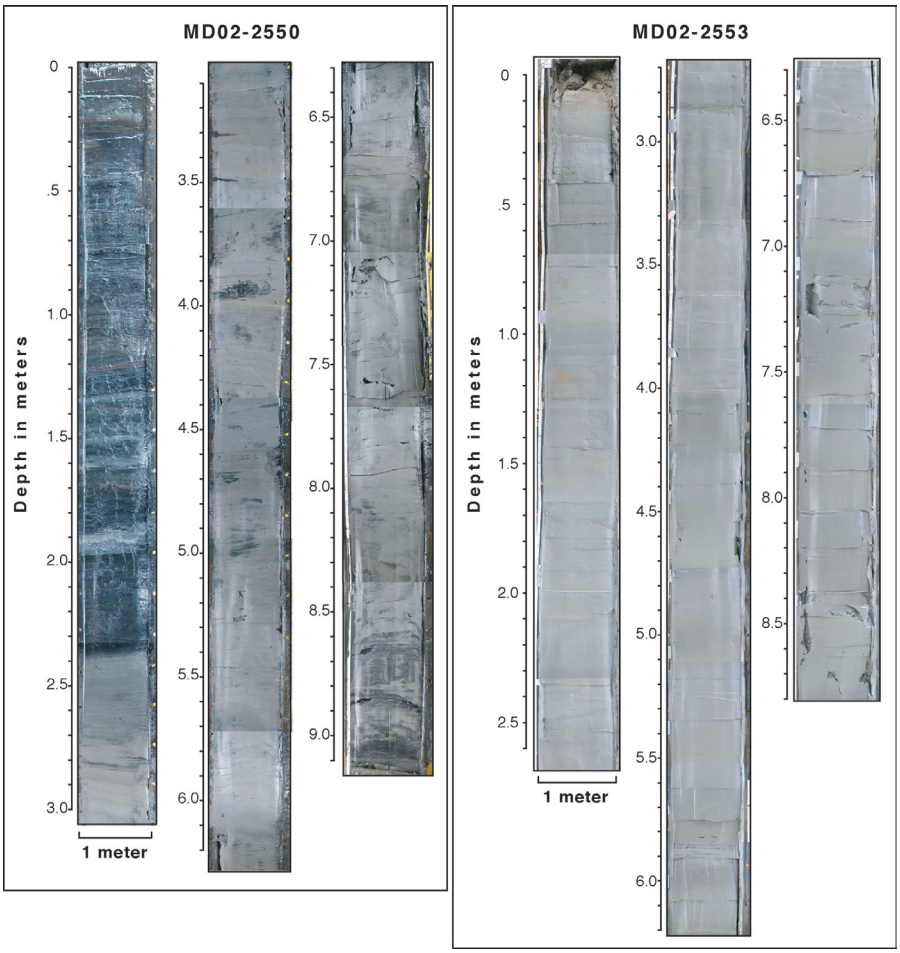

Figure 5. Photomosaic of box cores MD02-2550 (Orca Basin) and MD02-2553 (Pigmy Basin). Brightness differences and contrasting angles in laminations are due to camera angle and lighting.

and others, 1984). Hill and others (2004) estimate an average sediment accumulation rate of >50 cm per 1,000 year in the vicinity of the box core through radiocarbon dating from an adjacent piston core (MD02-2551). Their similar radiocarbon work on box core MD02-2550 indicates the middle Holocene may be missing (ca. 3 – 6.5 thousand years (ka)) between 175 and 190 cm (B. Flower, University of South Florida, oral commun., 2002). Throughout the core, signs of bioturbation are absent, and lamina thickness is variable. Evidence of gas vesicules occurs periodically.

A closeup of the several sieved fractions of the Orca Basin core shows an abundance of coccoliths, radiolarian tests, and spicules in a matrix of clay particles (fig. 6). Clay particles are identified by their silicate composition, determined using EDS, as are some trace amounts of quartz grains. Sand is not a major constituent in these samples; the coarse fraction was observed to contain mainly foraminifera and pteropods.

Grain-size analyses were performed every 10 cm over the top 3 m of the box core. Results show a predominance of clayey-silt throughout this section (fig. 7), with an overall coarsening upward in the core.

Trace-metal concentrations were measured in the top 2 m of the core. The results do not show marked variability in this section, with the top 0.5 m having the most consistency (fig. 8). Below 140 cm, there appears to be a slight increase in the concentration of some metals (Co, Mn, Ti, V, Y, Zn) and an increase in variability. This change is accompanied by a decrease in Na, which could indicate change in sediment texture if Na is a proxy for porosity. Selected trace-metal concentrations normalized to Al show some increase in the trace-metal component within the top 40 cm for Pb and Ni, relative to the rest of the core, but not a lot of variability (fig. 9). Deviations in the normalized trace-metal component at the base of the section (150–200 cm), in conjunction with the observation that approximately 20 cm may be missing, suggest that transport mechanisms may be active that are not evident in the upper 1 m of core. Selected trace-metal concentrations compared to samples acquired in the Mississippi River and Atchafalaya River Deltas indicate some variability (table 1). Average concentrations of Cu and Ni were similar to concentrations in the delta samples, whereas concentrations of Co, Pb, V, and Zn were lower.

Table 1. Average concentrations of selected trace metals from the basins compared to various locations around the northern Gulf of Mexico.

[*, peat and sand samples not included (intervals where > 50 percent of sample is > 36 micrometers (μm)) (Flocks and others, 2002); **, from Landrum (1995); ***, from Trefry and others (1995); —, not available]

Estuary/Basin	Co	Cu	Ni	Pb	V	Zn
Orca Basin (n=25)	6	21	23	14	78	48
Pigmy Basin (n=21)	11	37	35	16	137	89
Atchafalya Delta (n=42)*	10	19	25	20	95	76
Miss. Sub-deltas (n=27)* (n=27)*	10	20	25	25	83	77
Pass A Loutre (n=26)*	10	20	24	19	75	77
Miss. R. suspended sed***	—	—	41	36	132	—
St. Bernard delta regtion**	29	19	22	26	47	120
Apalachicola Bay**	18	37	—	—	79	57
Barataria Basin**	25	22	26	18	23	98
Beaumont Area**	—	20	17	—	—	108
Corpus Christi**	—	15	15	17	—	93
Galveston Area**	—	27	22	34	—	62
Mississippi Sound**	13	20	—	—	80	74
Mobile Bay**	15	31	—	—	88	120
Pensacola Bay**	8	31	—	—	75	86
Perdido Bay**	27	46	—	—	49	161
Pontchartrain Estuary**	9	23	17	81	78	78

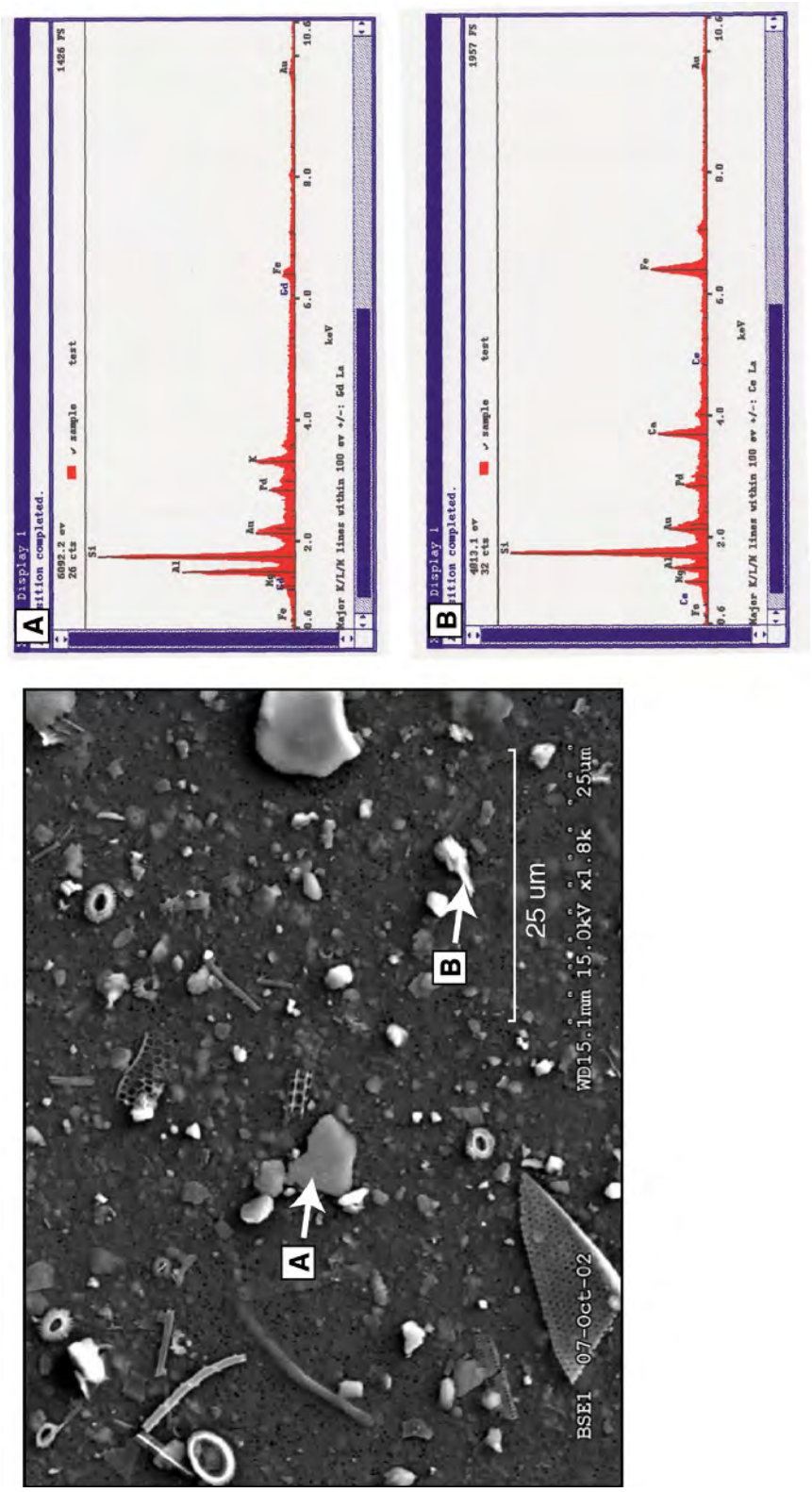

Figure 6. Scanning Electron Microscopy (SEM) image of particles less than 6 phi (φ); silt size) from box core MD02-2550, showing pelagic and hemipelagic material. Selected clay particles were analyzed for elemental composition using energy-dispersive spectroscopy (EDS; right), showing silicate composition and associated major cations. More SEM images with EDS analysis are included in the appendix to this chapter.

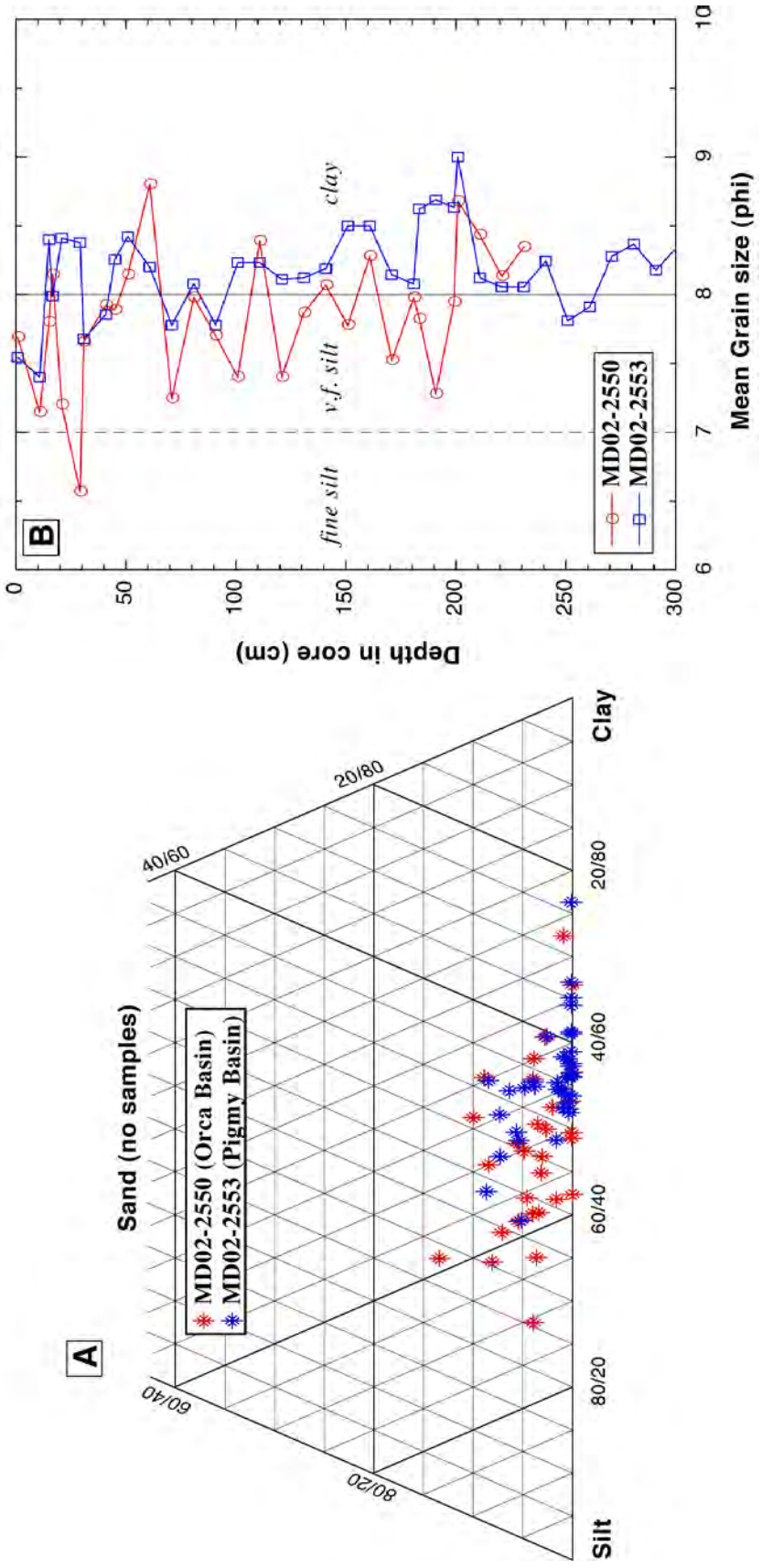

Figure 7. Grain-size analyses showing (A) distribution of samples and (B) trend and predominance of clay-size sediments.

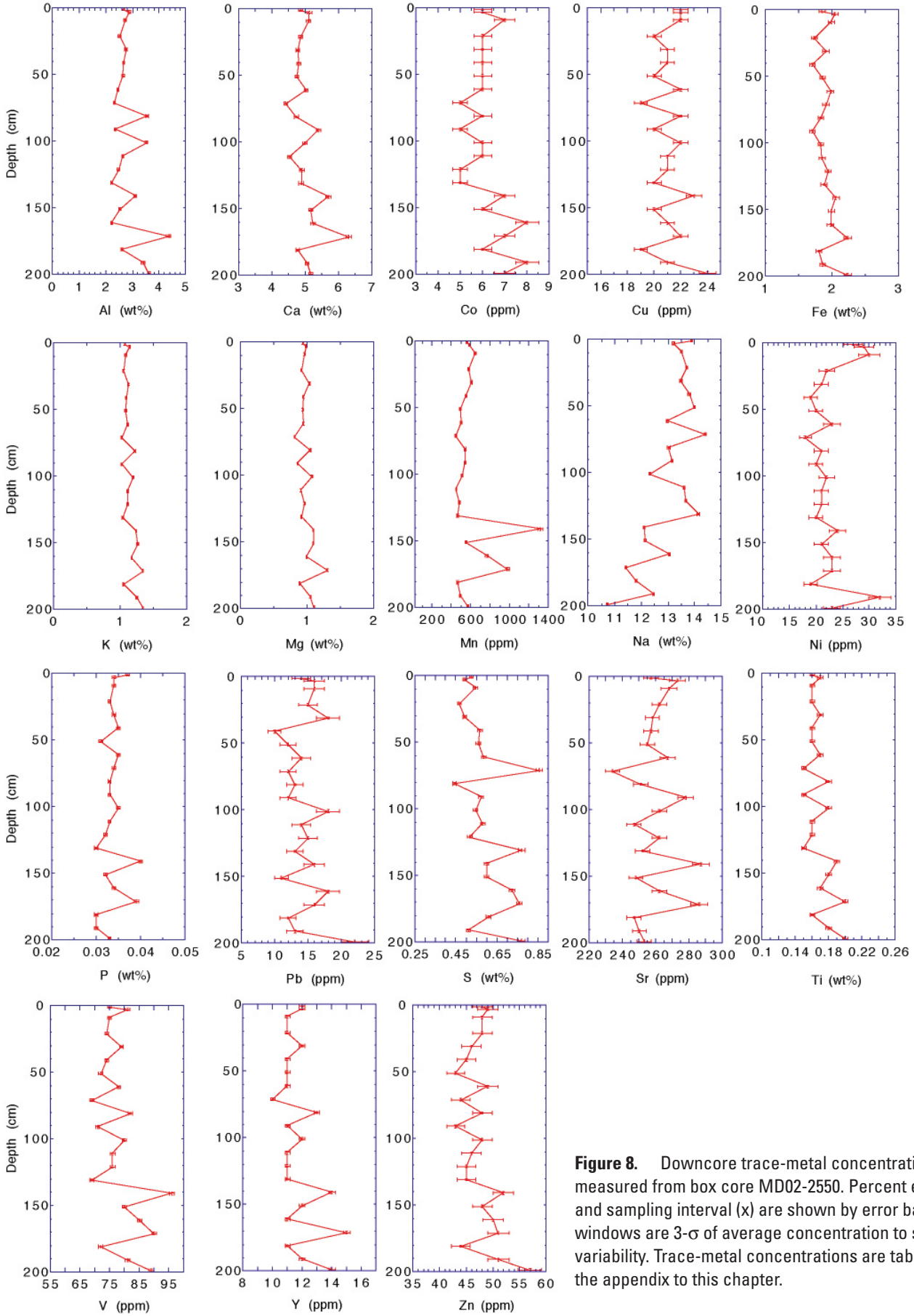

Figure 8. Downcore trace-metal concentrations measured from box core MD02-2550. Percent error (y) and sampling interval (x) are shown by error bars. Graph windows are 3-σ of average concentration to show variability. Trace-metal concentrations are tabulated in the appendix to this chapter.

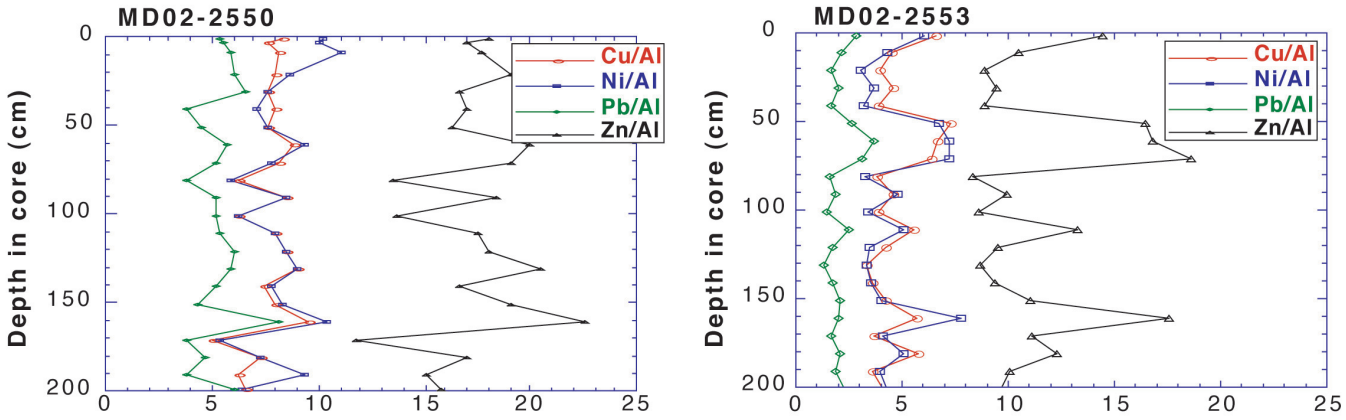

Figure 9. Selected trace-metal concentrations normalized to Al to reflect possible deviations from estimated background (environmental) conditions.

Pigmy Basin Sediments (box core MD02-2553)

Pigmy Basin has a maximum depth of about 2,240 m, with a sill depth of less than 1,700 m (fig. 10). Box core MD02-2553 was acquired in the central portion of the basin. Photographs of the sediments show gray, generally massive to faintly laminated muds throughout the length of the core (fig. 5). Black shading related to accumulation of organic material occurs throughout the core, and distinct concentrations of foraminifera occur at 65, 125, 127, 313, 315, and 442 cm downcore. There is no evidence of bioturbation or other physical disturbance to the sediments.

Comparison of SEM images between Orca and Pigmy Basins shows Pigmy sediments contain a similar amount of coccoliths, but no pteropods (figs. 6, 11); the basin has a lower preservation potential for aragonite. Poore and others (2004) estimate an average sediment accumulation rate of 50 cm per 1,000 years using AMS radiocarbon dating of planktonic foraminifera in the top 2 m of the core. However, through comparison with tree-ring dating, Poore and others (2005) suggest that small variations in sediment accumulation may exist. Variability in sedimentation may be due in part to a migrating source of fluvial clays. Throughout the 4,000 years of accumulation represented by this section of core, the primary discharge of the Mississippi River has varied in proximity to the basin by over 100 kilometers (km). Over that time, delta switching changed the course of the Mississippi River from the St. Bernard complex west to the Lafourche Delta, and then east to its current configuration (Frazier, 1967; Levin, 1991). Examination of the clay particles within the sample using EDS shows silicates with the presence of Al, K, Ca, Mn, and Fe (fig. 11).

Trace-metal concentrations within Pigmy Basin are consistently higher than those found in Orca Basin (with the understandable exception for Na and S) and other areas of the Mississippi River Delta (table 1). There is close correlation in trend between Ca, Sr, Al, and Y downcore (fig. 12). A less obvious, opposite trend can be seen in Ni, Pb, Ti, and Zn. This variance becomes more obvious when the latter constituents are normalized to Al (fig. 9). The increase in these constituents shown in figure 9 may be related to an enhanced terrestrial component.

Grain-size analysis indicates the sediments within Pigmy Basin are composed almost entirely of clay-size particles (fig. 7), with a smaller average diameter than sediments collected from Orca Basin. Mean grain size shows minimal variability around the silt/clay boundary (fig. 7), with possibly a slight coarsening-upward trend.

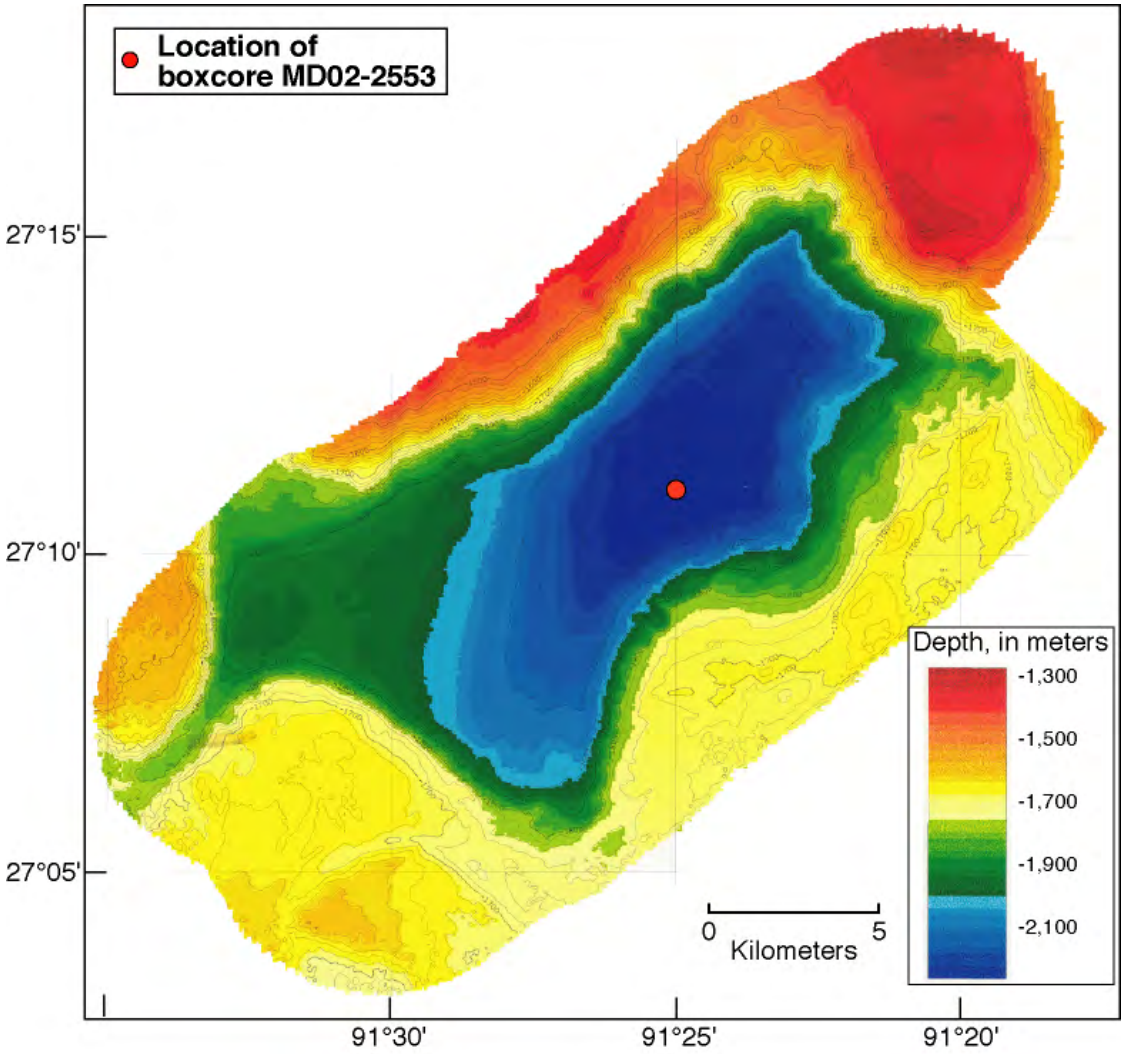

Figure 10. Bathymetric map of Pigmy Basin. Contours were generated from a geophysical survey conducted during the Paleoceanography of the Atlantic and Geochemistry (PAGE) 127 campaign. Location of box core MD02-2553 shown (red dot). Location of Pigmy Basin is shown in figure 1.

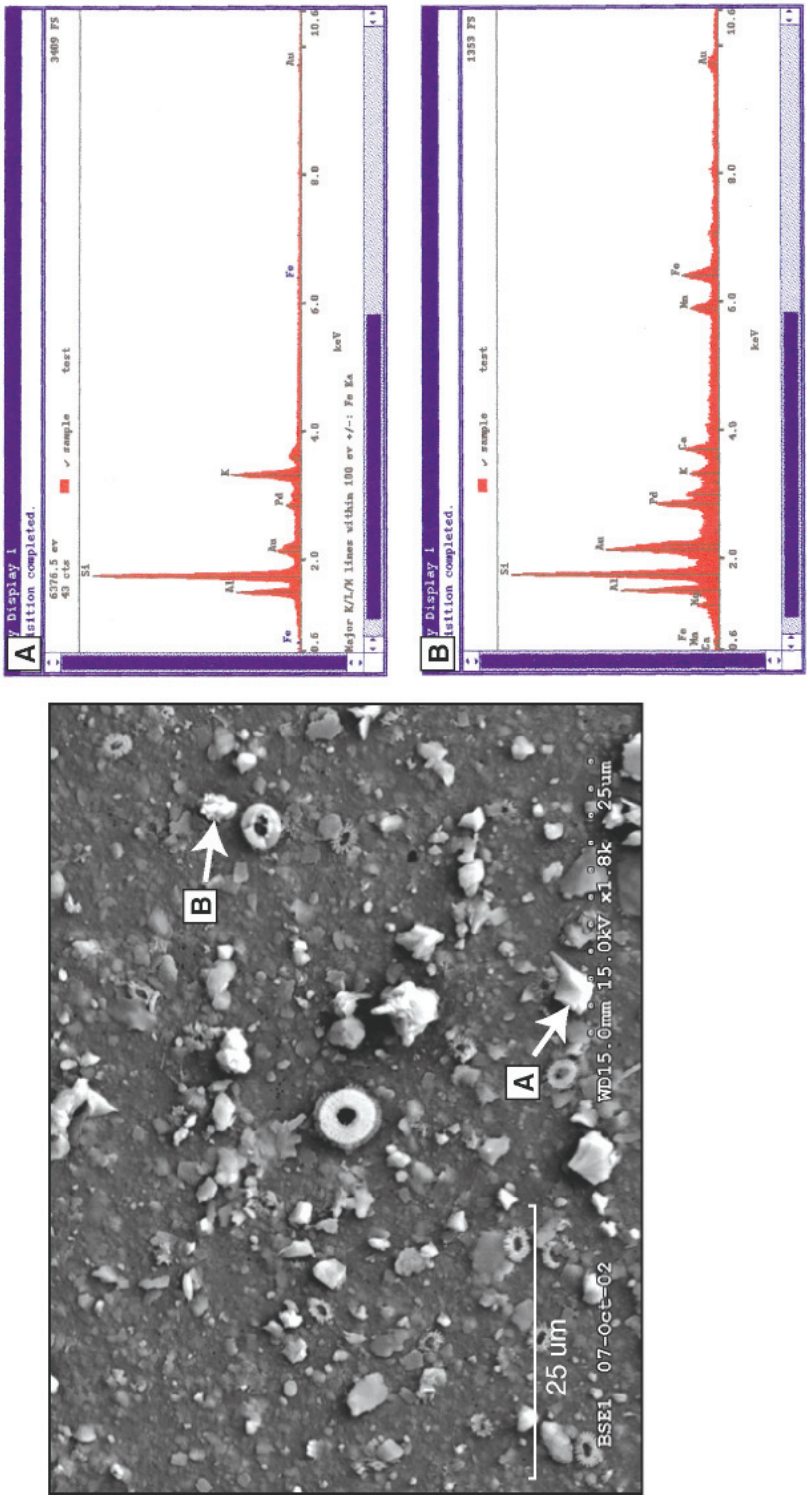

Figure 11. Scanning Electron Microscopy (SEM) image of particles less than 6 phi (θ); silt size) from box core MD02-2553, showing pelagic and hemipelagic material. Selected clay particles were analyzed for elemental composition using energy-dispersive spectroscopy (EDS; right), showing silicate composition and associated major cations. More SEM images with EDS analysis are included in the appendix to this chapter.

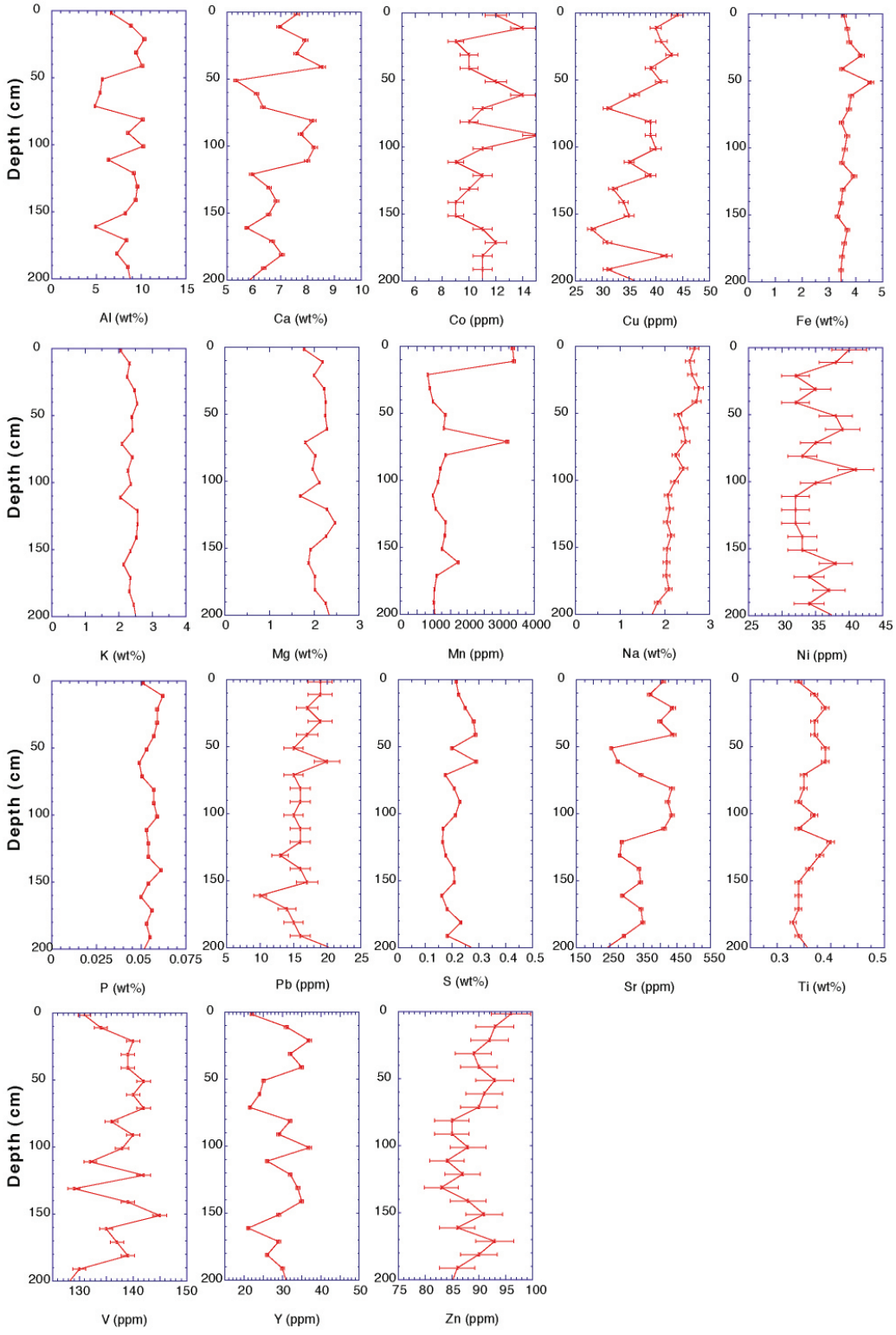

Figure 12. Downcore trace-metal concentrations measured from box core MD02-2553. Percent error (y) and sampling interval (x) are shown by error bars. Graph windows are 3-σ of average concentration to show variability. Trace-metal concentrations are tabulated in the appendix to this chapter.

Conclusion

Textural analyses of sediments collected from Orca and Pigmy Basins indicate the sediments to be well-sorted very fine silts and clays. There is little variability downcore in the top 2 m, with perhaps a slight coarsening upward in both basins. Sediments collected from Pigmy Basin have a smaller average grain size, about the 8-phi class, than Orca Basin sediments. Sediments from Pigmy Basin can be described as silty-clay, and those from Orca Basin can be characterized as clayey-silt. SEM imagery from the sediments show both basins contain abundant foraminifera. Orca Basin sediments contain abundant pteropods, whereas the Pigmy Basin sediments do not. EDS analysis through SEM show the clay particulate to contain the major cations (Ca, Mn, Fe, and Al), although clay species cannot be determined at this time. Some minor quartz and carbonate material were also found.

Trace-metal analysis demonstrates little variability in the top 2 m of sediment. Subtle trends in both basins indicate correlation in some constituents (for example, Al, Ca, Sr, and Y), possibly coincident with a mass balance in others (for example, Ni, Pb, Ti, and Zn). These variances may reflect an inconsistent fluvial component. The low-oxygen and hypersaline conditions in Orca Basin correspond to higher S and Na concentrations in the Orca sediments, and metal concentrations in Pigmy Basin are consistently higher than in Orca Basin. Lower sediment concentrations of certain soluble metals, such as Fe and Mn in Orca Basin as compared to Pigmy Basin, may reflect remobilization and precipitation processes that occur above the sea floor, in the brine, and in seawater columns (Trefry and others, 1984).

Table 1 lists trace-metal concentrations measured within various coastal and estuarine sediments from the northern Gulf of Mexico. The sediments were collected by surface grab and shallow sediment cores, and reflect the modern distribution of trace metals within the coastal environment. Compared to these analyses, the sediments from Orca Basin indicate similar or lower concentrations, whereas those from Pigmy Basin indicate significantly higher values (table 1). Comparison of the abundance of clay within the samples to selected trace metals (Cu, Pb) across these environments indicates a possible correlation. The higher clay fraction in the shelf-slope basin cores supports a higher concentration of Cu than in various facies of deltaic sediments (fig. 13). Although Cu and other metals may have an affinity for clay particulate, the Pb profile in the figure shows that correlation between trace-metal concentration and percentage of fine-grained material is not consistent. This suggests that Pb may have alternate or more complex transport mechanisms.

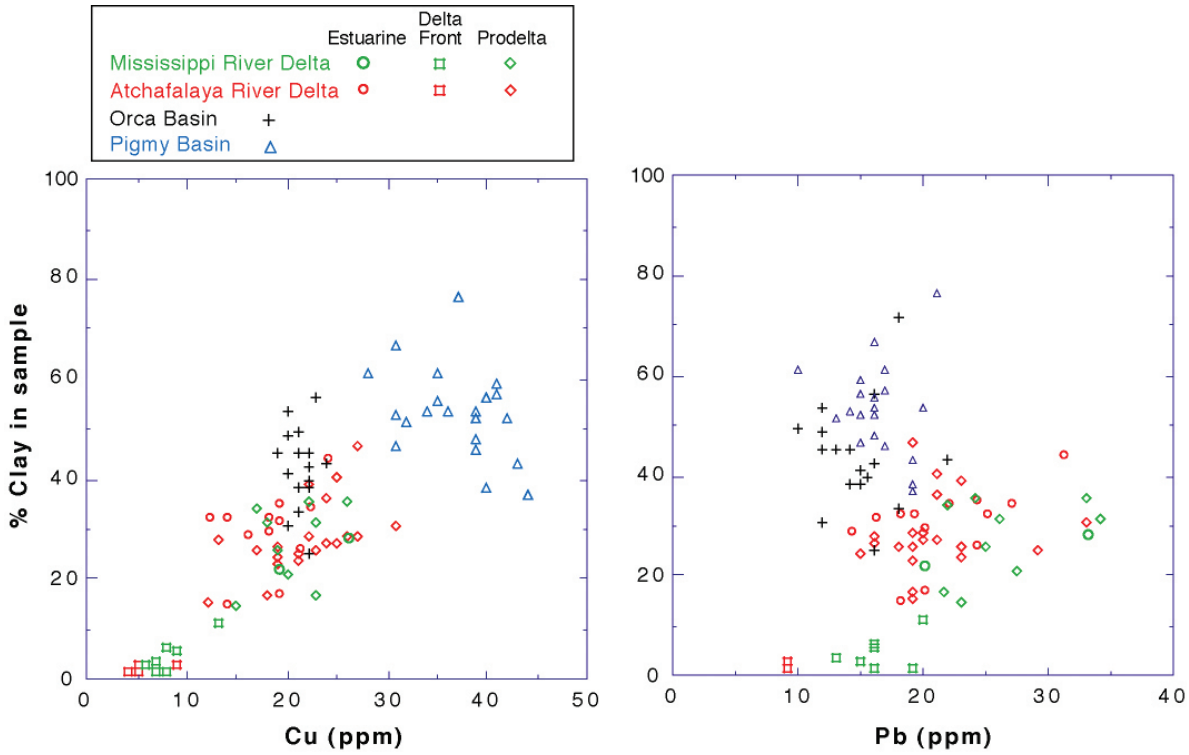

Figure 13. Clay-size constituent in relation to selected trace-metal (Cu, Pb) concentrations in samples collected from various environments in the northern Gulf of Mexico, from Flocks and others (2002). Samples from the deltas are divided into depositional facies associated with transgressive-phase delta development.

Acknowledgments

The authors thank Bill Waite and Pat Hart for assistance during the cruise and for contributing digital images and maps, Noreen Buster for the SEM analyses, and Nick Ferina and Chandra Dreher for sample preparation and grain-size analyses. Comments and review from Dick Poore, Brian Bossak, and Barbara Lidz are greatly appreciated.

References

Bouma, A., 1981, Submarine canyon-fan systems in a diapirically controlled area, Gulf of Mexico—sedimentary Environments of the North Atlantic during the Quaternary: Proceedings of the National Council for Scientific Research (NCSR) International Colloquium no. 325, 18 p.

Bouma, A., and Coleman, J., 1986, Intraslope basin deposits and relation to continental shelf, northern Gulf of Mexico: American Association of Petroleum Geologists Bulletin, v. 70, no. 9, p. 1178.

Bouma, A., Martin, R., and Bryant, W., 1980, Shallow structure of upper continental slope, central Gulf of Mexico: Proceedings, Offshore Technology Conference, v. 4, no. 12, p. 583–592.

DiMarco, M., Ferrel, R., Jr., and Tye, R., 1986, Clay mineralogy of Cubits Gap crevasse splay, Mississippi Delta: Gulf Coast Association of Geological Societies Transactions, v. 36, p. 441–447.

Flocks, J., Kindinger, J., Ferina, N., and Dreher, C., 2002, Sediment-hosted contaminants and distribution patterns in the Mississippi and Atchafalaya River Deltas: Gulf Coast Association of Geological Societies Transactions, v. 52, p. 277–289.

Flower, B., Hastings, D., Hill, H., and Quinn, T., 2004, Phasing of deglacial warming and Laurentide Ice Sheet meltwater in the Gulf of Mexico: Geology, v. 32, no. 7, p. 597–600.

Frazier, D., 1967, Recent deltaic deposits of the Mississippi River—their development and chronology: Gulf Coast Association of Geological Societies Transactions, v. 17, p. 287–315.

Grant, A., and Middleton, R., 1998, Contaminants in sediments—using robust regression for grain-size normalization: Estuaries, v. 21, p. 197–203.

Hill, H., Flower, B., Hollander, D., and Quinn, T., 2004, Evidence for oceanic/continental climate linkages during freshwater inputs to the Gulf of Mexico: EOS Transactions, American Geophysical Union, v. 47, no. 85, Fall Meeting Supplemental Abstract PP44A-07.

Horowitz, A., 1991, A primer on sediment-trace element chemistry: Boca Raton, Florida, Lewis Publishers, 136 p.

Jasper, J., and Gagosian, R., 1990, The sources and deposition of organic matter in the Late Quaternary Pigmy Basin, Gulf of Mexico: Geochimica et Cosmochimica Acta, v. 54, p. 1117–1132.

Kindinger, J., Flocks, J., Kulp, M., Penland, S., and Britsch, L., 2001, Sand resources, regional geology and coastal processes for the restoration of the Barataria barrier shoreline: U.S. Geological Survey Open-File Report 01–384, 69 p.

Landrum, K., 1995, Trace-metal variability of estuarine sediments, St. Benard geomorphic region, Louisiana: Gulf Coast Association of Geological Societies Transactions, v. 65, p. 365–370.

Levin, D., 1991, Transgressions and regressions in the Barataria Bight region of coastal Louisiana: Gulf Coast Association of Geological Societies Transactions, v. 41, p. 408–431.

Poore, R., Pavich, M., and Grissino-Mayer, H., 2005, Record of the North American southwest monsoon from Gulf of Mexico sediment cores: Geology, v. 33, no. 3, p. 209–212.

Poore, R., Quinn, T., and Verardo, S., 2004, Century-scale movement of the Atlantic intertropical convergence zone linked to solar variability: Geophysical Research Letters, v. 31, L12214, 4 p.

Raiswell, R., and Canfield, D., 1998, Sources of iron for pyrite formation in marine sediments: American Journal of Science, v. 298, no. 3, p. 219–245.

Stearns, S., Tieh, T., and Presley, B., 1986, Mineralogy and incipient diagenesis in sediments of Pigmy Basin, northern Gulf of Mexico: American Association of Petroleum Geologists Bulletin, v. 70, no. 5, p. 652.

Swarzenski, P., 2001, Evaluating basin/shelf effects in the delivery of sediment-hosted contaminants in the Atchafalaya and Mississippi River Deltas: U.S. Geological Survey Open-File Report 01–215, accessed October 17, 2006, at *http://gulfsci.usgs.gov/missriv/reports/ofrshelf/index.html*

Tompkins, R., and Shephard, L., 1979, Orca Basin—depositional process, geotechnical properties and clay mineralogy of Holocene sediments within an anoxic hypersaline basin, northwest Gulf of Mexico: Marine Geology, v. 33, p. 221–238.

Trefry, J., Naito, K., Trocine, R., and Metz, S., 1995, Distribution and bioaccumulation of heavy metals from produced water discharges to the Gulf of Mexico: Water Science Technology, v. 32, no. 2, p. 31–36.

Trefry, J., Presley, B., Keeney-Kennicutt, W., and Trocine, R., 1984, Distribution and chemistry of manganese, iron, and suspended particulates in Orca Basin: Geo-Marine Letters, v. 4, p. 125–130.

Walker, N., Roberts, H., Stone, G., Bentley, S., Huh, O., Sheremet, A., Rouse, L., Inoue, M., Welsh, S., Hsu, S., and Myint, S., 2002, Satellite-based assessment of sediment transport, distribution and resuspension associated with the Atchafalaya River discharge plume: Gulf Coast Association of Geological Societies Transactions, v. 52, p. 967–973.

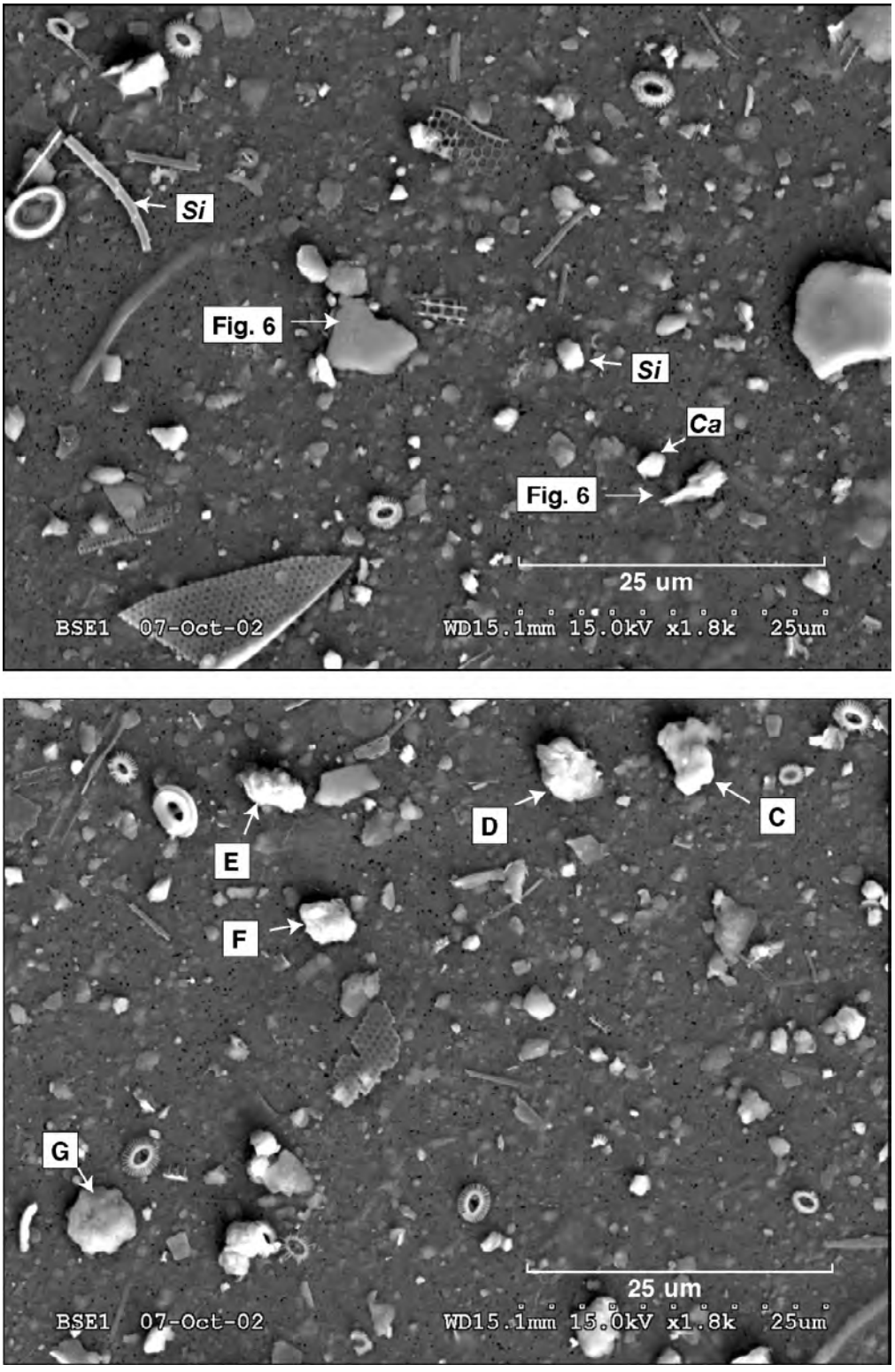

Attachment 1. SEM images of a <6-phi sample from box core MD02-2550 (Orca Basin). Letters mark particles that have been analyzed using EDS, results shown in subsequent attachments. Italicized letters list element (Si = silicon, Ca = calcium, etc.) found in particle.

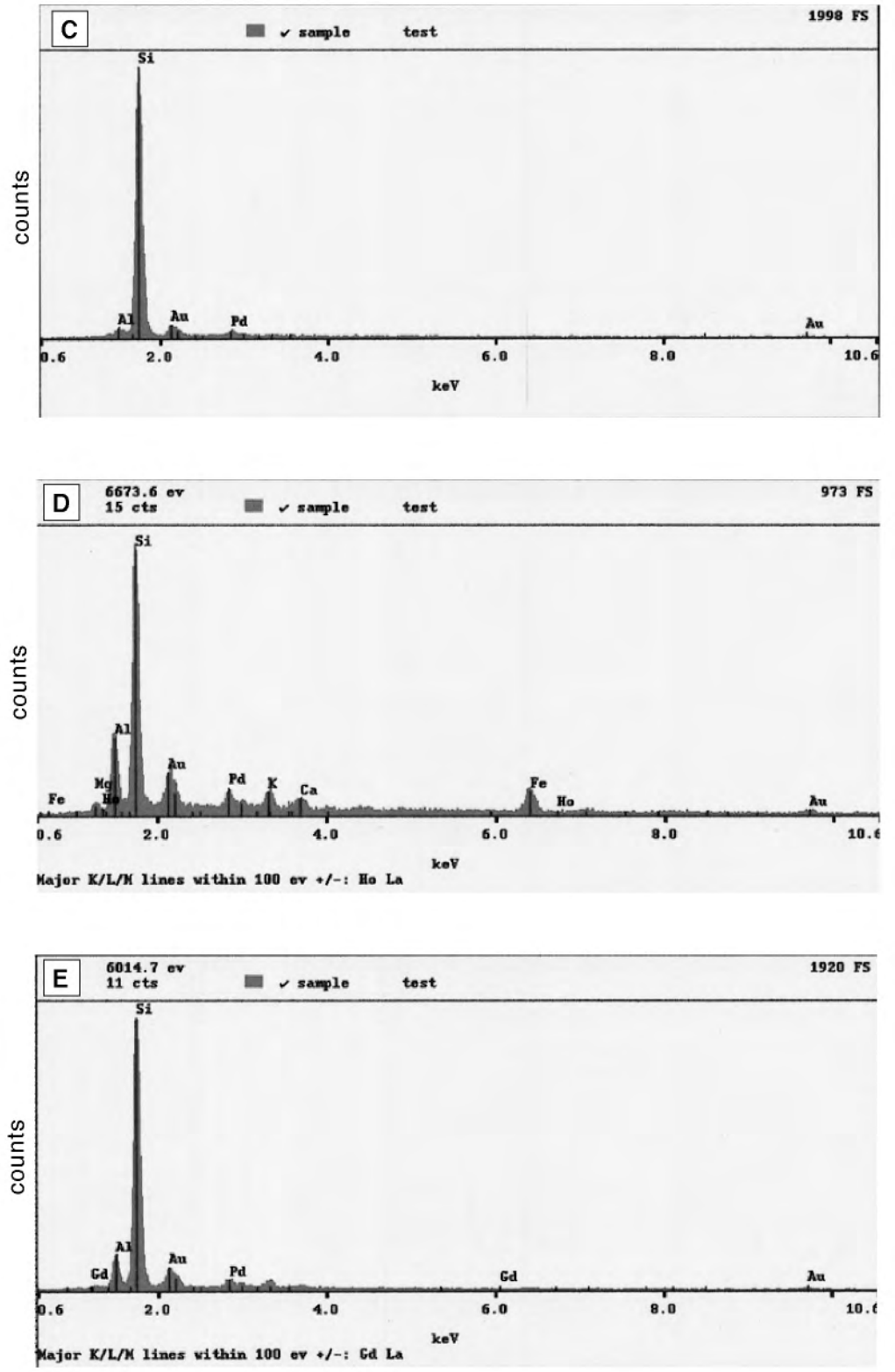

Attachment 2. EDS spectrum showing relative elemental composition of particles marked in Attachment 1. X-axis shows energy level, y-axis represents counts. The samples were coated with Au/Pd.

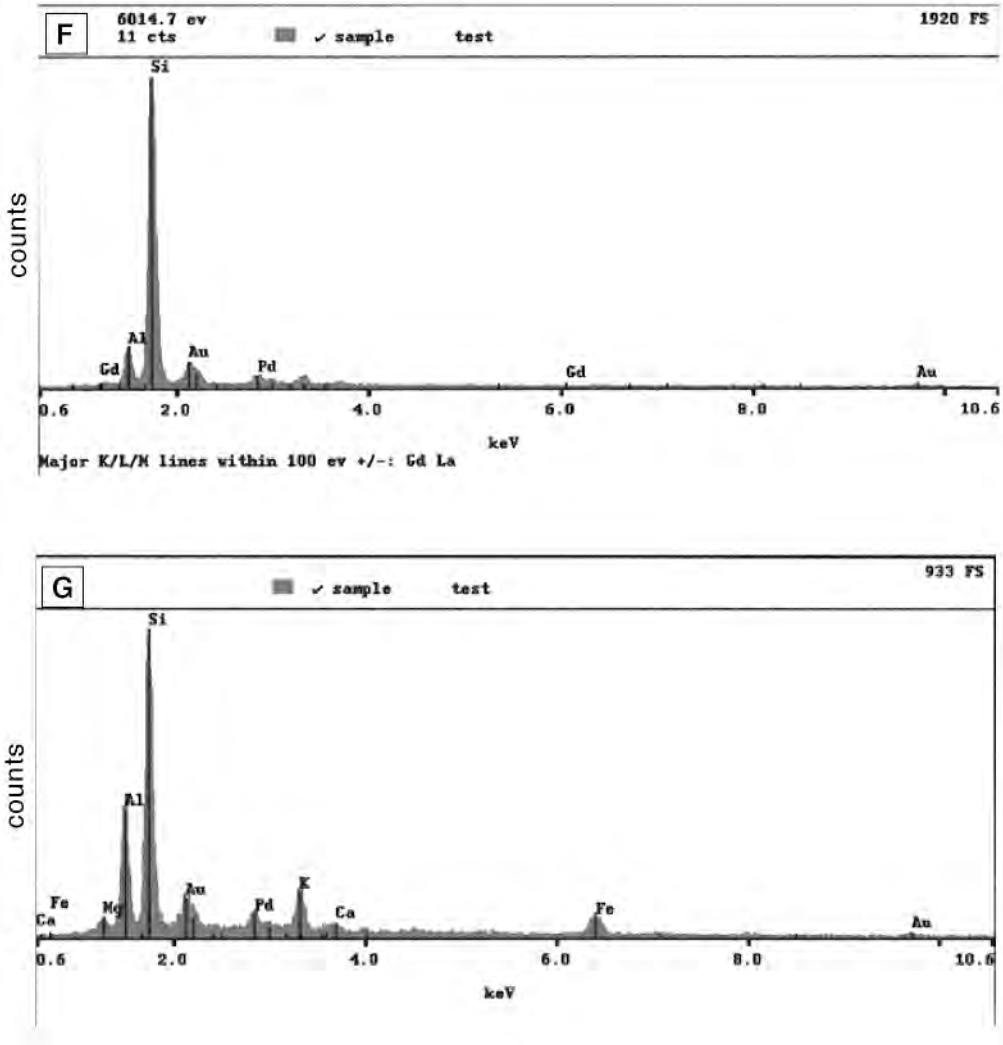

Attachment 3. EDS spectrum showing relative elemental composition of particles marked in Attachment 1. X-axis shows energy level, y-axis represents counts. The samples were coated with Au/Pd.

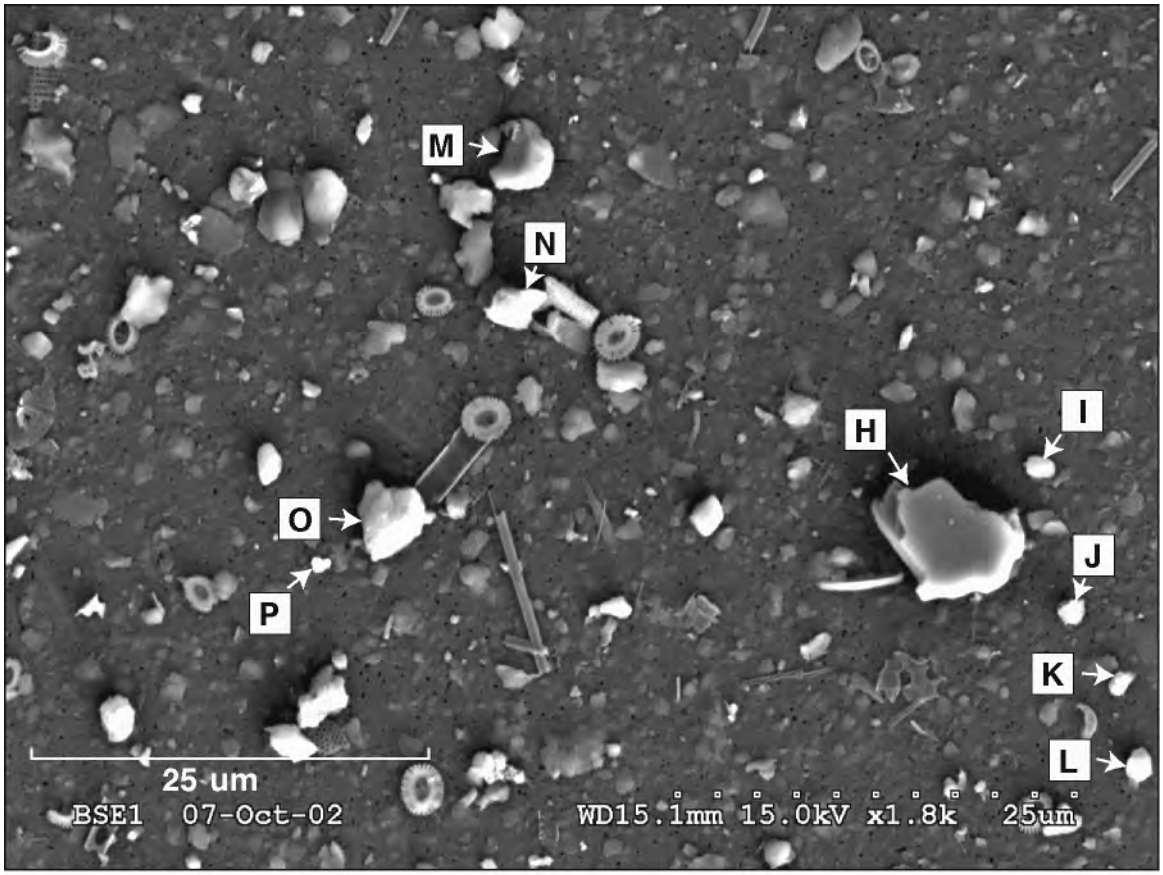

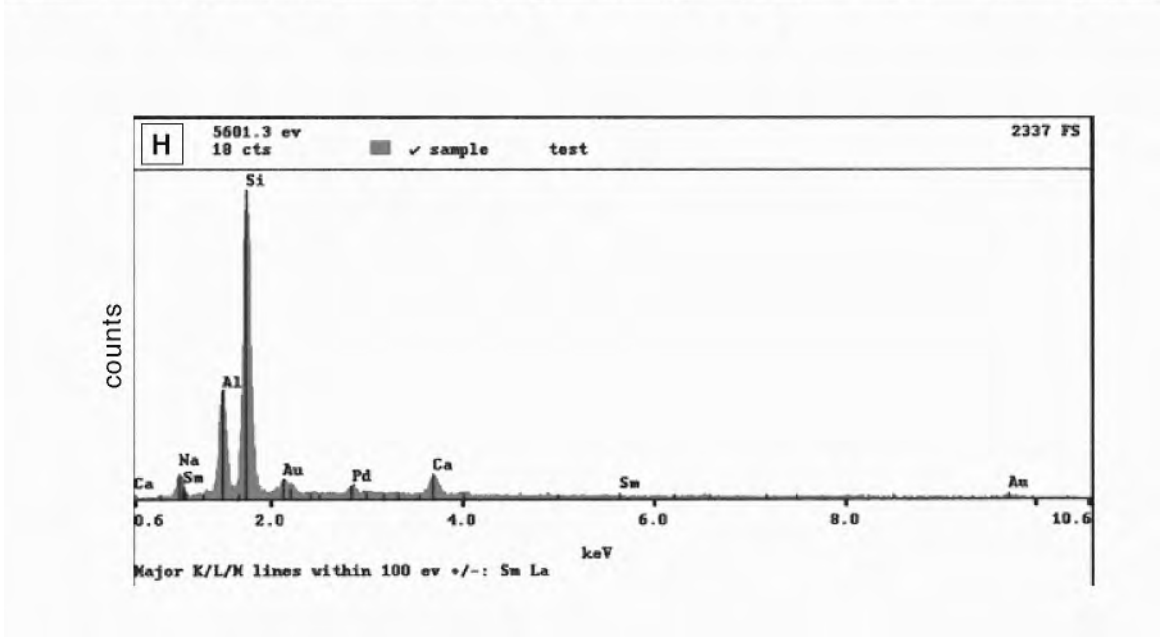

Attachment 4. Top: SEM images of a <6-phi sample from box core MD02-2550 (Orca Basin). Letters mark particles that have been analyzed using EDS, results shown in subsequent attachments. Bottom: EDS spectrum showing relative elemental composition of particles "H" shown in above image. X-axis shows energy level, y-axis represents counts. The samples were coated with Au/Pd.

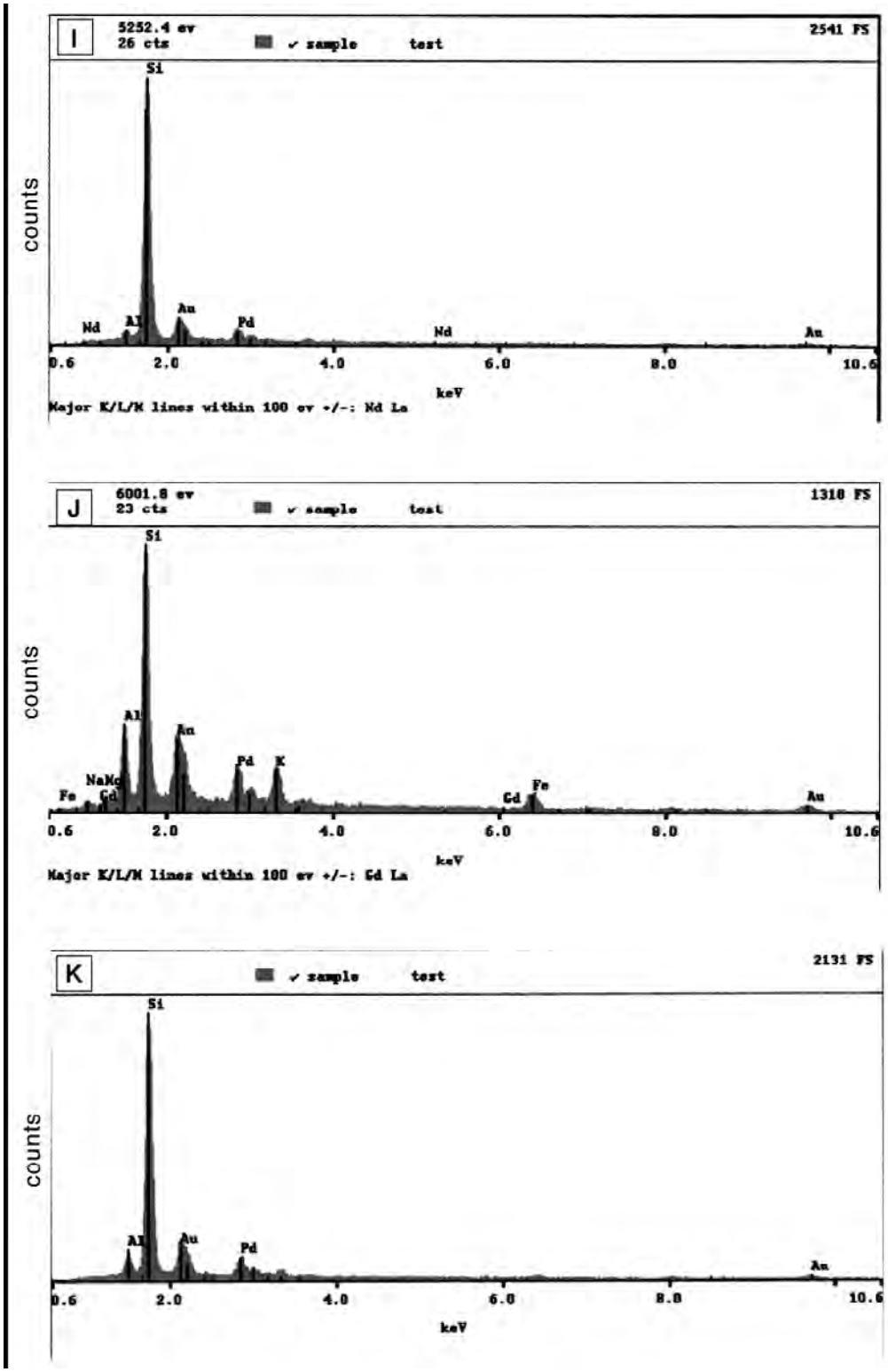

Attachment 5. EDS spectrum showing relative elemental composition of particles marked in Attachment 4. X-axis shows energy level, y-axis represents counts. The samples were coated with Au/Pd.

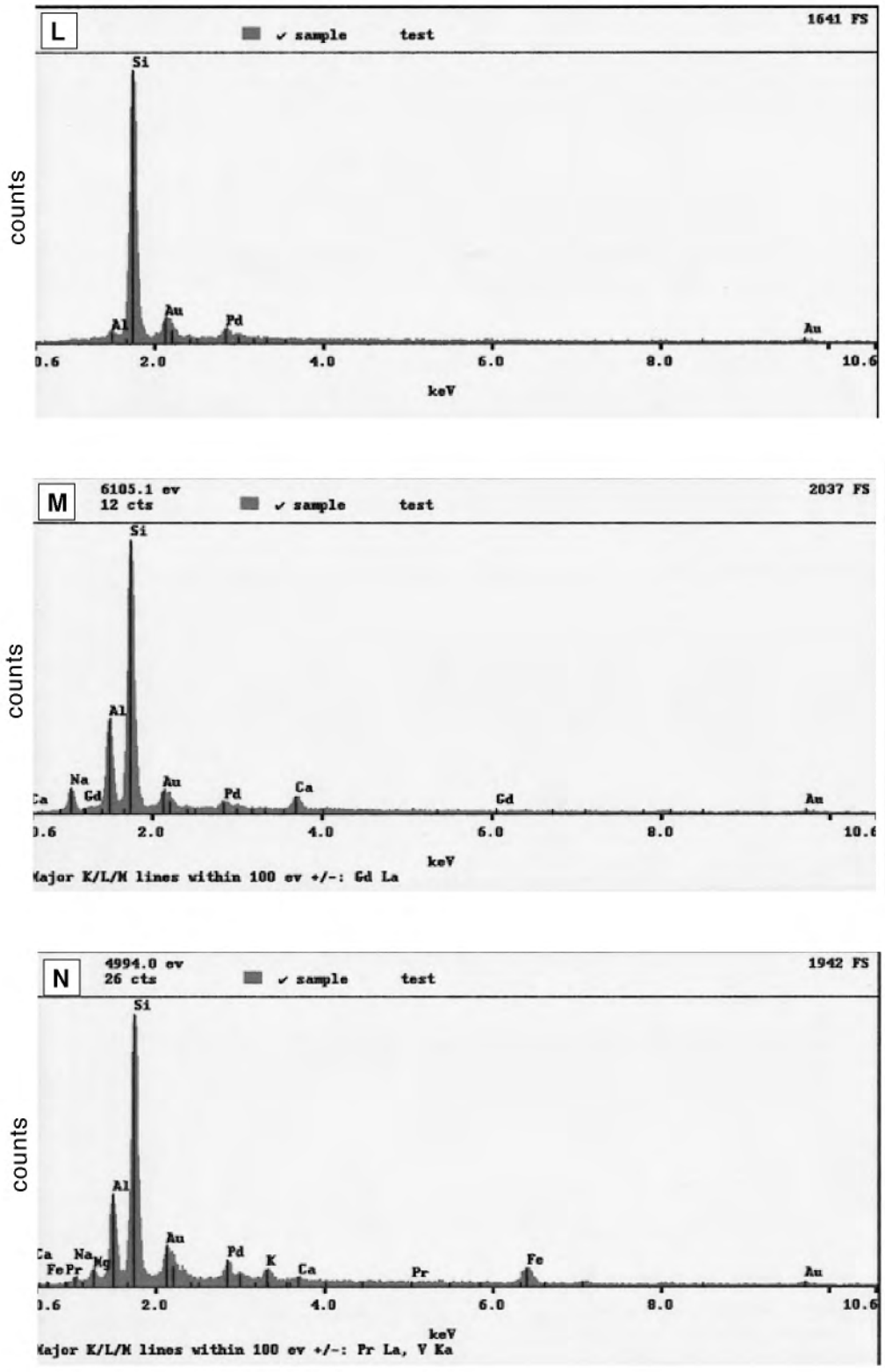

Attachment 6. EDS spectrum showing relative elemental composition of particles marked in Attachment 4. X-axis shows energy level, y-axis represents counts. The samples were coated with Au/Pd.

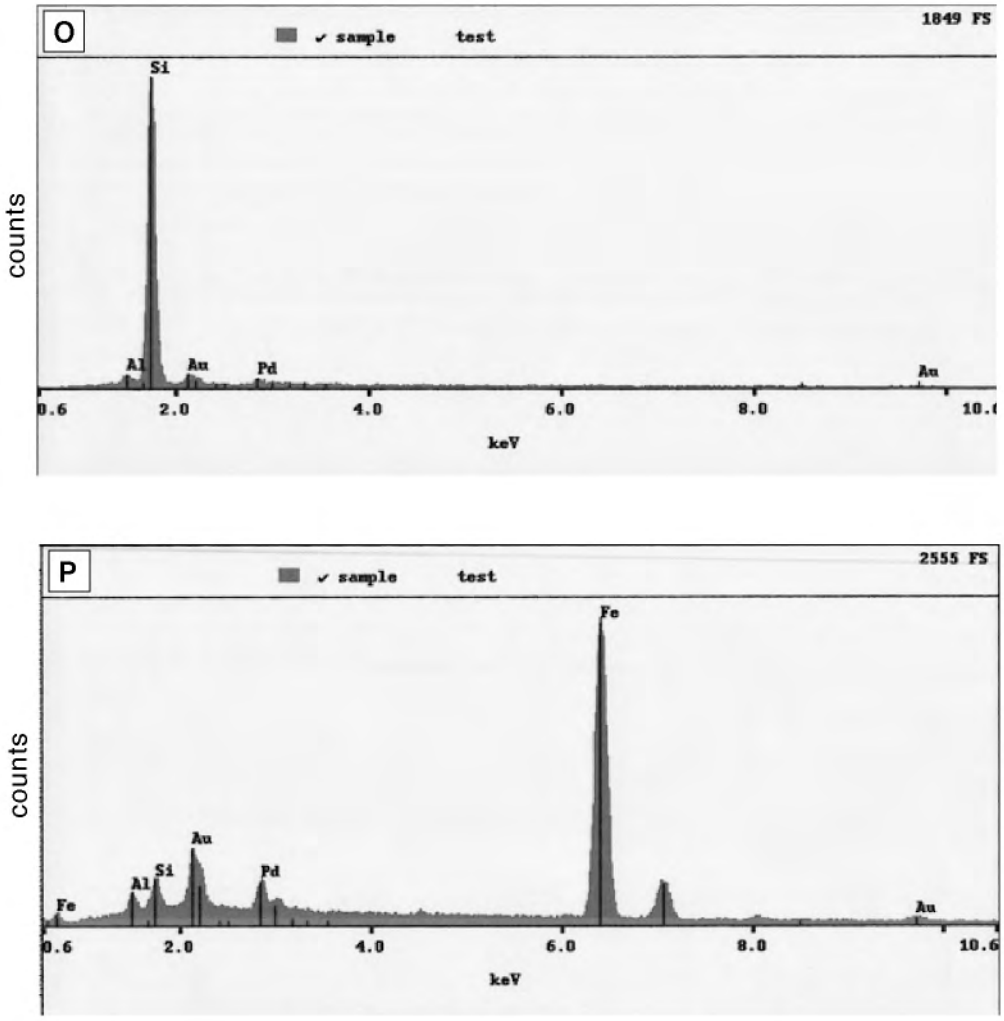

Attachment 7. EDS spectrum showing relative elemental composition of particles marked in Attachment 4. X-axis shows energy level, y-axis represents counts. The samples were coated with Au/Pd.

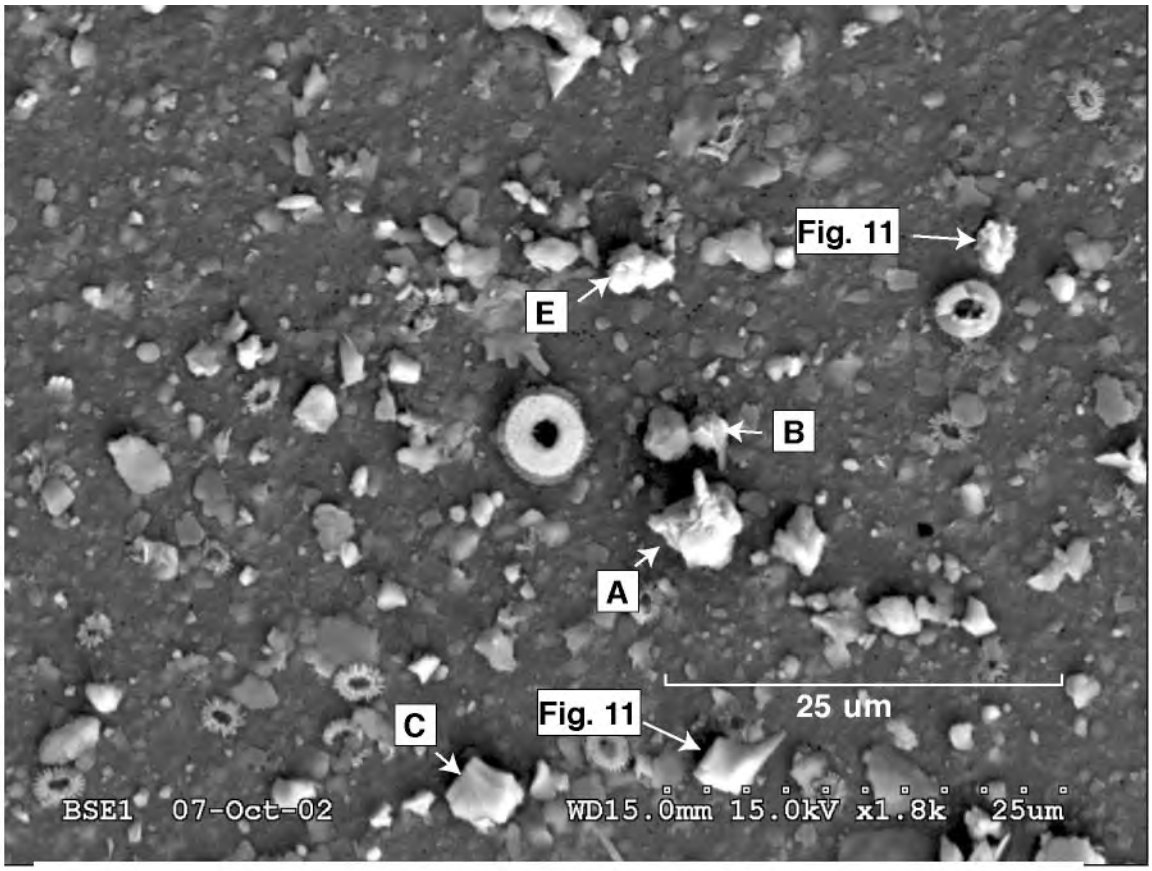

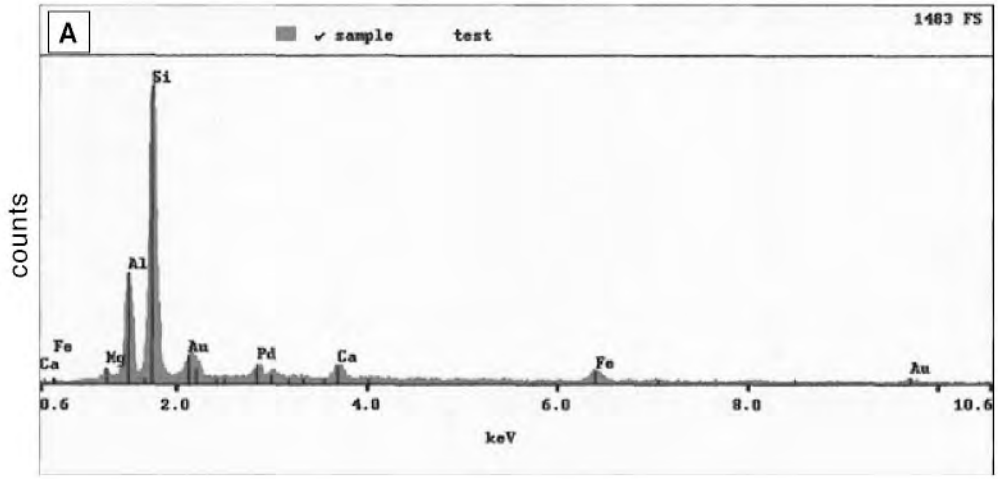

Attachment 8. Top: SEM images of a <6-phi sample from box core MD02-2553 (Pigmy Basin). Letters mark particles that have been analyzed using EDS, results shown in subsequent attachments. Bottom: EDS spectrum showing relative elemental composition of particle "A" marked in the above image. X-axis shows energy level, y-axis represents counts. The samples were coated with Au/Pd.

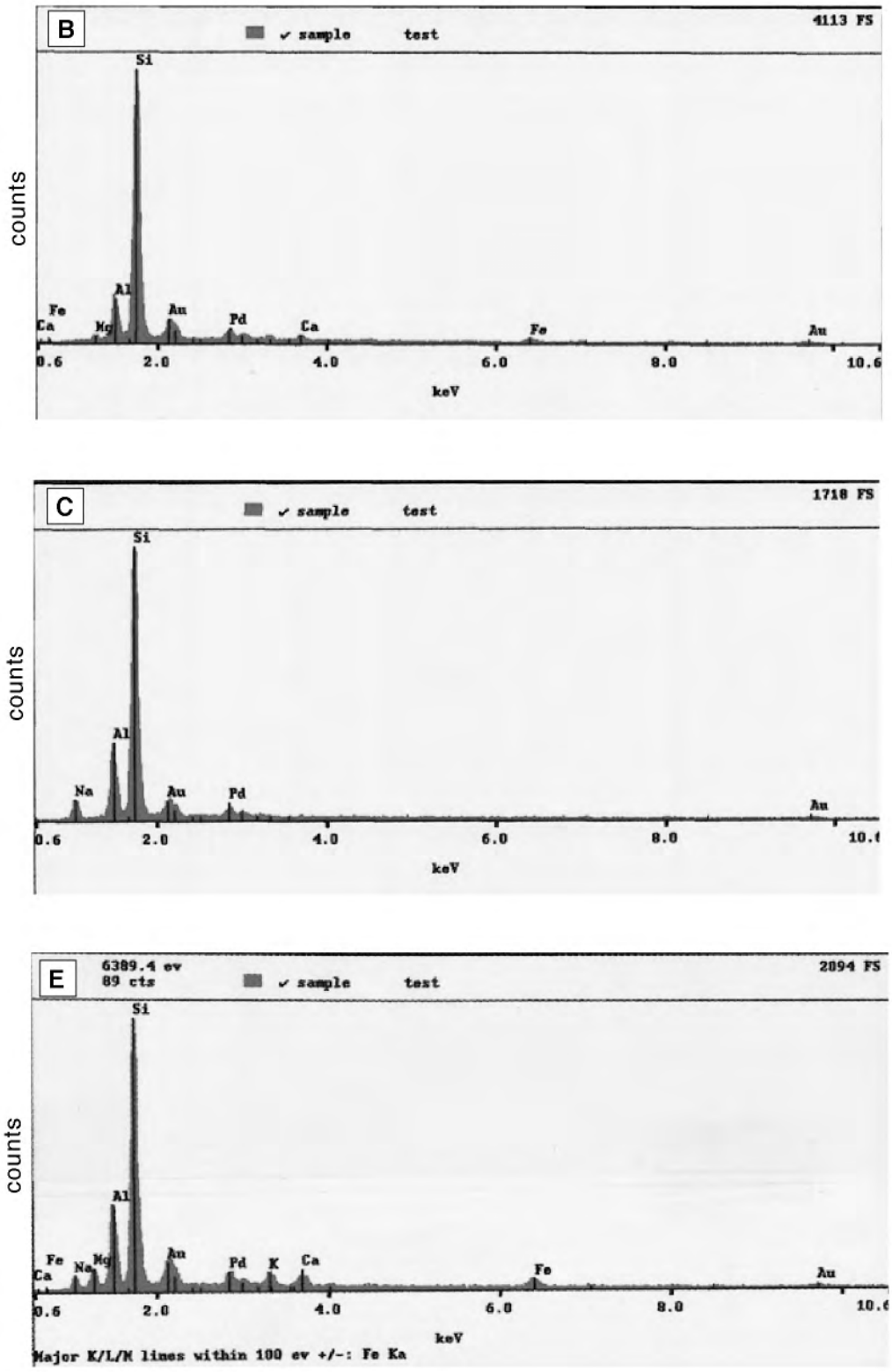

Attachment 9. EDS spectrum showing relative elemental composition of particles marked in Attachment 8. X-axis shows energy level, y-axis represents counts. The samples were coated with Au/Pd.

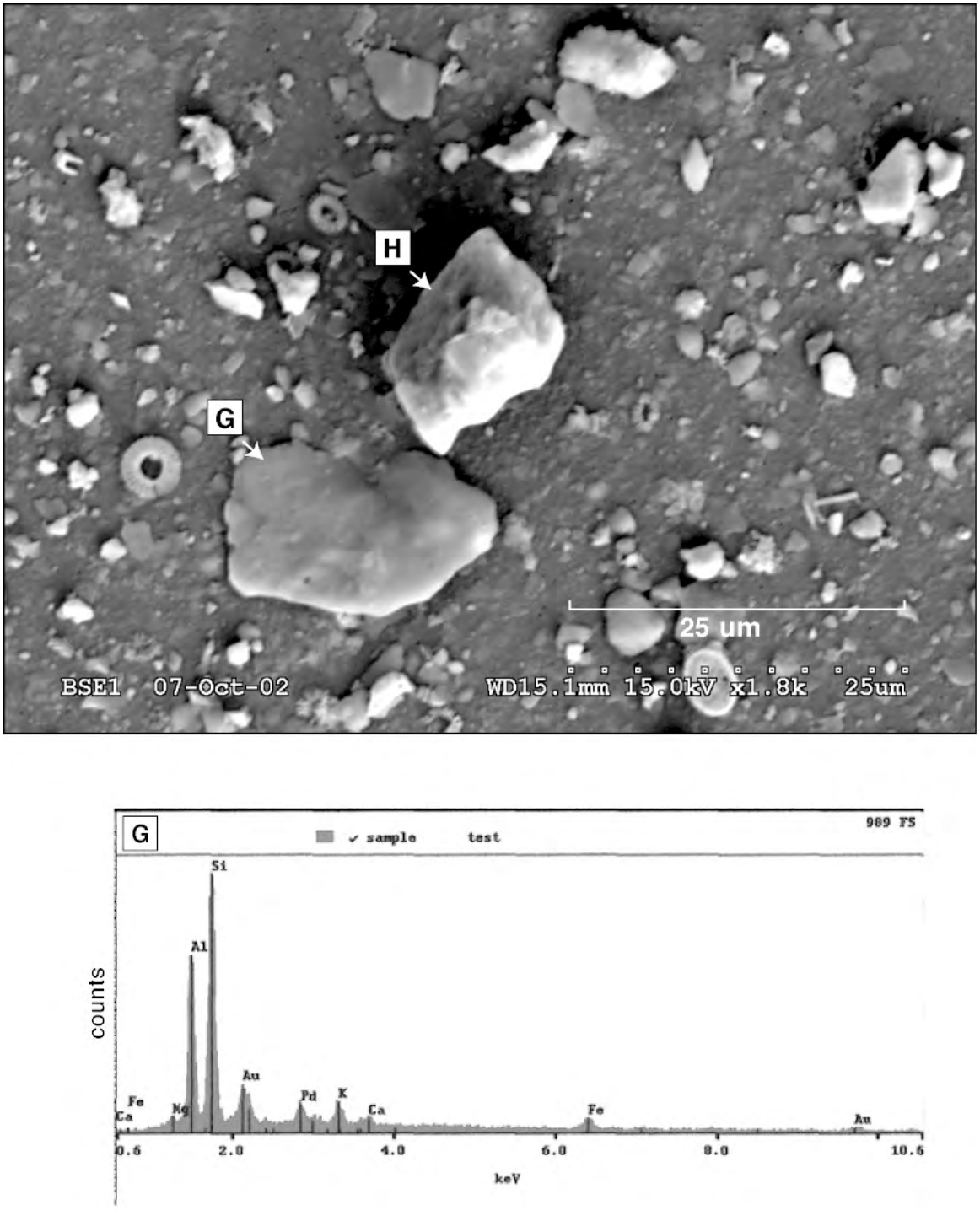

Attachment 10. Top: SEM images of a <6-phi sample from box core MD02-2553 (Pigmy Basin). Letters mark particles that have been analyzed using EDS, results shown in subsequent attachments. Bottom: EDS spectrum showing relative elemental composition of particle "G" marked in the above image. X-axis shows energy level, y-axis represents counts. The sample was coated with Au/Pd.

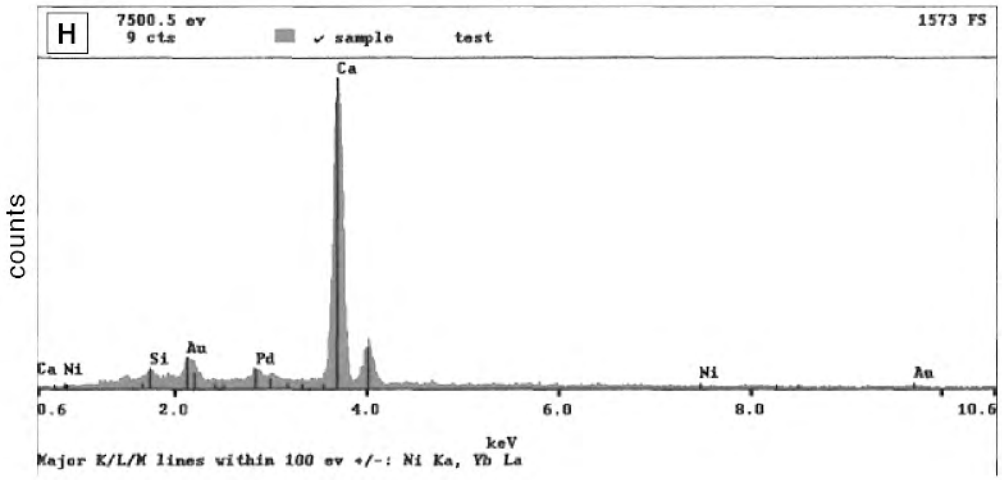

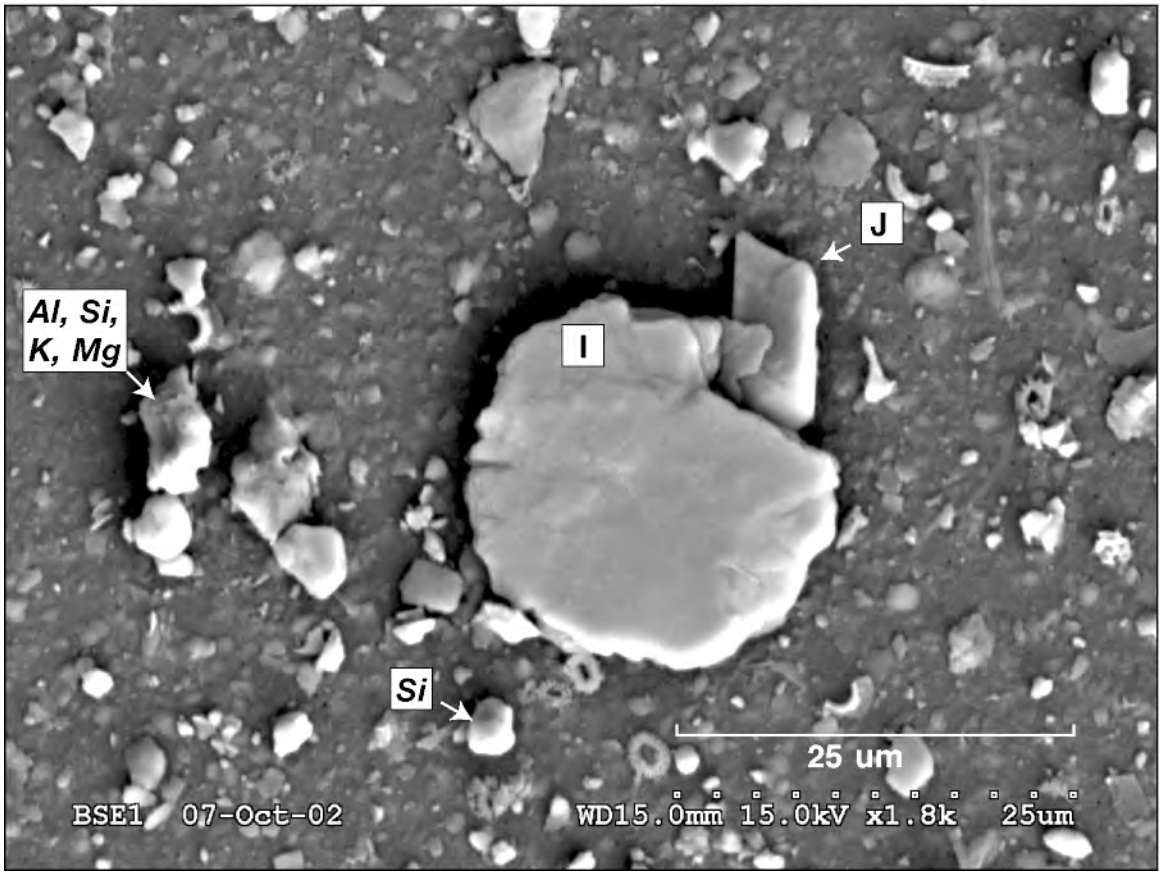

Attachment 11. Top: EDS spectrum showing relative elemental composition of particle "H" marked in Attachment 10. X-axis shows energy level, y-axis represents counts. The sample was coated with Au/Pd. Bottom: SEM images of a <6-phi sample from box core MD02-2553 (Pigmy Basin). Letters mark particles that have been analyzed using EDS, results shown in subsequent attachments. Italicized letters list element (Si = silicon, Al = aluminum, etc.) found within particle.

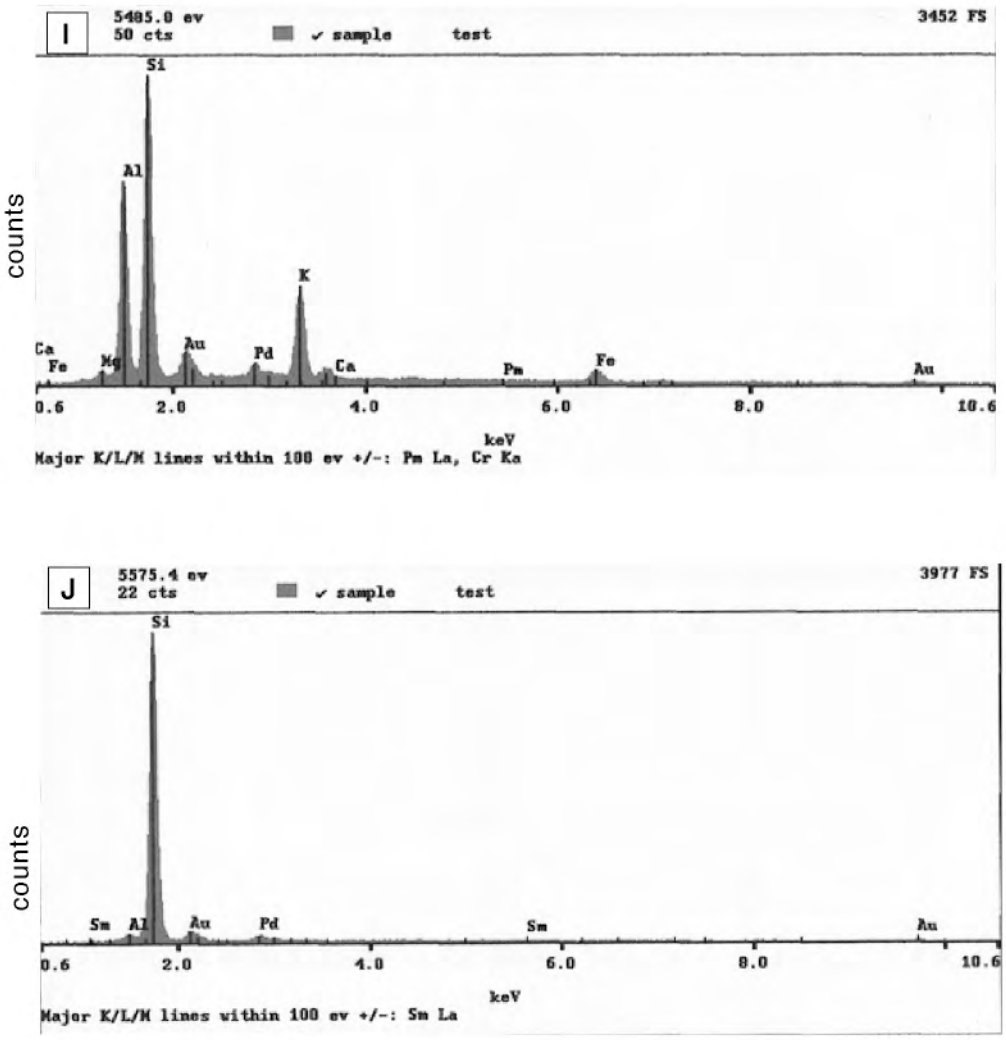

Attachment 12. EDS spectrum showing relative elemental composition of particles marked in Attachment 11. X-axis shows energy level, y-axis represents counts. The samples were coated with Au/Pd.

Attachment 13. Downcore chemical analysis of the top 2 m of box core MD02-2550 (Orca Basin). Measured using ICP-OES. Attachment 14 includes certification analysis for these data.

REPORT 25582 CODE 1F-TOTAL DIGESTION ICP																								
SAMPLE	Depth	Ag	Cd	Cu	Mn	Mo	Ni	Pb	Zn	Al	Be	Bi	Ca	Co	Fe	K	Mg	Na	P	Sr	Ti	V	Y	S
NUMBER	cm	ppm	ppm	ppm	ppm	ppm	ppm	ppm	ppm	%	ppm	ppm	%	ppm	%	%	%	%	%	ppm	%	ppm	ppm	%
MD02-2550 0-2	1	-0.3	-0.3	22	547	4	28	13	48	2.51	1	-2	4.78	6	1.81	1.04	0.90	13.59	0.036	254	0.16	73	11	0.515
MD02-2550 0-2 /R	1	-0.3	-0.3	21	567	3	26	15	49	2.81	1	-2	4.92	6	1.89	1.10	0.96	14.16	0.037	261	0.16	76	12	0.534
MD02-2550 2-4A	3	-0.3	-0.3	23	579	3	27	16	48	2.85	1	-2	5.09	6	1.98	1.15	0.99	13.32	0.033	273	0.16	82	12	0.486
MD02-2550 2-4B	3	-0.3	-0.3	23	613	3	33	20	53	2.99	1	-2	5.27	7	2.15	1.15	0.99	13.20	0.035	282	0.17	82	13	0.515
MD02-2550 2-4C	3	-0.3	-0.3	21	581	2	26	14	45	2.79	1	-2	4.99	5	1.98	1.12	0.96	13.12	0.033	263	0.17	79	12	0.479
MD02-2550 8-10	9	-0.3	-0.3	22	650	5	30	16	48	2.73	1	-2	5.10	7	1.99	1.08	0.96	13.49	0.034	268	0.16	75	11	0.545
MD02-2550 20-22	21	-0.3	-0.3	20	578	2	22	15	48	2.52	1	-2	4.86	6	1.73	1.05	0.91	13.71	0.033	262	0.16	74	11	0.464
MD02-2550 30-32	31	-0.3	-0.3	21	613	1	21	18	46	2.76	1	-2	4.78	6	1.91	1.12	1.03	13.48	0.034	258	0.17	79	12	0.492
MD02-2550 40-42	41	-0.3	-0.3	21	553	-1	19	10	45	2.67	1	-2	4.80	6	1.70	1.09	0.94	13.80	0.035	257	0.16	74	11	0.567
MD02-2550 50-52	51	-0.3	-0.3	20	492	2	20	12	43	2.64	1	-2	4.75	6	1.86	1.08	0.93	13.99	0.031	255	0.16	72	11	0.560
MD02-2550 60-62	61	-0.3	-0.3	22	503	2	23	14	49	2.46	1	-2	5.02	6	1.98	1.11	0.94	12.98	0.035	267	0.17	78	11	0.585
MD02-2550 70-72	71	-0.3	-0.3	19	447	1	18	12	44	2.31	1	-2	4.40	5	1.91	1.02	0.81	14.41	0.034	234	0.15	69	10	0.856
MD02-2550 80-82	81	-0.3	-0.3	22	539	-1	21	13	48	3.55	1	-2	4.73	6	1.83	1.22	1.04	13.03	0.033	251	0.18	82	13	0.444
MD02-2550 90-92	91	-0.3	-0.3	20	539	-1	20	12	43	2.35	1	-2	5.39	5	1.70	1.02	0.85	13.16	0.033	278	0.15	71	11	0.572
MD02-2550 100-102	101	-0.3	-0.3	22	510	2	22	18	48	3.52	1	-2	4.98	6	1.83	1.19	1.07	12.31	0.035	262	0.18	80	12	0.546
MD02-2550 110-112	111	-0.3	-0.3	21	451	1	21	14	46	2.63	1	-2	4.52	6	1.85	1.11	0.90	13.61	0.033	247	0.16	76	11	0.580
MD02-2550 120-122	121	-0.3	-0.3	21	487	1	21	15	45	2.48	1	-2	4.89	5	1.94	1.11	0.96	13.68	0.032	262	0.16	76	11	0.517
MD02-2550 130-132	131	-0.3	-0.3	20	464	-1	20	13	45	2.21	1	-2	4.87	5	1.88	1.04	0.91	14.15	0.030	252	0.15	69	11	0.770
MD02-2550 140-142	141	-0.3	-0.3	23	1319	2	24	16	52	3.11	1	-2	5.69	7	2.06	1.24	1.09	12.11	0.040	287	0.19	96	14	0.601
MD02-2550 150-152	151	-0.3	-0.3	20	552	1	21	11	48	2.53	2	-2	5.16	6	1.99	1.26	1.09	12.16	0.032	248	0.18	80	12	0.599
MD02-2550 160-162	161	-0.3	-0.3	21	766	10	23	18	50	2.22	1	-2	5.23	8	1.98	1.17	0.99	13.05	0.034	262	0.17	85	11	0.724
MD02-2550 170-172	171	-0.3	-0.3	22	984	2	23	16	51	4.36	1	-2	6.29	7	2.23	1.34	1.30	11.42	0.039	286	0.20	90	15	0.760
MD02-2550 180-182	181	-0.3	-0.3	20	480	2	19	9	45	2.53	1	-2	4.91	6	1.83	1.07	0.90	11.72	0.030	255	0.16	74	11	0.615
MD02-2550 180-182/R	181	-0.3	-0.3	19	455	3	19	14	43	2.68	1	-2	4.62	5	1.76	1.04	0.85	11.89	0.031	239	0.16	70	11	0.604
MD02-2550 190-192	191	-0.3	-0.3	21	496	5	32	13	51	3.40	1	-2	5.05	8	1.86	1.25	1.04	12.46	0.030	250	0.18	81	12	0.512
MD02-2550 198-200	199	-0.3	-0.3	24	570	2	23	22	57	3.62	1	-2	5.16	7	2.23	1.34	1.10	10.71	0.033	253	0.20	89	14	0.770

Attachment 14. Downcore chemical analysis of the top 2 m of box core MD02-2553 (Pigmy Basin). Measured using ICP-OES. Table includes certification analysis and notifications.

REPORT 25582 CODE 1F-TOTAL DIGESTION ICP																								
SAMPLE	Depth	Ag	Cd	Cu	Mn	Mo	Ni	Pb	Zn	Al	Be	Bi	Ca	Co	Fe	K	Mg	Na	P	Sr	Ti	V	Y	S
NUMBER	cm	ppm	ppm	ppm	ppm	ppm	ppm	ppm	ppm	%	ppm	ppm	%	ppm	%	%	%	%	%	ppm	%	ppm	ppm	%
MD02-2553 0-2	1.5	-0.3	-0.3	44	3360	5	40	19	96	6.65	2	-2	7.61	12	3.55	2.06	1.77	2.67	0.051	408	0.34	131	22	0.215
MD02-2553 10-12	11	-0.3	-0.3	40	3394	2	38	19	93	8.86	3	-2	6.95	14	3.68	2.32	2.18	2.56	0.062	368	0.37	134	31	0.225
MD02-2553 20-22	21	-0.3	-0.3	41	823	-1	32	17	92	10.37	3	-2	7.93	9	3.76	2.25	1.99	2.61	0.059	438	0.39	140	37	0.250
MD02-2553 30-32	31	-0.3	-0.3	43	883	-1	35	19	89	9.43	3	-2	7.58	10	4.20	2.47	2.22	2.76	0.059	399	0.37	139	32	0.281
MD02-2553 40-42	41	-0.3	-0.3	39	974	-1	32	17	90	10.11	3	-2	8.56	10	3.47	2.55	2.25	2.71	0.057	439	0.37	139	35	0.268
MD02-2553 50-52	51	-0.3	-0.3	41	1348	2	38	15	93	5.64	3	-2	5.34	12	4.56	2.39	2.24	2.30	0.053	254	0.39	142	25	0.200
MD02-2553 60-62	61	-0.3	-0.3	36	1305	-1	39	20	91	5.41	3	-2	6.11	14	3.82	2.41	2.28	2.42	0.049	273	0.39	140	24	0.290
MD02-2553 70-72	71	-0.3	-0.3	30	3215	-1	35	14	89	4.78	2	-2	6.28	11	3.77	2.08	1.78	2.55	0.050	341	0.35	140	21	0.182
MD02-2553 70-72/R	71	-0.3	-0.3	32	3181	-1	35	16	91	4.88	2	-2	6.41	11	3.71	2.10	1.81	2.38	0.051	344	0.35	144	22	0.169
MD02-2553 80-82	81	-0.3	-0.3	39	1355	-1	33	16	85	10.18	2	-2	8.21	10	3.46	2.40	2.02	2.24	0.057	434	0.35	136	32	0.209
MD02-2553 90-92	91	-0.3	-0.3	39	1201	-1	41	16	85	8.53	2	-2	7.75	15	3.67	2.27	1.96	2.42	0.057	422	0.34	140	29	0.229
MD02-2553 100-102	101	-0.3	-0.3	40	1129	-1	35	15	88	10.23	3	-2	8.27	11	3.59	2.36	2.11	2.22	0.059	435	0.37	138	37	0.213
MD02-2553 110-112	111	-0.3	-0.3	35	973	-1	32	16	84	6.33	2	-2	8.00	9	3.47	2.05	1.68	2.07	0.053	411	0.34	132	26	0.167
MD02-2553 120-122	121	-0.3	-0.3	39	1056	-1	32	16	87	9.17	3	-2	5.93	11	3.93	2.56	2.28	2.11	0.054	285	0.40	142	32	0.165
MD02-2553 130-132	131	-0.3	-0.3	32	1352	-1	32	13	83	9.58	2	-2	6.57	10	3.52	2.56	2.46	2.05	0.054	279	0.38	129	34	0.177
MD02-2553 140-142	141	-0.3	0.3	34	1338	2	33	16	88	9.37	3	-2	6.85	9	3.45	2.52	2.26	2.14	0.061	337	0.36	139	35	0.207
MD02-2553 150-152	151	-0.3	-0.3	35	1247	-1	33	17	91	8.23	3	-2	6.56	9	3.31	2.35	1.91	2.05	0.054	341	0.34	145	29	0.209
MD02-2553 160-162	161	-0.3	-0.3	28	1727	1	38	10	86	4.89	2	-2	5.74	11	3.68	2.14	1.87	2.04	0.050	287	0.34	135	21	0.162
MD02-2553 170-172	171	-0.3	-0.3	31	1089	3	34	14	93	8.35	3	-2	6.69	12	3.57	2.35	2.01	2.03	0.056	342	0.34	137	29	0.162
MD02-2553 180-182	181	-0.3	-0.3	42	1024	-1	37	15	90	7.30	2	-2	7.05	11	3.49	2.31	2.01	2.09	0.053	348	0.33	139	26	0.233
MD02-2553 190-192	191	-0.3	-0.3	31	1004	1	34	16	86	8.51	2	-2	6.37	11	3.44	2.44	2.25	1.84	0.055	292	0.34	130	30	0.183
MD02-2553 200-202	201	-0.3	-0.3	37	1044	2	38	21	85	8.84	2	-2	5.77	11	3.44	2.51	2.34	1.70	0.051	234	0.36	128	31	0.288
STANDARDS:																								
AL-1			0.03	3	31	0.1	2	4.5	8	9.841	2.7	0.03	0.274	0.2	0.052	0.116	0.021	7.856	0.016	80	0.007	2	6.8	0.0085
AL-I		-0.3	-0.3	2	16	2	-1	5	7	12.34	3	-2	0.37	-1	0.06	0.12	0.03	6.52	0.014	89	-0.01	-2	4	0.022
SDC-1 cert		0.041	(.08	30	883	(.25	38	25	103	8.338	3.0	0.26	1.001	17.9	4.825	2.722	1.019	1.521	0.069	183	0.606	102	40	0.065
SDC-1		-0.3	-0.3	44	963	2	33	20	99	6.53	4	-2	1.04	15	4.75	2.73	1.10	1.48	0.050	168	0.62	99	36	0.075
DNC-1 cert		(.027	(.182	96	1154	(.7	247	6.3	66	9.687	1	(.02	8.055	54.7	6.94	0.19	6.06	1.39	0.037	145	0.287	148	18	(0.039
DNC-1		-0.3	-0.3	107	1243	-1	277	8	64	7.75	-1	-2	8.45	51	7.26	0.18	6.93	1.53	0.023	144	0.31	157	20	0.079
SCO-1 cert		0.134	0.14	28.7	410	1.37	27	31	103	7.24	1.84	0.37	1.87	10.5	3.59	2.30	1.64	0.67	0.090	174	0.38	131	26	0.063
SCO-1		-0.3	-0.3	29	409	3	26	28	99	5.07	2	-2	1.85	9	3.37	2.14	1.67	0.65	0.066	152	0.35	130	21	0.075
GXR-6 cert		1.3	(1	66	1008	2.4	27	101	118	17.68	1.4	(.29	0.179	13.8	5.58	1.87	0.61	0.1	0.035	35	0.498	186	14	0.016
GXR-6		0.5	-0.3	67	1151	4	18	103	120	15.95	2	-2	0.28	7	5.36	2.38	1.04	0.12	0.045	57	0.53	182	24	0.017
GXR-2 cert		17	4.1	76	1008	(2.1	21	690	530	16.46	1.7	(.69	0.929	8.6	1.86	1.37	0.85	0.56	0.105	160	0.3	52	17	0.031
GXR-2		15.9	3.1	78	813	3	17	696	503	5.30	2	-2	0.68	7	1.66	1.15	0.65	0.50	0.045	121	0.29	51	9	0.024
GXR-1 cert		31	3.3	1110	853	18	41	730	760	3.52	1.22	1380	0.958	8.2	23.64	0.05	0.22	0.05	0.065	275	0.036	80	32	0.257
GXR-1		31.2	2.5	1201	967	23	39	798	722	1.38	1	1168	0.90	3	24.36	0.04	0.20	0.05	0.048	291	0.02	85	38	0.292
GXR-4 cert		4	(.86	6520	155	310	42	52	73	7.20	1.9	19	1.01	14.6	3.09	4.01	1.66	0.56	0.120	221	0.29	87	14	1.770
GXR-4		3.0	-0.3	6044	153	311	38	46	69	4.63	2	17	1.00	11	2.76	3.85	1.81	0.48	0.096	204	0.21	82	15	1.895
Note: Certificate data underlined are recommended values; other values are proposed except those preceded by a "(" which are information values.																								
Barite, gahnite, chromite, cassiterite, zircon, sphene, magnetite, and sulphates may not be totally dissolved.																								
Aluminium and Yttrium may only be paritally extracted.																								
Sulphur associated with barite will not be extracted. Rutile, ilmenite and monazite may not be fully extracted.																								

Attachment 15. Downcore grain-size analysis of box core MD02-2550 (Orca Basin), measured using laser diffraction. Depth is to midpoint of 2-cm interval. Mean values are in phi.

Grainsize_DataTable		% finer than										
Sample I.D.	Depth mdpt (m)	5%	10%	16%	25%	50%	75%	84%	90%	95%	Inman Mean	Sorting Value
2550-000-002	0.020	10.284	9.752	9.247	8.674	7.610	6.624	6.123	5.610	4.336	7.685	1.532
2550-008-010	0.090	9.837	9.103	8.555	8.029	7.059	6.159	5.728	5.287	4.487	7.142	1.371
2550-020-022	0.210	10.204	9.655	9.171	8.651	7.694	6.834	6.426	6.030	5.467	7.798	1.310
2550-040-042	0.410	10.414	9.951	9.506	8.977	7.985	7.155	6.790	6.460	6.019	8.148	1.259
2550-050-052	0.510	10.091	9.434	8.857	8.273	7.207	6.144	5.549	4.654	2.743	7.203	1.809
2550-052-054	0.530	10.010	9.352	8.784	8.183	6.944	5.318	4.342	3.496	2.776	6.563	2.343
2550-060-062	0.610	10.185	9.614	9.106	8.566	7.577	6.667	6.210	5.745	4.689	7.658	1.411
2550-070-072	0.710	10.375	9.886	9.410	8.855	7.828	6.911	6.441	5.916	4.131	7.925	1.469
2550-080-082	0.810	10.410	9.939	9.475	8.912	7.835	6.847	6.309	5.685	3.369	7.892	1.614
2550-090-092	0.910	10.430	9.989	9.578	9.093	8.130	7.222	6.706	6.023	4.631	8.142	1.535
2550-100-102	1.010	10.727	10.414	10.108	9.703	8.751	7.891	7.502	7.105	6.102	8.805	1.299
2550-106-108	1.070	10.155	9.569	9.039	8.461	7.356	6.169	5.459	4.592	3.237	7.249	1.935
2550-110-112	1.110	10.422	9.949	9.475	8.896	7.832	6.924	6.476	6.014	5.167	7.976	1.441
2550-120-122	1.210	10.281	9.732	9.207	8.623	7.579	6.648	6.194	5.762	4.929	7.700	1.431
2550-126-128	1.270	10.317	9.782	9.244	8.608	7.412	6.199	5.565	4.882	3.861	7.404	1.863
2550-140-142	1.410	10.526	10.119	9.717	9.212	8.214	7.404	7.058	6.750	6.345	8.388	1.231
2550-160-162	1.610	10.129	9.521	8.977	8.401	7.337	6.322	5.817	5.319	4.520	7.397	1.541
2550-170-172	1.710	10.398	9.908	9.412	8.812	7.711	6.759	6.325	5.960	5.547	7.869	1.426
2550-180-182	1.810	10.446	9.996	9.553	9.010	7.960	7.040	6.583	6.122	5.503	8.068	1.444
2550-198-200	1.990	10.402	9.923	9.446	8.863	7.740	6.664	6.101	5.570	4.705	7.773	1.646
2550-210-212	2.110	10.520	10.102	9.682	9.149	8.106	7.252	6.867	6.512	6.008	8.275	1.318
2550-230-232	2.310	10.418	9.956	9.506	8.959	7.856	6.597	5.533	4.007	2.795	7.520	2.476
2550-240-242	2.410	10.442	9.992	9.551	9.013	7.957	6.969	6.412	5.797	4.756	7.982	1.608
2550-250-252	2.510	10.501	10.081	9.667	9.147	8.059	6.921	5.974	4.434	2.763	7.821	2.357
2550-254-256	2.550	10.350	9.857	9.380	8.807	7.631	6.145	5.183	4.280	3.270	7.281	2.264
2550-260-262	2.610	10.416	9.964	9.534	9.010	7.951	6.920	6.346	5.774	4.853	7.940	1.618
2550-270-272	2.710	10.637	10.282	9.934	9.483	8.520	7.742	7.419	7.144	6.797	8.677	1.169
2550-280-282	2.810	10.605	10.231	9.856	9.363	8.321	7.433	7.004	6.544	5.680	8.430	1.410
2550-290-292	2.910	10.514	10.094	9.675	9.140	8.055	7.094	6.594	6.061	5.231	8.135	1.540
2550-300-302	3.010	10.581	10.193	9.806	9.295	8.222	7.321	6.887	6.414	5.395	8.346	1.441

Attachment 16. Downcore grain-size analysis of boxcore MD02-2553 (Pigmy Basin), measured using laser diffraction. Depth is to midpoint of 2-cm interval. Mean values are in phi.

Grainsize_DataTable Sample I.D.	Depth mdpt (m)	% finer than 5%	10%	16%	25%	50%	75%	84%	90%	95%	Inman Mean	Sorting Value
2553-000-002	0.010	10.377	9.871	9.340	8.667	7.414	6.288	5.739	5.134	3.997	7.540	1.766
2553-010-012	0.110	10.422	9.943	9.437	8.770	7.460	6.149	5.362	4.337	3.166	7.400	2.217
2553-014-016	0.150	10.576	10.192	9.811	9.319	8.282	7.396	6.982	6.564	5.895	8.397	1.377
2553-016-018	0.170	10.507	10.083	9.651	9.085	7.919	6.866	6.335	5.852	5.195	7.993	1.617
2553-020-022	0.210	10.637	10.275	9.911	9.404	8.269	7.345	6.921	6.499	5.908	8.416	1.453
2553-028-030	0.290	10.539	10.139	9.748	9.248	8.221	7.372	6.997	6.655	6.145	8.373	1.296
2553-030-032	0.310	10.493	10.052	9.589	8.966	7.704	6.497	5.774	4.790	3.179	7.682	2.088
2553-040-042	0.410	10.503	10.074	9.636	9.050	7.835	6.698	6.066	5.400	3.872	7.851	1.825
2553-044-046	0.450	10.544	10.144	9.749	9.237	8.156	7.219	6.764	6.297	5.655	8.256	1.470
2553-050-052	0.510	10.679	10.341	10.001	9.530	8.365	7.337	6.836	6.329	5.762	8.419	1.600
2553-060-062	0.610	10.628	10.263	9.897	9.388	8.170	7.056	6.495	6.007	5.437	8.196	1.690
2553-070-072	0.710	10.557	10.150	9.725	9.139	7.862	6.552	5.837	5.138	3.796	7.781	2.000
2553-080-082	0.810	10.583	10.199	9.814	9.292	8.094	6.958	6.336	5.774	5.076	8.075	1.759
2553-090-092	0.910	10.557	10.152	9.737	9.168	7.917	6.644	5.823	4.788	3.291	7.780	2.190
2553-100-102	1.010	10.651	10.293	9.934	9.433	8.252	7.160	6.527	5.913	5.250	8.231	1.760
2553-110-112	1.110	10.623	10.263	9.904	9.416	8.250	7.157	6.568	6.013	5.542	8.236	1.702
2553-120-122	1.210	10.623	10.261	9.900	9.400	8.172	6.978	6.332	5.802	5.270	8.116	1.799
2553-130-132	1.310	10.565	10.173	9.777	9.245	8.073	7.000	6.459	5.983	5.425	8.118	1.631
2553-140-142	1.410	10.630	10.263	9.895	9.380	8.160	7.067	6.484	5.959	5.341	8.190	1.711
2553-150-152	1.510	10.710	10.389	10.066	9.619	8.461	7.425	6.941	6.450	5.872	8.503	1.584
2553-160-162	1.610	10.686	10.352	10.020	9.562	8.436	7.439	6.981	6.526	5.941	8.500	1.518
2553-170-172	1.710	10.570	10.180	9.793	9.274	8.117	7.054	6.488	5.929	5.298	8.141	1.672
2553-180-182	1.810	10.583	10.197	9.809	9.281	8.087	6.963	6.339	5.758	5.042	8.074	1.761
2553-182-184	1.830	10.632	10.277	9.929	9.472	8.470	7.651	7.307	6.997	6.540	8.618	1.237
2553-190-192	1.910	10.703	10.383	10.070	9.657	8.632	7.700	7.317	6.987	6.582	8.694	1.335
2553-198-200	1.990	10.691	10.360	10.032	9.587	8.546	7.641	7.237	6.840	6.226	8.635	1.374
2553-200-202	2.010	10.805	10.529	10.257	9.891	8.919	8.048	7.737	7.510	7.290	8.997	1.191
2553-210-212	2.110	10.621	10.249	9.870	9.340	8.130	7.010	6.376	5.763	4.630	8.123	1.788
2553-220-222	2.210	10.644	10.284	9.920	9.410	8.162	6.925	6.200	5.563	4.446	8.060	1.924
2553-230-232	2.310	10.635	10.272	9.901	9.377	8.113	6.894	6.202	5.598	4.214	8.052	1.890
2553-240-242	2.410	10.614	10.242	9.865	9.359	8.230	7.196	6.635	6.086	5.439	8.250	1.636
2553-250-252	2.510	10.574	10.187	9.797	9.272	8.062	6.764	5.830	4.526	2.844	7.814	2.373
2553-260-262	2.610	10.592	10.207	9.817	9.282	8.057	6.808	5.998	5.171	3.517	7.907	2.056
2553-270-272	2.710	10.658	10.308	9.960	9.481	8.317	7.221	6.590	5.980	5.370	8.275	1.751
2553-280-282	2.810	10.693	10.358	10.020	9.546	8.386	7.323	6.722	6.044	5.059	8.371	1.751
2553-290-292	2.910	10.610	10.238	9.865	9.361	8.192	7.103	6.500	5.882	4.966	8.183	1.740
2553-300-302	3.010	10.669	10.324	9.976	9.491	8.322	7.278	6.744	6.206	5.602	8.360	1.643

Attachment 17. Texture analysis of cores MD02-2550 and MD02-2553, determined from grain-size analysis. Sand, silt, and clay refer to >4 phi, 4 – 8 phi, and <8 phi, respectively. Inman mean values are in phi.

Sample I.D.	depth (m)	Sand %	Silt %	Clay %	Inman mean	Inman sorting
2550-000-002	0.020	4.596	55.700	39.650	7.685	1.532
2550-008-010	0.090	3.945	70.570	25.500	7.142	1.371
2550-020-022	0.210	1.622	57.420	41.030	7.798	1.310
2550-040-042	0.410	0.086	50.370	49.480	8.148	1.259
2550-050-052	0.510	8.085	61.400	30.470	7.203	1.809
2550-052-054	0.530	13.396	58.350	28.240	6.563	2.343
2550-060-062	0.610	4.025	57.890	38.100	7.658	1.411
2550-070-072	0.710	4.863	50.130	44.990	7.925	1.469
2550-080-082	0.810	5.560	48.900	45.540	7.892	1.614
2550-090-092	0.910	3.956	42.200	53.730	8.142	1.535
2550-100-102	1.010	0.917	27.110	71.940	8.805	1.299
2550-106-108	1.070	7.100	58.490	34.420	7.249	1.935
2550-110-112	1.110	3.085	51.680	45.270	7.976	1.441
2550-120-122	1.210	3.389	58.020	38.560	7.700	1.431
2550-126-128	1.270	5.436	57.990	36.490	7.404	1.863
2550-140-142	1.410	0.000	43.431	56.590	8.388	1.231
2550-160-162	1.610	3.657	63.230	33.270	7.397	1.541
2550-170-172	1.710	0.011	57.570	42.340	7.869	1.426
2550-180-182	1.810	0.129	51.000	48.810	8.068	1.444
2550-198-200	1.990	3.156	53.540	43.280	7.773	1.646
2550-210-212	2.110	0.261	46.680	53.080	8.275	1.318
2550-230-232	2.310	9.977	43.710	46.330	7.520	2.476
2550-240-242	2.410	3.509	47.670	48.760	7.982	1.608
2550-250-252	2.510	8.897	39.610	51.520	7.821	2.357
2550-254-256	2.550	8.435	49.960	41.580	7.281	2.264
2550-260-262	2.610	2.674	48.710	48.630	7.940	1.618
2550-270-272	2.710	0.000	33.320	66.730	8.677	1.169
2550-280-282	2.810	2.767	38.010	59.330	8.430	1.410
2550-290-292	2.910	2.003	46.470	51.460	8.135	1.540
2550-300-302	3.010	3.879	39.940	56.240	8.346	1.441

sample I.D.	depth (m)	Sand %	Silt %	Clay %	Inman mean	Inman sorting
2553-000-002	0.010	5.005	58.050	36.800	7.540	1.766
2553-010-012	0.110	8.524	52.990	38.400	7.400	2.217
2553-014-016	0.150	0.762	41.250	58.030	8.397	1.377
2553-016-018	0.170	1.483	50.580	47.950	7.993	1.617
2553-020-022	0.210	0.010	42.700	57.240	8.416	1.453
2553-028-030	0.290	0.004	43.496	56.520	8.373	1.296
2553-030-032	0.310	7.165	49.620	43.200	7.682	2.088
2553-040-042	0.410	5.265	48.710	46.030	7.851	1.825
2553-044-046	0.450	1.002	44.870	54.130	8.256	1.470
2553-050-052	0.510	0.000	41.022	58.910	8.419	1.600
2553-060-062	0.610	1.291	44.760	53.900	8.196	1.690
2553-070-072	0.710	5.518	47.570	46.790	7.781	2.000
2553-080-082	0.810	0.298	47.500	52.140	8.075	1.759
2553-090-092	0.910	7.181	44.710	47.980	7.780	2.190
2553-100-102	1.010	0.018	43.890	56.090	8.231	1.760
2553-110-112	1.110	0.000	43.984	55.980	8.236	1.702
2553-120-122	1.210	0.020	46.130	53.780	8.116	1.799
2553-130-132	1.310	0.227	47.970	51.700	8.118	1.631
2553-140-142	1.410	0.618	45.620	53.810	8.190	1.711
2553-150-152	1.510	0.000	38.716	61.270	8.503	1.584
2553-160-162	1.610	0.006	38.940	61.040	8.500	1.518
2553-170-172	1.710	0.331	46.830	52.900	8.141	1.672
2553-180-182	1.810	0.795	47.120	52.050	8.074	1.761
2553-182-184	1.830	0.000	35.680	64.410	8.618	1.237
2553-190-192	1.910	0.000	32.950	67.000	8.694	1.335
2553-198-200	1.990	0.001	34.730	65.170	8.635	1.374
2553-200-202	2.010	0.000	23.670	76.350	8.997	1.191
2553-210-212	2.110	3.664	43.260	53.090	8.123	1.788
2553-220-222	2.210	3.840	42.600	53.560	8.060	1.924
2553-230-232	2.310	4.664	42.860	52.430	8.052	1.890
2553-240-242	2.410	0.282	43.930	55.960	8.250	1.636
2553-250-252	2.510	8.316	40.220	51.430	7.814	2.373
2553-260-262	2.610	6.215	42.430	51.280	7.907	2.056
2553-270-272	2.710	0.015	42.480	57.620	8.275	1.751
2553-280-282	2.810	2.453	38.060	59.480	8.371	1.751
2553-290-292	2.910	1.399	43.890	54.630	8.183	1.740
2553-300-302	3.010	0.429	41.690	57.980	8.360	1.643

Chapter 14

Methane-Derived Authigenic Carbonates from the IMAGES VIII/PAGE 127 Gas Hydrate and Paleoclimate Cruise on the RV *Marion Dufresne* in the Gulf of Mexico, 2–18 July 2002

Yifeng Chen[1, 2], Ryo Matsumoto[1], and William Ussler III[3]

Methane-derived authigenic carbonates from the IMAGES VIII/PAGE 127 gas hydrate and paleoclimate cruise on the RV Marion Dufresne *in the Gulf of Mexico, 2–18 July 2002; chapter 14* in *Winters, W.J., Lorenson, T.D., and Paull, C.K., eds., 2007, Initial report of the IMAGES VIII/PAGE 127 gas hydrate and paleoclimate cruise on the RV* Marion Dufresne *in the Gulf of Mexico, 2–18 July 2002: U.S. Geological Survey Open-File Report 2004–1358.*

Abstract

Authigenic carbonates were sampled in piston cores collected from the Tunica Mound and the Mississippi Canyon areas on the continental slope of the northern Gulf of Mexico during a cruise conducted on the RV *Marion Dufresne* in July 2002. Carbonates are present as hardgrounds, porous crusts, concretions or nodules, and shell fragments with or without carbonate cements. The carbonate samples recovered during the cruise occurred at gas-venting sites, which likely overlie gas hydrate-bearing sediments. Electron microprobe, X-ray diffraction (XRD), and thin-section investigations indicate that these carbonates are high magnesium calcite (6–21 mole (mol %) $MgCO_3$), with a significant presence of framboidal pyrite. All carbonates are depleted in ^{13}C ($\delta^{13}C$ = –61.9 to –31.5 parts per thousand (‰) Peedee Belemnite (PDB)), indicating that the carbon is derived mainly from anaerobic methane oxidation (AMO). Age estimates based on ^{14}C dating of shell fragments and on regional sedimentation rates indicate that these authigenic carbonates formed within the last 1,000 years in the Mississippi Canyon region and within the last 5,500 years at Tunica Mound. The oxygen isotopic composition of carbonates ranges from +3.4 to +5.9‰ PDB. Oxygen isotopic compositions and Mg^{2+} contents of the carbonates, in conjunction with current in situ temperatures of bottom seawater and sediment, indicate that some of these carbonates (especially from cores associated with underlying massive gas hydrates) precipitated in or near equilibrium with present bottom-water conditions. On the other hand, those carbonates more enriched in ^{18}O are interpreted to have precipitated from ^{18}O-rich fluids, which are thought to have been derived from dissociation of gas hydrates. The dissociation of gas hydrates in the northern Gulf of Mexico within the last 5,500 years may be caused by nearby salt movement and related brines.

Introduction

The co-occurrence of authigenic carbonates and gas venting has been documented at many gas hydrate sites (for example, the Blake Ridge (Naehr and others, 2000); the Cascadia Margin (Bohrmann and others, 1998); the Gulf of Mexico (Sassen and others, 2004)). In these areas, the carbon in the carbonates was mainly derived from methane. Thus, carbonate precipitation may be related to the decomposition of gas hydrates.

Determining the age of authigenic carbonate is difficult. Some researchers hypothesize that gas hydrate-related authigenic carbonates formed during the last glacial maximum (LGM) (Bohrmann and others, 1998; Aloisi and others, 2000). This interpretation, however, assumes that the lowered sea level during the Pleistocene epoch reduced pressure on the ocean margins and triggered gas hydrate dissociation.

Because ^{14}C datable shell fragments were mixed with some sampled authigenic carbonates in the northern Gulf of Mexico (GOM), some chronological control is available that

[1] University of Tokyo, 7-3-1 Hongo, Bunkyo-ku, Tokyo 113-0033, JAPAN.

[2] Nanjing Institute of Geography and Limnology, Chinese Academy of Sciences, 73 East Beijing Road, Nanjing 210008, CHINA.

[3] Monterey Bay Aquarium Research Institute, 7700 Sandholdt Road, Moss Landing, CA 95039 USA.

helps constrain the time of formation of these authigenic carbonates. High-resolution seismic profiles across the core sites and regionally well-known sedimentation rates (Coleman and others, 1983; Rowan and Weimer, 1998) also help constrain the time of carbonate formation.

Geochemical data are presented for carbonates recovered from piston cores obtained from the northern Gulf of Mexico (fig. 1). Core information, including water depths and locations, is presented in Appendix A. The data document variations in the carbon and oxygen isotopes, chemical compositions, mineralogy, and the timing of the carbonate precipitation. The carbon isotopic values suggest carbonate carbon is derived from anaerobic oxidation of methane. The variations in oxygen isotopes together with other geochemical proxies provide evidence for the relations between authigenic carbonate and gas hydrates.

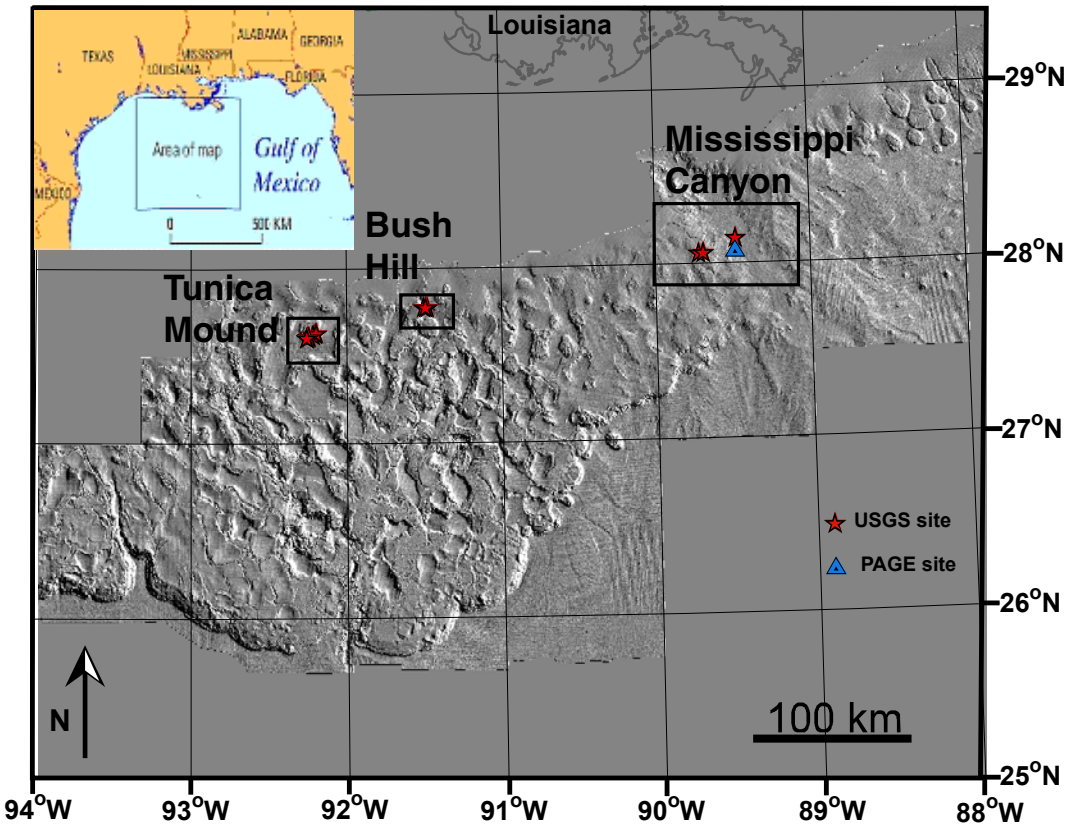

Figure 1. Coring locations of carbonates and pore water in the northern Gulf of Mexico during the July 2002 RV *Marion Dufresne* Cruise (MD-02). Carbonates were recovered from two areas—the Tunica Mound and the Mississippi Canyon.

Geological Background and Sampling

The northern Gulf of Mexico is a passive continental margin characterized by more than 10 kilometers (km) of sediments of Mesozoic-Cenozoic age, which are well-suited for the generation and accumulation of large oil and gas reservoirs. The extensive salt deposits and salt thrusts within this margin provide an excellent environment for both hydrocarbon accumulation and migration (Sassen and others, 1994). During the Late Triassic period, rifting of the Gulf of Mexico led to the formation of many subbasins; these basins were then floored by thick salt (Louanne/Werner formations) during Middle Jurassic marine incursions (Salvador, 1987) and formed the main structural features of the northern Gulf of Mexico. Since the Cenozoic era, the long history of ongoing salt diapirism has resulted in structural deformation, faulting, fracturing, and sediment slumping, all of which provide conduits for upward seepage of gaseous and liquid hydrocarbons. Authigenic carbonate minerals and gas hydrates on the sea floor and within sediments are the cumulative products of these extensive hydrocarbon seeps (for example, Brooks and others, 1984; Roberts and Aharon, 1994). Authigenic carbonates are so pervasive in the northern GOM that carbonate mounds and hydrate-related hills may exceed a kilometer in diameter (Neurauter and Roberts, 1992). These authigenic carbonates may cap gas hydrate-bearing strata and provide a temporal record of hydrocarbon seeps.

During July 2002, the research vessel (RV) *Marion Dufresne* was used to investigate the occurrence and distribution of gas hydrate in the shallow subsurface of the northern Gulf of Mexico (fig. 1). A giant Calypso piston corer was used to obtain sediment samples up to 38 meters (m) in length (Winters and others, this volume, chapter 3). Authigenic carbonates were recovered between 0 and 27 meters below the sea floor (mbsf) in sediments from several different geological environments: (1) on or near sea-floor sediments on the crest of a salt diapir at Tunica Mound (cores MD02-2543G, 2544G, 2545G), (2) in shallow subbottom sediment over a gas chimney (MD02-2570, 2571C2) west of the Mississippi Canyon, (3) near a salt diapir at Tunica Mound (MD02-2546), and (4) in sediment associated with gas hydrates (MD02-2569 and MD02-2573GHF) on the floor of the Mississippi Canyon (figs. 2–3). Prior to this cruise, carbonate samples typically were recovered in the Gulf of Mexico only from near-surface

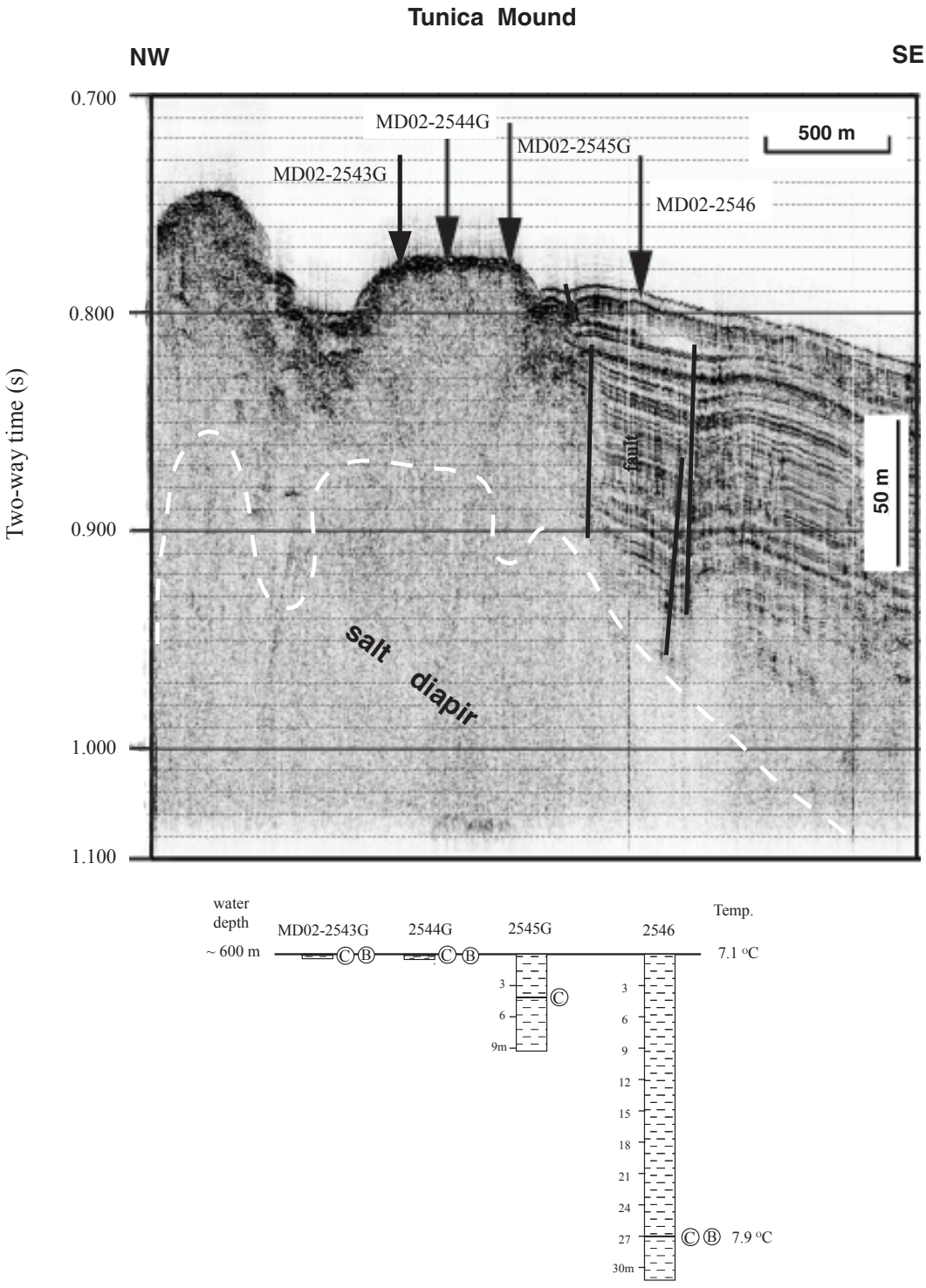

Figure 2. Upper: Seismic profile oriented northwest–southeast across the Tunica Mound sea-floor area of Garden Bank Block 386 on the upper continental slope. Locations of cores containing carbonates are indicated with arrows. Note the underlying salt diapir and the well-defined faults, which function as conduits for gas and fluids to migrate to the sea floor. This has created a variety of vent-related features. Lower: Graphic logs showing the lithology and distribution of carbonates in cores (C = carbonate nodules/crusts/hardgrounds; B = bivalves shell fragments).

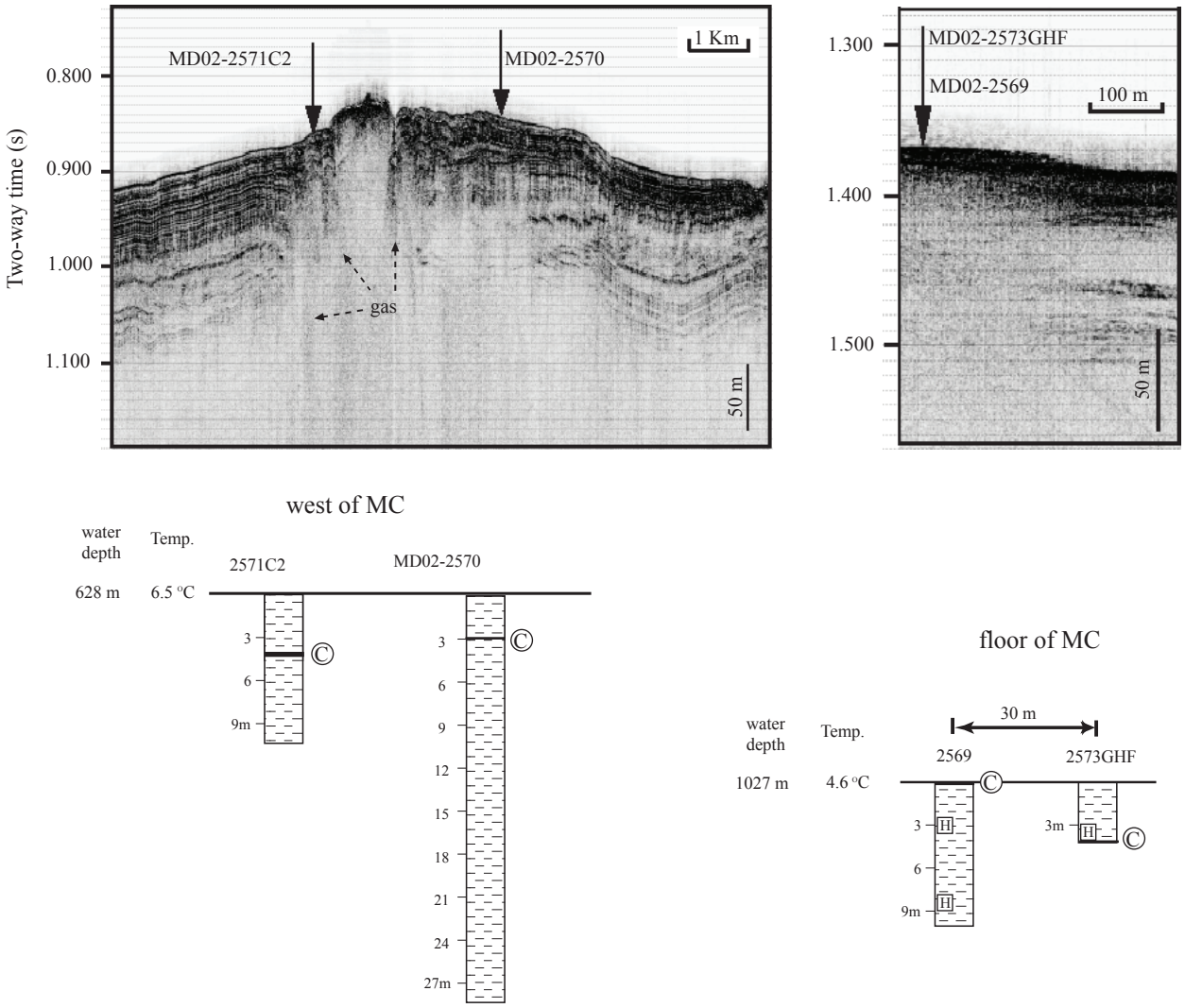

Figure 3. Upper: Seismic profile oriented northwest–southeast across a site west of the Mississippi Canyon (MC) and in the central MC sea-floor area. Locations of cores containing carbonates are indicated with arrows. Lower: Graphic logs showing lithology and distribution of carbonates in cores (C = carbonate nodules/crusts/hardgrounds; H = gas hydrates).

sediment by using submersibles (Roberts and Aharon, 1994; Aharon and others, 1997).

Methods

The carbonates (number of samples (n) = 25) in hand samples were petrographically and geochemically examined. Bulk mineralogy (n = 35) was determined on pressed powder mounts by using a Mac Science MXP3 Powder X-ray Diffractometer (XRD) at the University of Tokyo. The XRD patterns were obtained from 0º to 40º 2θ at a scanning speed of 2º 2θ/min. The weight percentages of minerals were estimated using the peak weights (Müller, 1967) with an estimated error of ±5%. Carbon-coated, polished thin sections were made from selected authigenic carbonates and examined by electron microprobe analyses by using a JEOL Superprobe 733 – II to provide detailed chemical compositions of calcite. In addition, concentrations of Ca, Mg, Mn, Fe, Sr, and Ba were determined. The analytical precision is 1% for Ca, 2% for Mg, 4% for Mn and Fe, and 9% for Sr and Ba.

Oxygen and carbon isotope compositions (n = 34) were measured on the same set of samples by XRD. Carbon dioxide gas was produced by reaction with 100-% phosphoric acid at 25 ºC for 24 hours, and the purified CO_2 gas was analyzed using a Finnigan MAT 252 Mass Spectrometer at the University of Tokyo. The isotopic compositions are given relative to the Peedee Belemnite (PDB) reference, with a precision of ±0.2‰ for both $\delta^{13}C$ and $\delta^{18}O$ values.

Pore waters for stable oxygen isotope analyses were collected by squeezing 10-centimeter (cm) long, whole-round core sections at about 3-m intervals (Ussler and Paull, this

volume, chapter 8). Oxygen isotopic compositions of 155 pore-water samples were determined using the H_2O–CO_2 equilibration method (Epstein and Mayeda, 1953). The resulting CO_2 was purified and collected by cryogenic transfer. Stable oxygen isotope ratios of CO_2 also were measured on a Finnigan MAT 252 mass spectrometer at the University of Tokyo. Oxygen isotope measurements on the pore waters are reported in standard delta notation (δ) with respect to Standard Mean Ocean Water (SMOW). The cumulative (vacuum line and mass spectrometer) accuracy and precision of oxygen isotopic measurements are ±0.2‰ and ±0.06‰, respectively.

The ^{14}C measurements were made on shell fragments with and without carbonate cements (n = 2) in core MD02-2543G. To remove contaminants, each shell fragment was carefully stripped of adhering sediments under a microscope, repeatedly placed into deionized water in an ultrasonic bath, and leached using l molar (M) HCl. The washing was finished with a final rinsing with deionized water, and the sample was dried in a desiccator in a vacuum line. Under vacuum, the shell was reacted with phosphoric acid, and the evolved CO_2 was reduced to obtain graphite targets prepared following the method described by Miyairi and others (2004). The ^{14}C concentration was measured using accelerator mass spectrometry (AMS) in a Pelletron 5UD Tandem accelerator at the Research Center for Nuclear Science and Technology, University of Tokyo. The analytical precision was ±0.5%. The age was calculated as years before present (BP, years from A.D. 1950), and errors are expressed as ± 1 standard deviation (σ).

Results

Occurrence of Authigenic Carbonates

Authigenic carbonates were collected at the Tunica Mound in cores MD02-2543G, 2544G, 2545G, and 2546 with water depths ranging between 579 and 595 m. The geothermal gradient at these sites was 29 degrees Celsius per kilometer (°C/km), with a bottom-water temperature of 7.1 ºC at these sites (Labails, this volume, chapter 6). Seismic profiles of this site (fig. 2) show that Tunica Mound is underlain by a large salt diapir. The authigenic carbonates were found at the top of core MD02-2543G and occurred as broken pieces of hardgrounds, with or without carbonate-cemented shell fragments being present (fig. 3). Carbonates recovered from core MD02-2544G consisted of porous crusts with noncemented shell fragments (fig. 4) on the sea floor. One large, hard and irregularly shaped concretion was obtained at 4.25 mbsf in core MD02-2545G (fig. 4). A semi-consolidated concretion, with a small cemented shell fragment was at ~27 mbsf in core MD02-2546. This was the deepest concretion recovered during the cruise (fig. 4). No gas hydrates were found or inferred to have existed in any of the cores collected at the Tunica Mound (Paull and others, 2005); however, this area is characterized with gas venting.

Authigenic carbonates also were recovered from two cores (MD02-2569 and 2573GHF) on the floor of the Mississippi Canyon in a gas hydrate area at water depths of 1,032 and 1,027 m, respectively, and bottom-water temperature of 4.6 ºC (fig. 3). Both cores were observed to contain gas hydrates. Carbonates in MD02-2569 occurred as irregular hard nodules in sediments just below the sea floor, underlain by two layers of massive gas hydrates (fig. 3). One layer occurred at ~3 mbsf, as a chunk of gas hydrate filling the entire 10-cm diameter core liner (fig. 5). Carbonates in core MD02-2573GHF were found coexisting with small pieces of gas hydrate, distributed as porous concretions in irregular shapes (fig. 5).

The authigenic carbonates recovered in cores MD02-2570 and 2571C2 are near a gas chimney west of the Mississippi Canyon (fig. 3) in 631 and 664 m of water. Bottom-water temperature is 6.5 ºC, and a geothermal gradient of 36 °C/km (Labails and others, this volume, chapter 6) is present in the area. In core MD02-2570, round semi-consolidated carbonate nodules were obtained at ~3 mbsf; whereas, the carbonates in core MD02-2571C2 were ~35 cm thick and occurred as semi-consolidated nodules and slabs. One ~2-cm-thick carbonate slab has a round hole of ~0.5 cm in diameter, which may be a conduit for gas venting (fig. 5).

In summary, most of the authigenic carbonate samples occurred on the sea floor or in shallow sediments (that is, ≤5 mbsf) surrounding gas vents, except for one sample obtained at ~27 mbsf in core MD02-2546.

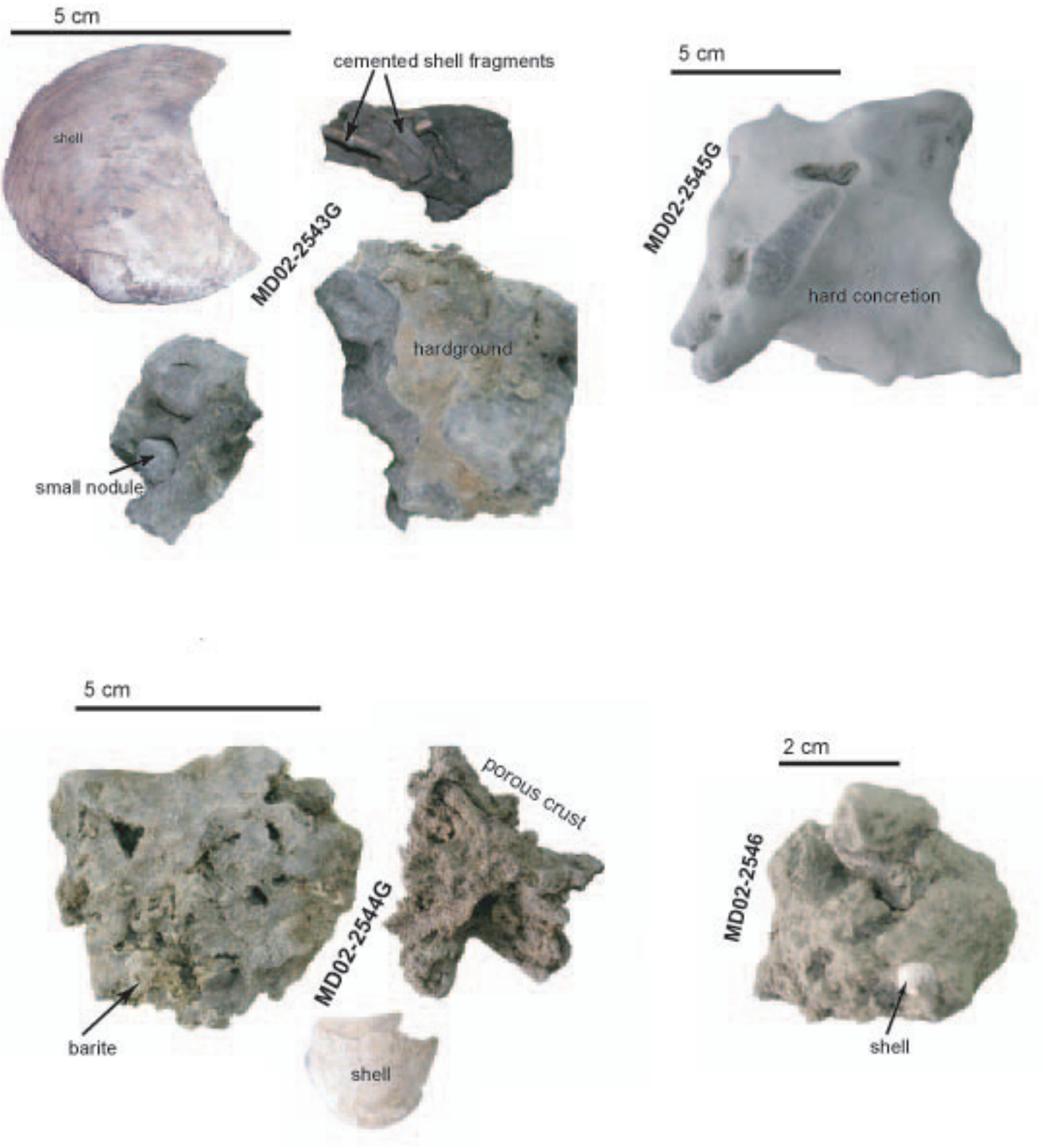

Figure 4. Specimens of carbonates in piston cores from the Tunica Mound in the northern Gulf of Mexico.

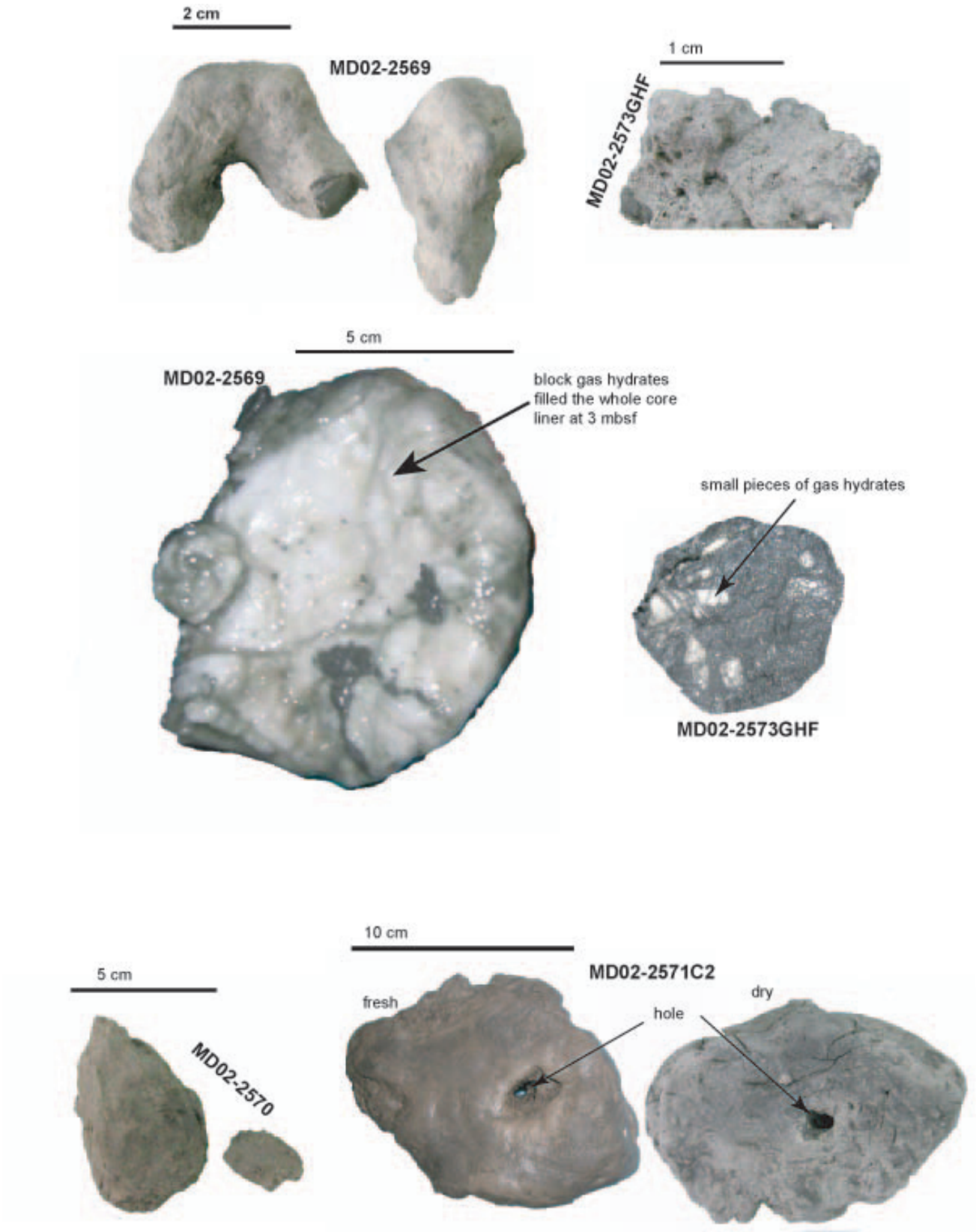

Figure 5. Specimens of carbonates from piston cores from the Mississippi Canyon in the northern Gulf of Mexico. A sample from core MD02-2571C2 has a hole that is probably a gas conduit for the upward migration of methane. Specimens of gas hydrates were recovered in cores MD02-2569 and 2573 (photographs provided by W. Winters and T. Lorenson, respectively).

Petrography and Mineralogy

Observations of thin sections showed that the predominant micritic authigenic carbonates were developed within fine-grained clastic sediments. Silt-sized quartz grains, foraminifera (mostly planktonic), bivalve shell fragments, and framboidal pyrites were noted as well as numerous cavities. The cavities were cemented with micritic carbonates, organic matter, and some framboidal pyrites. Barite was identified (≤5%) in only one sample (MD02-2544G) (fig. 6).

Thirty-one authigenic carbonates and one bivalve shell were analyzed by XRD. The samples are composed primarily of calcite and quartz with subordinate amounts of dolomites and pyrites. Calcite content ranges from 41 weight percent (wt%) to 94 wt%, with a mean of 73 wt%. Differences in mineralogy by area are not obvious among crust, hardground and nodules.

The position of the major diffraction peak *d*(104) of calcite varies between 2.978 and 3.014 angstroms (Å; fig. 7). The shift of *d*(104) values away from that of stoichiometric calcite (3.035 Å) is caused by substitution of Mg^{2+} for Ca^{2+}, as well as by other divalent ions. Most calcites centered around 2.998 Å, indicating a $MgCO_3$ content of approximately 12 molar percent (mol%) based on the standard calibration curves from Müller (1967). However, two extreme values of calcite *d*(104) were measured, which indicate that $MgCO_3$ content in the calcite ranges from 6 mol% to 20 mol%.

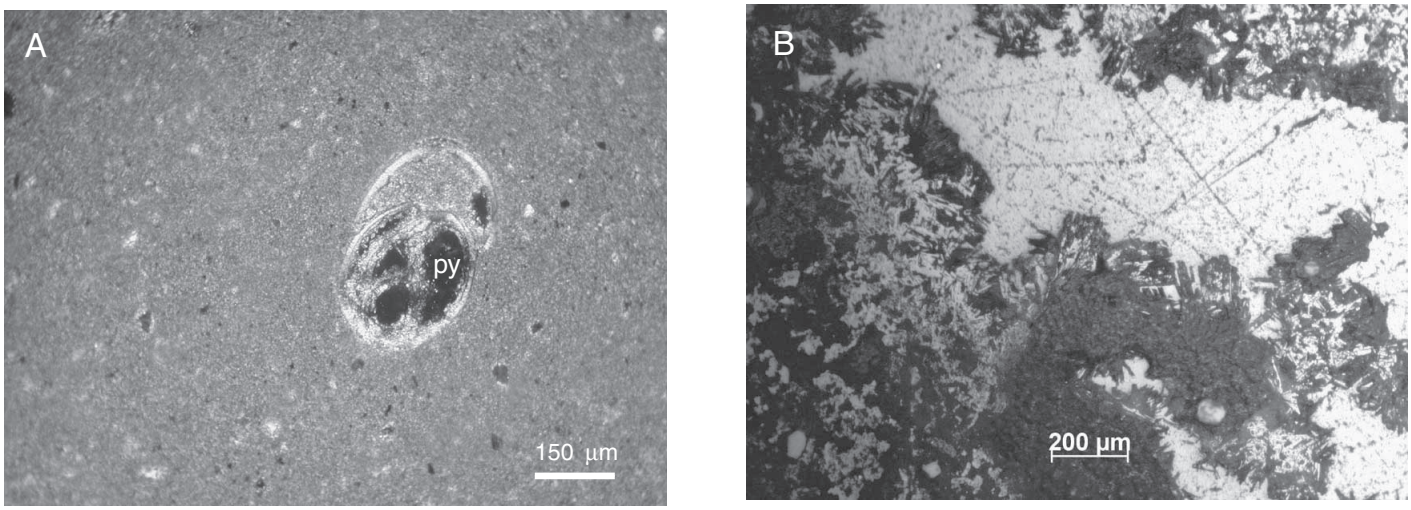

Figure 6. Thin-section photomicrographs of carbonates. (A) Micritic carbonates developed within silt-sized quartz grains (shining spots), framboidal pyrite (py) formed inside the cavities of formas (polarized light, sample MD02-2543G hardground). (B) Bladed crystals of barite developed within the cavities around micritic calcites (polarized light, sample MD02-2544G porous nodule).

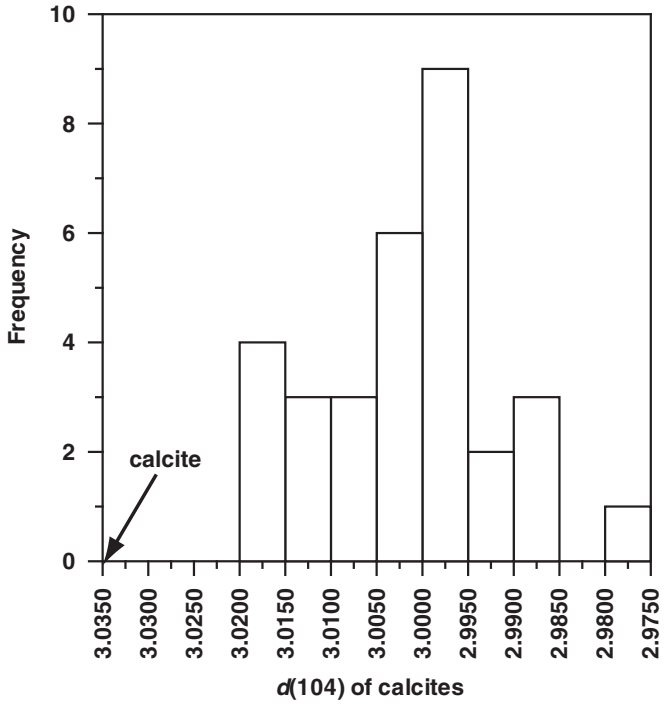

Figure 7. Distribution of *d*(104) values for calcite of 31 authigenic carbonates.

Geochemistry

Chemical Compositions of Calcite

Seventeen authigenic carbonate samples were measured by electron microprobe. The data indicate that all carbonates are high magnesium calcite, with 6 to 21 mol% Mg^{2+} (table 1), which are consistent with the shifts of *d*(104) determined by XRD analysis. These carbonates also contain minor amounts of FeO and MnO (table 1), which indicate carbonates have precipitated in reducing environments.

Stable Carbon and Oxygen Isotopic Compositions of Carbonates

Stable isotopes of carbon and oxygen were measured on 23 bulk authigenic carbonate samples and on 11 micro drilled samples from carbonate nodules in cores MD02-2545G, MD02-2569, and MD02-2571C2 A20-25cm (table 2). Except for a shell fragment ($\delta^{13}C_c$ = –3.1‰), all the carbonates are extremely depleted in ^{13}C, with $\delta^{13}C_c$ values ranging from –35.8 to –61.9‰. The oxygen isotopes of carbonates ($\delta^{18}O_c$) range from +3.4 to +5.9‰ (table 2; fig. 8).

Table 1. Chemical compositions of calcite in authigenic carbonates analyzed by electron microprobe analysis.

Core no.	Molar percent					Point no.	Sample no.
	Cacium	Magnesium	Iron	Manganese	Strontium		
MD02-2543G	89.3 (42.7–100)	10.0 (0.0–55.2)	0.6 (0.0–17.9)	0.0 (0.0–3.4)	0.1 (0.0–2.1)	840	5
MD02-2544G	93.6 (79.9–100)	6.1 (0.0–19.6)	0.2 (0.0–11.3)	0.0 (0.0–0.3)	0.0 (0.0–0.5)	521	3
MD02-2545G	89.6 (52.6–100)	9.5 (0.0–46.8)	0.9 (0.0–7.7)	0.0 (0.0–0.3)	0.0 (0.0–0.3)	74	1
MD02-2546	77.6 (71.0–84.7)	21.3 (15.3–25.3)	1.1 (0.0–4.5)	0.0 (0.0–0.0)	0.0 (0.0–0.0)	47	1
MD02-2569	83.0 (50.2–100)	16.6 (0.0–49.3)	0.3 (0.0–0.6)	0.0 (0.0–0.6)	0.0 (0.0–0.4)	179	2
MD02-2573GHF	83.5 (54.2–99.2)	15.8 (0.8–45.6)	0.6 (0.0–4.7)	0.0 (0.0–0.4)	0.1 (0.0–0.3)	50	1
MD02-2570	80.9 (51.7–100)	18.2 (0.0–48.1)	0.8 (0.0–2.4)	0.0 (0.0–0.5)	0.0 (0.0–0.3)	193	3
MD02-2571C2	83.7 (50.6–100)	15.3 (0.0–49.4)	1.0 (0.0–6.0)	0.1 (0.0–1.5)	0.0 (0.0–0.4)	123	1

Note: Data shown in average (range); point no., number of points; sample no., number of thin sections.

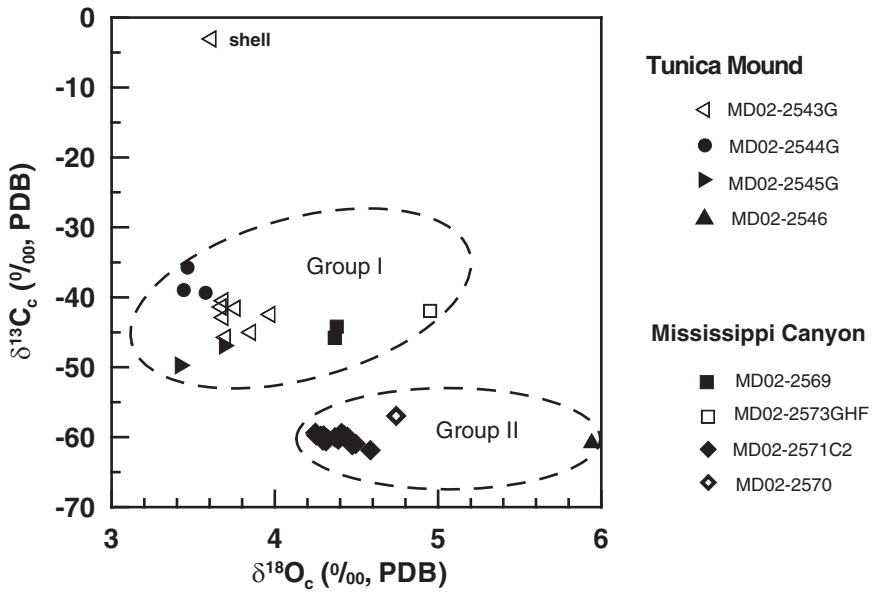

Figure 8. Carbon and oxygen isotopic compositions of carbonates.

Table 2. Geological setting and results of isotopic and Mg^{2+} contents of carbonates, $\delta^{18}O$ values of interstitial water sampled from the upper 6 meters of sediment cores, and calculated carbonate precipitated water oxygen isotopes.

[m, meters; mbsf, meters below sea floor; $\delta^{13}C_c$, the stable carbon isotope of carbonate; PDB, Peedee Belemnite; $\delta^{18}O_c$, the stable oxygen isotope of carbonate; Mg, magnesium; mol%, molar percent; Bottom water temperature, measured bottom water temperature (Labails and others, 2007); °C, degrees Celsius; Temperature, assumed carbonate precipitated temperature; $\delta^{18}C_{w(cal)}$, calculated carbonate precipitated water oxygen isotope; SMOW, standard mean ocean water]

Core no.	Water depth (m)	Depth (mbsf)	Location structure	$\delta^{13}C_c$ (PDB)	$\delta^{18}O_c$ (PDB)	Mg (mol%)	Bottom water temperature (°C)	Temperature (°C)	$\delta^{18}O_{w(cal)}$ (SMOW)
Tunica Mound									
MD02-2543G C.C. TOP hardground	579	0.03	over salt diapir	–42.9	3.7	11	7.1	7.1	1.0
MD02-2543G C.C. TOP porous crust	579	0.03	over salt diapir	–42.5	4.0				
MD02-2543G C.C. TOP small nodule	579	0.03	over salt diapir	–45.7	3.7				
MD02-2543G C.C. TOP hardground with the small nodule	579	0.03	over salt diapir	–40.5	3.7				
MD-02-2543G C.C. TOP shell cements	579	0.03	over salt diapir	–41.4	3.7	9	7.1	7.1	1.1
MD02-2543G C.C. TOP shell	579	0.03	over salt diapir	–3.1	3.6	0	7.1	7.1	0.7
MD02-2543G C.C. A	579	0.15	over salt diapir	–45.0	3.8				
MD02-2543G C.C. C	579	0.15	over salt diapir	–41.6	3.7	10	7.1	7.1	1.1
MD02-2544G C.C. A	584	0.1	over salt diapir	–39.0	3.4	7	7.1	7.1	0.9
MD02-2544G C.C. A porous crust	584	0.1	over salt diapir	–39.4	3.6				
MD02-2544G C. C. B	584	0.1	over salt diapir	–35.8	3.5	6	7.1	7.1	1.0
MD02-2545 inner rim	588	4.23	over salt diapir	–49.7	3.4				
MD02-2545 outer rim	588	4.23	over salt diapir	–46.9	3.7				
MD02-2545	588	4.23	over salt diapir	–48.3	3.6	10	7.1	7.1	1.0
MD02-2546	595	26.95	near salt diapir	–60.8	5.9	21	7.1	7.1	2.5
MD02-2546	595	26.95	near salt diapir	–60.8	5.9	21	7.1	7.9	2.7
Mississippi Canyon									
MD02-2569 inner rim	1,032	0.03	over salt diapir	–45.8	4.4				
MD02-2569 outer rim	1,032	0.03	over salt diapir	–44.2	4.4				
MD02-2569	1,032	0.03	over salt diapir	–45.0	4.4	17	4.6	4.6	0.7
MD02-2573 GHF	1,027	4.2	over salt diapir	–41.9	5.0	16	4.6	4.6	1.3
MD02-2570	631	2.95	gas chimney	–57.0	4.7	18	6.5	6.5	1.4
MD02-2571C2 A 0–5 cm	664	4.28	gas chimney	–61.1	4.5				
MD02-2571C2 A 5–10 cm	664	4.34	gas chimney	–60.0	4.4				
MD02-2571C2 A ~10 cm	664	4.37	gas chimney	–59.7	4.4				
MD02-2571C2 440 cm	664	4.4	gas chimney	–61.9	4.6				
MD02-2571C2 A 10–15 cm	664	4.4	gas chimney	–59.4	4.4				

Table 2. Geological setting and results of isotopic and Mg^{2+} contents of carbonates, $\delta^{18}O$ values of interstitial water sampled from the upper 6 meters of sediment cores, and calculated carbonate precipitated water oxygen isotopes. — Continued

[m, meters; mbsf, meters below sea floor; $\delta^{13}C_c$, the stable carbon isotope of carbonate; PDB, Peedee Belemnite; $\delta^{18}O_c$, the stable oxygen isotope of carbonate; Mg, magnesium; mol%, molar percent; Bottom water temperature, measured bottom water temperature (Labails and others, 2007); °C, degrees Celsius; Temperature, assumed carbonate precipitated temperature; $\delta^{18}C_{w(cal)}$, calculated carbonate precipitated water oxygen isotope; SMOW, standard mean ocean water]

Core no.	Water depth (m)	Depth (mbsf)	Location structure	$\delta^{13}C_c$ (PDB)	$\delta^{18}O_c$ (PDB)	Mg (mol%)	Bottom water temperature (°C)	Temperature (°C)	$\delta^{18}O_{w(cal)}$ (SMOW)
MD02-2571C2 A 15–20 cm	664	4.46	gas chimney	–59.9	4.4	15	6.5	6.5	1.3
MD02-2571C2 A 20–25 cm #1	664	4.52	gas chimney	–60.4	4.4				
MD02-2571C2 A 20–25 cm #2	664	4.52	gas chimney						
MD02-2571C2 A 20–25 cm #3	664	4.52	gas chimney	–60.5	4.3				
MD02-2571C2 A 20–25 cm #4	664	4.52	gas chimney	–59.8	4.3				
MD02-2571C2 A 20–25 cm #5	664	4.52	gas chimney	–60.6	4.3				
MD02-2571C2 A 20–25 cm #6	664	4.52	gas chimney	–59.7	4.3				
MD02-2571C2 A 20–25 cm #7	664	4.52	gas chimney	–59.8	4.3				
MD02-2571C2 A 20–25 cm #8	664	4.52	gas chimney	–61.0	4.5				
MD02-2571C2 A 25–30 cm	664	4.58	gas chimney	–59.4	4.2				

Stable Oxygen Isotopic Compositions of Interstitial Water

Because all sampled carbonates occurred within the upper 5 m of sediment (except for core MD02-2546), the stable oxygen isotopic values of interstitial water ($\delta^{18}O_{IW}$) from the upper 6 m of sediment were accounted for in this study. These $\delta^{18}O_{IW}$ values remain almost constant with depth for the upper 6 m in each core, and most of the values (n = 30 of 34) range from +0.7‰ to +1.0‰, with a mean of +0.8‰. Thus, we can regard these $\delta^{18}O_{IW}$ values as reflecting the regional bottom seawater oxygen isotope ($\delta^{18}O_{sw}$), except for four samples in core MD02-2543G, which have values ranging from –0.6‰ to –0.4‰. These four samples may be out of place because they came from the upper 0.15 m of a core with a bent barrel. The negative $\delta^{18}O_{IW}$ values may have been caused by diagenetic reactions at low temperatures with the underlying patchy tephra in the core. Because the carbonates in core MD02-2543G were just below the sea floor, we will assume $\delta^{18}O_{IW}$ values of these carbonates are the same as the regional $\delta^{18}O_{sw}$.

There was no interstitial water available for $\delta^{18}O$ analysis in cores MD02-2544G, 2573GHF, and 2571C2 because of the lack of sediment recovery. The carbonates in these cores occurred within 5 mbsf, thus we assume that $\delta^{18}O_{IW}$ values of the host sediment are the same as the regional $\delta^{18}O_{sw}$ values. The $\delta^{18}O_{IW}$ value of the pore water sampled from the same horizon that contained the carbonates at ~27 mbsf in core MD02-2546 is +1.3‰.

^{14}C Ages of Shells

Results of ^{14}C analyses show that a shell and carbonate-cemented shell in core MD02-2543G have $\Delta^{14}C = –361.1 \pm 4.7‰$ ($\delta^{13}C = –3.1‰$), and $\Delta^{14}C = –499.5 \pm 5.0‰$, respectively. Based on the conventional ^{14}C age calculation (Stuiver and Polach, 1977), these two shells may have ages of 3,600 ± 60 years BP and 5,560 ± 80 years BP, respectively.

Discussion

Carbon Isotopic Variations of Carbonates

The sources of carbon in the pore fluids in the Gulf of Mexico include: (1) methane ($\delta^{13}C = –120$ to $–30‰$), (2) oil fractions ($\delta^{13}C = –25$ to $–28‰$) (Aharon and others, 1997), (3) sedimentary organic matter ($\delta^{13}C = –25‰$ on average), (4) marine biogenic carbonate ($\delta^{13}C = ~0‰$), and (5) seawater CO_3^{2-} with a $\delta^{13}C$ value of $\delta^{13}C = 0 \pm 3‰$ (Anderson and Arthur, 1983).

In order to identify the carbon source and the carbonate-forming mechanism for the authigenic carbonates, carbon isotope analyses were carried out on the same subsamples, which also were analyzed mineralogically. Because carbonate carbon isotope values (from –35.8 to –61.9‰) are lower than those found in any known carbon source other than methane, this is an indication that methane is the major carbon source of the carbonates. Supporting this conclusion is the occurrence of framboidal pyrite in these carbonates, which requires

anoxic conditions to form. Thus, these carbonates probably were formed near conditions of anaerobic methane oxidation (AMO) by sulfate reduction. One of the effects of AMO is to generate HCO_3^- and to increase the alkalinity of the pore fluids, which contributes to the precipitation of authigenic carbonates. Moreover, the addition of methane carbon to the pore fluid dissolved inorganic carbon (DIC) pool, which decreases the $\delta^{13}C$ value of the DIC, may result in authigenic carbonates with low $\delta^{13}C$ values (Paull and others, 1992; Greinert and others, 2001). In contrast, the carbon isotope values of the shells are much higher (–3.1‰), suggesting that the carbon came mainly from seawater bicarbonate.

Two general mechanisms generate methane in the marine environment: microbial methane formed by CO_2-reduction and thermogenic-methane generated during organic matter maturation (Bernard and others, 1978; Whiticar, 1999). The $\delta^{13}C$ values of microbial methane typically are <-60‰. Conversely, thermogenic methane with the $\delta^{13}C$ values typically are >-50‰ (Bernard and others, 1978).

According to the $\delta^{13}C_c$ values of –35.8 to –61.9‰, carbonates can be classified into two groups: Group I ($\delta^{13}C_c$ = –35.8 to –49.7‰) and Group II ($\delta^{13}C_c$ = –59.4 to –61.9‰) (fig. 8). Group I carbonates were found in Tunica Mound cores MD02-2543G, 2544G, and 2545G but not in core MD02-2546, and in both cores (MD02-2569 and 2573GHF) containing gas hydrates from the floor of the Mississippi Canyon. At Tunica Mound, carbonate $\delta^{13}C_c$ values range from –35.8 to –49.7‰ with a mean of –42.6‰. At the floor of the Mississippi Canyon, the carbonate $\delta^{13}C_c$ values are in a tight range of –41.9 to –45.8‰ with a mean of –44.0‰. Group II carbonates were recognized in both cores (MD02-2570 and 2571C2) near a gas chimney west of the Mississippi Canyon and a core (MD02-2546) on the flank of Tunica Mound. The carbonate $\delta^{13}C$ values range from –59.4 to –61.9‰, with an average of –60.3‰.

The distinction in the carbon isotopic values in groups I (–35.8 to –49.7‰) and II (–59.4 to –61.9‰) may reflect the variation in the source of the methane carbon, particularly if the carbon comes from thermogenic or microbial sources. The group II values clearly indicate that microbial methane carbon dominates in the DIC pool from which the carbonates precipitated. However, the group I carbonates may be coming from either primarily thermogenic methane sources or may indicate more dilution of the DIC pool with carbon from other sources; for example, microbial methane carbon diluted by seawater DIC, or a mixture of microbial and thermogenic methane carbon. Localized conduits, for example faults and fractures, caused by salt movement from the migration of thermogenic hydrocarbons from great depth in the sedimentary section to the sea floor are common in the Gulf of Mexico (fig. 2, for example).

Ages of Carbonates

The age of the authigenic carbonates can be estimated from known regional sedimentation rates and(or) ^{14}C measurements of associated shells.

Tunica Mound: Carbonates at Tunica Mound are from Garden Banks Block 386 (GB 386), and in this area the sedimentation rate is 7 to 11 meters per thousand years (m/k.y.) for the upper sedimentary section (Rowan and Weimer, 1998; Cooper and Hart, 2003). The carbonates in core MD02-2546 occurred at about 27 mbsf in the stratified sediments inferred from the seismic profile (fig. 2). If constant sedimentation rates are assumed, this suggests the nodule is only 4,000 years old.

Carbonates recovered from cores MD02-2543G, 2544G, and 2545G occurred on the top of Tunica Mound. Because erosion is occurring here, the sedimentation rates cannot be used to determine the sediment ages. Fortunately, shell fragments were also recovered together with these carbonates (fig. 3). The ^{14}C measurements of the shell and carbonate-cemented shell in core MD02-2543G yielded ages of 3,600 ± 60 yearsr BP and 5,560 ± 80 years BP, respectively. These calculated ages suggest the carbonate-cemented shell is about 2,000 years older than the shell without cements. Because the top of Tunica Mound is believed to be eroding, shells of different ages may be in close proximity. Moreover, the apparently older carbonate-cemented shell may have survived longer because it was protected from erosion due to the carbonate-cemented cover. Authigenic carbonates from other cores (MD02-2544G and 2545G) are very near the location of MD02-2543G (on top of Tunica Mound). Thus, they are likely to be of similar ages (younger than 5,500 years).

Mississippi Canyon: The authigenic carbonates in the Mississippi Canyon occurred from the sea floor to 4.6 mbsf in stratified sediments interpreted from seismic profiles (fig. 2); therefore, we can use the known sedimentation rates to constrain the ages of the authigenic carbonates in these sediments. The average sedimentation rates at the upper slope of the Mississippi Canyon are 15 to 20 m/k.y. because of sediment instabilities during the last 20 ka (Coleman and others, 1983). Because the carbonate concretions in the sediment cannot be older than the sediment deposits, the carbonates probably precipitated in recent times (less than 1,000 years ago).

In summary, all the authigenic carbonates collected during this cruise precipitated very recently—less than 5,500 years in the Tunica Mound and less than 1,000 years ago in the Mississippi Canyon region.

Oxygen Isotopic Variations of Carbonates and Gas Hydrate Dissociation

The oxygen isotopic composition of any particular sample of authigenic carbonate is controlled by a combination of factors, including (1) sample mineralogy and chemistry,

(2) temperature of carbonate precipitation, and (3) pore-fluid isotopic composition (Anderson and Arthur, 1983). To investigate if the analyzed $\delta^{18}O$ values of the carbonates are in equilibrium with ambient waters and to determine the factors that are critical to the $\delta^{18}O$ of the authigenic carbonates, the following oxygen isotope fraction equations were used:

Magnesium calcite: $1000\ln\alpha = 2.78 * (10^6/T^2) - 2.89 + 0.06 * \text{mol \% } MgCO_3$ (Friedman and O'Neil, 1977); and

Aragonite: $t = 19.9 - 4.34 * [\delta^{18}O_{arag\ (PDB)} - \delta^{18}O_{w\ (SMOW)}]$ (Hudson and Anderson 1989).
In these equations:

$$\alpha = \frac{1030.91 + 1.03091 * d^{18}O_{c(PDB)}}{1000 + d^{18}O_{w(SMOW)}}$$

representing the oxygen isotope fractionation between the carbonate and the water in which it precipitated;

T is the absolute temperature (K); and
t is the Celsius temperature (°C).

According to ^{14}C dating and sedimentation rates, authigenic carbonates collected during this cruise have precipitated within the last few thousand years; therefore, influence of the last glacial-interglacial cycles on bottom seawater temperatures and oxygen isotopes can be ignored. Thus, present in situ bottom-seawater temperatures are similar to those at which these authigenic carbonates were precipitated.

Because the authigenic carbonates were precipitated in non-eroded sediment, we estimated the temperature at which these carbonates were precipitated according to the heat-flow data measured by Labails and others (this volume, chapter 6). Using these temperatures, the $\delta^{18}O_w$ of the water in equilibrium with these carbonates was calculated.

Tunica Mound: Because bivalves live on the sea floor, we assumed that they formed at current bottom-water temperature. The $\delta^{18}O$ of water for the formation of shell material in core MD02-2543G was calculated to be +0.7‰, using a present bottom-seawater temperature of 7.1 ºC. This is in agreement with the measured regional $\delta^{18}O_{sw}$ (fig. 9).

Erosion is believed to have caused the carbonates in cores MD02-2543G and 2544G to be exposed at the sea floor. We assumed that the present bottom-water temperature of 7.1 ºC represents the temperature at which these carbonates were formed. The theoretical $\delta^{18}O_w$ values for these carbonates at the Tunica Mound were calculated from +0.9 to +1.1‰, close to the measured present regional $\delta^{18}O_{sw}$ (fig. 9). Therefore, it is reasonable to infer that these carbonates from Tunica Mound precipitated in or near isotopic equilibrium with present regional bottom water, and this also confirms that carbonates in cores MD02-2543G, 2544G, and 2545G have originally

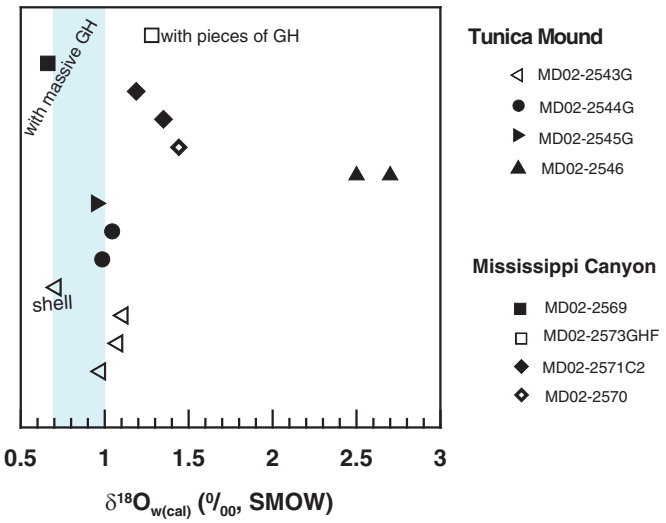

Figure 9. Calculated carbonate precipitated water oxygen isotopes. The blue shaded area represents present bottom-water oxygen isotopes (+0.7 to +1.0‰). There is no specific vertical scale.

precipitated in very recent times in the shallow subbottom sediment.

For the carbonate nodule in core MD02-2546, we assumed that the nodule was precipitated in the sediments not deeper than the present subbottom depth (~27 mbsf). Therefore, the nodule precipitated between the present bottom-seawater temperature of 7.1 ºC and a subsurface temperature of 7.9 ºC (which was estimated from heat-flow data). Then the calculated $\delta^{18}O_w$ values for carbonate in core MD02-2546 are from +2.7 to +2.5‰, which are much higher than those of the present observed pore water (+1.3‰) or the present bottom water (+ 0.7‰) (fig. 9).

Mississippi Canyon: Authigenic carbonates in core MD02-2569 present in shallow sea-floor sediment are underlain by two horizons of massive gas hydrate at 3 and 6 mbsf, respectively. The bottom-water temperature of 4.6 °C suggests carbonates precipitated from water with an oxygen isotope composition of +0.7‰, which is in agreement with present $\delta^{18}O_{sw}$ (fig. 9). Therefore, carbonate in core MD02-2569 precipitated in or near isotopic equilibrium with present regional bottom water.

The carbonates in core MD02-2573GHF coexisted with pieces of gas hydrate at 4.2 mbsf. Because a geothermal gradient was not determined at that site because of a bent core barrel, we assumed the nodule precipitated at a bottom-water temperature of 4.6 °C. The carbonates were calculated to have precipitated from water of much heavier oxygen isotope $\delta^{18}O_w$ = +1.3‰ (fig. 9; table 2); however, core MD02-2573 is only 30 m away from core MD02-2569.

Authigenic carbonates in cores MD02-2570 and MD02-2571C2 occurred at 2.95 and ~4.4 mbsf in the sediments, respectively, with a bottom-water temperature of 6.5 °C and

a geothermal gradient of 36 °C/km. The calculated in situ temperature of the carbonate-bearing sediments are all 6.6 °C. There is only a negligible 0.1 °C difference from present bottom-water temperature. Assuming a bottom-water temperature of 6.5 °C as the precipitation temperature of these carbonates, the calculated $\delta^{18}O_w$ for the precipitated carbonates are +1.3 and +1.4‰, respectively. These values are heavier than the present $\delta^{18}O_{sw}$ values (fig. 9).

In summary, the calculated $\delta^{18}O_w$ values for authigenic carbonates in cores MD02-2546, 2573GHF, 2570, and 2571C2 are from +1.3 to 2.7‰, which are +0.5 to +1.9‰ higher than present $\delta^{18}O$ values of in situ bottom water or pore water in the northern Gulf of Mexico. The possible sources for the ^{18}O-enriched water are (1) LGM (Last Glacial Maximum) northern Atlantic bottom seawater ($\delta^{18}O \sim +1.7$ to +1.8‰) (Schrag and others, 2002), (2) deep-seated fossil brines ($\delta^{18}O > +3.0$‰) (Gat, 1996), and (3) fluids from gas hydrates dissociation ($\delta^{18}O \sim +2.9$‰) (for example, Hesse and Harrison, 1981; Matsumoto, 1989).

The first option can be ruled out because the authigenic carbonates precipitated in very recent time —younger than 5,500 years ago. The bottom-seawater $\delta^{18}O_{sw}$ cannot be affected by the LGM bottom seawater oxygen isotope fractionation and should be the same as the present measured values (+0.7 to +1.0‰). As for the second possibility, some of the pore-water samples contained anomalously high Cl^- concentrations (1,000 millimoles (mM) to 2,161 mM) (Ussler and Paull, this volume, chapter 8). However, their $\delta^{18}O_{IW}$ values vary from –0.9 to +1.3‰, which indicates that high salinity pore waters do not carry water with an isotopic composition that is distinctive from seawater. These anomalously high pore-water salinities are not derived from deep-seated brines but are from the simple dissolution of salts. Therefore, deep-seated fossil brines with heavy $\delta^{18}O$ values can also be excluded as the source of the ^{18}O-enriched water.

^{18}O-enriched carbonates that may be related to gas hydrate dissociation have been reported for a number of cold seep environments worldwide (for example, Matsumoto, 1989; Aloisi and others, 2000; Naehr and others, 2000; Pierre and others, 2000; Greinert and others, 2001). During the formation of gas hydrates from interstitial water, the water containing heavier oxygen isotopes is preferentially incorporated into the gas hydrate structure (Davidson and others, 1983; Matsumoto, 2000). Therefore, gas hydrate decomposition liberates ^{18}O-enriched water molecules, which can contribute between 1 and 2.9‰ to the ^{18}O enrichment of the interstitial waters (Hesse and Harrison, 1981).

Formation and decomposition of gas hydrates are observed to be ongoing in the northern GOM (Milkov and Sassen, 2003). This evidence leads us to conclude that dissociation of pre-existing gas hydrate must have provided the ^{18}O-enriched water incorporated into the anomalously heavy ^{18}O in carbonates in core MD02-2546 at the Tunica Mound, in core MD02-2573GHF where carbonates coexisted with pieces of gas hydrates, and in cores MD02-2570 and 2571C2 at the Mississippi Canyon region. Group II carbonates in cores MD02-2546, 2570, and 2571C2 were derived from microbial methane. Thus, all these carbonates are related to the dissociation of gas hydrate.

During the last 5,500 years, it is not possible that bottom seawater temperature increased or the sea level dropped to trigger the dissociation of gas hydrates associated with cores MD02-2546, 2573GHF, 2570, and 2571C2. The northern Gulf of Mexico, however, is characterized by ongoing salt diapirism since the Cenozoic era. The salt movement has caused uplift of sediment layers and faulting and fracturing of sediments, which led to (1) a decrease in geo-pressures of the associated gas hydrate-hosting sediment horizons and (2) an increase in pore-water salinity of nearby gas hydrate-bearing sediments. As a consequence, decomposition of gas hydrates was triggered in the associated sediment horizons. The seismic profile across the Tunica Mound (fig. 2) clearly shows a large, shallow salt diapir existing near core MD02-2546. The Cl^- concentrations of core MD02-2569, which is just 30 m from core MD02-2573GHF, indicate that a salt diapir underlies this core also (Ussler and Paull, this volume, chapter 8). The seismic profile across core MD02-2570 and 2571C2 (fig. 4) shows gas chimneys in the sediment, which may also have been caused by the upward migration of underlying salt. Thus, we can conclude that nearby salt movement probably caused the dissociation of gas hydrate associated with these cores.

Summary and Conclusions

Carbonates sampled from various subbottom depths in sediments at the Tunica Mound and the Mississippi Canyon region in the northern Gulf of Mexico are dominated by authigenic, micritic high magnesium calcite. The $\delta^{13}C$ values of carbonates indicate that these authigenic carbonates precipitated from DIC produced by microbially mediated anaerobic oxidation of methane.

The $\delta^{18}O$ values indicate that some carbonates, including those from core MD02-2569 (with underlying massive gas hydrate), precipitated in or near equilibrium with present bottom-water temperature. Others, from core MD02-2573GHF (with underlying small pieces of gas hydrates) for example, precipitated from ^{18}O-enriched fluids caused by the decomposition of gas hydrates away from present bottom-water and pore-water equilibrium. That is, some authigenic carbonates at cold seeps in the northern Gulf of Mexico are derived from the dissociation of gas hydrates, but others are probably only associated with methane venting from deep hydrocarbon gases. The dissociation of gas hydrates in the northern Gulf of Mexico within the last 5,500 years probably was caused by salt migration.

Authigenic carbonates recorded the history of fluxes from gas hydrates in the Gulf of Mexico. Procedures used during this study on authigenic carbonates can also be used in other geologic settings, such as the Nankai Trough.

Acknowledgments

We appreciate the opportunity provided by the U.S. Geological Survey (USGS) to participate in the cruise of the RV *Marion Dufresne* during 2002. The authors thank Rendy Keaten and Patrick Mitts for their help with collecting samples. Financial support for this work was provided by the Grant-in-Aid from the Ministry of Education and Science and the Research Grant from JAPEX.

References

Aharon, P., Schwarcz, H.P., and Roberts, H.H., 1997, Radiometric dating of submarine hydrocarbon seeps in the Gulf of Mexico: GSA Bulletin, v. 109, no. 5, p. 568–579.

Aloisi, G., Pierrre, C.M., Rouchy, J., Foucher, J.P., Woodside, J., and the MEDINAUT Scientific Party, 2000, Methane-related authigenic carbonates of eastern Mediterranean Sea mud volcanoes and their possible relation to gas hydrate destabilization: Earth and Planetary Science Letters, v. 184, p. 321–338.

Anderson, T.F., and Arthur, M.A., 1983, Stable isotopes of oxygen and carbon and their application to sedimentologic and paleoenvironmental problems, *in* Arthur, M.A., Anderson, T.F., Kaplan, I.R. and Veizer, J., eds., Stable isotopes in sedimentary geology, SEPM Short Course No. 10, 1–1—1–151.

Bernard, B.B., Brooks, J.M., and Sackett, W.M., 1978, Light hydrocarbons in recent Texas continental shelf and slope sediments: J. Geophys. Res., v. 83, p. 4053–4061.

Bohrmann, G., Greinert, J., Suess, E., and Torres, M., 1998, Authigenic carbonates from the Cascadia subduction zone and their relation to gas hydrate stability: Geology, v. 26, no. 7, p. 647–650.

Brooks, J.M., Kennicutt, M.C., II, Fay, R.T., McDonald, T.J., and Sassen, R., 1984, Thermogenic gas hydrates in the Gulf of Mexico: Science, v. 225, p. 409–411.

Coleman, J.M., Prior, D.B., and Lindsay, J.F., 1983, Deltaic influences on shelf edge instability processes: SEPM Special Publication 33, p. 121–137.

Cooper, A.K., and Hart, P.E., 2003, High-resolution seismic-reflection investigation of the northern Gulf of Mexico gas-hydrate-stability zone: Marine and Petroleum Geology, v. 19, p. 1275–1293.

Davidson, D.W., Leaist, D.G., and Hesse, R., 1983, Oxygen-18 enrichment in the water of a clathrate hydrate: Geochim. Cosmochim. Acta, v. 47, p. 2293–2295.

Epstein, S., and Mayeda, T., 1953, Variation of O^{18} content of waters from natural sources: Geochimica et Cosmochimica Acta, v. 4, p. 213–224.

Friedman, I., and O'Neil, J.R., 1977, Compilation of stable isotope fractionation factors of geochemical interest, *in* Fleishcher, M., eds., Data of geochemistry, 6th ed., U.S. Geological Survey Professional Paper 440–KK, 11 p.

Gat, J.R., 1996, Oxygen and hydrogen isotopes in the hydrologic cycle: Annual Review of Earth and Planetary Sciences, v. 24, p. 225–262.

Greinert, J., Bohrmann, G., and Suess, E., 2001, Gas hydrate-associated carbonates and methane-venting at Hydrate Ridge—Classification distribution and origin of authigenic lithologies, *in* Paull, C.K., and Dillon, P.W., eds., Natural gas hydrates—occurrence, distribution, and dynamics: Geophys. Monogr., v. 124, p. 99–113.

Hesse, R., and Harrison, W.E., 1981, Gas hydrates (clathrates) causing pore-water freshening and oxygen isotope fractionation in deep-water sedimentary sections of terrigenous continental margins: Earth and Planetary Science Letters, v. 55, p. 453–462.

Hudson, J.C., and Anderson, T.F., 1989, Ocean temperatures and isotopic compositions through time, *in* Clarkson, E.N.K., Curry, G.B., and Rolfe, W.D.I., eds., Environments and physiology of fossil organisms: Trans. R. Soc. Edinb. v. 80, p. 183–192.

Labails, Cinthia, Géli, Louis, Sultan, Nabil, Novosel, Ivana, and Winters, W.J., 2007, Thermal measurements from the Gulf of Mexico Continental Slope—Results from the PAGE cruise, Chapter 6, *in* Winters, W.J., Lorenson, T.D., and Paull, C.K., eds., Initial report of the IMAGES VIII/PAGE 127 gas hydrate and paleoclimate cruise on the RV *Marion Dufresne* in the Gulf of Mexico, 2–18 July 2002: U.S. Geological Survey Open-File Report 2004–1358, 9 p.

Matsumoto, R., 1989, Isotopically heavy oxygen-containing siderite derived from the decomposition of methane hydrate: Geology, v. 17, no. 8, p. 707–710.

Matsumoto, R., 2000, Methane hydrate estimates from the chloride and oxygen isotopic anomalies—Examples from the Blake Ridge and Nankai Trough sediments: Annals of the New York Academy of Sciences, v. 912, p. 39–50.

Milkov, A.V., and Sassen, R., 2003, Two-dimensional modeling of gas hydrate decomposition in the northwestern Gulf of Mexico—Significance to global change assessment: Global and Planetary Change, v. 36, p. 31–46.

Miyairi, Y., Yoshida, K., Miyazaki, Y., Matsuzaki, H., and Kaneoka, I., 2004, Improved ^{14}C dating of a tephra layer (AT tephra, Japan) using AMS on selected organic fractions: Nuclear Instruments and Methods in Physics Research B, v. 223–224, p. 555–559.

Müller, G., 1967, Methods in sedimentary petrology, *in* Engelhardt, W.V., Füchtbauer, H., and Müller, G., eds., translated by Schmincke Hans-Ulrich, Sedimentary petrology Part 1: New York/London, Stuttgart Hafner Publishing Co., p. 179–213.

Naehr, T.H., Rodriguez, N.M., Bohrmann, G., Paull, C.K., and Botz, R., 2000, Methane-derived authigenic carbonates associated with gas hydrate decomposition and fluid venting above the Blake Ridge diapir, *in* Paull, C.K., Matsumoto, R., Wallace, P.J., and Dillon, W.P., eds., Proc. ODP Sci. Res., v. 164, p. 285–300.

Neurauter, T.W., and Roberts, H.H., 1992, Seismic and visual observation of seepage related structure on the continental slope, northern Gulf of Mexico: 24th Annual Offshore Technology Conference, Paper OTC 6850, May 4–7, 1992, Houston, Texas, p. 355–362.

Paull, C.K., Chanton, J.P., Neumann, A.C., Coston, J.A., and Martens, C.S., 1992, Indicators of methane-derived carbonates and chemosynthetic organic carbon deposits—Examples from the Florida Escarpment: J. Soc. Sediment Geol. Palaios, v. 7, p. 361–375.

Paull, C.K., Ussler, W., III, Lorenson, T., Winters, W., and Dougherty, J., 2005, Geochemical constraints on the distribution of gas hydrates in the Gulf of Mexico: Geology, DOI 10.1007/s00367-005-0001-3, 8 p.

Pierre, C., Rouchy, J.M., and Gaudichet, A., 2000, Diagenesis in the gas hydrates sediments of the Blake Ridge, Mineralogy and stable isotope compositions of the carbonate and sulphide minerals, *in* Paull, C.K., Matsumoto, R., Wallace, P.J., and Dillon, W.P., eds., Proc. ODP Sci. Res., v. 164, p. 139–146.

Roberts, H.H., and Aharon, P., 1994, Hydrocarbon-derived buildups of the northern Gulf of Mexico—A review of submersible investigations: Geo-Mar. Lett., v. 14, p. 135–148.

Rowan, M.G., and Weimer, P., 1998, Salt-sediment interaction, northern Green Canyon and Ewing Bank (offshore Louisiana), northern Gulf of Mexico: AAPG Bulletin, v. 82 no. 5B, p. 1055–1082.

Salvador, A., 1987, Late Triassic-Jurassic paleogeography and origin of Gulf of Mexico basin: AAPG Bull., v. 71, p. 419–451.

Sassen, R., MacDonald, I.R., Requejo, A.G., Guinasso, N.L., Kennicutt, M.C., II, Sweet, S.T., and Brooks, J.M., 1994, Organic geochemistry of sediments from chemosynthetic communities, Gulf of Mexico slope: Geo-Marine Letters, v. 14, p. 110–119.

Sassen, R., Roberts, H.H., Carney, R., Milkov, A.V., DeFreitas, D., Lanoil, B., and Zhang, C.L., 2004, Free hydrocarbon gas, gas hydrate, and authigenic minerals in chemosynthetic communities of the northern Gulf of Mexico continental slope—Relation to microbial processes: Chemical Geology, v. 205, p. 195–217.

Schrag, D.P., Adkins, J.F., McIntyre, K., Alexander, J.L., Hodell D.A., Charles, C.D., and McManus, J.F., 2002, The oxygen isotopic composition of seawater during the last glacial maximum: Quaternary Science Reviews, v. 21, p. 331–342.

Stuiver, M., and Polach, H.A., 1977, Discussion—Reporting of ^{14}C data: Radiocarbon, v. 19, no. 3, p. 355–363; accessed October 10, 2006, at *http://www.radiocarbon.org/Pubs/Stuiver/index.html*

Whiticar, M.J., 1999, Carbon and hydrogen isotope systematics of bacterial formation and oxidation of methane: Chemical Geology, v. 161, p. 291–314.

Back: Samples of gas hydrate recovered from Calypso giant piston core MD02–2569.